



Advanced Concept Studies for Supersonic Commercial Transports Entering Service in the 2018-2020 Period Phase 2

John Morgenstern and Michael Buonanno
Lockheed Martin, Palmdale, California

Jixian Yao, Mugam Murugappan, Umesh Paliath, Lawrence Cheung, Ivan Malcevic, Kishore Ramakrishnan, Nikolai Pastouchenko and Trevor Wood
GE Global Research, Niskayuna, New York

Steve Martens, Phil Viars, Trevor Tersmette, Jason Lee, Ron Simmons, and David Plybon
GE Aviation, Cincinnati, Ohio

Juan Alonso, Francisco Palacios, Trent Lukaczyk, and Gerald Carrier
Stanford University, Stanford, California

NASA STI Program . . . in Profile

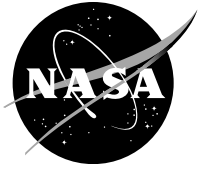
Since its founding, NASA has been dedicated to the advancement of aeronautics and space science. The NASA Scientific and Technical Information (STI) Program plays a key part in helping NASA maintain this important role.

The NASA STI Program operates under the auspices of the Agency Chief Information Officer. It collects, organizes, provides for archiving, and disseminates NASA's STI. The NASA STI Program provides access to the NASA Technical Report Server—Registered (NTRS Reg) and NASA Technical Report Server—Public (NTRS) thus providing one of the largest collections of aeronautical and space science STI in the world. Results are published in both non-NASA channels and by NASA in the NASA STI Report Series, which includes the following report types:

- **TECHNICAL PUBLICATION.** Reports of completed research or a major significant phase of research that present the results of NASA programs and include extensive data or theoretical analysis. Includes compilations of significant scientific and technical data and information deemed to be of continuing reference value. NASA counter-part of peer-reviewed formal professional papers, but has less stringent limitations on manuscript length and extent of graphic presentations.
- **TECHNICAL MEMORANDUM.** Scientific and technical findings that are preliminary or of specialized interest, e.g., "quick-release" reports, working papers, and bibliographies that contain minimal annotation. Does not contain extensive analysis.
- **CONTRACTOR REPORT.** Scientific and technical findings by NASA-sponsored contractors and grantees.
- **CONFERENCE PUBLICATION.** Collected papers from scientific and technical conferences, symposia, seminars, or other meetings sponsored or co-sponsored by NASA.
- **SPECIAL PUBLICATION.** Scientific, technical, or historical information from NASA programs, projects, and missions, often concerned with subjects having substantial public interest.
- **TECHNICAL TRANSLATION.** English-language translations of foreign scientific and technical material pertinent to NASA's mission.

For more information about the NASA STI program, see the following:

- Access the NASA STI program home page at <http://www.sti.nasa.gov>
- E-mail your question to help@sti.nasa.gov
- Fax your question to the NASA STI Information Desk at 757-864-6500
- Telephone the NASA STI Information Desk at 757-864-9658
- Write to:
NASA STI Program
Mail Stop 148
NASA Langley Research Center
Hampton, VA 23681-2199



Advanced Concept Studies for Supersonic Commercial Transports Entering Service in the 2018-2020 Period Phase 2

John Morgenstern and Michael Buonanno
Lockheed Martin, Palmdale, California

Jixian Yao, Mugam Murugappan, Umesh Paliath, Lawrence Cheung, Ivan Malcevic, Kishore Ramakrishnan, Nikolai Pastouchenko and Trevor Wood
GE Global Research, Niskayuna, New York

Steve Martens, Phil Viars, Trevor Tersmette, Jason Lee, Ron Simmons, and David Plybon
GE Aviation, Cincinnati, Ohio

Juan Alonso, Francisco Palacios, Trent Lukaczyk, and Gerald Carrier
Stanford University, Stanford, California

Prepared under Contract NNC10CA02C

National Aeronautics and
Space Administration

Glenn Research Center
Cleveland, Ohio 44135

Acknowledgments

This work was funded by the NASA N+2 Supersonic program administered by Peter Coen at the NASA Langley Research Center and Clayton Meyers at the NASA Glenn Research Center under prime contract (Lockheed Martin (LM)) NNC10CA02C. LM would like to thank them and many others at NASA including Susan Cliff, Don Durston, Bruce Storms, Maureen Delgado, Jonathan Seidel, Teresa Monaco, Lori Ozoroski, Richard Campbell, Eric Walker, Floyd Wilcox and Linda Bangert for their helpful contributions, editorial support and encouragement on this program. LM would also like to acknowledge GE Global Research Center including specifically Steve Martins, Jixian Yao, and Phil Viars; and Stanford University including Juan Alonso and his team, for contributing written material, data, and ideas for this N+2 Phase 2 final report.

Trade names and trademarks are used in this report for identification only. Their usage does not constitute an official endorsement, either expressed or implied, by the National Aeronautics and Space Administration.

Level of Review: This material has been technically reviewed by NASA technical management OR expert reviewer(s).

Available from

NASA STI Program
Mail Stop 148
NASA Langley Research Center
Hampton, VA 23681-2199

National Technical Information Service
5285 Port Royal Road
Springfield, VA 22161
703-605-6000

This report is available in electronic form at <http://www.sti.nasa.gov/> and <http://ntrs.nasa.gov/>

Executive Summary

Lockheed Martin Aeronautics Company (LM), working in conjunction with General Electric Global Research (GE GR) and Stanford University, executed a 19 month program responsive to the NASA sponsored “N+2 Supersonic Validation: Advanced Concept Studies for Supersonic Commercial Transports Entering Service in the 2018-2020 Period” contract. The key technical objective of this effort was to validate integrated airframe and propulsion technologies and design methodologies necessary to realize a supersonic vehicle capable of meeting the N+2 environmental and performance goals.

The N+2 program is aligned with NASA’s Supersonic Project and is focused on providing system-level solutions capable of overcoming the efficiency, environmental, and performance barriers to practical supersonic flight. The N+2 environmental and performance goals are outlined in the technical paper, AIAA-2014-2138 (Ref. 1) along with the validated N+2 Phase 2 results. Our Phase 2 efforts built upon our Phase 1 studies (Ref. 2) and successfully demonstrated the ability to design and test realistic configurations capable of shaped sonic booms over the width of the sonic boom carpet.

Developing a shaped boom configuration capable of meeting the N+2 shaped boom targets is a key goal for the N+2 program. During the LM Phase 1 effort, LM successfully designed and tested a shaped boom trijet configuration (1021) capable of achieving 85 PLdB under track (forward and aft shock) and up to 28° off-track at Mach 1.6. In Phase 2 we developed a refined configuration (1044-2) that extended the under 85 PLdB sonic boom level over the entire carpet of 52° off-track at a cruise Mach number of 1.7. Further, the loudness level of the configuration throughout operational conditions calculates to an average of 79 PLdB. These calculations rely on propagation employing Burger’s (sBOOM) rounding methodology, and there are indications that the configuration average loudness would actually be 75 PLdB. We also added significant fidelity to the design of the configuration in this phase by performing a low speed wind tunnel test at our LTWT facility in Palmdale, by more complete modelling of propulsion effects in our sonic boom analysis, and by refining our configuration packaging and performance assessments.

Working with General Electric, LM performed an assessment of the impact of inlet and nozzle effects on the sonic boom signature of the LM N+2 configurations. Our results indicate that inlet/exhaust stream-tube boundary conditions are adequate for conceptual design studies, but realistic propulsion modeling at similar stream-tube conditions does have a small but measurable impact on the sonic boom signature.

Previous supersonic transport studies have identified aeroelastic effects as one of the major challenges associated with the long, slender vehicles particularly common with shaped boom aircraft (Ref. 3). Under the Phase 2 effort, we have developed a detailed structural analysis model to evaluate the impact of flexibility and structural considerations on the feasibility of future quiet supersonic transports. We looked in particular at dynamic structural modes and flutter as a failure that must be avoided. We found that for our N+2 design in particular, adequate flutter margin existed. Our flutter margin is large enough to cover uncertainties like large increases in engine weight and the margin is relatively easy to increase with additional stiffening mass. The lack of major aeroelastic problems probably derives somewhat from an early design bias. While shaped boom aircraft require long length, they are not required to be thin. We intentionally developed our structural depths to avoid major flexibility problems. So at the end of Phase 2, we have validated that aeroelastic problems are not necessarily endemic to shaped boom designs.

Experimental validation of sonic boom design and analysis techniques was the primary objective of the N+2 Supersonic Validations contract; and in this Phase, LM participated in four high speed wind tunnel tests. The first so-called Parametric Test in the Ames 9x7 tunnel did an exhaustive look at variation effects of the parameters: humidity, total pressure, sample time, spatial averaging distance and number of measurement locations, and more. From the results we learned to obtain data faster and more accurately, and made test condition tolerances easy to meet (eliminating earlier 60 percent wasted time when

TABLE 1.—N+2 ENVIRONMENTAL AND PERFORMANCE GOALS, AND VALIDATED PHASE 2 RESULT
[*Measurements of low N-wave dive booms suggest that Burger's alone may result in loudness as much as 5 PLdB too high.]

	NASA N+2 Supersonic Transport (2018-2020) Goals	LM N+2 Phase 2 Predicted and Validated Status
Environmental Goals		
Sonic Boom	85 PLdB up to 20° off-track (NASA specified goal)	<85 PLdB over full carpet 79* PLdB average (sBOOM)
Airport Noise (cumulative below stage 3)	10 to 20 EPNdB	21.55 (GE - predicted)
Cruise Emissions	<10 EINOx	5 EINOx
Performance Goals		
Cruise Speed	Mach 1.6 to 1.8 shaped boom flight	Mach 1.7 (1.8 over water)
Range	4,000 nmi	5,500 nmi
Payload (passengers)	35 to 70 passengers	82 pax
Fuel Efficiency (passenger-nmi per lb of fuel)	3.0	3.13 (using GE engines)

condition tolerances could not be held). The next two tests used different tunnels. The Ames 11 ft tunnel was used to test lower Mach numbers of 1.2 and 1.4. There were several difficulties using this tunnel for the first time for sonic boom including having to shift the measurement Mach numbers to 1.15 and 1.3 to avoid flow problems. It is believed that the 11 ft could be used successfully to measure sonic boom but there are likely to be a number of test condition restrictions. The Glenn 8x6 ft tunnel was used next and the tunnel has a number of desirable features for sonic boom measurement. While the Ames 9x7 can only test Mach 1.55 to 2.55 and the 11 ft can only test Mach 1.3 and lower, the Glenn 8x6 can test continuously from Mach 0.3 to 2.0. Unfortunately test measurement accuracy was compromised by a reference pressure drift. Post-test analysis revealed that the drift occurred when Mach number drifted slightly. Test measurements indicated that if Mach number drift is eliminated, results from the 8x6 would be more accurate, especially at longer distances, than results from the 9x7. The fourth test in the 9x7, called LM4, used everything we learned to comprehensively and accurately measure our new 1044-02 configuration with a full-carpet shaped signature design. Productivity was 8 times greater than our Phase 1 LM3 test. Measurement accuracy and repeatability was excellent out to 42 in. However, measurements at greater distances require the rail in the aft position and become substantially less accurate. Further signature processing or measurement improvements are needed for beyond near-field signature validation.

Stanford University

Stanford University, in collaboration with LM and NASA, developed an adjoint-based capability for the inverse shape design of supersonic configurations to match a target equivalent area distribution. Stanford derived, implemented, and tested a preliminary version of an adjoint solver that is able to produce sensitivities (gradients) of cost functions derived from the aircraft's equivalent area distribution with respect to arbitrary numbers of design variables that affect the shape of the aircraft. Using CAPRI, a CAD-neutral software interface, Stanford successfully applied the adjoint-based techniques to the N+2 trijet configuration. The Stanford Final Report is attached in Appendix B.

General Electric

GE Global Research and Aviation supported Lockheed Martin in this Phase 2 NASA sponsored 'N+2 NRA—System Level Experimental Validations for Supersonic Transport Aircraft' program. Based on Lockheed Martin provided updated requirements and targets, GE modified an adaptive cycle engine with FLADE tip propulsion system expected to meet or exceed the environmental goals set by NASA, from

the recent Phase 1 program. This propulsion system takes advantage of cooled cooling air to extend the overall pressure ratio of the engine and increase thermal efficiency. A low noise, high performance exhaust system takes advantage of the innovative adaptive feature, the FLADE tip on the second fan stage, to provide a third air stream to feed the inverted velocity profile and fluid shield on the exhaust for lower noise capability. A trapped vortex pilot Mini-Burner is also incorporated in the exhaust to provide augmented transonic thrust and potential take-off noise abatement.

A limited trade study was performed for three fan pressure ratios, 2.45, 2.55 and 2.65. The highest fan pressure ratio propulsion system has the best performance and weight impact but based on the jet noise assessment a fan pressure ratio of 2.55 is retained as the target.

The flowpath of the IVP/Shield nozzles tested in Phase 1 was updated to mitigate the overexpansion at low power conditions that led to unsteady flow separation. A new exhaust nozzle configuration was required to fully mitigate this issue. The new exhaust configuration allows the primary exhaust to operate in a purely convergent mode as well as a convergent-divergent mode. This change resulted in higher internal nozzle performance across a wider range of the operational map. Large eddy simulations of the Phase 1 cutback configuration show very good comparisons to measured acoustic data and Phase 2 results show a much improved flow field.

Analysis was performed of the Lockheed Martin supersonic inlet coupled with a two-stage counter-rotating FLADED fan configuration that was designed and tested under the VAATE program. Lockheed Martin supplied an inlet/boundary condition with inlet auxiliary doors open, downstream of the inlet centerbody and struts. The acoustic analysis again shows the dominant tonal energy is related to the wakes from the inlet struts. The GE GR final report is attached in Appendix C.

Contents

Executive Summary	iii
Stanford University	iv
General Electric	iv
1.0 Introduction	1
1.1 Subject/Relevancy	1
2.0 N+2 Configuration Refinement	3
2.1 Cruise Mach Trade	4
2.2 Sonic Boom Signature Improvement	4
2.3 Configuration Maturation	9
2.3.1 OML Refinement	9
2.3.2 Landing Gear Integration	13
2.3.3 Vehicle Packaging	14
2.3.4 Cabin Layout	15
2.3.5 Mass Properties	16
2.3.6 Aerodynamics	19
2.4 Vehicle Sizing and Mission Performance	20
2.4.1 Vehicle Airport Operations and Configuration	22
2.5 Propulsion Integration and Sensitivity Analysis	24
2.5.1 Inlet Design	24
2.5.2 Auxiliary Inlet Design	26
2.5.3 Propulsion System Sensitivity Analyses	26
2.6 LTWT Test	30
2.6.1 Model Design	31
2.6.2 Test Planning	34
2.6.3 Test Analysis and Results	37
3.0 N+2 Structural and Aeroelastic Analysis	52
3.1 Introduction	52
3.1.1 Purpose	52
3.1.2 Objectives	53
3.1.3 Scope/Tasks	53
3.2 Configuration and Structural Arrangement	54
3.2.1 Configuration and Systems Layout	54
3.2.2 Control Surface Sizing and Definition	57
3.2.3 PreCEPT	57
3.3 Structural Design Criteria and Design Loads	57
3.3.1 Structural Design Criteria and Design Load Cases	57
3.3.2 Linear Aerodynamic Maneuver Loads	64
3.3.3 CFD-Loads Model and Trim Scheme	68
3.3.4 Loads Summary	71
3.4 Finite Element Modeling	75
3.4.1 Geometry Processing for FEM Development	75
3.4.2 Meshing 2D Shells on the Surface Geometry	77
3.4.3 Meshing 1D Bars and Rod Elements	80
3.4.4 Additional FEM Details	81
3.4.5 FEM Element and Node Numbering	86
3.4.6 FEM Include File Structure	89
3.4.7 Material Property Definition	91
3.4.8 Nonstructural Mass—0D Elements	93
3.4.9 FEM Morphing to Increase Aft-Deck and Tail Stiffness	96

3.5	Structural Sizing.....	99
3.5.1	Approach.....	99
3.5.2	Design Criteria.....	100
3.5.3	Design Variables and Zones	104
3.5.4	Core and Stiffener Trade Studies.....	114
3.5.5	Final Sizing Results	115
3.5.6	Stress, Strain, and Deflection Plots.....	120
3.5.7	Mode Shapes and Frequencies (With Focus on Final Design).....	134
3.6	Aeroelastic Analysis.....	138
3.6.1	Aeroelastic Model.....	138
3.6.2	Comparison of MSC.NASTRAN With FAMAS Results.....	139
3.6.3	Flutter Results.....	141
3.6.4	Aft Deck Stiffening Alternative.....	150
3.7	Structural Deformation Effects on Sonic Boom.....	151
3.8	Conclusions and Recommendations in Sections 5.0 and 6.0	156
4.0	N+2 Sonic Boom Testing and Analyses.....	156
4.1	Ames 9x7-0250 Parametric Test	156
4.2	Ames 11-0249 Boeing Test.....	158
4.2.1	Background and Overview	158
4.2.2	Test Description.....	159
4.2.3	Test Conduct.....	162
4.2.4	Test Observations and Issues	166
4.2.5	Test Conclusion and Recommendations.....	171
4.3	Glenn 8x6-12-002 Boeing Test	173
4.4	Ames 9x7-0254 LM4 Test	177
4.5	Test Planning (Productivity Tolerances, Test Models, Processing).....	179
4.6	Model Design	183
4.7	Test Description	188
4.8	Oil and Stereo-RBOS Flow Visualization.....	189
4.9	Test Analysis and Results	201
5.0	Summary and Conclusions	211
5.1	N+2 Configuration Refinement.....	211
5.1.1	Quiet Shaped Boom	211
5.1.2	Quiet, Clean, Efficient Propulsion	212
5.1.3	Efficient, High Performance Vehicle.....	212
5.2	N+2 Structural and Aeroelastic Analysis	213
5.3	N+2 Shaped Sonic Boom Testing and Analysis	213
6.0	Recommendations	214
6.1	N+2 Configuration Refinement.....	214
6.2	N+2 Structural and Aeroelastic Analysis	215
6.3	N+2 Shaped Sonic Boom Testing and Analysis	215
Appendix A	—Acronym List.....	217
Appendix B	—N+2 NRA—System Level Experimental Validations for Supersonic Transport Aircraft	219
Appendix C	—Development of Design Capabilities Within the NASA/LMCO N+2 Supersonics Effort	325
References	375

List of Figures

Figure 1.—LM N+2 Organization	2
Figure 2.—N+2 Phase 2 Configuration Evolution (left to right): 1021, 1040, 1043, 1044	3
Figure 3.—N+2 Phase 2 Baseline Vehicle 3-View	3
Figure 4.—Mach Effect on Ground Signatures	5
Figure 5.—Configuration 1021 Full-Carpet Loudness	6
Figure 6.—Configuration 1021 Signature, 5.6 R/(b/2), SOC 4,000 nmi Mission	6
Figure 7.—DOE Design Variable Sweep	7
Figure 8.—Phi = 40° Pressure Gradients, Configuration 1040 (top) and 1043 (bottom)	7
Figure 9.—SOC Full-Carpet Loudness Comparison, 4,000 nmi Mission	8
Figure 10.—CFD Result of Representative Inlet and C-D Nozzle	8
Figure 11.—Propulsion Effects on Signature, 5.6 R/(b/2)	8
Figure 12.—Configuration 1044-2 Full-Carpet Loudness	9
Figure 13.—Configuration 1021 Issues To-Fix	10
Figure 14.—Configuration 1021 Versus 1040	10
Figure 15.—Configuration 1040 Versus 1043	10
Figure 16.—Configuration 1044 High-Alpha Pitch-Up Due to Wing Apex Vortex Formation	11
Figure 17.—Configuration 1043 Versus 1044	12
Figure 18.—Configuration 1044 Versus 1044-2	12
Figure 19.—Configuration 1044 Versus 1044-3b	13
Figure 20.—Main Landing Gear Retraction Concept	13
Figure 21.—Engine FOD Considerations: Inlet Suction (top) and NLG Water Spray	14
Figure 22.—Configuration 1044 Ground Operation Clearance	14
Figure 23.—Configuration 1044 Inboards	15
Figure 24.—Two-Class, 80 Passenger Cabin Layout	16
Figure 25.—Nominal Passenger Cabin Cross-Section	16
Figure 26.—Empty Weight (left) and Empty Weight Fraction (right) Comparison	18
Figure 27.—Configuration 1044 In-Flight CG Envelope	18
Figure 28.—Configuration 1044 Drag Polars	19
Figure 29.—Configuration 1044 L/D Versus CL	19
Figure 30.—L/D _Max Versus Mach Comparison	20
Figure 31.—Sizing Mission Profile	21
Figure 32.—N+2 Phase 2 Design Space	21
Figure 33.—Mission Performance Comparison: Flight Profile (top) and L/D (bottom)	22
Figure 34.—Global Shaped Boom Supersonic Service Network	24
Figure 35.—N+2 Phase 2 Mach 1.7 Inlet	25
Figure 36.—Mach 1.7 Inlet Recovery Caine Curve	25
Figure 37.—Inlet Peak Recovery Versus Free-Stream Mach	25
Figure 38.—Streamline (left), Mach (center) and Pressure Recovery (right) Maps	27
Figure 39.—Configuration 1044-3b scaled M1.7 Inlet and Non-Proprietary Plug Nozzle	27
Figure 40.—Plume effects on Equivalent Area (top), 5.6 R/(b/2) Signature (middle) and Ground Signature (bottom): Configuration 1044-3b, SOC 4,000 nmi Mission	28
Figure 41.—Configuration 1044 Centerline Nacelle Un-Adapted (top) Versus Adapted Grid (bottom) CFD Solutions	29
Figure 42.—Grid Adaption Effects on Configuration 1044-2 5.6 R/(b/2) Signature (top) and Ground Signature (bottom), SOC 4,000 nmi Mission	29
Figure 43.—LTWT Wind Tunnel Circuit	30
Figure 44.—LTWT Test and Model Support Capability	30
Figure 45.—Model Changeable Part Options	31
Figure 46.—V-Tail Dihedral, Incidence and Rudder Variations	32

Figure 47.—Options for Canard, Extended Gear, Nacelle Removal and Centerline Vertical Tail	33
Figure 48.—Leading Edge Plain and Krueger Flaps with 2 Deflections Each.....	33
Figure 49.—Trailing Edge Deflection Parts	34
Figure 50.—1044-2 Model in Test Section at High Alpha.....	35
Figure 51.—Naming Notation for Flap Deflections	37
Figure 52.—Measurement Extremes, Balance Limits and Reference Quantities.....	37
Figure 53.—LTWT332 Output Files of Test Measurements and Photography.....	38
Figure 54.—ColSelect ASCII Data Contains these 118 Key Variables	39
Figure 55.—Weight Tares Taken (28) for Any Significant Configuration Change	41
Figure 56.—Run Schedule (Illegible but) Included Here for Identification	42
Figure 57.—Pitch Stability Assessment.....	43
Figure 58.—Smoke Showing Wing Vortex Impingement on V-Tail	44
Figure 59.—Roll Stability Assessment.....	44
Figure 60.—Yaw Stability Assessment	45
Figure 61.—Pitch-Up Control Concepts Exploration.....	46
Figure 62.—Configuration 1044-2 Pitch Break Surface Oil-Flow Visualization.....	47
Figure 63.—Aft Deck Flap Control Power Assessment	48
Figure 64.—Ruddervator Control Power Assessment	49
Figure 65.—Ruddervator Size Variation Comparison, Open (baseline) and Closed (50-percent oversize)	50
Figure 66.—Alternate Planform Study	51
Figure 67.—Low-boom supersonic flight requirements raise natural aeroelasticity concerns	52
Figure 68.—N+2 Structural Analysis Tasks and Schedule.....	53
Figure 69.—Cabin Layout for the 1044-2 Configuration	54
Figure 70.—Layout of Major Subsystems	55
Figure 71.—Concepts for Major Load Paths Developed to Accommodate Cabin and Subsystems Layout (Early Concept)	55
Figure 72.—Concept for the Shear Ties Attaching the Forward Wing to the Fuselage	56
Figure 73.—Final Structural Layout for the 1044-3 Configuration.....	56
Figure 74.—N+2 Mach, Altitude Flight Envelope	59
Figure 75.—Sample V-n Diagram	59
Figure 76.—A uniform pressure is applied to the cabin (left figure) and cargo bay (right figure).....	61
Figure 77.—Application of Landing and Ground Handling Loads to FEM	64
Figure 78.—Linear Aerodynamic Model for Loads and Flutter Analysis	65
Figure 79.—Spline Verification—Wing Up-Bending	65
Figure 80.—Spline Verification—Fuselage Down-Bending.....	66
Figure 81.—Spline Verification—Wing Down-Bending	66
Figure 82.—Support Point Definition.....	67
Figure 83.—Comparison of Linear Aero Model to LTWT Test Data (Mach 0.14)	67
Figure 84.—Comparison of Linear Aero Lift Coefficient with Test (Mach 1.7)	68
Figure 85.—Wedge Shaped Gaps Needed to Enable 30° of Trailing Edge Flap Actuation	69
Figure 86.—N+2 Configuration 1044-3 Surface Mesh used by Splitflow for CFD-Based Aeroelastic Analysis.....	69
Figure 87.—MDICE uses an Application Programming Interface to Transfer Forces and Deflections Between Aerodynamic and Structural Analyses.....	69
Figure 88.—Surface Patch Definitions for Fluid-Structure Interfaces	70
Figure 89.—Force Coefficient Convergence History of Trim Procedure Used to Enhance Grid Adaption about the Equilibrium Trim State	71
Figure 90.—CFD-based Cp Distribution for Load Case 600, illustrating Vortex Dominated Effects on the Upper Surface.....	73

Figure 91.—Isosurfaces of Vortex Magnitude colored with Helicity to Illustrate the Vortex Structure at $M=1.41$, $Nz=2.5$ (Load Case 600)	74
Figure 92.—Vector Plot of Applied Loads Colored by Z-Component of Force for Load Case 600 Illustrates Nonlinear Vortex Effects Captured by CFD-based Trim Process	74
Figure 93.—N+2 Raw Geometry Import into Hypermesh	75
Figure 94.—N+2 Analysis Geometry after PreCEPT Automated Organization and Cleanup	75
Figure 95.—N+2 fully trimmed surface geometry set prior to meshing.....	76
Figure 96.—N+2 Subassembly Map Exploded View.....	76
Figure 97.—N+2 Model Browser Showing High Level Assembly Structure	77
Figure 98.—N+2 Control Surface Hinge Definition in Offset State	77
Figure 99.—N+2 Element Density on Outer Wing Box.....	78
Figure 100.—N+2 Element Density on Inner Wing and Tail.....	78
Figure 101.—N+2 Element Density Fuselage	78
Figure 102.—N+2 OML Material Direction Definition	79
Figure 103.—N+2 Substructure Material Direction Definition.....	80
Figure 104.—N+2 Bar and Rod Element Mesh Definition	80
Figure 105.—N+2 Landing Gear Models	82
Figure 106.—N+2 Landing Gear Include File Hierarchy	82
Figure 107.—N+2 Main Landing Gear Attachment.....	83
Figure 108.—N+2 Landing Gear Doors in Closed Position.....	83
Figure 109.—N+2 Main Landing Gear Doors Offset to show CBUSH Connections to Vehicle.....	83
Figure 110.—N+2 Typical Control Surface Hinge Structure (Bow-tie).....	84
Figure 111.—N+2 Control Surface Modeling Details on Trailing Edge Structures.....	84
Figure 112.—N+2 Control Surface Loads used for Free-body Hinge Moment Checks.....	84
Figure 113.—N+2 Propulsion System Suspension Interface Model	85
Figure 114.—N+2 Propulsion System Suspension Properties.....	85
Figure 115.—N+2 Discrete Spring Attachment of Forward Wing to Fuselage.....	85
Figure 116.—Property Set Maturation.....	92
Figure 117.—N+2 Metallic Usage and Overall Composition	93
Figure 118.—N+2 Property Type Counts.....	93
Figure 119.—N+2 Distributed Masses	94
Figure 120.—N+2 Element Sets for Weight Statement Breakdown	94
Figure 121.—N+2 Smeared Make-up Mass for FEM REV70	95
Figure 122.—N+2 Fuel Tanks and Fuel System Distributed Masses	95
Figure 123.—N+2 Miscellaneous Distributed Masses	96
Figure 124.—N+2 Morphing Shapes Show Magnitude of Thickness Increases	97
Figure 125.—N+2 Aft Deck Morphing Process	97
Figure 126.—N+2 Morphing of the Tail Thickness	98
Figure 127.—N+2 Trailing Edge Darts for CFD Loads Generation	98
Figure 128.—Structural Sizing Approach	99
Figure 129.—477 Buckling Panels on Inner Wing Skin.....	100
Figure 130.—367 Buckling Panels on Inner Wing Substructure.....	101
Figure 131.—252 Buckling Panels on Upper and Lower Outer Skin.....	101
Figure 132.—265 Buckling Panels on Outer Wing Substructure	102
Figure 133.—40 Panels on Tail Skins	103
Figure 134.—44 Panels on Tail Substructure	103
Figure 135.—346 Buckling Panels on Fuselage OML	104
Figure 136.—Composite Inner Wing Skin Design Zones—109 Zones, 327 Independent Design Variables.....	105
Figure 137.—Aluminum Inner Wing Skin Design Zones—9 Zones, 9 Independent Design Variables.....	105

Figure 138.—Titanium Inner Wing Skin Design Zones—9 Zones, 9 Independent Design Variables.....	106
Figure 139.—Composite Inner Wing Substructure Design Zones—82 Zones, 82 Independent Design Variables	106
Figure 140.—Aluminum Inner Wing Substructure Design Zones—15 Zones, 15 Independent Design Variables	107
Figure 141.—Titanium Inner Wing Substructure Design Zones—22 Zones, 22 Independent Design Variables	107
Figure 142.—Composite Outer Wing Skin Design Zones—52 Zones, 156 Independent Design Variables.....	108
Figure 143.—Composite Outer Wing Substructure Design Zones—59 Zones, 59 Independent Design Variables	108
Figure 144.—Aluminum Outer Wing Substructure Design Zones—2 Zones, 2 Independent Design Variables	109
Figure 145.—Titanium Outer Wing Substructure Design Zones—2 Zones, 2 Independent Design Variables.....	109
Figure 146.—Composite Tail Skin Design Zones—20 Zones, 60 Independent Design Variables	110
Figure 147.—Composite Tail Substructure Design Zones—17 Zones, 17 Independent Design Variables.....	110
Figure 148.—Titanium Tail Substructure Design Zones—6 Zones, 6 Independent Design Variables.....	111
Figure 149.—Composite Fuselage OML Design Zones—71 Zones, 213 Independent Design Variables.....	111
Figure 150.—Aluminum Fuselage OML Design Zones—5 Zones, 5 Independent Design Variables.....	112
Figure 151.—Aluminum Fuselage Substructure Design Zones—1 Zone, 1 Independent Design Variable	112
Figure 152.—Composite Fuselage Substructure Design Zones—87 Zones, 87 Independent Design Variables	113
Figure 153.—Titanium Fuselage Substructure Design Zones—3 Zones, 3 Independent Design Variables.....	113
Figure 154.—Titanium Center Pylon Design Zones—3 Zones, 3 Independent Design Variables.....	114
Figure 155.—Core Thickness Trade Study.....	115
Figure 156.—Stiffener Spacing Trade Study.....	115
Figure 157.—Tail Deformation for LC 400 (2.5 g Pull-Up, Mach 2.0, DTOW2)	116
Figure 158.—Inner Wing Composite Skin Thickness (Includes 0.5 in. core).....	117
Figure 159.—Inner Wing Composite Substructure (Includes 0.25 in. core)	117
Figure 160.—Inner Wing Metallic Substructure	118
Figure 161.—Outer Wing Composite Skin Thickness (includes 0.5 in. core).....	118
Figure 162.—Outer Wing Substructure Thickness (composite includes 0.25 in. core).....	119
Figure 163.—Tail Composite Skin Thickness (includes 0.5 in. core)	119
Figure 164.—Tail Substructure Thickness (composite includes 0.25 in. core)	120
Figure 165.—Fuselage OML Thickness (includes 0.5 in. core)	120
Figure 166.—Strain XX Load Case LC300—Upper Wing Skin.....	121
Figure 167.—Strain XX Load Case LC300—Lower Wing Skin	122
Figure 168.—Strain XX Load Case LC300—Upper Inner Wing Skin	123
Figure 169.—Strain XX Load Case LC400—Upper Inner Wing Skin	124
Figure 170.—Strain XX Load Case LC400—Lower Inner Wing Skin	125
Figure 171.—Strain XX Load Case LC400—Upper Tail Skin	126
Figure 172.—Strain XX Load Case LC400—Lower Tail Skin.....	127
Figure 173.—Von Mises Stress—Load Case LC400—Lower Inner Wing.....	128

Figure 174.—Von Mises Stress—Load Case LC400—Lower Inner Wing.....	129
Figure 175.—Von Mises Stress—Load Case LC5730—Lower Inner Wing (Landing Gear Attachment Area)	130
Figure 176.—Max Shear Stress—Load Case LC400—Lower Inner Wing Skin	131
Figure 177.—Deflection LC400	132
Figure 178.—Deflection LC300	133
Figure 179.—Deflection LC600	133
Figure 180.—N+2 Rigid Body Mode Shapes 1 to 3 for Rev 70 and 71	135
Figure 181.—N+2 Rigid Body Mode Shapes 4 to 6 for Rev 70 and 71	136
Figure 182.—N+2 Rigid Body Mode Shapes 7 to 9 for Rev 70 and 71	137
Figure 183.—N+2 Rigid Body Mode Shapes 10, 11, and 18 for Rev 70 and 71	138
Figure 184.—Modal Convergence Study (Mach 0.9, Symmetric Boundary Conditions, DTOW)	139
Figure 185.—Damping Versus Dynamic Pressure from NASTRAN	140
Figure 186.—Damping Versus Velocity (KEAS) from FAMAS	141
Figure 187.—FEM017-REV70 Flutter Boundary—Symmetric Boundary Conditions.....	142
Figure 188.—FEM017-REV70 Flutter Boundary—Antisymmetric Boundary Conditions	143
Figure 189.—Mach 0.95 Antisymmetric Boundary Conditions, Zero Fuel Weight.....	143
Figure 190.—Likely Spurious Results at Mach 1.1, Antisymmetric Boundary Conditions at DTOW	144
Figure 191.—N+2 Flutter Boundary Engine Mass Trade Study—Symmetric Boundary Conditions	145
Figure 192.—Damping and Frequency Versus Dynamic Pressure for Symmetric BCs, Mach 0.95, DTOW2, 40 percent Increase in Engine Mass	146
Figure 193.—Critical Symmetric Flutter Mode, Aft Deck Bending, Tail Bending and Torsion, $q_f = 1164 \text{ psf}$, $f = 5.5 \text{ Hz}$	147
Figure 194.—Engine Mass Trade Study—Antisymmetric Boundary Conditions	148
Figure 195.—Damping and Frequency Versus Dynamic Pressure for Antisymmetric BCs, Mach 0.7, DTOW2, 40 Percent Increase in Engine Mass	149
Figure 196.—Critical Antisymmetric Flutter Mode, Tail Bending and Torsion, $q_f = 1556 \text{ psf}$, $f = 9.3 \text{ Hz}$	150
Figure 197.—Aft Deck Stiffening Alternative by Pylon Height Extension Above Wing	150
Figure 198.—Fuel Tank Layout and Tank Burn Sequence at Beginning and End of Cruise	152
Figure 199.—Aeroelastic increments in Total Z-Force Normalized by Total Lift for the Beginning of Cruise.....	152
Figure 200.—Aeroelastic Increments in Total Z-Force Normalized by Total Lift for End of Cruise	153
Figure 201.—Comparison of the Z Deflections for the Beginning and End of Cruise Trim States	153
Figure 202.—Comparison of Planform Surface Pressure Coefficient for Rigid and Flexible Simulations at Start of Cruise	154
Figure 203.—Comparison of Empennage Surface Pressure Coefficient for Rigid and Flexible Simulations at Start of Cruise	154
Figure 204.—Comparison of Ground Signatures for Rigid and Flexible Simulations at Start of Cruise	155
Figure 205.—Comparison of Ground Loudness Carpets for Rigid and Flexible Simulations at Start of Cruise	156
Figure 206.—Tunnel Ambient DPP Versus Humidity	157
Figure 207.—Beyond Near-Field Measurements Appear Rounded and Missing Detail.....	158
Figure 208.—Aircraft Performance (44 in.) and Boom (16 in.) Models	160
Figure 209.—The 14 in. RF1.0 Rail Attached to Floor of 11 ft Transonic Tunnel (Note Non-Conformal Structural Attachment ~8 in. Aft of LE)	160
Figure 210.—Drawings of 11 ft Transonic Tunnel Test Section.....	161

Figure 211.—The 11 ft Wind Tunnel Layout—Boeing N+2 Exploratory Sonic Boom Test (side view).....	162
Figure 212.—Schlieren Images from 11 ft Transonic Tunnel	163
Figure 213.—Boeing Boom1 Model and RF1.0 Rail in 11 ft Transonic Tunnel	164
Figure 214.—Boeing PM1 Sting-Mounted Large Scale Performance Model	165
Figure 215.—Schlieren Image of Upstream Shocks Interfering With Boeing PM1 Sting-Mounted Large Performance Model.....	166
Figure 216.—Boeing BM1 Sonic Boom Model (close upper) Over RF1.0 Rail (lower).....	167
Figure 217.—Humidity per Run Number Throughout Test	169
Figure 218.—Schlieren Images Show Ambient Shocks From Upstream Interfering with Boeing BM1 Sonic Boom Model	170
Figure 219.—The 11 ft Test Section Slot Baffles as Possible Disturbance Sources and Repairs	171
Figure 220.—The 8x6 with Angled Bleed Holes on Walls, Model Hardware on Floor Strut and RF1.0 Rail on Ceiling.....	174
Figure 221.—Glenn 8x6 has Greater P_{static} Variations Than Ames 9x7, Which Distort Slope and Zero of Measurements at Every Rail Orifice.....	174
Figure 222.—Better Signature Detail Marred by Varying Level Drift.....	175
Figure 223.—Glenn 8x6 Ambient/Reference Drift Too Large (even at same strut height)	176
Figure 224.—Change in Reference Measurements Correlates With Change in Tunnel Mach	176
Figure 225.—Mach Change With Model Position Not Proportional (red increasing H, blue decreasing H).....	176
Figure 226.—Orifice Reference Pressures Change in Direct Proportion to Mach Variation	177
Figure 227.—The Far-Field Correction Method Provides Consistent Results Matching the Uncorrected Data's ∞ Distance Asymptote	178
Figure 228.—As the 70° Flat-Plate Model is Advanced Through the Flow-Field, Rail Measurements Quantify How Reflected Shock Strength Varies With Model Span	179
Figure 229.—The Model is Moved Back and Up for a Reference Measurement But May Still be Measured on the Rail—Orifices Not Ahead of the Model are Omitted from Spatial Averaging	179
Figure 230.—Automatic Reference Measurement Trimming Removes Only the Data With Model Intrusion and Keeps the Good Data for Resolving the Trailing Signature.....	180
Figure 231.—Omitting a Fraction of the Highest/Lowest Measurements Extremes, Smooths and Sharpens the Spatially Averaged Signature.....	180
Figure 232.—Reverse Aging, Averaging, then Re-Aging Achieves a Slight Sharpening of the Spatially Averaged Signature	181
Figure 233.—Doubled Rail Increases Position Options and Translation Length—Improving Measurement Accuracy, Plus No Stopping to Move Rail between Near and Far Measurements.....	182
Figure 234.—LM4 Wind Tunnel Model of 1044-2 Configuration.....	183
Figure 235.—Symmetry Plane Pressure Contours: No Blade (left) and With Blade (right)	183
Figure 236.—Blade Effects on Model Signature	184
Figure 237.—Blade Effects on Centerline Flow-Through Nacelle.....	185
Figure 238.—Centerline Flow-Through Nacelle Mach (left) and Pressure Recovery Map (right)	185
Figure 239.—Surface Pressure Contour Comparison.....	186
Figure 240.—Edge Thickness Effect on Model Signature [M=1.7, AoA=2.1, H=5.4(b/2)]	186
Figure 241.—LM4 Model CFD Boundary Layer Comparisons	186
Figure 242.—Predicted Boundary Layer Effects on LM4 Signature.....	187
Figure 243.—The 19 Percent Smaller 1044-2 Model Improved Spatial Averaging Positioning	187
Figure 244.—The 70° Flat-Plate Model Fabricated to Improve Measurement and Calibration of Reflected Shock Distortions	188
Figure 245.—Flat-Plate Approximates 1044-2 Wing Planform	188
Figure 246.—Hardware and 1044-2 Model Prepared for Testing	189

Figure 247.—Test Oil Flow (top) Showed Fully Attached Flow, Like Turbulent CFD (bottom).....	190
Figure 248.—Close-Up of 1021-01 Oil Streaks Showed Fully Attached Flow, Like Turbulent CFD (Some persistent separation streaks formed during tunnel start-up at low Re)	191
Figure 249.—Dramatic Upper Surface Flow Coloration Showed That Strong Pressure Disturbances are Isolated From Underneath the Wing Until Its Trailing Edge, as Intended	192
Figure 250.—Lower Surface Produced Little Flow Disturbance, Supporting Its Intended Mission to Quantify Shock Reflection Strength as a Function of Local Span.....	193
Figure 251.—Blade Support for 1021-01 (top) and 1044-02 (bottom) Showed Attached Flow Until Vortex Separation Region Identified by Dashed Red Line	194
Figure 252.—Upper and Lower Surface Oil Flows on 1044-02 Indicated Fully Attached Flow	195
Figure 253.—Upper Surface Oil Flow Strongly Showed Rib Pattern Shocks From Blade Trip Discs and Bow Shock Waves From Wing Trip Discs.....	195
Figure 254.—Legacy 69° Delta Wing-Body Model Oil Streaks Indicating Attached Flow and Dramatic Oil Evacuation Behind Diamond Airfoil Maximum Thickness Ridge.....	196
Figure 255.—Mottled Oil at the Root and Outboard Wing and Oil Void Streak at the Nose (bottom) Are Not Flow Phenomena, But Rather, Persistent Features From the Initial Oil Application (top)	196
Figure 256.—RBOS of 1021-01 Shaped Boom Model Made Nose and Underwing Nacelle Shocks Apparent, Otherwise, Only Background Flow-Field Variations	198
Figure 257.—Flat-Plate Model Created Little Disturbance between Nose Shock and Trailing Edge.....	198
Figure 258.—RBOS Wake Visualization by Shading on DY (see Figure 260)	199
Figure 259.—RBOS Side-View Validated Lack of Disturbance Below Flat-Plate between Nose Shock and Trailing Edge and Successful Isolation of Blade Disturbance.....	199
Figure 260.—RBOS of 1044-02 Shaded DX (top) and DY (bottom)	200
Figure 261.—RBOS of 1044-02 Illustrated that Shaped Boom Disturbances are Lower in Magnitude than Ambient Disturbances and only Subtly Visible Behind the Wing	201
Figure 262.—The 69° Delta Wing-Body Shocks Weakened and Harder to See at Smaller Size.....	201
Figure 263.—Excellent Test-to-Test Match (validated before proceeding with LM4)	202
Figure 264.—There Does Appear To Be Better and Worse Locations For Measuring in the Tunnel—Selective Data Processing Might Improve Results	203
Figure 265.—The 70° Flat-Plate Delta Model Produces Little Disturbance Under Itself So Reflections Could Be Characterized to Improve Flow-Field Calibration	203
Figure 266.—Measurement Fell Between Turbulent and Laminar Solutions	204
Figure 267.—Predictions Matched Measurements for Roll Angles from 0° to 60°	205
Figure 268.—Large Predicted Nacelle Effect is Matched by Measurements at 0° and 40° Roll	206
Figure 269.—Still Matching Well at 13 Semi-Span ($b/2$) Distance at 0° and 40° Roll.....	207
Figure 270.—Signature Uncertainty and Detail Degraded With Increased Measurement Distance but Aft Rail (17 to 21 semi-spans distance) Position Responsible for Part of Degradation.....	207
Figure 271.—Measurements and Match Showed More Uncertainty Than Required, Further Measurement Processing Improvements Needed.....	208
Figure 272.—Despite a Small Model a "Nonshaped" Boom Design of 3 Coalesced Shocks is Far Less Scattered by Tunnel Distortions.....	209
Figure 273.—Effect of Alpha Coalesced Into Only a Shock Magnitude Change and Small Recompression Detail Difference.....	210
Figure 274.—In Roll, Wing Trailing Edge Shocks Different While Leading Edge Shocks Similar—Because Leading Edge Swept Near Mach Cone	210

List of Tables

Table 1.—N+2 Environmental and Performance Goals, and Validated Phase 2 Result	iv
--	----

Table 2.—Phase 2 Configuration Progression	3
Table 3.—Breguet Range Parameter versus Mach	4
Table 4.—Configuration 1044 Weight Statement	17
Table 5.—Detailed Mission Statement and Maximum Range	21
Table 6.—Detailed Mission Statement, Shaped Boom	22
Table 7.—General Characteristics for Airframe Noise Calculation	23
Table 8.—Configuration and Design Weights Data	58
Table 9.—N+2 Design Speeds	58
Table 10.—Maneuver Load Cases	60
Table 11.—Cabin Pressure as a function of altitude	60
Table 12.—Landing Load Cases	62
Table 13.—Ground Handling Load Cases	63
Table 14.—Trim Deflections for Symmetric Maneuver Load Cases	72
Table 15.—Trim Deflections for Antisymmetric Component of Maneuver Load Cases	72
Table 16.—Weights and CG for final maneuver load calculations	72
Table 17.—N+2 Shell Element Counts by Subassembly	79
Table 18.—N+2 Bar and Rod Element Counts by Subassembly	81
Table 19.—N+2 FEM Numbering Master Schema	86
Table 20.—N+2 Element Type Breakdown and Counts	89
Table 21.—N+2 NASTRAN FEM Include File Structure	90
Table 22.—Basic Material Property Values	91
Table 23.—Design Criteria for Structural Sizing	100
Table 24.—Weight Summary of Sized FEMs	116
Table 25.—N+2 Vehicle modal frequencies for REV 70 and 71	134
Table 26.—Comparison of NASTRAN and FAMAS	139
Table 27.—FEM Weights and CG Locations for Flutter Analysis (FEM017-REV70)	142
Table 28.—Engine Masses for Trade Study	145
Table 29.—Minimum Flutter Dynamic Pressure versus Engine Mass (Symmetric Boundary Conditions)	145
Table 30.—Minimum Flutter Dynamic Pressure versus Engine Mass (Antisymmetric Boundary Conditions)	148
Table 31.—Flight condition and weight states for Beginning and End of Cruise States	152
Table 32.—Trim States Obtained with a CFD-Based Aeroelastic Trim Approach	152
Table 33.—Boeing Model Reference Dimensions and Size	160
Table 34.—N+2 Environmental and Performance Goals, and Validated Phase 2 Result (Table 1 Repeat)	211

Advanced Concept Studies for Supersonic Commercial Transports Entering Service in the 2018-2020 Period Phase 2

John Morgenstern and Michael Buonanno

Lockheed Martin

Palmdale, California 93599

Jixian Yao, Mugam Murugappan, Umesh Paliath, Lawrence Cheung, Ivan Malcevic,
Kishore Ramakrishnan, Nikolai Pastouchenko, and Trevor Wood

GE Global Research

Niskayuna, New York 12309

Steve Martens, Phil Viars, Trevor Tersmette, Jason Lee, Ron Simmons, and David Plybon

GE Aviation

Cincinnati, Ohio 45215

Juan Alonso, Francisco Palacios, Trent Lukaczyk, and Gerald Carrier

Stanford University

Stanford, California 94305

1.0 Introduction

1.1 Subject/Relevancy

The National Aeronautics and Space Administration's (NASA) Supersonics Project is aligned with the Aeronautics Research Mission Directorate (ARMD) principles of maintaining intellectual stewardship of aeronautical core competencies for the nation in the supersonic flight regime and of focusing research in areas that are appropriate to NASA's unique capabilities. The Supersonics Project is a broad-based effort designed to develop knowledge, capabilities and technologies that support vehicles that fly in the supersonic speed regime. A major focus of this effort is eliminating the efficiency, environmental and performance barriers to practical supersonic cruise vehicles.

The Supersonic project invests a significant portion of its allocated budget in NASA Research Announcement (NRA) solicitations—including the N+2 Supersonics Validation program. The objective of the NRA investment is to stimulate innovation in integrated transportation concepts and to create an environment for collaboration among NASA researchers, commercial organizations, and academia. This investment is primarily focused at foundational level research, but has also been used to aid the project in developing integrated systems concepts. These concepts can be used to both conduct trade studies to determine the requirements for future supersonic aircraft and to assess the effectiveness of the project's work content at overcoming the barriers to supersonic flight. LM's N+2 Supersonic Validations contract fits into NASA's N+2 Supersonic Program as shown in Figure 1.

The N+2 Supersonic Validations program (supersonic vehicle anticipated to enter service in 2018-2020) directly aligns with these NRA and Supersonic Project goals and focuses on the validation of methodologies to successfully design and develop a shaped boom supersonic air vehicle. The N+2 effort is divided into elements that focus on foundational, discipline, multidiscipline and integrated system level challenges. To achieve these multi-faceted goals, the N+2 effort requires multi-discipline analysis and optimization (MDAO) efforts between airframe and propulsion industries to address system integration.

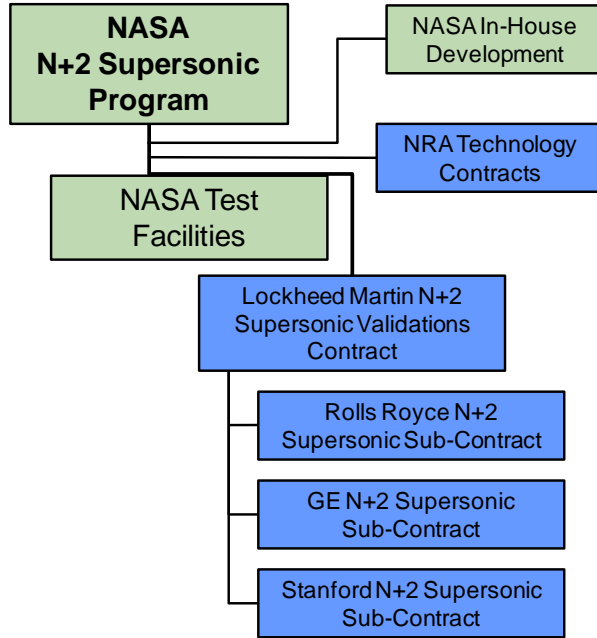


Figure 1.—LM N+2 Organization

Integrated vehicle design is performed to simultaneously achieve supersonic cruise efficiency, shaped sonic boom signatures, as well as low take-off noise. Other, integrated design concerns include:

- Sonic Boom Reduction
- Cruise Efficiency
- Aero-Propulsive-Servo-Elasticity
- Airport Noise
- Light Weight Structure for Airframe/Propulsion Systems
- High Altitude Emissions

A key element of the Supersonics Project (and N+2 program) is systems level validation testing, which leverages the substantial investments made by the project (both internally and through the NRA). The system level validation will provide proven capabilities that will be able to address the efficiency, environmental and performance challenges of future supersonic aircraft. The LM N+2 program conducts shaped boom testing and nozzle testing to achieve these goals.

The N+2 Supersonic program generates knowledge that can benefit the Nation. Therefore, this report (and related papers at technical conferences) seeks to share the program's findings, disseminate test results and validate component and system analysis tools that will support the design of an environmentally and economically viable product.

Meeting or surpassing these goals stimulates innovation and advances the pursuit of revolutionary conceptual designs. System-level multi-disciplinary analysis and optimization (MDAO) and out of the box thinking allows for tool and technology validation. This fosters an environment of innovation and generates excitement for future supersonic travel.

Overall, the N+2 effort is driven by the need for design and testing validations to meet the efficiency, environmental, and performance barriers to practical supersonic flight. Results from these efforts advance tools and technologies necessary for integrated supersonic design.

2.0 N+2 Configuration Refinement

The LM N+2 low-boom vehicle configuration evolved significantly during the Phase 2 effort. Figure 2 provides an overview of OMLs evaluated, while brief description of each configuration is given in Table 2.

Low-boom signature improvements and configuration refinements took place concurrently, resulting in a highly realistic design with a full-carpet, 4-PLdB reduction over Phase 1 boom loudness, Figure 3. Aerodynamic and mass properties database were developed for the baseline design and used in sizing and mission performance analyses. A sized, 335,000 lb-class vehicle with a 5,500 nmi range was selected as the going-forward design.

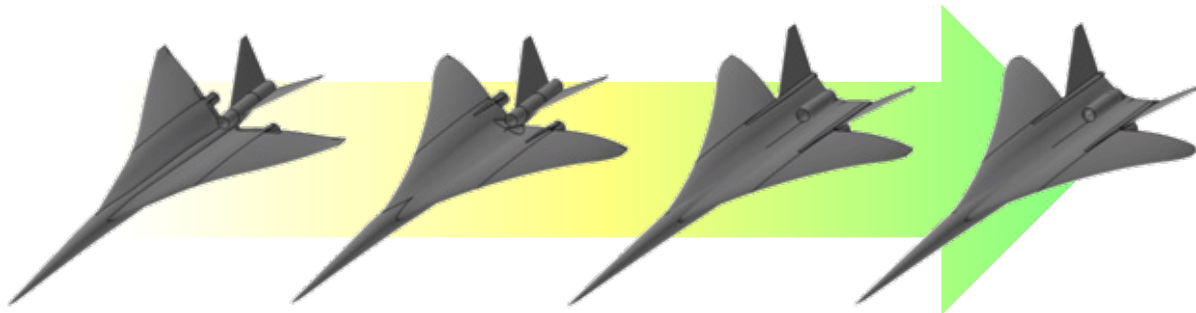


Figure 2.—N+2 Phase 2 Configuration Evolution (left to right): 1021, 1040, 1043, 1044

TABLE 2.—PHASE 2 CONFIGURATION PROGRESSION

Configuration	Description	Note
1021	Phase 1 baseline	LM3 OML
1040	Configuration 1021 DOE refinement	
1043	Aft-deck	
1044	Propulsion effects/Phase 2 baseline	
1044-2	Stanford optimization	LM4 and LTWT OML
1044-3b	Post-1044 mod rollup	
1044-X	Sized going-forward design	

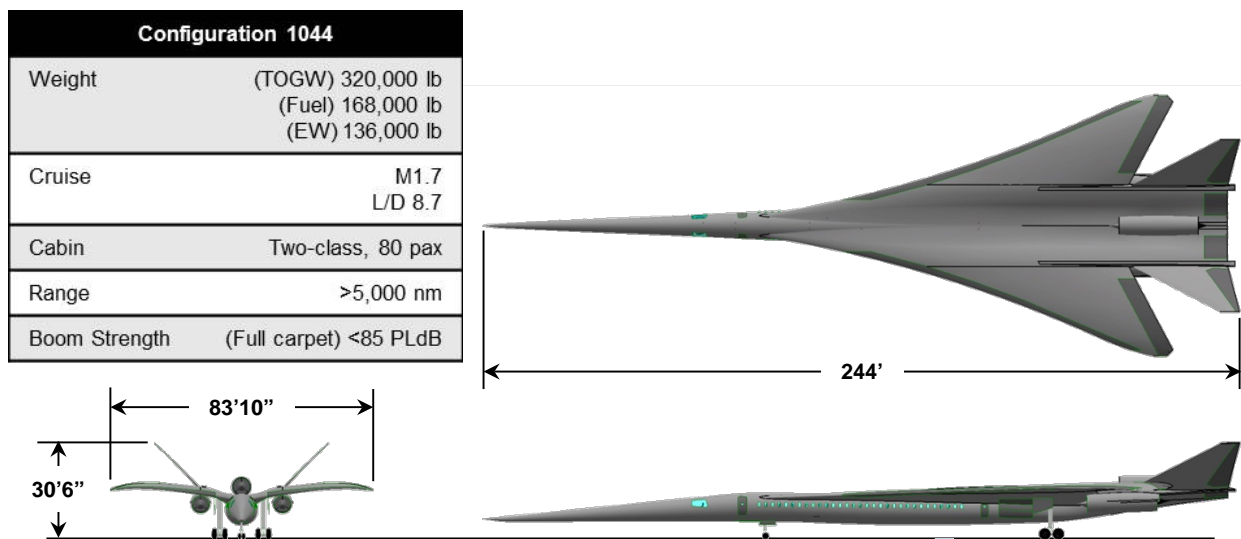


Figure 3.—N+2 Phase 2 Baseline Vehicle 3-View

2.1 Cruise Mach Trade

A zero-order cruise Mach trade was performed at the start of Phase 2 effort to evaluate the practicality of M1.6-plus cruise. Breguet range parameter, defined as $(M / SFC * L/D)$, was used to identify the cruise Mach that delivers best range performance, while predicted boom signatures were examined to characterize Mach-driven effects.

Range parameter calculation inputs extracted from Configuration 1021 aerodynamic database and GE62_FLF4 engine deck are tabulated in Table 3. The analysis assumed constant L/D via climbing cruise, as well as altitude-independent specific fuel consumption. As shown, range parameter continued to increase until around M1.7 before dropping off.

Analysis of Configuration 1021-based boom signatures showed an expected steepening of front shock slope due to increased shock strength at higher Mach, Figure 4. Upon closer examination it was found that the front shock slope also steepens with increasing off-track angle even though the magnitude of pressure rise is lower. This is attributed to the coalescing of shock, i.e., aging, over the longer distance traveled before the shock reaches ground. Note that as the roll angle increases, the swath of area affected by the boom also increases. As such, off-track signature shaping could be as critical, if not more so, than under-track signature shaping, and need to be addressed early on as oppose to trying to recover the signature after the fact.

Based on the above findings, as well as environmental (jet emission) and health (high-altitude radiation exposure) considerations, M1.7 was selected as the design cruise Mach for the Phase 2 effort, with M1.8 for over-water, boom-unconstrained operation pending engine cycle update.

2.2 Sonic Boom Signature Improvement

Phase 1 final under-track signature at the SOC of the 4,000-nmi low-boom mission was 85 PLdB and less than 87 PLdB across the full carpet, Figure 5. The predicted boom loudness corresponds to a 0.26 psf N-wave based on 1 ms/psf rise time, slightly higher than the target 0.22 psf N-wave. As shown in Figure 6, the aft shock is a well-shaped ramp consists of multiple small spikes out to 20° off-track. At 30° off-track, the aft shock split into two distinct sharp spikes due to shock coalescence, resulting in increased loudness. This trend continued through approximately 40° off-track, at which point the trend reversed. The front ramp remains well-shaped across the full carpet.

TABLE 3.—BREGUET RANGE PARAMETER VERSUS MACH

Mach	Range parameter
1.4	15.9
1.6	16.9
1.7	17.2
1.8	17.0

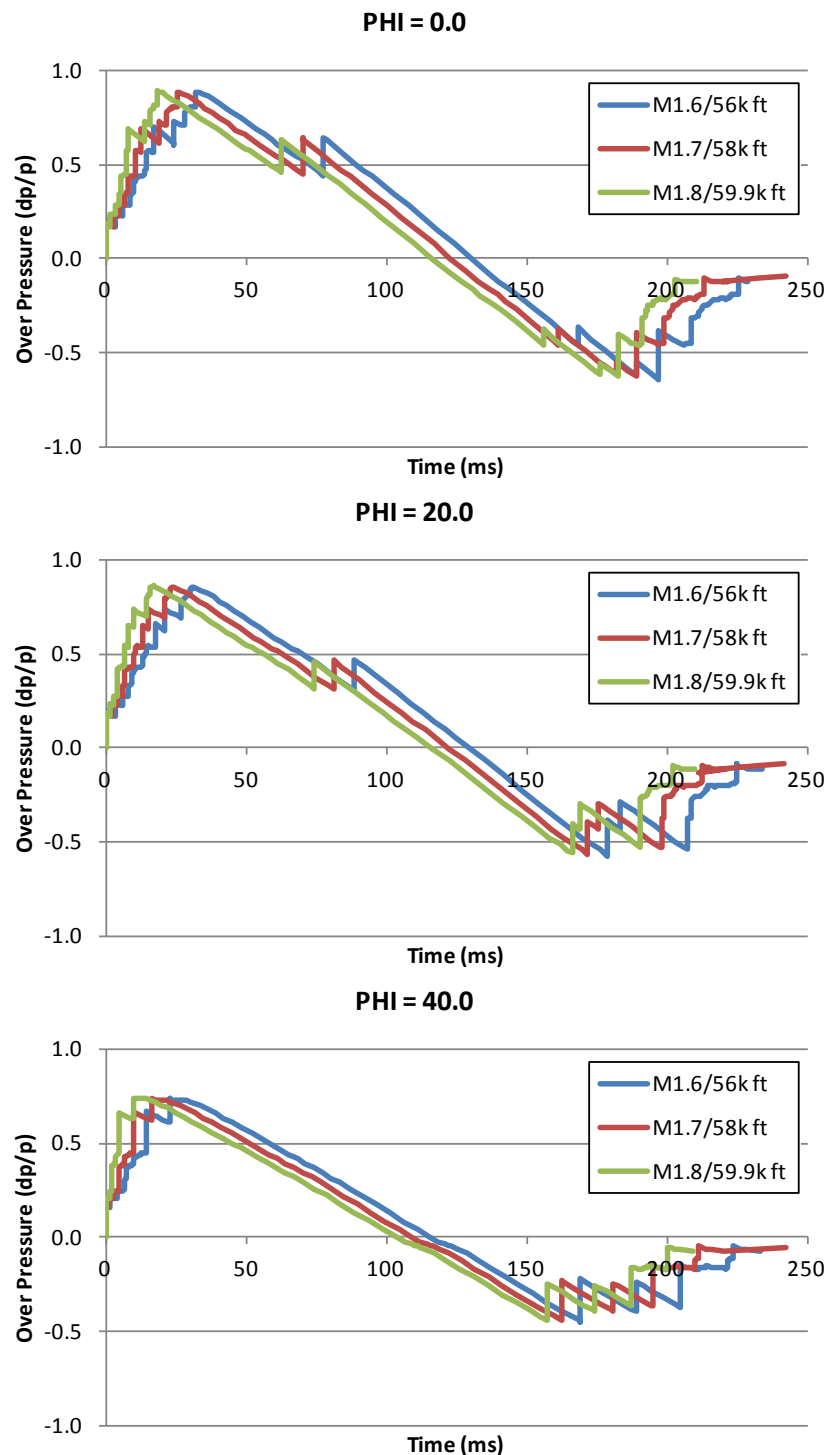


Figure 4.—Mach Effect on Ground Signatures

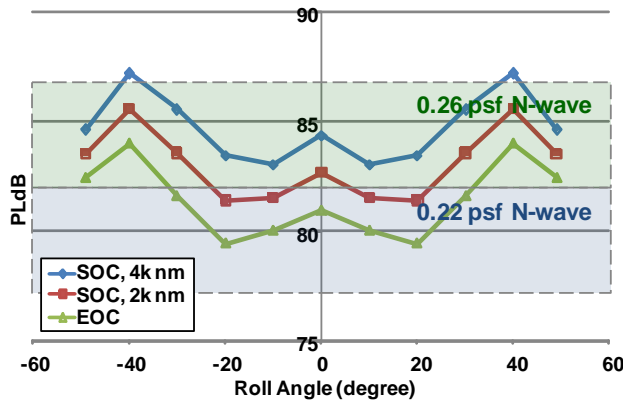


Figure 5.—Configuration 1021 Full-Carpet Loudness

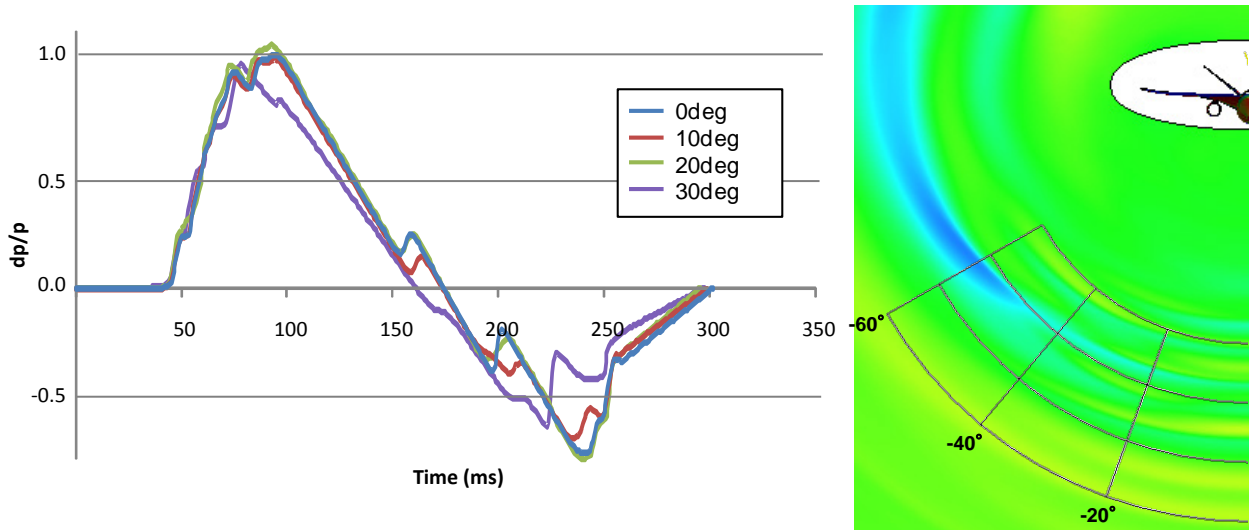


Figure 6.—Configuration 1021 Signature, 5.6 R/(b/2), SOC 4,000 nmi Mission

Using Configuration 1021 as a starting point, a 23-design variable DOE was performed to screen fuselage, wing and tail geometric parameters that have largest impact on boom signature, Figure 7. Response surface equations were generated for eight selected design variables and entered into a generic optimization routine to attempt to simultaneously improve configuration realism and boom signature. The resulting configuration, designated Configuration 1040, has better aerodynamic performance and packaging efficiency but no significant improvement in signature. It was concluded that the incremental adjustments to the POD design were not sufficient to eliminate the off-track lift gap between the wing and centerline v-tails, and that alternate approach is needed.

To address the off-track lift gap issue, the aft-deck concept explored as part of Phase 1 configuration trade studies was revisited. The original concept was to extend the inboard wing TE aft to increase vehicle cross-sectional area at off-track angles. The concept was taken one step further in Phase 2 by splitting up the centerline v-tails and moving it outboard. The outboard wing pylons were enlarged and extended aft to pick up the newly-relocated canted vertical tails. Comparison of near-field pressure gradient at 40° off-track angle shows the LE shock coming off the semi-span v-tails weakened the strong expansion fan coming off the wing TE, Figure 8. Configuration 1043 full-carpet signature shows that the aft-deck/v-tails relocation successfully revert the increasing trend at high off-track angles, Figure 9. Separately, front shock signature is further reduced by lengthening of the nose spike to shallow out the front shock ramp. Overall full-carpet loudness is now less than 85 PLdB.

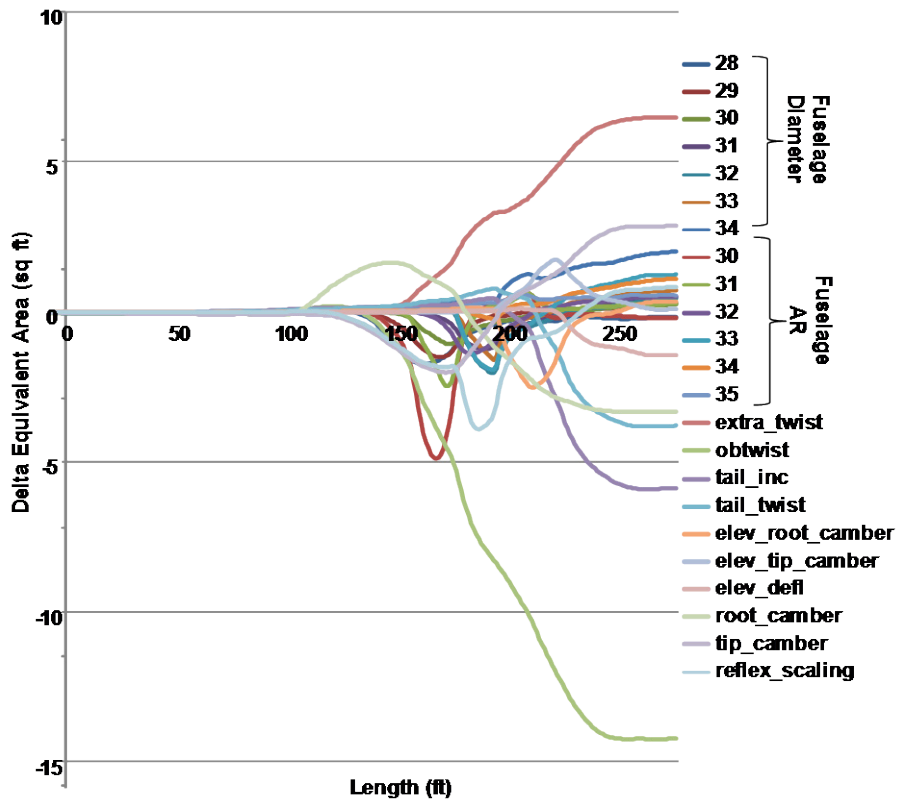


Figure 7.—DOE Design Variable Sweep

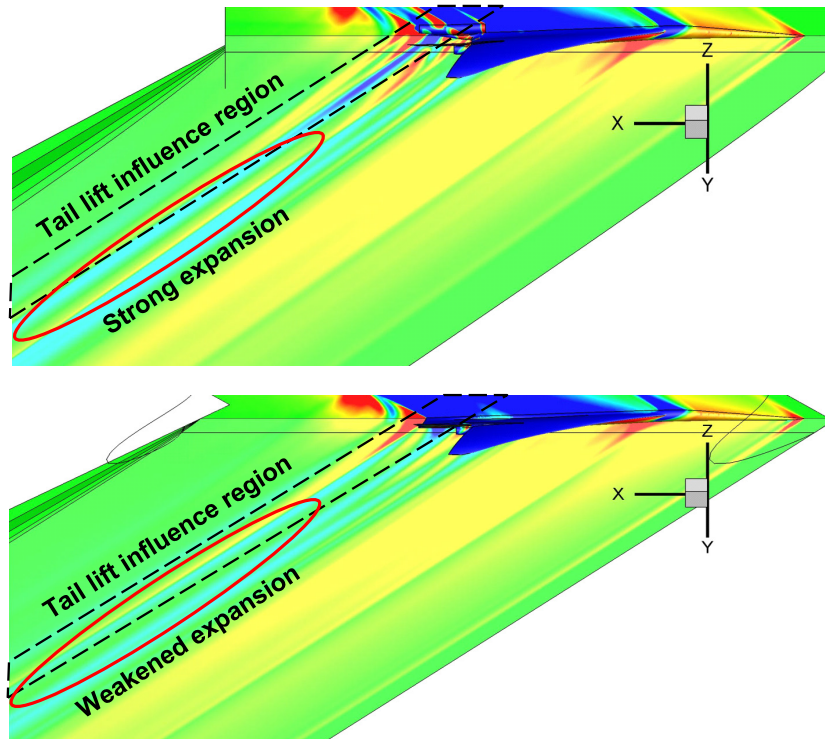


Figure 8.— $\Phi = 40^\circ$ Pressure Gradients, Configuration 1040 (top) and 1043 (bottom)

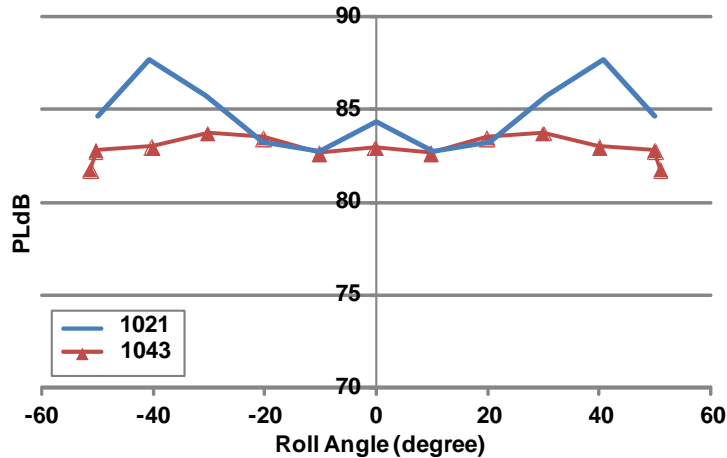


Figure 9.—SOC Full-Carpet Loudness Comparison, 4,000 nmi Mission

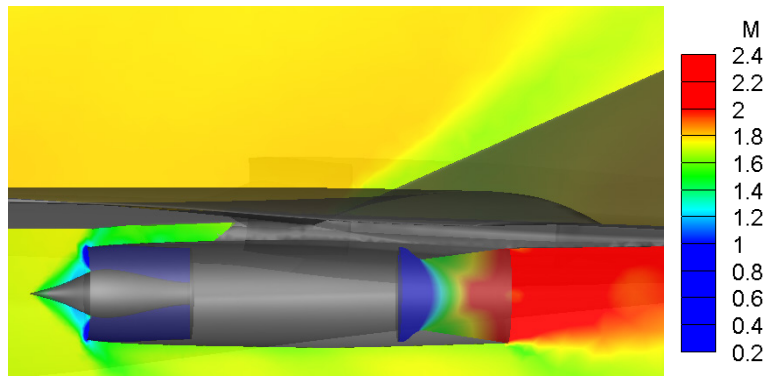


Figure 10.—CFD Result of Representative Inlet and C-D Nozzle

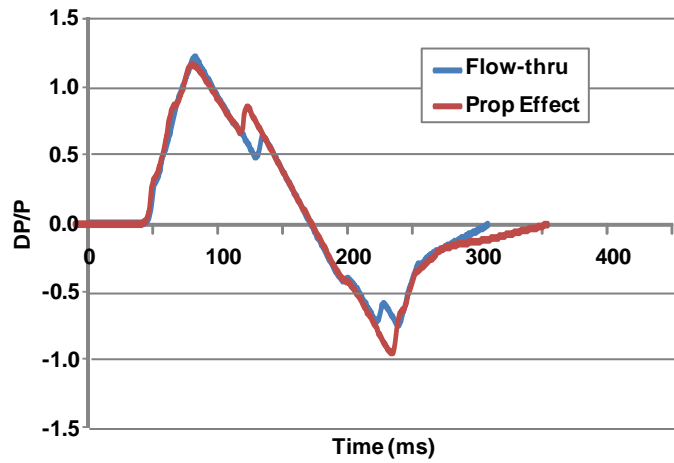


Figure 11.—Propulsion Effects on Signature, 5.6 R/(b/2)

Up to this point, flow-through nacelles were used in the signature analysis. To improve boom signature fidelity, notional M1.7 inlet centerbody and convergent-divergent nozzle were incorporated under Configuration 1044, Figure 10. As illustrated in Figure 11, inlet spillage and exhaust plume altered the local flow field characteristics, resulting in an approximately 2-PLdB increase in boom loudness. The signature hit was recovered through adjustment of under-wing reflex geometry and equivalent area offset.

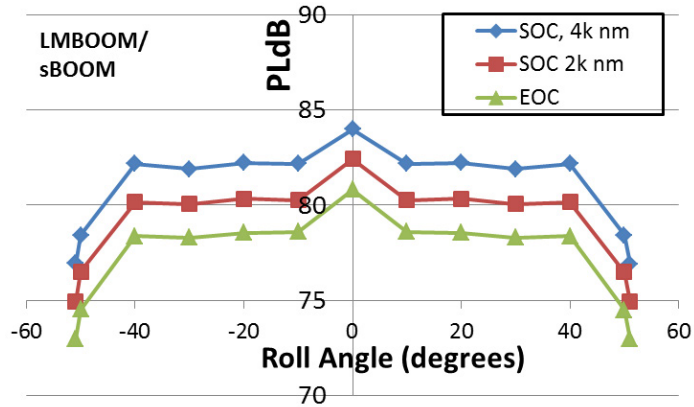


Figure 12.—Configuration 1044-2 Full-Carpet Loudness

The full-carpet signature of the final configuration that came out of the signature improvement effort is shown in Figure 12. Configuration 1044's average loudness at the start of cruise (SOC) of the 4,000 nmi low-boom mission is 82 PLdB, 80 PLdB at mid-cruise and 78 PLdB at EOC. The results equal to approximately a 4-PLdB reduction over the Phase 1 final signature.

2.3 Configuration Maturation

Vehicle configuration realism was significantly enhanced under the Phase 2 effort. Design deficiencies identified at the end of Phase 1 were addressed while additional refinements were incorporated. Detailed structure layout was created in support of FEM analysis, and low-speed wind tunnel test conducted to assess stability and control characteristics.

2.3.1 OML Refinement

Several design aspects of Configuration 1021 were deemed nonideal and required further refinement, Figure 13. The fuselage cross-section was shaped primarily to meet equivalent area target, resulting in a varying cross-section that encroached upon cabin space and increased manufacturing complexities. In addition, available fuselage volume was insufficient for subsystems packaging. The droop nose severely reduced forward cabin height and resulted in breaks in cabin attitude. Unrefined landing gear layout resulted in excessive gear length that constrained retraction options, as well as undesirable on-ground cabin inclination. Aerodynamically, the dihedral high-wing resulted in excess roll in sideslip.

Incremental changes were introduced under Configuration 1040 to address Phase 1 design deficiencies, Figure 14. Fuselage volume was increased to minimize cabin space encroachment and to provide additional packaging volume. Excessive nose droop was reduced to improve cabin layout. Upper surface wing-body blend was added to increase fuel volume and to improve structural load path. The outboard engine pylons were extended above upper wing surface to increase structural stiffness while doubling as anti-shock bodies to improve off-track area distribution. Finally, wing dihedral was reverted to improve roll stability in sideslip.

Additional refinements were incorporated along with the outboard relocation of v-tails under Configuration 1043, Figure 15. To support the v-tails at their new semi-span location, outboard engine pylons were further enlarged and extended aft, while the inboard portion of the wing was extended aft to bridge the gap between the pylon and fuselage for additional structural support. Nose droop angle was further reduced, which required lengthening of nose to compensate off-track front shock steepening due to aging. The centerline nacelle, no longer supporting the v-tails, was shortened to eliminate excess length and reduce drag.

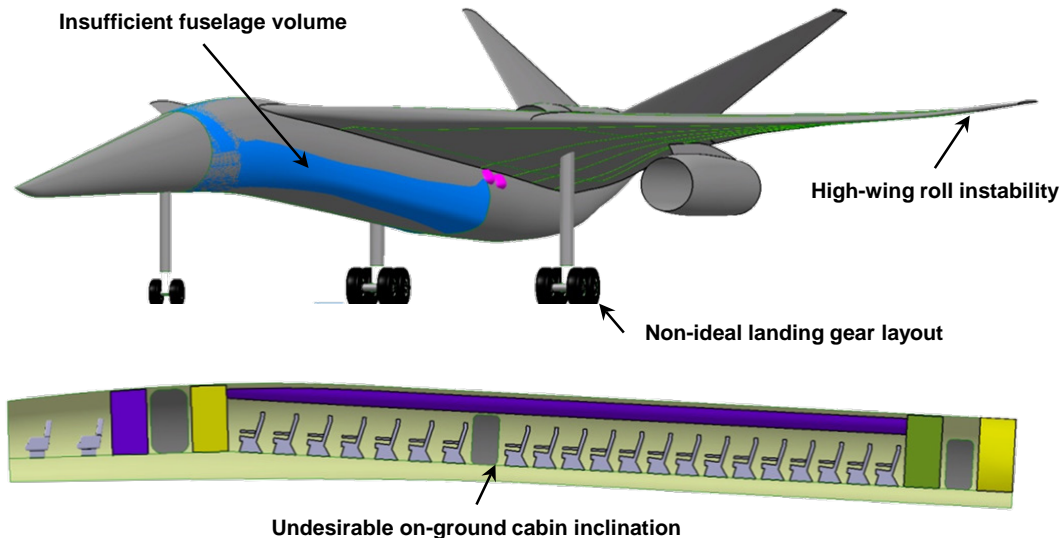


Figure 13.—Configuration 1021 Issues To-Fix

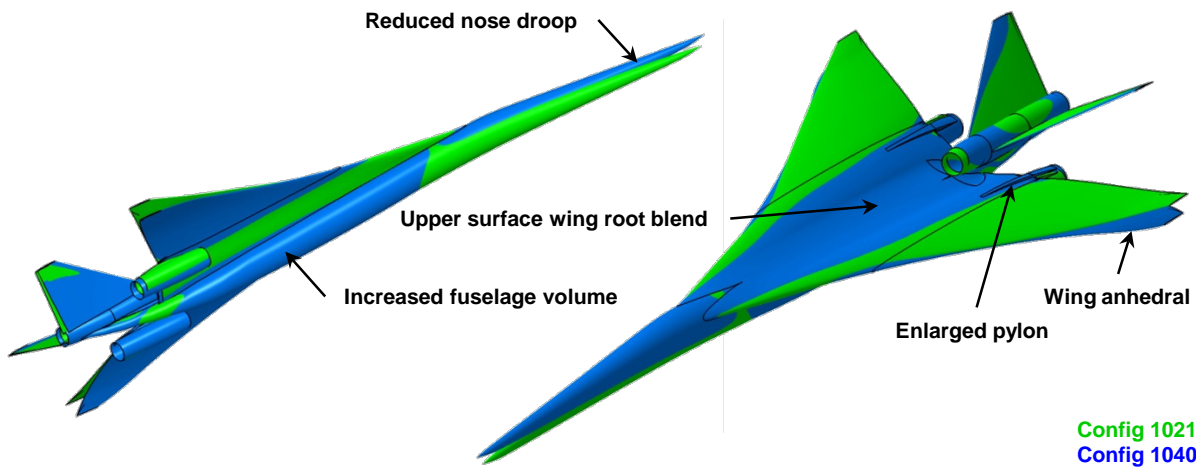


Figure 14.—Configuration 1021 Versus 1040

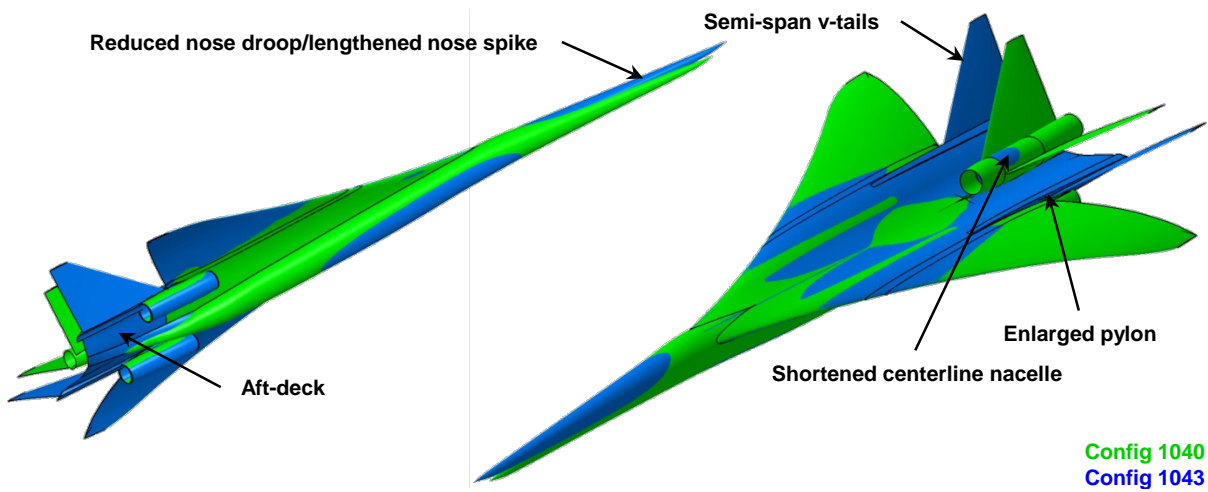


Figure 15.—Configuration 1040 Versus 1043

Internal review by LM Tech Fellows from design and structure disciplines identified high-alpha pitch-up as a potential complication that warrants further investigation. Low-speed CFD analysis using clean configuration confirmed worsening of pitch-break due to wing-root vortices impinging on the semi-span v-tails, Figure 16. Given the limited usefulness of clean configuration aerodynamics at high alpha and impracticality of running hundreds of CFD cases to explore stability and control concepts, LM proposed and received NASA authorization to plan, build, and test LTWT wind tunnel model to assess low-speed aerodynamic characteristics and control surface effectiveness (see Section 2.6 LTWT Test).

Configuration 1044 marked the end of boom signature improvement as well as vehicle OML freeze in support of discipline analyses and database generation, Figure 17. Lower surface wing reflex, designed to attenuate shock coming off of outboard nacelles, was modified to match the altered flow pattern from the newly introduced inlet centerbody. Aft-deck trailing edge was un-swept to better shield nozzle exhaust from impacting the aft shock signature. Finally, wingtip trailing edge was cropped to reduce tip drag.

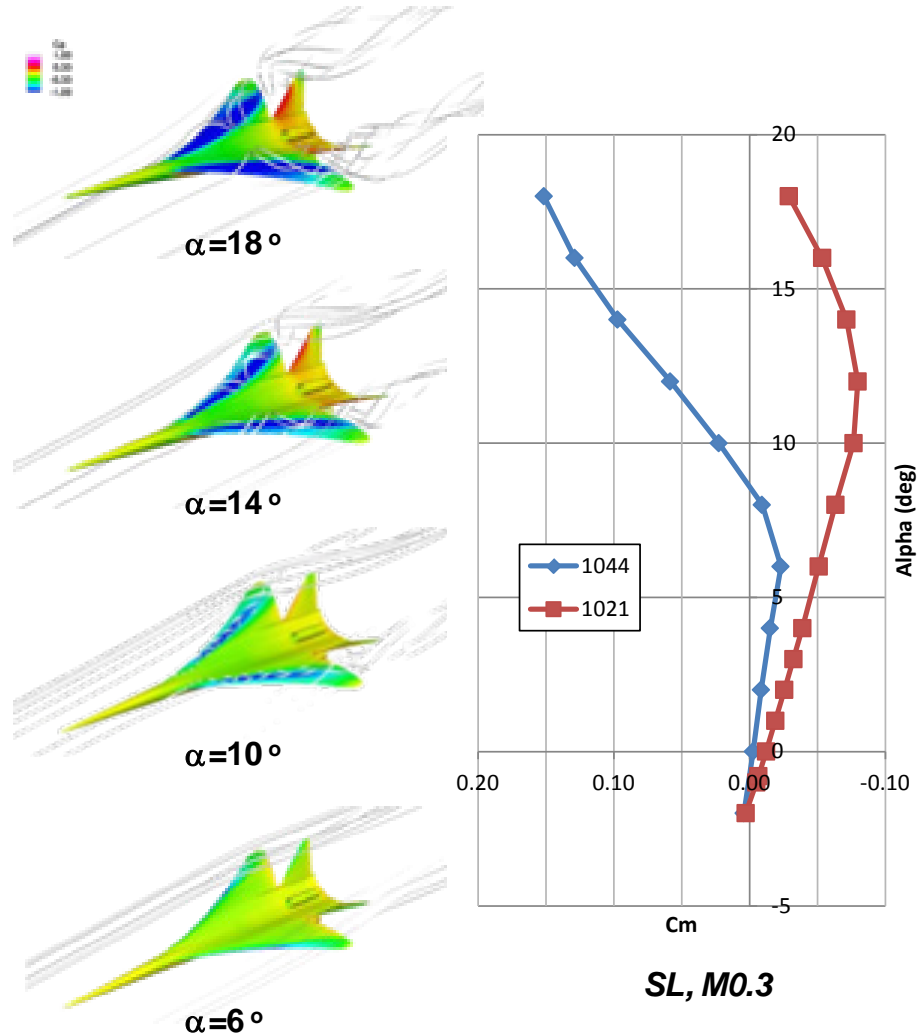


Figure 16.—Configuration 1044 High-Alpha Pitch-Up Due to Wing Apex Vortex Formation

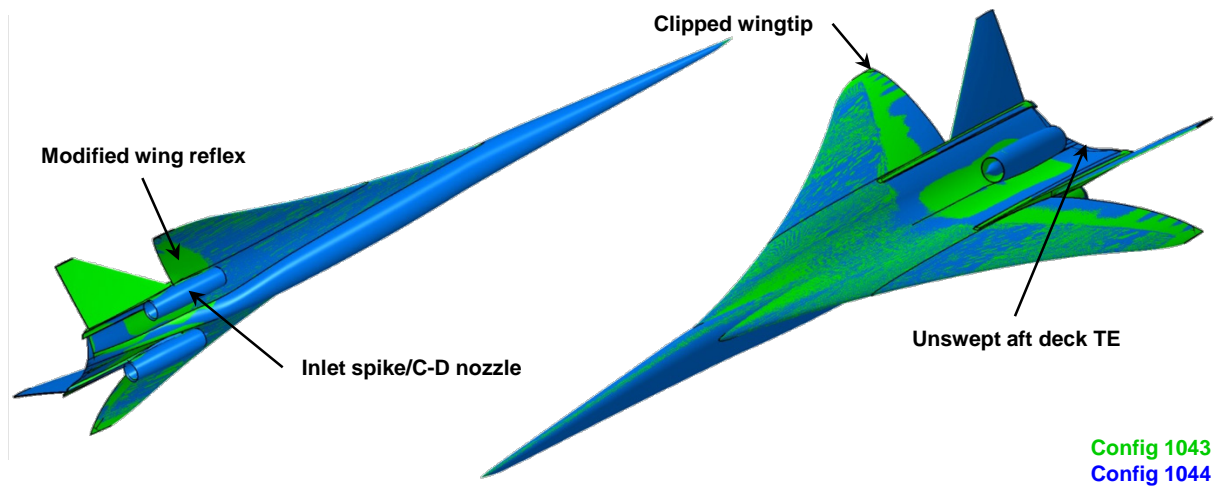


Figure 17.—Configuration 1043 Versus 1044

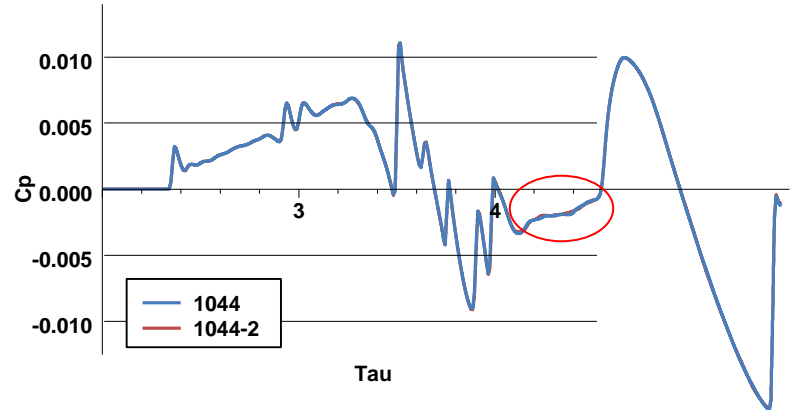
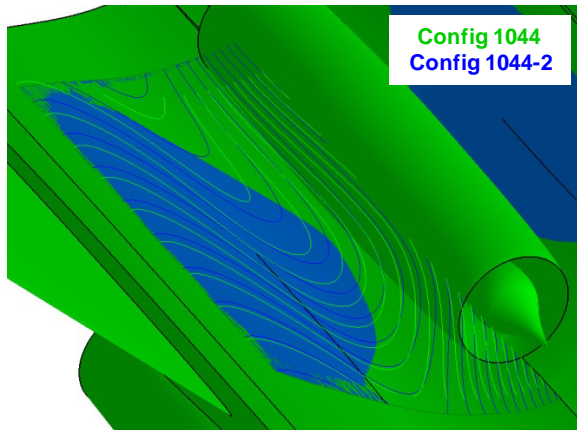


Figure 18.—Configuration 1044 Versus 1044-2

Two additional rounds of modifications were made post-Configuration 1044 to capture new information as they became available. No further update to the 1044-based database were made either because the magnitude of changes was sufficiently small and unlikely to affect the results, or the purpose of modifications was to simply document lessons-learned for future work. The first post-Configuration 1044 update, designated Configuration 1044-2, implemented one of Stanford-recommended OML refinements based on adjoint-based optimization results. CFD analysis predicted the aft-deck upper surface modification reduce drag by approximately one-percent with negligible effect to the boom signature, Figure 18. Additional discussion on Stanford adjoint-based optimization can be found in Appendix C. The modified OML was used in the design of both LTWT and LM4 wind tunnel models.

Configuration 1044-3b served as a repository of design changes based on discipline analysis results, Figure 19. Captured OML modifications include: aft-deck-fuselage fillet to remove load path discontinuity; enlarged outboard engine pylons to increase structure stiffness; scaled inlet to match engine mass flow requirement; simplified, nonexport control GE plug nozzle and nacelle closeout; straightened aft-deck TE to improve body flap integration; and raised v-tails to reduce interaction with wing root vortices at high-alpha. Configuration 1044-3b OML was used to perform propulsion system sensitivity trades (see Section 2.5.3).

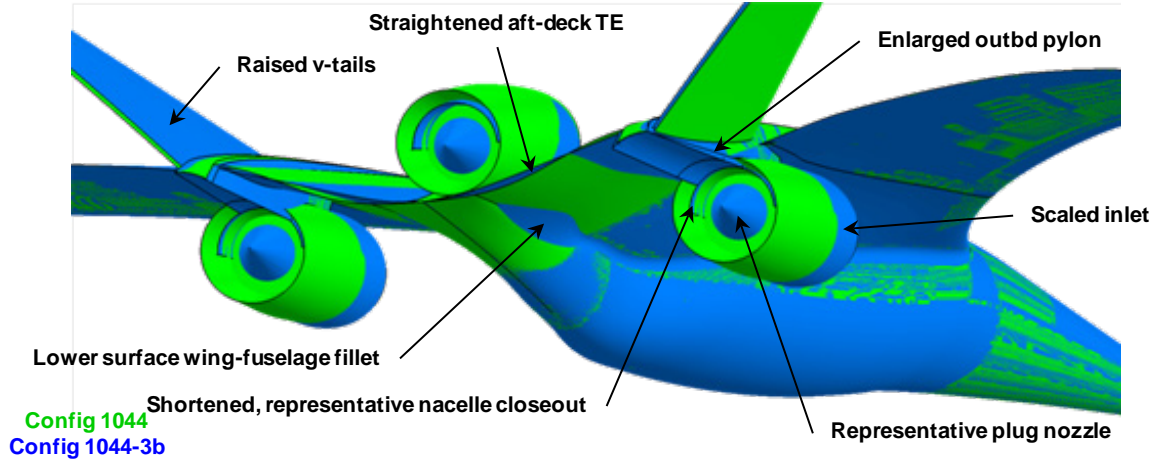


Figure 19.—Configuration 1044 Versus 1044-3b

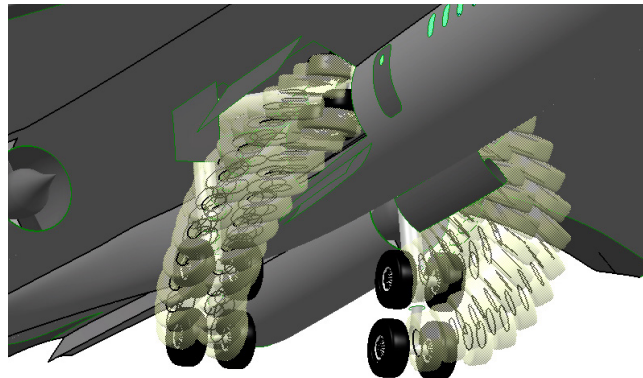


Figure 20.—Main Landing Gear Retraction Concept

2.3.2 Landing Gear Integration

Configuration 1044 posted some inherent landing gear integration issues. The high-wing arrangement led to an elevated CG and favored a wide wheel track to produce an acceptable turnover angle. However, the location of the outboard engines constrained the span-wise location of the wing-mounted main gear. Main gear ground contact point, and hence the length of the main strut, is defined by tip-back and tail-strike angles. The extended length prevented the main gear from retracting directly inboard into the fuselage, and instead required a forward and inboard retracting scheme with a highly-inclined trunnion axis, Figure 20. The nose gear is located as far forward as static load distribution permits to minimize forward fuselage cantilever, as well as maximize the base of the turnover angle. Static nose gear load varies from 7.5-percent at TOGW to 9.6-percent at ZFW. The 25.5x8.0-14 nose and H44.5x16.5-21 main tires were selected assuming a seven-percent safety factor and zero-growth due to the stringent vehicle weight limit imposed by boom signature requirements.

The location of the nose and main gear relative to the TE-mounted outboard engines is a potential FOD (foreign object damage) concern. As illustrated in Figure 21, debris and water spray kicked up by the nose wheels have a direct path to the engine inlet. Although the same cannot be said for the main wheels, objects dislodged from the main wheelwell either on the ground or in flight could be ingested by the engine depending on the strength of inlet suction and object's trajectory. Additional analysis is needed to characterize the flow field around the inlet to determine the probability of such occurrence.

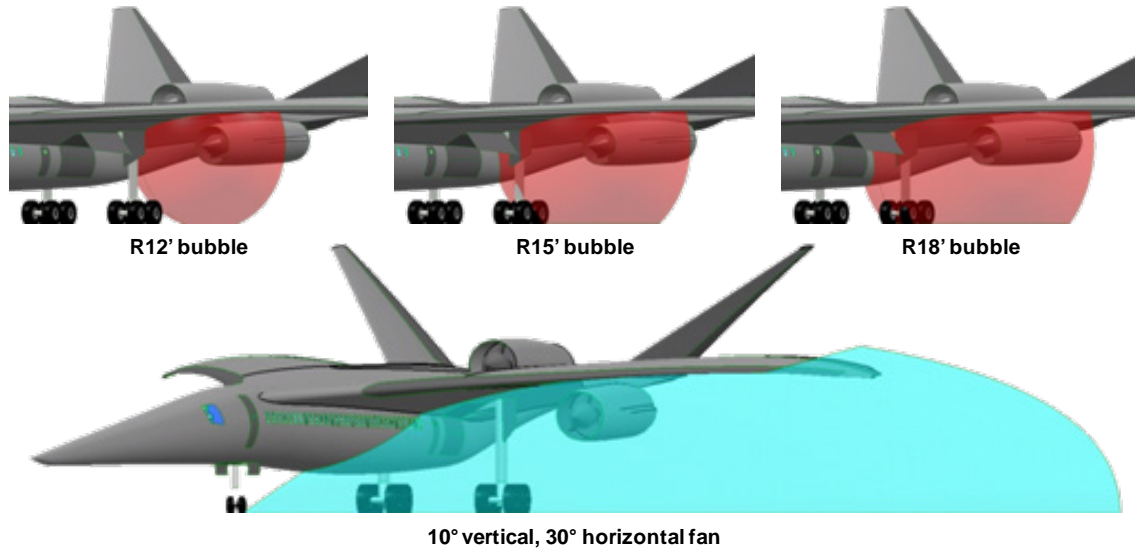


Figure 21.—Engine FOD Considerations: Inlet Suction (top) and NLG Water Spray

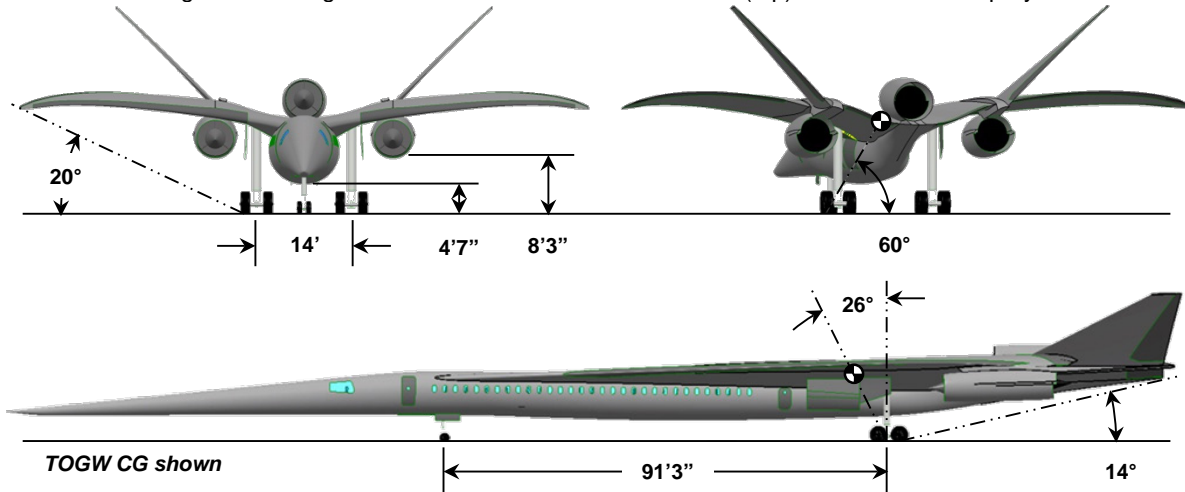


Figure 22.—Configuration 1044 Ground Operation Clearance

Configuration 1044 ground clearances are shown in Figure 22. The fuselage is nearly level with a minimum ground clearance of 4 ft, 7 in., while the bottom of the outboard nacelles is over 8 ft off the ground. Tail-strike angle is 14° with ample clearance for control surface deflection. Turnover angle, ranging from 58° at ZFW to 60° at TOGW, is comparable to typical high-wing transports but considered borderline for ground-based aircraft. Minimum turning radius is 52 ft, 8 in. assuming a maximum nose wheel steering angle of $\pm 60^\circ$, allowing the aircraft to make a 180° turn on a 150-ft wide runway.

2.3.3 Vehicle Packaging

Configuration 1044 inboard profiles are shown in Figure 23. The simplistic bones, developed based on common practices and prior supersonic aircraft design experiences, were used to define major load paths and usable volume. The layout also served as starting reference for the detailed structure layout in support of FEM analysis (see Section 3.4). 26-in. fuselage frame spacing was selected assuming composite sandwich skin with improved buckling strength over conventional aluminum structure. Longerons, keels and fuselage tube together provided longitudinal bending stiffness. Wing bending loads were carried inboard via spars orientated parallel to wing TE and into the wing box located aft of the main wheel well, while shear ties were used to transfer loads into fuselage frames in the absence of wing

carry-throughs in the main cabin. The slender, boom shaping nose forward of cockpit is treated as a light-weight aerodynamic fairing.

The location of the full-depth main wheel well effectively established the aft-most limit of the main cabin, resulting in a forward CG bias with the passenger aboard. The main wheel well also prevented the cargo hold, which is required to be pressurized to accommodate live cargo, being located directly aft of the cabin. As such, two separate pressure vessels are required, resulting to design inefficiencies and weight penalties. The fuselage under-floor space is of insufficient height to carry cargo and is used primarily for ducting, plumbing and wire routing.

Wing, aft-deck and center wing-box fuel tanks were laid out to counteract the forward payload CG and to minimize the need of in-flight fuel pumping and/or ballast to maintain desired vehicle attitude. Total fuel capacity is 176,000 lb assuming an 80-percent packaging factor. Aircraft subsystems, as functionality permits, were clustered toward the rear of the vehicle aft of the cargo hold to take advantage of the available volume, as well as shifting aircraft empty weight CG further aft.

2.3.4 Cabin Layout

Phase 2 baseline cabin layout assumed 80 passengers in two-class seating arrangement, Figure 24. Note that the fuselage still has a slight bulge around the mid-section due to equivalent area matching. The goal is to completely eliminate the cross-section variation to simplify cabin layout and to reduce manufacturing complexity. Two Type B exit doors are located in the front and two Type C service doors in the rear of cabin. Overhead emergency exits are envisioned for water-landing evacuation, where the cabin is likely to be submerged due to the high-wing arrangement. The 10- by 18-in. windows are spaced 26 in. apart, providing each seat-row with at least one window to reduce claustrophobia.

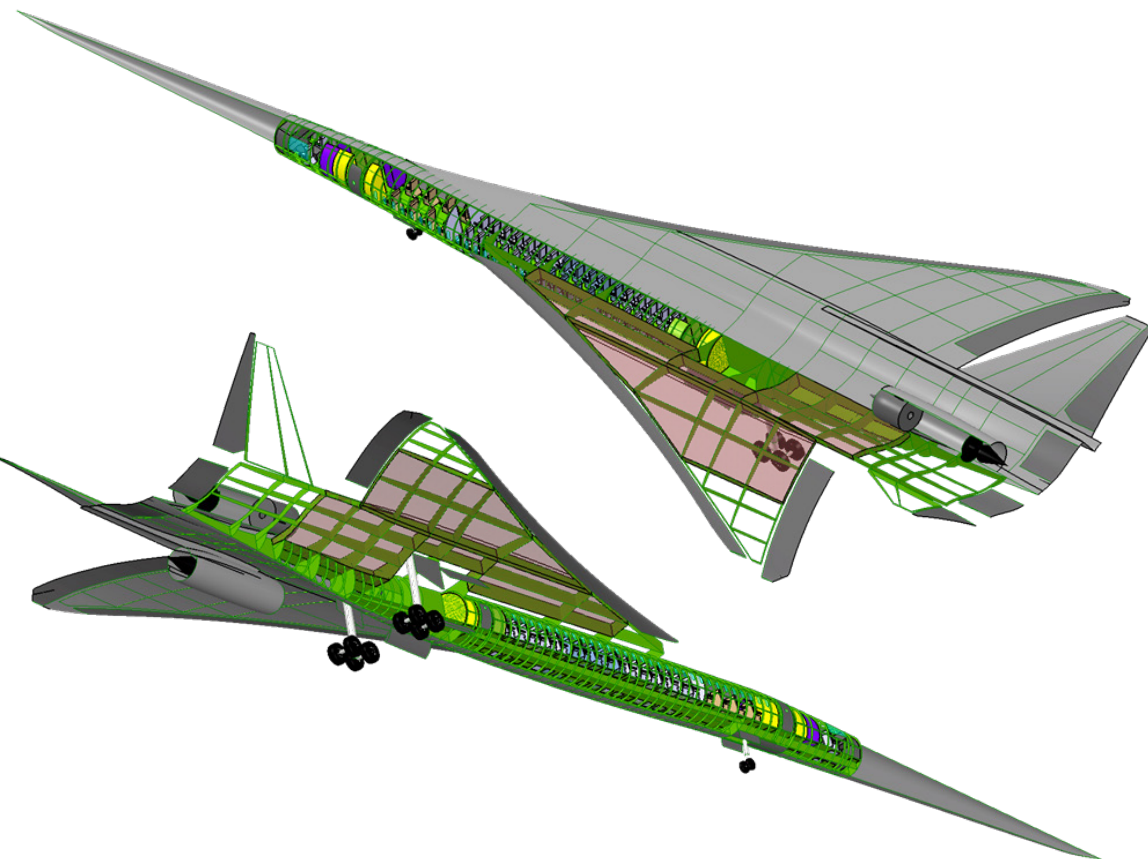


Figure 23.—Configuration 1044 Inboards

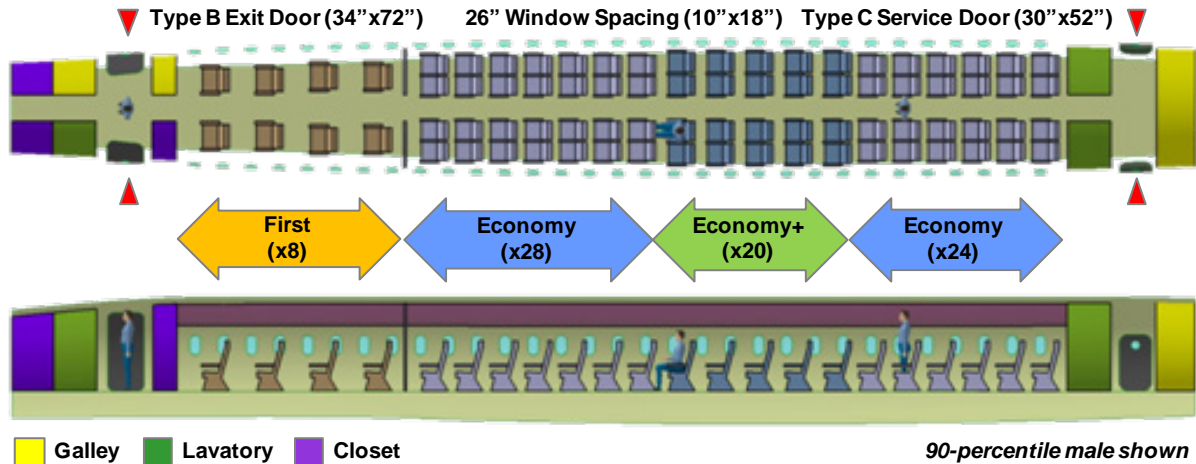


Figure 24.—Two-Class, 80 Passenger Cabin Layout

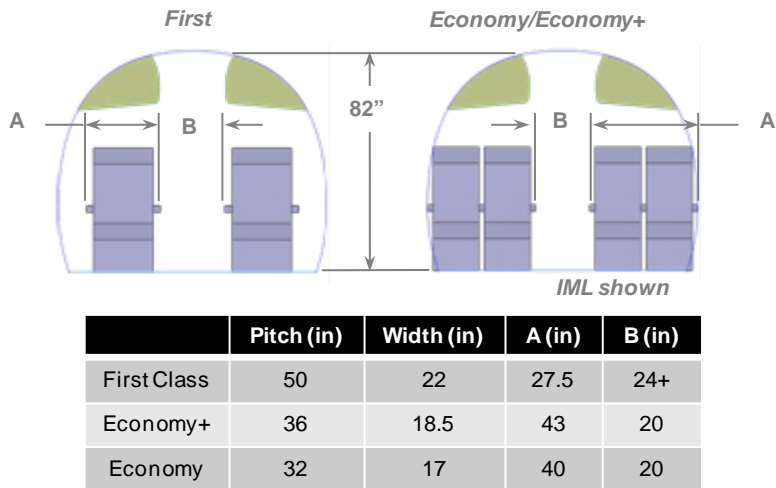


Figure 25.—Nominal Passenger Cabin Cross-Section

The First-class section featured eight 50-in. pitch seats in two-abreast arrangement and is serviced by the forward galley and lavatory located adjacent to the forward exits. The Economy-class section featured 72 32-in.-plus pitch seats in four-abreast arrangement and is serviced by a pair of lavatories and the aft galley. Nominal cabin cross-sections are shown in Figure 25. Seat-width varied from 22 in. in the First-class to 17 in. in Economy-class. Aisle height is 82 in. throughout the cabin, with a slight reduction forward of the forward exits due to nose droop. Minimum aisle width is 24 in. in the First-class and 20 in. in the Economy-class. Overhead bins are sized to accommodate standard carry-on luggage, while additional closet space are located forward of the First-class section.

2.3.5 Mass Properties

Parametric weight estimation developed under Phase 1 effort was reviewed for accuracy before being adopted for Phase 2 work: weight double-bookings were eliminated; vehicle model was updated to reflect the change in configuration; assumptions and known component weights were updated. Configuration 1044 geometry was then entered into the spreadsheet to generate the detailed weight buildup as shown in Table 4. Note that a 6-percent empty weight margin was added for conservatism, and that the gross weight was limited to 320,000 lb via fuel off-load to match the boom signature-specified vehicle weight.

The effect of the forward payload CG is evident given the 56-in./0.06MAC CG shift between OEW and ZFW. Using fuel to counteract the payload CG shift proved effect, as the TOGW CG was returned to FS2,045/0.51MAC.

TABLE 4.—CONFIGURATION 1044 WEIGHT STATEMENT

AN Group	Weight (lb)	X CG (FS) Gear Up
Wing	31,503	2,070.9
Aft Deck	6,934	2,567.9
V-Tail	4,013	2,713.9
Body	15,086	1,554.2
Nose Landing Gear	1,371	931.2
Main Landing Gear	11,096	2,004.2
Nacelle 1	4,260	2,339.1
Nacelle 2	2,363	2,570.9
Inlet 1	1,742	2,285.9
Inlet 2	2,581	2,307.1
Structure	80,949	2,061.5
Engine & Nozzle 1	14,533	2,407.1
Engine & Nozzle 2	7,266	2,533.3
Start & Controls	309	1,957.2
Fuel System	2,506	2,054.5
Propulsion	24,614	2,402.8
Flight Controls	3,525	2,331.4
Aux Power	1,008	2,478.1
Instruments	277	1,353.6
Hydraulics	2,354	2,178.9
Electrical	3,337	2,356.6
Avionics	986	774.8
Furnishings	9,097	1,482.3
ECS	2,688	1,622.4
Load & Handling	54	1,747.2
Systems	23,326	1,834.4
Margin	7,733	2,085.6
EW	136,622	2,085.6
Std Operating Items	2,930	1,109.6
Unusable Fuel and Oil	2,056	2,090.8
Operating Equipment	4,986	1,514.2
OEW	141,608	2,065.4
Passengers	13,600	1,428.1
Baggage	2,400	1,983.9
Payload	16,000	1,511.5
ZFW	157,608	2,009.2
Fuel	162,560	2,079.9
TOGW	320,168	2,045.1

Calculated empty weight and empty weight fractions were compared against developmental and production supersonic cruise aircraft, Figure 26. As illustrated, the predicted empty weight show high correlation with historical trend, while empty weight fraction fell into the low end of the range primary due to the application of advanced light-weight composite materials.

First-pass fuel-burn sequence was used to create the in-flight CG envelope shown in Figure 27. The aircraft is shown to be neutral to stable in-flight throughout the entire mission. Although the stated goal is to achieve supersonic cruise attitude without aerodynamic trim, the vehicle as currently configured could not meet the objective with fuel management alone. However, potential aeroelastic consideration-driven structure thickening could increase aft-deck fuel volume and shift the CG envelope to the right.

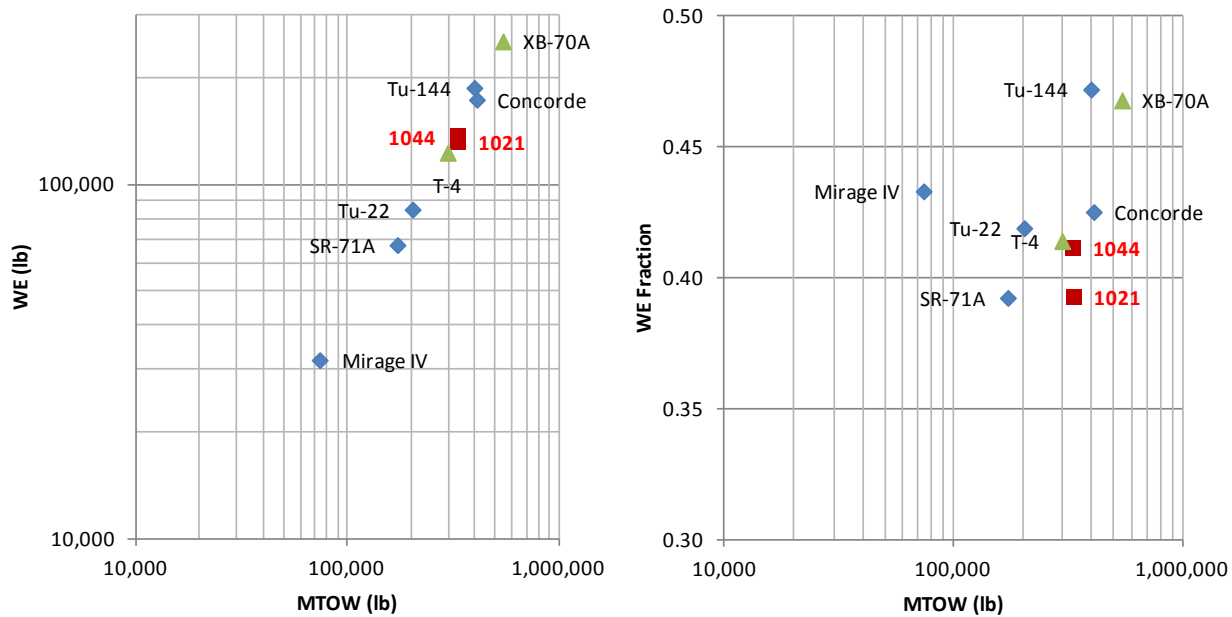


Figure 26.—Empty Weight (left) and Empty Weight Fraction (right) Comparison

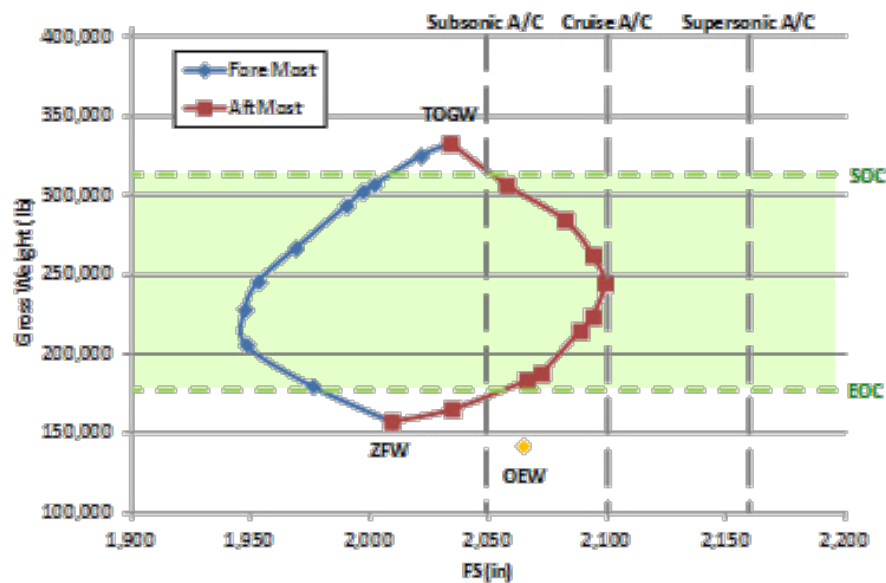


Figure 27.—Configuration 1044 In-Flight CG Envelope

2.3.6 Aerodynamics

Navier-Stokes CFD-based aerodynamic database was developed with Configuration 1044 OML and used in performance and sizing analysis. Forces and moments were calculated with realizable k-e turbulent model at specific Mach/altitude combinations. Drag polar and L/D versus CL plots at 40,000 ft are shown in Figure 28, Figure 29, respectively. Configuration 1021 and 1044 maximum L/D versus Mach comparison is shown in Figure 30. Overall, Configuration 1044 subsonic performance is slightly worse due to added aft-deck wetted area, while supersonic performance is similar. Further drag reduction is possible using Stanford adjoint-based optimization.

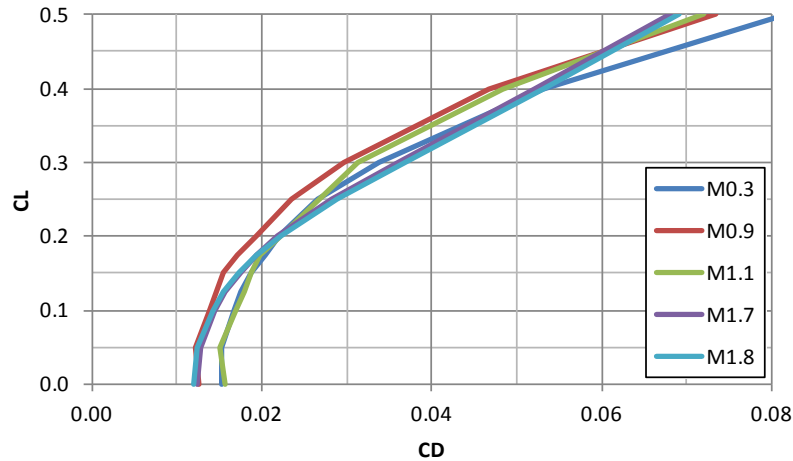


Figure 28.—Configuration 1044 Drag Polars

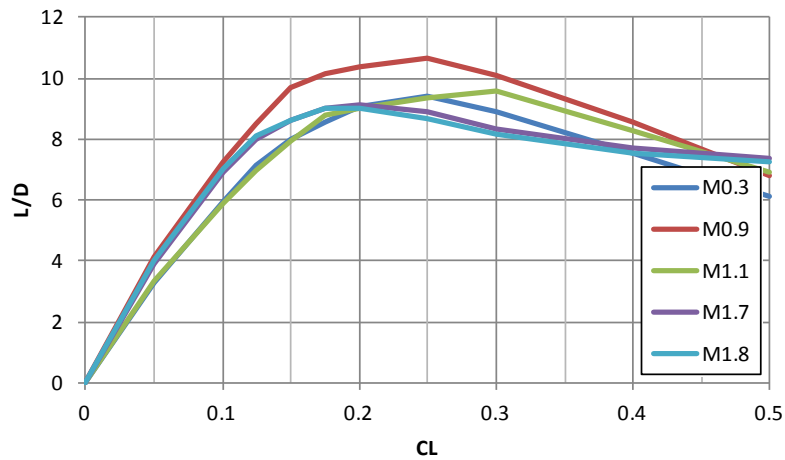


Figure 29.—Configuration 1044 L/D Versus CL

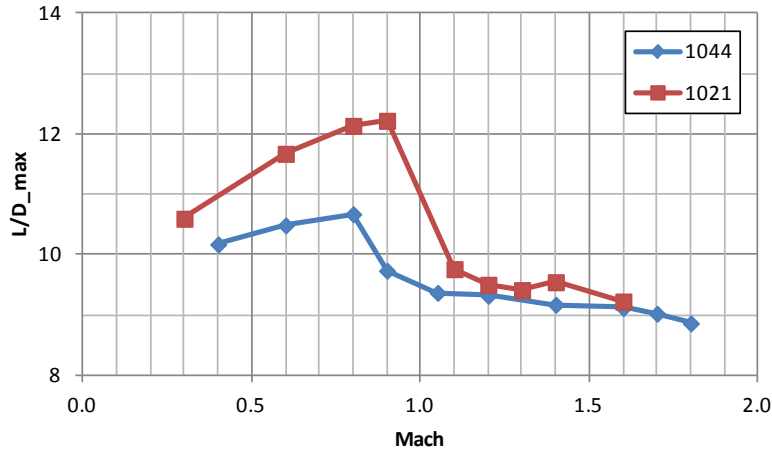


Figure 30.—L/D_{max} Versus Mach Comparison

2.4 Vehicle Sizing and Mission Performance

Vehicle sizing and performance analysis were conducted using ASSET mission code with fixed-geometry/weight option, i.e., the vehicle was not optimized and the range is a fallout of available fuel. The default maximum range mission profile is shown in Figure 31. The mission started with a 5-min ground warm-up/takeoff, followed by a 250 KEAS climb to 10,000 ft, where the vehicle performed a level acceleration to M0.9 before climbing again at 360 KEAS. Upon reaching 36,000 ft, the vehicle performed a level transonic acceleration to M1.28 before initiating the final climb to best cruise altitude at 400 KEAS. Cruise climb with a ceiling of 60,000 ft was employed to achieve best L/D and range. At the end of the cruise, the vehicle decelerate from cruise Mach to M1.4 at altitude before initiating a 250 KEAS descent to 10,000 ft, where it loitered for 5 min at best endurance before landing with an 8-percent reserve. Note that no distance and time credits were given to both loiter and landing.

For the low-boom mission, in which case the TOGW was limited to 283,000 lb via fuel offload, the transonic acceleration altitude was raised from 36,000 to 40,000 ft to reduce boom loudness while everything else remained unchanged.

Design space sweep with TOGW and ESF variations was performed to identify the optimum combination that delivers maximum range. Baseline GE62_LFL4 engine thrust and TSFC were scaled using ESF. At any given TOGW, payload weight remains fixed while engine weight, and hence OEW, is a function of ESF. The difference in OEW then became the fuel weight delta that is applied to the baseline fuel weight.

For the design space sweep, TOGWs of 300,000, 320,000 and 340,000 lb and ESFs of 1.0, 1.1, 1.2, and 1.3 were selected. Results were plotted against fuel volume and balanced field length constraints and shown in Figure 32. For the un-sized Configuration 1044, an additional 150 nmi range can be gained either by fixing the TOGW at 320,000 lb while up-sizing the engine by 15 percent, or by increasing gross weight to 330,000 lb, i.e., maximum fuel capacity (red limit on plot), while holding the ESF to 1.0. Further improvement in range can be achieved by increasing both TOGW and ESF at the same time. The shape of the plot indicated maximum range occurs somewhere between ESF of 1.1 and 1.2 across TOGW range considered. Using maximum fuel weight as constraint, a design point corresponds to a TOGW of 335,000 lb and ESF of 1.15 were selected and designated as Configuration 1044-X. Estimated balanced field length is in the low 10,000s, matching subsonic vehicles like 747-400 and near Concorde's mid-9,000s.

Figure 33 compares Configuration 1044-X as-flown maximum-range and low-boom mission profiles and performance, while detailed mission statements are given in Table 5 and Table 6, respectively. While the data show some subtle differences such as initial cruise altitude and climb cruise profile, the vehicle

was able to achieve an average cruise L/D of 8.7 in both missions. For the maximum-range case, the vehicle is capable of reaching a destination 5,500 nmi away in just over 6 hr. As of the low-boom case, airport-to-airport distance is 4,150 nmi with a 4.8-hr trip time.

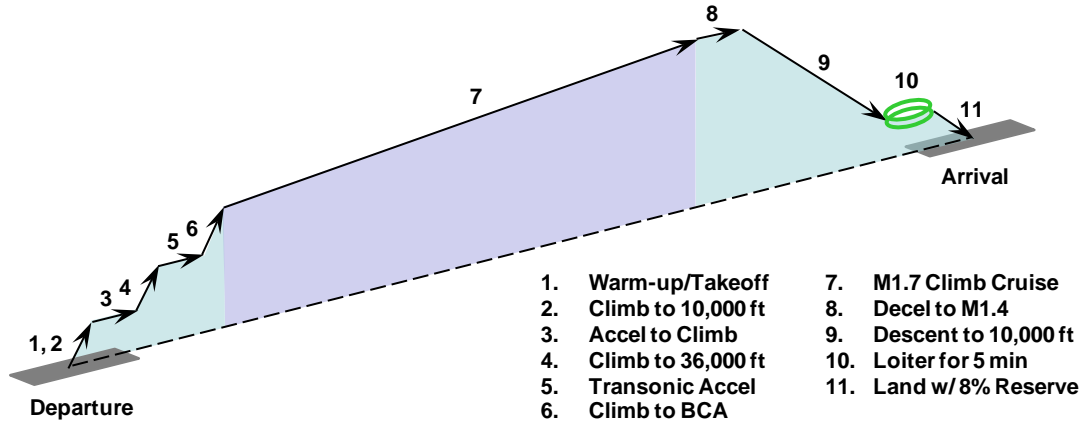


Figure 31.—Sizing Mission Profile

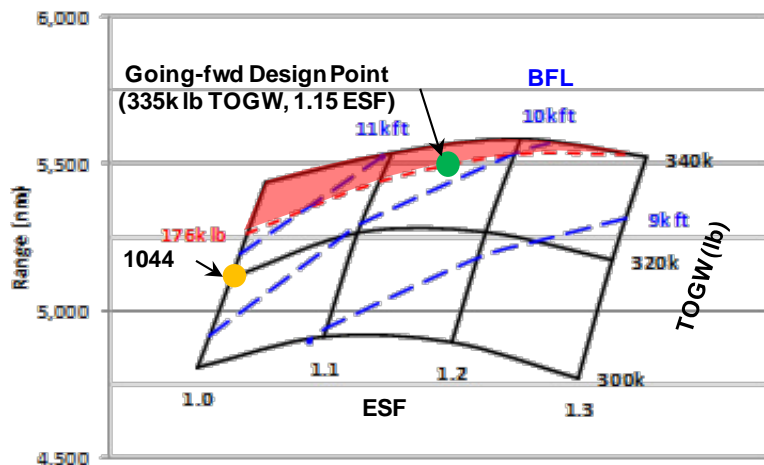


Figure 32.—N+2 Phase 2 Design Space

TABLE 5.—DETAILED MISSION STATEMENT AND MAXIMUM RANGE

Segment	Description	Initial alt (ft)	Initial Mach	Initial weight (lb)	Seg fuel (lb)	Seg distance (nmi)	Mission time (min)	Average L/D	Average SFC
1	WUTO	0	0.00	335,000	1,245	0	5.0	-----	0.71
2	Climb	0	0.38	333,755	3,391	10	7.2	7.61	0.89
3	Accel	10,000	0.45	330,364	992	4	7.9	9.68	0.94
4	Climb	10,000	0.66	329,372	7,719	68	16.0	10.20	1.03
5	Accel	36,000	0.90	321,653	4,992	65	22.4	9.35	1.06
6	Climb	36,000	1.28	316,661	6,773	97	29.2	8.73	1.14
7	Cruise	48,000	1.70	309,888	133,216	5,088	342.3	8.73	0.94
8	Decel	60,000	1.70	176,672	93	22	343.8	9.21	2.95
9	Descent	60,000	1.42	176,579	1,972	146	363.9	10.47	2.32
10	Loiter	10,000	0.50	174,608	1,341	0	368.9	10.49	0.97
11	Reserve	-----	----	-----	14,0808	-----	-----	-----	-----

TABLE 6.—DETAILED MISSION STATEMENT, SHAPED BOOM

Segment	Description	Initial alt (ft)	Initial Mach	Initial weight (lb)	Seg fuel (lb)	Seg distance (nmi)	Mission time (min)	Average L/D	Average SFC
1	WUTO	0	0.00	283,000	1,245	0	5.0	-----	0.71
2	Climb	0	0.38	281,755	2,377	7	6.5	8.84	0.89
3	Accel	10,000	0.45	279,377	742	3	7.1	10.24	0.94
4	Climb	10,000	0.66	278,636	7,549	77	16.2	9.91	1.04
5	Accel	40,000	0.90	271,087	5,593	85	24.4	9.25	1.09
6	Climb	40,000	1.41	265,494	3,806	59	28.4	8.22	1.16
7	Cruise	51,000	1.70	261,688	89,386	3,753	259.3	8.74	0.95
8	Decel	60,000	1.70	172,210	92	22	260.7	9.71	2.95
9	Descent	60,000	1.42	172,210	1,976	146	280.9	10.43	2.32
10	Loiter	10,000	0.50	170,233	1,329	0	285.9	10.40	0.98
11	Reserve	-----	----	-----	9,920	-----	-----	-----	-----

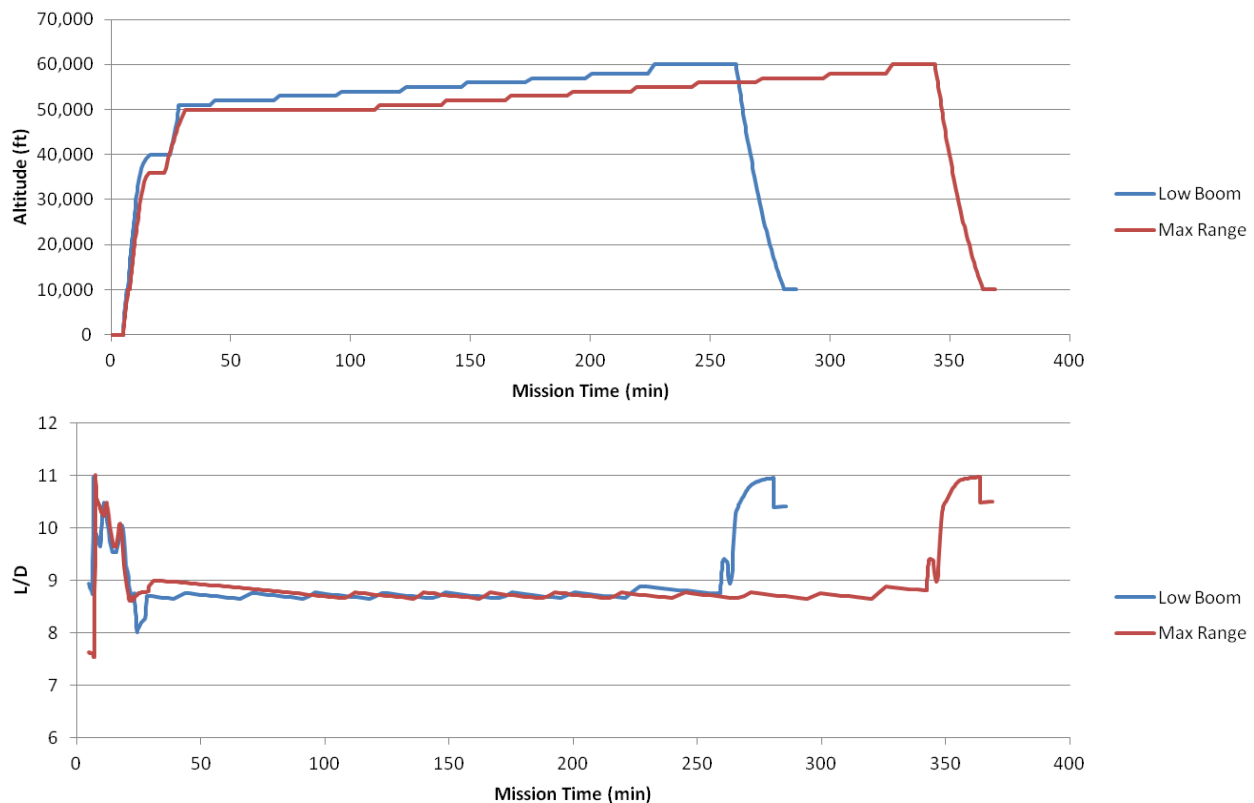


Figure 33.—Mission Performance Comparison: Flight Profile (top) and L/D (bottom)

2.4.1 Vehicle Airport Operations and Configuration

The 1044-X vehicle takes advantage of unique supersonic configuration characteristics during takeoff and landing operations. An N+2 vehicle and propulsion system is sized and designed to the certification noise conditions. Generally sideline noise is dominant. Our propulsion solution balances the sideline noise and thrust requirement with the cruise thrust requirement to develop a solution that satisfies both as efficiently and with a light of a propulsion system as possible. It has been LM's objective to reduce the

stringency of the takeoff thrust and throttle setting through integrated exploitation of propulsion, airframe, acoustics, certification rules and safety considerations. The operational procedures result in relatively high speeds with greater excess power, for lower throttle settings and thereby lower noise (particularly for critical noise conditions). Further as a noise sized vehicle, N+2 designs must incorporate comprehensive noise reduction technologies throughout: turbomachinery, combustors, inlet (acoustic liners, choking), nozzle, airframe (gap seals), propulsion-airframe interaction (acoustic liners), flaps (unslotted), landing gear (shrouds) and airframe excrescences (streamlined). Table 7 tabulates characteristics for airframe noise calculations.

TABLE 7.—GENERAL CHARACTERISTICS FOR AIRFRAME NOISE CALCULATION

Trailing Edge Noise		Flap/Elevon Side Edge					
Maximum takeoff weight, lb	322,000						
Maximum landing weight, lb	220,000	Number of flap side edges	6				
Wing area, ft ²	3,600	(For each flap side edge)					
Wing span, ft	83.8	Flap chord, ft	11.67	8.33	8.33	6.33	6.33 4.42
Horizontal tail area, ft ²	545 (total)	Flap maximum thickness at side edge, ft	1.125	0.7	0.7	0.5	0.5 0.32
Horizontal tail span, ft	14.7 (1 side)	Flap sweep angle, deg	39	39	39	39	39 39
Vertical tail area, ft ²	N/A	Flap span, ft	10.75	10.75	6.6	6.6	6.6 6.6
Vertical tail span, ft	N/A	Flap deflection angle, deg - Approach	25	25	20	20	0 0
		Flap deflection angle, deg - Sideline	10	10	10	10	0 0
		Flap deflection angle, deg - Cutback	10	10	10	10	0 0
		Flap lift coefficient - Approach	1.5	1.5	1.25	1.25	0.25 0.25
		Flap lift coefficient - Sideline	0.75	0.75	0.75	0.75	0.25 0.25
		Flap lift coefficient - Cutback	0.75	0.75	0.75	0.75	0.25 0.25
		Total lift coefficient - Approach	0.767				
		Total lift coefficient - Sideline	0.548				
		Total lift coefficient - Cutback	0.515				
Main Landing Gear		Slat					
Number of main gear	2	Number of slats per wing	4				
Number of tires per main gear strut	4	(For each slat)					
Main gear alignment angle, deg	0	Slat chord length, ft	2	2	2	2	
Main gear strut length, ft	11	Slat span length, ft	21	16.4	26.7	24	
Main gear strut diameter, ft	1.33	Slat sweep angle, deg	75	72	67	67	
Main gear tire diameter, ft	3.7	Slat gap (inches) - Approach	0.25	0.25	0.25	0.25	
Main gear tread width, ft	1.25	Slat gap (inches) - Sideline	0.25	0.25	0.25	0.25	
Local flow velocity into gear (ft/sec)	265	Slat gap (inches) - Cutback	0.25	0.25	0.25	0.25	
Nose Landing Gear		Slat deployment angle, deg - Approach	35	35	35	35	
Number of nose gear	1	Slat deployment angle, deg - Sideline	35	35	35	35	
Number of tires per strut of nose gear	2	Slat deployment angle, deg - Cutback	35	35	35	35	
Nose gear strut length, ft	4.4	Slat lift coefficient - Approach					
Nose gear strut diameter, ft	0.6	Slat lift coefficient - Sideline					
Nose gear tire diameter, ft	1.1	Slat lift coefficient - Cutback					
Nose gear tread width, ft	0.67	Total lift coefficient - Approach	0.767				
Local flow velocity into gear (ft/sec)	280	Total lift coefficient - Sideline	0.548				
		Total lift coefficient - Cutback	0.515				

* The landing gear are intended to have strut/linkage shrouding that reduce their wake about 60 percent and anti-FOD (xFOD) spats over the wheels that also reduce drag and noise

Flap to flap edges should have flexible seals during same deflection and LE simple flap deflects as one with flush seals between every segment.



Figure 34.—Global Shaped Boom Supersonic Service Network

Figure 34 shows the potential global supersonic service network based on the predicted Configuration 1044-X performance. Although the envisioned vehicle does not have the range to provide nonstop service between some extremely distance city-pair, i.e., Los Angeles to Dubai, a one-stop flight with a stop-over at London can still significantly reduce actual flight time, 8.8 versus 16.5 hr.

2.5 Propulsion Integration and Sensitivity Analysis

Propulsion system was continuously updated during Phase 2 effort. The flow-through nacelles were first updated with notional inlet centerbody and convergent-divergent nozzle, and later with LM-developed M1.7 inlet and GE-furnished nozzle and closeout lines. Off-design and grid-size sensitivities were examined to guide future effort.

2.5.1 Inlet Design

A clean-sheet, M1.7 inlet was developed to improve propulsion system realism as well as to assess low-speed fan noise characteristics. The inlet is of bleed-less, external-compression type developed based on 2D MOC analysis, with geometrical parameters (capture area, strut axial location, etc.) referenced to GE62_FLF fan diameter, Figure 35. The nonmoving axisymmetric center-body is supported by three radial struts positioned at 0°, 130° and 230° to reduce flow resonance. Note that actual geometry of the GE fan spool has yet to be defined, resulting in the mismatch at the fan face interface that will need to be revised in the future.

Figure 36 shows the inlet recovery Caine curve. The peak performance corresponds to fan face Mach of 0.525 and corrected mass flow rate of 831 lb/sec, which is approximately four-percent less than the 860 lb/sec required by the 1.0-scale GE62_FLF4 engine. As such, the as-drawn inlet capture area need to be increased in the next design iteration to match performance requirements.

Figure 37 shows the peak recovery versus free-stream Mach plot with the inset showing engine fan face pressure recovery map. As illustrated, boundary layer buildup and flow separation over the center-body resulted in a significant region of low pressure around the hub. Future design iterations will attempt to reduce flow distortion through center-body/strut shaping and boundary layer control techniques such as microvanes and boundary layer blowing.

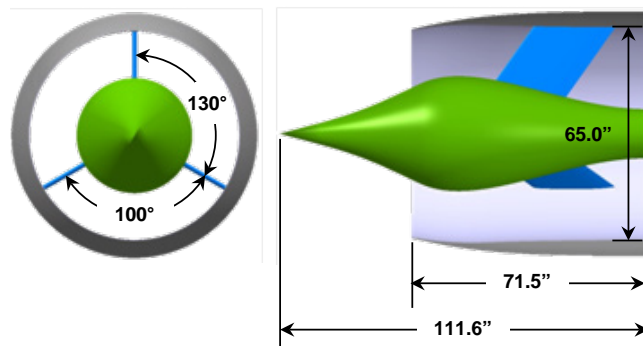


Figure 35.—N+2 Phase 2 Mach 1.7 Inlet

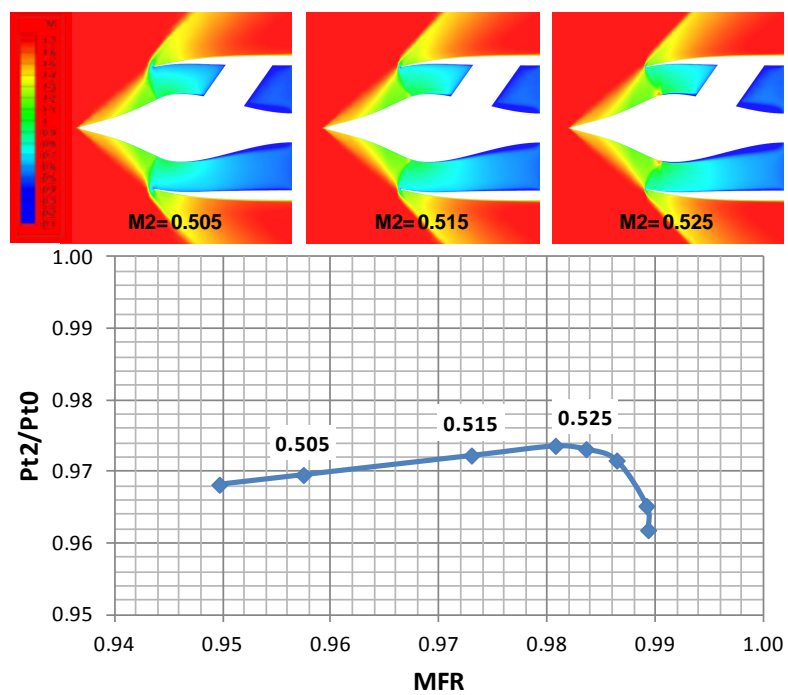


Figure 36.—Mach 1.7 Inlet Recovery Caine Curve

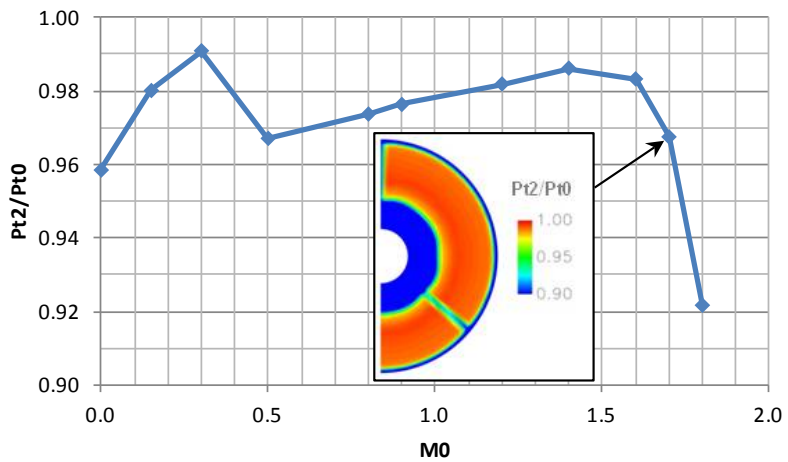


Figure 37.—Inlet Peak Recovery Versus Free-Stream Mach

LM is pleased to note that the M1.7 inlet was independently evaluated by NASA and received favorable reviews. The first-pass inlet with its strikingly short diffuser duct achieved the same critical performance level as the Gulfstream Dual Stream Inlet (0.965 at 0.972 vs. 0.965 at 0.969, respectively) yet with the simplicity of the Gulfstream Single Stream Inlet. Stability margin at the design cruise Mach was found to be greater or equal to 45-percent, well above the HSCT goal of 10-percent. The inlet is also tolerant to changes in free-stream Mach, capable of operating between M1.6 and M1.8.

2.5.2 Auxiliary Inlet Design

Translating cowl ahead of center-body strut LE was selected to provide auxiliary airflow during low-speed operations. Note that actuation mechanism and support structure has yet to be defined. Figure 38 shows the M0.1 and M0.3 flow characteristics and performance of the inlet with the cowl extended. Insufficient lip radius at the cowl and nacelle lips resulted in nonideal flow separation at very low speed but improves with increasing Mach. Translating shroud to increase lip radius is being investigated to improve pressure recovery. Overall fan face pressure recovery at M0.01 and M0.3 is 0.872 and 0.989, respectively.

2.5.3 Propulsion System Sensitivity Analyses

Exhaust plume and grid adaptation sensitivity analyses were performed to assess the effects of NPR and grid density variations. The analyses were based on Configuration 1044-3b OML with the most up-to-date propulsion geometry: 1.04-scale M1.7 inlet; GE FluidShield nacelle closeout, and simplified, nonproprietary GE plug nozzle, Figure 39.

The impact of plume size on signature was evaluated by varying NPR. Figure 40 shows the effect of reduced NPR signature. The loss of lift associated with reduced plume size allowed the aft shocks to coalesce and increased the boom loudness.

Boom signature sensitivity due to grid density was evaluated to determine the suitability and cost-effectiveness of grid adaption. As illustrated by Figure 41 and Figure 42 grid adaption provides better resolution of flow features around and inside the nacelle. Comparison of predicted signature shows a small (approximately 1 PLdB) but measureable impact primarily due to reduced inlet spillage with the adapted grids. However, the improved fidelity came with a price, namely, an approximately eight-fold increase in computational cost as the number of cells ballooned from four million un-adapted to 19 million adapted. As such, un-adapted grids are preferred at the conceptual design stage where rapid configuration turn-around is required, while adapted grids are more suitable for high-fidelity signature predictions prior to design-freeze. Furthermore if the correct amount of spillage is known, the inlet boundary condition of the un-adapted solution could be adjusted to match, producing even more nearly the same result as the adapted solution.

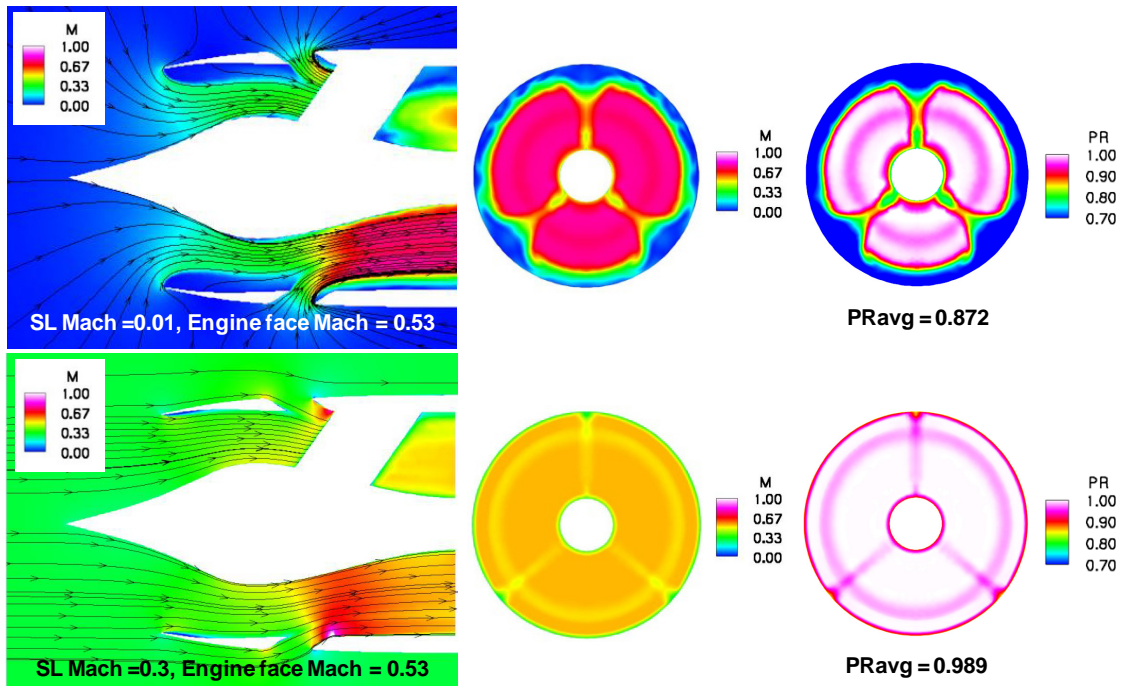


Figure 38.—Streamline (left), Mach (center) and Pressure Recovery (right) Maps

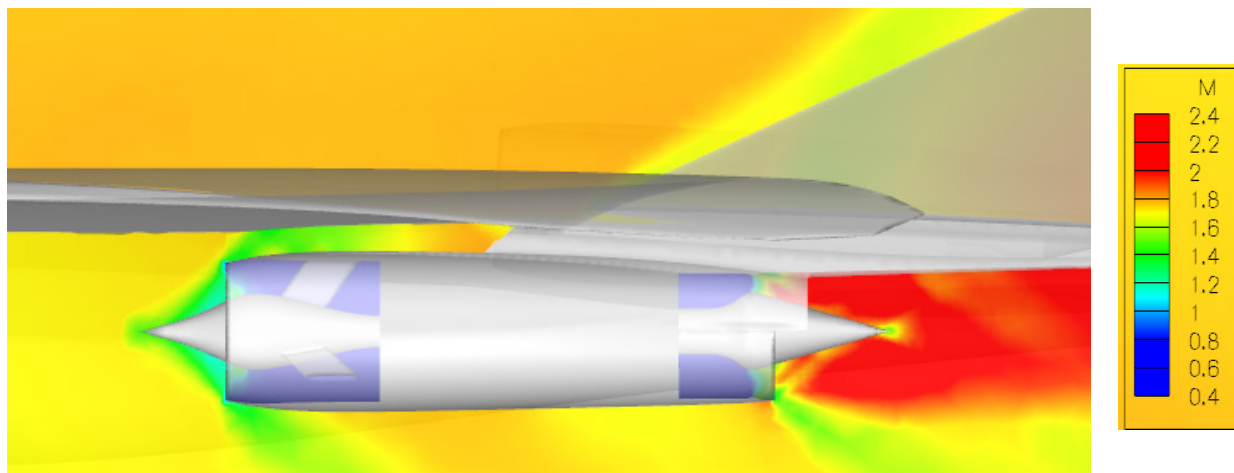


Figure 39.—Configuration 1044-3b scaled M1.7 Inlet and Non-Proprietary Plug Nozzle

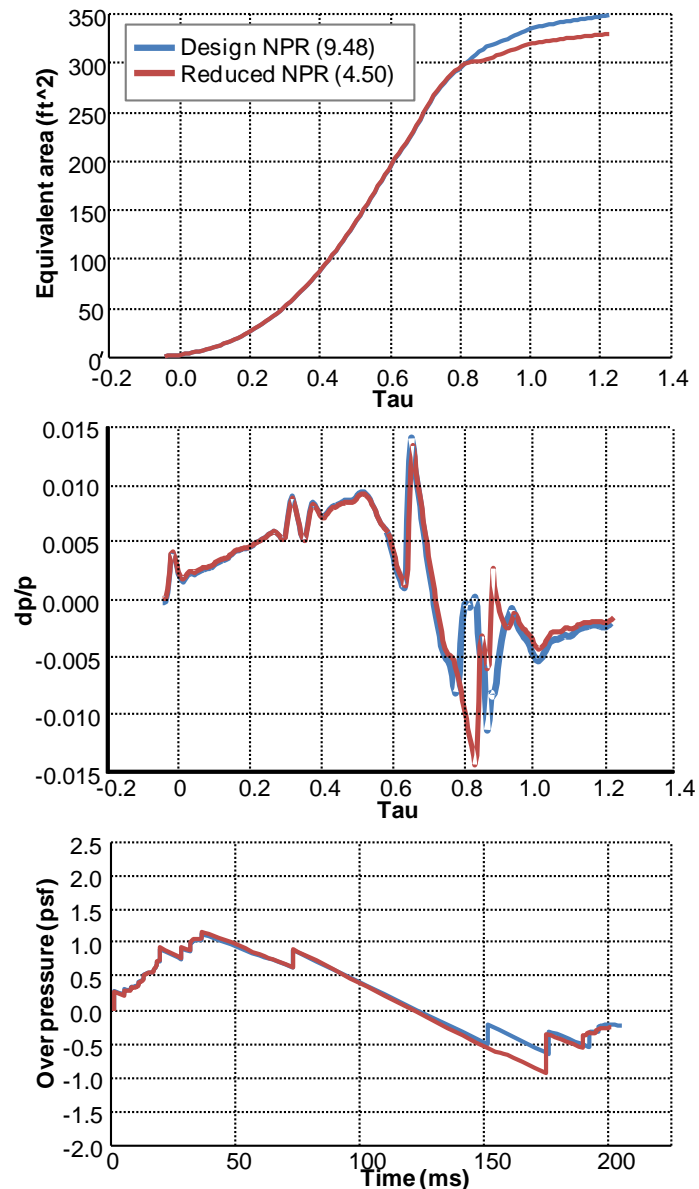


Figure 40.—Plume effects on Equivalent Area (top), 5.6 R/(b/2) Signature (middle) and Ground Signature (bottom): Configuration 1044-3b, SOC 4,000 nmi Mission

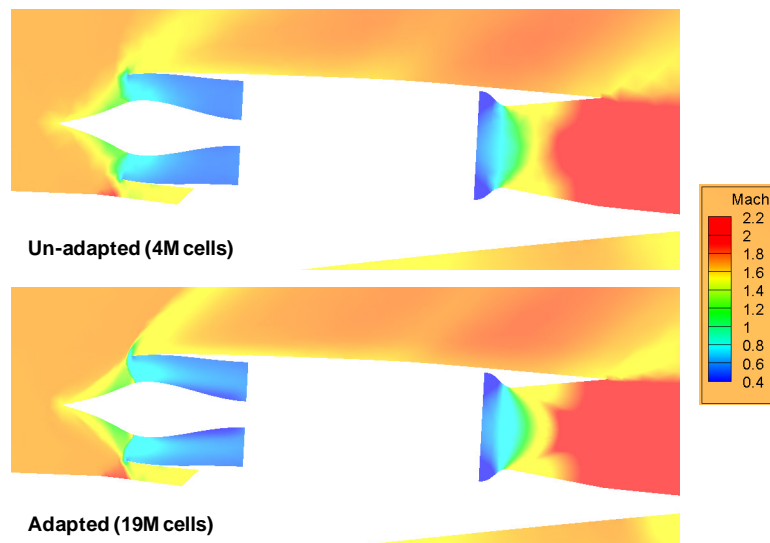


Figure 41.—Configuration 1044 Centerline Nacelle Un-Adapted (top)
Versus Adapted Grid (bottom) CFD Solutions

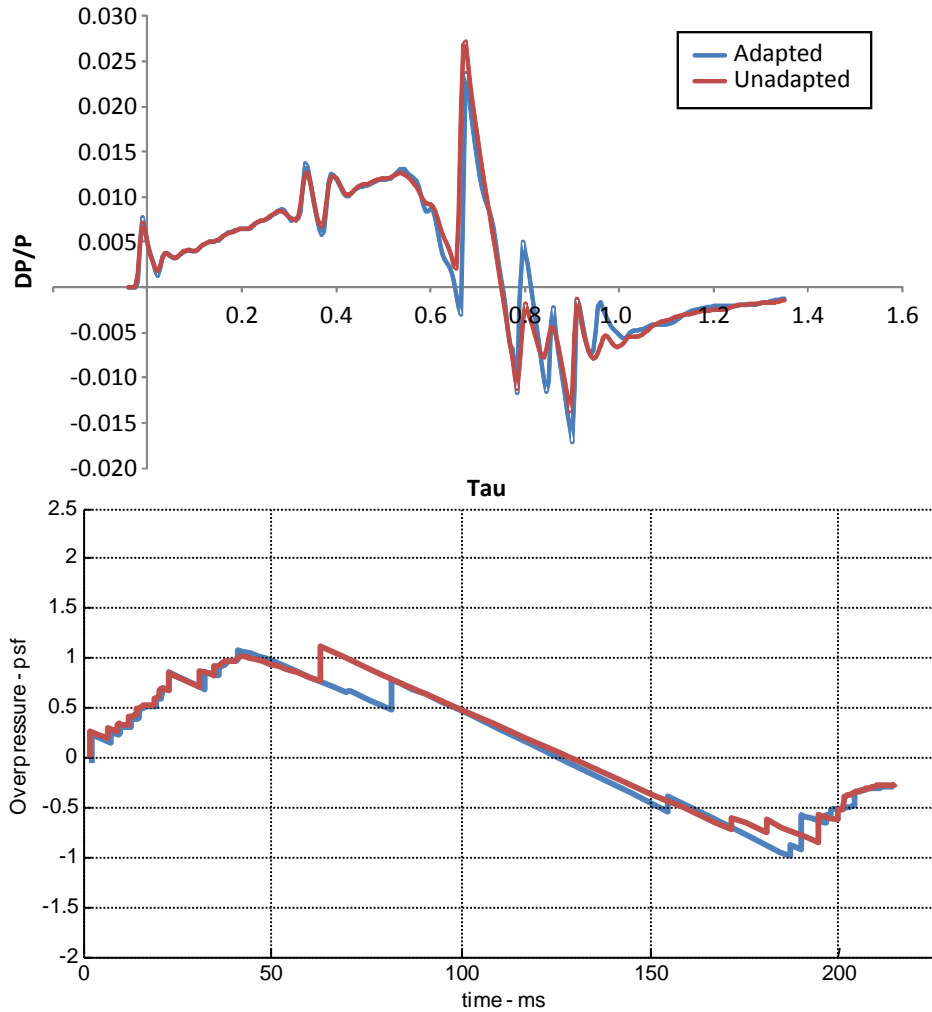


Figure 42.—Grid Adaption Effects on Configuration 1044-2 5.6 R/(b/2)
Signature (top) and Ground Signature (bottom), SOC 4,000 nmi Mission

2.6 LTWT Test

The N+2 program conducted a low-speed wind tunnel test to look at stability and control characteristics of the 1234 Configuration. The test was conducted at the Lockheed Martin Experimental Fluid Dynamics Center using the Low Turbulence Wind Tunnel (LTWT).

The LTWT no. 332 test was conducted primarily between September 20 to 27, 2012, with a handful of runs on October 2 to 3, 2012, with 569 runs obtained in 8 days of occupancy time. Not all days were full days, so test time was about 60 hr. The test was attended by Mike Buonanno, John Morgenstern, Bob Langberg, and Shawn Whitcomb. The test was also observed by Don Durston of NASA Ames.

The LTWT in Figure 43, provides a low-cost, high-value testing option and is commonly used to quickly obtain nonlinear aerodynamic effects, such as vortex interaction between wing/forebody areas and vertical tails. This capability is particularly valuable in the conceptual phase of a vehicle design. The tunnel provides metric data using six component balances and can be used for surface flow and smoke flow visualization.

The LTWT features a 2x3 ft test section, and operates up to Mach 0.15 and dynamic pressures of up to 32 psf (115 mph), Figure 44. Most tests are run at 25 to 30 psf. The tunnel is a closed circuit and has a large settling chamber with flow straightening screens. Models can be sting or blade supported, with measurements made using an internal Mk61 Task 0.75-in. six-component balance. In addition, floor-supported half-span models can be tested using a six-component floor balance. The N+2 model was designed for sting and blade supports and will be described below. A simulated ground plane can be installed in the tunnel to measure ground effects as well.

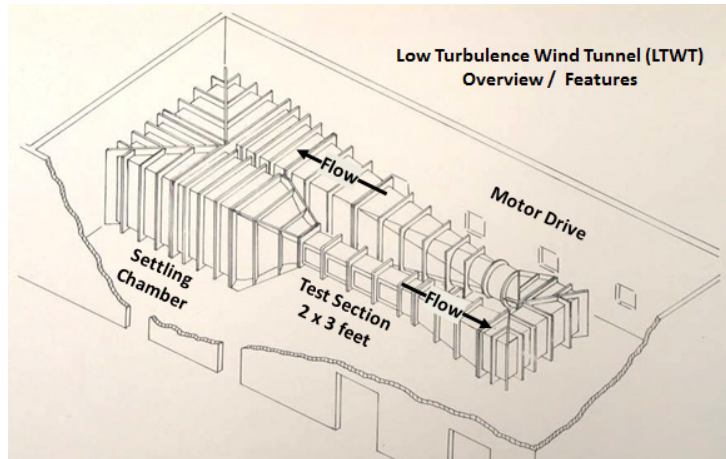


Figure 43.—LTWT Wind Tunnel Circuit

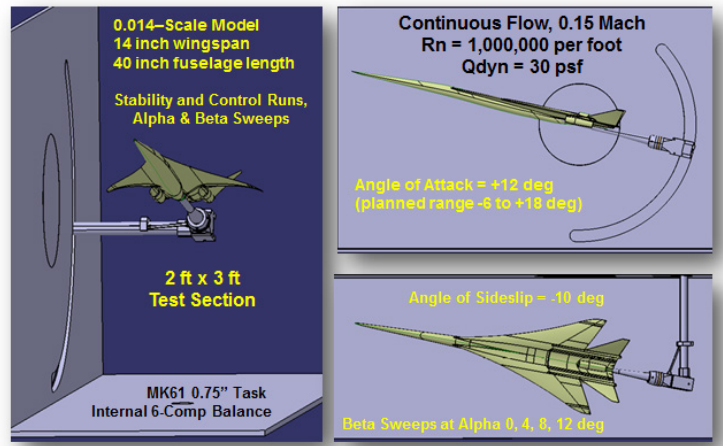


Figure 44.—LTWT Test and Model Support Capability

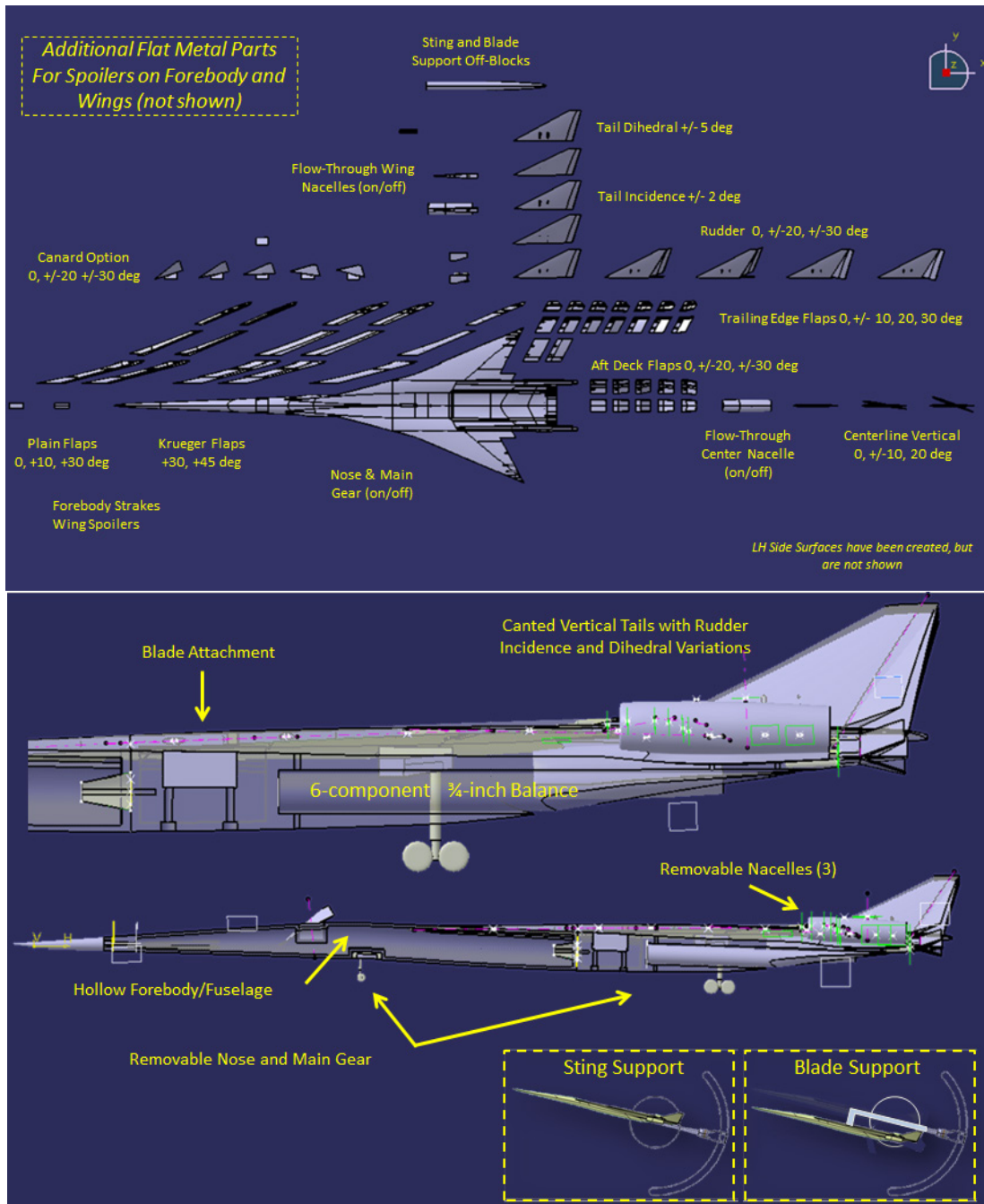


Figure 45.—Model Changeable Part Options

2.6.1 Model Design

The model is the Lockheed Martin N+2, Configuration no.1044, which features the aft deck, three engines, and canted vertical tails, Figure 45. It is the same loft as the model testing in the LM4 test at the NASA Ames 9x7 Supersonic Wind Tunnel, (97-0254) in October 2012. The model is fabricated out of stereolithography resin (SLA) and uses steel pins and tape to join removable parts for proper alignment and strength. In addition, bent metal parts made of 0.025 in. brass sheet stock can be used to fabricate strakes and flaps as desired. The model contains a machined aluminum sleeve designed for the balance

interface. This aluminum sleeve is bonded inside the models and uses two locating pins for repeatable balance attachment.

The LTWT model is sting supported but also has provisions for blade mounting for Ground Effects measurements. Control surfaces were available on the RH and LH sides of the model, but were at times tested on the LH side only to obtain six-component incremental forces and moments.

The V-tail dihedral and incidence have parts for angle variations, and two different size rudders were tested, Figure 46. A removable centerline vertical tail was built and tested, though it is not part of the baseline configuration.

The three flow-through engine nacelle parts are removable, but were always present on the model in the configurations tested.

Landing gear and doors are modeled with extended (compressed/loaded condition) and retracted gear configurations, Figure 47. A deflectable canard was fabricated, but not tested.

Leading edge flaps of two types were tested, Figure 48, with plain flaps at $+10^\circ$ and $+30^\circ$, and Krueger flaps at $+30^\circ$ and $+45^\circ$. Leading edge flaps were broken into three spanwise segments which could be deflected in various combinations.

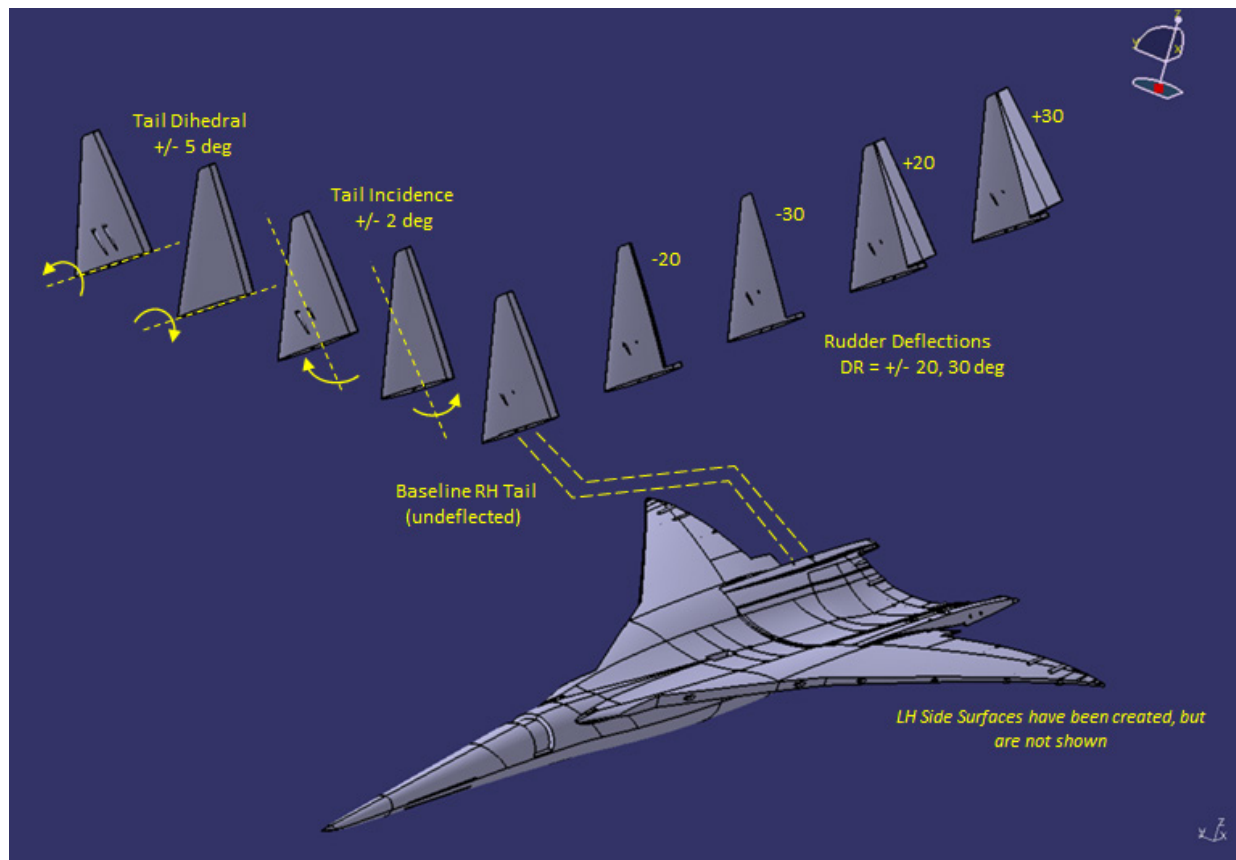


Figure 46.—V-Tail Dihedral, Incidence and Rudder Variations

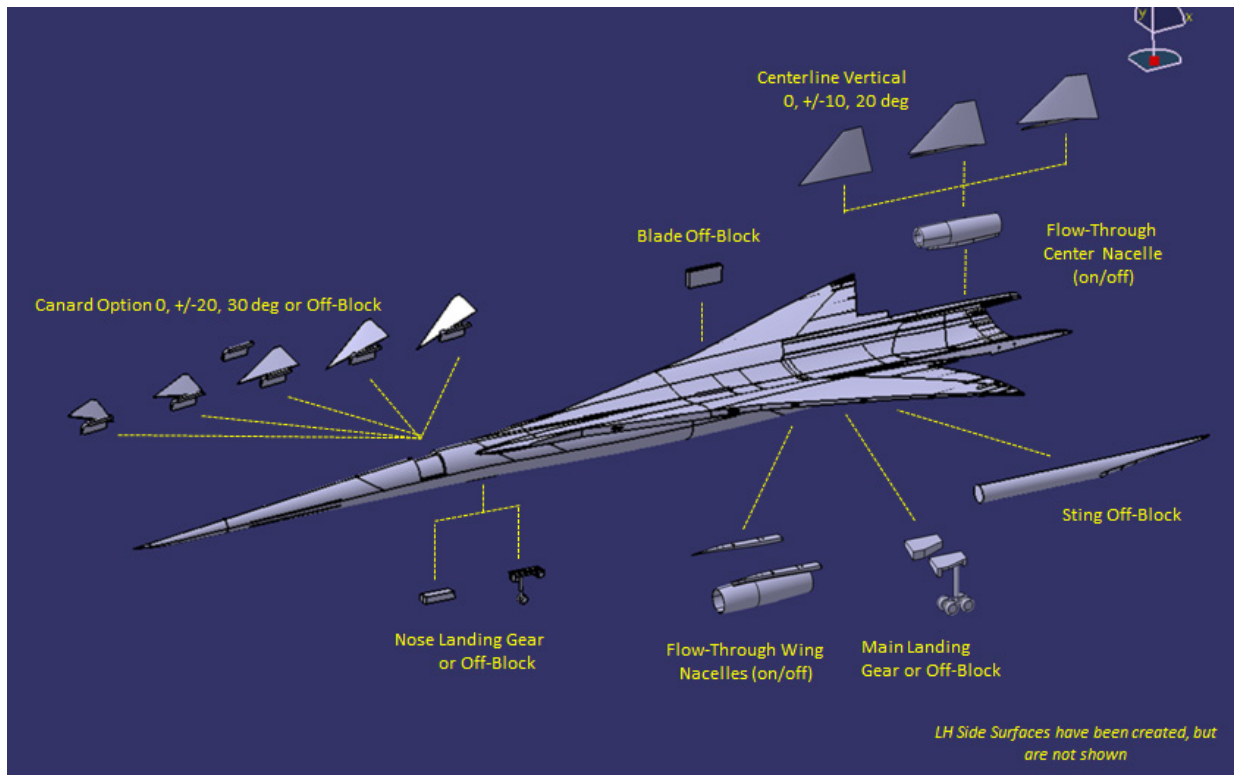


Figure 47.—Options for Canard, Extended Gear, Nacelle Removal and Centerline Vertical Tail

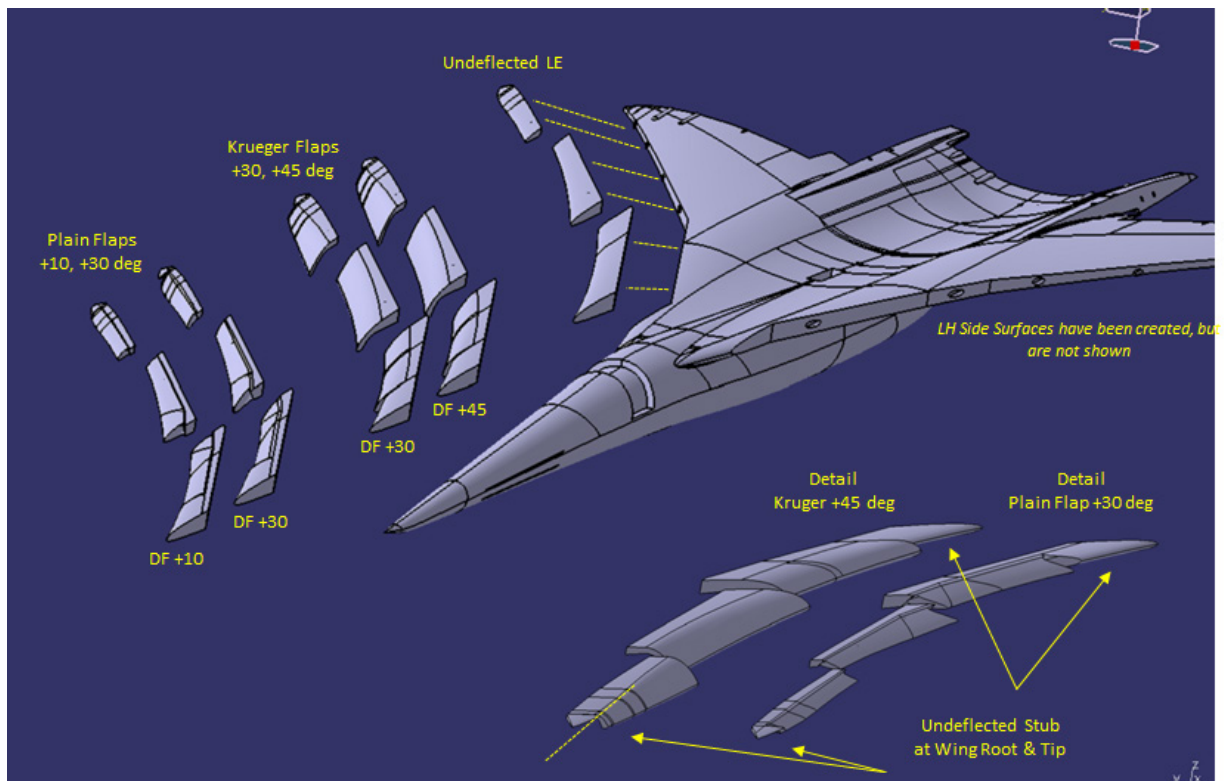


Figure 48.—Leading Edge Plain and Krueger Flaps with 2 Deflections Each

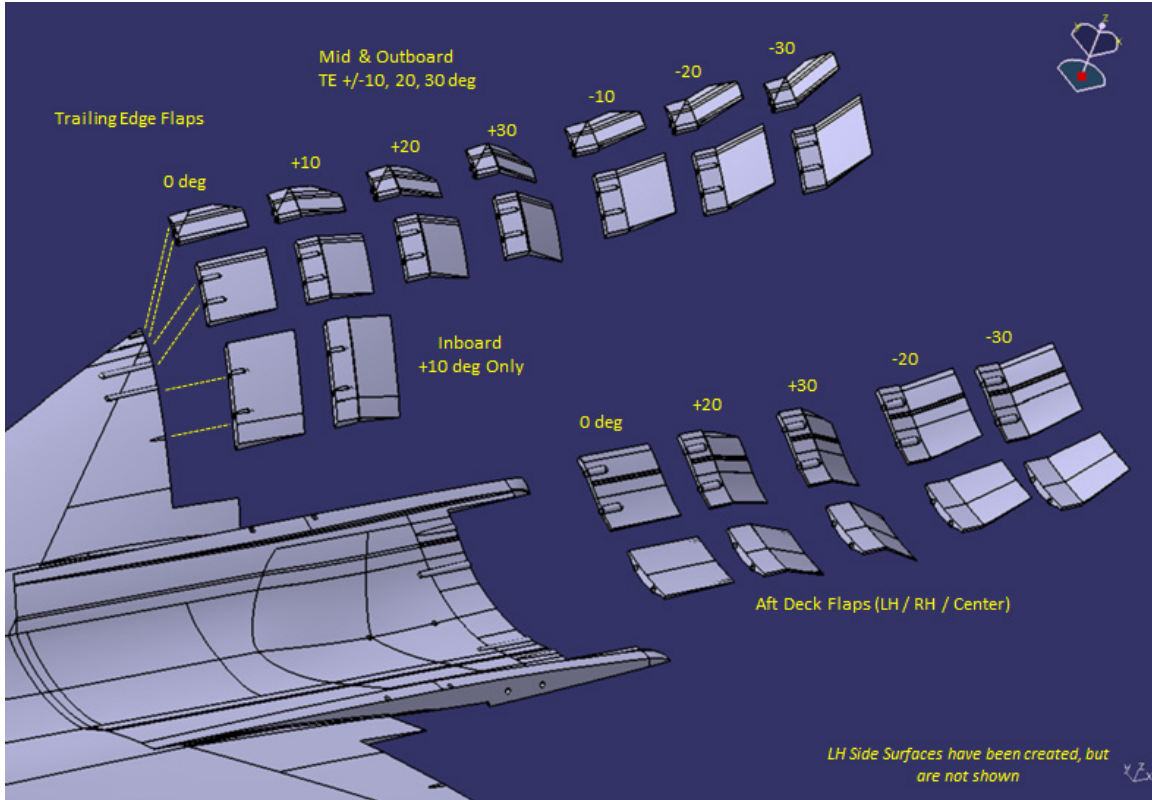


Figure 49.—Trailing Edge Deflection Parts

Trailing edge flaps (Ailerons and Elevators) were available in three segments on each of the wings and also in three segments on the aft deck, Figure 49. Deflections of $\pm 10^\circ$, 20° , 30° were available on the wing TE parts (except only 10° inboard), and deflections of $\pm 20^\circ$, 30° on the aft deck.

Bent metal parts were fabricated and taped in various locations and configurations, size, and orientations. Outboard wing Vortex Flaps (upper and/or lower surface devices for roll and directional control) were tested; these are a pop-up device like a spoiler, which may avoid aeroelastic issues. Wing Root / Fuselage junction deployable control surface options to explore vortex impingement on tails and pitch break. Forebody chine or strake options, symmetric and asymmetric were used to explore impact on lift and pitching moment characteristics.

2.6.2 Test Planning

The test focused on stability and control characteristics of the no. 1044 configuration, primarily at low speeds appropriate for take-off and landing evaluation. A large number of control surfaces were measured and evaluated, including alternate parts which are not in the baseline configuration. The incremental effect of landing gear and doors were evaluated and the aerodynamic changes in ground effect (IGE) were measured.

Goals of the test and the control effectors are as follows: Low-speed stability and control characteristics and control power increments were evaluated using yawed polars ranging from alpha -8° to $+16^\circ$ which were conducted at 0° , $\pm 5^\circ$, $\pm 10^\circ$ beta, Figure 50.



Figure 50.—1044-2 Model in Test Section at High Alpha

Flow visualization studies of vortex flow structures were conducted in the smoke tunnel and documented with still images and video recording. Surface flow (oil flow) visualizations were conducted with a kerosene/talc mixture to show surface flow patterns and areas of attached flow, separation, and flow reversals.

Ground effects were evaluated with the aircraft model supported by an upper surface blade and a simulated ground plane was installed in the tunnel. Landing gear were set in a deployed state to simulate take-off and landing configurations.

The vast majority of the 561 test runs were made to measure basic stability and control effects (494 runs). Necessary balance angle measurements and model weight tares were conducted as needed (29 runs). Surface flow visualization was performed in 18 runs, and 20 runs were devoted to ground effects measurements. Of the 561 runs, 8 runs (nos. 195 to 202 were bad—incorrectly conducted) and are not of value. Smoke flow visualization runs were conducted on the 2nd day of testing and do not have run numbers assigned.

In developing the test matrix, a number of discrete index/variables were assigned to define the overall configurations. A six-digit integer is used to represent the support, nacelles, and tails as listed. The major categories of configurations are listed with their configuration numbers below:

Configuration Nos. Tested

- 1st digit: (1) is Sting, (2) is Blade
- 2nd and 3rd digits: (11) = Nacelles ON, (always)
- 4th and 5th digits: LH & RH Tails, (1) On (0) Off (2,3) Dihedral (5,7) Incidence
- 6th digit: Center Vert Tail, (1) = 100 percent size, (2) 150 percent size

Baseline Configuration

- 111110 == (111) Sting, (110) Tails ON, Center Tail OFF (baseline)

Tail On/Off Variations

- 111111 == (111) Sting, (111) Tails ON, Center Tail ON
- 111001 == (111) Sting, (001) Tails OFF, Center Tail ON
- 111002 == (111) Sting, (002) Tails OFF, Lg Ctr Tail ON
- 111000 == (111) Sting, (000) Tails OFF, Center Tail OFF

Canted Tail Variations, RH & LH

- 111220 == (111) Sting, (220) Tail Dihedral +5, Center Tail OFF
- 111330 == (111) Sting, (330) Tail Dihedral -5, Center Tail OFF
- 111550 == (111) Sting, (550) Tail Incidence -2, Center Tail OFF
- 111770 == (111) Sting, (770) Tail Incidence +2, Center Tail OFF

Blade Support for Ground Effects

- 211110 == (211) Blade, (110) Tails ON, Center Tail OFF

In addition control surface deflections are represented in the test matrix, with the following sign convention and variable names, Figure 51. “LEF” and “DE” refer to leading edge flap and trailing edge flap parts respectively. The location, inboard/mid/outboard is indicated with the letter “I” / “M” / “O” and the RH/LH side of the control is indicated with the last letter in a configuration name. Rudders and Canards are similarly defined with “DR” and “DC”, followed by location and side.

The sign convention is positive leading edge down for LE flaps, positive trailing edge down for aft end controls and canards. Rudders are positive trailing edge to the left.

Finally, miscellaneous bent metal parts are assigned numbers and descriptions and are documented in the run matrix as they were run. The text in the run matrix documents the size of the part and its location and orientation on the model. Configuration photos were taken prior to each run to document the configuration and state of the model. A summary of conditions and measurement extremes, balance limits and reference quantities are in Figure 52.

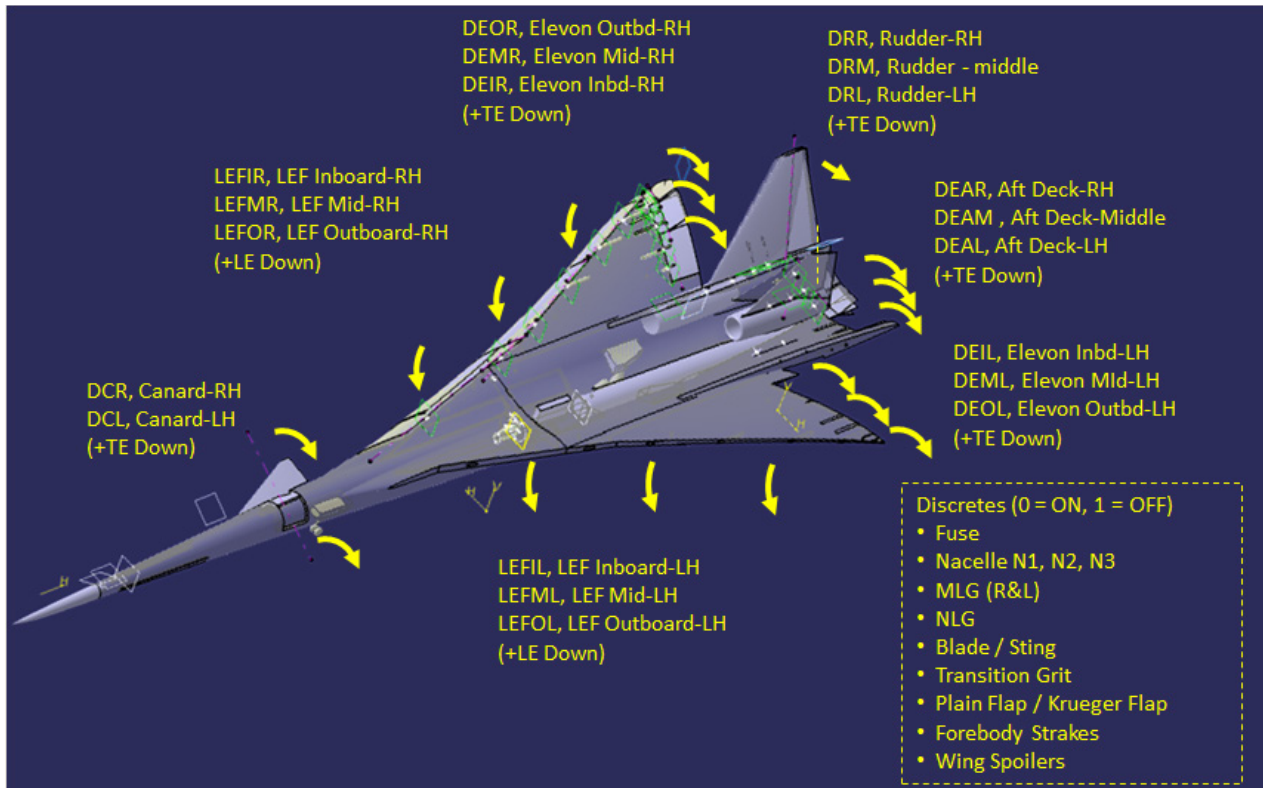


Figure 51.—Naming Notation for Flap Deflections

Summary of LTWT Test #332, Sept 2012, 569 Runs, 11748 total data points.

	TEST	RUN	POINT	ALPHA (deg)	BETA (deg)	Qdyn (psf) (psf)	VEL (ft/sec)	VKTS (kts)	MACH	RNFT	
Min	332	1	1	-16.61	-10.12	0	0	0	0	0	
Max	332	569	23	17.82	10.37	27.3076	160.82	95.22	0.14	0.89	
Stability Axis Coeffs, at MRC, not BMC											
	CLS	CDS	CMS	CRS	CNS	CYS					
Min	-0.820	-0.065	-0.213	-0.064	-0.072	-0.198			Sref	0.7056 ft ²	
Max	1.454	0.465	0.295	0.064	0.052	0.161			Cref	11.0260 in	
Balance Limits											
	NFBALA	AFBALA	PMBALA	RMBALA	YMBALA	SFBALA			FSBAL	BLBAL	WLBAL
	(lbf)	(lbf)	(in-lb)	(in-lb)	(in-lb)	(lbf)			28.700	0.000	2.850
	60	30	90	60	50	40			FSMRC	BLMRC	WLMRC
									28.493	0.000	3.661

Figure 52.—Measurement Extremes, Balance Limits and Reference Quantities

2.6.3 Test Analysis and Results

Overall, the test showed the vehicle to be controllable in all axes with the control surfaces as defined. Handling qualities should be excellent, especially at the low angles-of-attack used throughout all flight—except for takeoff and landing approach, where handling should still be acceptable with room for improvement with further refinement of strake design and pitch-up reduction. In fact, pitch-up handling is

good using the best performing flap configuration, but it would be desirable to have a simpler means of pitch-up suppression than a full leading edge flap.

LTWT #322 testing encompassed:

Total of 569 runs

- 28 Wt Tares and Sting Deflection Check (SAG)
- 18 Surface Flow Visualization
- N/A Smoke Flow Vis (no run #'s), est 2 to 3 hr total time in smoke tunnel
- 18 Blade Supported IGE runs
- 494 Stability and Control Runs (excluding 8 “bad” runs, which had an incorrect config)

The test acquired:

- Low Speed Stability and Control Power
 - Angle of Attack = -6 to +15°; Sideslip = $\pm 10^\circ$
 - Wing LE (IB,MB,&OB), Plain (0, +10, +30) and Kreuger (0, +30, +45)
 - Left Wing TE (IB,MB,&OB): 0, ± 10 , ± 20 , ± 30
 - Left Deck TE: 0, ± 10 , ± 20 , ± 30
 - Left Tail deflections: 0, ± 10 , ± 20 , ± 30
- Flow Visualization of Vortex Flow Structures
 - Surface Oil Flow
 - Smoke Tunnel Mount
- Allow for alternate blade mount for future IGE or clean tail configuration

Test repeatability may be as good as:

CL = ± 0.002

CrS = better than ± 0.0001

CD = ± 0.0001

CnS = better than ± 0.0001

Cm = ± 0.0002

CYS = ± 0.0002

Figure 53 and Figure 54 describe data files available from the test. During the test, weight tares were taken for repeatability and any time there was a configuration change that might change the model weight. Figure 55 describes the new configuration for each 28 weight tares that were taken during the test. Figure 56 shows a shrunken version of the Run Matrix for confirmation that one has the correct file.

Name	Date modified	Type	Size
2012_10_2_16_53_25.M2TS	10/2/2012 4:54 PM	AVCHD Video	24,737 KB
colsel_wHeight_10062012.zip	10/6/2012 4:16 PM	WinZip File	2,807 KB
ltwt_322_Reduction_eplot_parameters_for_release.xlsx	10/6/2012 4:14 PM	Microsoft Excel W...	1,297 KB
LTWT_Matrix_v4a.xlsx	10/3/2012 3:40 PM	Microsoft Excel W...	102 KB
LTWT332_Nplus2_1044_test_working_plots_use_TOC_and_bookmarks.pdf	10/6/2012 4:56 PM	PDF File	8,224 KB
ltwt332_Nplus2_Photo_Binder1.pdf	9/27/2012 10:40 AM	PDF File	212,494 KB
ltwt332_Nplus2_Photo_Binder2.pdf	9/27/2012 6:08 PM	PDF File	250,128 KB
ltwt332_Nplus2_Photo_Binder3.pdf	10/6/2012 9:19 AM	PDF File	63,111 KB

Figure 53.—LTWT332 Output Files of Test Measurements and Photography

TEST	1 Test Number	
RUN	2 Run Number	
POINT	3 Point Number	
WALANG	47 Support System Wall Angle, Uncorrected, from JSF Motion Control File	deg
FLRANG	48 Support System Floor Angle, Uncorrected, from JSF Motion Control File	deg
TRANS	49 Support System Translation Position, Uncorrected, from JSF Motion Control File	in
ROLL	54 Roll Pod Roll Angle	deg
WALANGV	73 Support System Wall Angle, Cont Swp Sched Velocity	deg/s
WALANGA	81 Support System Wall Angle, Cont Swp Sched Acceleration	deg/s ²
ALPHA	125 Angle of Attack (with Flow angularity and Wall correction)	deg
BETA	126 Angle of Sideslip (with Flow angularity correction)	deg
Q	132 Dynamic Pressure, corrected for compressibility & QFACT & Blockage (QFACTOR)	psf
PT	136 Tunnel Total Pressure	psf
TT	137 Tunnel Total Temperature, Rankine	deg R
PS	138 Tunnel Static Pressure	psf
TS	139 Tunnel Static Temperature, Rankine	deg R
MACH	148 Mach Number	
RNFT	149 Reynolds Number per Foot (millions)	million/ft
RNCREF	151 Reynolds Number based on CREF (millions)	million
SREF	152 Reference Area for Non-Dimensionalization, Full-Span	ft ²
CREF	153 Reference Length for PM Non-Dim, Full-Span	inches
BREF	154 Reference Length for RM&YM Non-Dim, Full-Span	inches
FSBAL	155 Fuselage Station of Balance Center	inches
BLBAL	156 Buttline of Balance Center	inches
WLBAL	157 Waterline of Balance Center	inches
FSMRC	158 Fuselage Station of Moment Reference Center	inches
BLMRC	159 Buttline of Moment Reference Center	inches
WLMRC	160 Waterline of Moment Reference Center	inches
ACAV	165 Cavity Area (Axial projected area only with scarf angle functionality)	ft ²
DALPHA_WALL	172 Wall Correction to Alpha, Additive = f[tunnel section geom, CL, BWING, SWING, PHIM]	deg
CPCAVA	174 PCAV/Q = Average (of NCPC, usually 1) Cavity Pressure Coefficients	-
HMRC	176 Height of MRC (corrected for sting & balance deflection)	inches
HOB	177 Height of MRC / BREF (HMRC/BREF)	-
CONFIG	193 Config or Model #, 1 or 2	1,2,3
SWCLRC	194 Config SWCLR = 11111, Support (1=Sting,2=Blade), WingNac, CtrNac, Ltail, Rtail, Ctrtail	111110, ...
LEFOL	195 Deflection LEF OB Left, + LE down	deg
LEFML	196 Deflection LEF MB Left, + LE down	deg
LEFIL	197 Deflection LEF IB Left, + LE down	deg
LEFIR	198 Deflection LEF IB Right, + LE down	deg
LEFMR	199 Deflection LEF MB Right, + LE down	deg
LEFOR	200 Deflection LEF OB Right, + LE down	deg
DEOL	201 Deflection TE OB Left, + TE down	deg
DEMOL	202 Deflection TE MB Left, + TE down	deg
DEIL	203 Deflection TE IB Left, + TE down	deg
DEAL	204 Deflection Aft Deck TE Left, + TE down	deg
DEAM	205 Deflection Aft Deck TE Mid, + TE down	deg
DEAR	206 Deflection Aft Deck TE Right, + TE down	deg
DEIR	207 Deflection TE IB Right, + TE down	deg
DEMR	208 Deflection TE MB Right, + TE down	deg
DEOR	209 Deflection TE OB Right, + TE down	deg
DRL	210 Deflection Rudder Left (+ TE left)	deg
DRM	211 Deflection Rudder Mid (+ TE left)	deg
DRR	212 Deflection Rudder Right (+ TE left)	deg
DCL	213 Deflection Canard Left, + TE down	deg
DCR	214 Deflection Canard Right, + TE down	deg
FSTR	215 Forebody Strakes	0,1,2,3,4

Figure 54.—ColSelect ASCII Data Contains these 118 Key Variables

WSPL	216 Wing Spoiler Left	0,1,2,3,4
WSPR	217 Wing Spoiler Right	0,1,2,3,4
WRDL	218 Wing Root Device Left	0,1,2,3,4
WRDR	219 Wing Root Device Right	0,1,2,3,5
SREFF	220 Sref Fullscale, ft	ft
CREFF	221 Cref Fullscale, ft	ft
BREFF	222 Bref Fullscale, ft	ft
FSMRCF	223 FSMRC, fullscale	in
GRIT	224 Grit Config	0,1,2,...
RUN_BASE	403 Run Number of Base Run	
CNFB	416 Coeff. Normal Force, Fully Corrected	Non-Dim
CAF	417 Coeff. Axial Force	Non-Dim
CPMB	418 Coeff. Pitching Moment	Non-Dim
CRMB	419 Coeff. Rolling Moment	Non-Dim
CYMB	420 Coeff. Yawing Moment	Non-Dim
CSFB	421 Coeff. Side Force	Non-Dim
DCNFB	422 Delta Coeff. Normal Force of Current Run - Base	Non-Dim
DCAF	423 Delta Coeff. Axial Force	Non-Dim
DCPMB	424 Delta Coeff. Pitching Moment	Non-Dim
DCRMB	425 Delta Coeff. Rolling Moment	Non-Dim
DCYMB	426 Delta Coeff. Yawing Moment	Non-Dim
DCSF	427 Delta Coeff. Side Force	Non-Dim
DCHFBA	428 Delta Coeff. Normal Force of Current Run - Base, Smoothed (Averaged)	Non-Dim
DCAFBA	429 Delta Coeff. Axial Force	Non-Dim
DCPMBA	430 Delta Coeff. Pitching Moment	Non-Dim
DCRMB	431 Delta Coeff. Rolling Moment	Non-Dim
DCYMB	432 Delta Coeff. Yawing Moment	Non-Dim
DCSFBA	433 Delta Coeff. Side Force	Non-Dim
CLS	434 Coeff. Lift, Stability Axis, Fully Corrected	Non-Dim
CDS	435 Coeff. Drag	Non-Dim
CMS	436 Coeff. Pitching Moment	Non-Dim
CRS	437 Coeff. Rolling Moment (Stab Axis)	Non-Dim
CNS	438 Coeff. Yawing Moment (Stab Axis)	Non-Dim
CYS	439 Coeff. Side Force	Non-Dim
DCLS	440 Delta Coeff. Lift, Stability Axis, from Base Run	Non-Dim
DCDS	441 Delta Coeff. Drag	Non-Dim
DCMS	442 Delta Coeff. Pitching Moment	Non-Dim
DCRS	443 Delta Coeff. Rolling Moment (Stab Axis)	Non-Dim
DCNS	444 Delta Coeff. Yawing Moment (Stab Axis)	Non-Dim
DCYS	445 Delta Coeff. Side Force	Non-Dim
DCLSA	446 Delta Coeff. Lift, Stability Axis, from Base Run, Smoothed (Averaged)	Non-Dim
DCDSA	447 Delta Coeff. Drag	Non-Dim
DCMSA	448 Delta Coeff. Pitching Moment	Non-Dim
DCRSA	449 Delta Coeff. Rolling Moment (Stab Axis)	Non-Dim
DCNSA	450 Delta Coeff. Yawing Moment (Stab Axis)	Non-Dim
DCYSA	451 Delta Coeff. Side Force	Non-Dim
LOD	470 Lift Over Drag (CLS/CDS)	Non-Dim
LONG_STAB	495 Longitudinal Stability for alpha sweeps, local akima fit slope of -CMS vs. CLS	
LONG_STABN	497 Longitudinal Stability for alpha sweeps, local akima fit slope of -CMS_NEUTRAL vs. CLS	
CRS_BETA	502 Roll Stability for beta, local akima fit slope of CRS vs. BETA	
CNS_BETA	504 Directional Stability for beta, local akima fit slope of CNS vs. BETA	
CMS_NEUTRAL	506 CMS adjusted to Neutral Stability at Low Alpha	
CMS_NEUTRALZ	509 CMS adjusted to Neutral Stability at Low Alpha & pushed to Zero CM at CL=0	
CDS_BUOY	577 Drag Coefficient Correction due to Buoyancy, Additive	-
CAF_BUOY	604 Coeff. Axial Force Buoyancy Corr (Additive) (Based on CDS_BUOY_ALPHA_U & BETA)	-
KCMS3_CLS	615 Slope of Pitching Moment Coeff Add Corr for Tunnel Wall Eff on Tail Downwash - Vortex Based	-
CMS3_CLS	616 Pitching Moment Coeff Add Corr for Tunnel Wall Eff on Tail Downwash - Vortex Based	-
KCDS_CLS2	621 Type-In Induced Drag per CLS^2 - Add Corr for Tunnel Wall Eff - Vortex Based	-
CDS_CLS2	622 Induced Drag Add Corr for Tunnel Wall Eff - Vortex Based	-
PCAV1	1157 1st Cavity Pressure, = XD7U corrected for tunnel gradient	psf
PCAV2	1158 2nd Cavity Pressure, if required, = XD4U corrected for tunnel gradient	psf
RUN_BASED	1668 Run Number of Base Run for Delta-Delta	

Figure 54.—Concluded

Description	RUN
Model Sag	1
Abs Weight Tare Baseline	2
Inverted Abs Weight Tare Baseline	7
Abs Weight Tare Tails Off	19
Abs Weight Tare Center Tail Only	28
Abs Weight Tare L&R&Center Tails	37
Wgt Tare; Forebody Strake Rect Mid = 1, Alpha Cont Swp, Beta=0	72
Wgt Tare; Forebody Strake Tri Lower = 4, Alpha Cont Swp, Beta=0	89
Canard L&R = 0, Alpha Cont Swp, Beta=0	111
Wgt Tare; Forebody Strake Rect Short/Fwd Mid = 5, Alpha Cont Swp, Beta=0	120
Wgt Tare, Sym xtralB&LEFI&M-L&R = +30, Alpha Cont Swp, Beta=0	145
Wgt Tare, Forebody Entire Strakes#7, Sym LEFI&M-L&R = +30, Alpha Cont Swp, Beta=0	159
Wgt Tare, Forebody Long Strakes#8, Sym LEFI&M-L&R = +30, Alpha Cont Swp, Beta=0	168
Wgt Tare, Forebody Strakes#9, Sym LEFI&M-L&R = +30, Alpha Cont Swp, Beta=0	177
Wgt Tare, Forebody Strakes#10, Sym LEFI&M-L&R = +30, Alpha Cont Swp, Beta=0	186
Wgt Tare, FSTR#11, Sym LEFI&M-L&R = +30, Alpha Cont Swp, Beta=0	235
Wgt Tare, Re-Base LEF & FSTR#7, Sym LEFI&M-L&R = +30, Alpha Cont Swp, Beta=0	244
Wgt Tare, Gear On, (LEF&FSTR#7), Alpha Cont Swp, Beta=0	450
Wgt Tare, Ext Wing Aft and Ctr Tail Only, (LEF&FSTR#7), Alpha Cont Swp, Beta=0	456
Wgt Tare, Ext Wing Aft and Large Ctr Tail Only, (LEF&FSTR#7), Alpha Cont Swp, Beta=0	462
Model Sag, IGE Base LEF&FSTR#7, Sym LEFI&M-L&R = +30	496
Wgt Tare, IGE Base LEF&FSTR#7, Sym LEFI&M-L&R = +30	497
Wgt Tare, Big Roll/Yaw Fence LH Up/Lo, (LEF&FSTR#7), Alpha Cont Swp, Beta=0	518
Wgt Tare, Big Roll/Yaw Fence LH Up, (LEF&FSTR#7), Alpha Cont Swp, Beta=0	524
Wgt Tare, Small Roll/Yaw Fence LH Up, (LEF&FSTR#7), Alpha Cont Swp, Beta=0	535
Wgt Tare, Small Roll/Yaw Fence LH Lo / RH Up, (LEF&FSTR#7), Alpha Cont Swp, Beta=0	541
Wgt Tare, Small Roll/Yaw Fence LH Lo / RH Up, (LEF&FSTR#7), Alpha Cont Swp, Beta=0	552
Wgt Tare, Alt Plate Kreuger, (LEF&FSTR#7), Alpha Cont Swp, Beta=0	558
Wgt Tare, Alt Plate Kreuger, Tails Off, (LEF&FSTR#7), Alpha Cont Swp, Beta=0	564

Figure 55.—Weight Tares Taken (28) for Any Significant Configuration Change

Figure 57 shows longitudinal stability trends for the baseline configuration. Lift, pitching moment and percent stability are shown versus Alpha. Of note on these plots is the pitch break which occurs at about Alpha = 6° to 8°. This is a wing/planform tail-interaction effect. This is an interaction between wing/forebody vortex structure interacting with the tail which is dependent on alpha. This can be seen by comparing the tail-on / tail-off configurations. The vortex structure can be seen in Figure 58 in smoke flow visualization showing the interaction with the canted vertical tails.

Figure 59 shows rolling moment and directional stability trends with alpha. The negative CrBeta values at positive alpha are stable slopes. Figure 60 shows yawing moment and directional stability characteristics. The positive CnBeta values for Alphas up to 8° to 12° show good directional stability. At higher alphas, the tails have reduced effectiveness at angles of attach beyond the pitch break.

The effect of leading edge flaps on longitudinal characteristics is presented in Figure 61. Changes in lift are negligible, but favorable reduction in the pitch break are shown with the plain flaps deflected at 30° (leading edge down). The benefit is best when the gaps between flap segment is left open creating leading edge snags, but some benefit is gained even with flaps taped over. A long, low-aspect ratio Forebody Strake (FB#7) is shown in the photograph and on the data plots. Some benefit is obtained from the strake, but not as much as from the flap deflection. The flap deflection with open snags delays the pitch break by about 2°, and the change in stability is dramatically mitigated. Figure 62 shows surface flow visualization of the leading edge deflected 30° with the gaps open and taped over. The vortex created at the open snag can be clearly seen in two streaks on each wing originating at the gap in the leading edge flap.

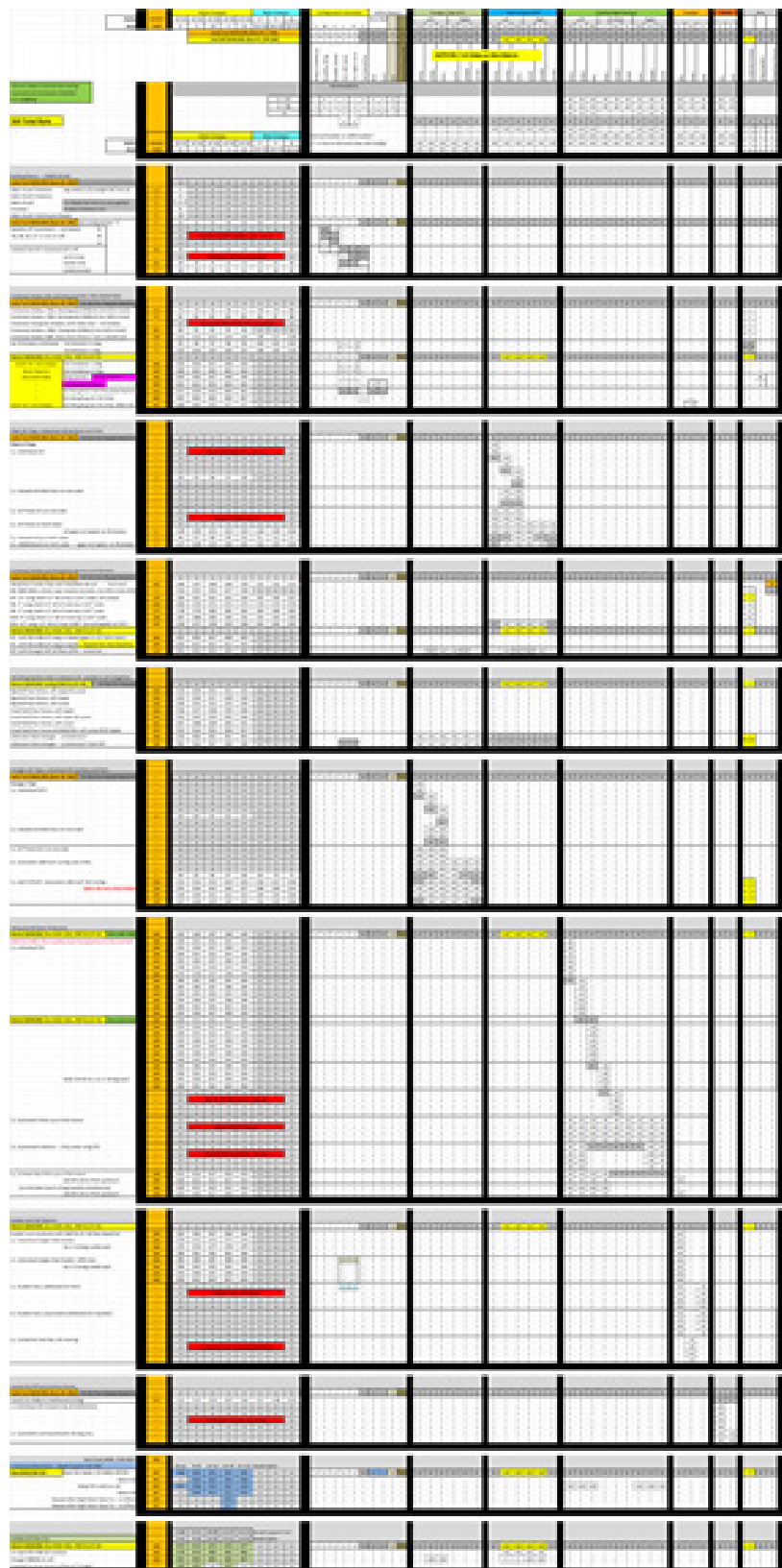


Figure 56.—Run Schedule (Illegible but) Included Here for Identification

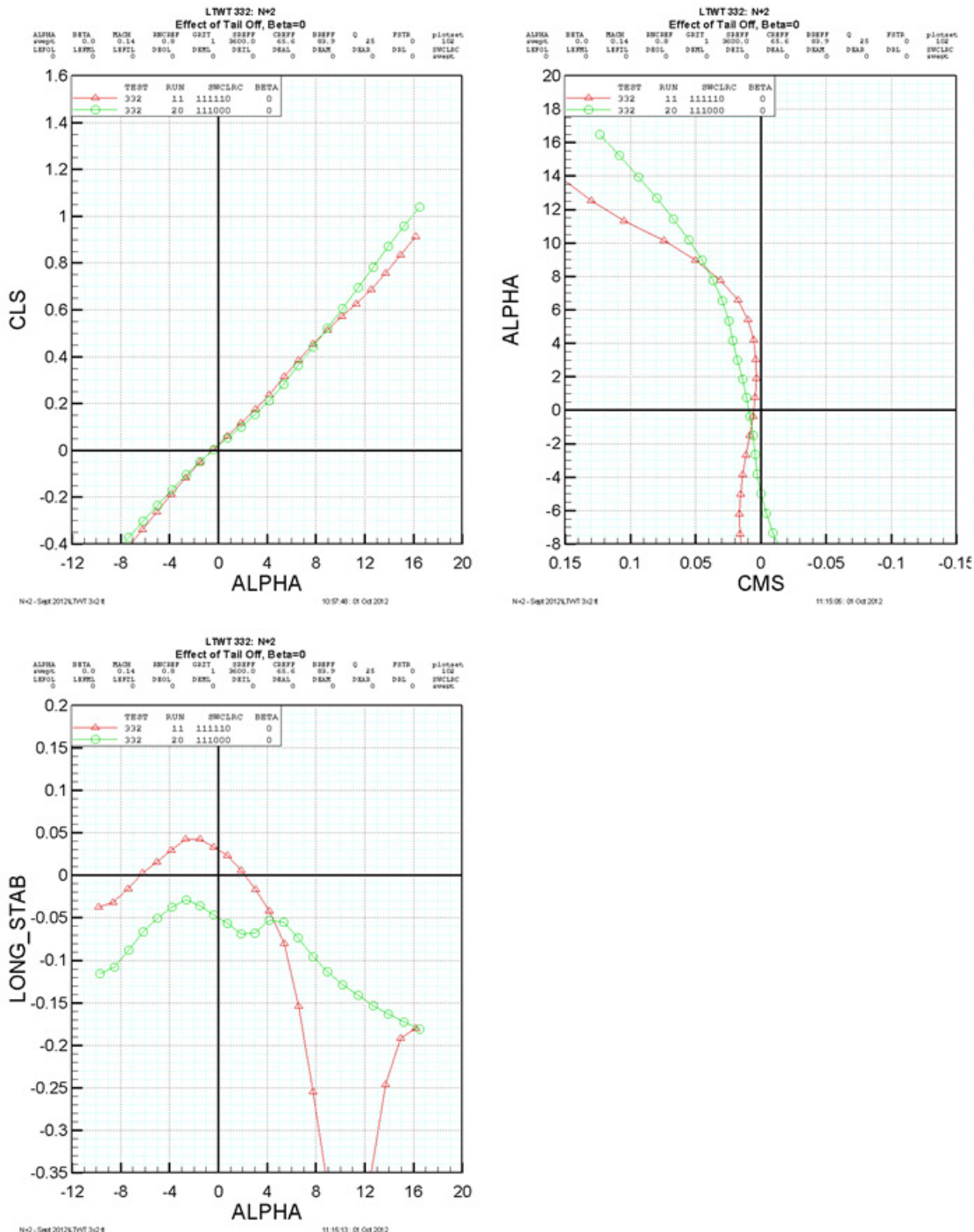


Figure 57.—Pitch Stability Assessment

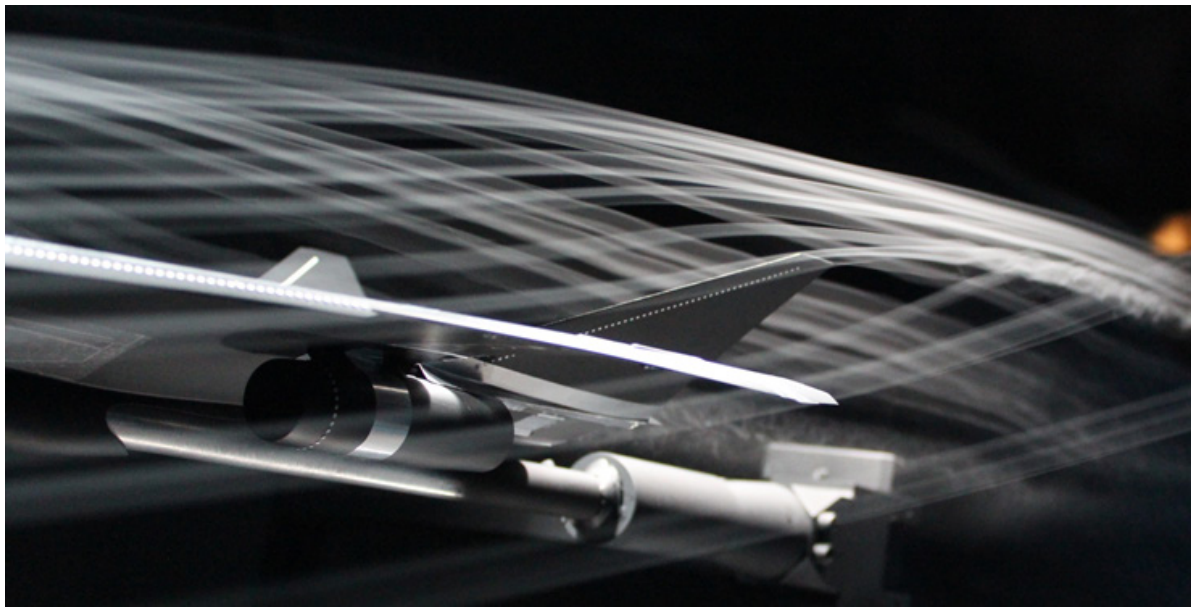


Figure 58.—Smoke Showing Wing Vortex Impingement on V-Tail

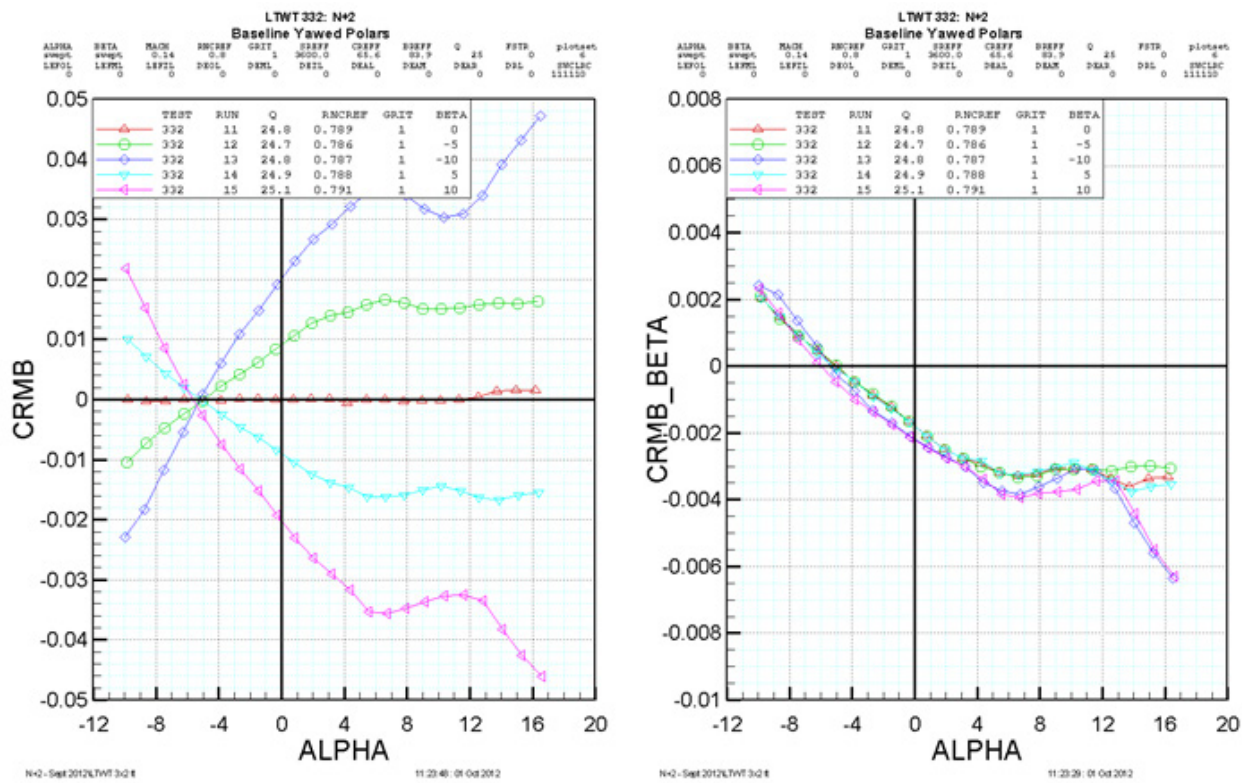


Figure 59.—Roll Stability Assessment

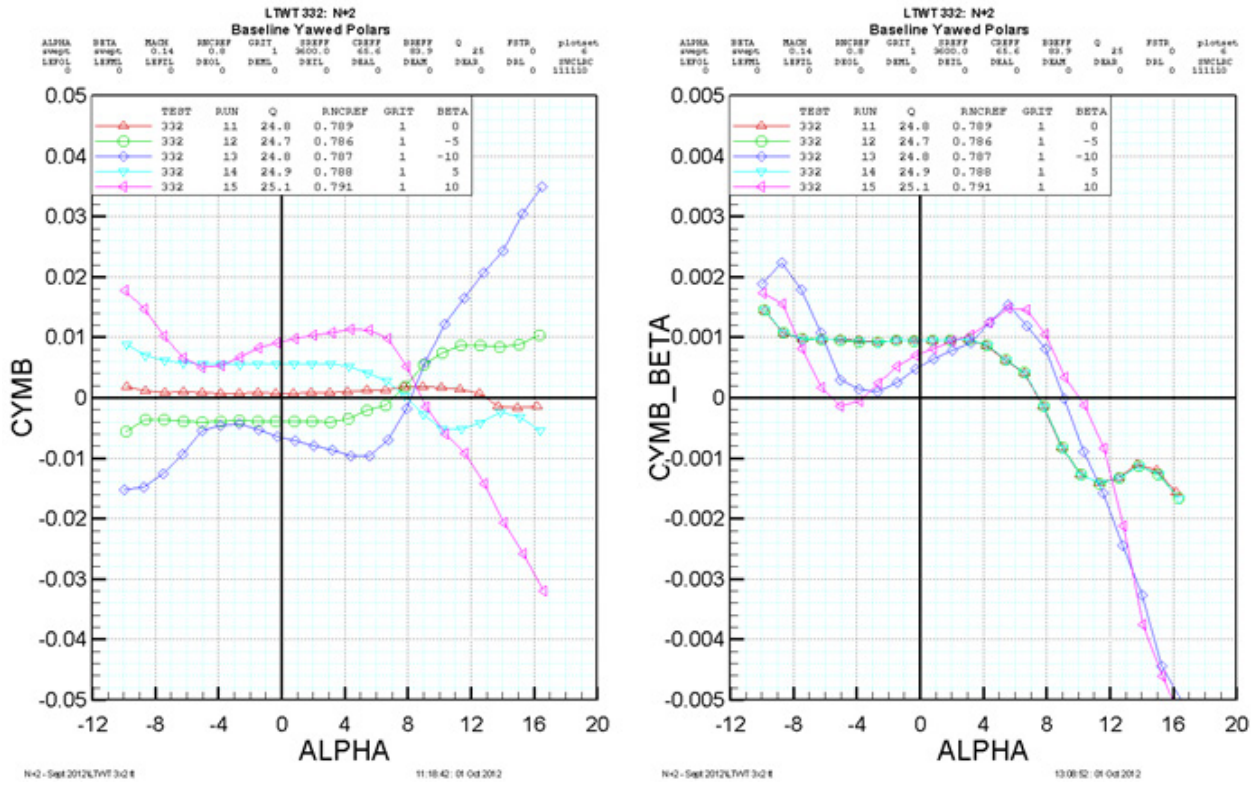


Figure 60.—Yaw Stability Assessment

The pitch control power of the left, outboard, aft deck flap is presented in Figure 63. Due to the long Delta Xfs moment arm to the CG, the control is effective in pitching moment. With its relative proximity to the centerline, the rolling moment is rather small.

Rudder control power on the canted vertical tails is shown for longitudinal and lateral moments in Figure 64. Due to the canted angle of the vertical tails, the rudder produces pitch, yaw and roll when deflected as expected. The degradation in roll effectiveness is due to the plotting of the stability axis coefficient with alpha. Had body axis incremental rolling moment been plotted, the surface would be constant with alpha as can be seen in the plot of side force, CY versus alpha. Figure 65 shows the effect of sizing the rudder by moving the hingeline to have 100 and 150 percent of the baseline rudder. Both configurations have the same physical tail area. As expected, the larger tail has greater control power. The proper rudder size requirements would be determined by a control power requirements analysis, but the nonlinear sensitivity due to tail size is documented in the wind tunnel data.

Finally, a planform variation is presented in Figure 66 where the canted vertical tails have been replaced with a web between the aft deck and the wing trailing edges. These parts are fabricated out of thin brass stock (0.025 in. thick) and taped in place with aluminum tape. This is a good example of the configuration explorations which can be accomplished quickly in the LTWT facility. The new planform shows excellent behavior in longitudinal stability and mitigates the pitch break found in the original baseline configuration by half.

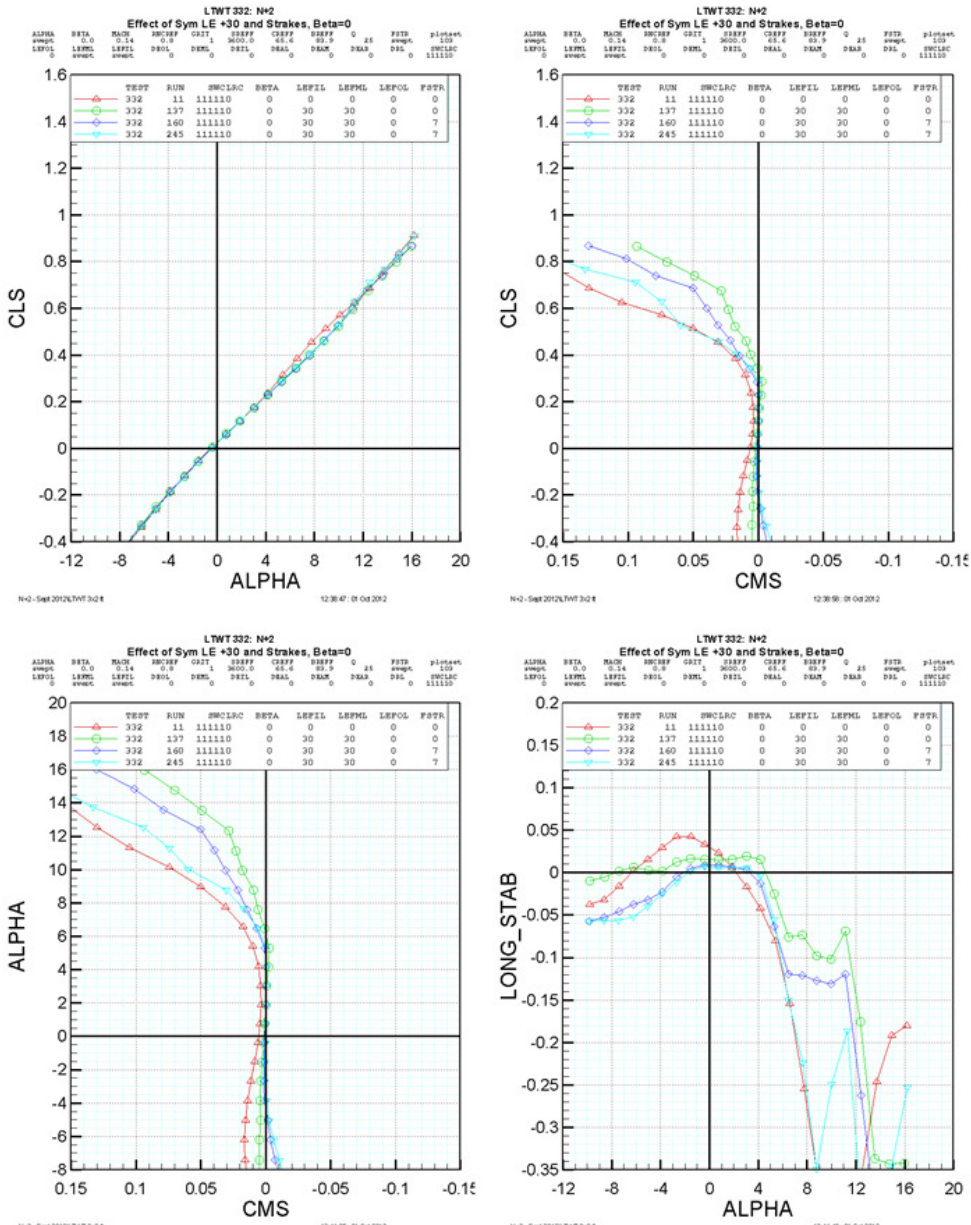
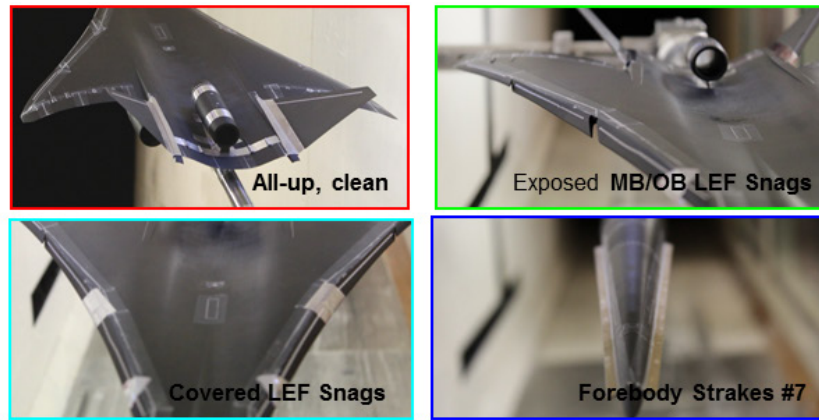


Figure 61.—Pitch-Up Control Concepts Exploration



Figure 62.—Configuration 1044-2 Pitch Break Surface Oil-Flow Visualization

The pitch control power of the left, outboard, aft deck flap is presented in Figure 63. Due to the long Delta Xfs moment arm to the CG, the control is effective in pitching moment. With its relative proximity to the centerline, the rolling moment is rather small.

Rudder control power on the canted vertical tails is shown for longitudinal and lateral moments in Figure 64. Due to the canted angle of the vertical tails, the rudder produces pitch, yaw and roll when deflected as expected. The degradation in roll effectiveness is due to the plotting of the stability axis coefficient with alpha. Had body axis incremental rolling moment been plotted, the surface would be constant with alpha as can be seen in the plot of side force, CY versus alpha. Figure 65 shows the effect of sizing the rudder by moving the hingeline to have 100 and 150 percent of the baseline rudder. Both configurations have the same physical tail area. As expected, the larger tail has greater control power. The proper rudder size requirements would be determined by a control power requirements analysis, but the nonlinear sensitivity due to tail size is documented in the wind tunnel data.

Finally, a planform variation is presented in Figure 66 where the canted vertical tails have been replaced with a web between the aft deck and the wing trailing edges. These parts are fabricated out of thin brass stock (0.025 in. thick) and taped in place with aluminum tape. This is a good example of the configuration explorations which can be accomplished quickly in the LTWT facility. The new planform shows excellent behavior in longitudinal stability and mitigates the pitch break found in the original baseline configuration by half.

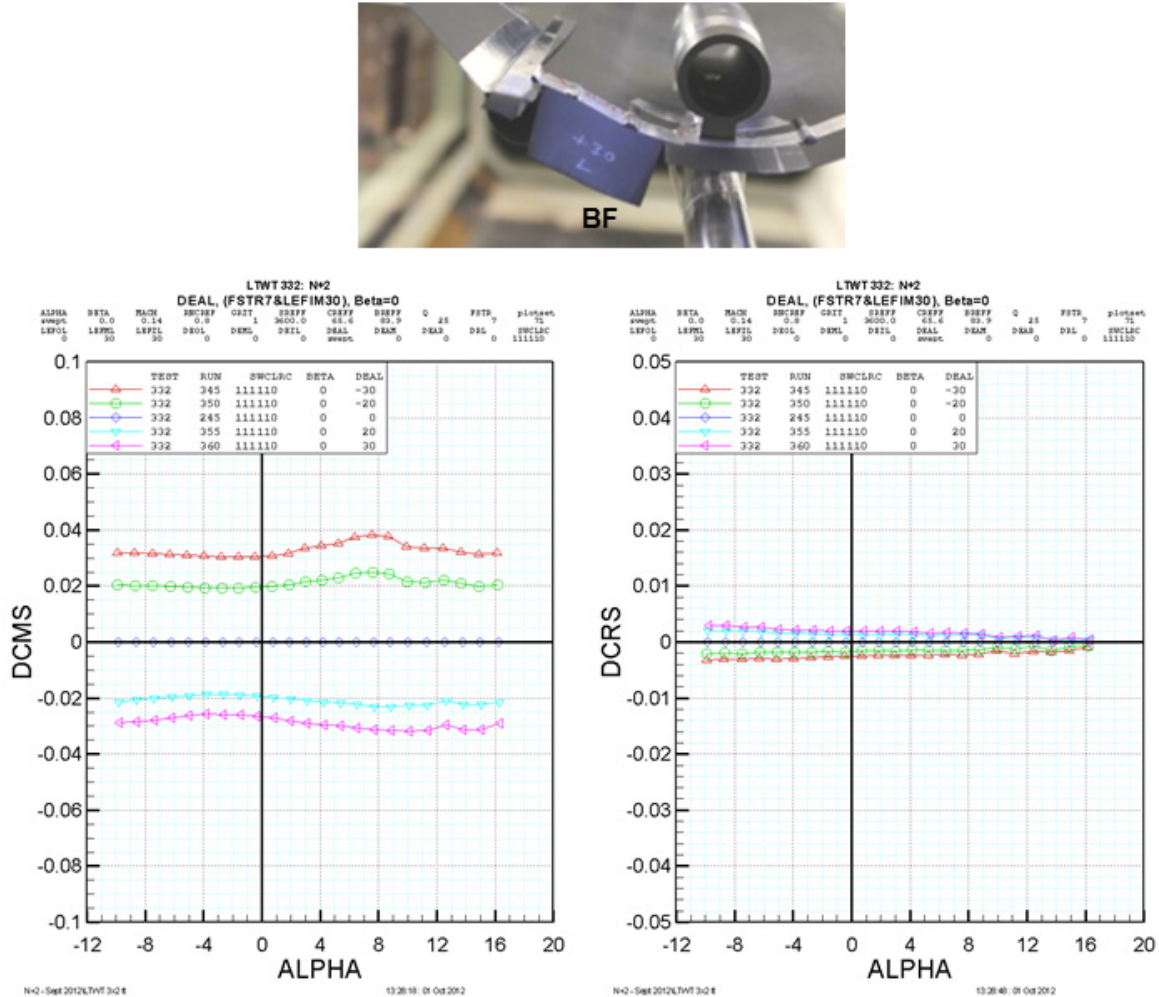


Figure 63.—Aft Deck Flap Control Power Assessment

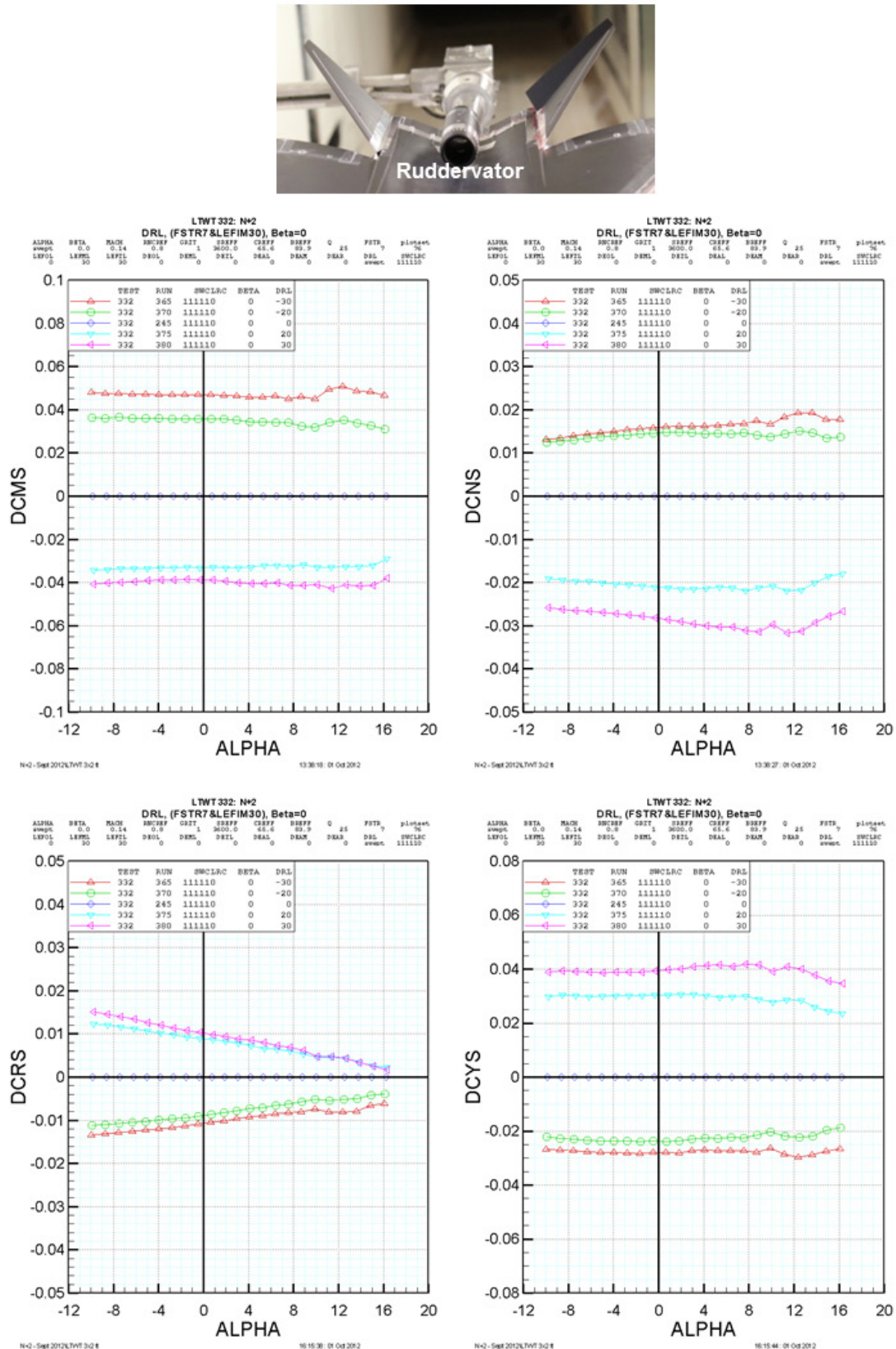


Figure 64.—Ruddervator Control Power Assessment

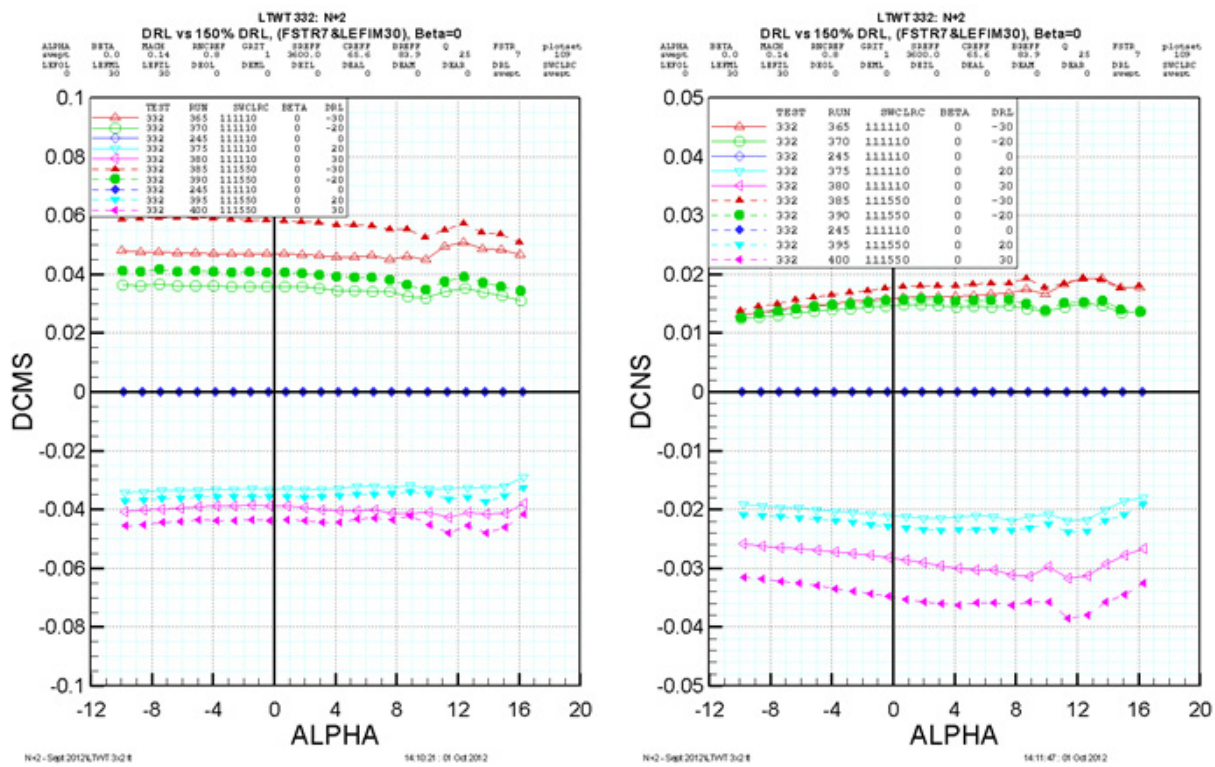


Figure 65.—Ruddervator Size Variation Comparison, Open (baseline) and Closed (50-percent oversize)

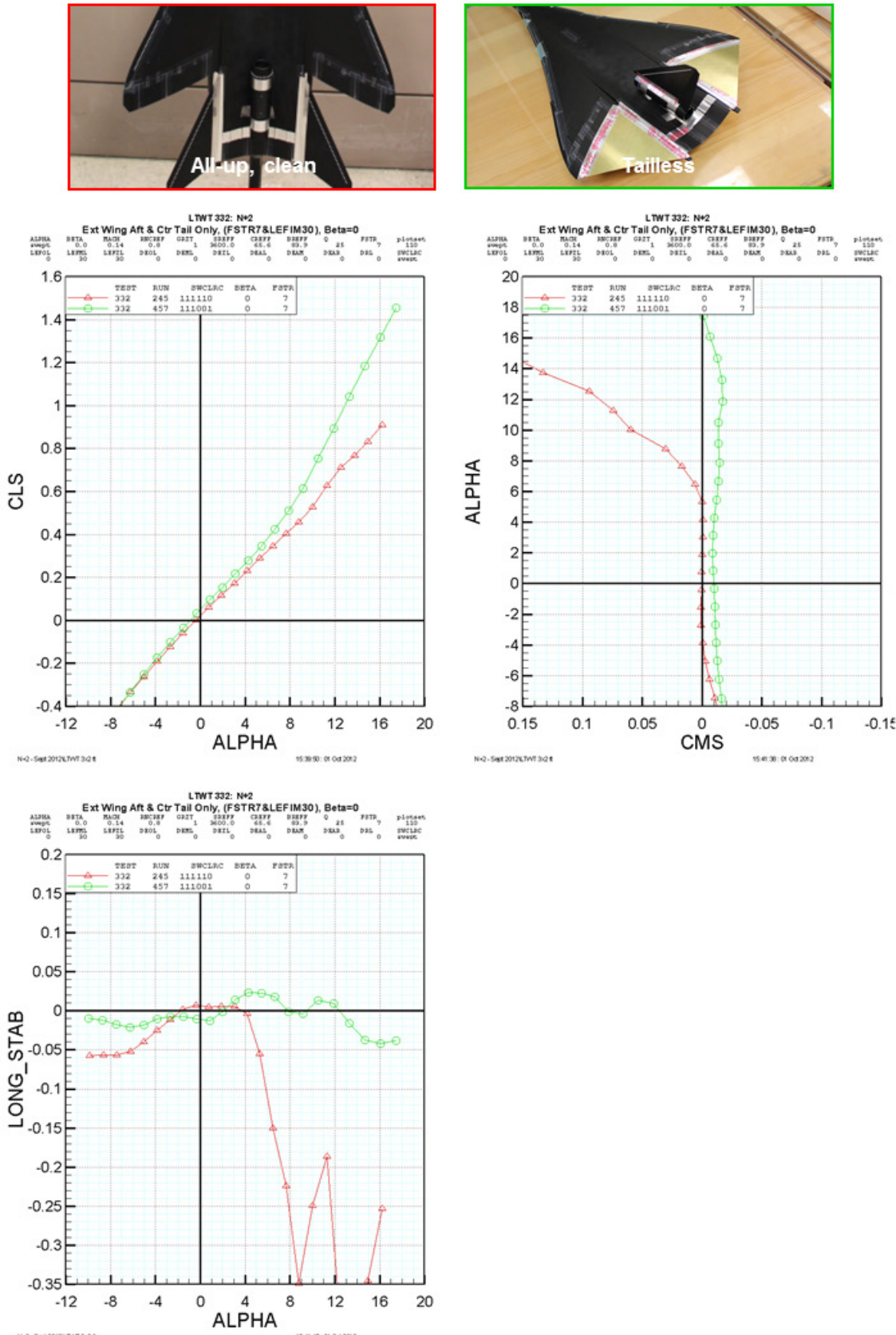


Figure 66.—Alternate Planform Study

3.0 N+2 Structural and Aeroelastic Analysis

3.1 Introduction

3.1.1 Purpose

Low-boom supersonic flight for a commercial transport places demanding requirements on aircraft configuration design. Sustained supersonic flight results in thin, plate-like lifting surfaces and long slender bodies with high fineness ratios. Shaped boom requirements also produce high fineness ratio vehicles with relatively large empennage sections on a thin aft deck as evidenced by the N+2 1044-3 configuration (see Figure 67).

These aircraft design features have raised obvious concerns about the aeroelastic characteristics of low-boom supersonic transports, both in terms of open-loop flutter speed and also interaction with the vehicle control laws due to the presence of low-frequency flexible modes that may interact with vehicle rigid body dynamics (i.e., aeroservoelasticity (Ref. 4)). These were also areas of concern for the High Speed Research program of the 1990's, which led to the fabrication and test of an aeroelastically-scaled semi-span wind tunnel model in the NASA Langley Transonic Dynamics Tunnel (Ref. 5).

As a result of these concerns and in the interest of addressing technical barriers to safe, efficient and economical supersonic flight, NASA, under the High Speed Program of the Fundamental Aeronautics Program, has funded Lockheed Martin to develop a full vehicle dynamic finite element model (FEM) of the N+2 1044-3 configuration. The purpose of this FEM is to be used as an analysis testbed by which aeroelastic and aeroservoelastic issues for low-boom supersonic configurations can be analyzed and addressed, including high fidelity computational analyses. This report discusses our approach and assumptions towards building the FEM and also initial linear open-loop flutter analysis.

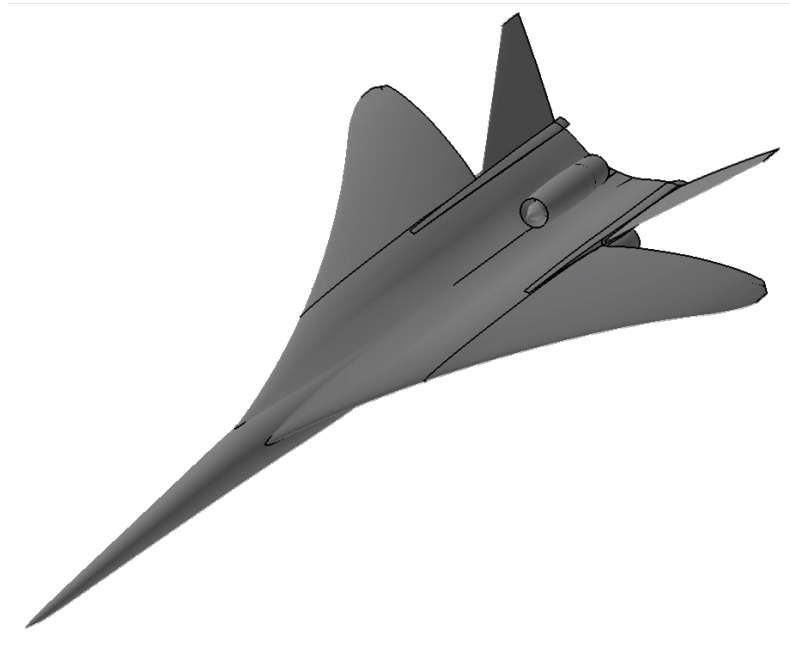


Figure 67.—Low-boom supersonic flight requirements raise natural aeroelasticity concerns

3.1.2 Objectives

The objectives of the structural analysis task are to develop a full-vehicle FEM suitable for aeroelastic analysis, provide configuration recommendations based on structural analysis, update the FEM with these recommendations, and perform linear open loop flutter analysis for an initial assessment of flutter. An essential deliverable of the project is the aeroelastic FEM, which will then be used by NASA for high-fidelity study of aeroelastic, aeroservoelastic, and aeropropulsive servoelastic challenges and development of associated tools.

3.1.3 Scope/Tasks

A FEM that is suitable for aeroelastic analysis requires that it have both representative stiffness and mass, including nonstructural mass, of the full vehicle. Towards this end, a preliminary structural layout of the vehicle, considering major loads paths and accounting for major cut-outs such as landing gear bays, cabin, cargo holds, major systems and control surfaces was developed. We then built a FEM of the structural design with materials appropriate for the temperature range and Mach number at which the vehicle will be flying. We assumed use of advanced composite materials, with some metallics at major load introduction points such as at landing gear and tail to body attachments. The FEM was then sized to a set of design load cases that were derived based on our structural design criteria assumptions and consisted of both maneuver and ground load cases. These criteria were based on FAR Part 25 and our experience from the Quiet Small Supersonic Transport (QSST) program. Aerodynamic loads were initially based on linear aerodynamics, but select cases were also based on CFD (Euler) aerodynamics. The loads also included inertial loads, which were derived through a distribution of nonstructural mass on the FEM, such that the total FEM weight and CG were consistent with the Level 1 mass properties statement of the vehicle. Nonstructural mass included fuel, system masses, passengers and cargo, engine masses, and other nonmodeled structural weight. Having developed a FEM sized to representative loads and to strength, buckling, and composite best-practices criteria, we then performed open-loop flutter analysis to determine critical flutter speed. In the course of these studies, we determined that the tail/aft-deck region deformed more than desired under load, and thus we thickened both the tail and the aft deck of the vehicle to produce a naturally stiffer structure. Each of these analyses will be explained in greater detail in the body of this report. Figure 68 shows our original program schedule with delineation of major technical tasks.

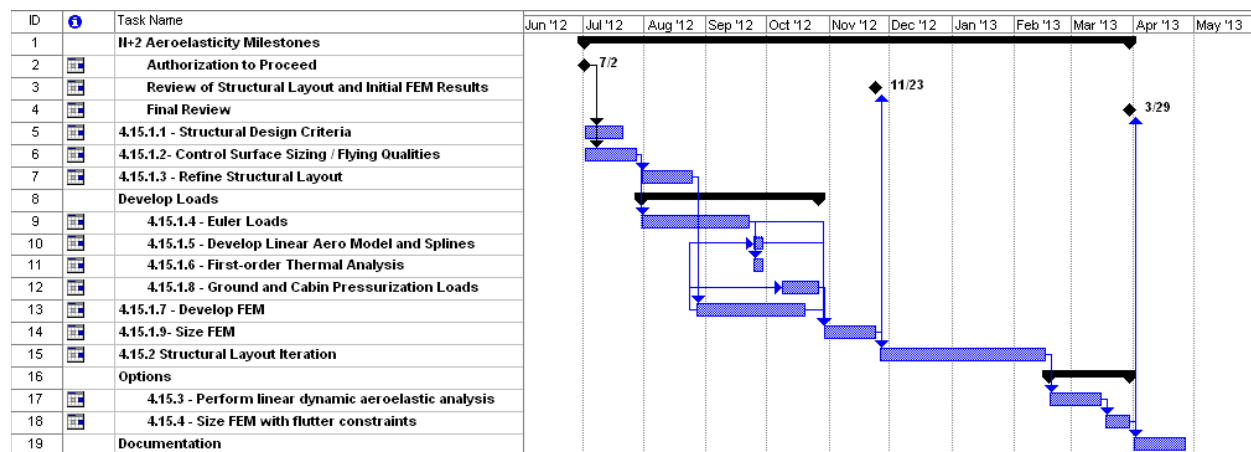


Figure 68.—N+2 Structural Analysis Tasks and Schedule

3.2 Configuration and Structural Arrangement

As a basis for the FEM development of the N+2 1044-3 configuration, we developed a representative structural layout, generating analysis-ready geometry using LM Aero's PreCEPT tool which facilitates the development of a full configuration FEM (Ref. 6). This section describes the approach used to develop a structural layout that accommodates major requirements such as cabin configuration and subsystem layout of the vehicle.

3.2.1 Configuration and Systems Layout

The general arrangement of the cabin and major internal subsystems is shown in Figure 69 and Figure 70. This configuration represents some significant structural challenges due to the lack of forward wing carry-through, a large cutout for main landing gear, and reduced structural depth towards the rear of the vehicle. Because of the unique vehicle configuration, an aft center-of-gravity (CG) is necessary, resulting in major subsystems being located toward the rear of the vehicle. This further limits the effective carry-through depth.

Figure 70 illustrates the approach taken to develop load paths that accommodate the cabin and subsystems layout. Longitudinal bending stiffness is provided primarily by large fore-aft keels within the wings. Major bulkheads around the main landing gear bay as well as wing carry-through aft of the main landing gear bay handle wing carry-through loads. The frame spacing throughout the fuselage was 26 in., and was largely determined by the spacing of the seating throughout the passenger cabin. This spacing drove much of the topology in the inner wing as well. The structural layout shown in Figure 71 represents an early approach, where the spars in the outer wing were distributed in a manner that aimed to direct load towards the wing carry through region. As the structural layout matured, it became difficult to resolve spacing issues near the intersection of these spars with the wing leading edge. As a result, a more uniform spacing approach was adopted.

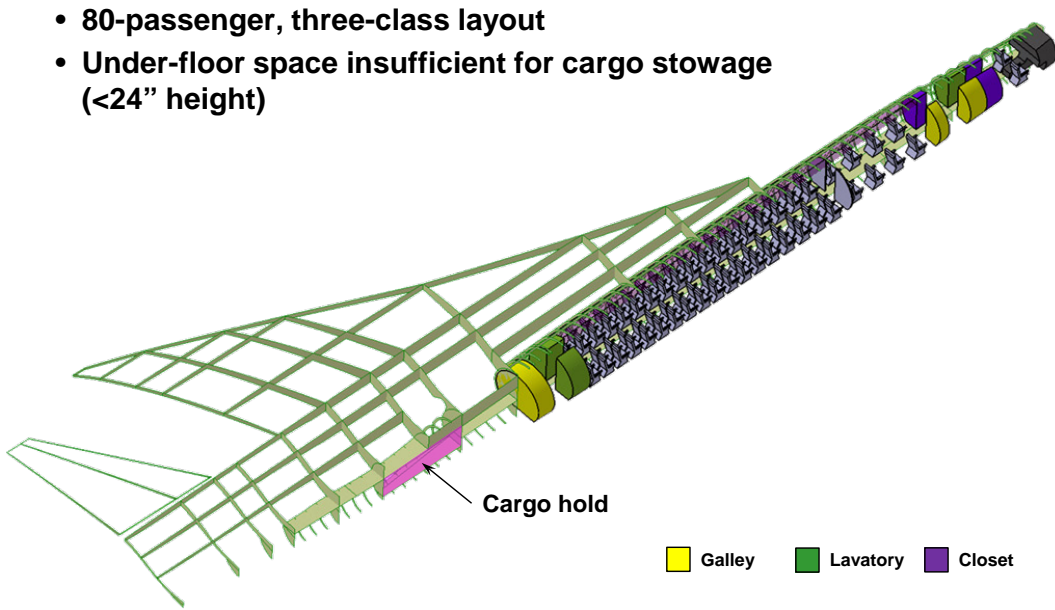


Figure 69.—Cabin Layout for the 1044-2 Configuration

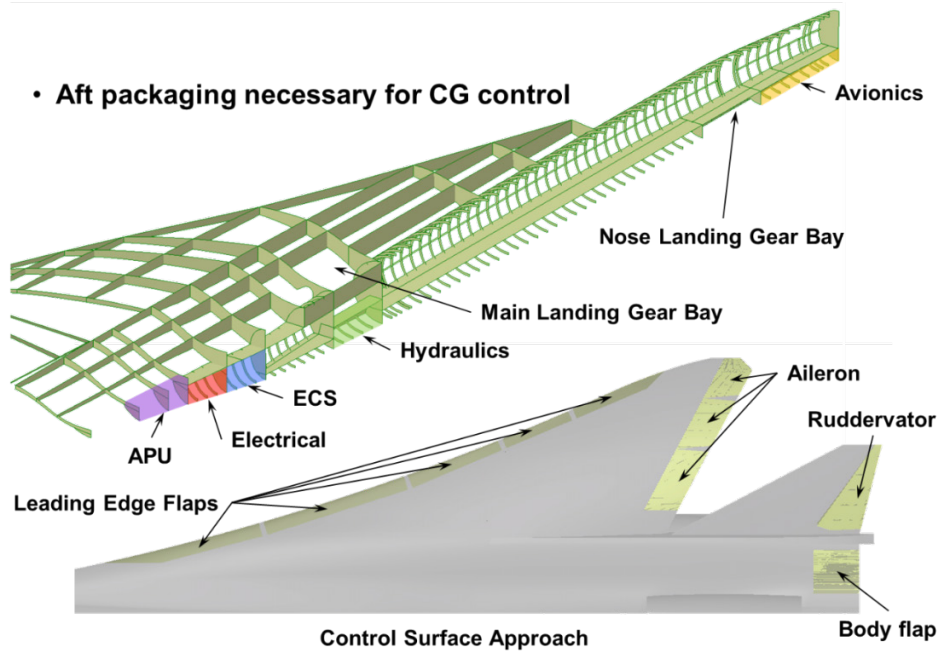


Figure 70.—Layout of Major Subsystems

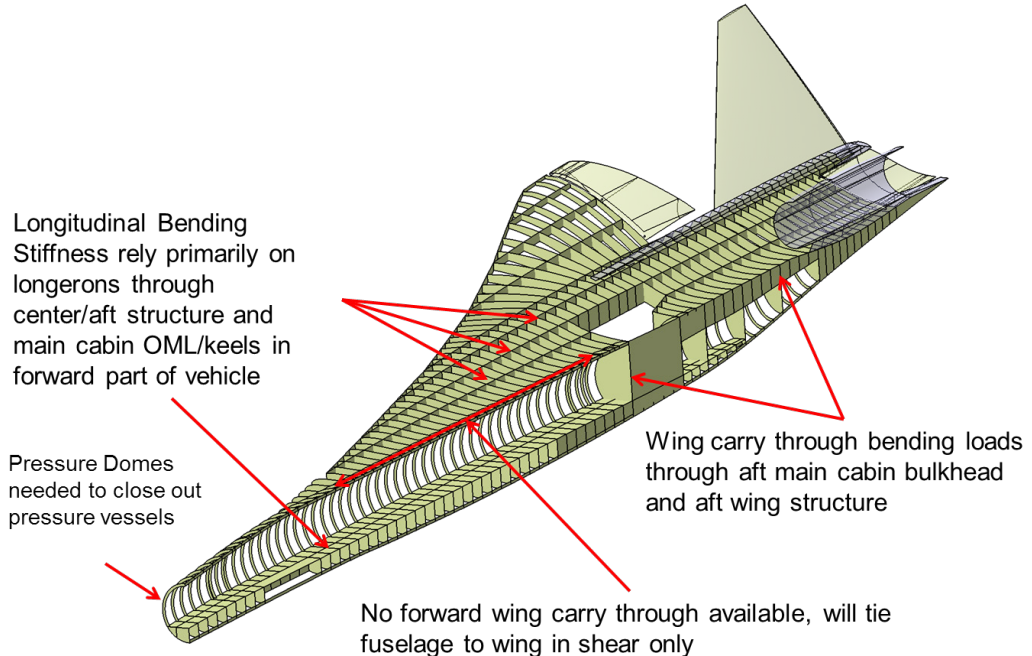


Figure 71.—Concepts for Major Load Paths Developed to Accommodate Cabin and Subsystems Layout (Early Concept)

Due to the lack of a forward wing carry-through, shear ties were used to avoid transmission of local bending loads into the fuselage OML, as described in Figure 72. Additional work is needed to mature this concept. However, in the absence of more detailed design and analysis work, we decided that this was a feasible solution to integrating the forward wing with the fuselage. The concept relies on the transmission of shear loads only through a pin/link-type arrangement. The goal of this approach is to avoid the

transmission of bending loads, and thus compression, into the fuselage, which may lack sufficient structural depth to accommodate these types of loads.

Figure 73 contains several views of the final structural arrangement; with an inset image of an early approach for comparison of the spar configuration on the outer wing (see also Figure 71 for this early concept). The final spar spacing on the outer wing is roughly 20 in., which is similar to spacing used on the Quiet Supersonic Transport (QSST). Control surface substructure was added to facilitate trimmed aeroelastic loads, and details like fuselage stringers, door framing, and pressure bulkheads were added to increase the applicability of the FEM towards characterizing the major structural aspects of the fuselage.

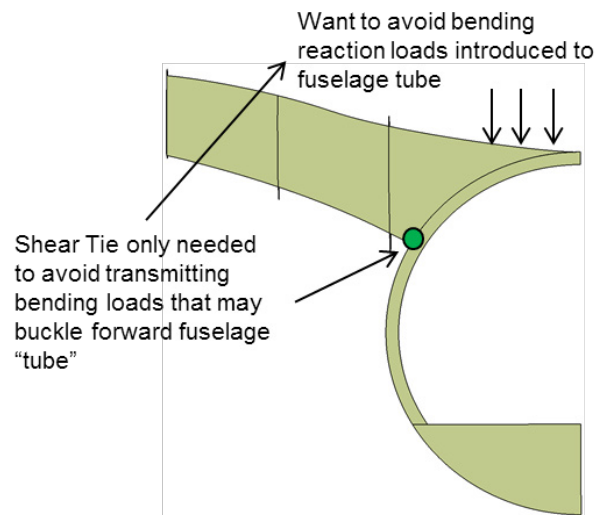


Figure 72.—Concept for the Shear Ties Attaching the Forward Wing to the Fuselage.

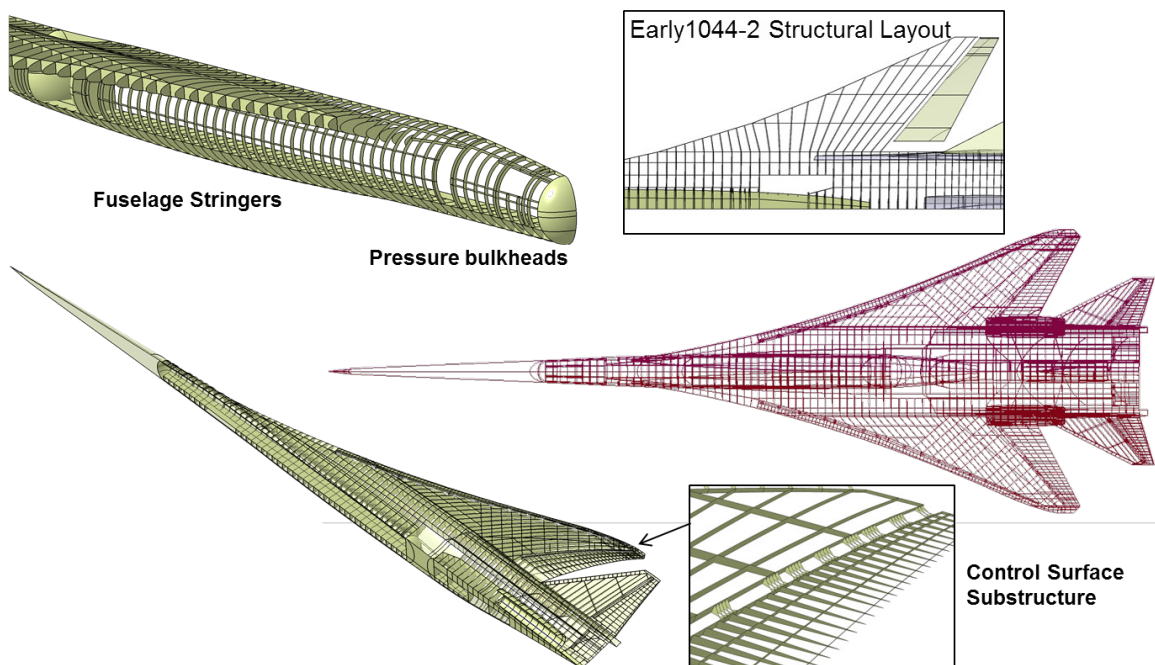


Figure 73.—Final Structural Layout for the 1044-3 Configuration

3.2.2 Control Surface Sizing and Definition

The control surface scheme used for this study is illustrated in Figure 70. The control surface suite consists of 4 leading edge flaps, 3 trailing edge flaps (flaperon and two ailerons), a ruddervator, and a body flap. A low turbulence wind tunnel test was conducted in September of 2012 to assess the effectiveness of the initial control surface layout and provide guidance for sizing. A variety of control surface configurations and planform modifications were tested. Overall, the vehicle exhibited good characteristics with the exception of an expected pitch up at low speed, due to the interaction of wing vortex with the canted vertical tails. Krueger flaps were initially considered for the leading edge devices. However, it was found that plain flaps were sufficient. The trailing edge flaps were shown to be sufficient in size, although the body flap size was reduced as a result of the test.

3.2.3 PreCEPT

LM Aero's PreCEPT tool was used to develop the geometry representing the structural layout. PreCEPT is a tool that implements a Smart Product Model, and using automation, creates components in CATIAV5 that contain geometry and metadata that are consumed during downstream analysis model development. PreCEPT is also linked with Altair's Hypermesh, which was used to develop the FEM. During the generation of the FEM, additional automation routines are used to perform cleanup, meshing, and material and property assignments, reducing the time required for model development. PreCEPT also supports a unique scripting language, which enables the automation of repetitive component creation. A majority of the structural layout for the N+2 configuration was scripted, with variables that would allow variable spacing throughout portions of the vehicle. These procedures were used to conduct alternative arrangements such as the early outer wing spar arrangement, to arrive at the final structural arrangement. Reference 6 has further detail about the PreCEPT tool.

3.3 Structural Design Criteria and Design Loads

We developed preliminary structural design criteria for the purposes of defining a set of design load cases to which the structural FEM would be sized. The main goal behind this task was to develop a set of preliminary design load cases that would be major drivers of the primary airframe structure. This exercise was not intended to be an exhaustive loads development process as would be done in a full-scale development program, but to provide select major load cases and thus produce a FEM that, overall, has representative stiffness for flutter analysis.

3.3.1 Structural Design Criteria and Design Load Cases

The N+2 gross weight of nearly 350,000 lb makes the vehicle applicable to FAR Part 25, and thus we pulled heavily from this document to define our structural design criteria. In addition, we also leveraged the design criteria and design load work that had been done in LM's Quiet Small Supersonic Transport (QSST) program (Document No. 422DS201, Ref. 7). This document facilitated identification of flight maneuver, landing and ground handling load cases.

Basic vehicle parameters and weights, important for loads calculations, are shown in Table 8. Maneuver and gust load cases were developed at 3 vehicle weights: Zero Fuel Weight (ZFW), which would be indicative of near landing, Design Take-off Weight (DTOW), indicative of near takeoff, and Design Take-off Weight 2 (DTOW2), corresponding to the beginning of the cruise segment. In addition, the Design Landing Weight is defined as the zero fuel weight plus 35 percent of available fuel. It is at this weight that sink speeds of 10 ft/s for landing load calculations are assumed. At the heavier DTOW, a sink speed of 6 ft/s is assumed for landing load calculations. The main and nose gear ground contact locations, relative to the vehicle center-of-gravity (CG) are needed in order to determine balanced loads at each gear for the ground and landing load cases.

TABLE 8.—CONFIGURATION AND DESIGN WEIGHTS DATA

Parameter	Value
Wing Reference Area	3600 ft ²
Wing Span	83 ft 10 in
Vehicle Length	244 ft
Main Gear Ground Contact Point	FS = 2,112.26 in., BL = \pm 84 in., WL = 89.61 in.
Nose Gear Ground Contact Point	FS = 1,002.64 in., BL = 0.0 in., WL = 126.85 in.
Zero Fuel Weight.....	157,608 lb
Design Landing Weight.....	220,308 lb
Design Take-off Weight (DTOW).....	332,732 lb
DTOW2 (Begin Cruise).....	301,210 lb
Total Fuel.....	175,124 lb

TABLE 9.—N+2 DESIGN SPEEDS

Design Speed	Value
Cruise Speed (V _C).....	400 KEAS
Dive Speed (V _D)	450 KEAS
Maneuvering Speed (V _A)	318 KEAS
Speed for Max Gust Intensity (V _B)	275 KEAS (FAR 25.335)
Landing Speed	169 KEAS
Cruise Mach Number (M _C).....	Mach = 1.8
Dive Mach Number (M _D)	Mach = 2.0

Table 9 shows the design speeds that were the basis of our preliminary design loads. While these speeds were defined with the guidance of FAR Part 25, this is not the complete list of structural design speeds. There are other speeds identified in FAR Part 25, such as flap speed and gear extended speed, but these were felt to not be as significant design drivers of primary airframe structure, such as wing box, fuselage, and tail structure.

As a companion to Table 9 is the Mach, Altitude flight envelope in Figure 74, which defines the vehicle maximum Mach number as a function of altitude. This envelope is also important from a flutter perspective as the vehicle is required to be flutter-free 15 percent beyond dive speed. While the N+2 vehicle cruises at Mach 1.8, provision is made in emergency situations to dive at Mach 2.0. The dark circles on the figure indicate where there are design load cases used for structural sizing.

Maximum and minimum design load factors are defined for this vehicle to be +2.5 g and -1 g, respectively, consistent with commercial transports. Several V-n diagrams which plot maximum and minimum maneuver load factor against vehicle speed (in knots equivalent or KEAS) were created at different gross weights and flight altitudes. In addition, gust load factors which are defined by standard discrete gust equations in FAR Part 25 are also included on the V-n diagram. From the V-n diagram analysis, one gust load case was identified for the design loads and is associated with a ZFW condition at 20,000 ft altitude. The discrete gust load factor for this case is 2.7 g and is identified in Figure 75 by the dark circle.

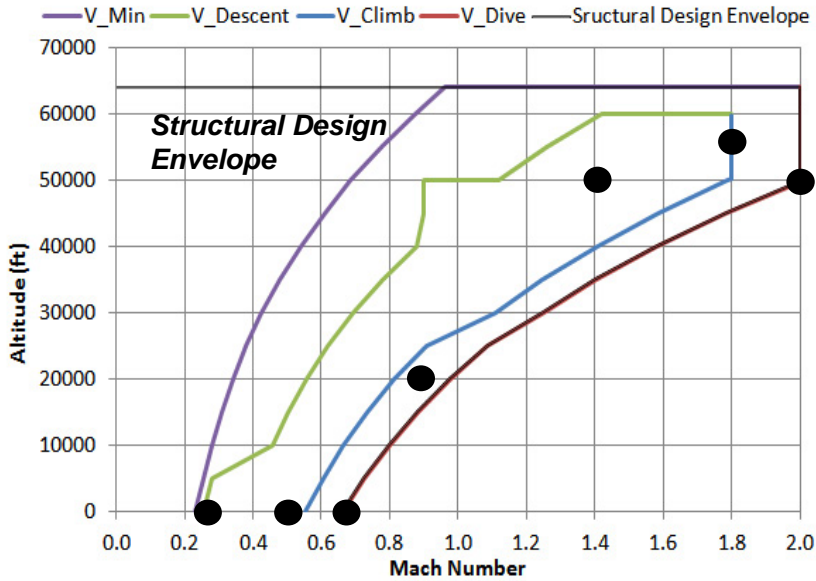


Figure 74.—N+2 Mach, Altitude Flight Envelope

Zero Fuel Weight Configuration at 20,000 feet

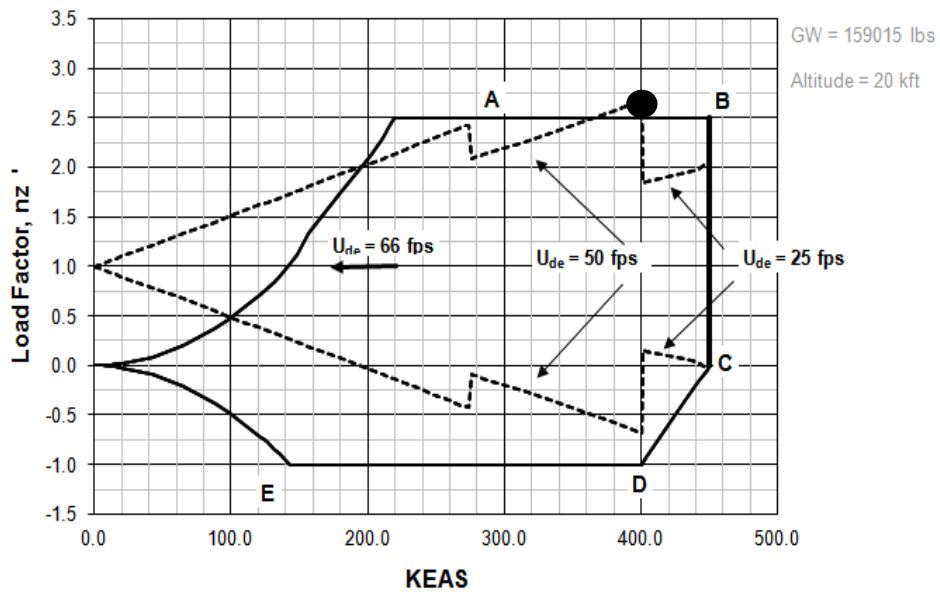


Figure 75.—Sample V-n Diagram

Table 10 is a summary of the maneuver load cases used for preliminary sizing of the structure that were developed based on the previous design criteria. They include a mix of pull-up and push-over maneuvers at various design speeds, altitudes, and gross weights. In addition, they include some asymmetric maneuvers, along with a gust case and a cruise condition. The landing condition is developed and the air loads associated with it are applied along with the gear loads to develop balanced landing load conditions.

Each of the maneuver load cases has an associated cabin pressure, as well, which is a function of altitude. The cabin pressure is maintained to be no less than that corresponding to an altitude of 6,000 ft. Thus above 6,000 ft there is a pressure difference between the cabin and the atmosphere which is defined in Table 11.

TABLE 10.—MANEUVER LOAD CASES

Case no.	Description	Mach	Speed (KEAS)	Nz	Weight	Altitude (ft)
100	Pull up	0.66	438.00	2.50	DTOW	Sea Level
200	Push over	0.66	438.00	-1.00	DTOW	Sea Level
300	Pull up	0.48	318.0	2.50	DTOW	Sea Level
400	Pull up	2.00	450.00	2.50	DTOW2	49,770
500	Push Over	2.00	450.00	-1.00	DTOW2	49,770
600	Pull up	1.41	318.00	2.50	DTOW	49,770
700	Pull up	0.66	438.00	2.50	ZFW	Sea Level
800	Push over	0.66	438.00	-1.00	ZFW	Sea Level
900	Pull up	2.00	450.00	2.50	ZFW	49,770
1000	Push over	2.00	450.00	-1.00	ZFW	49,770
1100	Steady roll (Roll rate = 30°/sec)	0.48	318.00	0.00	DTOW	Sea Level
1200	Abrupt roll (Roll accel = 30°/sec ²)	0.48	318.00	0.00	DTOW	Sea Level
1300	Steady roll (Roll rate = 30°/sec)	0.48	318.00	1.67	DTOW	Sea Level
1400	Abrupt roll (Roll accel = 30°/sec ²)	0.48	318.00	1.67	DTOW	Sea Level
1500	Landing 1g	0.26	169.00	1.00	DTOW	Sea Level
1600	Cruise 1g	1.80	357.00	1.00	DTOW	55,000
1700	Gust Loads	0.89	400.00	2.70	ZFW	20,000

TABLE 11.—CABIN PRESSURE AS A FUNCTION OF ALTITUDE

Altitude (ft)	Cabin Pressure (psi)	Ambient Pressure (psi)	Cabin ΔP (psi)
0	14.7	14.7	0
1000	14.18	14.18	0
2000	13.67	13.67	0
3000	13.18	13.18	0
4000	12.7	12.7	0
5000	12.23	12.23	0
6000	11.78	11.78	0
7000	11.78	11.34	0.44
8000	11.78	10.92	0.86
9000	11.78	10.51	1.27
10,000	11.78	10.11	1.67
20,000	11.78	6.76	5.02
30,000	11.78	4.37	7.41
40,000	11.78	2.72	9.06
50,000	11.78	1.68	10.1
60,000	11.78	1.04	10.74
64,000	11.78	1.04	10.74

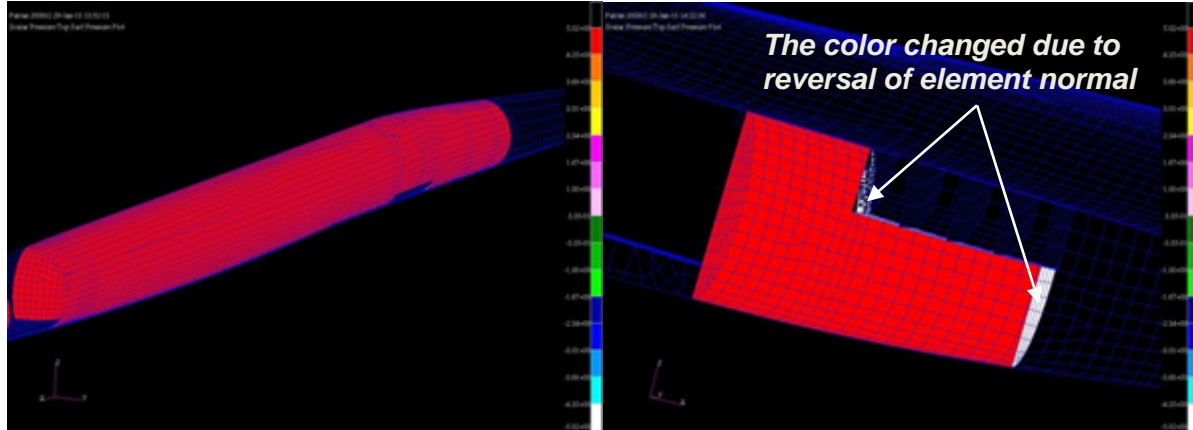


Figure 76.—A uniform pressure is applied to the cabin (left figure) and cargo bay (right figure)

The pressure difference was applied to the FEM, as shown in Figure 76, both to the main cabin and the cargo hold. The magnitude of the pressure depended on the altitude of the maneuver and was specified by the right hand column of Table 11.

Table 12 shows the landing load cases and associated gear reactions that were considered for N+2. A 1g air load was also applied to the vehicle for all landing cases. The vehicle gross weights that are reported are those corresponding to an earlier FEM, which was a little heavier than the mass properties weight target of 332,732 lb reported in Table 8. For the landing loads, we extensively leveraged previous work that had been done in the QSST program. Main and nose gear vertical reaction forces for the Level Landing (LL) case were scaled up based on the weight from the QSST reaction forces according to the following equation:

$$FZLL_{N+2} = FZLL_{QSST} \frac{Weight_{N+2}}{Weight_{QSST}} \quad (1)$$

For Spin-Up (SU) and Spring-Back (SB) load cases, the main and nose gear vertical reaction forces were scaled from Level Landing loads as follows:

$$FZ(SU \text{ or } SB)_{N+2} = 0.8 * FZLL_{N+2} \quad (2)$$

Fore and aft drag forces were computed from the vertical forces by:

$$FX_{N+2} = \pm 0.8 * FZ_{N+2} \quad (3)$$

The ground handling load cases are defined in Table 13. In this case, the reaction forces were computed according to FAR Part 25, Sections 25.471-25.507. No air loads were applied to the vehicle for these cases.

TABLE 12.—LANDING LOAD CASES

Design Takeoff Weight				Design Landing Weight		
Weight (lb)	334139			220308		
Xcg (in.)	2020			2069		
Zcg (in.)	256			243		
Sink Rate (ft/s)	6			10		
	Right MG	Left MG	Nose Gear	Right MG	Left MG	Nose Gear
Static Condition	FZ	153139	153139	27861	105885	105885
	FY	0	0	0	0	0
	FX	0	0	0	0	0
Level Landing	FZ	120290	120290	21341	264368	264368
	FY	0	0	0	0	0
	FX	30073	30073	5335	66092	66092
Air Load	FZ	334139			220307	
Spin-up Case	FZ	96232	96232	17073	211495	211495
	FY	0	0	0	0	0
	FX	76986	76986	13658	169196	169196
Air Load	FZ	334139			220307	
Spring-back Case	FZ	96232	96232	17073	211495	211495
	FY	0	0	0	0	0
	FX	-76986	-76986	-13658	-169196	-169196
Air Load	FZ	334139			220307	
Lateral Drift Landing	FZ	90218	90218	21341	198276	198276
	FY	22554	22554	5335	49569	49569
	FX	36087	36087	8536	79311	79311
Air Load	FZ	334139			220307	
One Gear Landing	FZ	120290	0	0	264368	0
	FY	0	0	0	0	0
	FX	30073	0	0	66092	0
Air Load	FZ	334139			220307	
Side Load Landing	FZ	60145	60145	0	132184	132184
	FY	48116	36087	0	105747	79311
	FX	0	0	0	0	0
Air Load	FZ	334139			220307	
Side Load Landing – L to R	FZ	60145	60145	0	105747	105747
	FY	-48116	-36087	0	-84598	-63448
	FX	0	0	0	0	0
Air Load	FZ	334139			220307	

TABLE 13.—GROUND HANDLING LOAD CASES

		Design Takeoff Weight			Design Landing Weight		
Weight (lb)		334139			220308		
Xcg (in.)		2020			2069		
Zcg (in.)		256			243		
Sink Rate (ft/s)		6			10		
		Right MG	Left MG	Nose Gear	Right MG	Left MG	Nose Gear
Static Condition	FZ	153139	153139	27861	105885	105885	8538
	FY	0	0	0	0	0	0
	FX	0	0	0	0	0	0
3-point Braked Roll	FZ	153139	153139	67875	127061	127061	39432
	FY	0	0	0	0	0	0
	FX	122511	122511	0	101649	101649	0
2-point Braked Roll	FZ	153139	153139	0	127061	127061	0
	FY	0	0	0	0	0	0
	FX	122511	122511	0	101649	101649	0
Dynamic Roll Braking	FZ	153139	153139	92275			
	FY	0	0	0			
	FX	122511	122511	0			
Turning Condition	FZ	153139	153139	27861	105885	105885	8538
	FY	76569	76569	13931	52942	52942	4269
	FX	0	0	6965	0	0	2134
Nwhl yaw and steering (1)	FZ	153139	153139	27861	105885	105885	8538
	FY	0	0	22289	0	0	6830
	FX	0	0	0	0	0	0
Nwhl yaw and steering (2)	FZ	153139	153139	47868	105885	105885	27815
	FY	0	0	-10118	0	0	-6671
	FX	122511	0	0	84708	0	0
Reversed Braking	FZ	153139	153139	0	105885	105885	0
	FY	0	0	0	0	0	0
	FX	-84226	-84226	0	-58237	-58237	0
2-G Taxi	FZ	306278	306278	83584	211769	211769	25614
	FY	0	0	0	0	0	0
	FX	0	0	0	0	0	0

The inertia relief capability in MSC.NASTRAN was used to compute inertia forces that balance the externally applied landing and ground handling forces for a free-free vehicle boundary condition (i.e., free to translate vertically, fore-aft, and pitch). As shown in Figure 77, ground reactions were applied at the ground contact points for the ground control cases and landing cases where side force was present. For the remainder of the landing cases, the vertical and drag forces were applied at the axle.

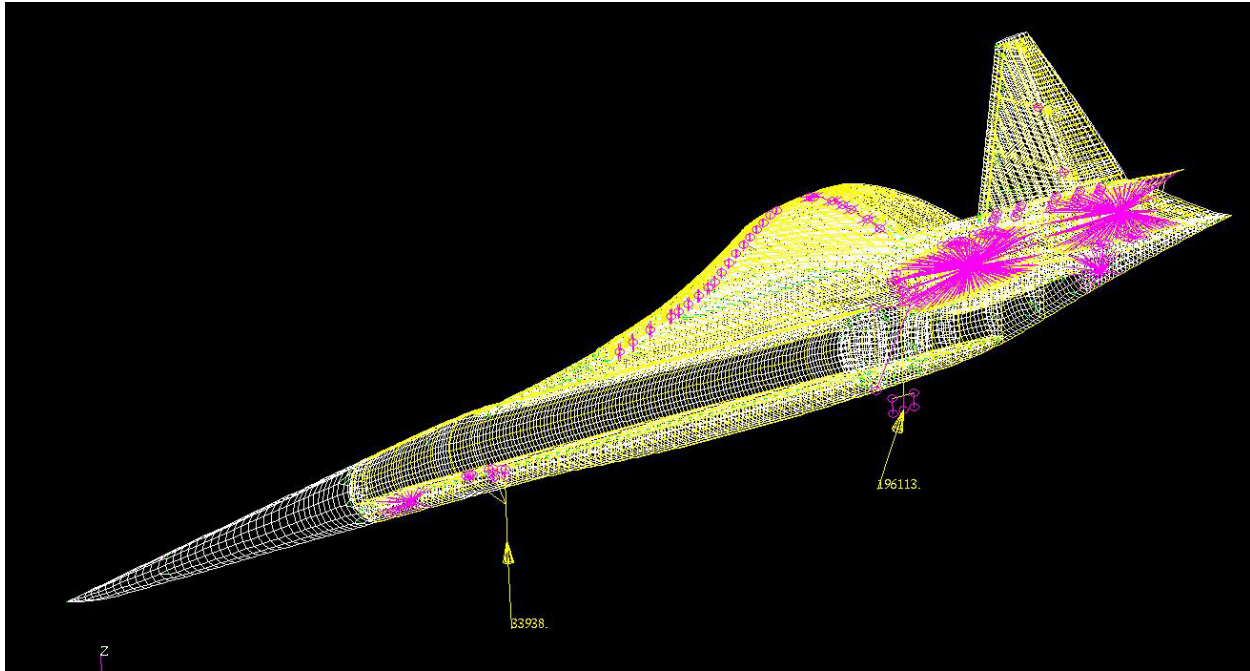


Figure 77.—Application of Landing and Ground Handling Loads to FEM

3.3.2 Linear Aerodynamic Maneuver Loads

External flight loads were computed via static aeroelastic analysis in MSC.NASTRAN (SOL144). We utilized the linear aerodynamic doublet-lattice method available in the solution and for initial loads calculations assumed rigid aerodynamics, eventually transitioning to flexible aerodynamics as the structural design matured. We also developed loads for a select number of cases using CFD (Euler) predictions as described in the next section.

Figure 78 shows the linear aerodynamic model used both for maneuver loads and flutter analyses. The lifting surface waterline is at $z=285.83$ in, which corresponds to the most inboard leading edge flap hinge point. As shown in the figure, there are 9 control surfaces, 4 leading edge flaps (LEF), 2 ailerons, 1 trailing edge flap (TEF), 1 body flap and 1 rudder. For this semispan aerodynamic model there are 1900 individual aerodynamic boxes. Guidelines for developing the model included: avoiding abrupt element size changes between panels, maintaining streamwise continuity between panels (which required splitting the control surfaces into several pieces), and aiming for boxes with aspect ratios of 1 to 2 as much as possible without letting the number of elements become excessive.

Aerodynamic forces were transferred to the structural model via infinite plate splines. Conversely, displacements from the structural model were then transferred to the aerodynamic model by the same splines (which can be derived through principles of virtual work). As a check of the spline quality, flexible modal displacements from the FEM were mapped to the aerodynamic model, and as seen from Figure 79 through Figure 81, the splines adequately transfer displacements from the FEM to the linear aerodynamic model.

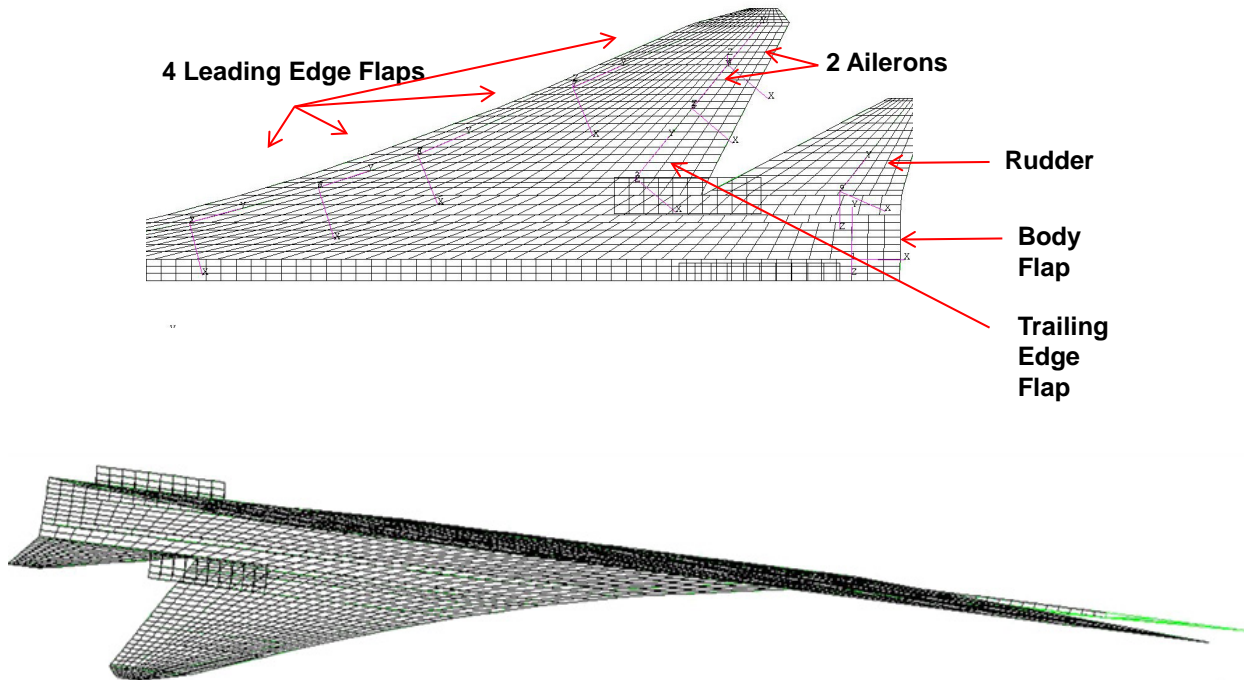


Figure 78.—Linear Aerodynamic Model for Loads and Flutter Analysis

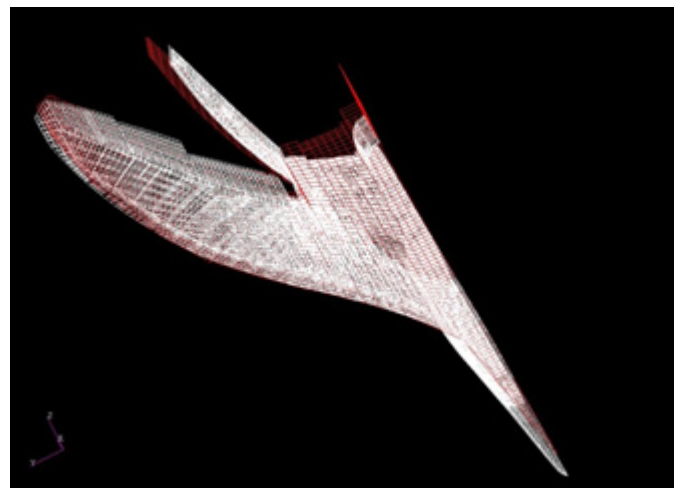


Figure 79.—Spline Verification—Wing Up-Bending

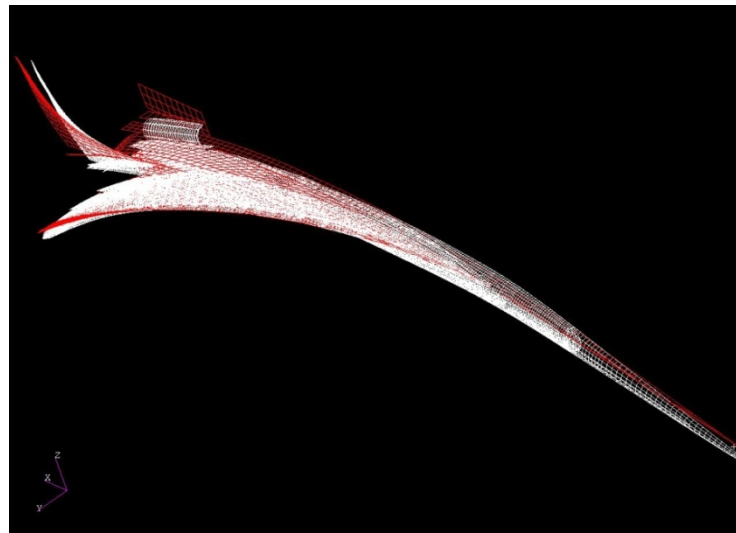


Figure 80.—Spline Verification—Fuselage Down-Bending

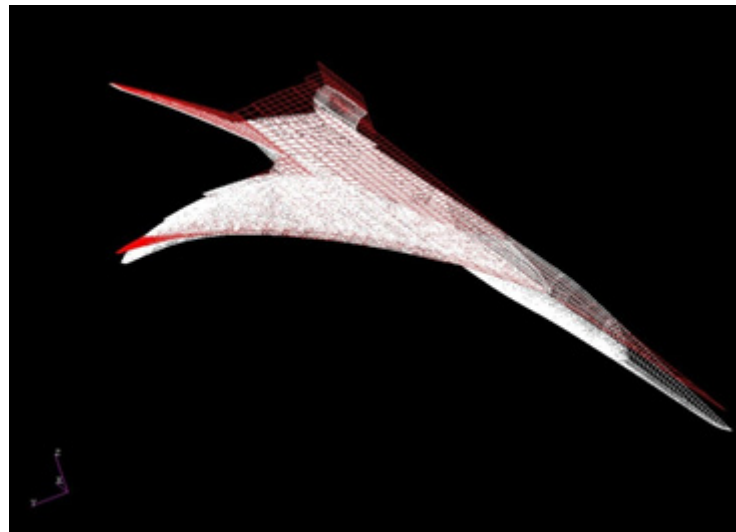


Figure 81.—Spline Verification—Wing Down-Bending

For both the maneuver load calculations and the landing/ground handling loads, the structural model was supported at a grid point on the symmetry plane. For symmetric trim cases, the support point is fixed in all degrees of freedom except in vertical translation and pitch. For antisymmetric cases, only rigid body roll is free at the support point. The support point is shown in Figure 82 and was developed to not add stiffness to the FEM.

For the symmetric maneuvers of Table 10, the trim variables were angle of attack (AOA) and body flap. For cases where the body flap deflection exceeded 30°, trailing edge control surfaces on the main wing were scheduled to deflect with the body flap in a 1:1 ratio. The two wing ailerons were used to trim the vehicle in roll and were linked together to deflect equally.

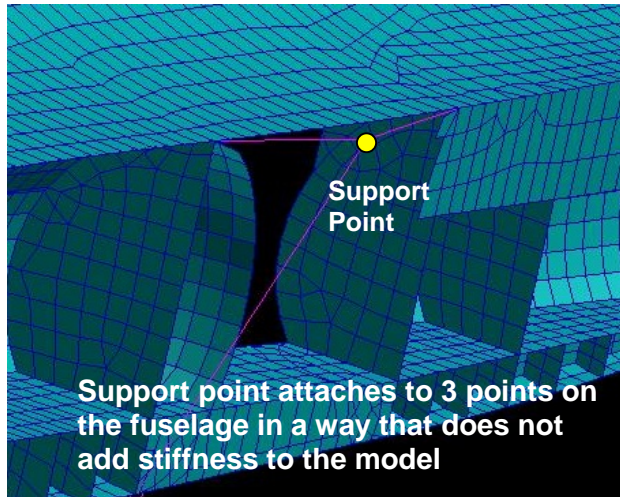


Figure 82.—Support Point Definition

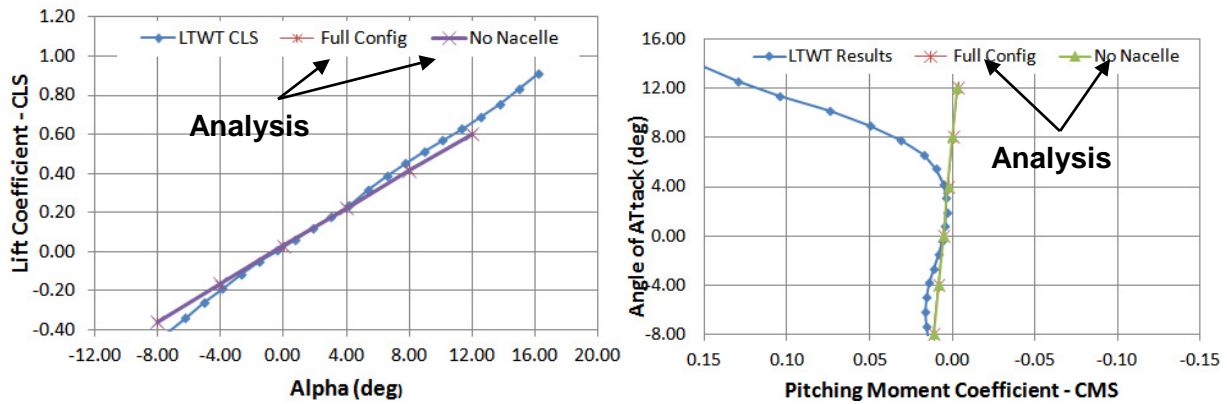


Figure 83.—Comparison of Linear Aero Model to LTWT Test Data (Mach 0.14)

Figure 83 shows a comparison of the linear aerodynamic model with Low Turbulence Wind Tunnel (LTWT) test results, for both lift and pitching moment. The Mach number is 0.14, and the LTWT data is a sweep in AOA from -8° to $+12^\circ$. Pitching moments were computed about the wind tunnel data moment reference center ($X=2035.21$ in., $Y=0$ in., $Z=261.5$ in.). The objective of this study was to compare linear aerodynamic results to LTWT test results and assess the impact of under-wing nacelle on lift and pitching moment. Rigid aerodynamics was assumed in this analysis as the wind tunnel model was rigid. For the linear aerodynamic model, geometric incidence of the fuselage and wing twist were modeled and are part of the linear data in the plots. In general, the lift curve of the linear aerodynamic model matches well that of the LTWT data, particularly at modest AOA (-4° to $+4^\circ$), and there is little impact to removing the under-wing cruciform nacelle. As expected the pitching moment trends of the linear model do not match wind tunnel test data well, not predicting at all the unstable pitch break at about 4° AOA. However, the slope of the pitch curve is matched reasonably well near 0° AOA.

Figure 84 is a comparison of the lift curve as predicted by the linear aerodynamic model and compared to supersonic (Mach 1.7) wind tunnel test data. The linear aerodynamic model matches the measured lift curve quite well, especially when fuselage incidence and wing twist are removed from the model. Based on this data and the previous figure, we decided to include the incidence and twist for subsonic maneuver load cases and remove it for supersonic load cases.

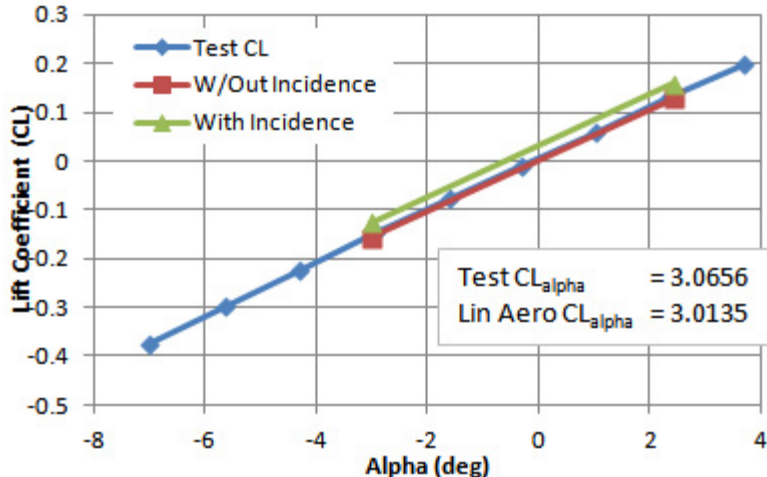


Figure 84.—Comparison of Linear Aero Lift Coefficient with Test (Mach 1.7)

3.3.3 CFD-Loads Model and Trim Scheme

CFD-based, trimmed flight loads were developed for select maneuver load cases of Table 10. To accomplish this, a CFD loads model with sufficient detail to allow the actuation of control surfaces was developed. The baseline control surface scheme consisted of 4 leading edge flaps, 3 trailing edge flaps, a body flap, and a ruddervator. Due to spanwise camber on the wing, the wedge-shaped gaps between the trailing edge flaps were generated in order to allow deflection of the control surfaces without collision up to 30°. Figure 85 shows the shape of the gaps, as well as the shape of the trailing edge flaps when deflected.

The trimmed CFD-based (Euler) maneuver loads were generated using LM Aero's computational aeroelasticity toolset, consisting of in-house aerodynamic and structural solvers linked together with the MultiDisciplinary Computing Environment (MDICE) (Refs. 8 and 9). MDICE is a commercial product maintained by CFD Research Corporation in Huntsville, AL. The aerodynamic portion of the CFD-based aeroelastic analysis was performed by LM Aero's in-house solver Splitflow. Splitflow is a Cartesian, Euler/Navier-Stokes Solver. It requires a triangulated surface grid as input, and generates its own volumetric grid. Figure 86 contains images of the surface mesh used by Splitflow. MDICE is used to coordinate the transfer of information between the aerodynamic and structural codes. MDICE uses an application programming interface (API) layer to link with analyses, transferring information between these processes in memory, thereby avoiding file-based transfer of data. Figure 87 contains an image of this process. MDICE also manages the execution of the simulation via a scripting language, thus enabling tailoring of the aeroelastic simulation to meet various goals and trim schemes.

The structural portion of the aeroelastic analysis is handled by LMMS, which is a linear structural analysis solver developed in-house. LMMS uses the normal modes computed by NASTRAN in combination with the nodes and element connectivity of the FEM to compute deflections due to loads transmitted from the aerodynamic analysis through MDICE. MDICE then maps the resulting deflections back to the aerodynamic grid in preparation for the next iteration of loads analysis. This process is repeated until convergence is achieved. LMMS also has utilities for computing deformation due to control surface deflections, which are superimposed on the elastic deflections before sending to MDICE.

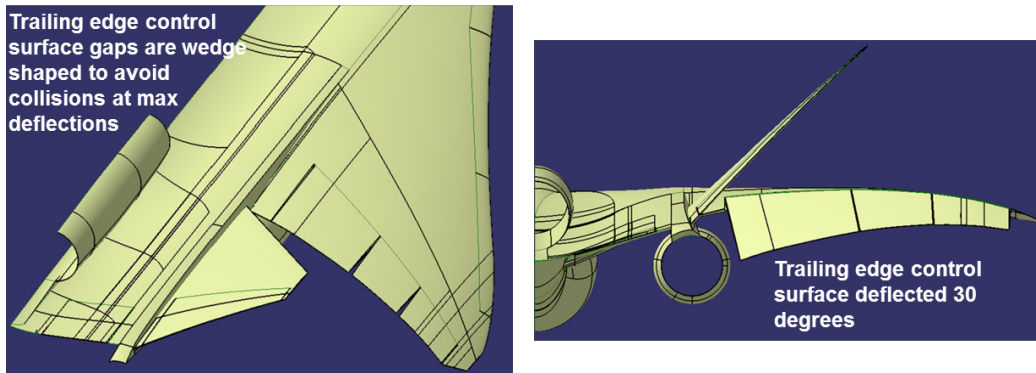


Figure 85.—Wedge Shaped Gaps Needed to Enable 30° of Trailing Edge Flap Actuation

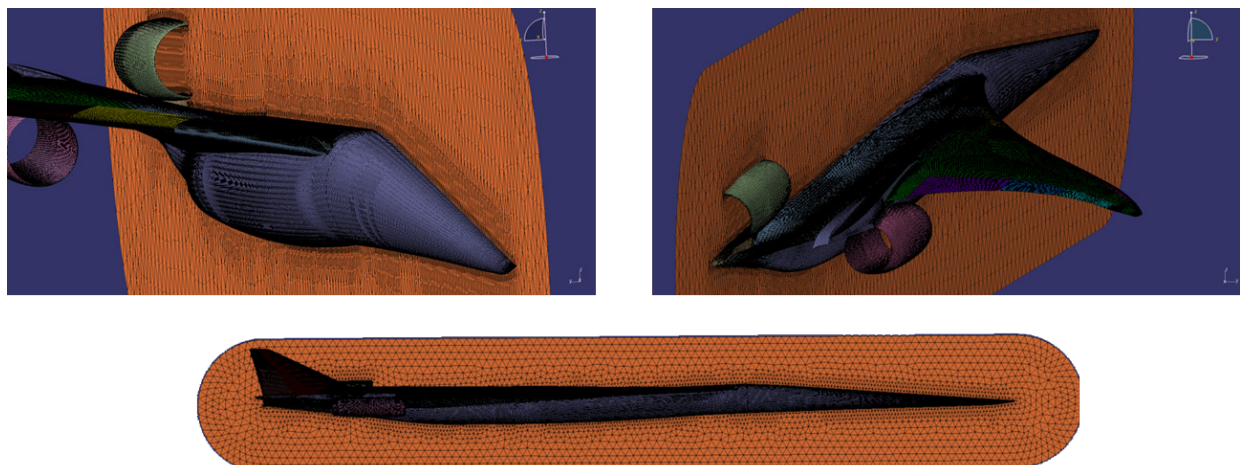


Figure 86.—N+2 Configuration 1044-3 Surface Mesh used by Splitflow for CFD-Based Aeroelastic Analysis

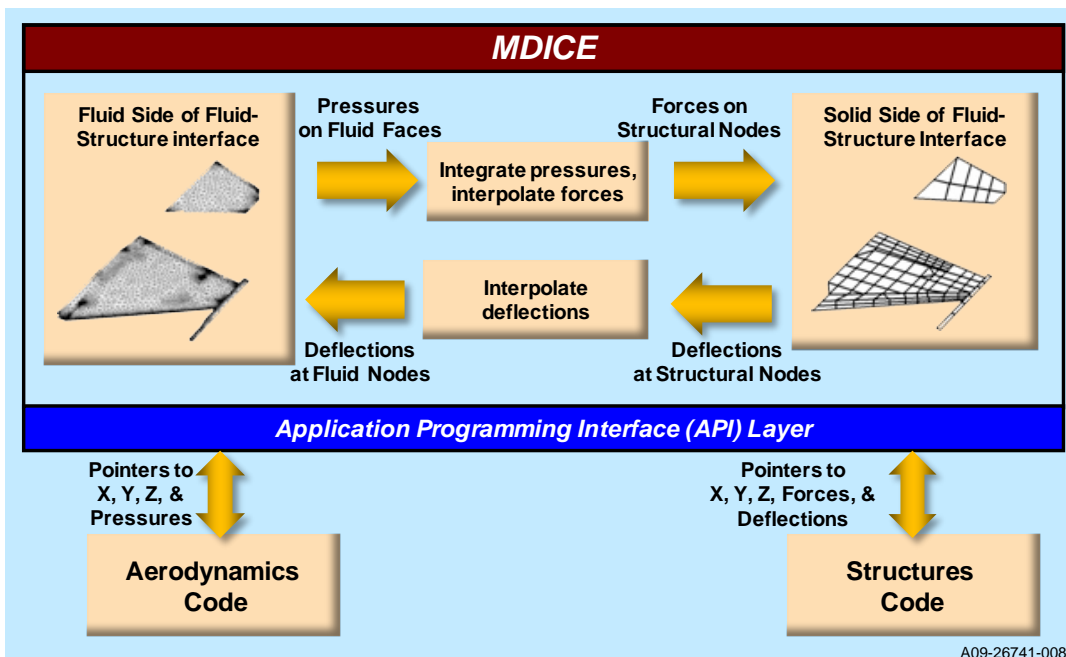


Figure 87.—MDICE uses an Application Programming Interface to Transfer Forces and Deflections Between Aerodynamic and Structural Analyses.

For most aeroelastic simulations, the surface meshes of both the fluid and structural models are segregated into individual patches which afford control over how forces and deflections are mapped between the disciplines. Corresponding pairs of aerodynamic and structural patches are referred to as fluid-structure interfaces. Control surfaces are usually separated in a manner distinct from the wing box, to allow the specification of control surface deflections without impacting the surrounding structure, as well as to capture aeroelastic phenomenon where there is a discontinuity between surfaces such as control surface blow-back. For the N+2 configuration, the surface mesh was discretized into 16 different patches, with an additional patch representing the symmetry plane to blend fuselage deformations into this portion of the mesh. Control surface deflections are generated by computing the needed motion on the structural model, and then super-imposing these deflections on the elastic deflections before they are passed to the fluids grid via MDICE. Figure 88 illustrates the discretization of the structural model surface mesh into these patches.

To develop trimmed flight loads, the overall vehicle force and moment coefficients are monitored during the aeroelastic simulation. An initial sensitivity analysis is done to develop coarse stability derivatives, then a two degree of freedom trim problem (usually involving angle of attack and a trim surface deflection angle) is solved to compute a new trim state. This trim state is incrementally approached using a relaxation factor, which applies a fraction of the difference between the current and computed trim state as an update to the current trim state to avoid numerical instabilities.

The aerodynamic solver, Splitflow, has the ability to adapt the volumetric grid based on changes to the surface geometry or to requested gradients in the flowfield. In order to focus the majority of the mesh refinement near the final equilibrium state, a multi-step process is followed during the trim solution. This phased approach begins with a coarse grid, which is used to develop stability derivatives based on trim variable perturbations. Next, a trim is performed without allowing adaptation of the volumetric mesh. This allows the geometry to move near the equilibrium state. Finally, grid adaption based on flowfield gradients is enabled to increase the fidelity of the flow solution and allow the geometry to reach the final trim state. Figure 89 shows the convergence history of the Z-Force Coefficient in a typical trim simulation with this approach.

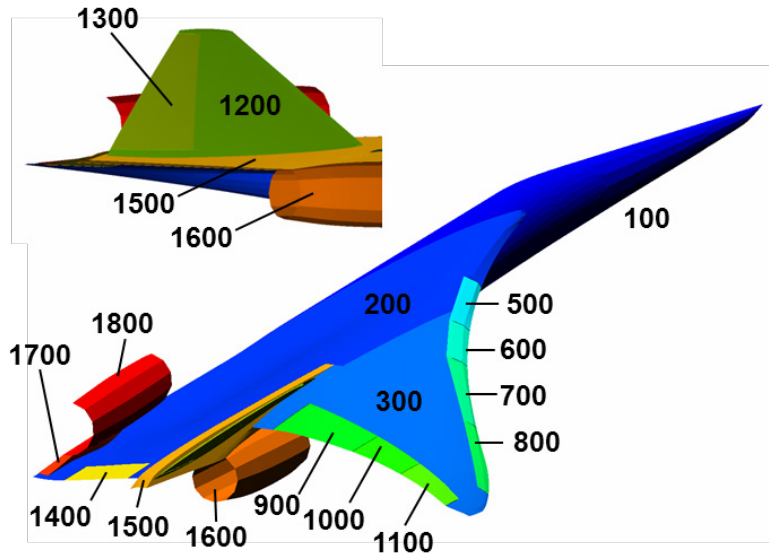


Figure 88.—Surface Patch Definitions for Fluid-Structure Interfaces

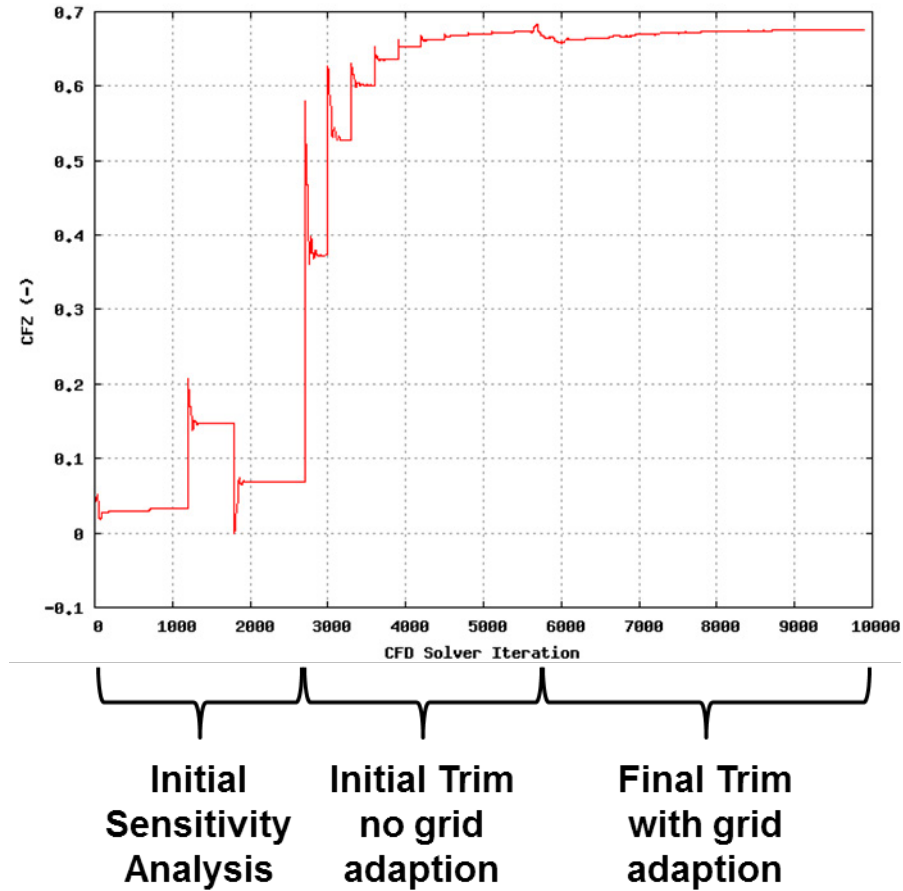


Figure 89.—Force Coefficient Convergence History of Trim Procedure Used to Enhance Grid Adaption about the Equilibrium Trim State

During the structural model development effort, portions of the upper aft deck between the centerline nacelle and tail boom were thickened to increase structural depth. Additionally, the vertical tail was thickened, and a fillet on the lower aft deck surface was smoothed out. Because this operation was performed directly on the FEM through a morphing procedure, updated CAD geometry was not available, and would have required a remesh of the aerodynamic model. An alternate approach was developed where the motion of the nodes due to the morphing process was converted to a mode shape. This mode shape was loaded by LMMS, treated as a structural deflection, and mapped to the aerodynamic model through the fluid structure interfaces defined for these portions of the vehicle. This allowed for a relatively quick update of the aerodynamic model without the need to go back to the CAD model.

3.3.4 Loads Summary

Table 14 and Table 15 show the final trimmed values for the maneuver load cases of Table 10. These flight loads were based on the FEM013 structural model and incorporated a thickening of the tail and aft deck to reduce deformation under load. The weights and CG locations assumed for the final maneuver load calculations are given in Table 16 and differ slightly from the weights of Table 8, because they were based on an earlier FEM.

The highlighted far-right columns of Table 14 are those load cases that were developed with CFD-based loads and their associated trim deflections. The CFD-results for load cases 300, 400 and 600 were selected for the final design loads because these were load cases that were major structural design drivers and because they also varied significantly from linear predictions due to their relatively high AOA, where

separation and vortex lift dominated more. Also, for the linear load cases that required more than 30° of body flap deflection to trim, the other wing control surfaces that were needed are shown in the column labeled “Linked to BF”.

TABLE 14.—TRIM DEFLECTIONS FOR SYMMETRIC MANEUVER LOAD CASES
[Cases that were used in final design loads are highlighted in gray.]

Case no.	Description	Mach	Speed (KEAS)	Nz	Weight	Altitude (ft)	Flexible Linear		Linked to BF	Rigid CFD		AOA (deg)
							Body Flap (deg)	AOA (deg)		Body Flap (deg)	TEF, AIL1, AIL2 (deg)	
100	Pull up	0.66	438	2.5	DTOW	Sea Level	-0.75	6.88		-3.58	0.00	6.15
200	Push over	0.66	438	-1	DTOW	Sea Level	3.64	-3.82		2.30	0.00	-3.34
300	Pull up	0.48	318	2.5	DTOW	Sea Level	-3.06	13.63		-0.99	0.00	10.73
400*	Pull up	2	450	2.5	DTOW2	49,770	-21.38	7.91	TEF	-8.88	-8.88	6.61
500	Push Over	2	450	-1	DTOW2	49,770	16.08	-3.02		17.03	17.03	-4.10
600*	Pull up	1.41	318	2.5	DTOW	49,770	-34.04	16.35	TEF, AIL1&2	-5.56	-5.56	12.45
700	Pull up	0.66	438	2.5	ZFW	Sea Level	-3.44	2.84		-2.98	0.00	2.92
800	Push over	0.66	438	-1	ZFW	Sea Level	4.72	-2.20		1.60	0.00	-2.01
900*	Pull up	2	450	2.5	ZFW	49,770	-24.88	4.60	TEF	-9.78	-9.78	3.60
1000	Push over	2	450	-1	ZFW	49,770	18.65	-1.68		15.75	15.75	-2.83
1100	Steady roll	0.48	318	0	DTOW	Sea Level	2.22	-0.77				
1200	Abrupt roll	0.48	318	0	DTOW	Sea Level	2.22	-0.77				
1300	Steady roll	0.48	318	1.67	DTOW	Sea Level	-1.31	8.85				
1400	Abrupt roll	0.48	318	1.67	DTOW	Sea Level	-1.31	8.85				
1500	Landing 1g	0.3	204	1	DTOW	Sea Level	-3.28	12.92		24.17	0.00	14.28
1600*	Cruise 1g	1.8	357	1	DTOW	55,000	-20.39	5.66	TEF	-10.09	-10.09	4.53
1700	Gust Loads	0.89	400	2.7	ZFW	20,000	-5.62	3.70		-4.97	0.00	3.79

TABLE 15.—TRIM DEFLECTIONS FOR ANTSYMMETRIC COMPONENT OF MANEUVER LOAD CASES

Case no.	Description	Mach	Speed (KEAS)	Nz	Weight	Altitude (ft)	AIL1	AIL 2
1100	Steady roll	0.48	318	0	DTOW	Sea Level	10.22	10.22
1200	Abrupt roll	0.48	318	0	DTOW	Sea Level	11.84	11.84
1300	Steady roll	0.48	318	1.67	DTOW	Sea Level	10.22	10.22
1400	Abrupt Roll	0.48	318	1.67	DTOW	Sea Level	11.84	11.84

TABLE 16.—WEIGHTS AND CG FOR FINAL MANEUVER LOAD CALCULATIONS

Configuration	Weight (lb)	X-CG (in.)	Y-CG (in.)	Z-CG (in.)
DTOW	333,167	2032.5	0.0	258.4
DTOW2	301,645	2061.6	0.0	256.11
ZFW	158,042	2006.4	0.0	244.48

3.3.4.1 CFD-Based Trimmed Load Results

Rigid CFD (Euler) trim solutions were generated for symmetric critical flight conditions as identified in Table 14. Good correlation between linear aerodynamic and CFD aerodynamics was obtained for subsonic and supersonic conditions at low angles of attack. Larger differences in the predicted trim state were noted at higher angles of attack. Based on these results, CFD-based results for load cases 300, 400, and 600 replaced the linear results for structural optimization. Vortex dominated flow features can be seen in the CFD-based results. Figure 90 shows the C_p distribution on the vehicle for load case 600, clearly illustrating the vortex scrub pattern on the upper surface of the wing and vertical tail. Figure 91 shows isosurfaces of vorticity magnitude colored by helicity, which gives more insight to the structure of the vortices for this condition. These effects can be seen in the applied loads once the pressures have been mapped to forces on the structural model. Figure 92 contains an image of the applied loads for load case 600, in which the vortex scrub over the upper wing surface is clearly seen as a region of higher load.

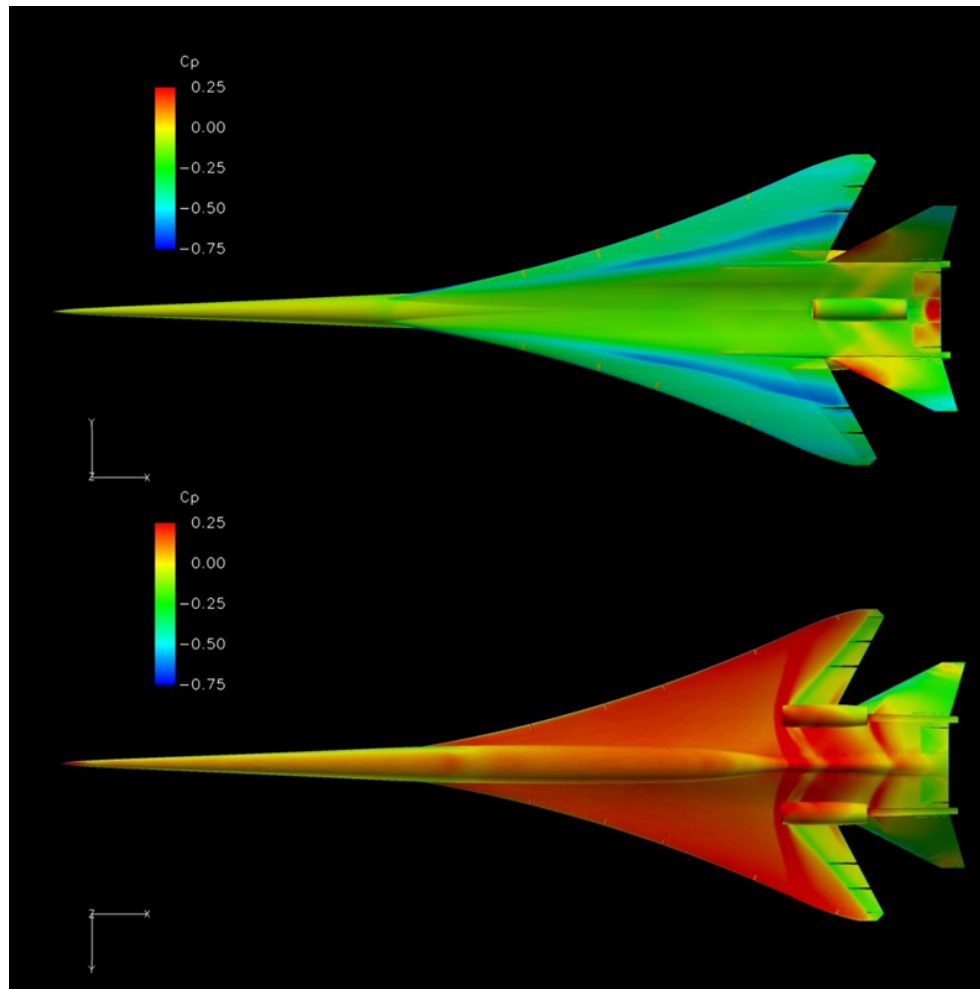


Figure 90.—CFD-based C_p Distribution for Load Case 600, illustrating Vortex Dominated Effects on the Upper Surface

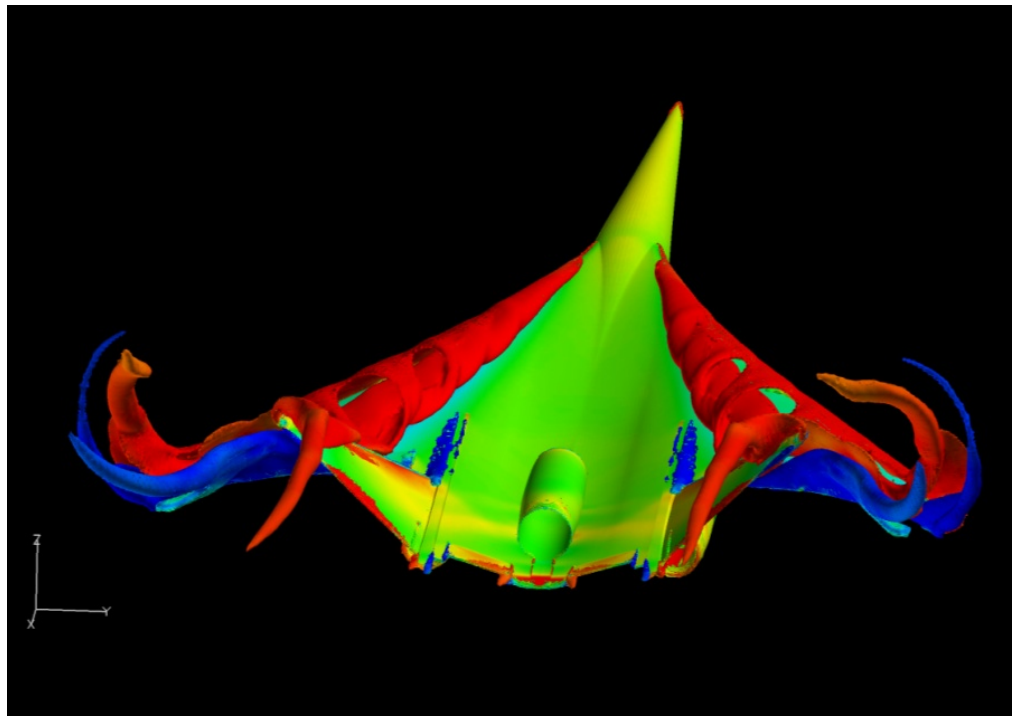


Figure 91.—Isosurfaces of Vortex Magnitude colored with Helicity to Illustrate the Vortex Structure at $M=1.41$, $Nz=2.5$ (Load Case 600)

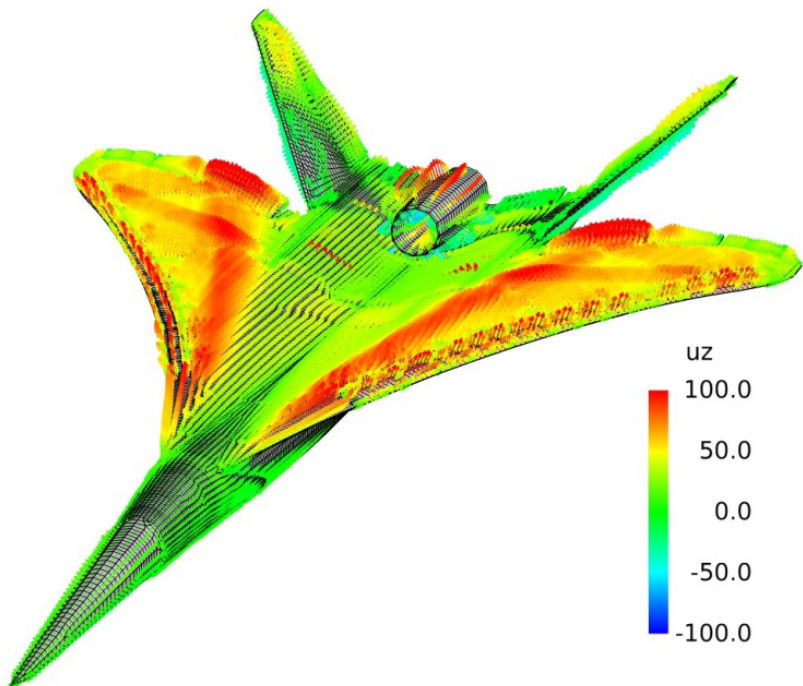


Figure 92.—Vector Plot of Applied Loads Colored by Z-Component of Force for Load Case 600 Illustrates Nonlinear Vortex Effects Captured by CFD-based Trim Process

3.4 Finite Element Modeling

3.4.1 Geometry Processing for FEM Development

Development of the N+2 vehicle FEM was assisted by PreCEPT. This tool operates in conjunction with CATIA V5 to produce a clean idealized geometry dataset which has metadata associated to each surface. The metadata enables automated organization and simplification of the geometry dataset after import into a dedicated FEM pre- and post-processor. Altair Hypermesh was used as the FEM processor for this effort due to its open architecture, integration with our PreCEPT tool, and overall usability.

Importing the CATIA V5 part file into a session of Hypermesh that is linked to PreCEPT allows automated identification, naming and organization of the surface data set. The following figures show the raw import geometry (11,631 surfaces, lines and points) and the organized surface set (approximately 1700 surfaces). The automated cleanup is possible because PreCEPT can discover and operate on the metadata associated to each surface.

The surfaces in Figure 94 that represent the substructures (ribs, spars, frames) and lifting surfaces (wing, fuselage OML) are only trimmed by their own boundary. A single spar or rib surface is not trimmed by the internal intersection of other substructure members or the top and bottom lifting surface. The internal surface intersections were executed and the resulting shared surfaces topologically stitched together to form the final analysis surface geometry. The final geometry set consisted of 6261 distinct surfaces belonging to 793 components (see Figure 95).

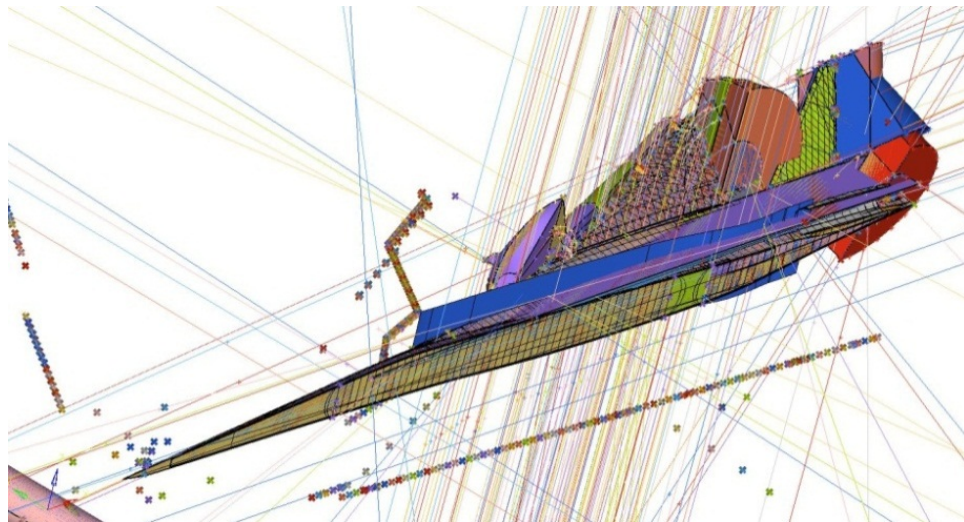


Figure 93.—N+2 Raw Geometry Import into Hypermesh

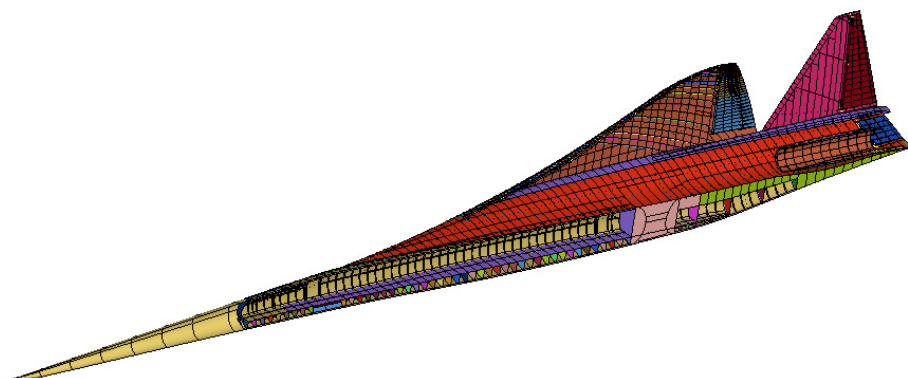


Figure 94.—N+2 Analysis Geometry after PreCEPT Automated Organization and Cleanup

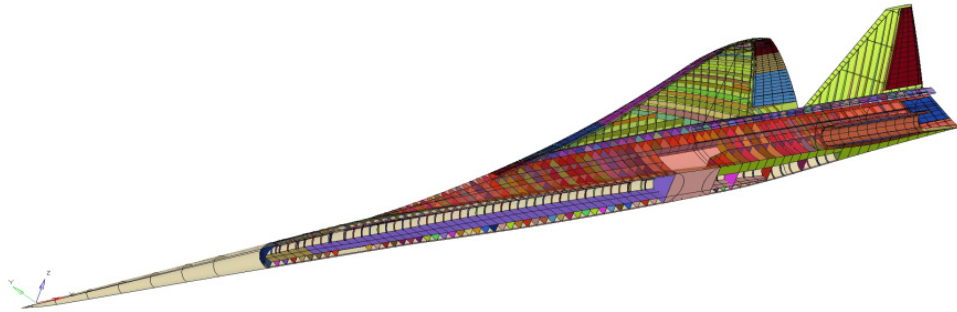


Figure 95.—N+2 fully trimmed surface geometry set prior to meshing

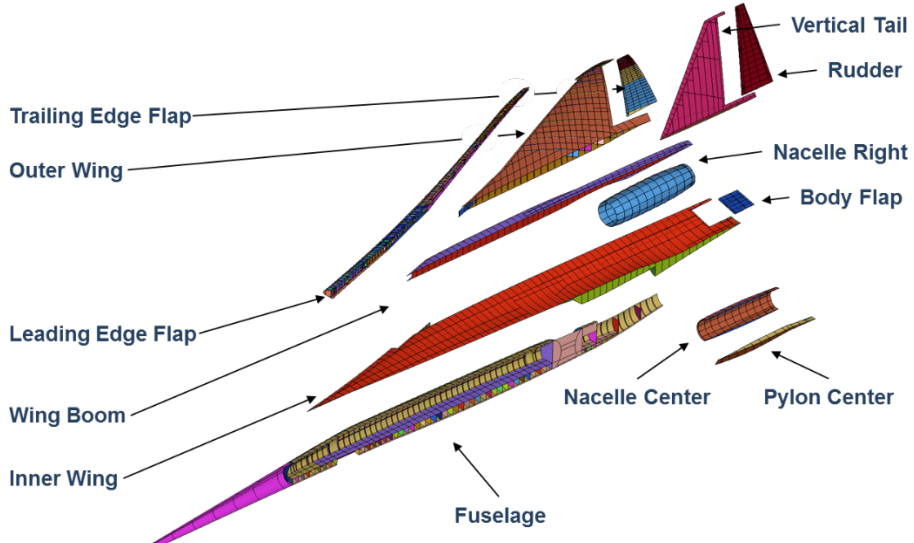


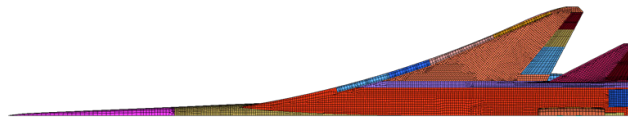
Figure 96.—N+2 Subassembly Map Exploded View

Minor manual geometry correction was performed as well as additional detailed component creation and organization that is reflected in the final Hypermesh database. In addition to the assembly/subassembly structures created automatically by PreCEPT, additional assembly structures were defined to aid discussion and exchange of data among the N+2 analysis team. Figure 96 shows pictorially the high level subassemblies created for this purpose.

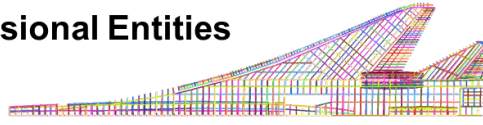
These high level assemblies were further subdivided into parent assemblies for 2D entities (surfaces and shells), and 1D entities (substructure caps and stiffeners). A third general category was defined as a collection of additional details. Figure 97 shows the Hypermesh model browser used to navigate these groupings.

Notional manufacturing breaks were defined and the components were offset to break the continuous surface topology. Figure 98 shows the control surfaces, nacelles, tail and fuselage in this offset position. After meshing was complete, the subassemblies were offset back to the original location but retained the desired topology breaks. The ability to identify and operate on both large components and small details of the model was invaluable during FEM development.

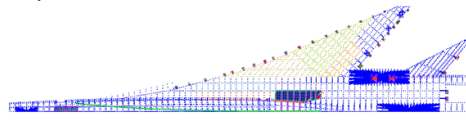
- **2 Dimensional Entities**



- **1 Dimensional Entities**



- **Other Details** (landing gear, control surface hinges, discrete connections between assemblies and mass smearing details)



Entities	ID	Color
Assembly Hierarchy		
Master Baseline	1	Grey
MfgAssy	761	Blue
BodyFlapRightAssy	757	Blue
BodyFlapLeftAssy	750	Blue
FuselagePressureDomes	756	Blue
FuselageRightAssy	762	Blue
LeftRightAssy	754	Blue
NacelleCenterAssy	752	Blue
NacelleRightAssy	753	Blue
PylonCenterAssy	751	Blue
RudderRightAssy	756	Blue
TeRightAssy	755	Blue
VehicleTailRightAssy	758	Blue
WingBoomRightAssy	760	Blue
WingInnerRightAssy	763	Blue
WingOuterRightAssy	759	Blue
myDMGAssy	770	Blue
myBodyFlapCaps	782	Blue
myFuselageCaps	776	Blue
myLEFCaps	778	Blue
myNacelleCenterCaps	783	Blue
myNacelleRightCaps	784	Blue
myPylonCenterCaps	787	Blue
myRudderCaps	780	Blue
myTEFCaps	779	Blue
myVerticalailCaps	781	Blue
myWingBoomCaps	785	Blue
myWingInneCaps	777	Blue
myWingOuterRight	786	Blue
myAddedDetails	775	Blue
myGearDoors	764	Blue
myGearStructures	788	Blue
myHingeStructures	772	Blue
myMassState	799	Blue
myModelInterconnectAssy	769	Blue
Scratch	886	Blue
Beam Section (5)		
Card (6)		
Component (2582)		
Include File (24)		
Load Collector (21)		
Load Step (1)		
Material (13)		
Property (3082)		
Set (142)		
System Collector (15)		
Tag (35)		
Title (1)		

Figure 97.—N+2 Model Browser Showing High Level Assembly Structure

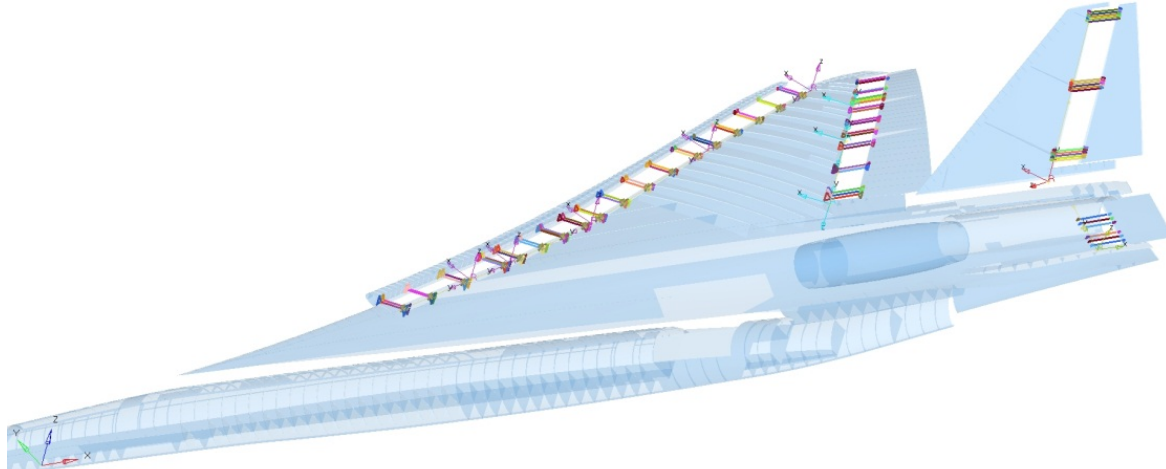


Figure 98.—N+2 Control Surface Hinge Definition in Offset State

3.4.2 Meshing 2D Shells on the Surface Geometry

Meshing the surface geometry was partly automated with PreCEPT and the Hypermesh automesh functionality. Extensive use of the element edge density interactive tools allowed for tuning of the auto-meshed surfaces to achieve the desired element density. Specifically, a minimum of 3 elements through the depth of the wing primary structures was generated to capture shear stress distributions. The lifting surfaces were adjusted to generate approximately 3x4 element densities on wing skin panels bounded by substructure. This was not a hard requirement but only a guideline. This resulted in an average OML element size of 6 to 9 in. The shell elements are located on the OML surfaces. The following figures show the mesh densities used in various portions of the model.

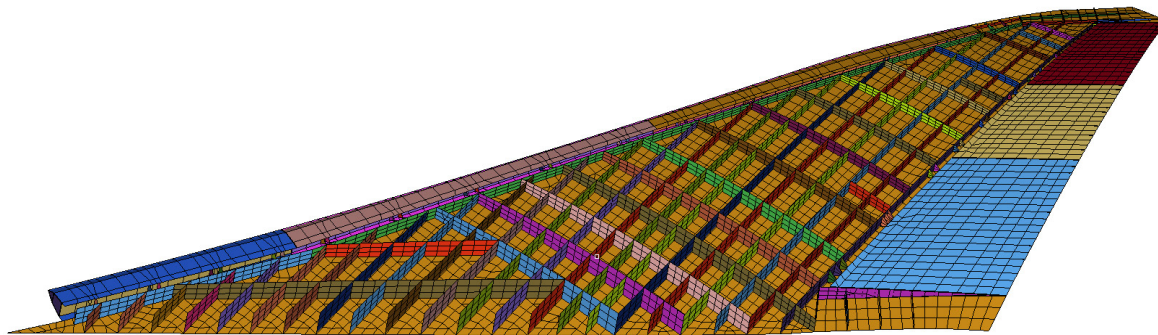


Figure 99.—N+2 Element Density on Outer Wing Box

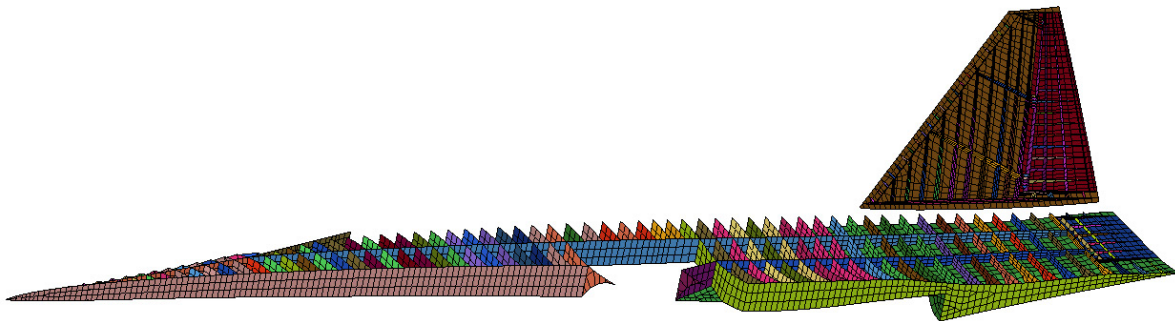


Figure 100.—N+2 Element Density on Inner Wing and Tail



Figure 101.—N+2 Element Density Fuselage

The 2D shell elements were output in NASTRAN format using CQUAD4 and CTRIA3 linear elements. Table 17 lists the 2D element counts for the various major subassemblies.

Material directions were generated for all 2D shell elements on the OML and substructure. Figure 102 shows the material directions on the lifting surfaces and fuselage. The OML material directions follow these guidelines.

- Inner wing - Positive span wise direction
- Outer wing - Parallel to trailing edge spar
- Tail - Parallel to trailing edge spar
- LE Control Surfaces - Parallel to trailing edge spar
- TE Control Surfaces - Parallel to leading edge spar
- Fuselage OML - Positive X axis
- Nacelle OML - Positive X axis
- Gear Doors - Positive X axis

TABLE 17.—N+2 SHELL ELEMENT COUNTS BY SUBASSEMBLY

Subassembly	2D Elements
Pylon Center	157
Nacelle Center	611
Nacelle Right	990
LEF	1153
TEF	1607
Rudder	932
Body Flap	326
Vertical Tail	2287
Wing Outer	7943
Wing Boom	3333
Fuselage (includes LG door)	7394
Wing Inner (includes LG door)	7614
Control Surface Stiffeners	192
FEM 2D Shell Elements	34539

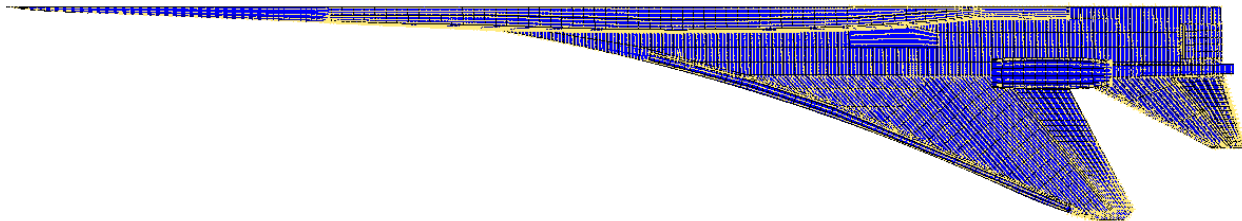


Figure 102.—N+2 OML Material Direction Definition

The substructure material directions are shown in Figure 103 and were determined using these guidelines.

- Ribs and Spars - Along the long direction of the substructure
- Generally in the plane of the parent lifting surface
- LE Control Surface - Positive Z axis (exception to above rule)
- Fuselage Floor - Positive X axis
- Under Floor Frame - Positive Z axis
- Pressure Domes - Rotation axis projected onto element surface

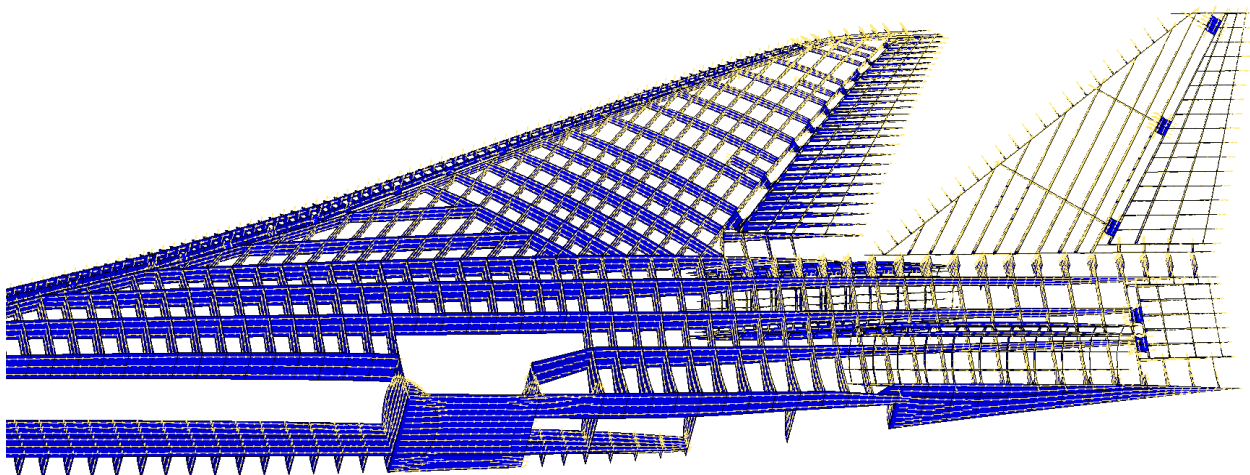


Figure 103.—N+2 Substructure Material Direction Definition

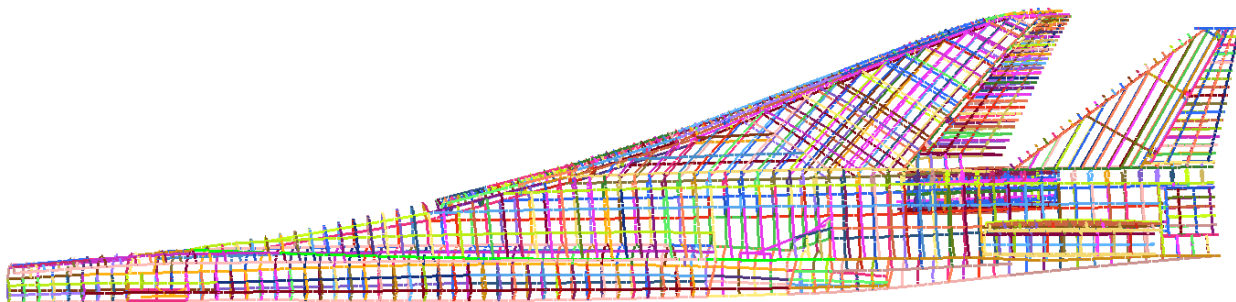


Figure 104.—N+2 Bar and Rod Element Mesh Definition

3.4.3 Meshing 1D Bars and Rod Elements

Substructure (ribs, spars, frames) in the wing, tail and fuselage are connected to the OML surfaces through some fastening scheme. This can be discrete fasteners, rivets, bonding or a combination. In the N+2 FEM development, that level of detail has not been determined so the substructure/lifting surface interfaces were modeled with continuous meshes. To account for the additional load carrying capability of substructure caps, a bar or rod element is typically constructed along the intersection node line and assigned a property that is appropriate for the construction concept being modeled.

After the shell meshing was completed, PreCEPT generated 1D elements along the top and bottom intersections of each substructure component (rib, spars, frames) with the associated lifting surfaces (upper wing skin, lower wing skin, fuselage OML). The 1D elements were collected into upper or lower cap components and organized into the appropriate subassembly structure in Hypermesh. This greatly accelerated adding this detail to the FEM. These 1D elements were configured as NASTRAN ROD elements.

Additional 1D elements were created in areas of the model that were not based on PreCEPT-generated components (primarily fuselage). The ring frame stiffeners around the fuselage were modeled with BAR elements that were 4 by 0.25 in. sections without end offsets. In those cases, tools native to the Hypermesh pre-processor were used to complete the element mesh construction. Figure 104 and Table 18 summarize the 1D element mesh.

TABLE 18.—N+2 BAR AND ROD ELEMENT COUNTS BY SUBASSEMBLY

Subassembly	1D Elements
Pylon Center	0
Nacelle Center	508
Nacelle Right	780
LEF	817
TEF	968
Rudder	554
Body Flap	200
Vertical Tail	758
Wing Outer	2436
Wing Boom	1059
Fuselage	3295
Wing Inner	2319
Miscellaneous Details	1128
FEM 1D Bar and Rod Elements	14822

3.4.4 Additional FEM Details

The details discussed in the following sections are landing gear, gear doors, control surface hinges and engine suspension modeling. These details were added through manual processes using available tools.

3.4.4.1 Landing Gear FEM

A landing gear model that provided load transfer from the ground handling cases into the primary substructure was added for both a gear up and gear down configuration. The landing gear was modeled with CBAR, CROD, RBAR and MPC elements. Figure 105 shows the basic configuration of the main landing gear retraction and extension path superimposed on the FEM and the details of the FE abstraction. The retracted FEM for the main gear folds in a similar fashion.

Modeling both configurations of the landing gear was required to account for both retracted and extended load cases being used in the optimization solution. When specific static cases were being run or modal analyses being executed, one of the configurations was commented out in the bulk data. To facilitate modification for these situations, the fixed portion of the landing gear model as well as the attachment to the airframe was placed in the ‘incLandingGearModel.bdf’ file. This file in turn includes one or both of the ‘incLandingGearExtended.bdf’ or ‘incLandingGearRetracted.bdf’ files. The ‘incLandingGearMasses.bdf’ file contains the concentrated masses associated with the fixed parts of the landing gear and is included at all times. This structure is illustrated in the Hypermesh include file browser in Figure 106.

The attachment of the main landing gear to the airframe primary substructure is shown in Figure 107. The attachment is modeled with rigid RBE2 to distribute the landing gear loads into the airframe. The landing gear section properties were estimated but not sized. Therefore, to prevent introduction of low frequency modes due to the un-sized landing gear, the steel material property was scaled up to provide a pseudo rigid structure that possessed reasonable mass and inertia properties and did not adversely affect the matrix solution.

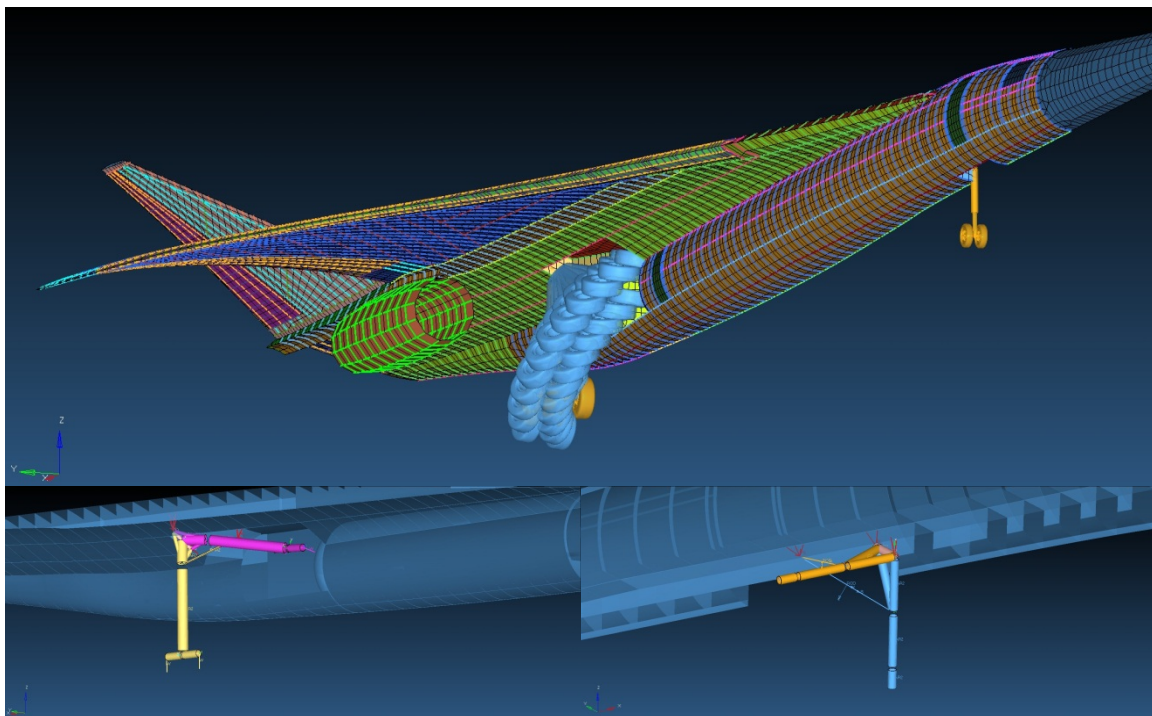


Figure 105.—N+2 Landing Gear Models

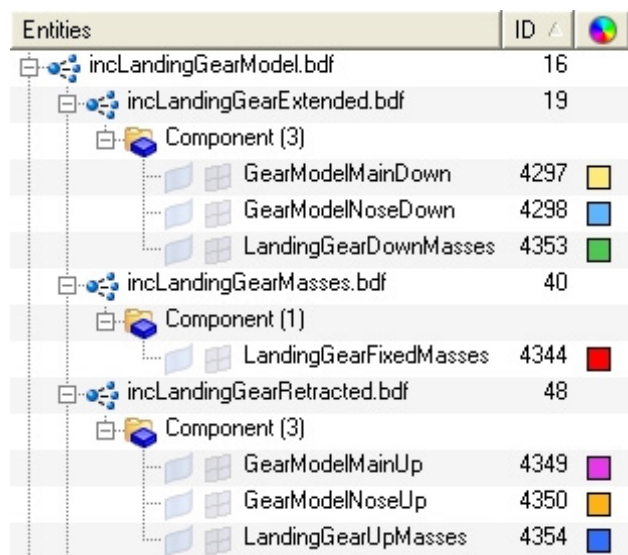


Figure 106.—N+2 Landing Gear Include File Hierarchy

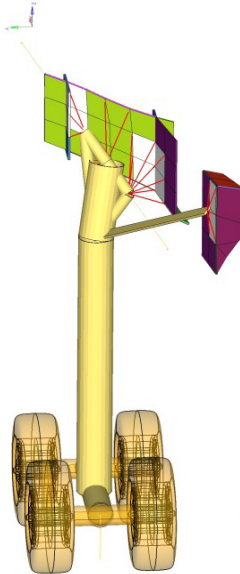


Figure 107.—N+2 Main Landing Gear Attachment



Figure 108.—N+2 Landing Gear Doors in Closed Position

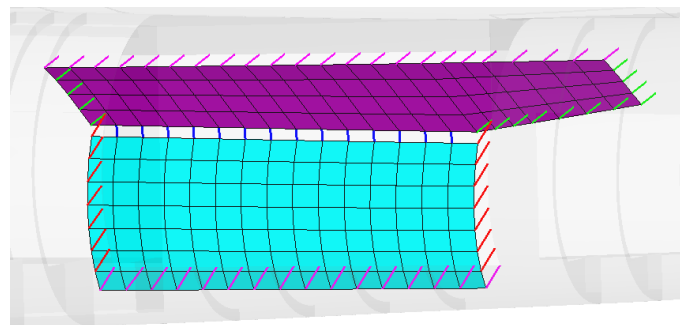


Figure 109.—N+2 Main Landing Gear Doors Offset to show CBUSH Connections to Vehicle

3.4.4.2 Landing Gear Doors

The landing gear doors were modeled as load introduction structures attached to the airframe with discrete springs to provide load transfer normal to the door due to aerodynamic pressure, but limited stiffness elsewhere. The gear doors were not sized in the optimization but the appropriate mass was rolled up into the appropriate subassembly (fuselage or wing). The gear doors were modeled in the door closed configuration. No open door configuration was explicitly modeled. Figure 108 and Figure 109 show the various details of the doors and door attachment.

The main landing gear doors were attached to the fuselage and lower wing substructure with hinge connections along the top and bottom edges, the sides were connected with radial springs. The seam between the doors was also modeled with springs but free in the seam direction. The doors are composite honeycomb skins with an aluminum stiffener frame.

3.4.4.3 Control Surface Hinges

The control surface hinge structures were modeled with a bow-tie structure (Figure 110) to provide a modeled representation of the hinge fitting mass and inertia and to provide coincident points for elastic connections on the defined hinge line.

PreCEPT-generated control surfaces enable automated generation of the mesh structures, local coordinate systems, and elastic connections for all control surfaces. The trailing edge control surfaces are shown in Figure 111. The local coordinate systems are defined with the Y-axis along the hinge line and a positive rotation deflects the control surface trailing edge downward. The hinges were locked in rotation (1.0×10^{10} in-lb/rad) and the bearing stiffness was set to a large value (1.0×10^9 lb/in).

Extensive checks were performed on the control surface load transfer to verify proper hinge operation. An individual load case (LC400) was selected from the linear aerodynamic model hinge moment results and was compared to the applied force free-body of each control surface (Figure 112). The free-body forces were resolved about a point on each hinge line using the control surface local coordinate system and summing the results for each hinge. The computed free-body hinge moments matched the panel aero hinge moment data.

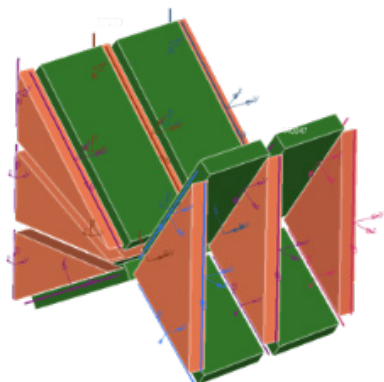


Figure 110.—N+2 Typical Control Surface Hinge Structure (Bow-tie)

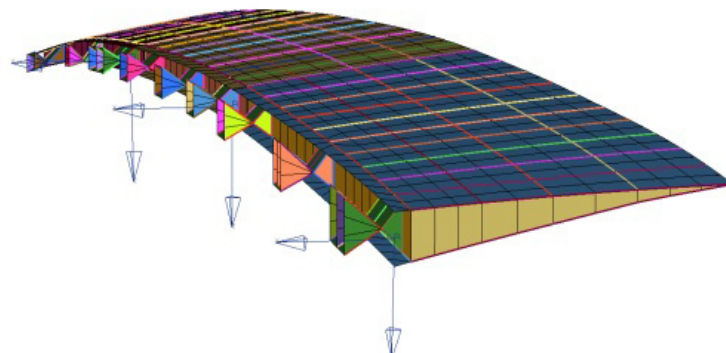


Figure 111.—N+2 Control Surface Modeling Details on Trailing Edge Structures

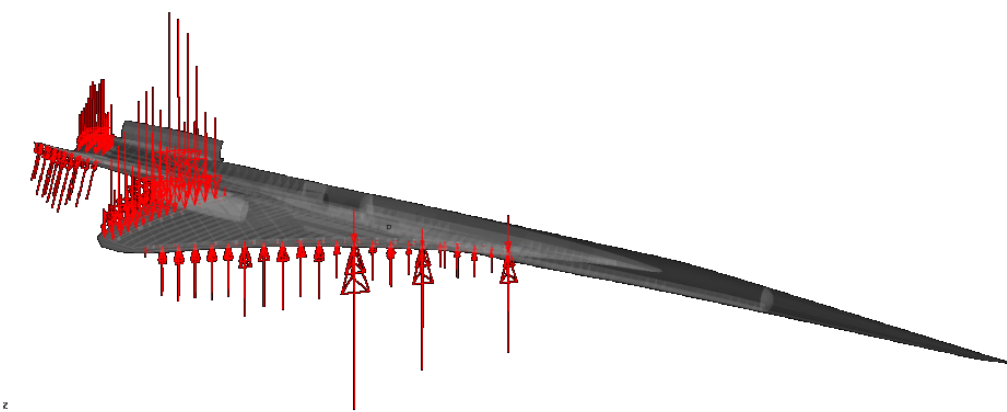


Figure 112.—N+2 Control Surface Loads used for Free-body Hinge Moment Checks

3.4.4.4 Engine Suspension System

The engine mass and nacelle structures are modeled as a single fore and aft coincident point connection to the center pylon and under wing pylon structures. The points are interconnected with CBUSH elastic elements. The stiffness properties of these springs represent the suspension system for each engine/nacelle subsystem. Figure 113 shows the definition of the suspension system model.

The engine mass was modeled as a concentrated mass along the center line of the nacelle and connected to the interior of the nacelle with a single RBE3 spider element to distribute the mass. The mass, inertia and stiffness properties for the right engine system are listed in Figure 114.

These values were selected to produce a first roll mode of approximately 3.5 Hz and a first pitch model of 6 to 10 Hz. These values were targeted after a literature search of other modern day aircraft with pylon-engine-nacelle arrangements.

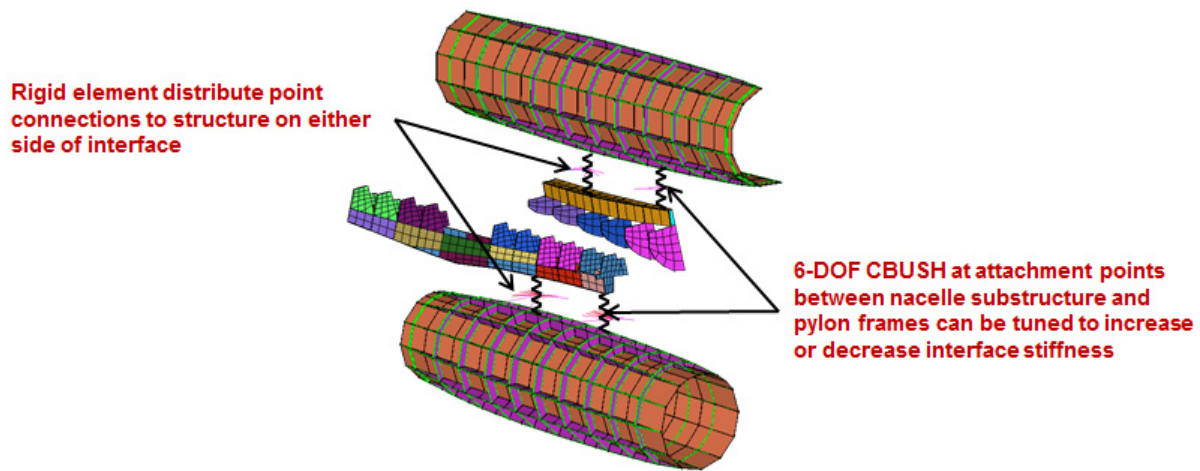


Figure 113.—N+2 Propulsion System Suspension Interface Model

Right Assy Mass = 11,275 lb Engine only = 7,226 lb	I_{xx} (lb-in 2)	I_{yy} (lb-in 2)	I_{zz} (lb-in 2)
About CG of nacelle/engine (2403.17, 157.263, 220.388)	4.574×10^6	26.84×10^6	26.83×10^6
About midpoint of suspension axis (2407.09 150.660 257.799)	20.85×10^6	42.79×10^6	27.49×10^6

	K_{tx} (lb/in)	K_{ty} (lb/in)	K_{tz} (lb/in)	K_{mx} (in-lb/rad)	K_{my} (in-lb/rad)	K_{mz} (in-lb/rad)
nacelleRightBraceAft	10.0×10^6	4.0×10^6	10.0×10^6	30.0×10^6	0	0
nacelleRightBraceFwd	0.04×10^6	4.0×10^6	10.0×10^6	10.0×10^6	0	0

Figure 114.—N+2 Propulsion System Suspension Properties

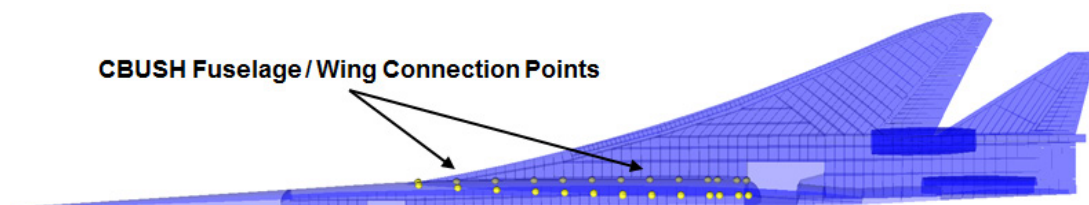


Figure 115.—N+2 Discrete Spring Attachment of Forward Wing to Fuselage

3.4.4.5 Wing—Fuselage Attachment

The wing forward of the main landing gear bay is only attached to the fuselage at select locations along the structural stiffeners on the fuselage and the forward root rib of the inner wing. This attachment is modeled with NASTRAN CBUSH elements as shown in Figure 115. The stiffness properties are essentially rigid in the translational degrees of freedom creating a pinned condition. Further definition of this attachment arrangement is needed to refine the model in this area. A trade study of attachment concepts and the effect on fuselage / wing interaction would be beneficial.

3.4.5 FEM Element and Node Numbering

The various subassemblies were individually renumbered according to a defined schema that was maintained in a spreadsheet. After the initial renumbering, element sets were exported in several formats to support use of the model in other software tools. The numbering schema is keyed by subcomponent names defined in the Hypermesh database. Table 19 defines the numbering used in this effort.

TABLE 19.—N+2 FEM NUMBERING MASTER SCHEMA

Assembly	Subcomponent	Element Start	Size	End
Miscellaneous at model level		1	999	999
		1000	1000	1999
		2000	3000	4999
		5000	5000	9999
Connections		10000	10000	19999
	cnxfuselage2innerwing	10000	1000	10999
	cnxpylon2nacellecenter	11000	500	11499
	cnxboom2nacelleright	11500	500	11999
	cnxboom2verticaltail	12000	500	12499
	cnxlef2innerwing	12500	500	12999
	cnxlef2outerwing	13000	500	13499
	cnxtef2outerwing	13500	500	13999
	cnxrudder2verticaltail	14000	500	14499
	cnxbodyflap2innerwing	14500	500	14999
	cnxnlg2fuselage	15000	100	15099
	cnxmlg2innerwing	15100	200	15299
	cnxnlgdoor2fuselage	15300	100	15399
	cnxmlgdoor2fuselage	15400	100	15499
	cnxmlgdoor2innerwing	15500	100	15599
	cnxmlgdoor2mlgdoor	15600	100	15699
OPEN		20000	10000	29999
		30000	20000	49999
AERO PANELS		100000	100000	199999
Inner Wing		200000	100000	299999
	innerwingUpperskin	200000	4000	203999
	innerwingLowerskin	204000	4000	207999
	innerwingInterior2D	210000	5000	214999
	innerwingInterior1D	215000	5000	219999
	innerwingOther	220000	5000	224999
	innerwingMainGearDoor	225000	1000	225999
	bodyflapUpperskin	230000	200	230199
	bodyflapLowerskin	230200	200	230399
	bodyflapInterior2D	230400	200	230599
	bodyflapInterior1D	230600	300	230899
	bodyflapOther	232000	0	231999
Boom		300000	100000	399999

TABLE 19.—N+2 FEM NUMBERING MASTER SCHEMA

Assembly	Subcomponent	Element Start	Size	End
	boomUpperskin	300000	1500	301499
	boomLowerskin	301500	1500	302999
	boomInterior2D	303000	3000	305999
	boomInterior1D	306000	2000	307999
Pylon		308000	2000	309999
	pylonOML	308000	500	308499
	pylonInterior2D	308500	500	308999
	pylonInterior1D	309000	500	309499
Outer Wing		400000	100000	499999
	outerwingUpperskin	400000	3000	402999
	outerwingLowerskin	403000	3000	405999
	outerwingInterior2D	410000	5000	414999
	outerwingInterior1D	415000	3000	417999
	outerwingOther	420000	0	419999
Wing Flaps		430000	20000	449999
	lefUpperskin	430000	400	430399
	lefLowerskin	430400	400	430799
	lefInterior2D	431000	500	431499
	lefInterior1D	431500	1000	432499
	lefOther	433000	0	432999
	tefUpperskin	440000	600	440599
	tefLowerskin	440600	600	441199
	tefInterior2D	441400	600	441999
	tefInterior1D	442000	1000	442999
	tefOther	443000	0	442999
Vertical Tail		500000	100000	599999
	vtailUpperskin	500000	3000	502999
	vtailLowerskin	503000	3000	505999
	vtailInterior2D	510000	5000	514999
	vtailInterior1D	515000	3000	517999
	vtailOther	520000	0	519999
	rudderUpperskin	540000	400	540399
	rudderLowerskin	540500	400	540899
	rudderInterior2D	541000	400	541399
	rudderInterior1D	541400	600	541999
	rudderOther	542000	0	541999
Fuselage		600000	100000	699999
	fuselageNoseFairing	600000	1000	600999
	fuselageOML	601000	9000	609999
	fuselageInterior2D	610000	5000	614999
	fuselageInterior1D	615000	5000	619999
	fuselageOther	620000	5000	624999
	fuselageNoseGearDoor	625000	1000	625999
	fuselageMainGearDoor	626000	1000	626999
	fuselageNoseGearStructure	630000	1000	629999
	fuselageMainGearStructure	631000	1000	630999
AERO		700000	100000	799999
Engine Nacelle		800000	100000	899999
	nacelleCenterUpperskin	800000	200	800199
	nacelleCenterLowerskin	800200	200	800399
	nacelleCenterInterior2D	800400	300	800699
	nacelleCenterInterior1D	802000	1000	802999

TABLE 19.—N+2 FEM NUMBERING MASTER SCHEMA

Assembly	Subcomponent	Element Start	Size	End
				-1
	nacelleRightUpperskin	803000	400	803399
	nacelleRightLowerskin	803400	400	803799
	nacelleRightInterior2D	803800	600	804399
	nacelleRightInterior1D	806000	2000	807999
Concentrated Masses		900000	100000	999999
	incNonStructuralMass.bdf	900000	3000	902999
	incWingSmearedMass.bdf	903000	5000	907999
	incAftDeckSmearedMass.bdf	908000	1000	908999
	incVerticalTailSmearedMass.bdf	909000	1000	909999
	incFuselageSmearedMass.bdf	910000	4000	913999
	incEngineStartAndControlsMasses.bdf	914000	1000	914999
	incWeightMargin.bdf	915000	15000	929999
	incFuelTank1Mass100pct.bdf	930000	1000	930999
	incFuelTank2Mass100pct.bdf	931000	1000	931999
	incFuelTank3Mass100pct.bdf	932000	1000	932999
	incFuelTank4Mass100pct.bdf	933000	1000	933999
	incFuelTank5Mass100pct.bdf	934000	1000	934999
	incFuelTank6Mass100pct.bdf	935000	1000	935999
	incFuelTank7Mass100pct.bdf	936000	1000	936999
	incFuelTank8Mass100pct.bdf	937000	1000	937999
	incFuelTank9Mass100pct.bdf	938000	1000	938999
	incFuelTank10Mass100pct.bdf	939000	1000	939999
	incFuelSystemMass.bdf	940000	4000	943999
	incUnusableFuelAndOilMass.bdf	944000	4000	947999

The node numbering is not as consistent because adjacent subcomponents share many nodes. Therefore, the numbering generally follows the same schema but will have inconsistencies due to the sharing of nodes between many subcomponents.

3.4.5.1 FEM Element/Node Counts

Table 20 lists the total counts for each NASTRAN element type. The data is consistent with the Hypermesh database used to export the basic N+2 FEM and the solution decks used for static and modal analyses. Specialty analyses such as linear panel aerodynamics or CFD cosimulation may incorporate additional elements to account for coupling/interaction between the multidisciplinary analyses.

The total number of nodes in the basic FEM is 28557. Two nodes are used as origin locations for coordinate systems and are not used by any structural elements. Again, for specialty analyses, additional nodes may be included as appropriate.

TABLE 20.—N+2 ELEMENT TYPE BREAKDOWN AND COUNTS

Element Category	Category Total	Element NASTRAN	Element Count
MASS	30122		
		CONM2:	30122
WELD	4		
		RBAR:	4
RIGID	35		
		RBE2:	35
RBE3	33		
		RBE3:	33
SPRING	213		
		CBUSH:	213
ROD	11932		
		CROD:	11932
BAR2	2890		
		CBAR:	2890
TRIA3	1412		
		CTRIA3:	1412
QUAD4	33127		
		CQUAD4:	33127
TRIA6	0		
QUAD8	0		
BAR3	0		
GAP	0		
PLOT	0		
JOINTS	0		
INTERFACE PANELS	0		
TETRA4	0		
PENTA6	0		
HEX8	0		
TETRA10	0		
PENTA15	0		
HEX20	0		
Total Elements	79768		79768

3.4.6 FEM Include File Structure

The model was further organized into an include file structure. This structure is retained in the delivery package for the FEM and is documented in the delivery package README.TXT file. Relevant portions of the file are reproduced in Table 21.

TABLE 21.—N+2 NASTRAN FEM INCLUDE FILE STRUCTURE

[[[[FE MODEL INCLUDE FILES]]]]	
incGridBasic.bdf	
incElementBasic.bdf	
incTailRootRibExtraAttach.bdf	
incLandingGearModel.bdf	>>> Stationary components of LG model <<<
incLandingGearExtended.bdf	>>> Included in LG model gear down config. [Commented out] <<<
incLandingGearRetracted.bdf	>>> Included in LG model gear up config. <<<
incLandingGearDoors.bdf	>>> Doors Closed <<<
incGenericProperties.bdf	
incProjectMaterials.bdf	
incProjectPcompProperties.bdf	>>> SIZED COMPOSITE PROPERTY DATASET <<<
incProjectMetalProperties.bdf	>>> SIZED METALLIC PROPERTY DATASET <<<
incProjectProperties.bdf	
incProjectPpushProperties.bdf	
incBoundaryConditions.bdf	>>> Symmetric boundary conditions <<<
incBoundaryConditions_AntiSYM.bdf	
incEngineStartAndControlsMasses.bdf	
incLandingGearMasses.bdf	
incFuelSystemMass.bdf	
incFuelTank10Mass100pct.bdf	
incFuelTank1Mass100pct.bdf	
incFuelTank2Mass100pct.bdf	
incFuelTank3Mass100pct.bdf	
incFuelTank4Mass100pct.bdf	
incFuelTank5Mass100pct.bdf	
incFuelTank6Mass100pct.bdf	
incFuelTank7Mass100pct.bdf	
incFuelTank8Mass100pct.bdf	
incFuelTank9Mass100pct.bdf	
incUnusableFuelAndOilMass.bdf	
incNonStructuralMass.bdf	>>> Non-structural mass parent file <<<
incBodyFlapActuatorMasses.bdf	
incRudderActuatorMasses.bdf	
incOutboardEngineMass.bdf	
incCenterEngineMass.bdf	
incPassengerMass.bdf	
incBaggageMass.bdf	
incStdOperatingItems.bdf	
incAuxPower.bdf	
incInstruments.bdf	
incAvionics.bdf	
incFurnishings.bdf	
incLEFActuatorMasses.bdf	
incTEFActuatorMasses.bdf	
incWeightMargin.bdf	
incAftDeckSmearedMass.bdf	>>> Make-up mass files <<<
incFuselageSmearedMass.bdf	
incVerticalTailSmearedMass.bdf	
incWingSmearedMass.bdf	

3.4.7 Material Property Definition

The physical properties and material properties of the N+2 vehicle evolved as the development effort matured. A brief discussion of this process is provided, followed by a summary of the final configuration.

3.4.7.1 Material Systems Used

The material systems and associated ID's used in the N+2 final FEM are summarized in Table 22.

3.4.7.2 Material Property Maturation Process

Automated methods were used early in the N+2 effort to generate metallic properties that sped FEM development. The properties were assigned to the PreCEPT components (ribs, spars, lifting surfaces, control surfaces, etc...) and named accordingly. Initial check-out solutions were performed with this property set.

The generic properties were replaced with a definition of an all-composite airframe that used sandwich panel construction for all surfaces. Additional properties were defined as the model matured to account for model details not present in the original PreCEPT definition. Thorough check-out solutions were performed with this property set.

A cloned copy of the composite property from the parent component was generated and assigned to each geometric surface and the associated elements. This greatly expanded the number of unique properties in the model but formed a basis set of properties for defining optimization design zones and buckling panels. The string 'Surf.xxxx' is appended to the master property for each component where 'xxxx' is replaced by the surface ID from the Hypermesh database. The automated generation and consistent naming of properties was invaluable in the FEM development process and enabled application of other semi-automated tools for manipulating the designed property zones used when sizing the vehicle. The design zone definition process merged many of these unique properties into constant property zones that were used for optimizing the structure. After reviewing the results of the optimization, the design zones were further subdivided in areas of active sizing. Lastly, metallic properties (titanium and aluminum) were introduced in critical load carrying areas. This maturation process is illustrated in Figure 116.

TABLE 22.—BASIC MATERIAL PROPERTY VALUES

Isotropic	ID
Generic Aluminum	1
Aluminum (typical)	100
Titanium (typical)	103
Stiff Aluminum	303
Stiff Steel	304
Cap Material	22000
Orthotropic	ID
Core	10056
Graphite fabric	20000
Graphite tape	20075

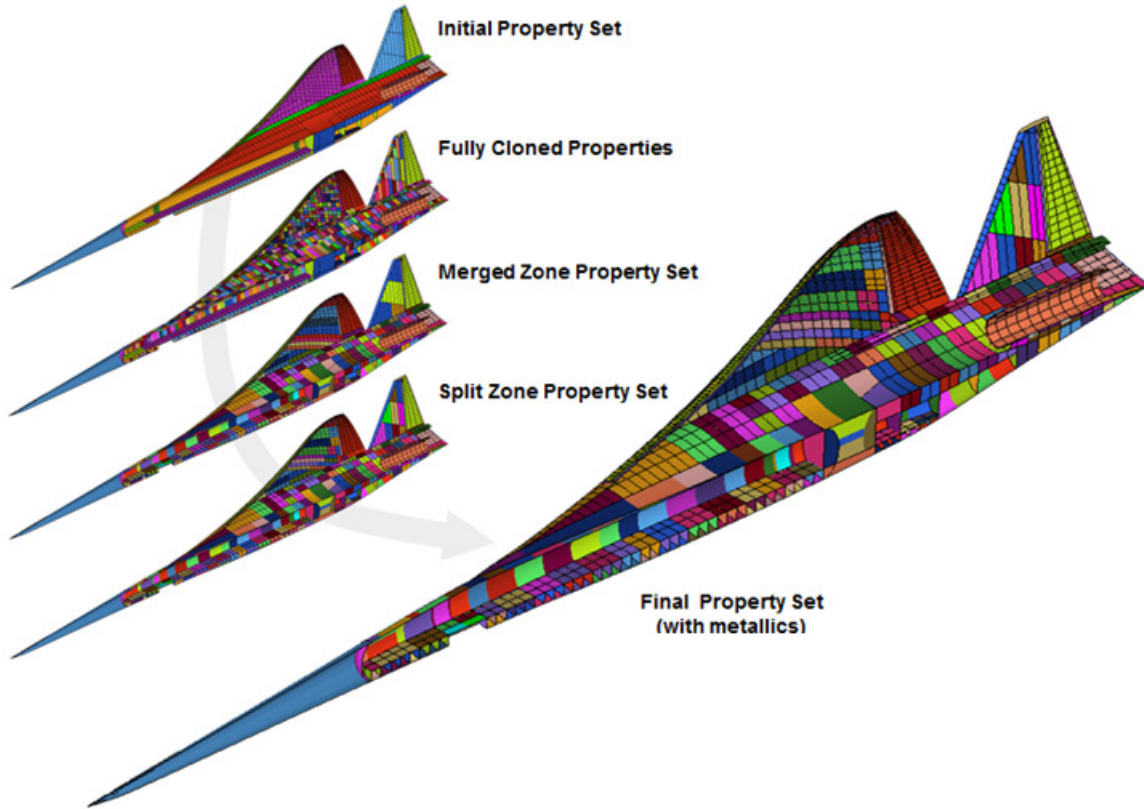


Figure 116.—Property Set Maturation

The introduction of metallic materials into the sizing process produced a FEM that was representative of material utilization on modern aircraft. Figure 117 summarizes the areas where metallics were used and shows a comparison to current commercial aircraft. The commercial aircraft compositions were determined from general literature sources and are approximate values. The N+2 composition percentages were: composites 55 percent, aluminum 26 percent, titanium 16 percent, and steel 3 percent.

The final property set consisted of 3165 properties of which 685 are currently used. The vast majority of those properties are the cloned PCOMPs for each OML and substructure surface. Most of these were subsequently merged in the design zone creation process. The property type breakdown and counts are shown in Figure 118.

The composite structures are sandwich construction consisting of carbon fiber facesheets over a honeycomb core. Various parts of the vehicle were assigned different core thicknesses based on trade studies discussed in Section 3.5.4. The structural optimization solution determined the total thickness of each facesheet ply direction (see Section 3.5.5 for final sizing results). The core thickness for the composites of major areas is below:

- OML Skins - 0.50 in.
- Substructure Webs - 0.25 in.
- Fuselage Interior - 0.25 in. (aft cabin floor is 0.75)
- Pressure Domes - 0.50 in.
- Access Doors - 0.75 in.
- Gear Doors - 0.75 in.

Metal usage in structural FEM

- Aluminum typical (cyan)
- Aluminum stiff (brown) nose fairing
- Titanium typical (blue)
- Steel stiff (yellow) landing gear tubes

Titanium used for:

- Tail root rib and stub TE spar
- Engine fwd and aft structures
- Control surface hinges
- Outboard wing root rib (aft 1/4) and stub TE spar
- Landing gear attachment (nose and main)

Aluminum used for:

- Door/Window frames or pillars
- Engine nacelle structures (not shown)
- Between titanium attachment structures to create continuous load path
- Some fuel boundaries

FEM overall material composition

- Modeled FEM Structure* = 30595.7 lb (using FEM14a facesheet thk)
- Comparable to current composite commercial A/C
A350 (52% Comp, 20% Al, 14% Ti, 7% Steel, 7% Misc.)
787 (50% Comp, 20% Al, 15% Ti, 10% Steel, 5% Other)

* Does not include the smeared makeup masses

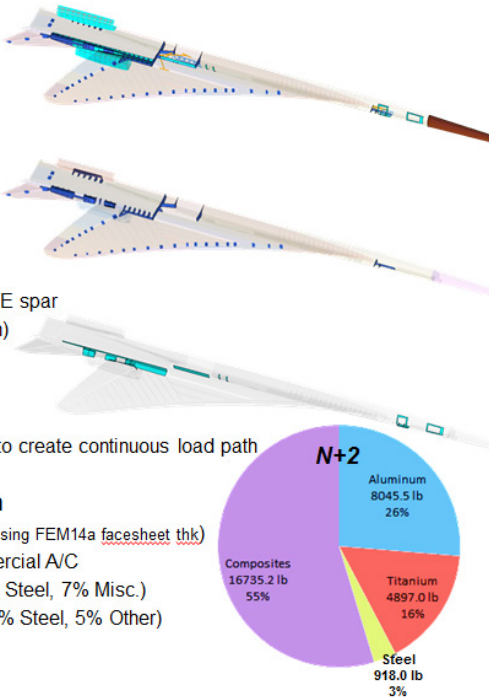


Figure 117.—N+2 Metallic Usage and Overall Composition

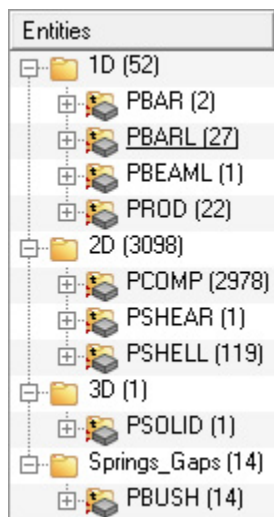


Figure 118.—N+2 Property Type Counts

This construction was modeled using NASTRAN PCOMP bulk data entries with ‘SMCORE’ specified in the LAM field. This allows modeling the total thicknesses of each ply direction without introducing an actual stacking sequence. The smeared approach is highly desirable when running optimization solutions since it reduces the potential design variables to 3 or 4 per property zone.

3.4.8 Nonstructural Mass—0D Elements

The modeled primary structural components of the N+2 FEM comprise 18 percent of the total gross take-off weight. The remainder is comprised of nonstructural masses for fuel, systems, payload, nonmodeled structure and growth margin. The weight statement provided by the mass properties group

defines estimates of these weights and also roll-ups to major subassembly target weights for each configuration.

These nonstructural masses are incorporated in the FEM by creating concentrated mass elements on the nodes that are located along intersections between the skin OML and the substructure. Extensive organization of these mass elements into 32 separate bulk data include files enables rapid updates and configuration of the vehicle model for various mass states (Figure 119).

This technique distributes the system masses over the proper area of the model without introducing spurious panel modes on the lifting surface OML. Discrete system masses were modeled at their center of gravity and connected to the FEM through constraint elements (RBE2 and RBE3).

The FEM was divided into major element groups that closely mapped to the weight statement subassemblies for primary structure. These groups are shown in Figure 120.

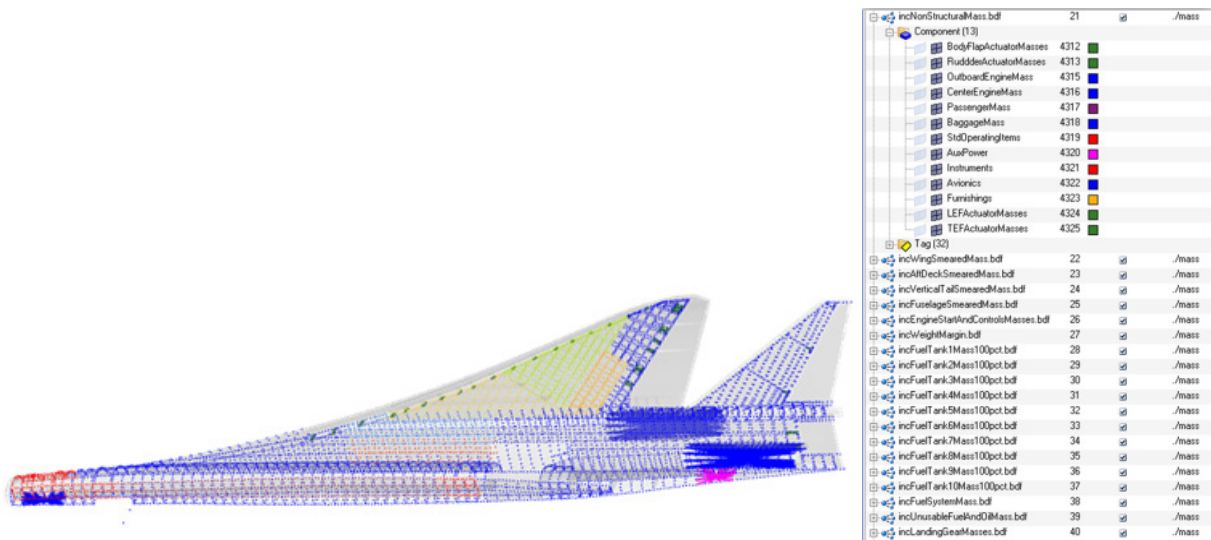


Figure 119.—N+2 Distributed Masses

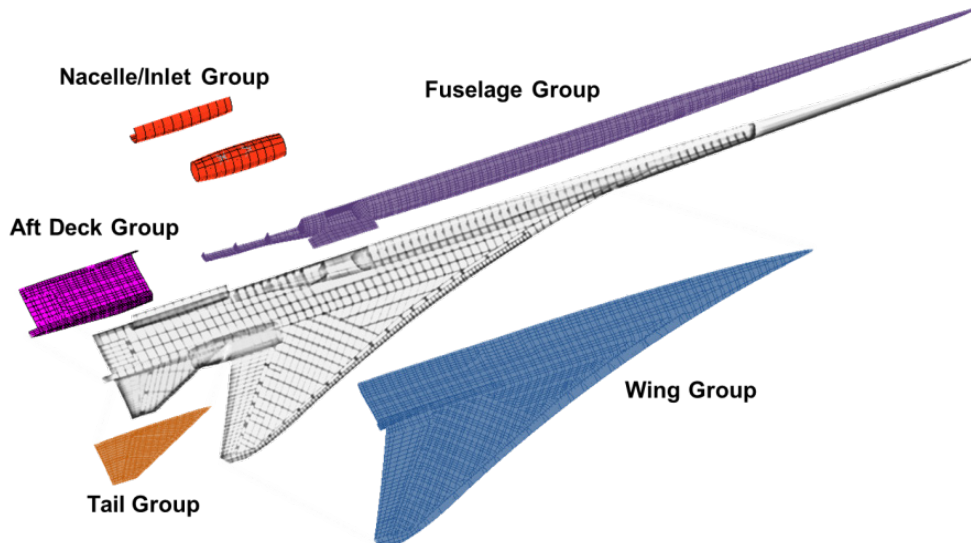


Figure 120.—N+2 Element Sets for Weight Statement Breakdown

These element sets were weighed and compared to the weight statement estimate. The difference was divided by the number of intersection nodes in each set and scaled to bring the total of the element group up to the weight statement estimate. When a new set of thicknesses were output from the gage optimization, these make-up or ‘smeared’ masses were re-scaled to recover the proper subassembly weight. This technique enables reuse of trimmed load sets for a given weight state of the air vehicle. Figure 121 shows the smeared masses for REV70 of the optimized airframe.

Figure 122 illustrates the distribution of the actual fuel mass as well as the distributed fuel system masses (pipes, pumps, etc...).

The remainder of the distributed masses is shown in Figure 123. Lastly, the growth margin mass was distributed over the entire vehicle. No nonstructural mass terms on structural elements were used.

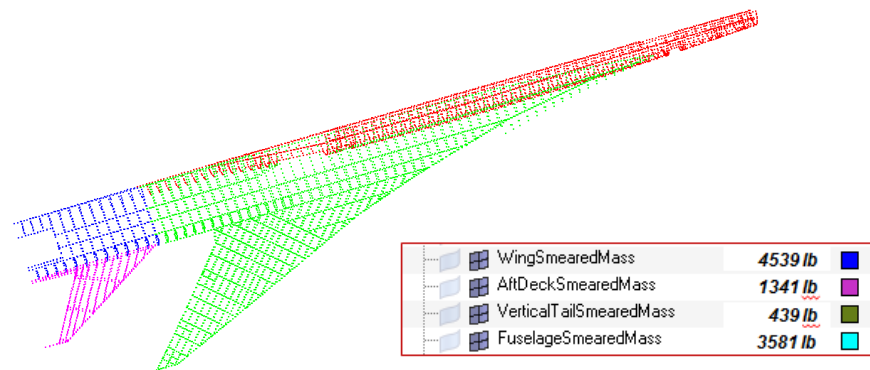


Figure 121.—N+2 Smeared Make-up Mass for FEM REV70

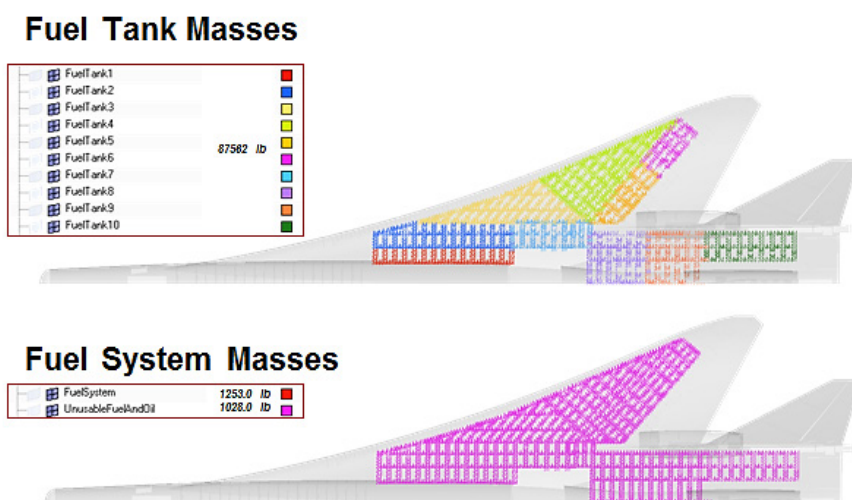


Figure 122.—N+2 Fuel Tanks and Fuel System Distributed Masses

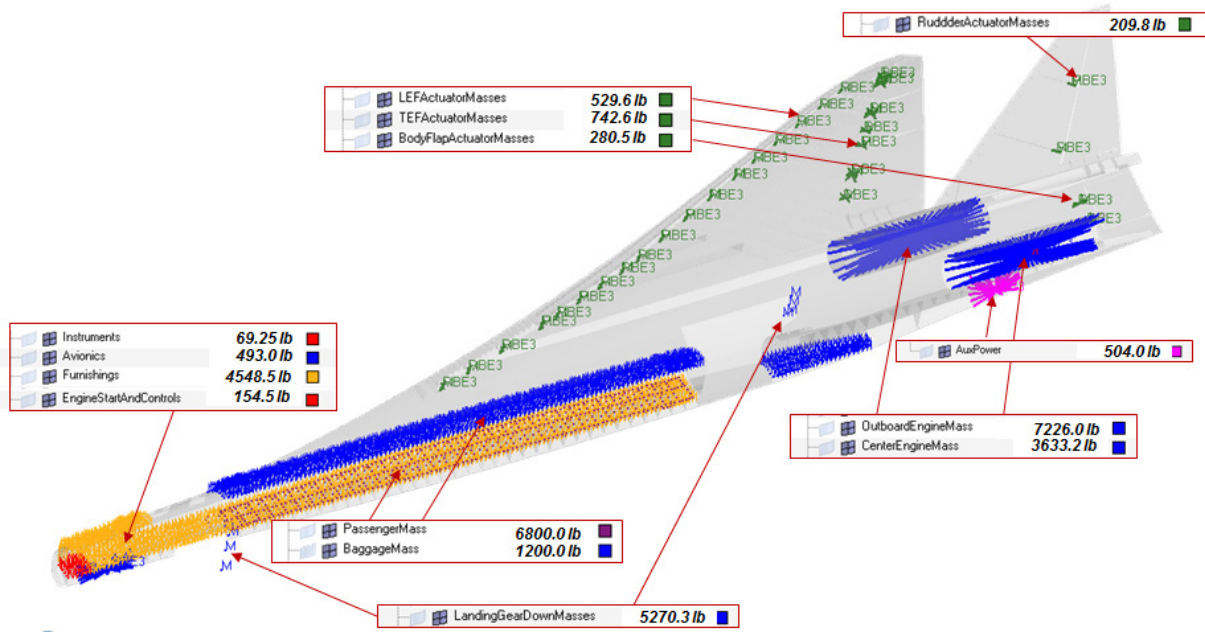


Figure 123.—N+2 Miscellaneous Distributed Masses

3.4.9 FEM Morphing to Increase Aft-Deck and Tail Stiffness

Morphing as applied to a FEM allows the mesh of the model to be deformed according to rules and/or equations that the user defines. This type of model modification changes the geometric properties of the model but does not disturb the node or element IDs, the element property assignments or existing load definitions. It is a desirable solution to geometric design changes when a significant number of man-hours have been invested in development of a FEM that has been distributed to other engineering disciplines that depend on a defined model numbering scheme. Significant rework can be involved if a published FEM must be renumbered or reconstructed.

In the course of sizing the N+2 vehicle, concerns arose over the tail and aft deck deflections under load. These concerns initiated an effort to modify the FEM to provide better load transfer from the tail to the centerline of the aft fuselage. Several options were considered and 3 modifications selected (Figure 124).

1. Thicken the aft deck up to 50 percent of the local depth to increase stiffness of the aft deck substructure and the tail attachment
2. Remove a sharp angle between the aft lower skin and the aft fuselage (referred to as a crease in the OML) to increase the minimum depth of the aft deck substructure
3. Increase the tail T/C by 26 percent from 2.5 to 3.16 percent to reduce bending of the tail structure

The morphing domains (related mesh entities) and the morphing handles (movable points on a domain) were constructed in Hypermesh. The data applied to the morph handles for the aft deck was generated by defining the desired profiles at 4 locations in the span wise direction and then performing a Matlab 3D surface fit to the profiles (Figure 125). The function returned by the surface fit was used to calculate the handle deflections. The morph shape was imported into Hypermesh and applied to the model.

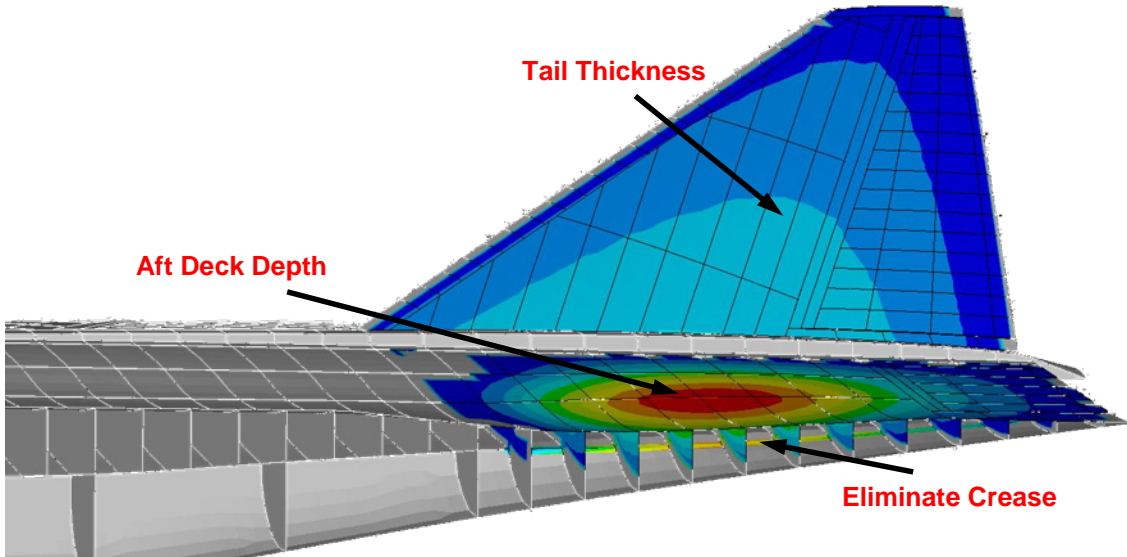


Figure 124.—N+2 Morphing Shapes Show Magnitude of Thickness Increases

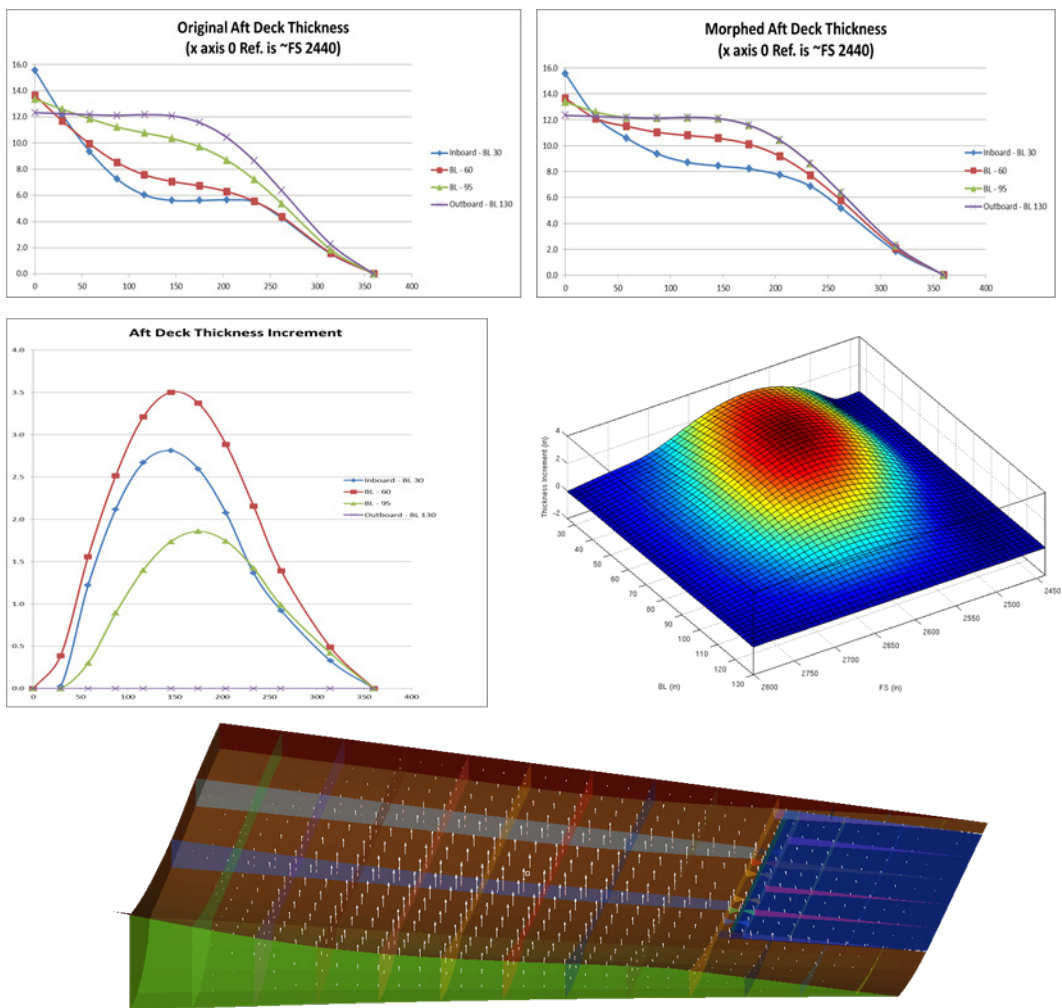


Figure 125.—N+2 Aft Deck Morphing Process

The tail morphing was done entirely in Hypermesh with the addition of constraints to prevent the leading and trailing edges from moving. The rudder hinge line was also constrained prior to the symmetric thickening of the tail (Figure 126).

Lastly, removing the crease in the OML was also done entirely in the preprocessor. However, all the morphing shapes (the perturbations applied) were exported and saved to provide an updating capability for prior versions of the N+2 FEM.

One additional morphing operation was performed but not incorporated into the structural FEM. The structural FEM used in the CFD loads mapping process requires that the control surfaces not collide when deflected for trimming. Therefore, the trailing edge ailerons and flaps were morphed to provide clearance when deformed during trimming (Figure 127). The morphing shape was developed along with the structural FEM for accurate mapping across the fluid structure interfaces used during the CFD aeroelastic analysis.

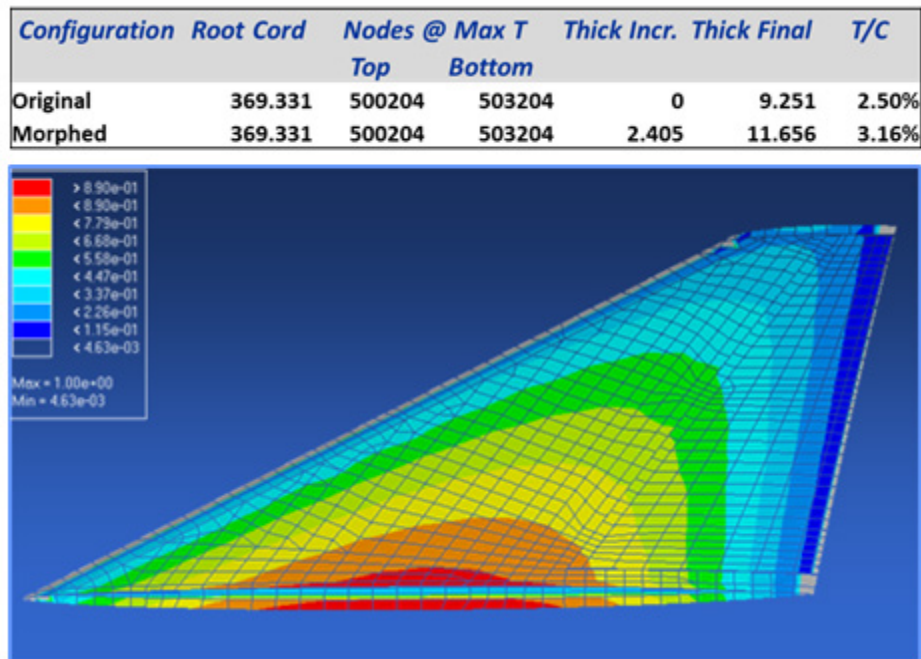


Figure 126.—N+2 Morphing of the Tail Thickness

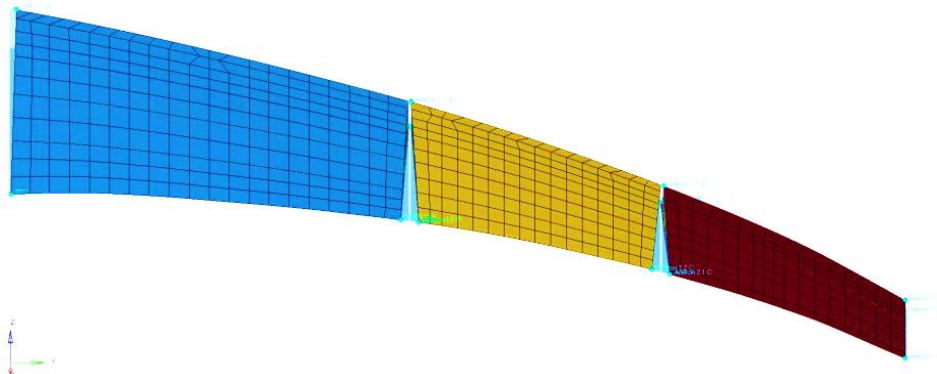


Figure 127.—N+2 Trailing Edge Darts for CFD Loads Generation

3.5 Structural Sizing

The structural gauges of the FEM were sized to the design load cases of Section 3.3 in order to arrive at an airframe with representative stiffness for a credible flutter analysis. We went through several iterations of structural sizing, starting with a coarse all-composite design model and then refining the model to have more design zones so as to avoid large zones being sized by small stress concentrations. In the end, we conducted a final sizing of the FEM with metallic and composite materials. It is the results of this final sizing that are summarized in this section.

3.5.1 Approach

Our process for sizing the structure is shown in Figure 128. The structural sizing is ultimately done in MSC.NASTRAN SOL200, which utilizes gradient based optimization to determine optimal gauges that minimize weight while satisfying strength, buckling, and manufacturability criteria. Our in-house tool, AS3, serves as a front-end to the SOL200 optimization by translating design variable definition, stress/strain constraint definition, and buckling panel definition from a simple format to the NASTRAN bulkdata format. The buckling constraints are implemented through an external function call by SOL200 to our in-house panel buckling routine, TM1A, which assumes simply supported boundary conditions. AS3 creates the bulkdata for the structural design variables and constraints, which is then combined with the rest of a ready-to-run SOL200 model that contains the basic FEM, design loads, design objective function (in our case weight), and case control statements.

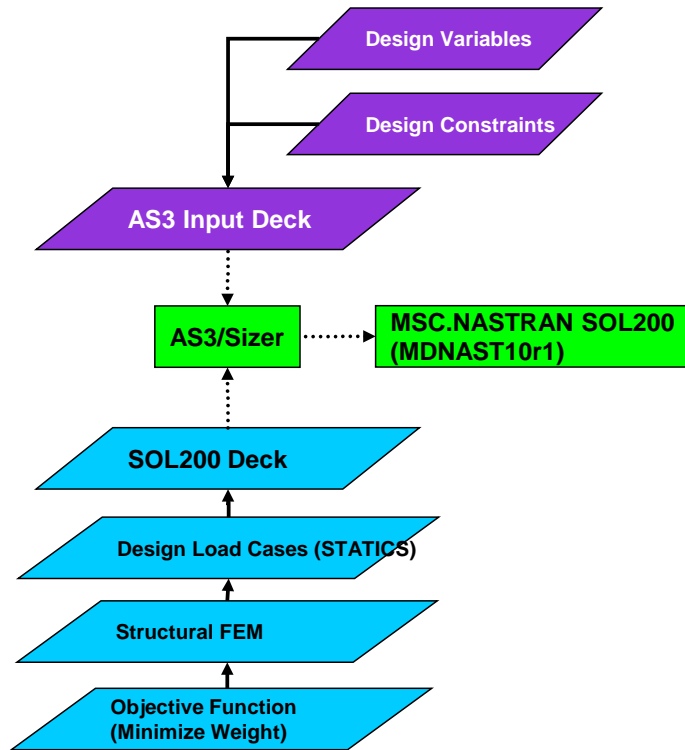


Figure 128.—Structural Sizing Approach

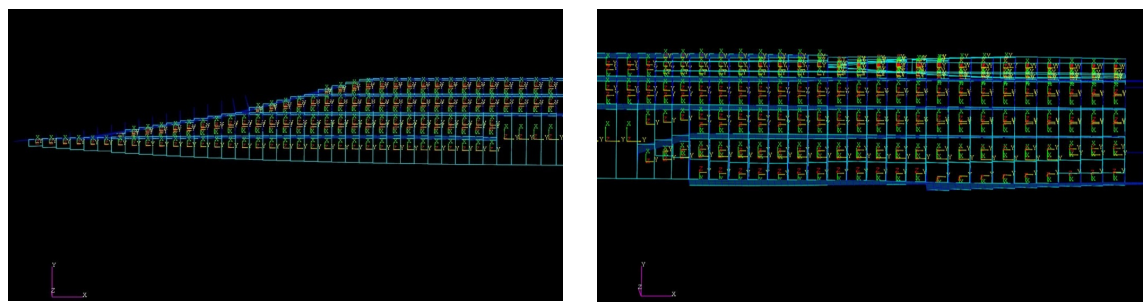
3.5.2 Design Criteria

Our design criteria for sizing the structure under the given set of design loads consisted of stress/strain criteria, minimum gauge criteria, ply percentage criteria for composites, and buckling criteria. These criteria were evaluated at ultimate load which was defined as 1.5 times the design limit load cases of Section 3.3. Table 23 summarizes the criteria for both the composite parts and metallic parts. The strength criteria were knocked down from their room temperature allowable to account for an elevated temperature of 210 °F which corresponds to an adiabatic wall temperature at a cruise condition of Mach 2.0, as specified in our Mach, Altitude envelope (see Figure 74). The ply percentage constraints, both minimum and maximum values, were based on our composite best-practices design guidelines. Ply percentage is defined as the ratio between the thickness of one material orientation (e.g., 0° plies) to the thickness of the overall laminate, not including the core thickness.

The buckling criteria are evaluated by MSC.NASTRAN SOL200 through an external function call to TM1A. Area averaged running loads from the FEM analysis (N_{xx}, N_{yy}, N_{xy}), along with current laminate definition, core thickness, and panel dimensions are provided by NASTRAN to TM1A, which then returns the buckling eigenvalue, which is constrained to be greater than 1.0 at ultimate load. Figure 129 to Figure 135 show the buckling panels that are defined as part of the structural sizing model. In total there are 1791 buckling panels. The total number of stress/strain criteria per load case is 199,524.

TABLE 23.—DESIGN CRITERIA FOR STRUCTURAL SIZING

Criteria	Graphite/BMI with Ti Core	Aluminum	Titanium
Strength criteria	Fiber strain based on damage tolerance allowable at elevated temp	von Mises \leq XX ksi Max Shear Stress \leq XX ksi	von Mises \leq XXX ksi Max Shear Stress \leq XX ksi
Minimum gauge	Skins—8 plies per facesheet Substructure—4 plies per facesheet	0.06 in.	0.06 in.
Ply percentage	Yes	No	No
Buckling	Yes—Core thickness remains constant	Yes—number of stiffeners remains constant	Yes—number of stiffeners remains constant



Close-up of Buckling Panels on Boom

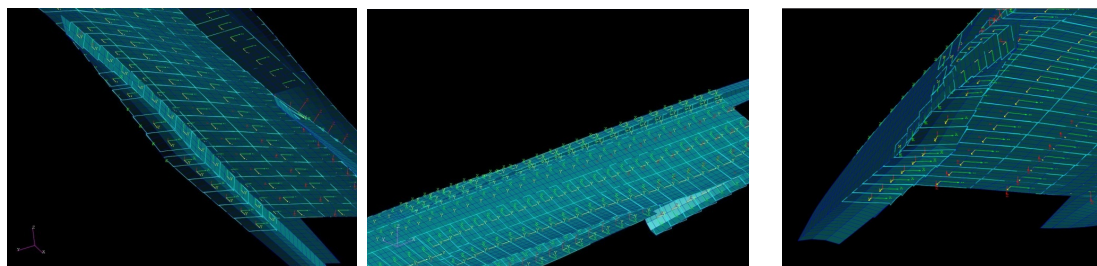


Figure 129.—477 Buckling Panels on Inner Wing Skin

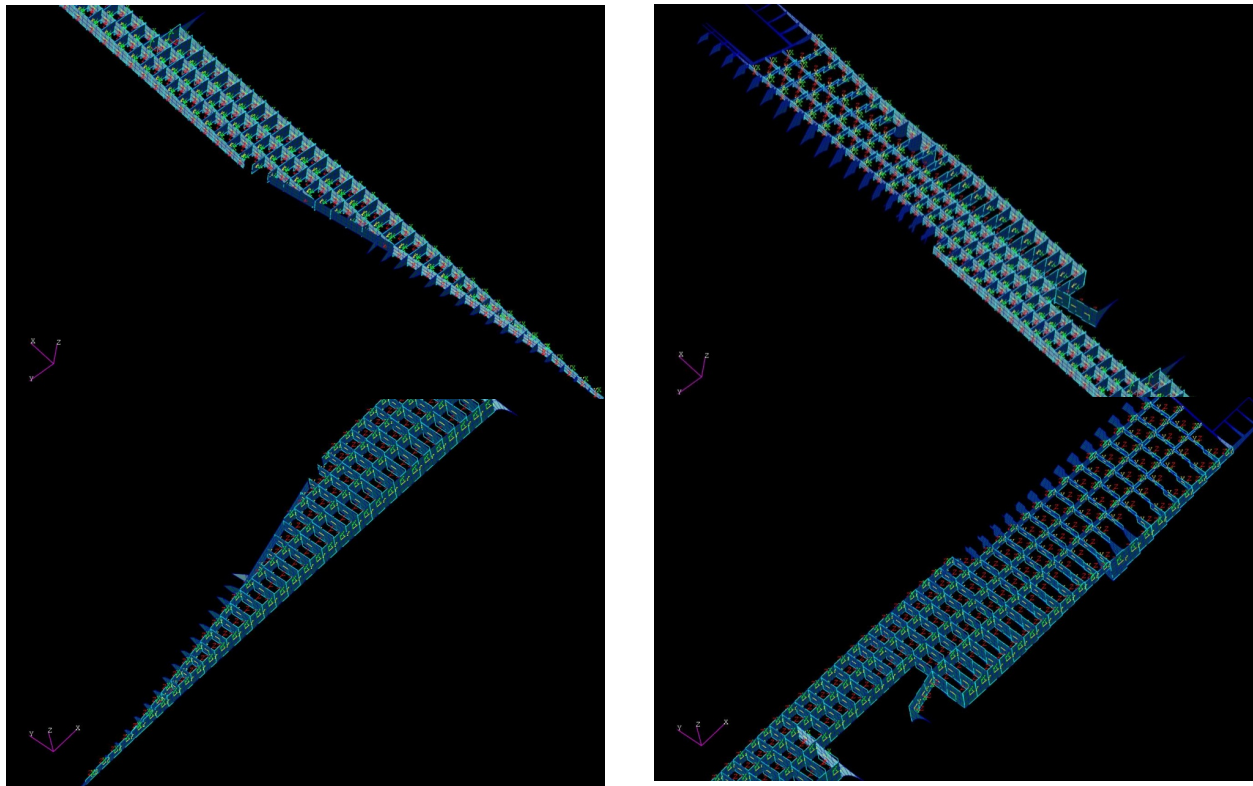


Figure 130.—367 Buckling Panels on Inner Wing Substructure

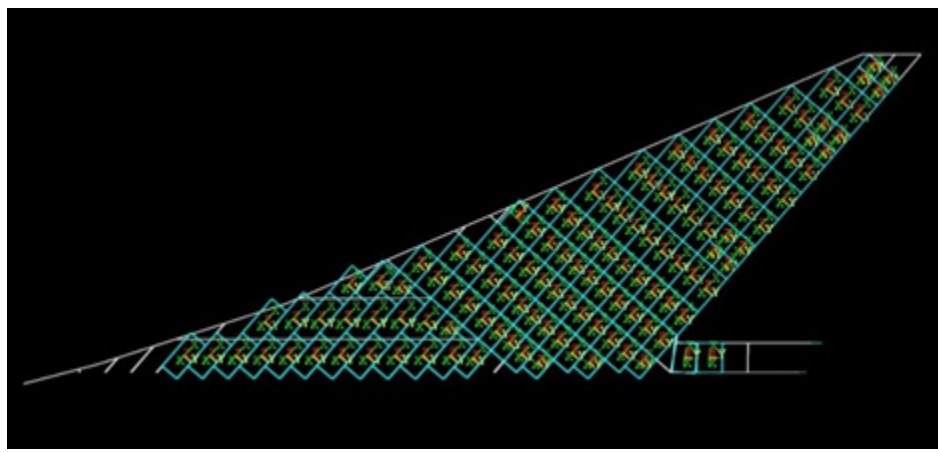


Figure 131.—252 Buckling Panels on Upper and Lower Outer Skin

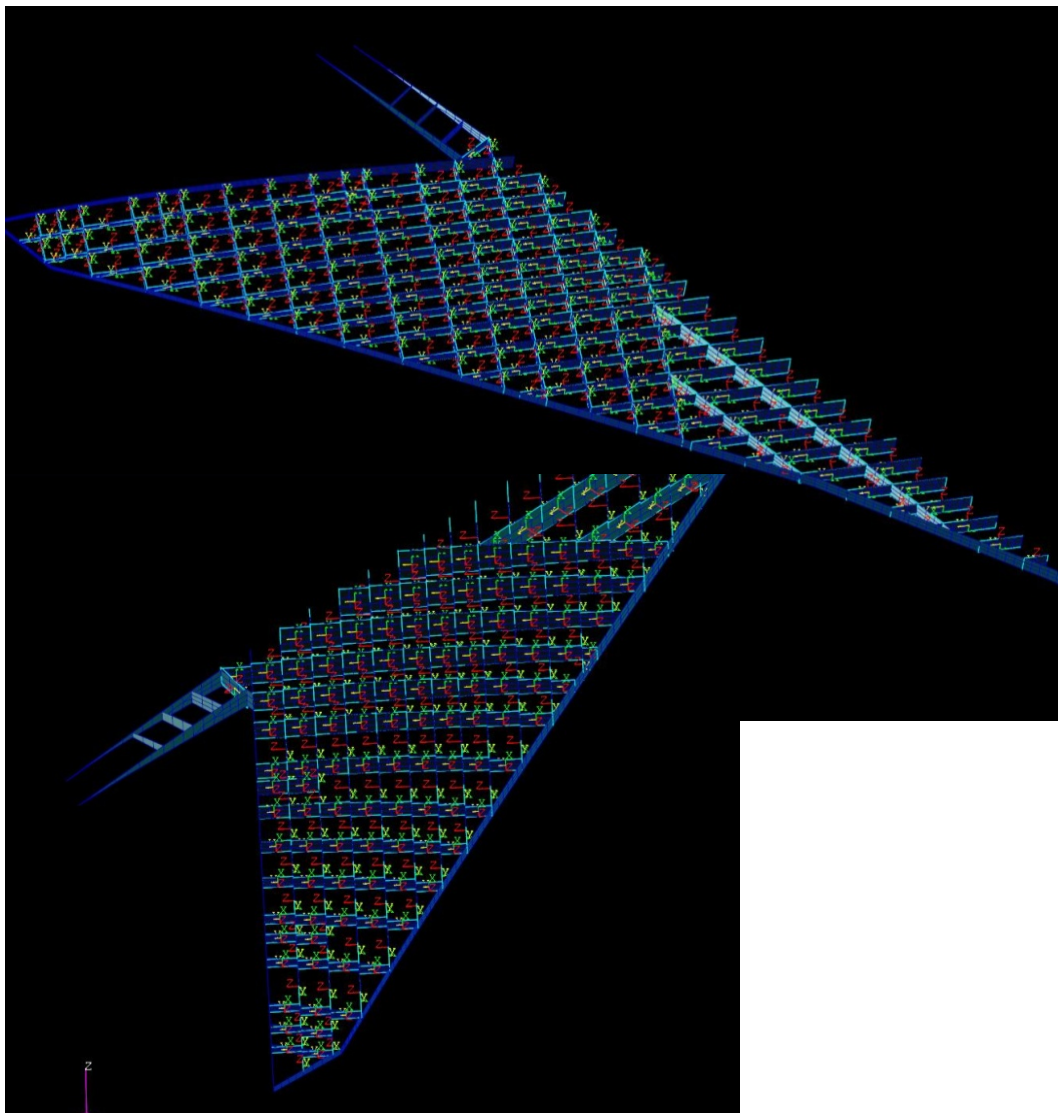


Figure 132.—265 Buckling Panels on Outer Wing Substructure

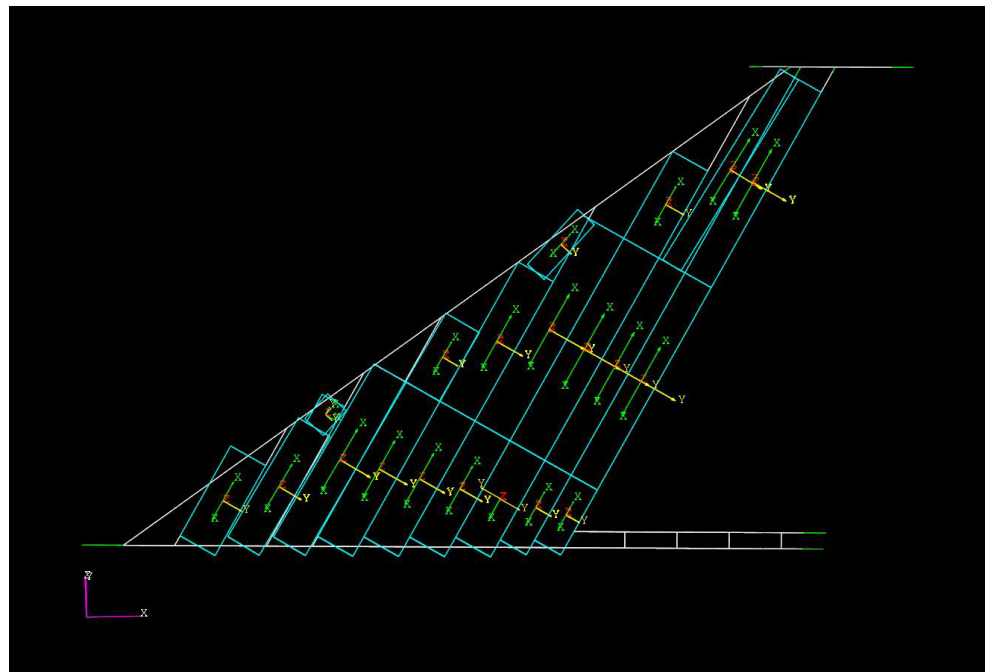


Figure 133.—40 Panels on Tail Skins

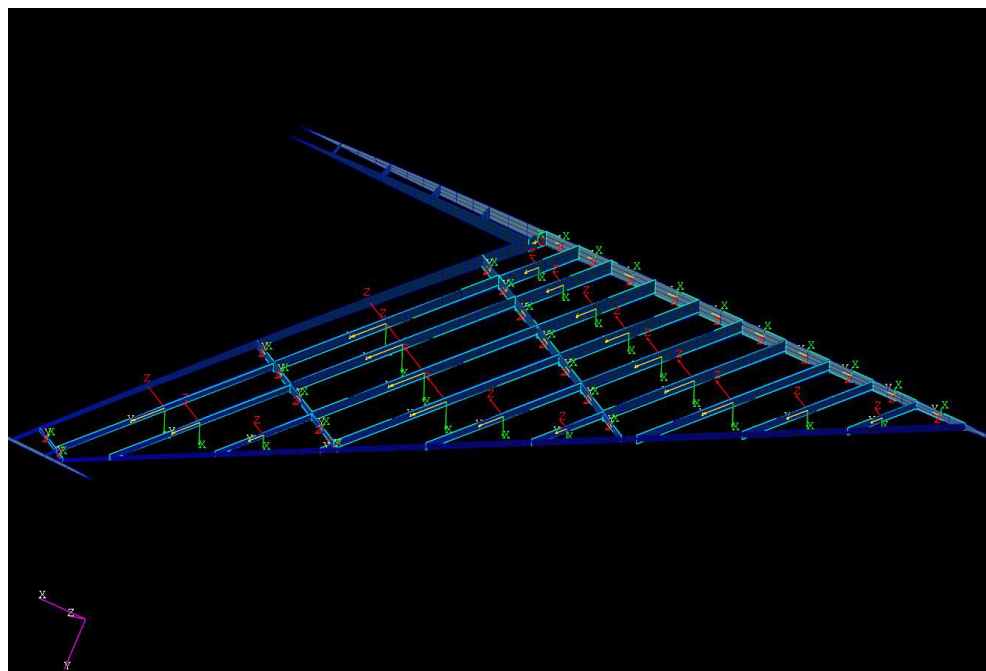


Figure 134.—44 Panels on Tail Substructure

Fuselage panels are curved to reflect curvature of fuselage OML

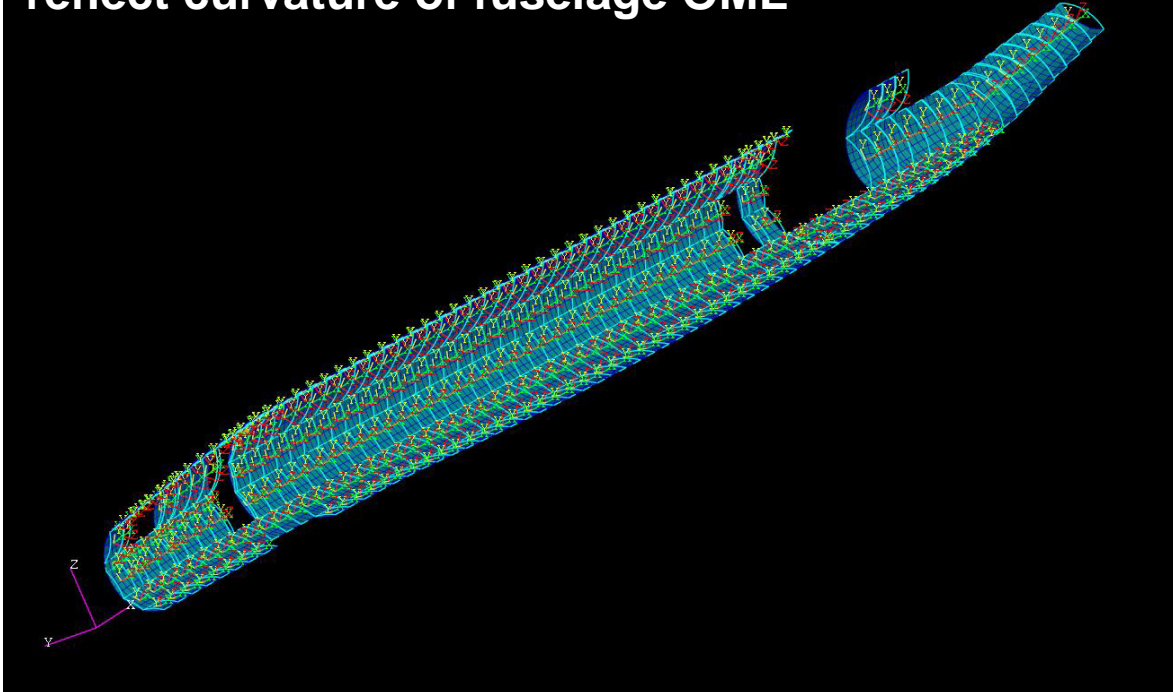


Figure 135.—346 Buckling Panels on Fuselage OML

3.5.3 Design Variables and Zones

The design variables for structural sizing are the thickness of the shell elements that comprise the primary structure of the vehicle. This includes the main outer wing box, tail wing box, inner wing and boom, and fuselage. We did not size the control surfaces, nor did we size the vehicle nose. As indicated in Section 3.4 the FEM makes significant use of composite materials with metallics used for major load introduction and bulkheads. We divided the designed shell elements of the airframe into constant property zones, where each element in the zone is assigned to the same property (either a PCOMP or PSHELL). The strategy behind breaking up the model into design zones was to have enough resolution such that the thickness of large panels was not being driven by a small stress or strain concentration, while at the same time keeping the number of independent design variables (and thus run-times) to a reasonable level. In the end, the sizing model contained 1078 independent design variables.

The elements associated with skins were comprised of a Graphite composite tape system with 4 material directions, 0° , 45° , -45° , and 90° directions. The thickness of each material direction was allowed to be a design variable, except that the $+45^\circ$ and -45° thickness were constrained to be equal in order to maintain a balanced laminate per composite design best practices. Thus there are 3 independent design variables for a composite skin design zone. The composite substructure (rib, spars, bulkheads, and longerons) were comprised of a Graphite composite fabric system, and we enforced these elements to be quasi-isotropic laminates (equal numbers of 0 , 45 , -45 , and 90), since ribs and spars tend to be shear dominant. Thus there is 1 independent design variable for a composite substructure property zone. For the metallic property zones, there is naturally only 1 design variable per zone, the thickness of the shell element, since metals are isotropic.

Figure 136 to Figure 154 show the design zones that were considered as part of the structural sizing, with the number of independent design variables per region also provided. Each uniquely colored region is an independent design zone.

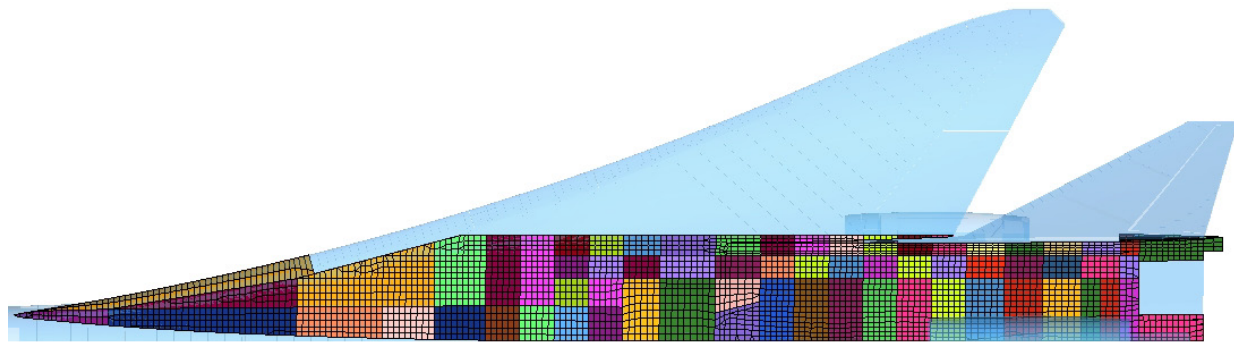


Figure 136.—Composite Inner Wing Skin Design Zones—109 Zones, 327 Independent Design Variables

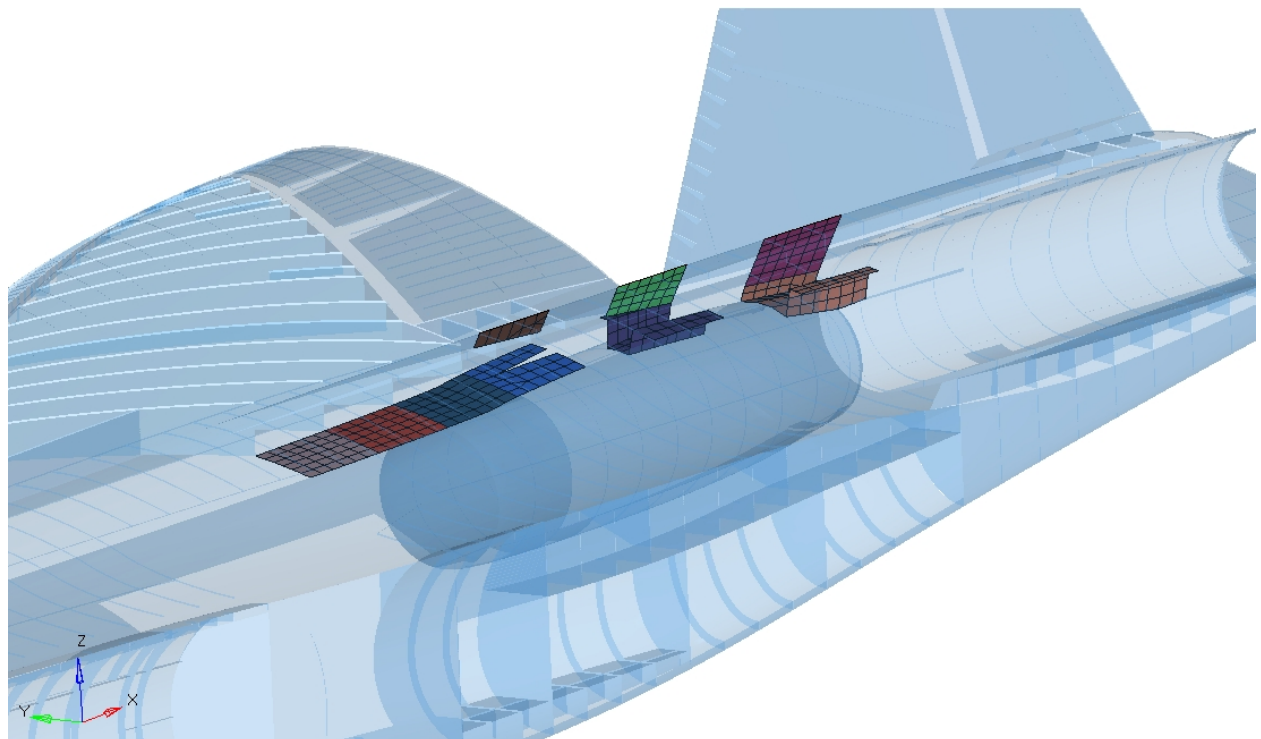


Figure 137.—Aluminum Inner Wing Skin Design Zones—9 Zones, 9 Independent Design Variables

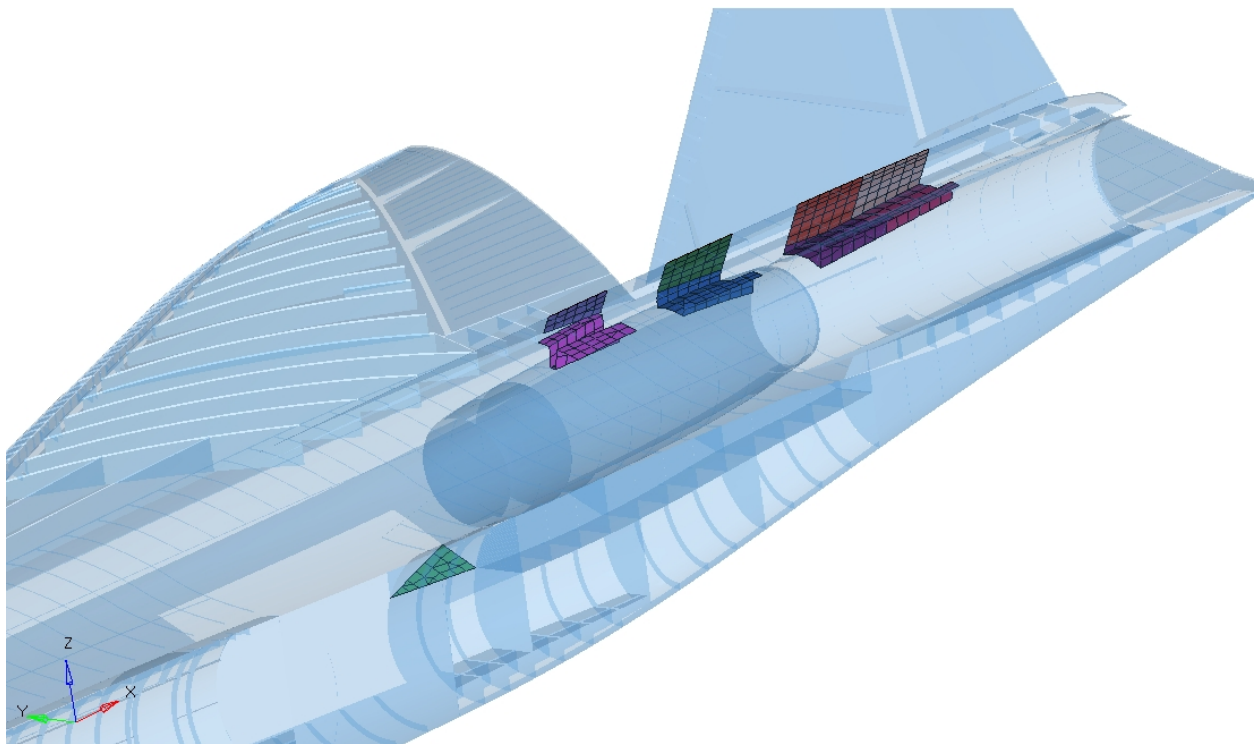


Figure 138.—Titanium Inner Wing Skin Design Zones—9 Zones, 9 Independent Design Variables

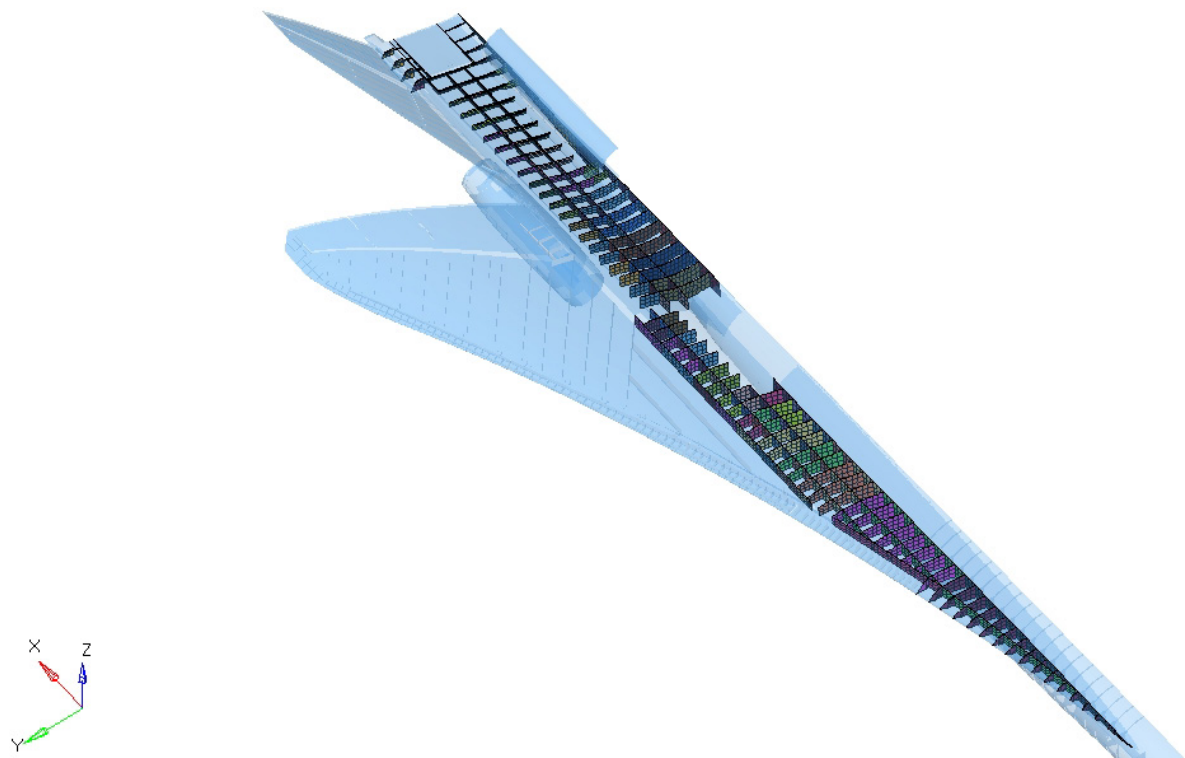


Figure 139.—Composite Inner Wing Substructure Design Zones—82 Zones, 82 Independent Design Variables

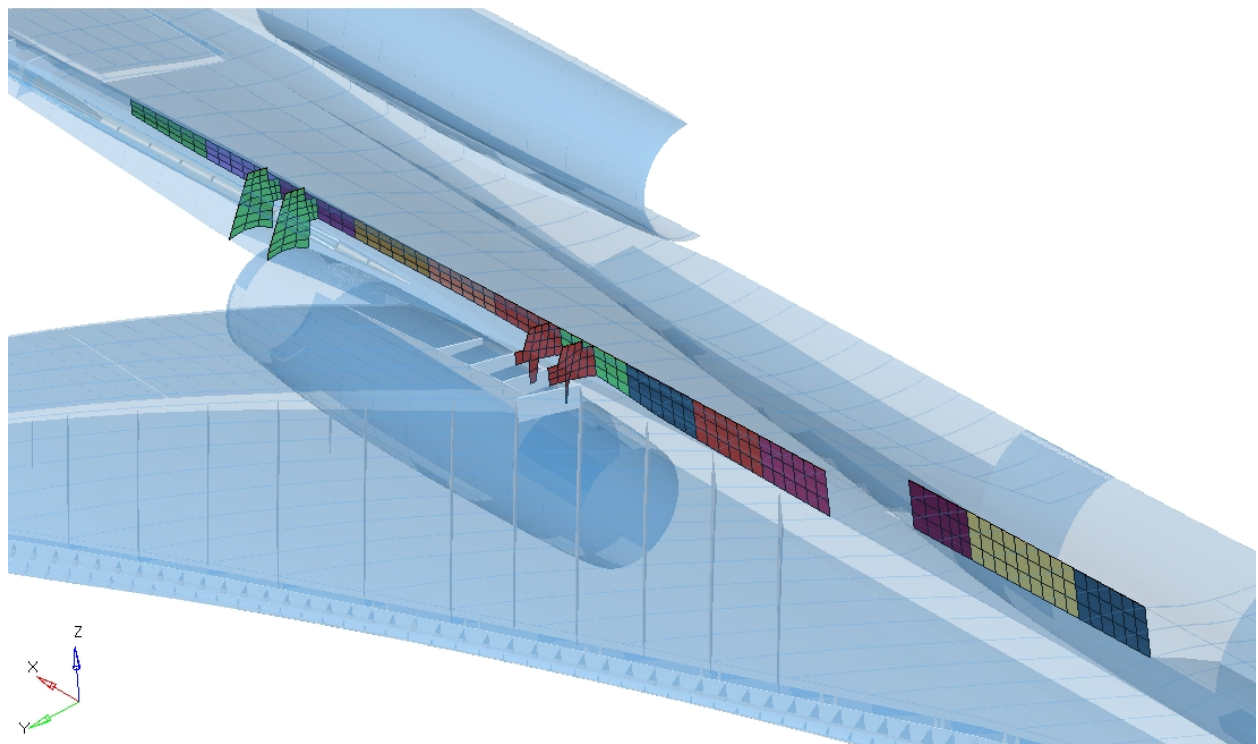


Figure 140.—Aluminum Inner Wing Substructure Design Zones—15 Zones, 15 Independent Design Variables

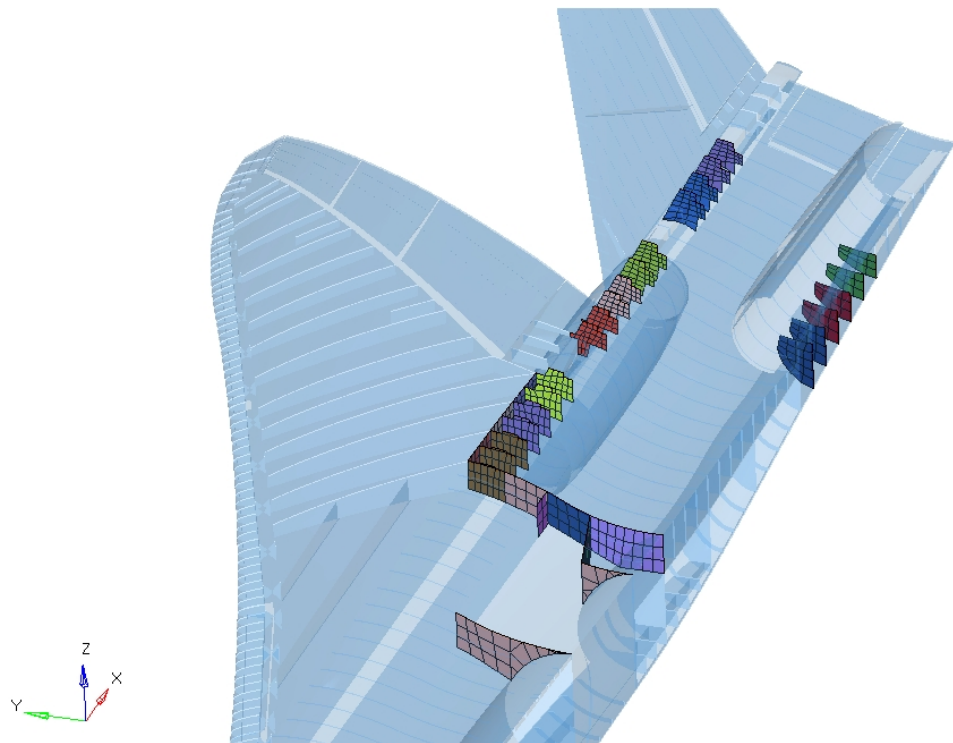


Figure 141.—Titanium Inner Wing Substructure Design Zones—22 Zones, 22 Independent Design Variables

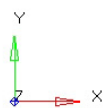
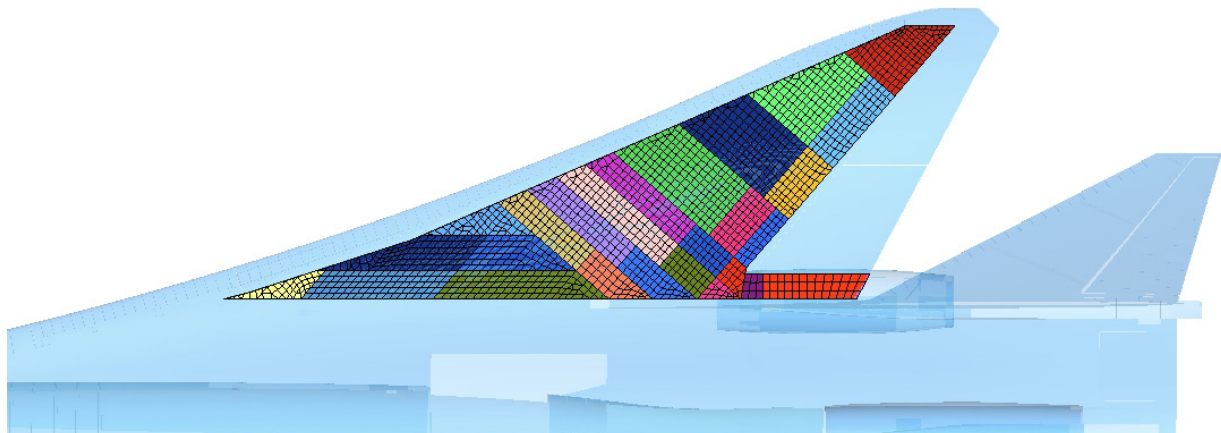


Figure 142.—Composite Outer Wing Skin Design Zones—52 Zones, 156 Independent Design Variables

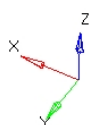
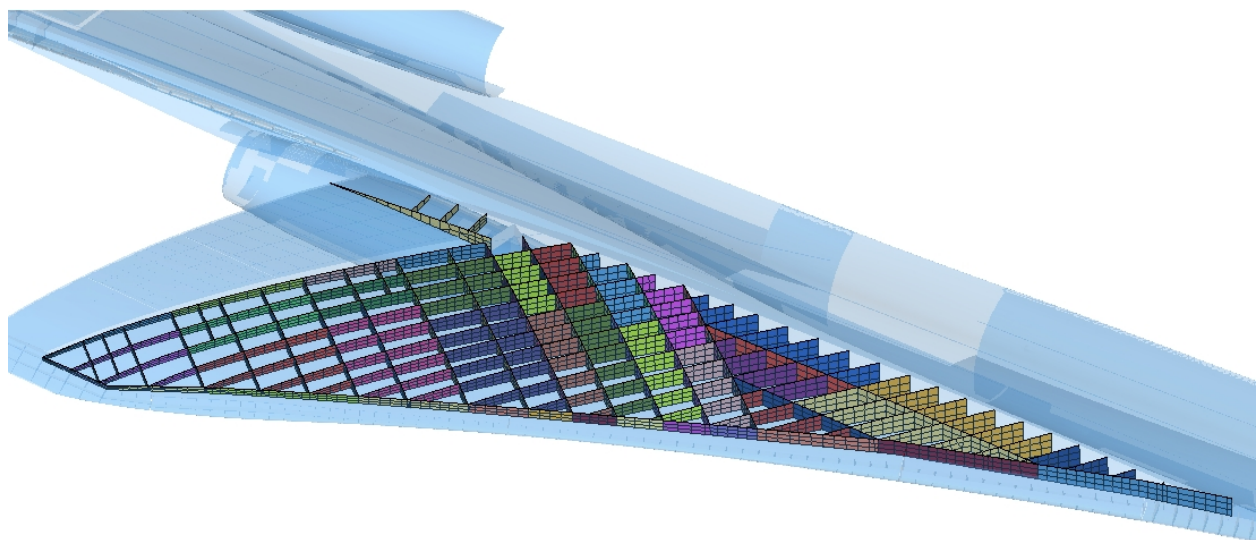


Figure 143.—Composite Outer Wing Substructure Design Zones—59 Zones, 59 Independent Design Variables

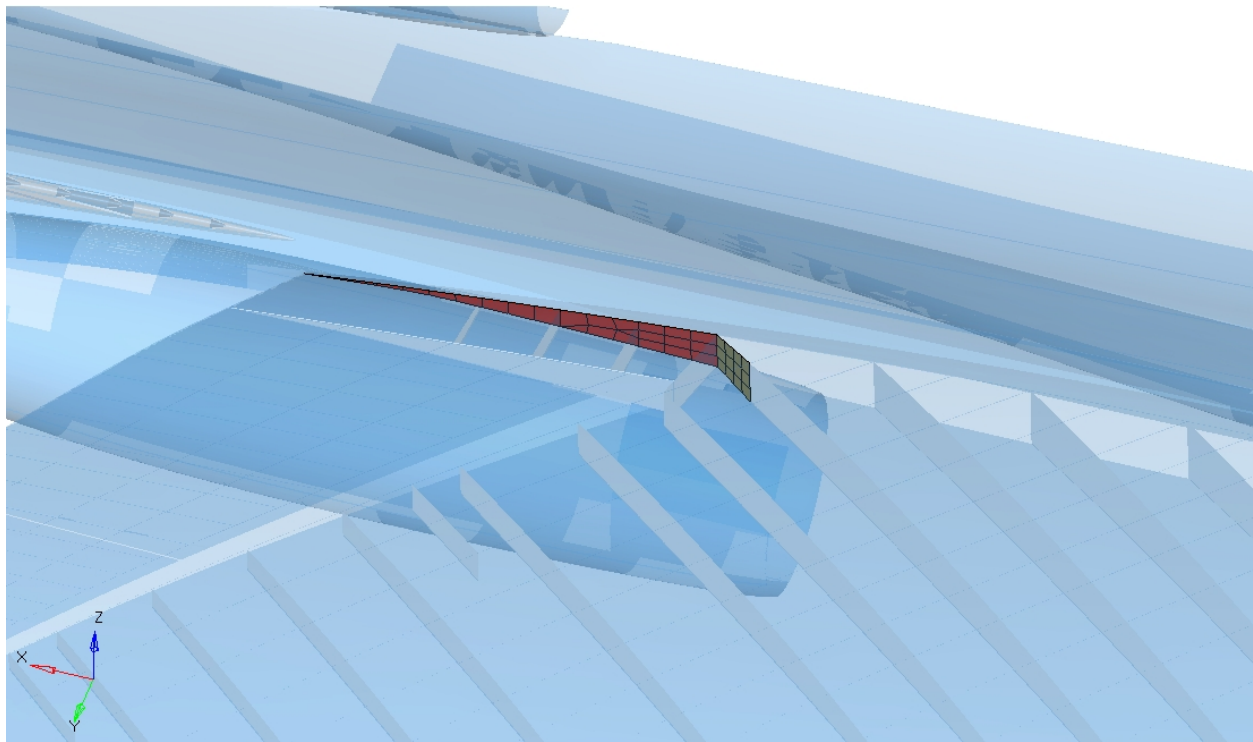


Figure 144.—Aluminum Outer Wing Substructure Design Zones—2 Zones, 2 Independent Design Variables

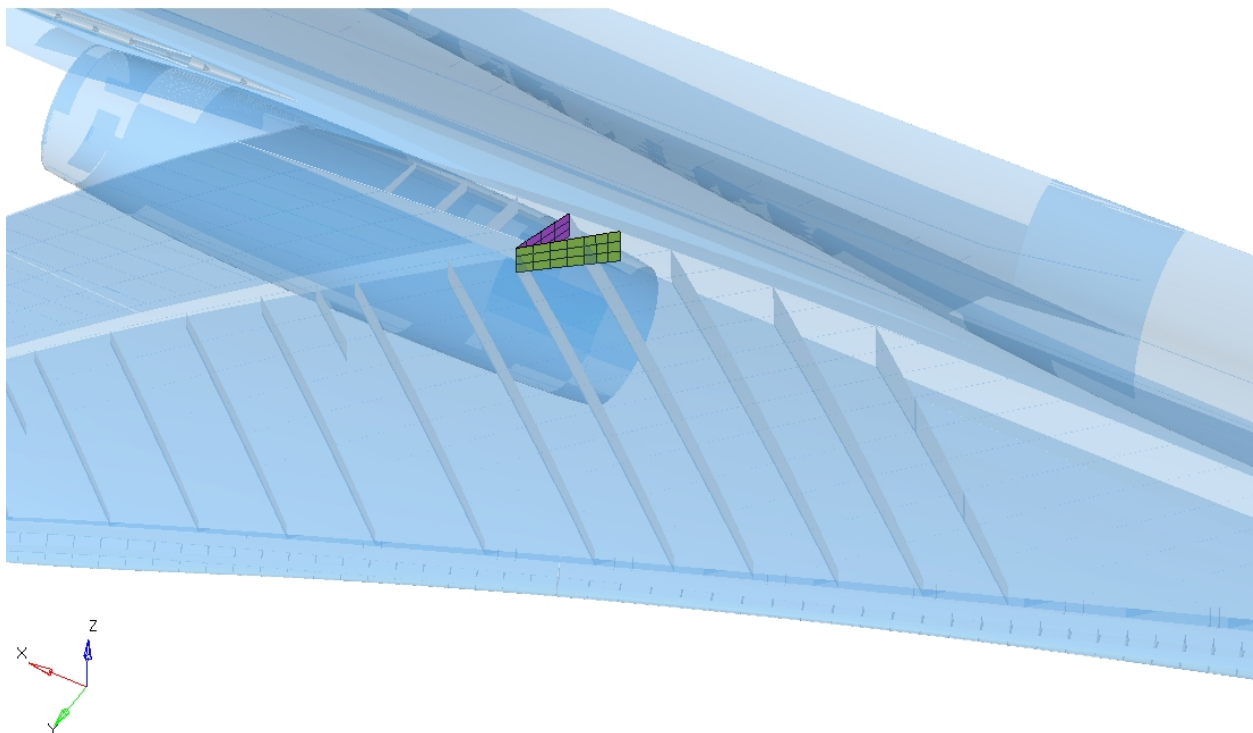


Figure 145.—Titanium Outer Wing Substructure Design Zones—2 Zones, 2 Independent Design Variables

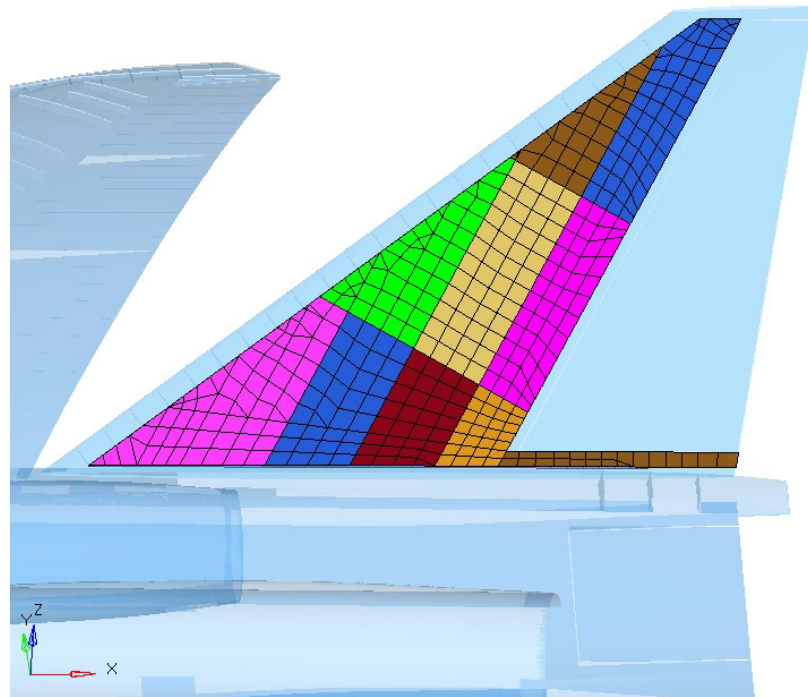


Figure 146.—Composite Tail Skin Design Zones—20 Zones, 60 Independent Design Variables

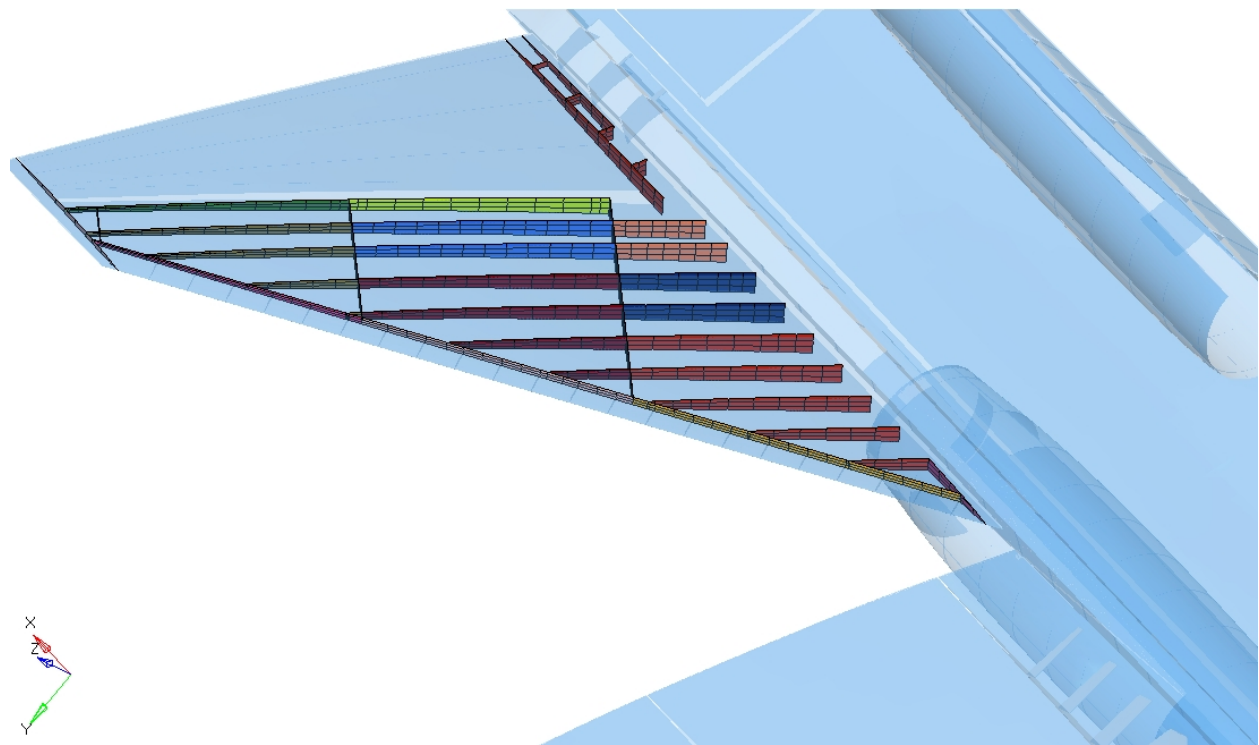


Figure 147.—Composite Tail Substructure Design Zones—17 Zones, 17 Independent Design Variables

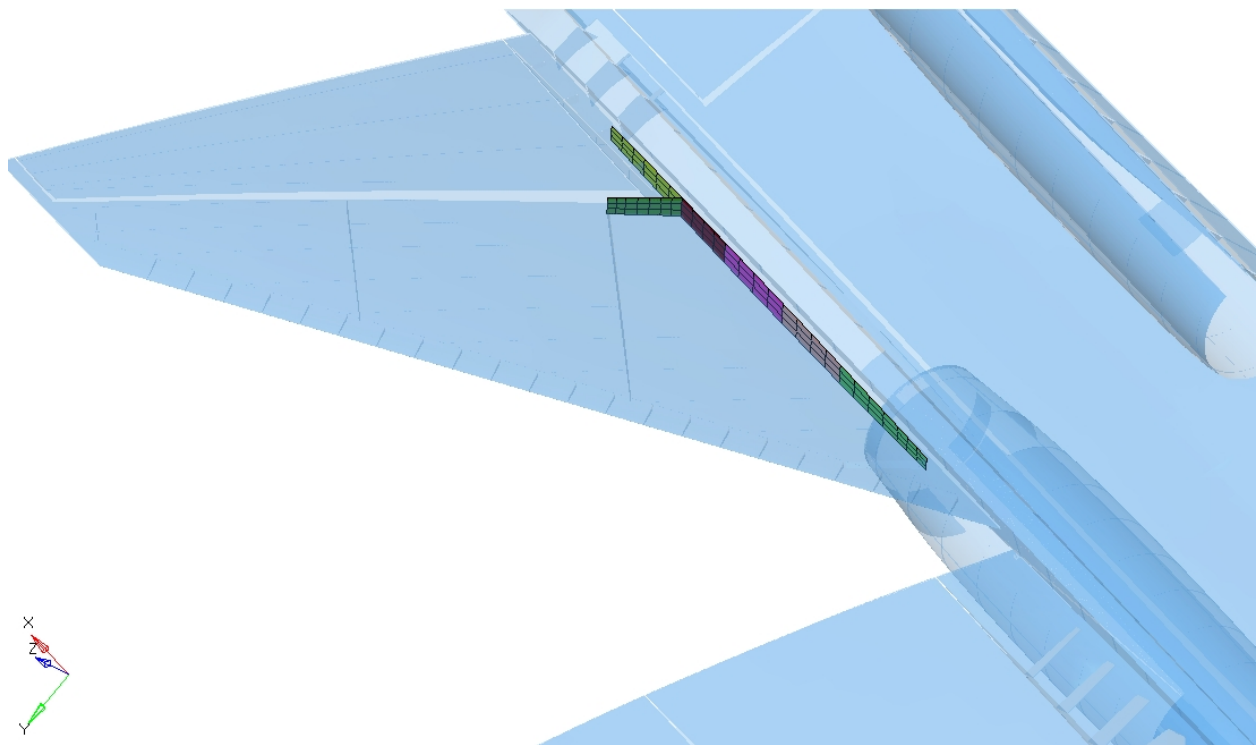


Figure 148.—Titanium Tail Substructure Design Zones—6 Zones, 6 Independent Design Variables

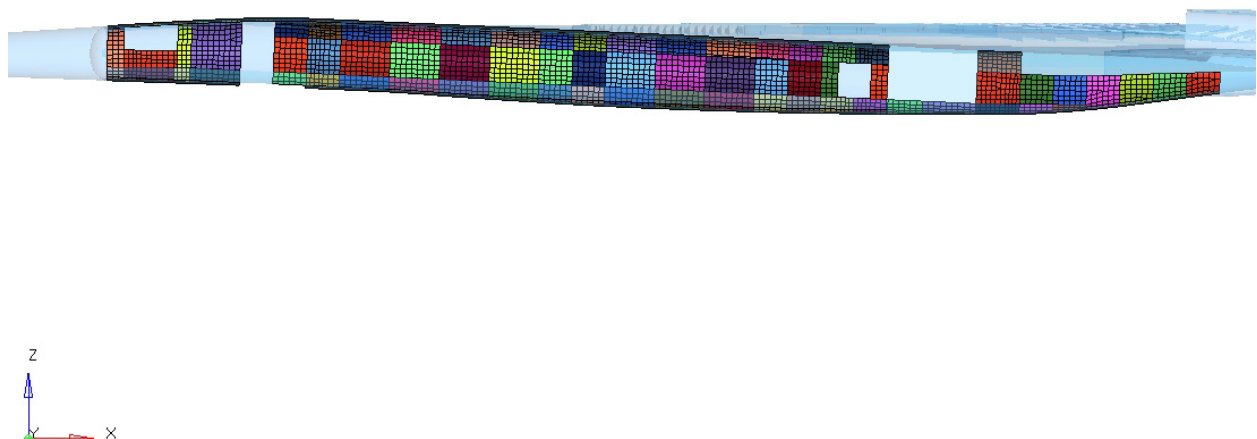


Figure 149.—Composite Fuselage OML Design Zones—71 Zones, 213 Independent Design Variables

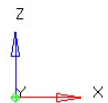


Figure 150.—Aluminum Fuselage OML Design Zones—5 Zones, 5 Independent Design Variables

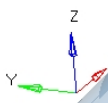
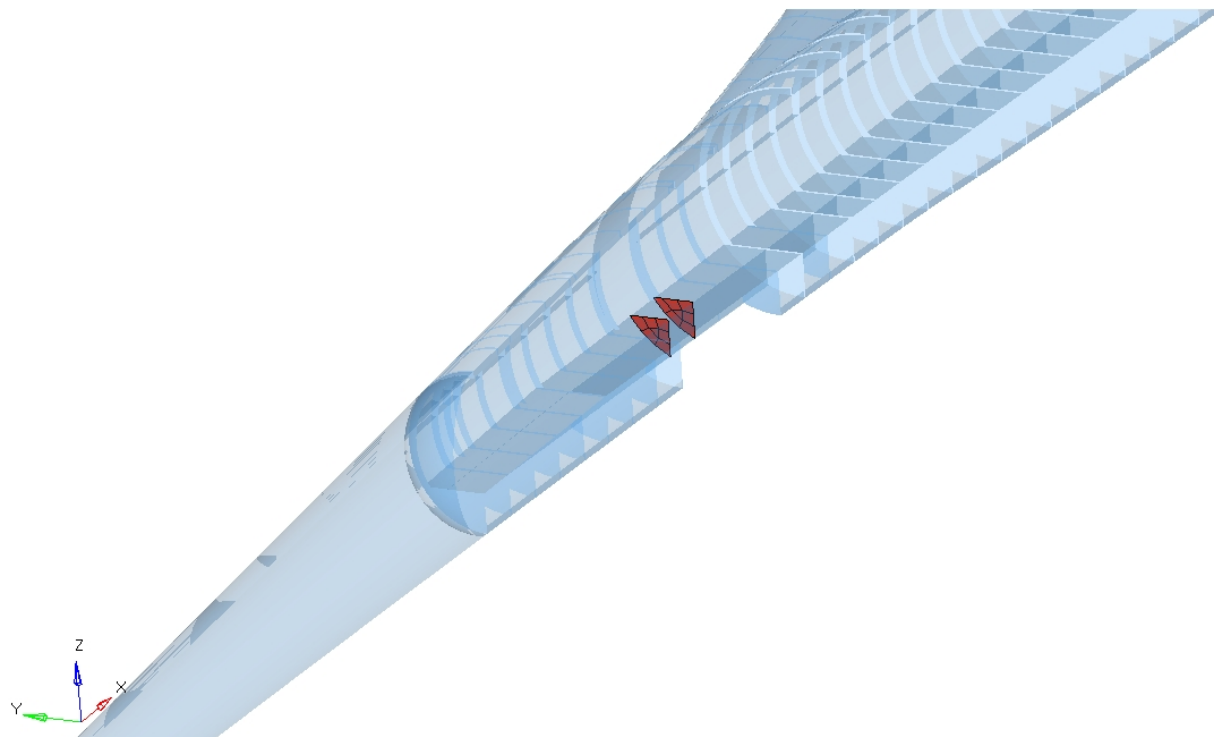


Figure 151.—Aluminum Fuselage Substructure Design Zones—1 Zone, 1 Independent Design Variable

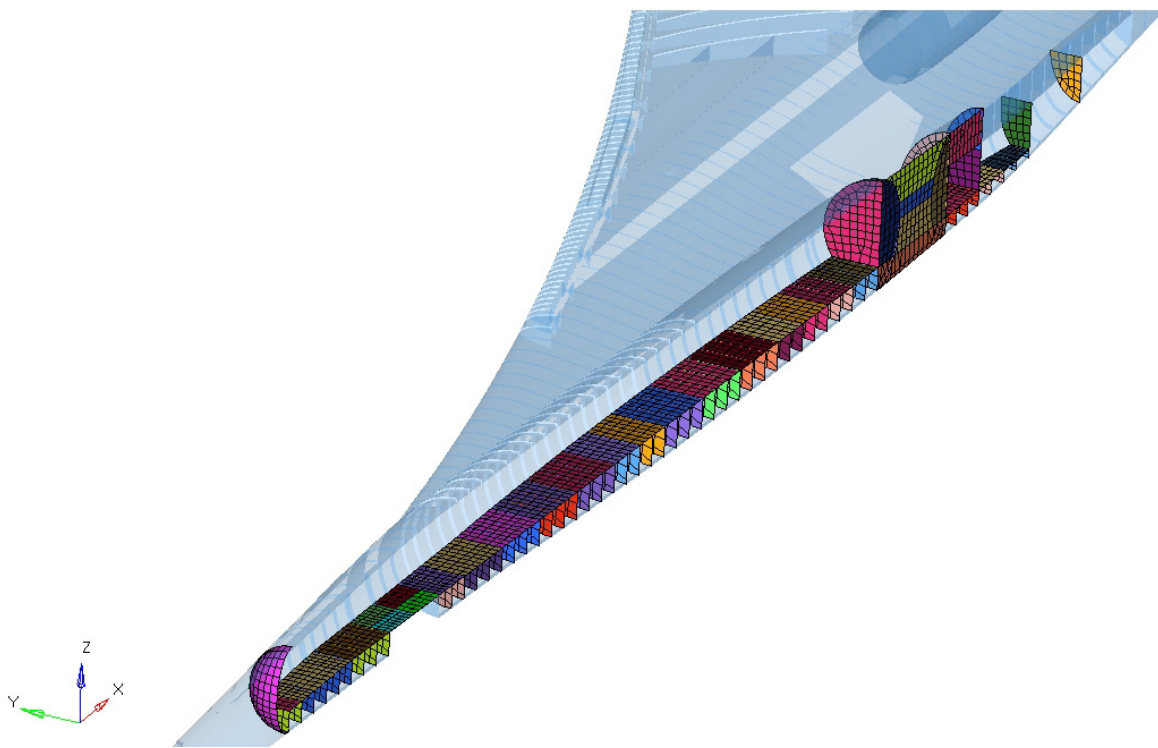


Figure 152.—Composite Fuselage Substructure Design Zones—87 Zones, 87 Independent Design Variables

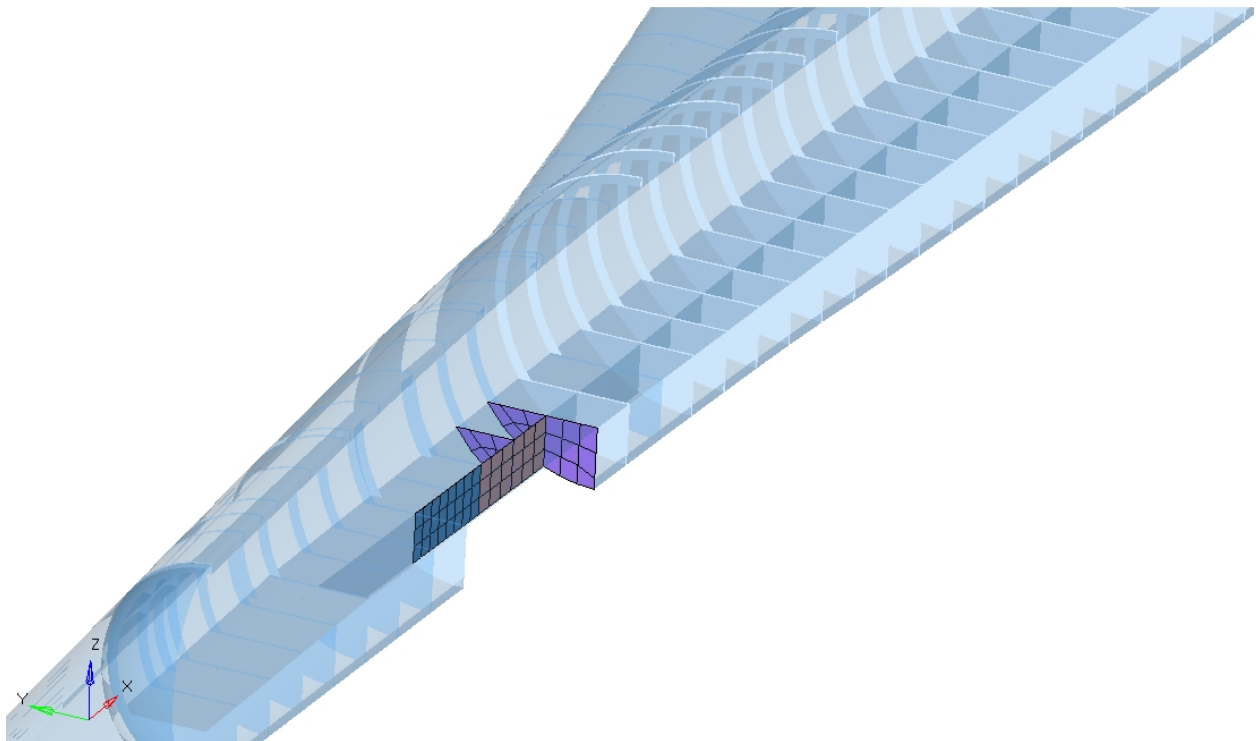


Figure 153.—Titanium Fuselage Substructure Design Zones—3 Zones, 3 Independent Design Variables

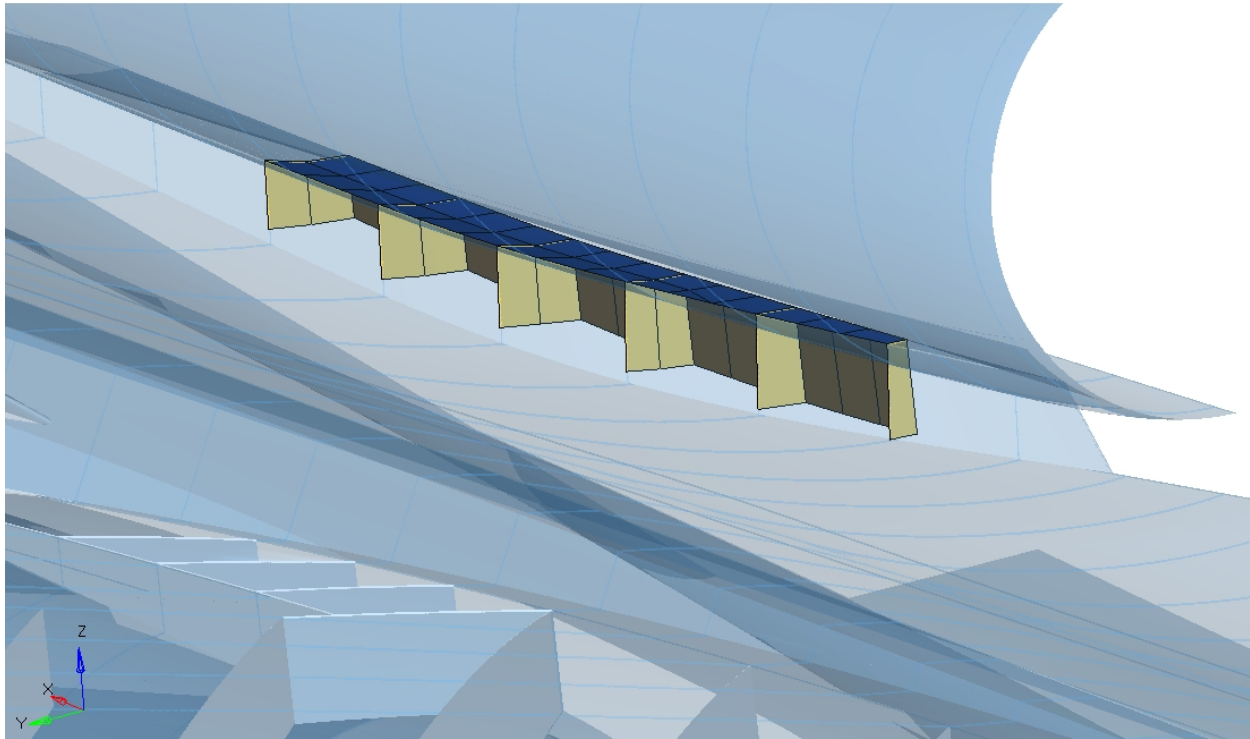


Figure 154.—Titanium Center Pylon Design Zones—3 Zones, 3 Independent Design Variables

3.5.4 Core and Stiffener Trade Studies

For the original FEM sizing studies with the all-composite vehicle, we had been assuming $\frac{3}{4}$ in. thick honeycomb core for all of the designed elements. Core thickness chiefly affects buckling margins, and we learned that the buckling criteria drove very little of the structural sizing. This suggested that our original assumptions for core thickness were too conservative and thus possibly carrying unnecessary amounts of core weight. Hence, we initiated a sizing trade study to look at variation in the core thickness and to identify the minimum weight core thickness on a global level. As shown in Figure 155, we conducted sizing with various combinations of skin and substructure core thickness (ranging in increments of 0.75, 0.5, and 0.25 in.). From the results of these studies, we concluded that on an overall level, 0.5 in. of core for the skins and 0.25 in. of core for the substructure was the minimum weight solution. Further optimization of the core thickness could be conducted for each panel, but this sort of detail optimization of each panel was beyond the scope of this study and felt to have little impact on the overall aeroelastic characteristics of the vehicle.

The metallic buckling panels were stiffened with discrete stringers. Like the core thickness, the stringer spacing principally influences the buckling margins. As a result, we conducted a trade study in the stringer spacing applied uniformly over every metallic panel. Figure 156 shows the results of this trade study, plotting the total weight of the sized elements plus the weight of the stiffeners (which are not modeled directly in the FEM but only on the buckling panel definition). Based on the results of this study, we selected 9 in. stringer spacing for all metallic buckling panels. Like the core thickness, further optimization could be performed on each individual panel, but that was beyond the scope of this activity.

Total Sized Element Weight versus Core Thickness

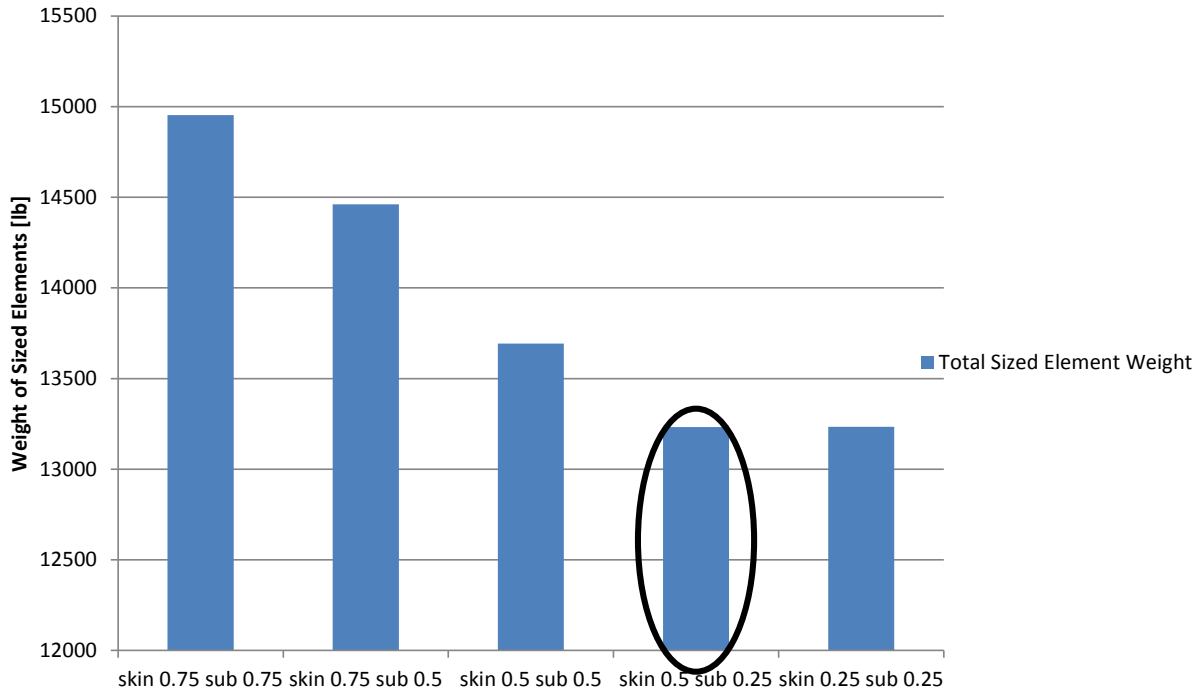


Figure 155.—Core Thickness Trade Study

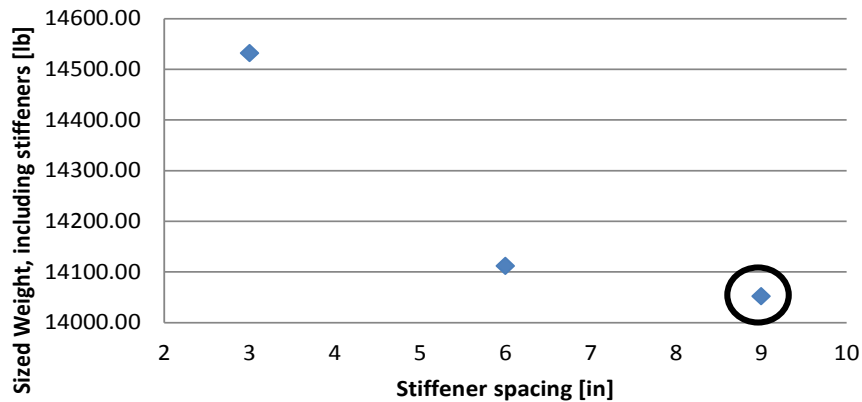


Figure 156.—Stiffener Spacing Trade Study

3.5.5 Final Sizing Results

The FEM was sized to the criteria of the previous section. This FEM was designated FEM017-REV70. Upon analysis of this structural design to the design loads, we discovered that tail deformation for one of the elevated g pull-ups (LC400) was still excessive, nearly 47 in. for a tail span of roughly 250 in. (see Figure 157). In discussions with subject matter experts in the field of nonlinear mechanics, beyond 10 percent displacement of the span of the surface, geometric nonlinearity begins to become more significant. Consequently, we also ran a sizing where we added a constraint on tail deformation for load case 400 to be less than 25 in. (roughly 10 percent of the tail span). This FEM was designated FEM017-REV71. A comparison of the mass properties of each FEM is found in Table 24.

As seen in Table 24, the inclusion of the displacement constraint on the tail adds 1731 lb to the airframe weight, with most of it being added to the aft deck and the rest being added to the tail. This is also reflected in the plots of sized airframe thickness, shown in Figure 158 to Figure 165.

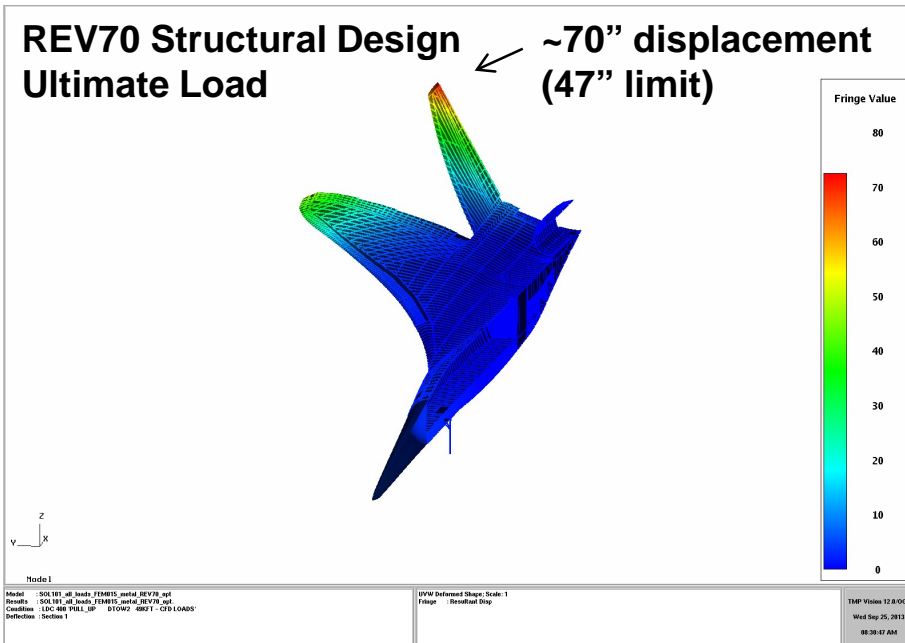


Figure 157.—Tail Deformation for LC 400 (2.5 g Pull-Up, Mach 2.0, DTOW2)

TABLE 24.—WEIGHT SUMMARY OF SIZED FEMS

Full Span	Mass Property Statement	FEM 017 Metal Rev70 SS Adjusted Mass	FEM 017 Metal Rev71 SS Adjusted Mass
Wing	31504.0	24818.3	24755.2
Aft Deck	6934.0	4252.0	5371.6
Tail	4014.0	3703.3	4504.3
Fuselage	15086.0	11891.5	11764.9
Subtotal	57538.0	44665.2	46395.9
Nacelle+Inlet (structure)	10946.0	12664.4	12664.4
NLG (structure + mass)	1377.0	1374.6	1374.6
MLG (structure + mass)	11096.0	11095.6	11095.6
Non-Fuel Sys Mass	76651.0	68007.0	68007.0
FEM Makeup Mass	0.0	19801.3	18070.6
Zero Fuel Weight	157608.0	157608.1	157608.1
Fuel Mass (updated)	175124.0	175124.0	175124.0
GTOW	332732	332732	332732
CG-X Gear Up)	2045.00	2021.75	2022.89
CG-Y			
CG-Z	257.10	258.39	258.51

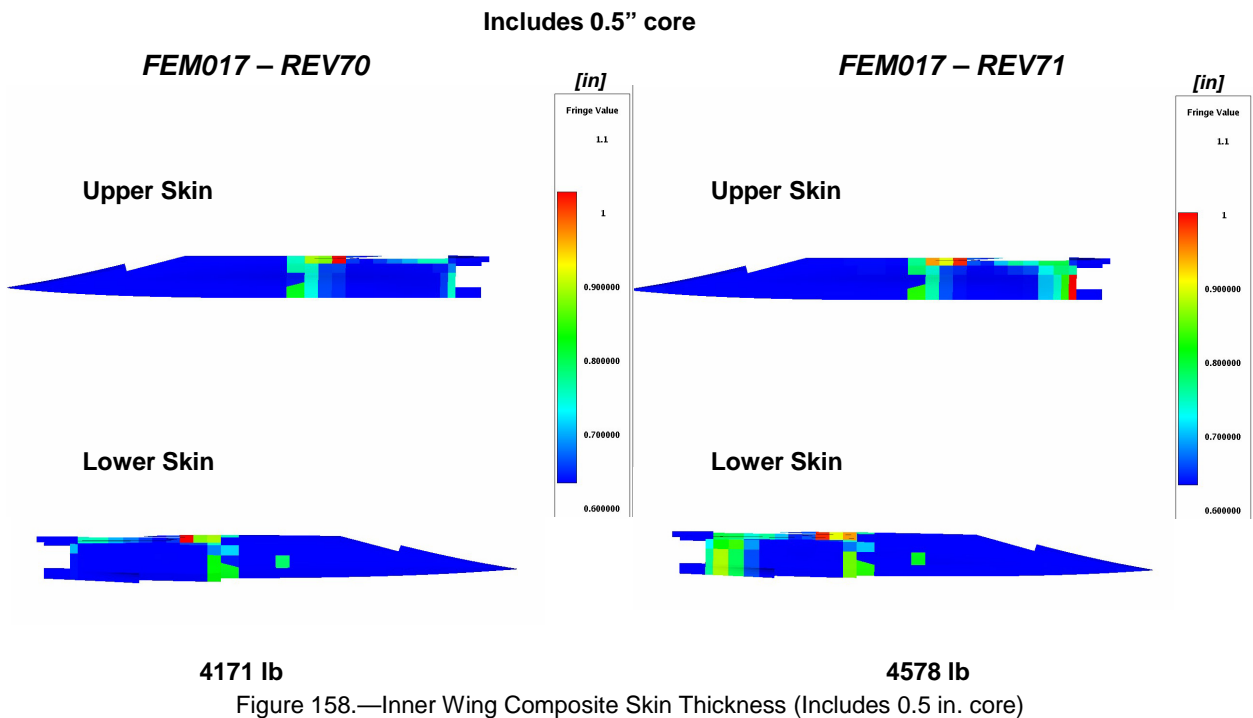


Figure 158.—Inner Wing Composite Skin Thickness (Includes 0.5 in. core)

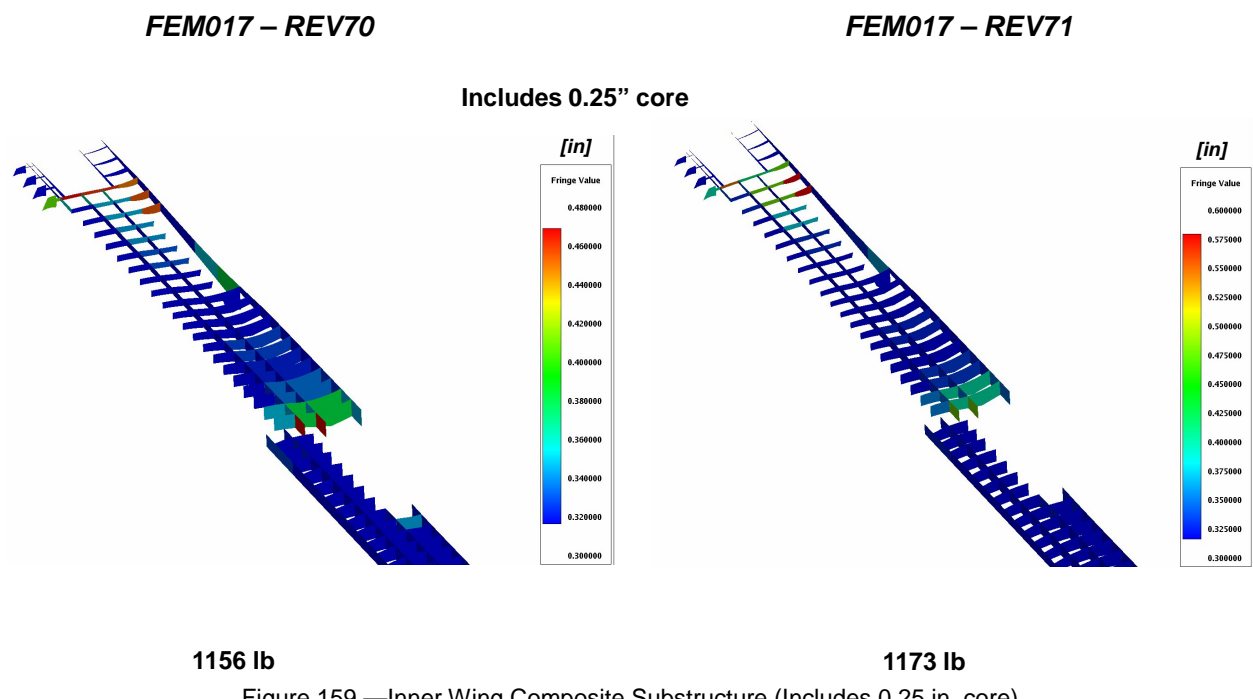
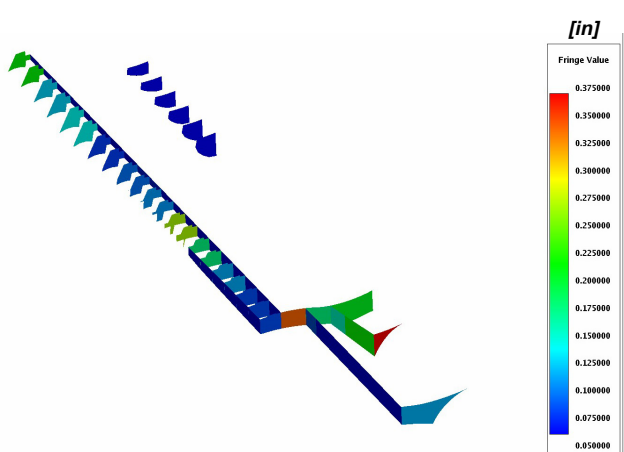
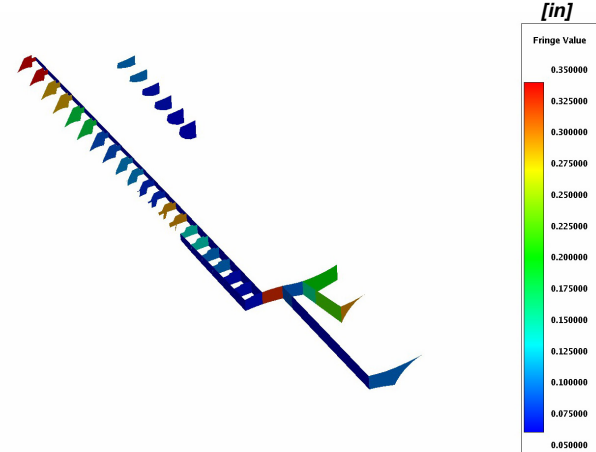


Figure 159.—Inner Wing Composite Substructure (Includes 0.25 in. core)

FEM017 – REV70



FEM017 – REV71

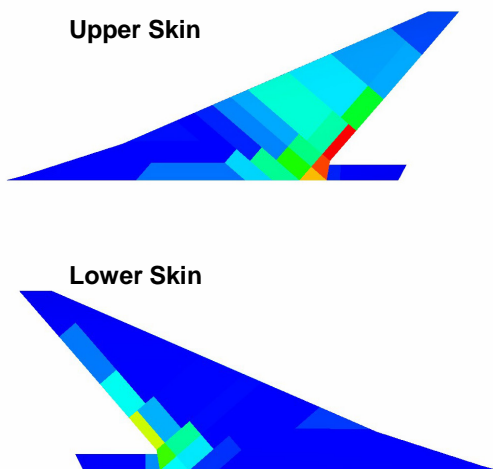


736 lb

760 lb

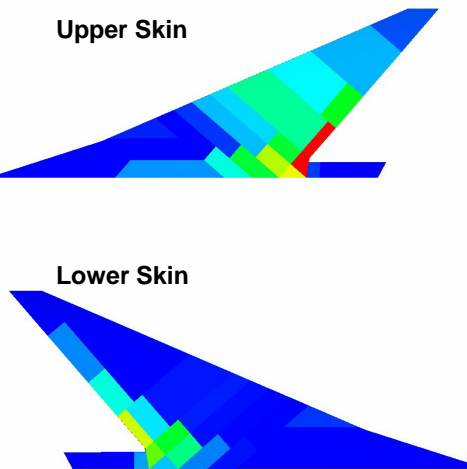
Figure 160.—Inner Wing Metallic Substructure

FEM017 – REV70



Includes 0.5" core

FEM017 – REV71



2226 lb

2243 lb

Figure 161.—Outer Wing Composite Skin Thickness (includes 0.5 in. core)

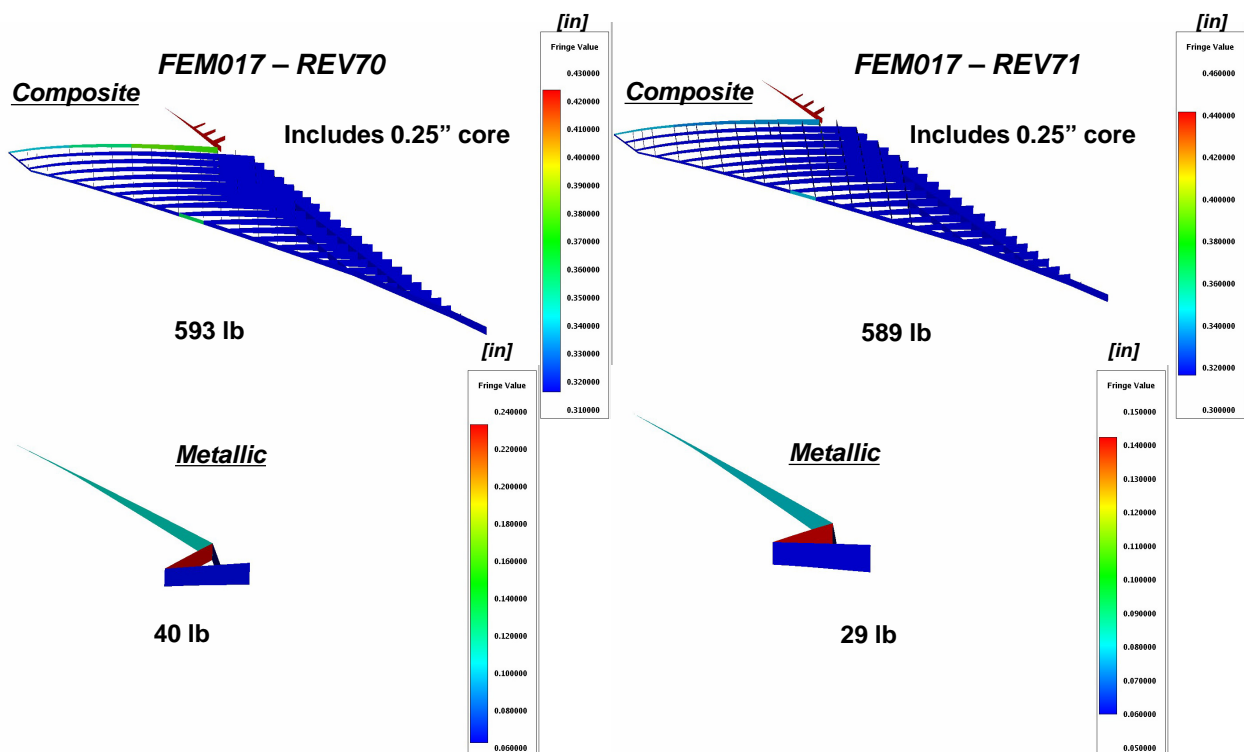


Figure 162.—Outer Wing Substructure Thickness (composite includes 0.25 in. core)

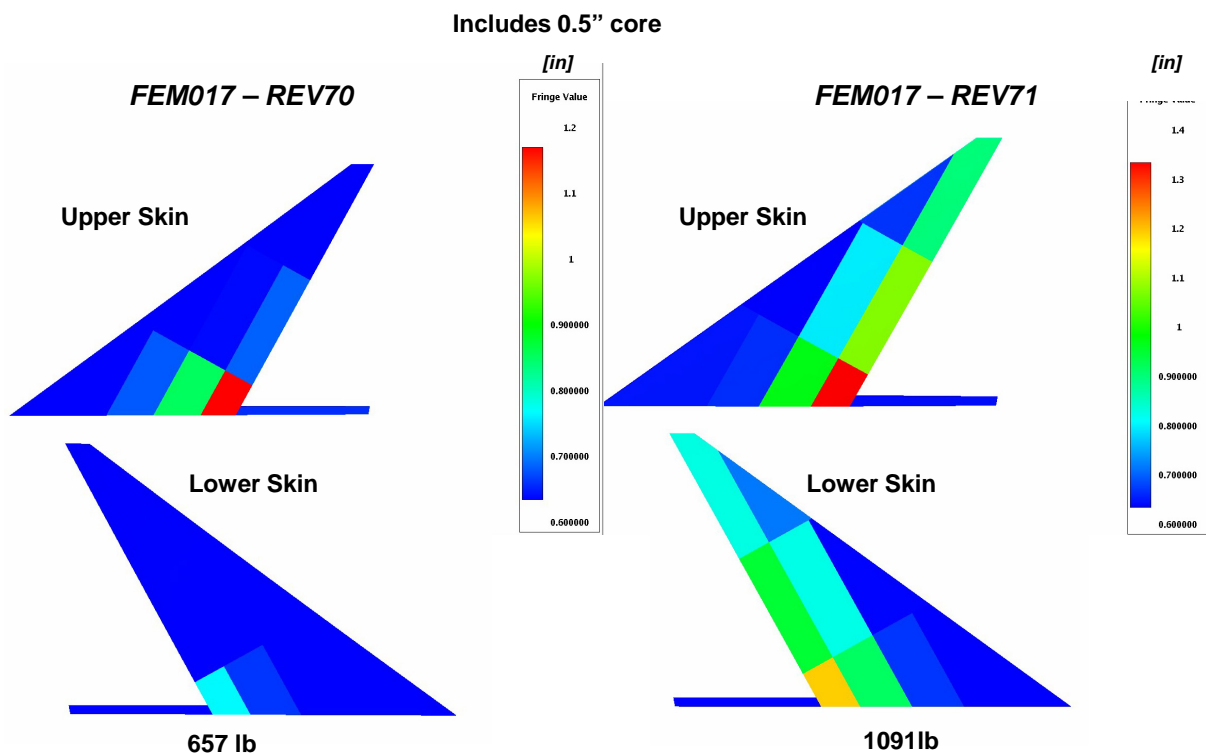


Figure 163.—Tail Composite Skin Thickness (includes 0.5 in. core)

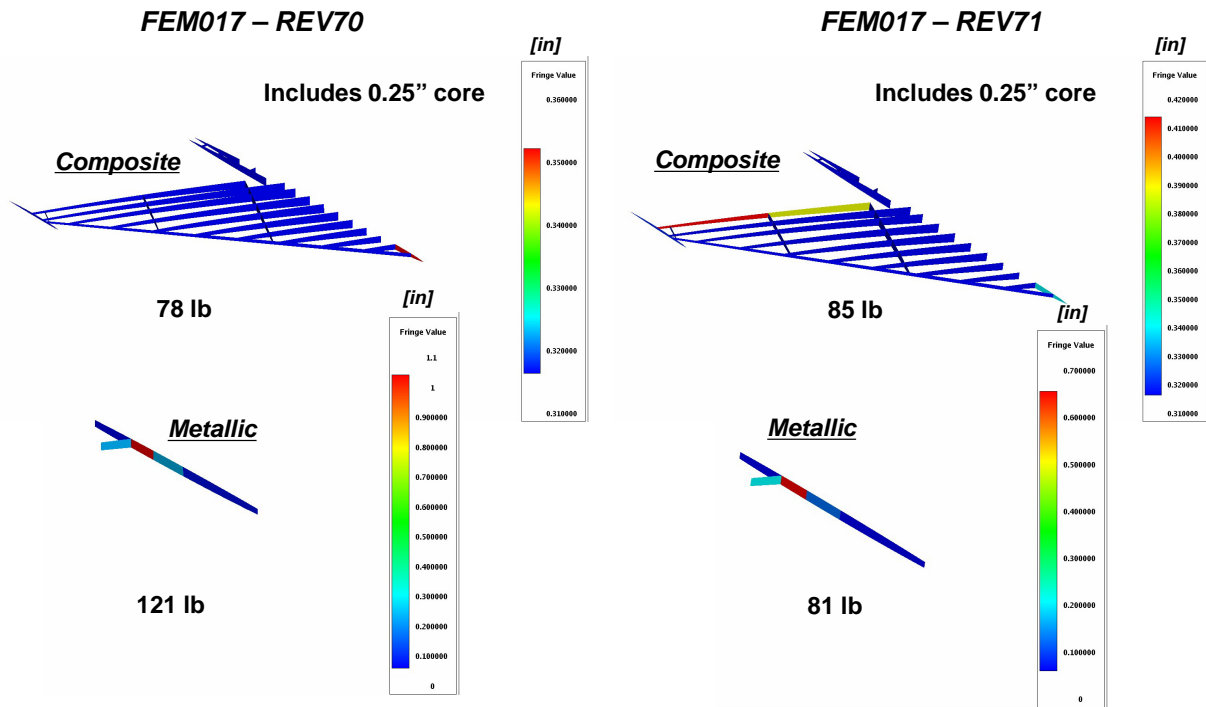


Figure 164.—Tail Substructure Thickness (composite includes 0.25 in. core)

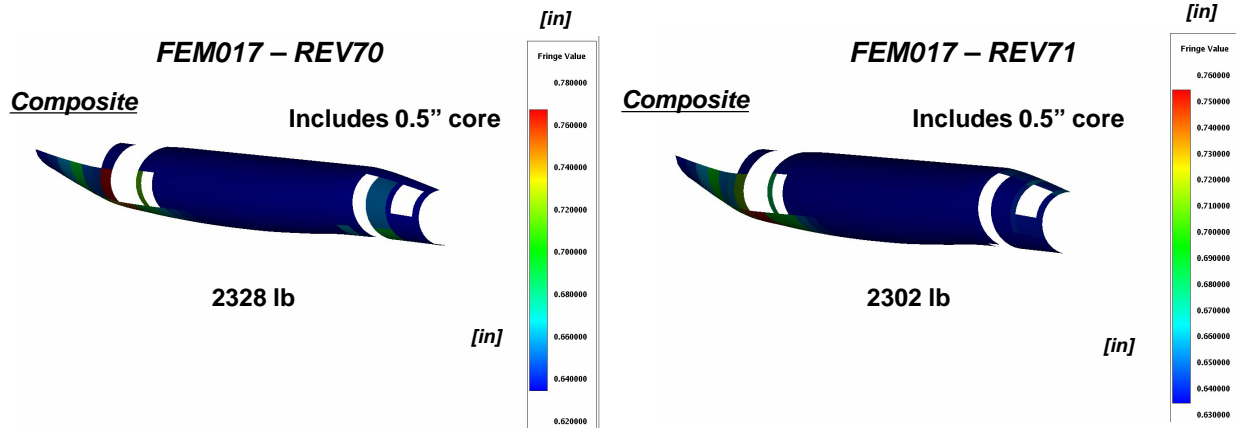


Figure 165.—Fuselage OML Thickness (includes 0.5 in. core)

3.5.6 Stress, Strain, and Deflection Plots

A select set of stress, strain and deformation plots is presented in this section. As with most FE analyses, the volume of data produced is very large and should be reviewed in a dedicated post-processing tool. However, these plots are representative of the sizing results. The use of a tail tip deflection constraint in the optimization is the difference between REV70 (without) and REV71 (with).

3.5.6.1 Strain Plots

Figure 166 to Figure 172, the strain plots, are average strain at the middle surface for each element set shown and are at ultimate load (includes 1.5 safety factor).

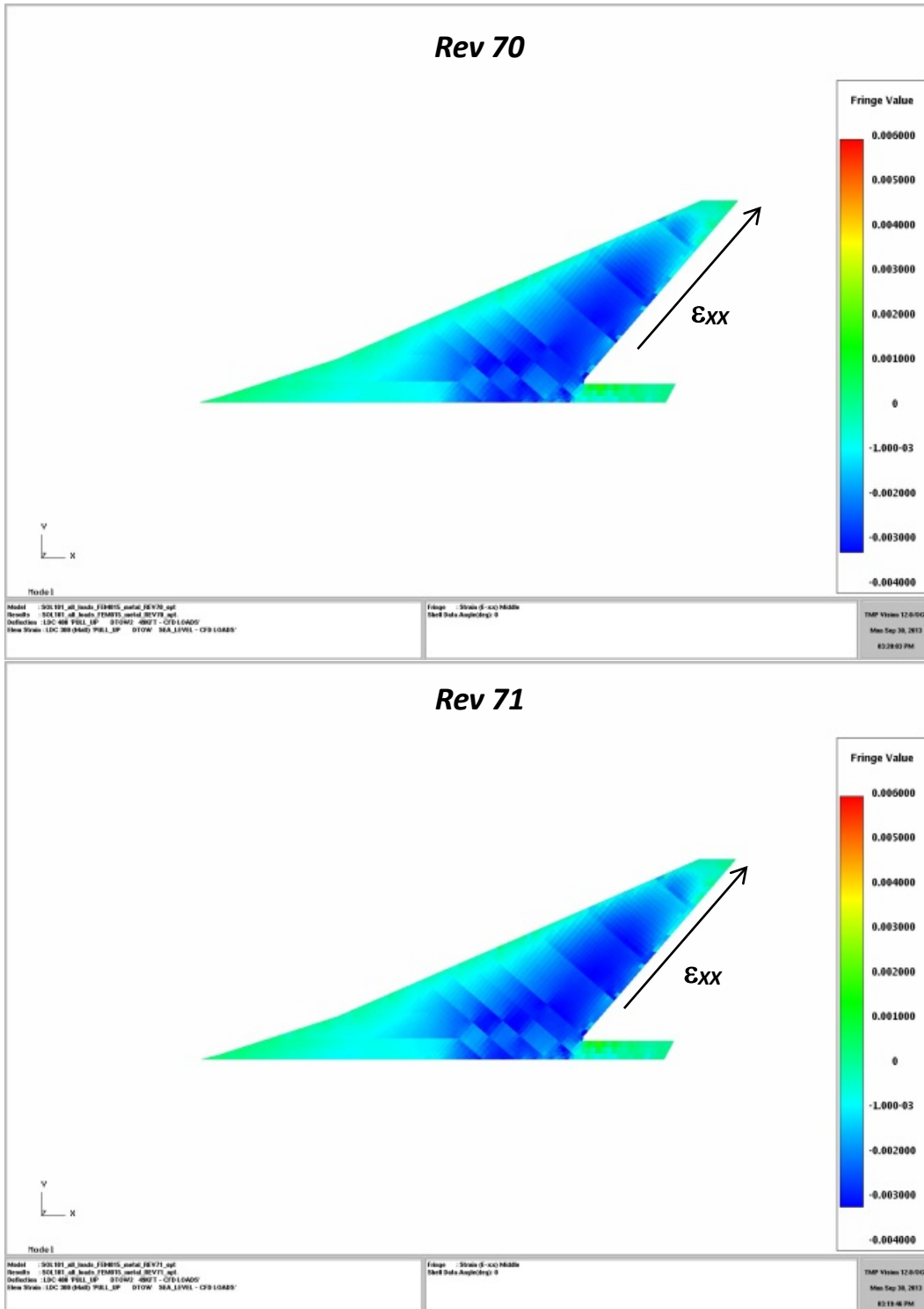


Figure 166.—Strain XX Load Case LC300—Upper Wing Skin

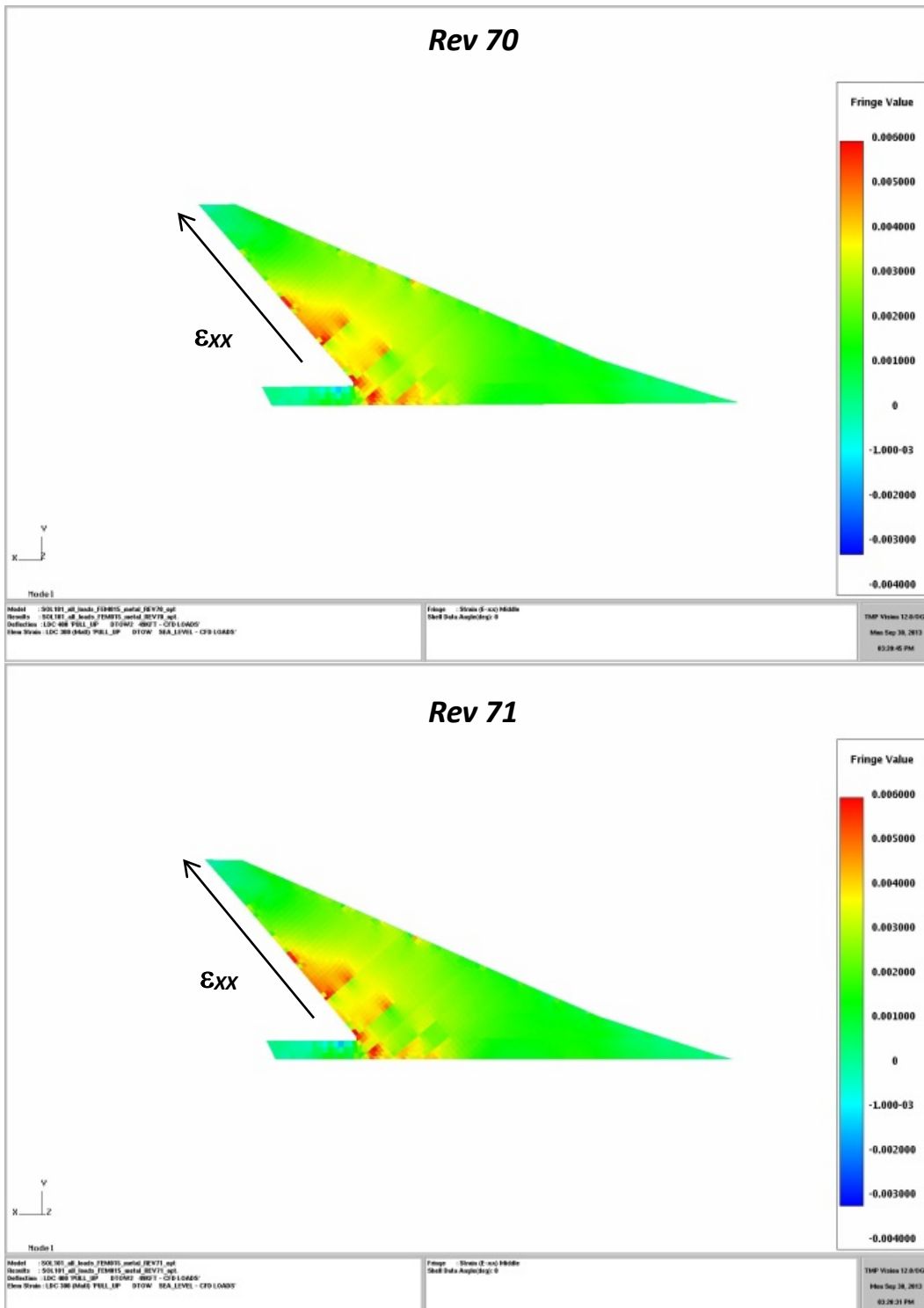


Figure 167.—Strain XX Load Case LC300—Lower Wing Skin

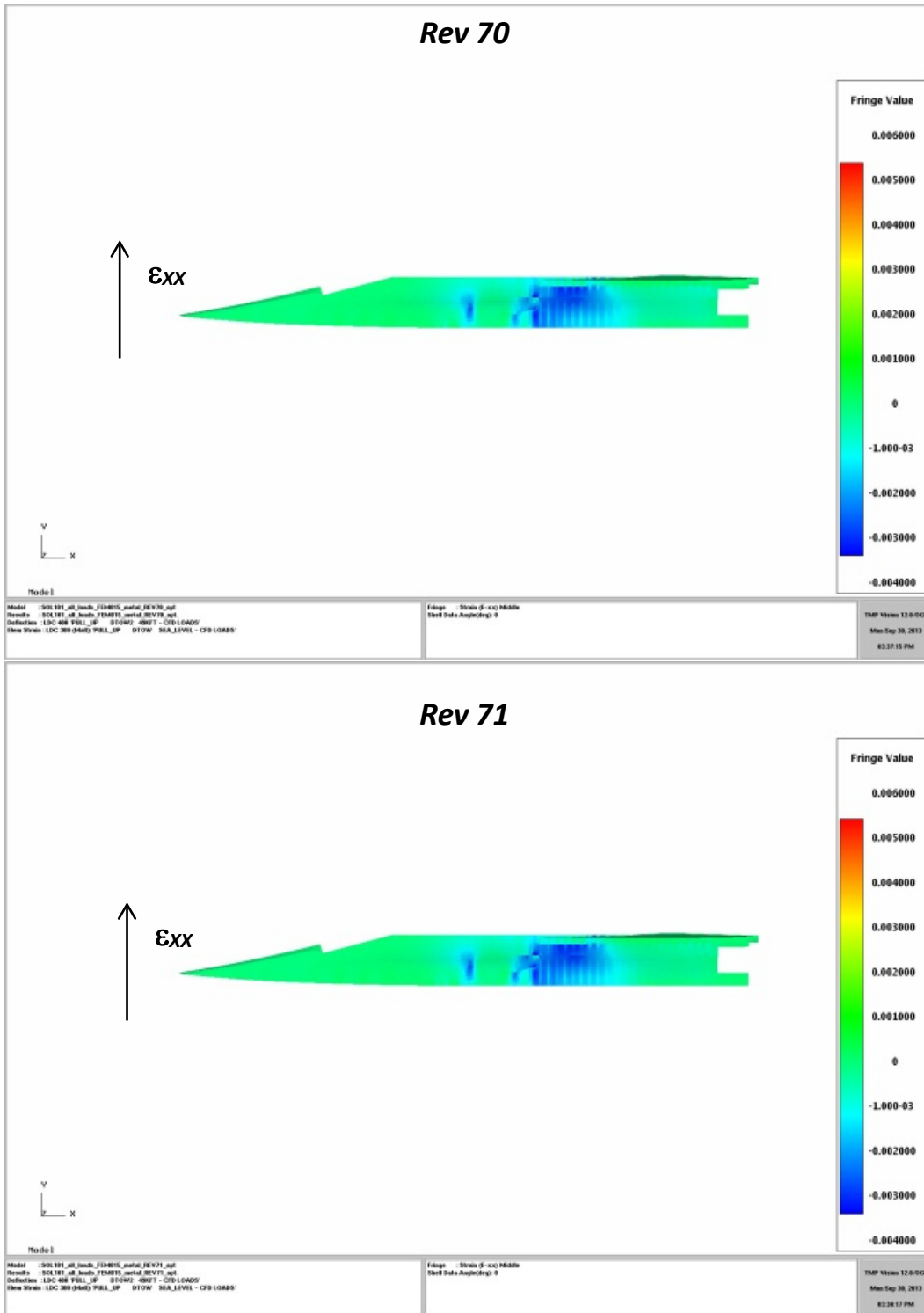


Figure 168.—Strain XX Load Case LC300—Upper Inner Wing Skin

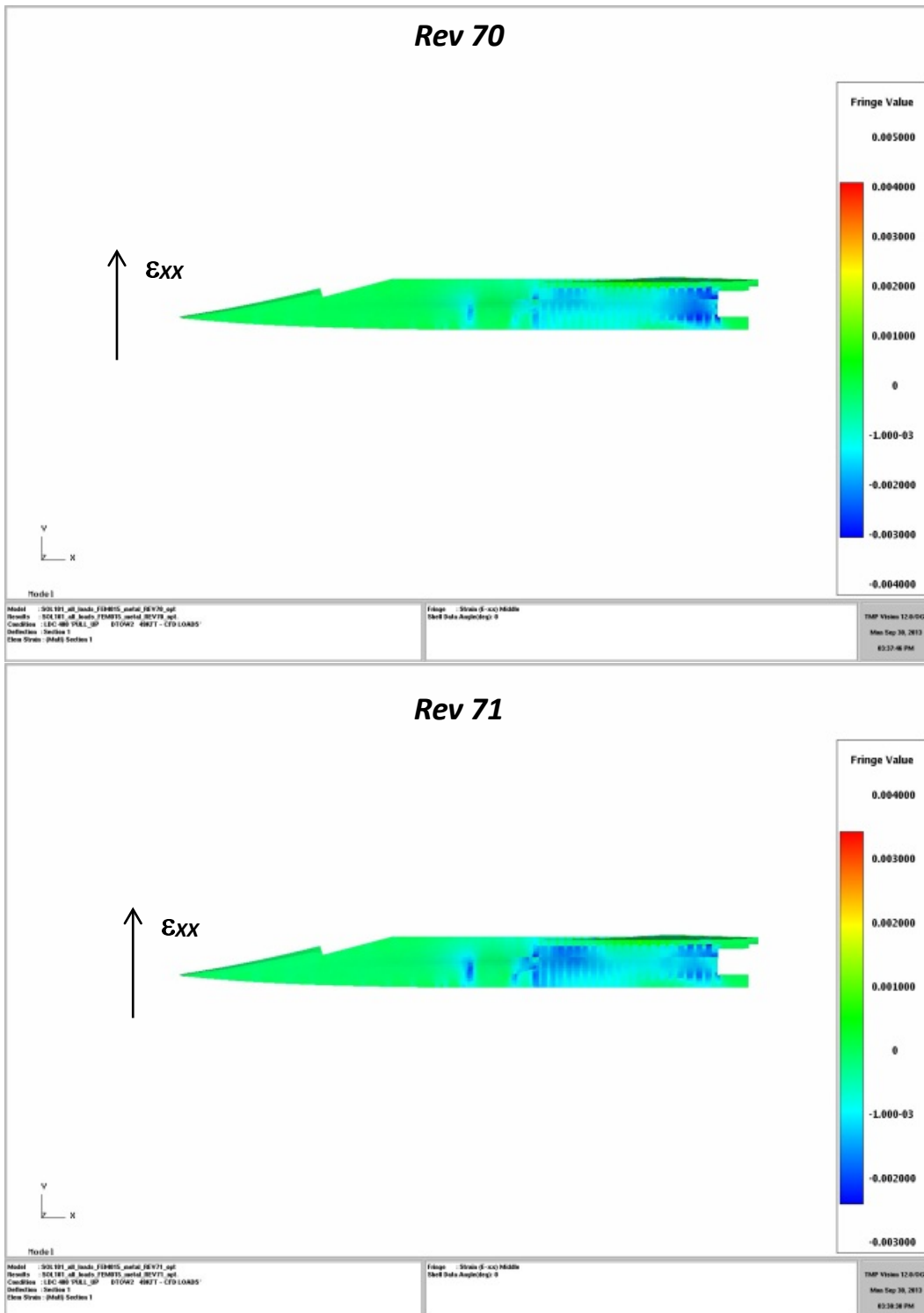


Figure 169.—Strain XX Load Case LC400—Upper Inner Wing Skin

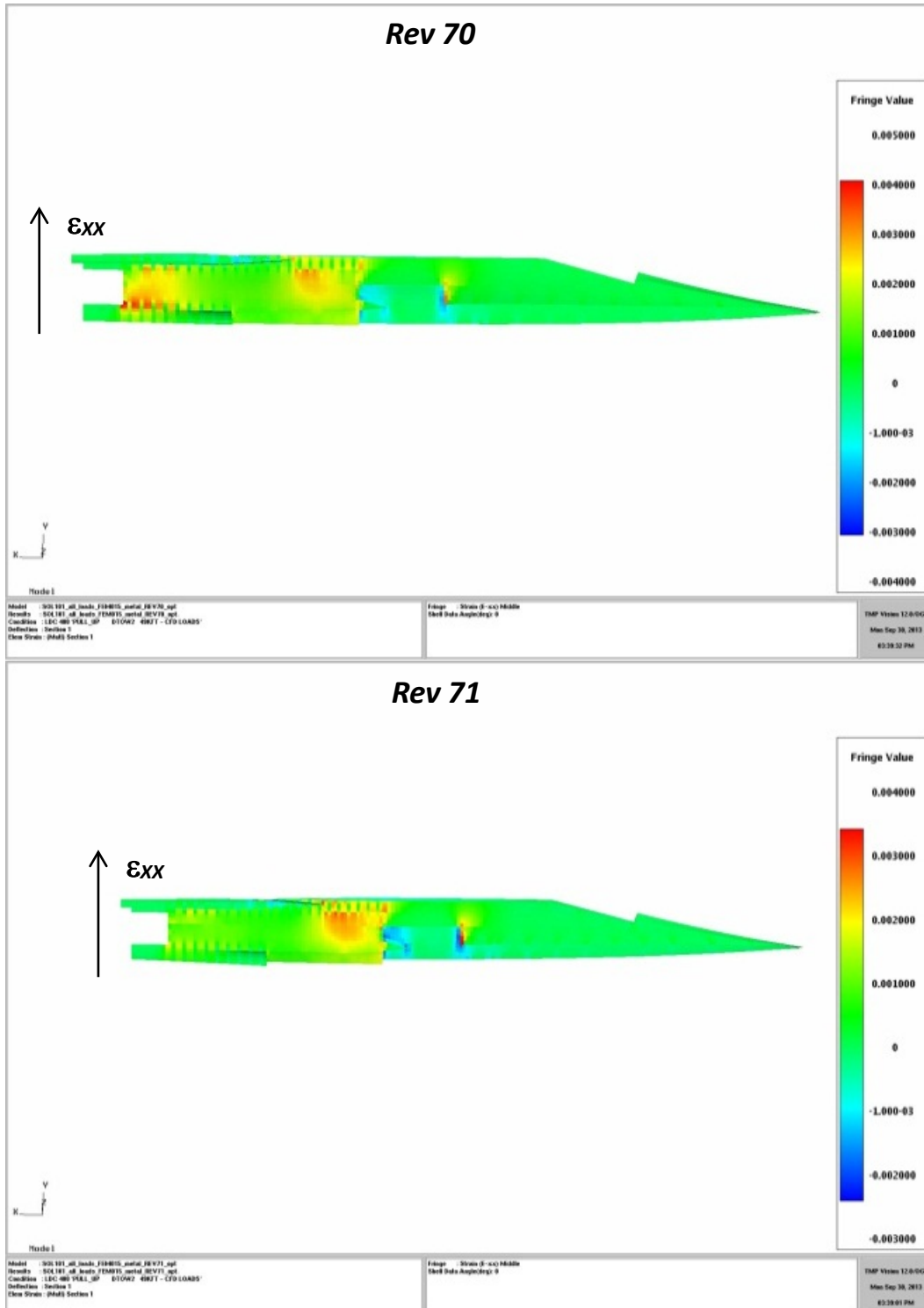


Figure 170.—Strain XX Load Case LC400—Lower Inner Wing Skin

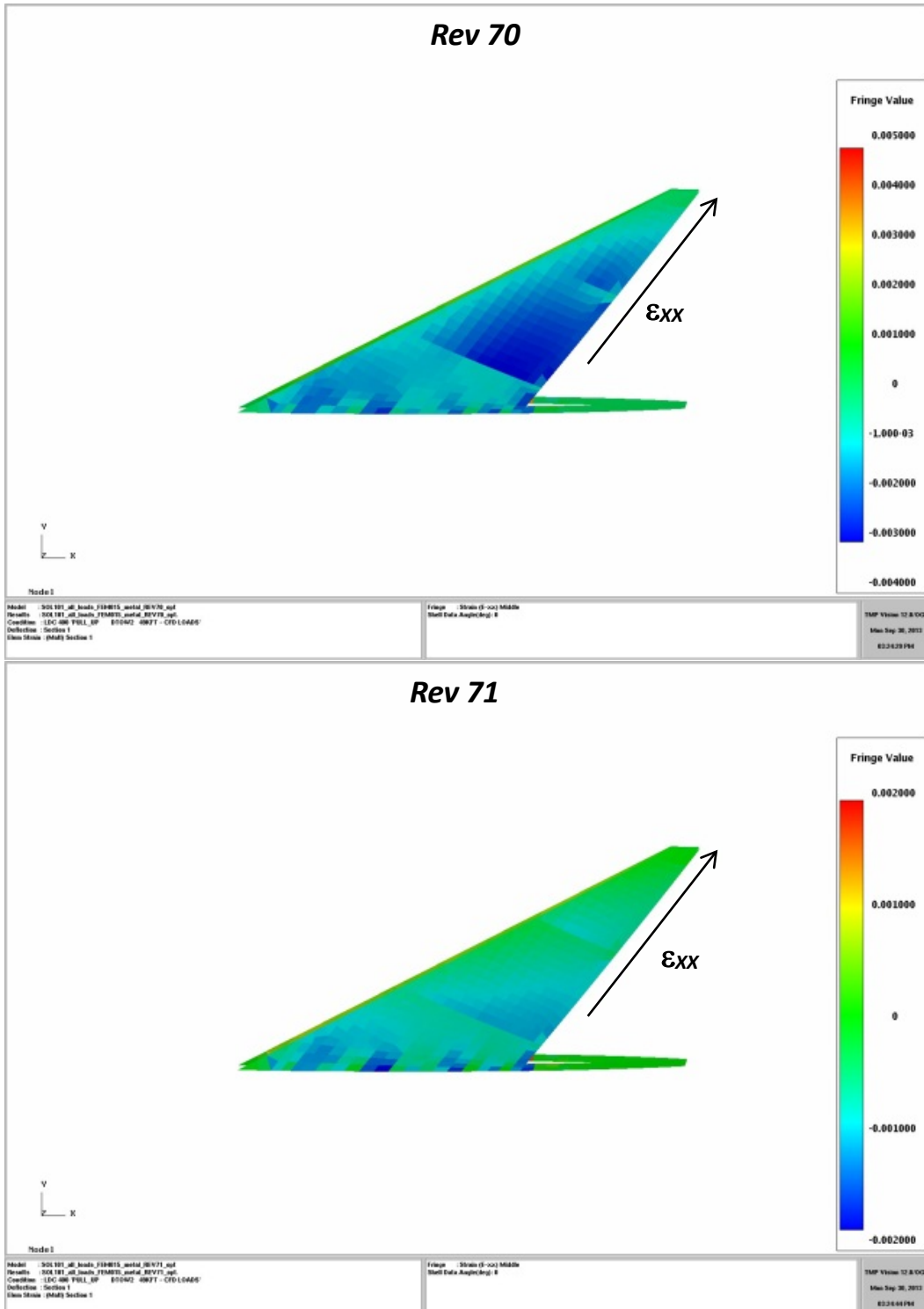


Figure 171.—Strain XX Load Case LC400—Upper Tail Skin

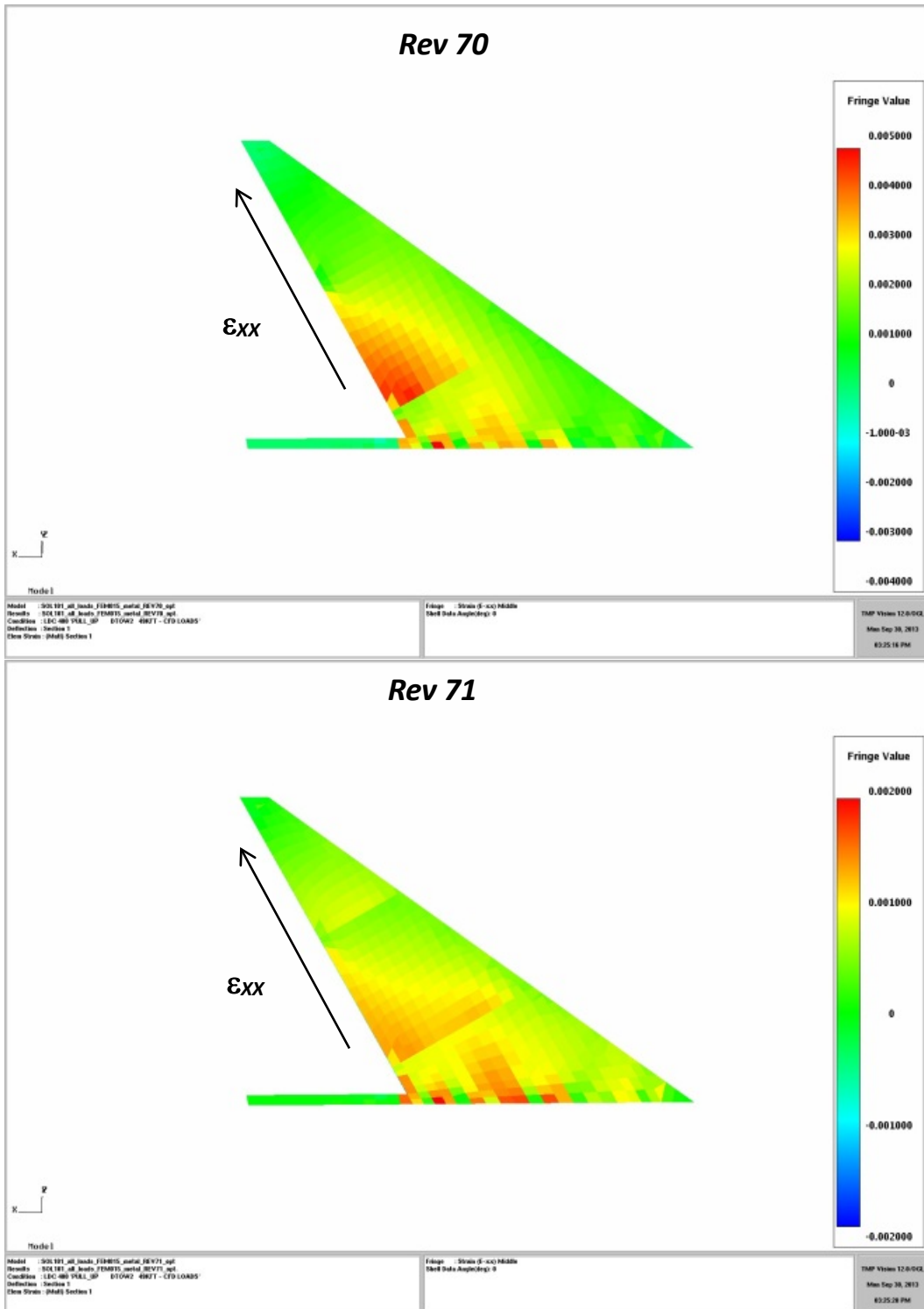


Figure 172.—Strain XX Load Case LC400—Lower Tail Skin

3.5.6.2 Stress Plots

Figure 173 to Figure 176, the maximum von Mises stress plots, focus on the metallic elements of the vertical tail and outboard engine mounting locations on the lower inner wing. The tail loads and engine nacelle loads must pass through these structures and they are the critical responses for load case 400. A

single plot of von Mises stress near the main landing gear attachment area on the lower inner wing is also shown. The plots shown, like the strain plots, are also under ultimate load (includes 1.5 safety factor).

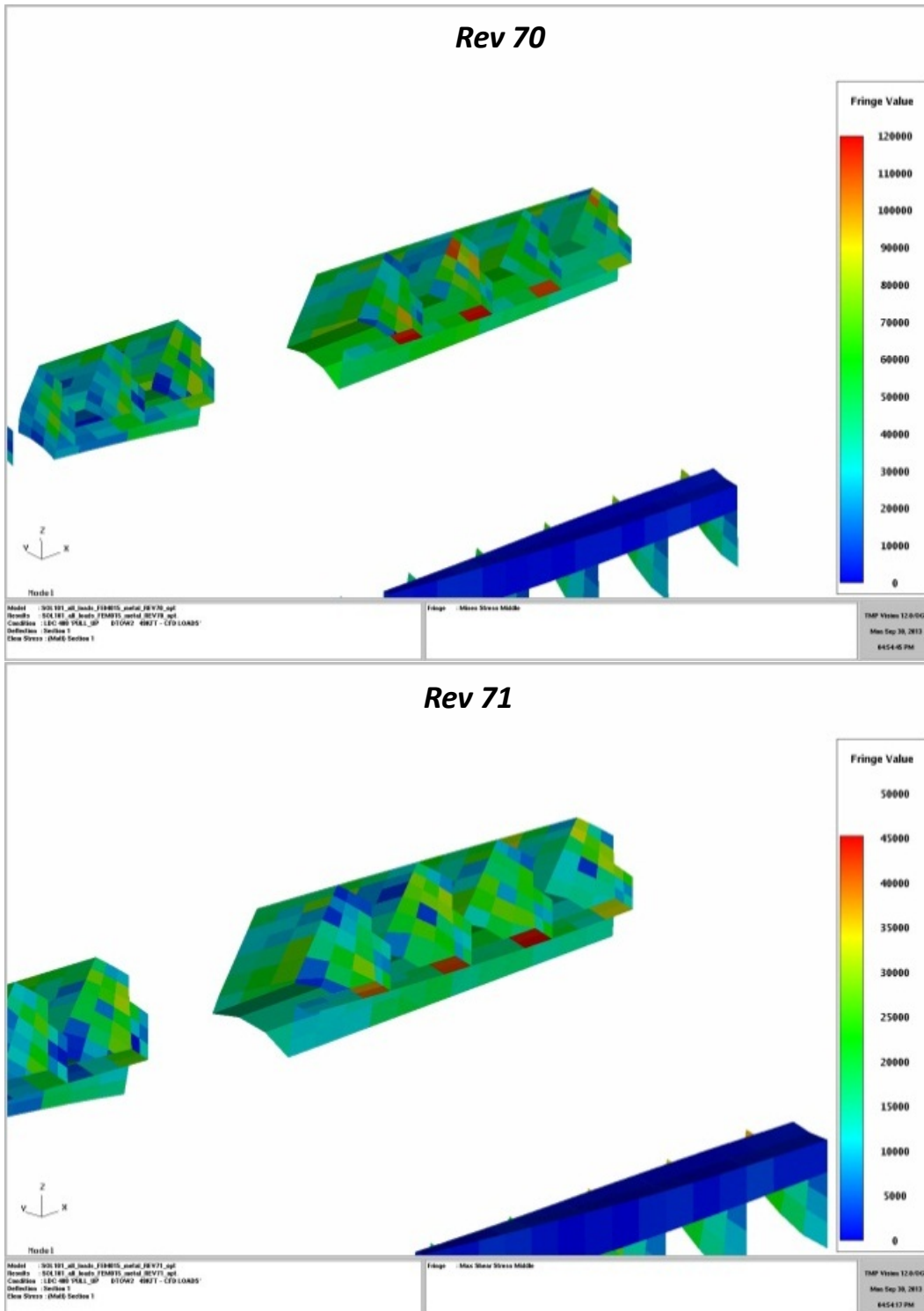


Figure 173.—Von Mises Stress—Load Case LC400—Lower Inner Wing

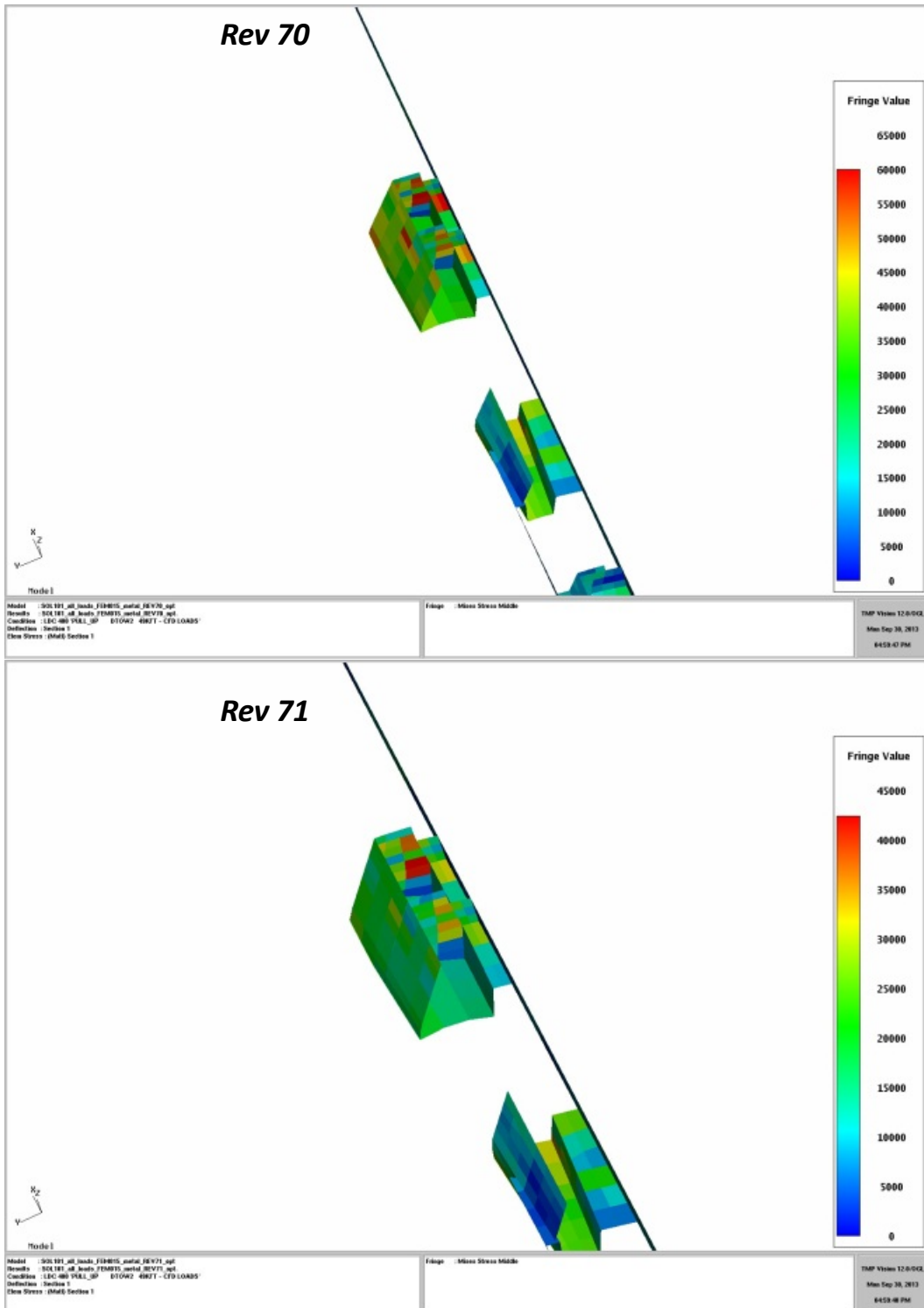


Figure 174.—Von Mises Stress—Load Case LC400—Lower Inner Wing

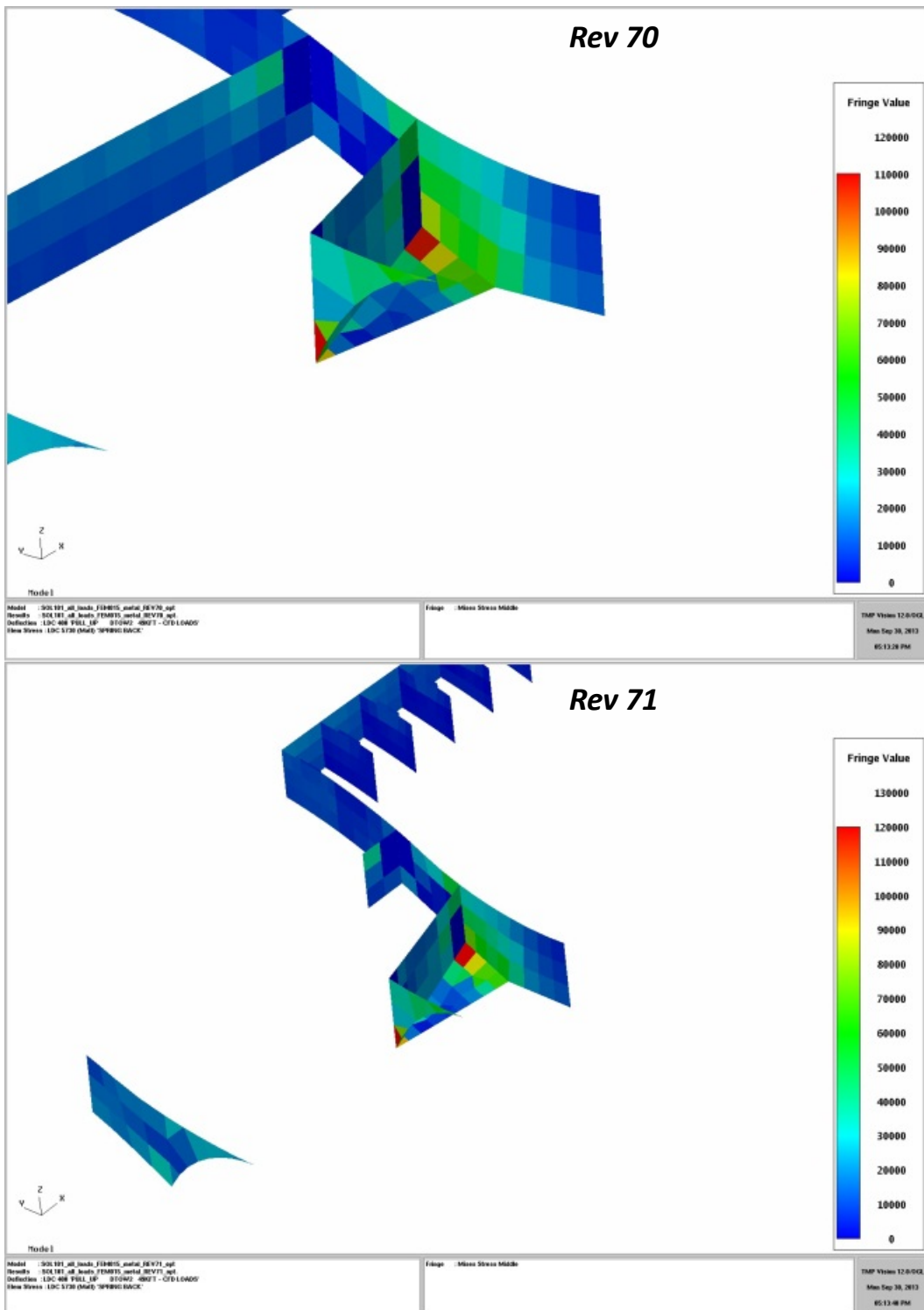


Figure 175.—Von Mises Stress—Load Case LC5730—Lower Inner Wing (Landing Gear Attachment Area)

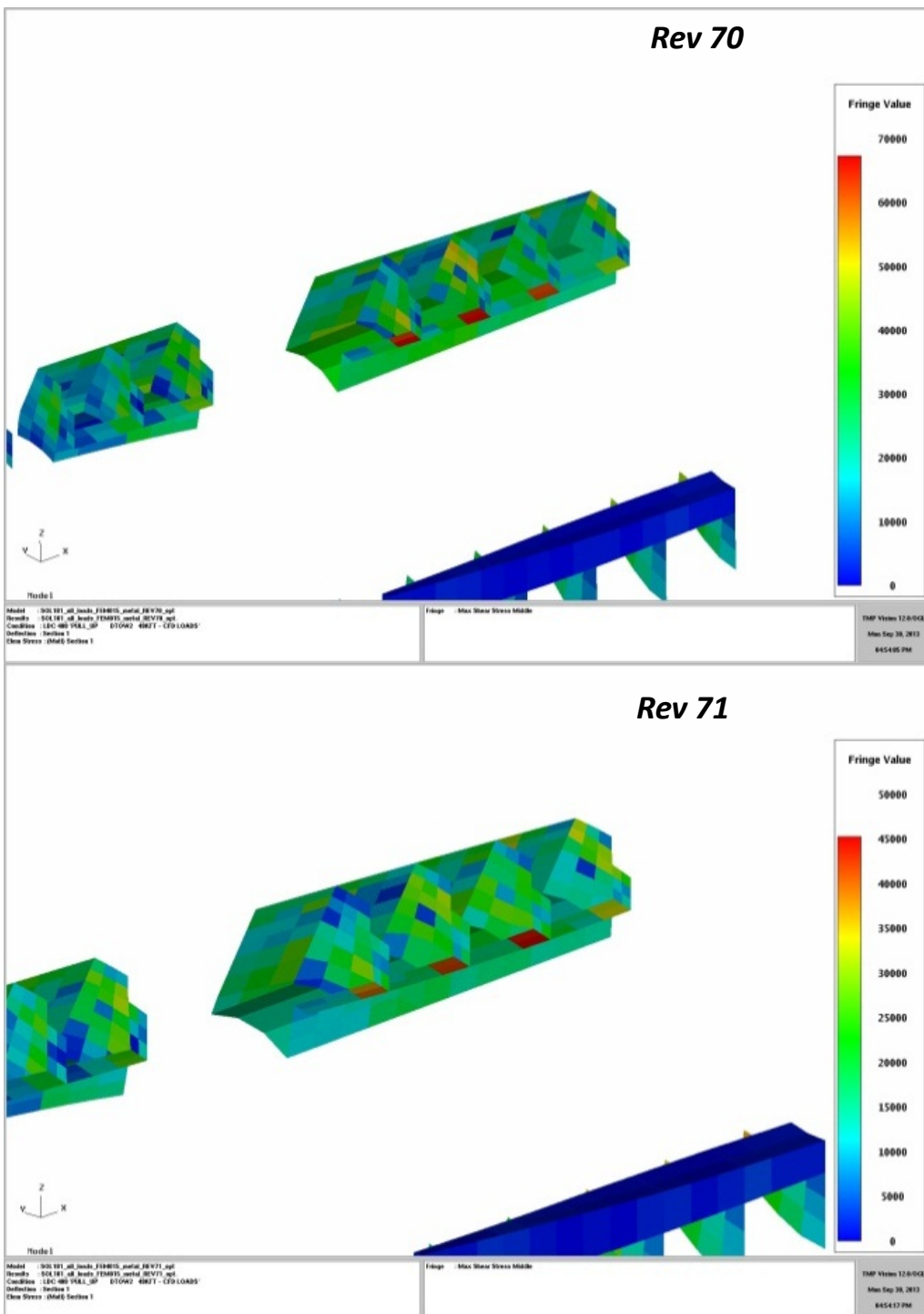


Figure 176.—Max Shear Stress—Load Case LC400—Lower Inner Wing Skin

3.5.6.3 Deflection Plots

The deflection plots (Figure 177 to Figure 179) clearly show the effect of the tail tip deflection constraint on the optimized vehicle. Figure 177 compares the displacement of REV70 and REV71 FEMs under load case 400 and shows that the REV71 FEM meets the tail displacement constraint of 37.5 in. under ultimate load (25 in. under limit).

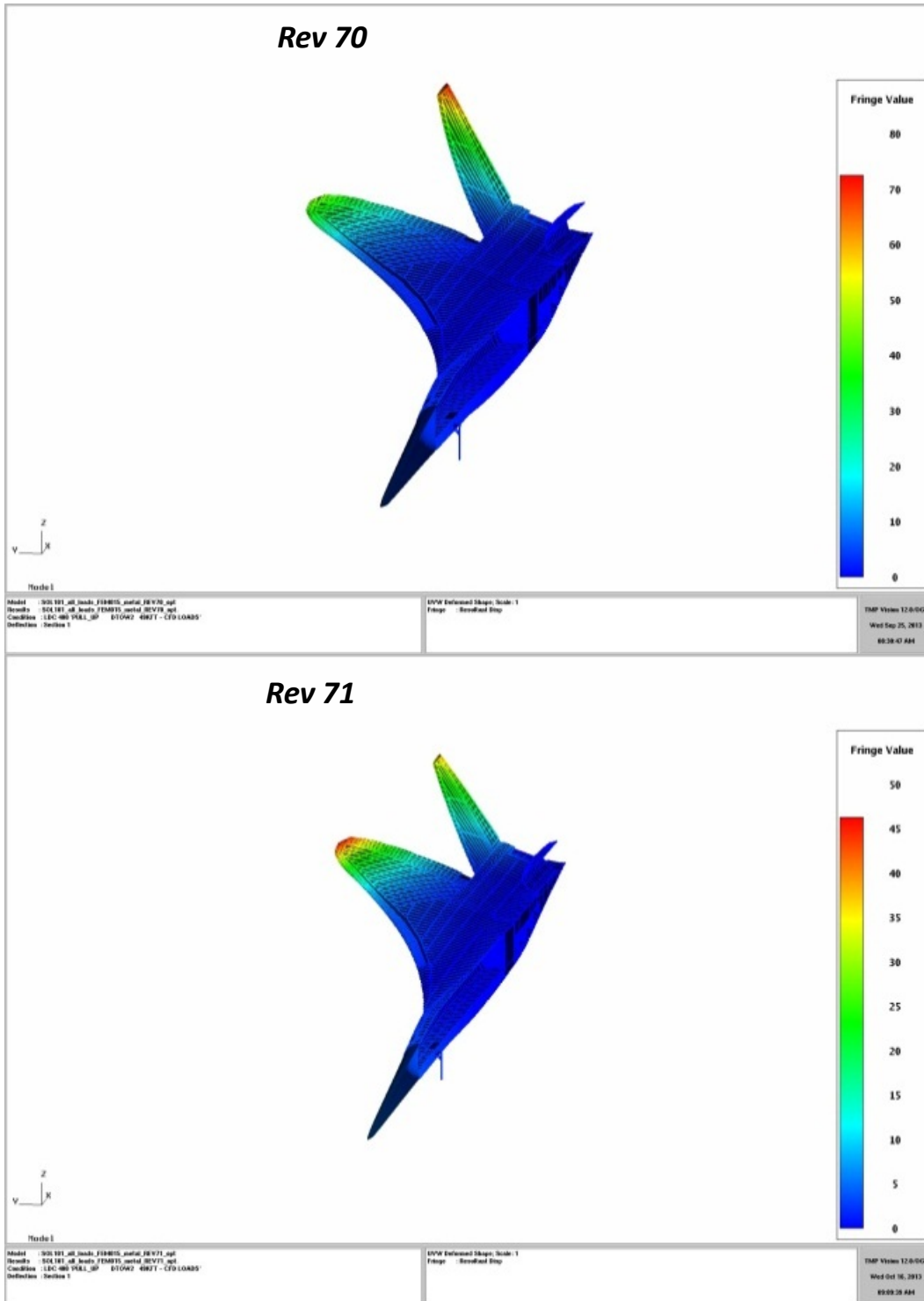


Figure 177.—Deflection LC400

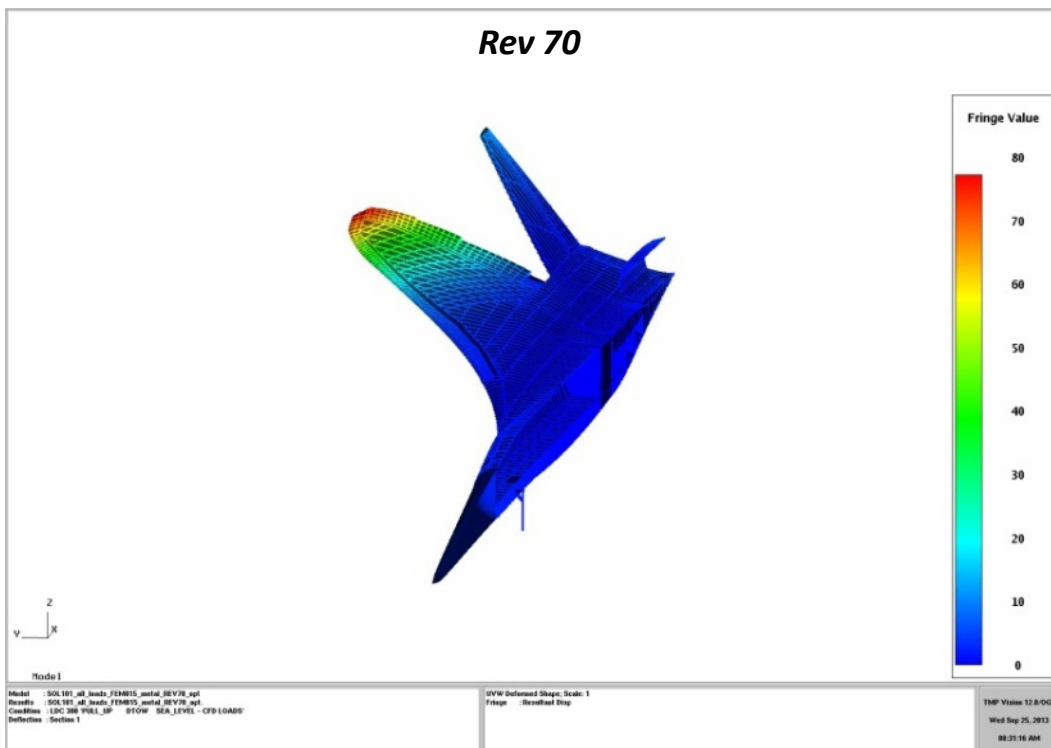


Figure 178.—Deflection LC300

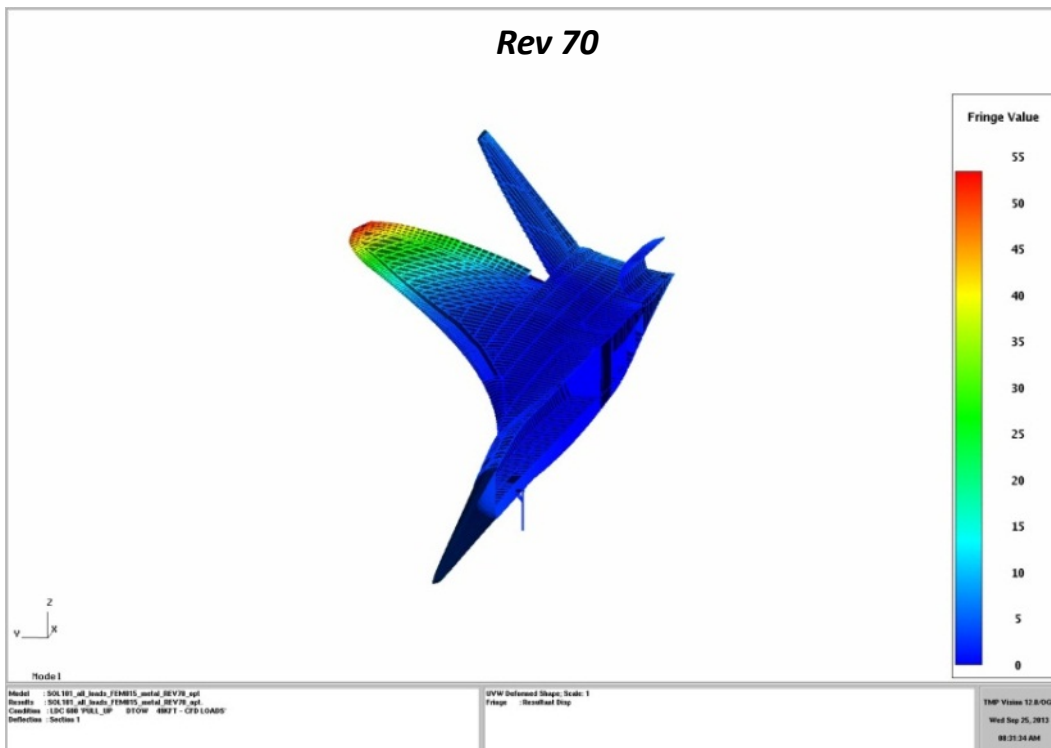


Figure 179.—Deflection LC600

3.5.7 Mode Shapes and Frequencies (With Focus on Final Design)

A modal solution was performed on both the Rev70 and Rev71 FEMs. The results of these analyses are presented in Table 25. The rigid body frequencies and mode shapes are characteristic of a free-free symmetric model that has symmetry boundary conditions enforced at the vehicle centerline.

The larger differences noted in modes 6, 7, 13, 16, and 20 are due to the effects of the engine nacelle suspension system coupling differently with different structural vehicle modes. The structural modes are directly affected by the gage optimization performed on each model. However, the suspension modes are relatively unaffected. Therefore, the engine inertia will couple or uncouple from adjacent structural modes as in an auxiliary mass system. Modes 12 to 17 show varying amounts of this behavior and involve much of the aft structure. Selected mode shapes are presented in Figure 180 to Figure 183 with a brief description of each.

TABLE 25.—N+2 VEHICLE MODAL FREQUENCIES FOR REV 70 AND 71

Mode no.	Rev 70, Frequency (Hz)	Rev 71, Frequency (Hz)	Diff. 70->71
1	0.00	0.00	0.0%
2	0.00	0.00	0.0%
3	0.00	0.00	0.0%
4	2.15	2.23	3.7%
5	2.42	2.44	1.0%
6	2.93	3.38	15.2%
7	3.50	3.67	4.8%
8	4.37	4.41	1.1%
9	5.33	5.60	5.0%
10	5.92	5.94	0.3%
11	7.07	7.34	3.8%
12	7.96	8.07	1.3%
13	8.24	9.36	13.5%
14	9.69	10.03	3.5%
15	10.54	10.85	2.9%
16	10.93	11.88	8.7%
17	12.26	12.28	0.1%
18	12.89	13.23	2.7%
19	13.66	14.14	3.5%
20	14.19	15.72	10.8%
21	15.34	16.04	4.6%

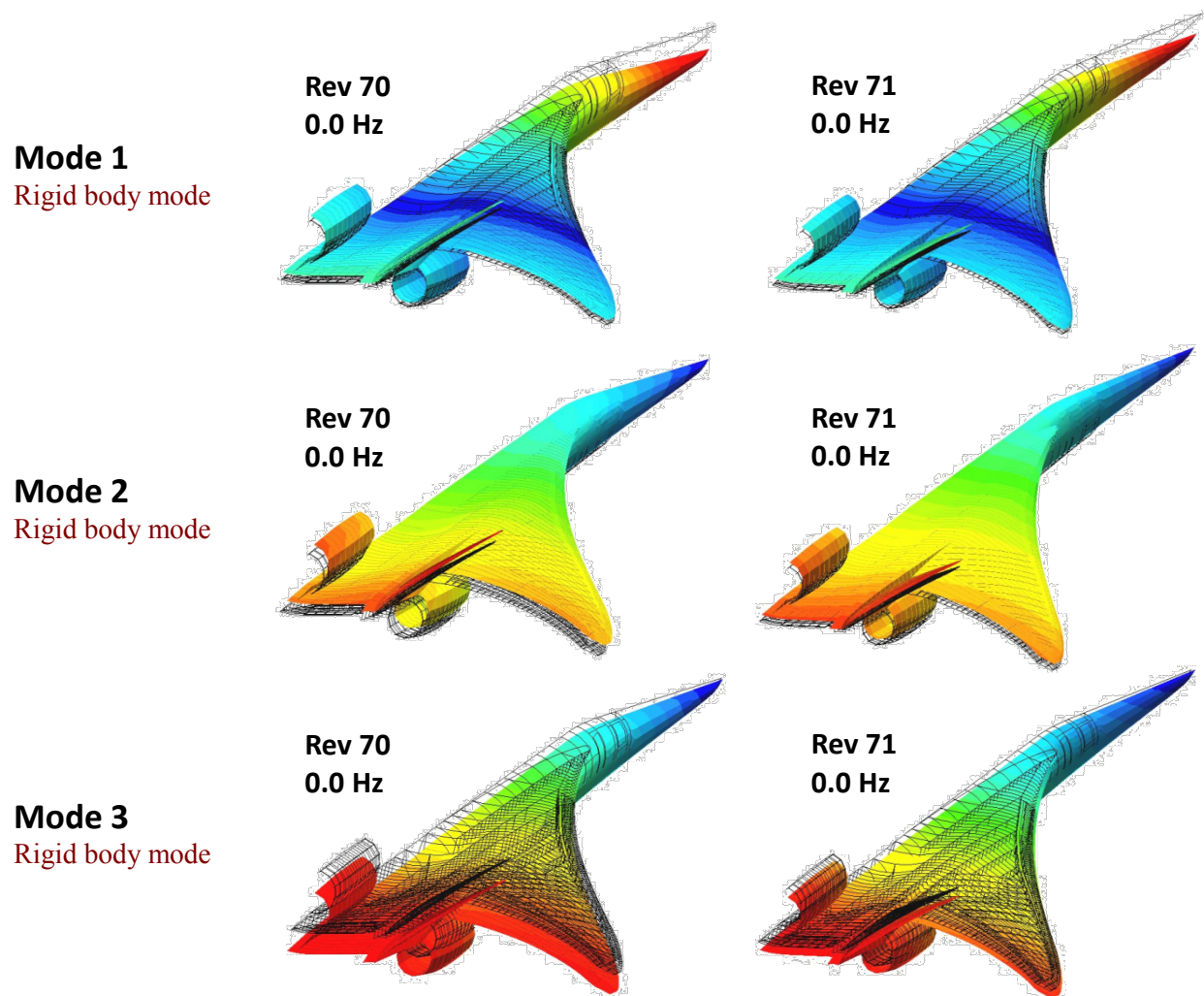


Figure 180.—N+2 Rigid Body Mode Shapes 1 to 3 for Rev 70 and 71

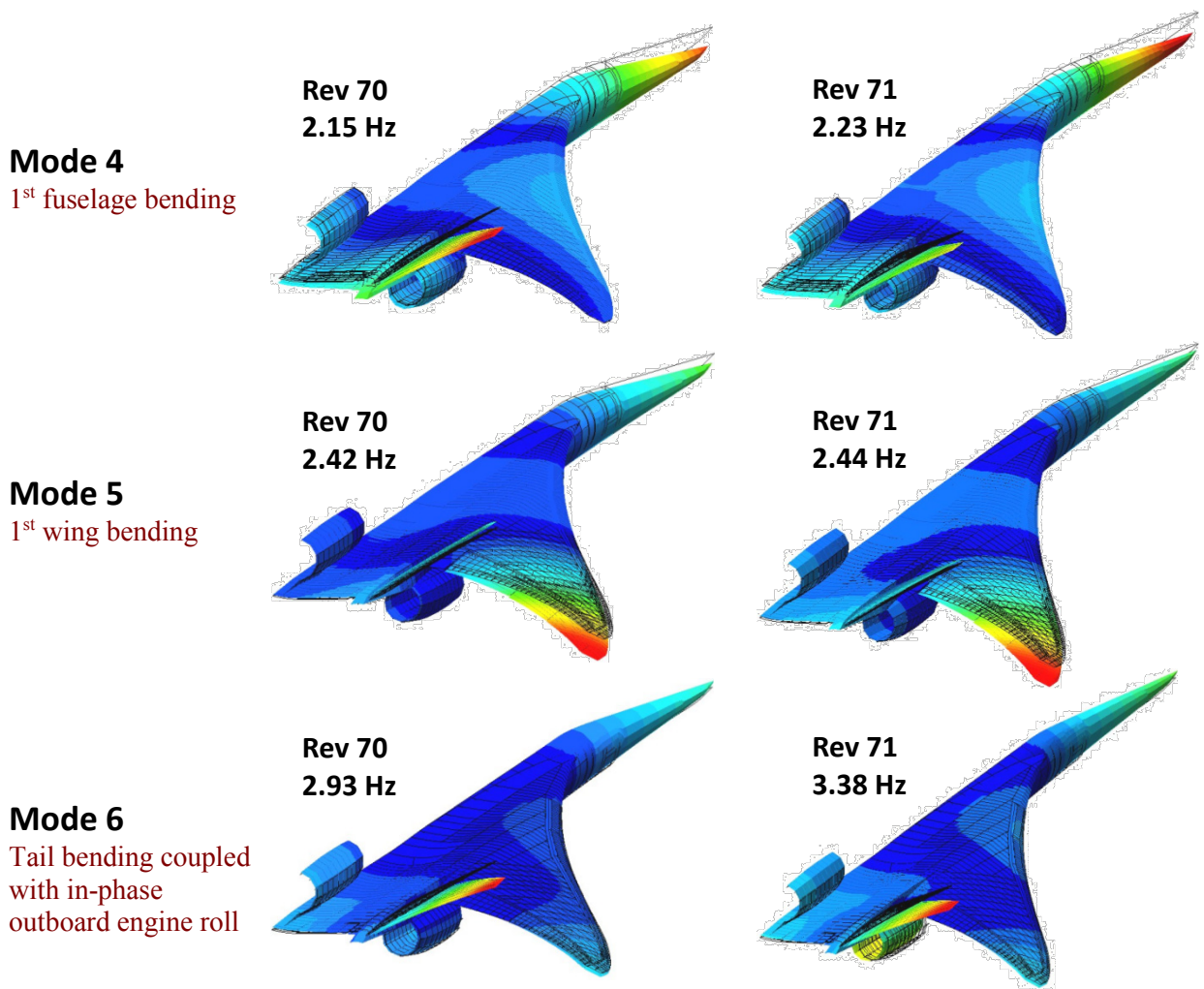
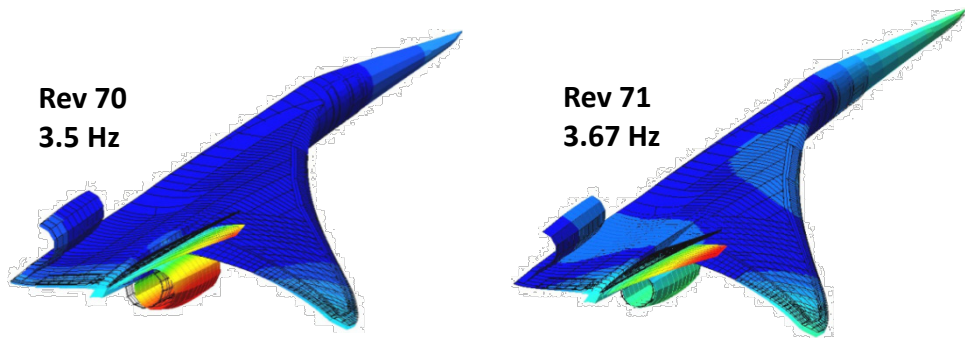
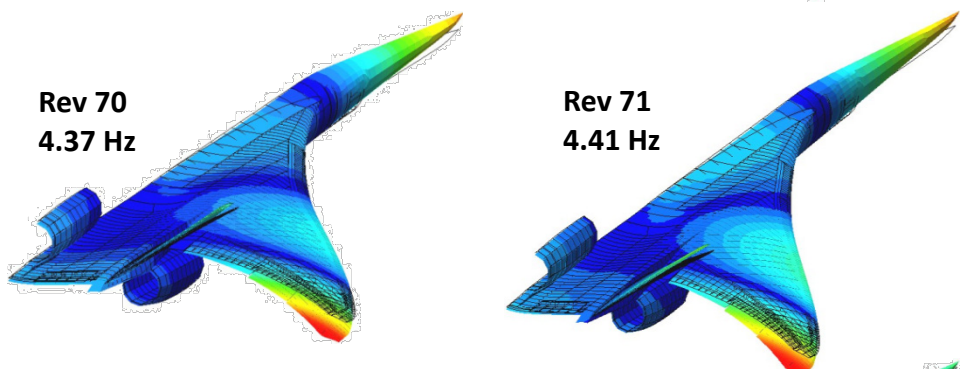


Figure 181.—N+2 Rigid Body Mode Shapes 4 to 6 for Rev 70 and 71

Mode 7
Tail bending coupled
with out-of-phase
outboard engine roll



Mode 8
2nd fuselage and 2nd
wing bending



Mode 9
Aft deck bending
coupled with tail
bending and weak
wing torsion

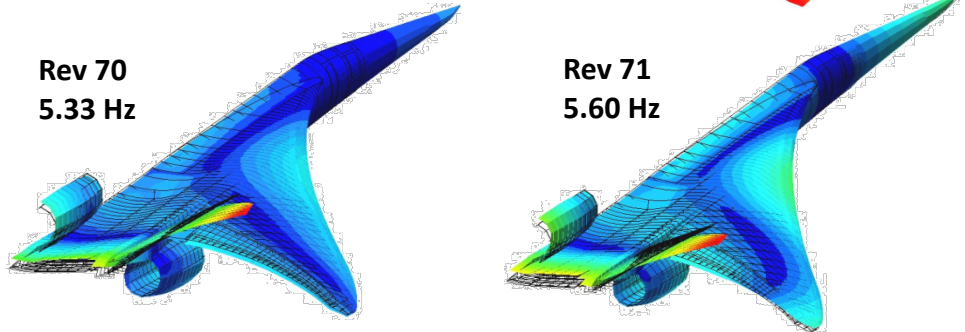


Figure 182.—N+2 Rigid Body Mode Shapes 7 to 9 for Rev 70 and 71

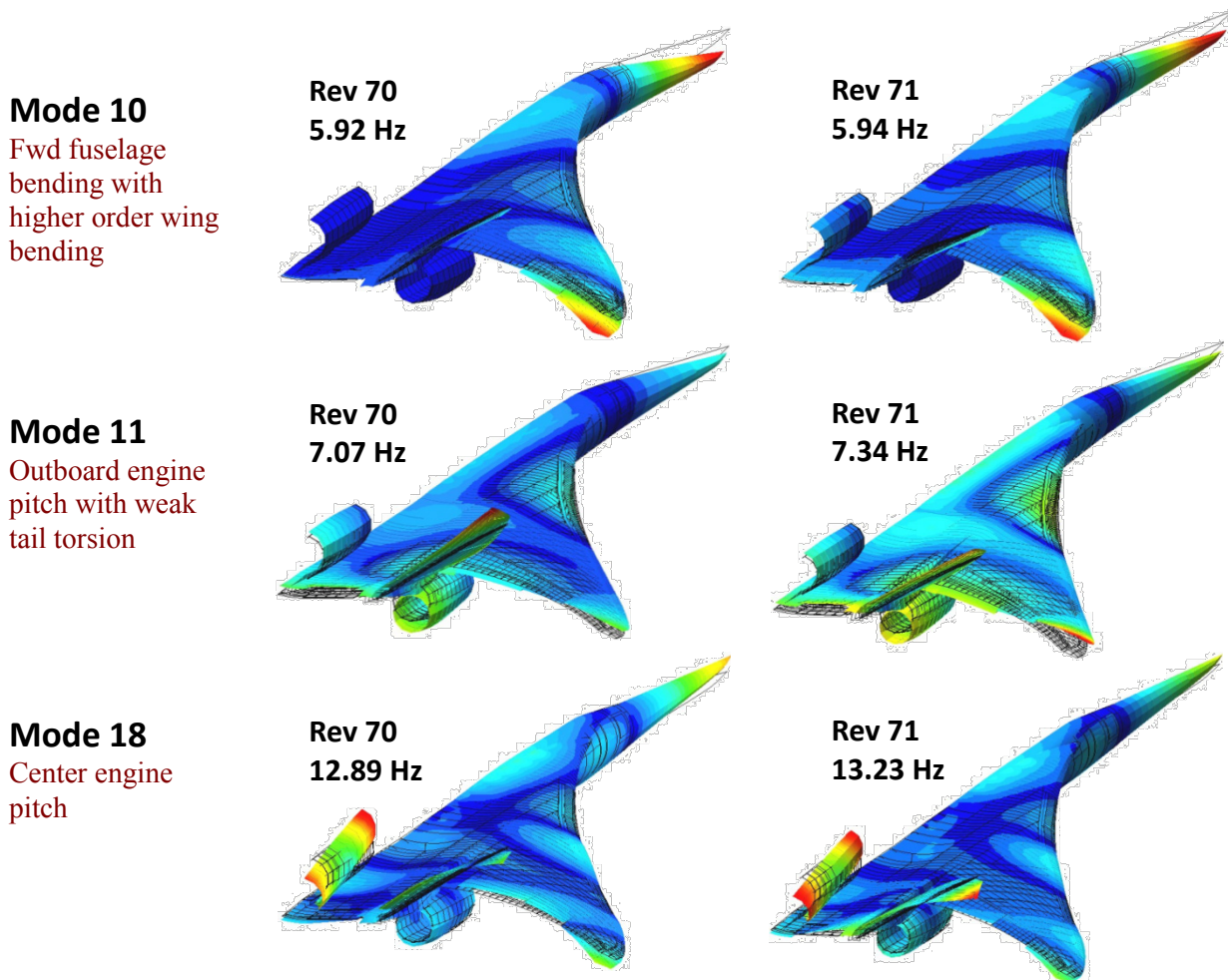


Figure 183.—N+2 Rigid Body Mode Shapes 10, 11, and 18 for Rev 70 and 71

3.6 Aeroelastic Analysis

Open-loop flutter analysis was performed on the final structural designs, FEM017-REV70 (sized without the constraint on tail displacement) and FEM017-REV71 (sized with the constraint on tail displacement). We utilized MSC.NASTRAN SOL145 for our flutter solutions which use the doublet lattice method for subsonic Mach numbers and ZONA51 for supersonic Mach numbers. The same linear aerodynamic model and spline model that was used for loads calculations in Section 3.3 was also used for flutter analysis.

3.6.1 Aeroelastic Model

Section 3.3 discusses the check on the quality of the spline models that provided transfer of forces and displacement between the linear aerodynamic model and the FEM. We also conducted a modal convergence study, plotting the critical flutter dynamic pressure as a function of the number of structural modes retained for the analysis. This trade is shown in Figure 184, where we looked at 22, 27, and 32 retained modes, including 3 rigid body modes for symmetric boundary conditions. Based on this study, we retained 27 modes for subsequent flutter analyses balancing accuracy of the flutter solutions with efficiency of the runs, since we had plans to run many trades.

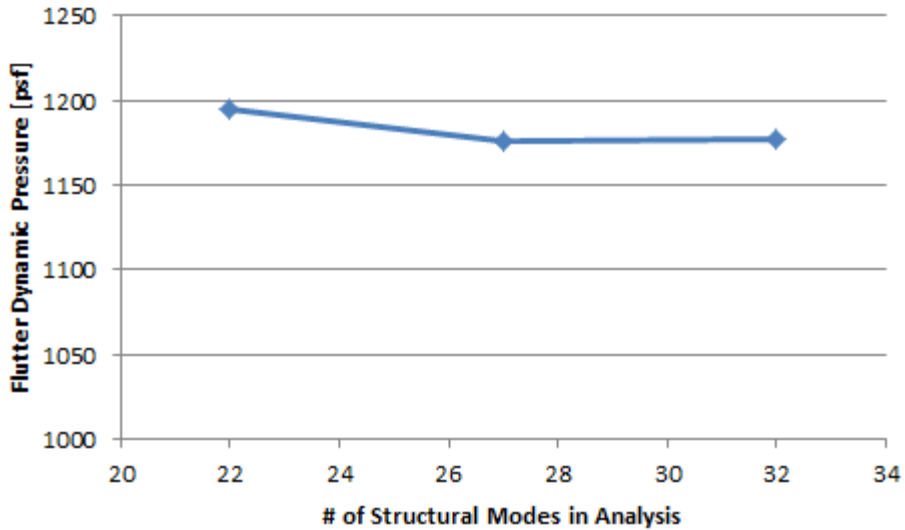


Figure 184.—Modal Convergence Study (Mach 0.9, Symmetric Boundary Conditions, DTOW)

TABLE 26.—COMPARISON OF NASTRAN AND FAMAS

Flutter Crossing	FAMAS Flutter Speed (KEAS)	FAMAS Flutter Dynamic Pressure (psf)	NASTRAN Flutter Dynamic Pressure (psf)	Percent Difference (FAMAS/NASTRAN)
1	562	1070	1071	-0.1%
2	704	1679	1653	1.6%
3	916	2842	2875	-1.1%

3.6.2 Comparison of MSC.NASTRAN With FAMAS Results

While we utilized MSC.NASTRAN for our flutter surveys, we also ran a flutter solution using our in-house PK flutter solver, FAMAS, as a check against the NASTRAN results (Table 26). FAMAS utilized the aerodynamic influence coefficient (AIC) matrices from NASTRAN as well as the structural mode shapes and frequencies, but the matched point PK aeroelastic root solver was performed by FAMAS. Figure 185 shows the damping versus dynamic pressure from NASTRAN, while Figure 186 shows damping versus KEAS from FAMAS. Not including the mildly unstable rigid body root, which is attributed to the vehicle being statically unstable, predicted by NASTRAN, both methods agree on the speed of 3 flutter crossings when converted to dynamic pressure. The comparison presented is for Mach 0.95, symmetric boundary conditions at DTOW. The analysis was done on an earlier all-composite FEM, hence the difference in the flutter dynamic pressure from subsequent, more recent, flutter analyses presented in the next section.

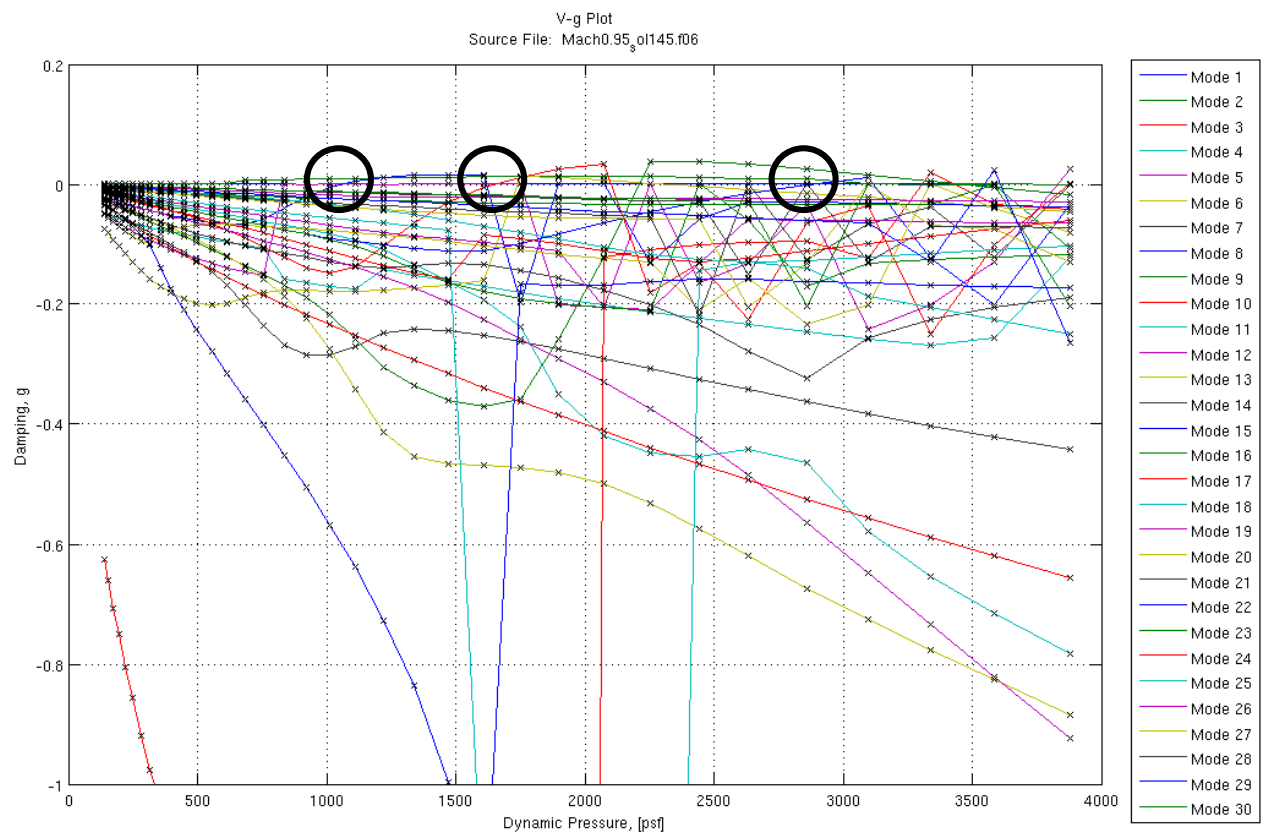


Figure 185.—Damping Versus Dynamic Pressure from NASTRAN

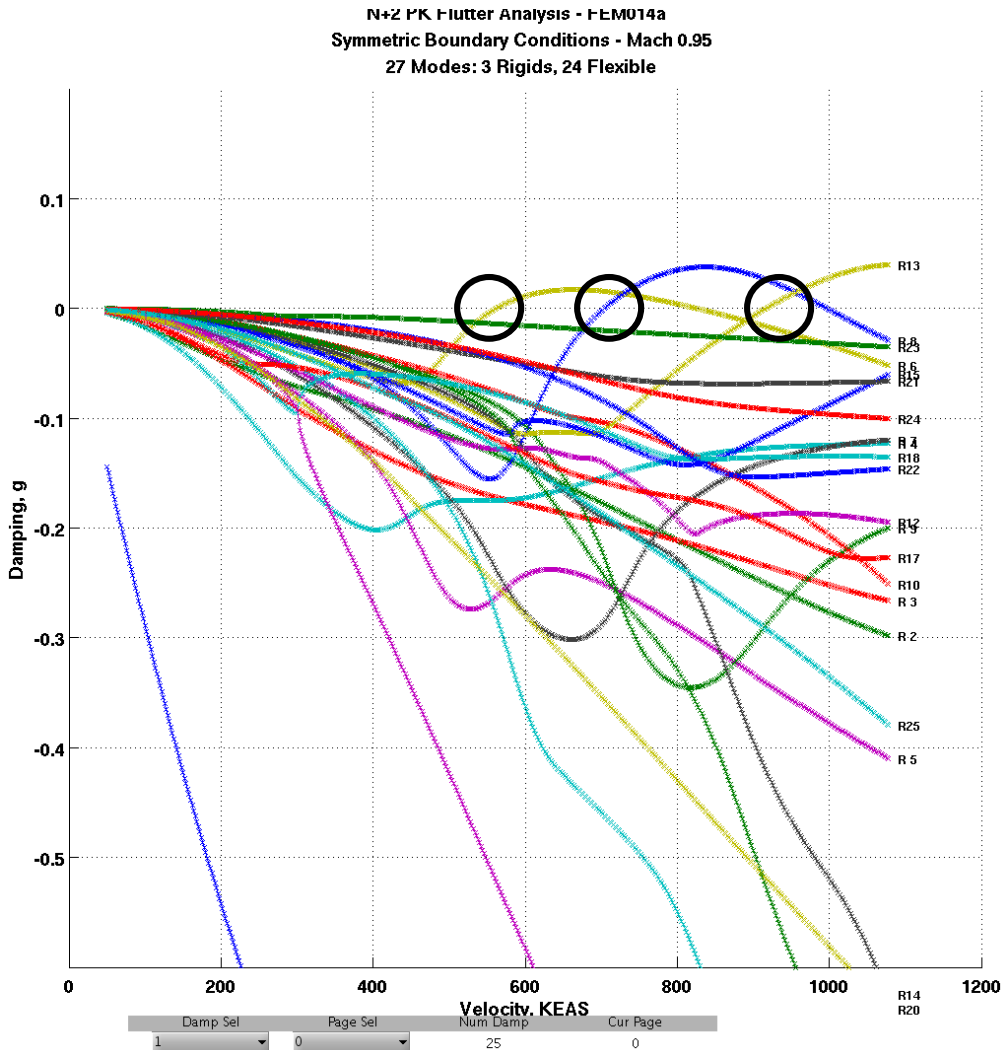


Figure 186.—Damping Versus Velocity (KEAS) from FAMAS

3.6.3 Flutter Results

Flutter analysis was initially performed on the FEM017-REV71 structural design, the design that included a displacement constraint on horizontal tail deflection for LC 400. However, for both symmetric and antisymmetric boundary conditions and for 3 gross weights: DTOW, DTOW2 and ZFW, there were no unstable flutter roots below 1600 psf and in most cases, especially for antisymmetric boundary conditions, there were none below 3500 psf (minimum required flutter dynamic pressure is roughly 900 psf for most Mach numbers). This stood in stark contrast to previous flutter analyses that we had performed on the all-composite FEM, where we saw critical flutter dynamic pressures around 1000 psf. As a result we speculated that inclusion of the displacement constraint considerably stiffened the tail and aft deck thereby increasing the flutter speed dramatically which was characterized largely by tail and aft deck bending. Consequently, we also ran flutter surveys on the FEM017-REV70 design which did not include the tail displacement constraints, and the results of these surveys are presented below, since the flutter speeds were much lower and closer to the flutter boundary. Table 27 shows the FEM weight and CG locations of the gross weight configurations of FEM017-REV70 that were considered as part of the flutter surveys.

Figure 187 shows the minimum flutter dynamic pressure as a function of Mach number and vehicle gross weight for symmetric boundary conditions. In addition, the minimum required flutter dynamic

pressure (including the 15 percent margin on flutter speed) is represented by the solid red line. Flutter dynamic pressure below this line would indicate that the vehicle flutter requirement is not met, and so, based on this linear flutter analysis, we conclude that flutter speed is not critical. The dashed lines indicate that a flutter root was not found within the dynamic pressure range of the analysis (up to about roughly 4000 psf). However, in this transonic region, a more appropriate nonlinear transonic flutter solver is needed. For the DTOW and DTOW2 flutter solutions, the flutter modes in the 3000 to 4000 psf range have a flutter frequency of about 10 to 12 Hz. The flutter modes that go unstable at lower dynamic pressure near 1500 to 2000 psf have flutter frequencies of about 5 to 6 Hz. The flutter frequency for the ZFW cases ranges from 6 to 7 Hz.

Figure 188 shows the minimum flutter dynamic pressure as a function of Mach number and vehicle gross weight for antisymmetric boundary conditions. In general, the flutter speeds are higher than in the symmetric cases, though further investigation is needed with a suitable transonic aerodynamic theory. This is particularly evident when looking at the frequency and damping versus dynamic pressure at Mach 0.95 and 1.1, as shown in Figure 189 and Figure 190. At Mach 0.95, there are several zero frequency roots that go unstable, where one as shown in Figure 189, looks like a divergence mode consist of lateral nose bending. However, it is somewhat questionable how realistic this mode is for a semi-span model and at Mach 0.95 with linear aerodynamic theory. The aeroelastic roots at Mach 1.1 are very sporadic with many unstable roots at low dynamic pressures, indicating that the results may be spurious. Both of these plots emphasize the need that future studies should look at flutter in the transonic regime with an appropriate transonic code.

TABLE 27.—FEM WEIGHTS AND CG LOCATIONS FOR FLUTTER ANALYSIS (FEM017-REV70)

Configuration	Semi-span FEM Weight (lb)	X-CG (in.)
DTOW	166,366	2021.8
DTOW2-AFT	150,605	2049.8
ZFW	78,804	1983.4

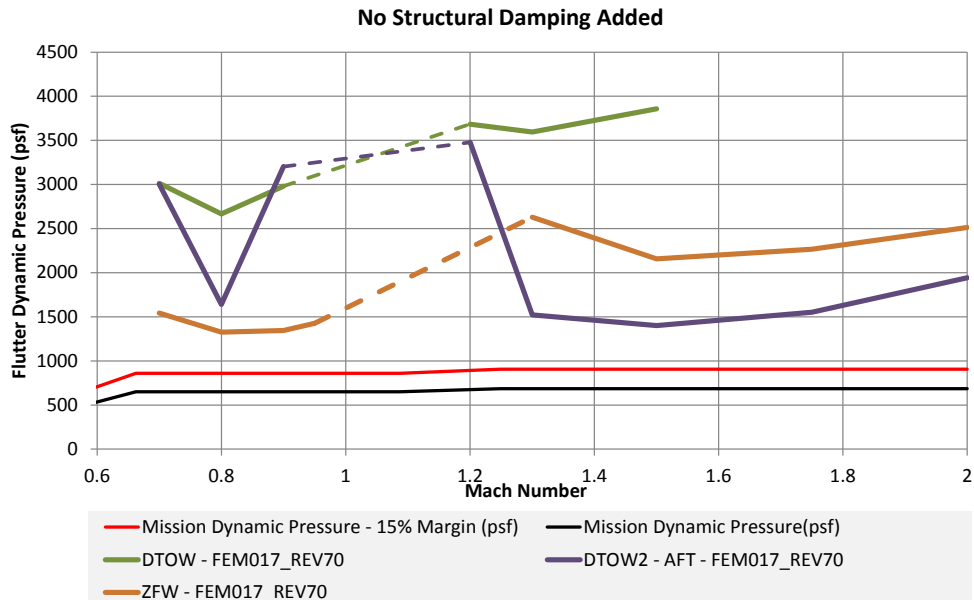


Figure 187.—FEM017-REV70 Flutter Boundary—Symmetric Boundary Conditions

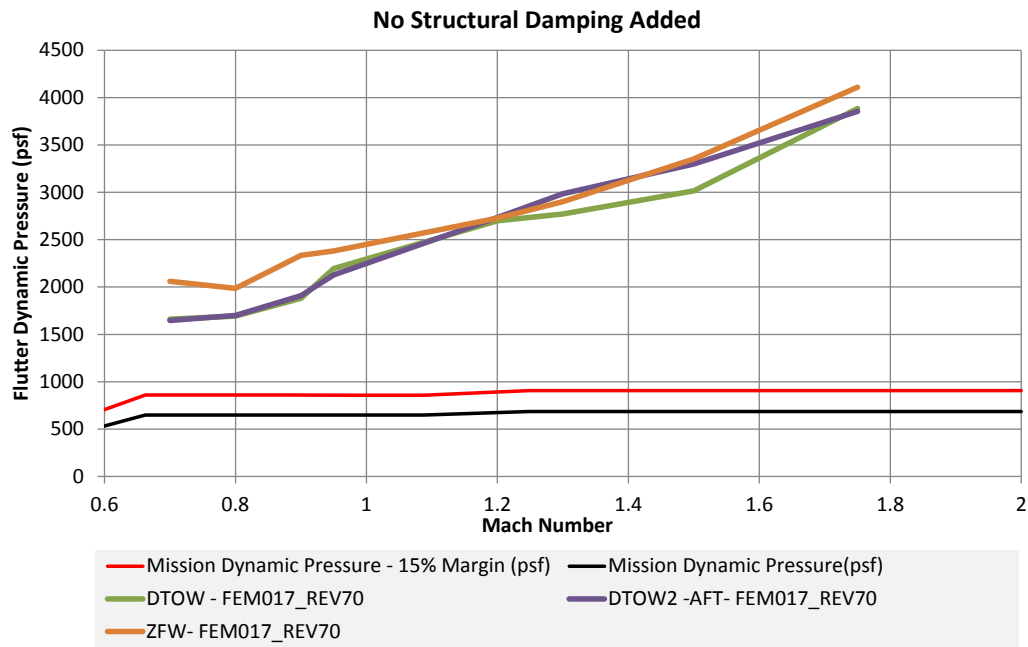


Figure 188.—FEM017-REV70 Flutter Boundary—Antisymmetric Boundary Conditions

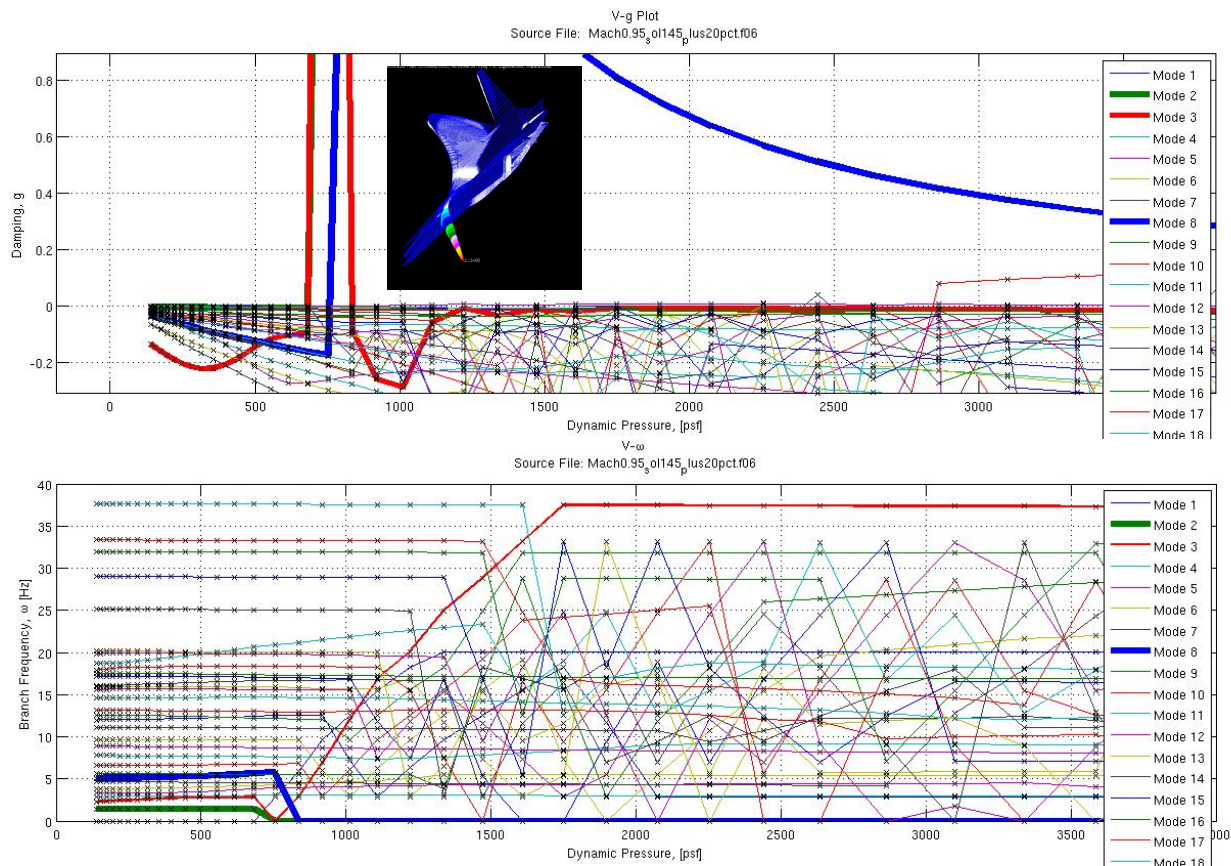


Figure 189.—Mach 0.95 Antisymmetric Boundary Conditions, Zero Fuel Weight

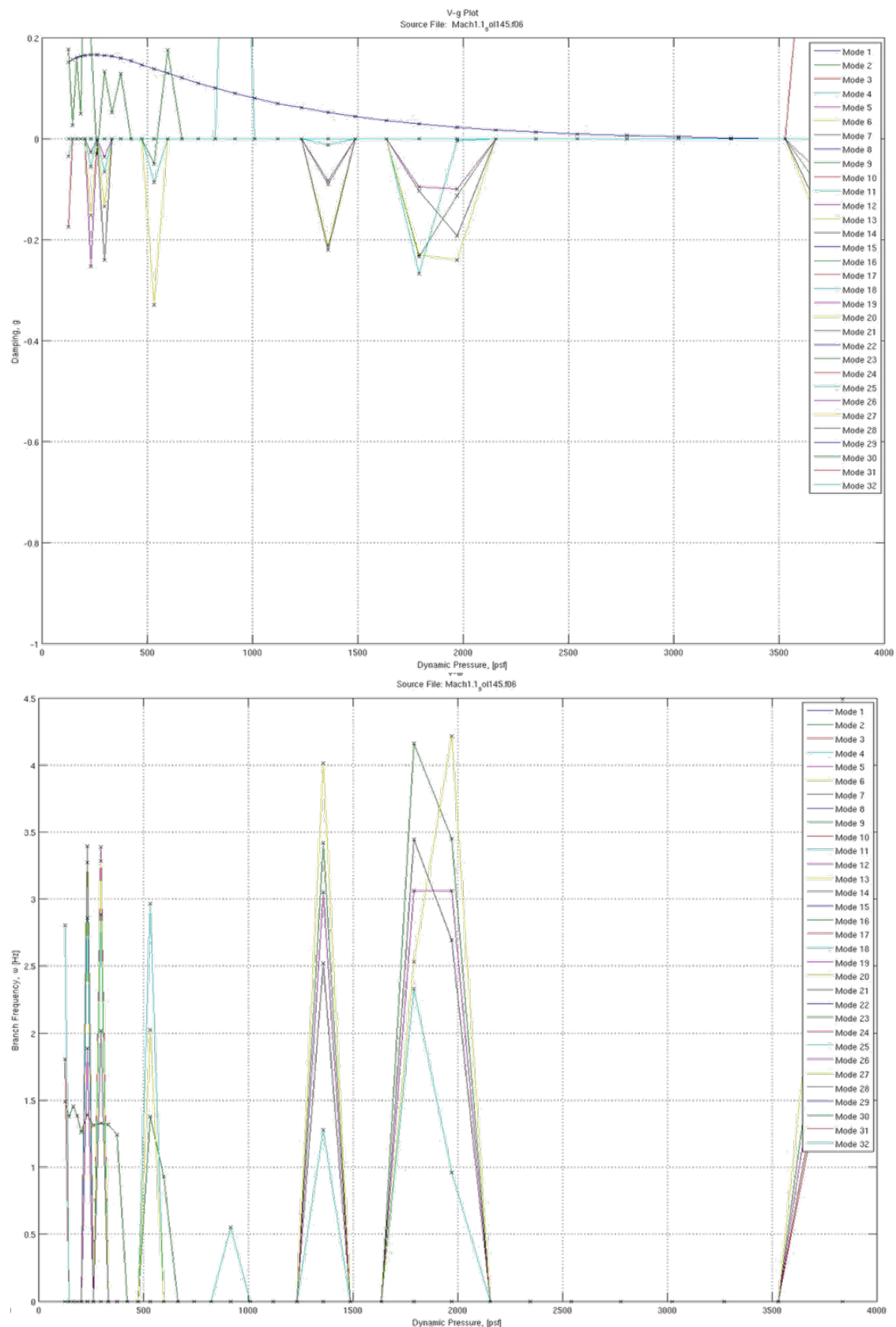


Figure 190.—Likely Spurious Results at Mach 1.1, Antisymmetric Boundary Conditions at DTOW

Since there is considerable uncertainty associated with the weight of the propulsion system and because the flutter mechanism involves aft-deck and tail bending near where the engines are mounted, we conducted a sensitivity study of flutter speed to increases in engine weight. We increased the engine weight from 20 percent of its baseline value to 40 percent above its baseline value, in an effort to bound the maximum amount of expected increase in engine weight.

Table 28 shows the weight per engine for each trade study. In addition, the engine moment of inertia was also increased in proportion to its weight by assuming a fixed radius of gyration for the baseline engine.

Figure 191 shows the flutter survey for symmetric boundary conditions for the 3 different engine weights. For the DTOW and DTOW2 gross weight conditions increasing the engine mass decreases the flutter dynamic pressure. For the ZFW condition increasing engine mass increases the flutter dynamic pressure, though the ZFW condition is not the critical weight for most Mach numbers. Table 29 summarizes the minimum flutter dynamic pressure for each of the engine weight studies. In general, a 40 percent increase in engine weight drops the critical flutter dynamic pressure by 12 percent, but still meeting the required flutter margin, though as mentioned earlier further analysis is needed with a transonic aeroelastic code.

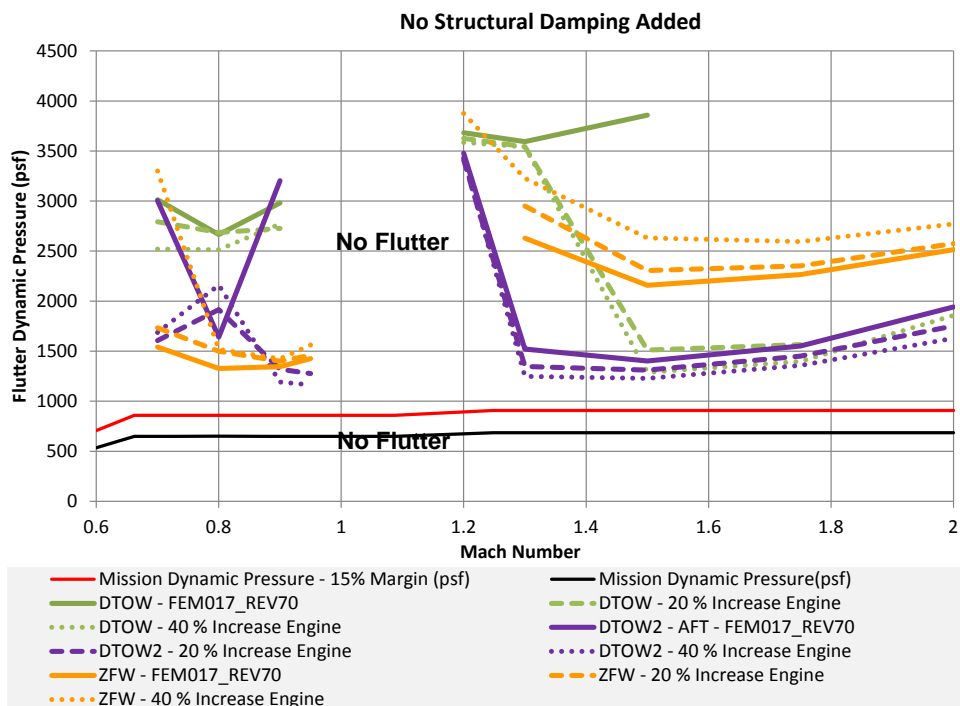


Figure 191.—N+2 Flutter Boundary Engine Mass Trade Study—Symmetric Boundary Conditions

TABLE 28.—ENGINE MASSES FOR TRADE STUDY

Percent Increase	Weight per Engine (lb)
0% (Baseline)	7,226
20%	8,671
40%	10,116

TABLE 29.—MINIMUM FLUTTER DYNAMIC PRESSURE VERSUS ENGINE MASS (SYMMETRIC BOUNDARY CONDITIONS)

Percent Increase	Minimum Flutter Dynamic Pressure (psf)	Weight (lb)	Mach
0% (Baseline)	1327	ZFW	0.8
20%	1277	DTOW2	0.95
40%	1164	DTOW2	0.95

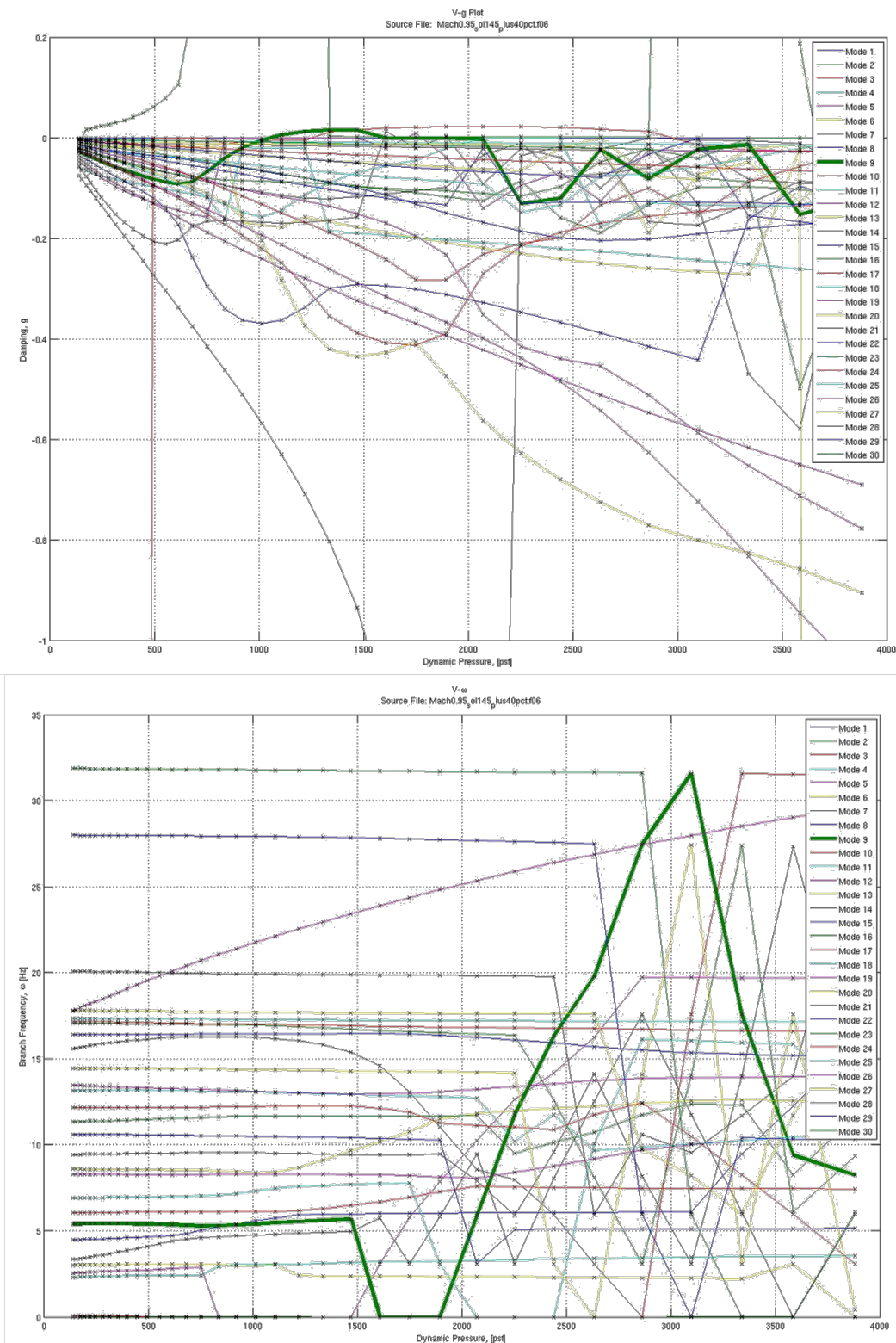


Figure 192.—Damping and Frequency Versus Dynamic Pressure for Symmetric BCs, Mach 0.95, DTOW2, 40 percent Increase in Engine Mass

Figure 192 and Figure 193 show the V-g, V-f plots and the flutter mode, respectively, of the critical flutter solution at Mach 0.95 with an increase of 40 percent engine mass and symmetric boundary conditions. The flutter crossing is highlighted by the dark green line and is a shallow-crossing hump mode that combines aft deck bending, tail bending and tail torsion. The mode that goes unstable even earlier is a rigid body mode (zero frequency) and is associated with the vehicle being statically unstable in this weight configuration (DTOW2 along the aft CG burn schedule).

Figure 194 shows the flutter survey for antisymmetric boundary conditions for the 3 different engine weights. In this case, the reduction in flutter dynamic pressure with an increase in engine mass is more modest, decreasing only 5 percent for a 40 percent increase in engine mass (see Table 30).

Figure 195 and Figure 196 show the V-g, V-f plots and the flutter mode, respectively, of the critical antisymmetric flutter solution at Mach 0.7 with an increase of 40 percent engine mass. The flutter crossing is highlighted by the dark turquoise line and is a steeper crossing than the symmetric flutter mode and combines tail bending and tail torsion.

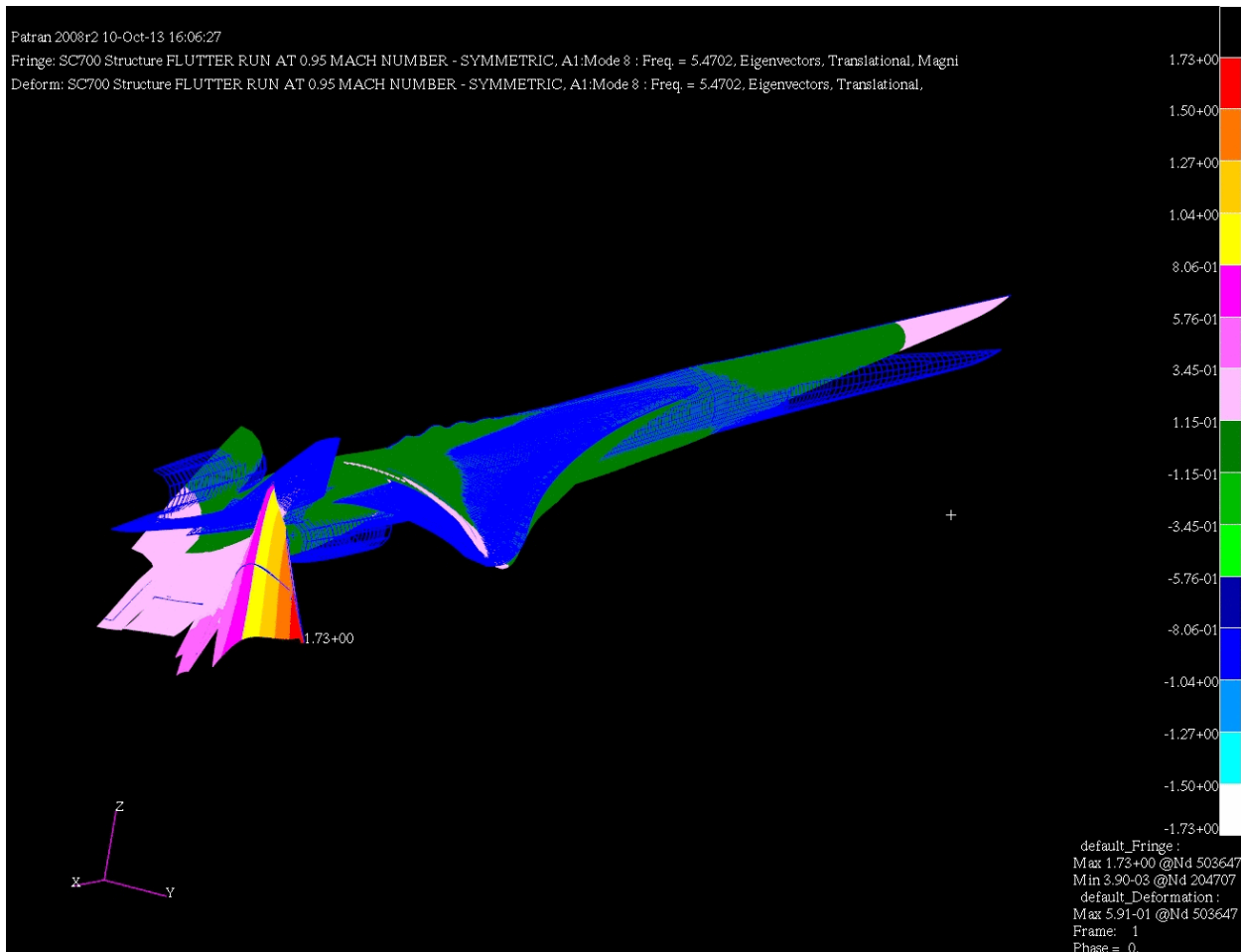


Figure 193.—Critical Symmetric Flutter Mode, Aft Deck Bending, Tail Bending and Torsion, $q_f = 1164 \text{ psf}$, $f = 5.5 \text{ Hz}$

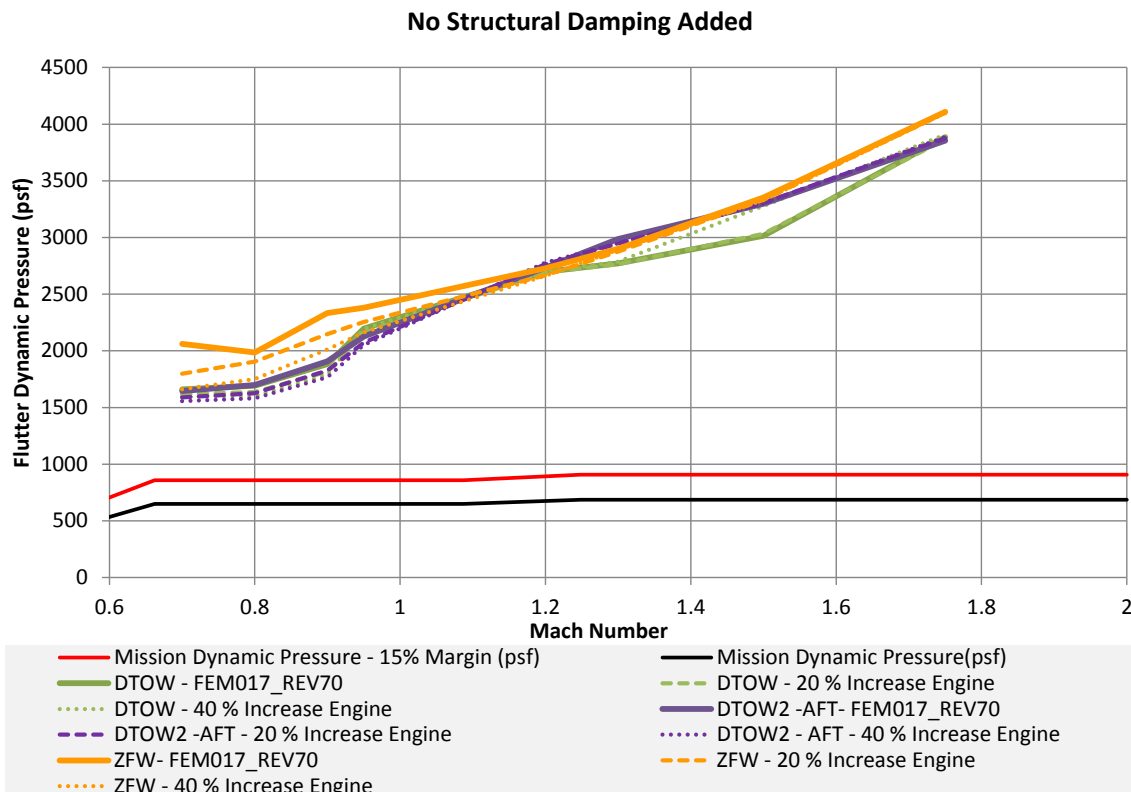


Figure 194.—Engine Mass Trade Study—Antisymmetric Boundary Conditions

TABLE 30.—MINIMUM FLUTTER DYNAMIC PRESSURE VERSUS
ENGINE MASS (ANTISYMMETRIC BOUNDARY CONDITIONS)

Percent Increase	Minimum Flutter Dynamic Pressure (psf)	Weight (lb)	Mach
0% (Baseline)	1646	DTOW2	0.7
20%	1590	DTOW2	0.7
40%	1556	DTOW2	0.7

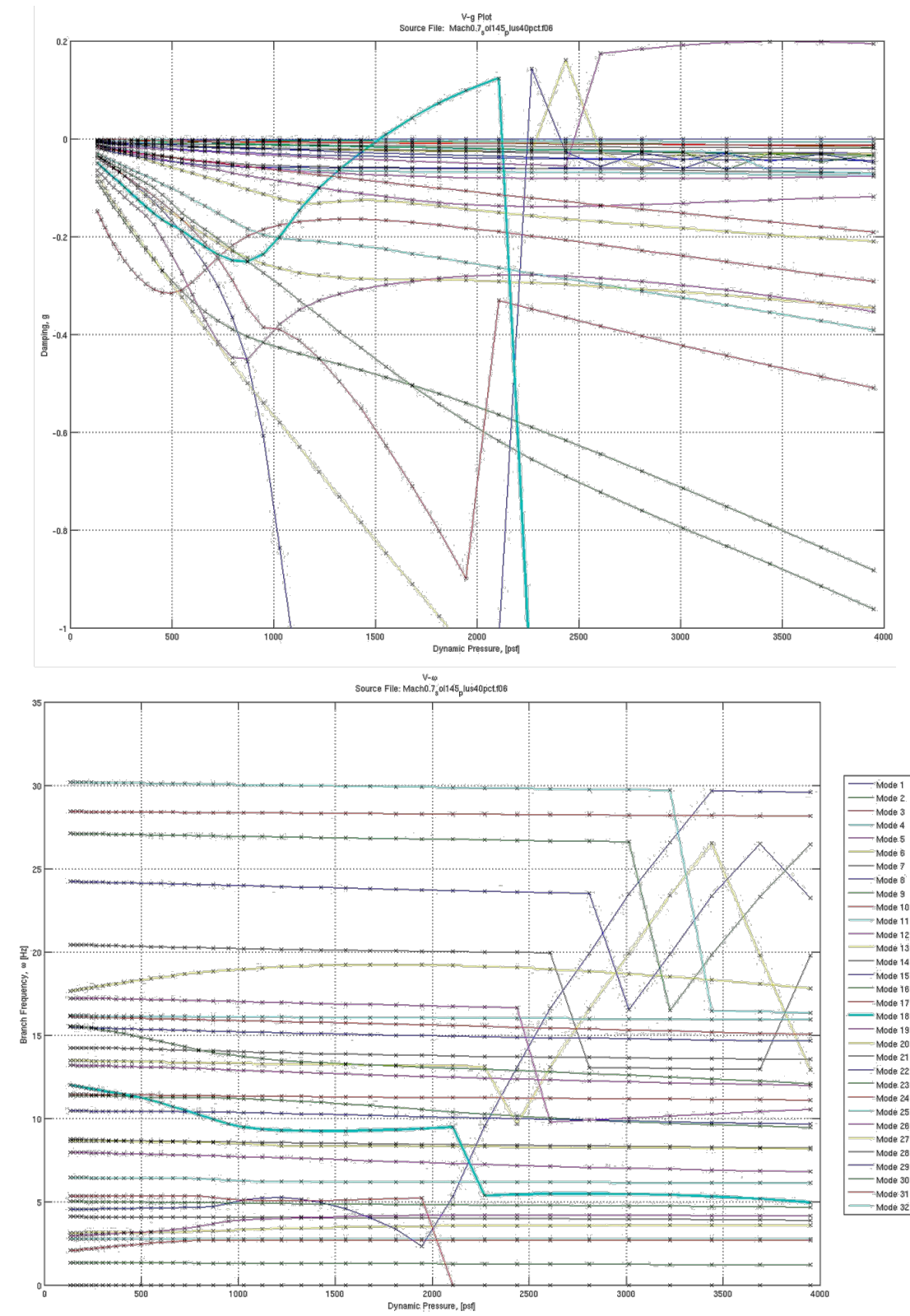


Figure 195.—Damping and Frequency Versus Dynamic Pressure for Antisymmetric BCs, Mach 0.7, DTOW2, 40 Percent Increase in Engine Mass

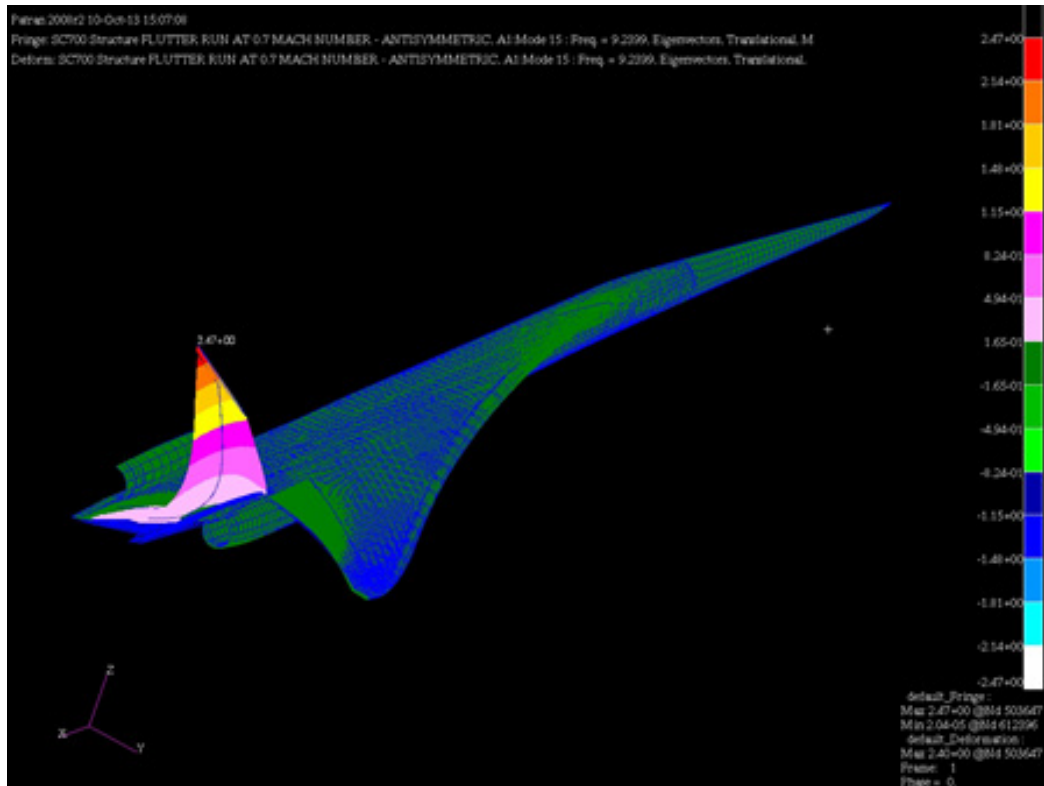


Figure 196.—Critical Antisymmetric Flutter Mode, Tail Bending and Torsion,
 $qf = 1556 \text{ psf}$, $f = 9.3 \text{ Hz}$

Increase pylon height until no further benefit
 (with little sonic boom / aero impact)

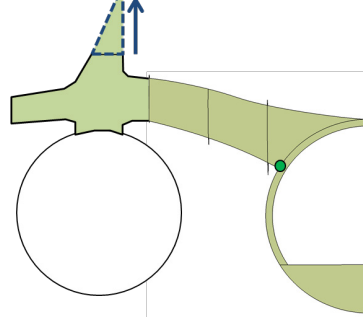


Figure 197.—Aft Deck Stiffening Alternative by
 Pylon Height Extension Above Wing

3.6.4 Aft Deck Stiffening Alternative

Boom shaping and wave drag are primarily sensitive to large changes in area or lift. There are wing rib/longerons that support the wing nacelles and carry back into the outer edges of the aft deck. They can be extended in height above the wing with little cross-sectional area increase. We would like to examine adding (like an above wing “T” stiffener) a pylon height extension, like Figure 197, as much as 24 in. in additional height: starting in the wing box, peaking in height around the start of the aft deck (wing TE) and carrying back to the TE of the aft deck and supporting the V-tails more rigidly in pitch and torsion.

3.7 Structural Deformation Effects on Sonic Boom

The impact of operational structural deflections on sonic boom was investigated. Structural deformations affecting boom shaping could come from:

1. Aeroelastic trim variations from beginning to end of cruise and during climb/descent
2. Control surface and structural deflections countering turbulence
3. Maneuver control surface and structural deflections

With regard to the third source listed above, nonemergency maneuvers are executed slowly, due to limited excess power available, so they seem unlikely to cause changes (but may limit maneuver rates). The second source, countering turbulence, involves aeroelastics, design, flight control system response and pilot response; while the first source involves only aeroelastics and vehicle design, so it should be most expedient to quantify the first source initially.

Our CFD-based aeroelastic tools were used to determine the aeroelastic trim state at the beginning and end of cruise. Those aeroelastic structural deflections are then analyzed with the high fidelity gridding scheme and CFD solver used for boom assessment. The aeroelastic trims require lift of the deformed geometry to equal weight and pitching moment to be zero about the specified center of gravity. The aeroelastic trim process includes structural deflections, as well as deflections from the control surfaces designated as pitch trim devices. Angle-of-attack is also included as a trim variable. Table 31 contains the flight conditions for the beginning and end of cruise states, as well as the vehicle weight and Fuselage Station (FS) CG location. The finite element model used to support this analysis was based on Configuration 1044-3, including thickness modifications made to the aft deck. The structural design used was FEM17 Rev 70, which was a design that included the results of metallic trades, and was structurally optimized without a vertical tail deflection constraint because the flutter analysis of Section 3.6.3 indicated that the additional weight of the deflection constraint was unnecessary.

To accurately model the mass distribution of the beginning and end of cruise states, spent fuel tanks masses were removed from the model and partial fuel tank masses were created based on an aft-CG fuel tank burn sequence. Figure 198 illustrates the tank layout, as well as the fuel tank burn sequence used. These fuel tank weights account for the additional 10.6 percent fuel volume available in tank 10 due to thickening of the aft deck.

With the fuel tanks modeled, the beginning of cruise CG location was at FS 2081.1 in, and the end of cruise state was located at FS 2025.3 in. These CG locations were used as the FS moment reference location in the trim analyses.

Table 32 contains the trim states obtained with the CFD-based Aeroelastic Approach. Rigid trim states using a CFD-based approach were also computed and are included for comparison. For the beginning of cruise state, the body flap was used as the only pitch trim control device. An increase in 10.44° in body flap deflection was needed to account for aeroelastic effects. For the end of cruise state, large body flap deflections were encountered due to the more forward CG, therefore the trailing edge flap and ailerons were used as well. For this state, only a modest increase of approximately 0.7° was needed to account for aeroelastic effects. To better understand the underlying factors producing these differences trim state, a comparison of aeroelastic increments in integrated loads for different portions of the vehicle was constructed. Normalizing these values relative to the total lift, and plotting these values over the vehicle illustrates the sources of largest change. Figure 199 contains a plot of the aeroelastic increments in the Z force for various parts of the vehicle, normalized by total lift for the beginning of cruise state. As can be seen, the vertical tail is unloading due to aeroelastic effects (negative percentage of total lift), and to compensate for this impact on the pitching moment, the body flap is increasing its deflection to generate more lift (positive percentage of total lift) to balance the vehicle. A comparison of the integrated force in the Z direction showed that the lift on the vertical tail was in the positive Z-direction during the rigid analysis, and that this was reduced to 52 percent of this value during the aeroelastic analysis. The wing also slightly unloads during this trim state as well.

TABLE 31.—FLIGHT CONDITION AND WEIGHT STATES FOR BEGINNING AND END OF CRUISE STATES

State	Mach	Weight (lb)	Altitude (ft)	Target CG FS (in.)
Cruise Start	1.7	261,688	48,400	2083
Cruise End	1.7	172,302	57,100	2047

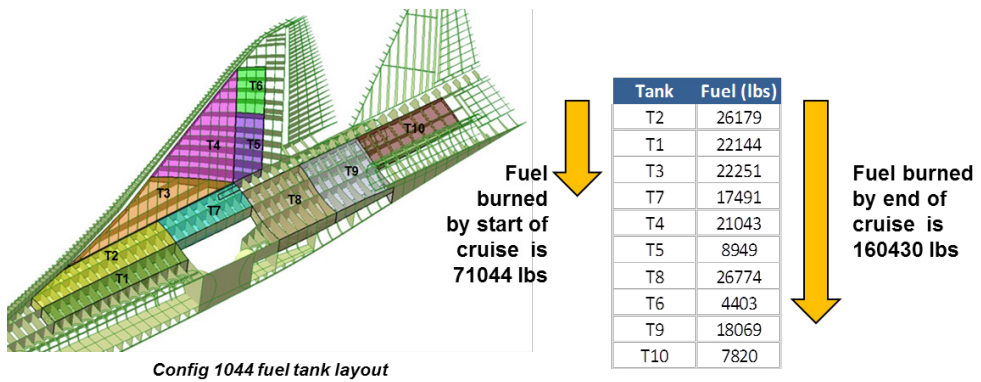


Figure 198.—Fuel Tank Layout and Tank Burn Sequence at Beginning and End of Cruise

TABLE 32.—TRIM STATES OBTAINED WITH A CFD-BASED AEROELASTIC TRIM APPROACH

	Cruise Start Rigid	Cruise Start Aeroelastic	Cruise End Rigid	Cruise End Aeroelastic
CX	0.00497	0.00531	0.00545	0.00495
CZ	0.13659	0.13661	0.13632	0.13633
CMY	0.00000	0.00000	0.00000	0.00000
ALPHA (deg)	2.25	2.27	2.67	2.57
LEF (deg)	0.00	0.00	0.00	0.00
TEF (deg)	0.00	0.00	-5.67	-4.98
BFLAP (deg)	-3.83	6.61	-5.67	-4.98

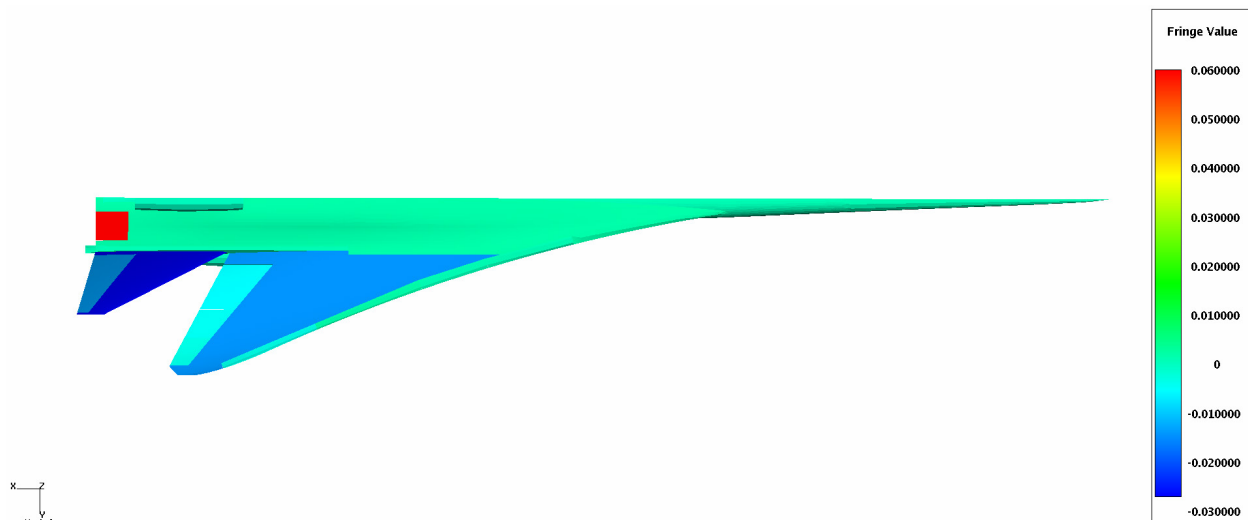


Figure 199.—Aeroelastic increments in Total Z-Force Normalized by Total Lift for the Beginning of Cruise

A similar plot for the end of cruise state is shown in Figure 200. For this trim state, the aeroelastic, integrated load on the vertical tail in the Z-direction was 70 percent of the rigid value, therefore a smaller aeroelastic increment compared to the beginning of cruise state. The more-forward CG also results in a smaller change in control surface deflection needed to balance the aeroelastic increment. The wing also shows a modest increase in lift, rather than the decrease shown at the beginning of cruise state. This is most likely due to the use of trailing edge control surfaces, which impose a positive or “wash-in” twist on the wing due to their downward load on the trailing edge of the wing. This trend can be seen in the comparison of Z-deflections for both trim states shown in Figure 201.

To assess the impact of these deflections on the boom signature of the vehicle, the deflections obtained for the trim states were mapped to the CFD mesh used for boom prediction. This was performed using the tools used during the CFD-based aeroelastic analysis. The aerodynamic models used in the aeroelastic trims were modified to allow control surface actuation during the simulation. These modifications were not present in the models used for boom assessment, therefore, only structural deflections (i.e., no control surface deflections) were mapped during this process.

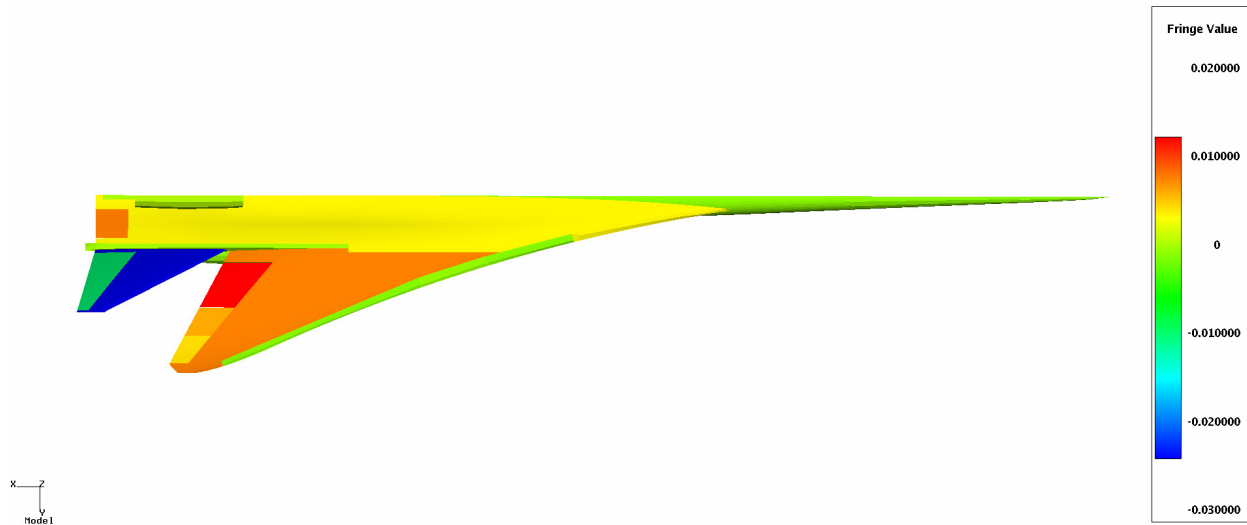


Figure 200.—Aeroelastic Increments in Total Z-Force Normalized by Total Lift for End of Cruise

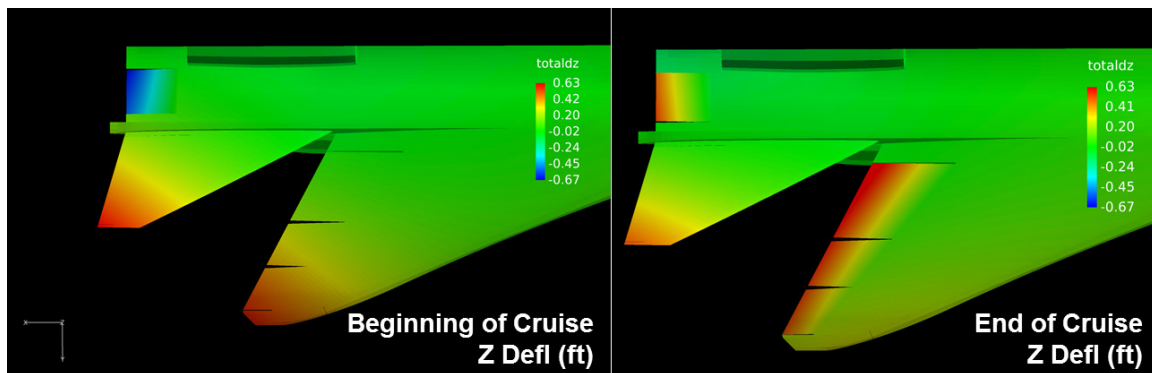


Figure 201.—Comparison of the Z Deflections for the Beginning and End of Cruise Trim States

Both rigid and deformed grids were analyzed at the Start of Cruise condition with a Mach number of 1.7 and an Angle of Attack of 2.1° in CFD++ using the Euler equations. Issues were encountered using grids that included the propulsion system details so flow-through propulsion systems were used instead to capture the incremental impact of structural deformation and control surface deflection to trim on sonic boom. A comparison of top surface pressures shown in Figure 202 shows that the loading on the wing changes only slightly, but that more significant changes occur around the centerline nacelle and empennage.

The region of increased pressure near the mid-point of the centerline nacelle is a result of the structural thickening applied to the FEM to increase the rigidity of the aft deck. A comparison of the loading on the bottom surface of the empennage shown in Figure 203 clearly shows the impact of the body flap deflection and the reduced tail loading due to aeroelastic washout.

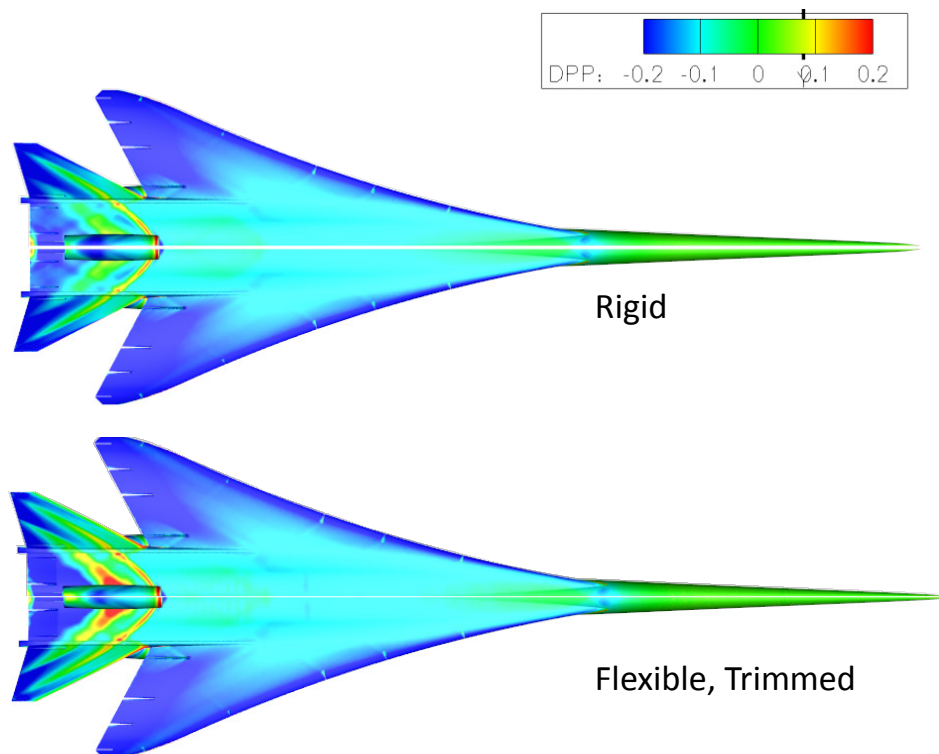


Figure 202.—Comparison of Planform Surface Pressure Coefficient for Rigid and Flexible Simulations at Start of Cruise

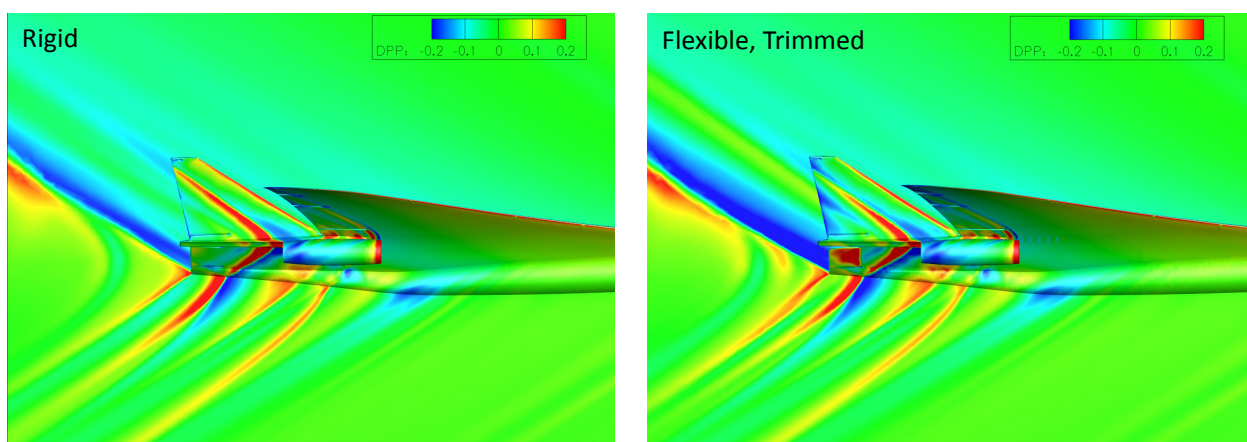


Figure 203.—Comparison of Empennage Surface Pressure Coefficient for Rigid and Flexible Simulations at Start of Cruise

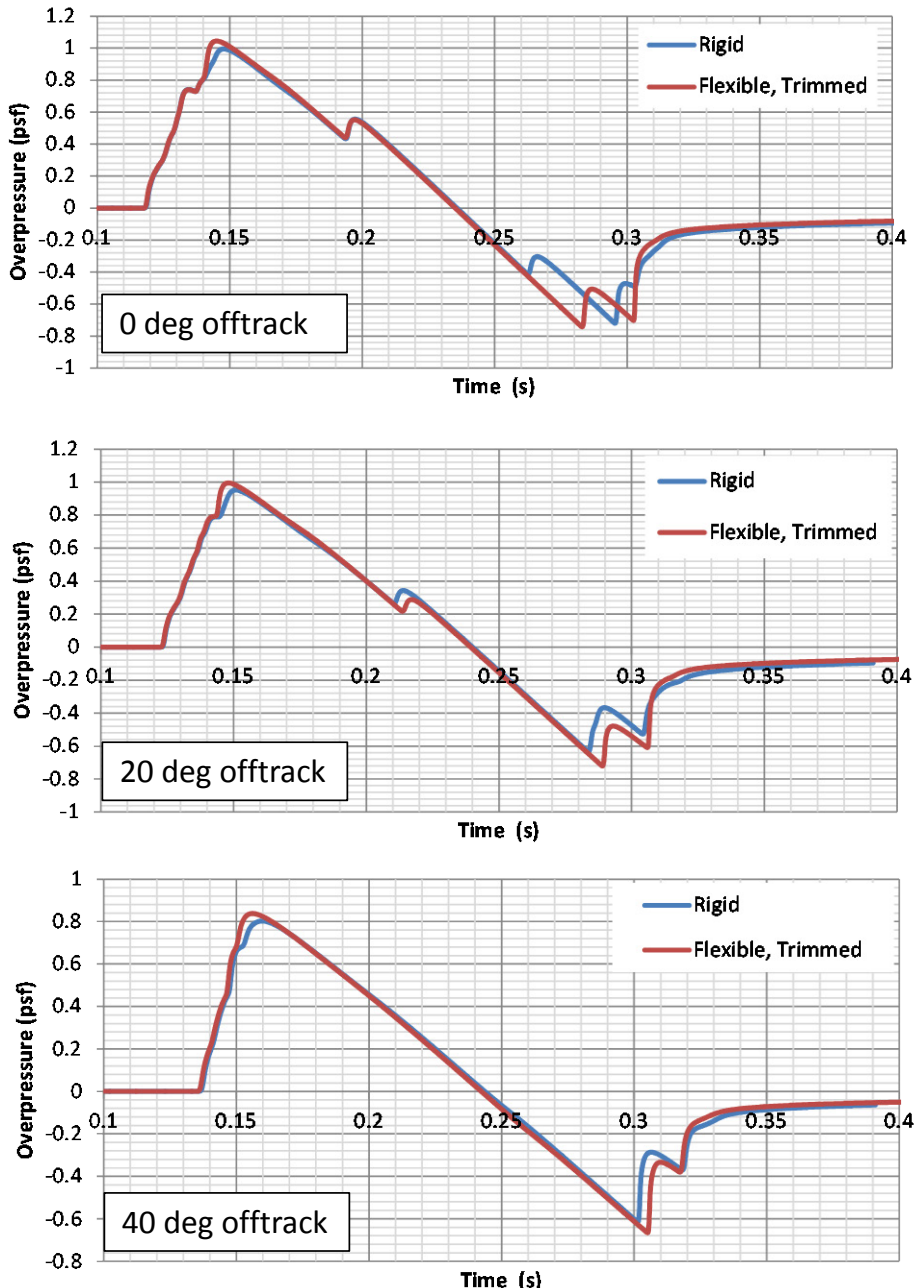


Figure 204.—Comparison of Ground Signatures for Rigid and Flexible Simulations at Start of Cruise

Off body pressures were extracted at a distance of 345 ft from both the rigid and flexible solutions and propagated to the ground using the Burgers-equation solver sBOOM. The comparison of the ground signatures shown in Figure 204 shows that flexibility effects only have a small impact on the front ramp portion of the signature, but there are significant changes to the aft part of the signal due to the changes in tail loading. A comparison of the carpet loudness of the two configurations, plotted in Figure 205, shows that the change in loudness varies between 0.5 and 4.0 PL dB across the carpet.

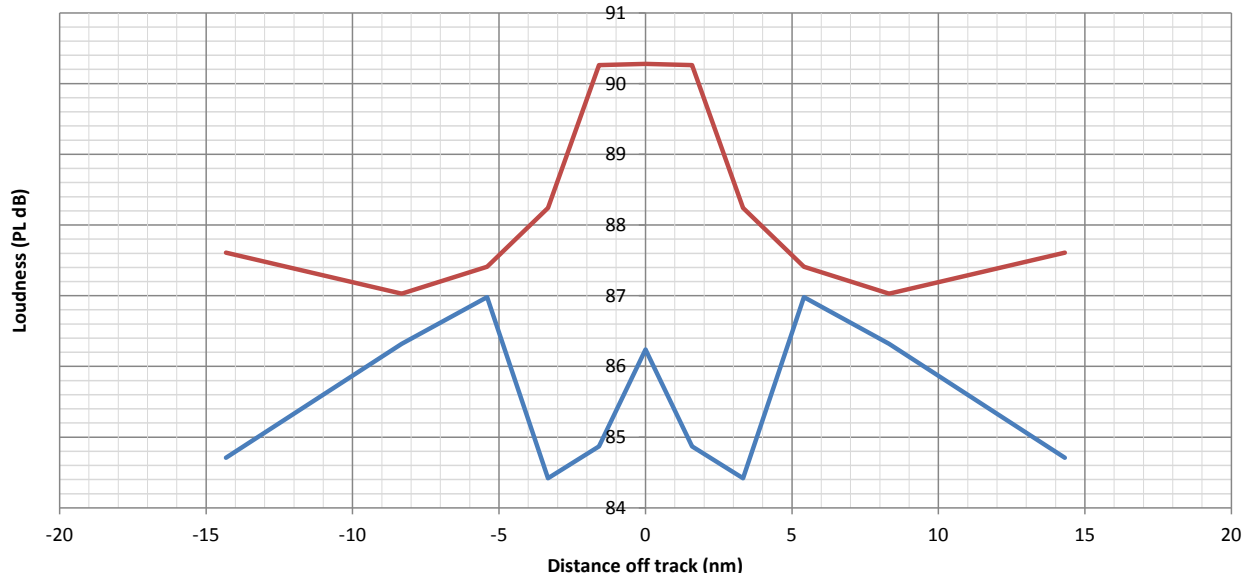


Figure 205.—Comparison of Ground Loudness Carpets for Rigid and Flexible Simulations at Start of Cruise

When considering these results it should be noted that the reason for significantly degraded sonic boom performance when flexibility effects are included is that the 1044 configuration was not designed to accommodate these effects. For future shaped boom design efforts, aeroelastic simulation should be used during the preliminary design phase to modify the aircraft jig shape so that the loading at the cruise design point matches the design loading and the vehicle produces the desired sonic boom characteristics. The design and analysis tools used to perform this work could also be used to modify the design to eliminate these adverse effects.

3.8 Conclusions and Recommendations in Sections 5.0 and 6.0

Conclusions and recommendations are compiled at the end of this report in Section 5.0 Conclusions and Section 6.0 Recommendations, respectively.

4.0 N+2 Sonic Boom Testing and Analyses

4.1 Ames 9x7-0250 Parametric Test

The “Parametric” test of April 2012 contributed to the productivity and accuracy improvements achieved on the final 97-0254 or LM4 test (Section 4.4). Test 97-0250 investigated tunnel flow control (particularly humidity and P_T), spatial averaging measurement procedures and beyond near-field measurement distances. It sought to better define limits for: humidity, P_T , sampling time, sampling translation distance, reference position and other parameters—for best productivity with still acceptable accuracy.

Just before the start of N+2 early in 2010, NASA ran two sonic boom tests to study the effect of humidity on sonic boom measurements. In the Ames 9x7 tunnel, lower humidity resulted in sharper sonic boom measurements and variations in humidity resulted in measurement changes (later understood to be due to ambient flow field pressure changes or pressure position shifts). However, humidity of 175, 200, and 225 ppm produced good measurements as long as that humidity value did not vary during a measurement set. So for the LM1-2 tests in November through December 2010, humidity was planned to be nominally 200 ppm ± 25 ; however, depending on outside weather and other conditions 225 ppm could

be time consuming to reach or even be unreachable. In testing over the next year and a half, humidity up to 350 ppm was found to provide acceptable results as long as it did not vary during a measurement set. Invariant humidity was originally defined to be the best the tunnel could achieve: ± 3 ppm. While the tunnel could hold this tolerance for several sets, it would often start drifting. When this happened during a measurement set, data acquisition was stopped until the tunnel was readjusted to a steady humidity—which often took large amounts of time (using manual flow adjustments). In fact, time spent initially evacuating the tunnel and refilling it with dry air to get dry enough to start, plus time spent readjusting the tunnel to a steady humidity was consuming as much as 60 percent of run time nonproductively. In LM3, running P_T (total pressure) at 2300 psf, instead of 1450 psf, made initially drying the tunnel faster and made holding humidity easier (presumably because the tunnel was closer to atmospheric pressure reducing leakage and requiring less dry air flow to maintain steady humidity). To reduce nonproductive time, the 97-0250 Parametric test further investigated humidity and P_T limitations using actual model signatures for assessments (Ref. 2).

The Parametric test investigated humidity and P_T thoroughly. Running humidity at 200, 300, 400 and 500 ppm showed that dryer air resulted in sharper signatures, fewer spurious measurement spikes and more flow-field consistency between measurement and reference runs. In addition, plotting the reference runs at different humidity levels in Figure 206 shows that the tunnel ambient flow does change with humidity changes. There is some level shift but also a shift of the pressure pattern forward on the rail that increases in displacement going from orifices 50 to 300. So humidity affects the ambient flow in the 9x7. However, other runs where ambient pressure was repeatedly measured for 15 min while the humidity slowly drifted as much as 100 ppm, did not show a conclusive link between changing humidity and the measured ambient pressure. So for humidity it was decided that testing would be done at whatever dry tunnel level was easy to achieve and hold that day and the variation would be kept as steady as possible. Humidity requirements were set at less than 350 ppm and no more than ± 15 ppm during a measurement set, which was always achieved without having to stop data acquisition.

For this tunnel, P_T has both coarse and fine control loops that are different for increasing or decreasing pressure in the settling chamber. After investigating rail pressure with the different control loops set to auto, manual and off, no effect was seen on the rail pressures due to P_T variations. A requirement of ± 3 psf tolerance was specified because in practice ± 1.5 psf was achieved by the tunnel controls. The following LM4 test was able to use these larger tolerance values to avoid stopping data acquisition while still obtaining accurate measurements.

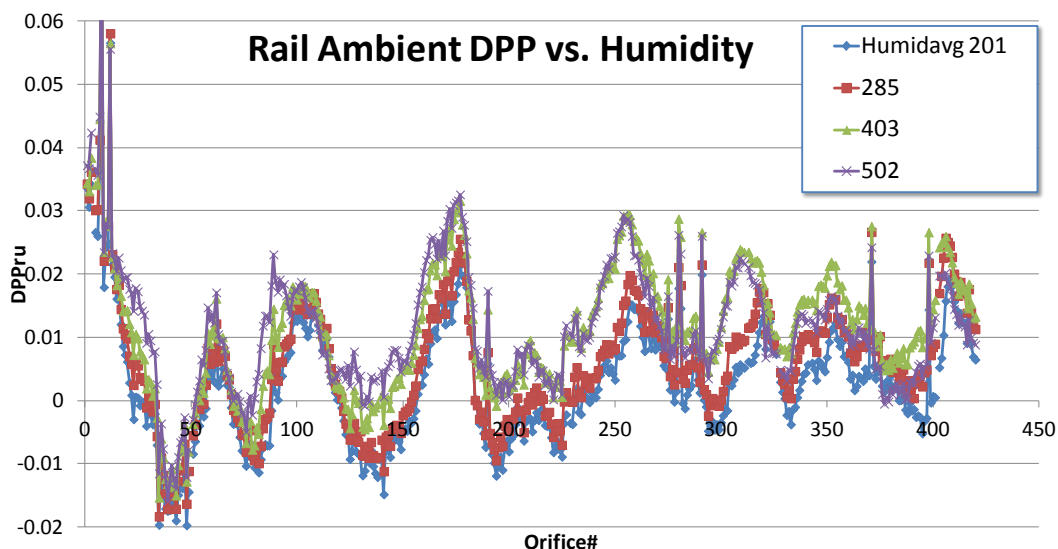


Figure 206.—Tunnel Ambient DPP Versus Humidity

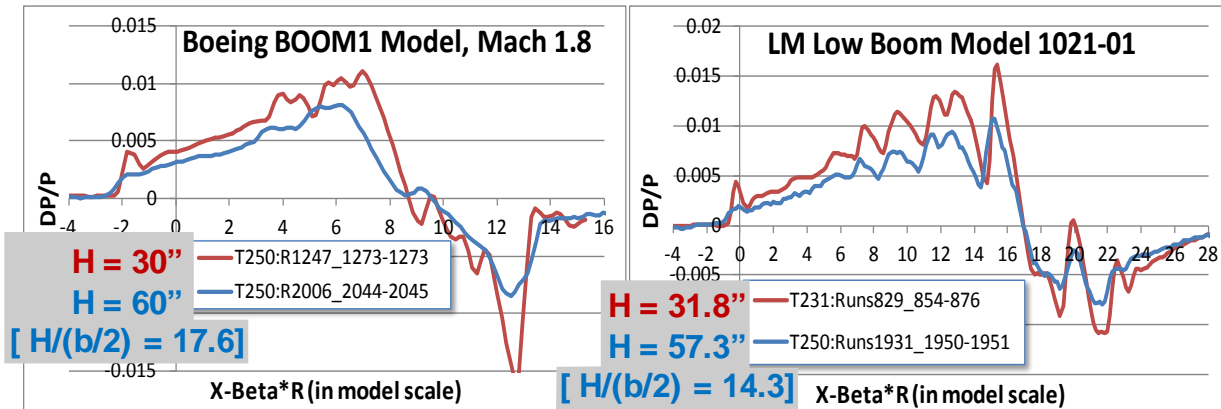


Figure 207.—Beyond Near-Field Measurements Appear Rounded and Missing Detail

This Parametric test also performed refined spatially averaged measurement sets for the 1021-01 Configuration validated in LM3. LM3 post-test analysis indicated that the 4 in. translation used for most LM3 measurements was insufficient for best accuracy (12+ in. is needed in the 9x7) but 30 sec time samples could be cut to 2 sec (excepting the reference measurement). Measurement set accuracy was improved and acquisition time was decreased from 50 min in LM3 to 20 min in this Parametric test.

Sonic boom propagation methodology requires starting signatures to be outside near-field interference distortion. Typically this requires the CFD or wind tunnel data to be 15 to 25 semispans [$R/(b/2)$] from the vehicle. The LM3 test measured the 1021-01 model at 5 and 8 semispans. The tunnel is capable of measuring the model up to 17 semispans; but to do so, the rail needed to be moved to the aft window blank and the adapter between the strut and roll mechanism needed to be rotated 180°. The rail reposition was not done in LM3 so it was first investigated in this Parametric test with spatial averaging. Both the Boeing BOOM1 model and the LM 1021-01 model were measured at the farthest distance possible with just a rail move, Figure 207. The smaller size of the Boeing model (about 16 in.) allowed a slightly greater measurement distance, more translation distance (21 in.) and more measurement points (39) than the LM 1021-01 model (12 in., 20 points). Unfortunately, there was not a published result for what the BOOM1 model's sonic boom should look like going from 9 to 18 semi-spans. There is general rounding/smearing of detail throughout the signature. The nose bluntness spike is almost gone. And there are some shape changes in the signature, like a higher end of ramp magnitude relative to the ramp ahead of it, that have not scaled in amplitude with square root of distance. CFD analyses of the 1021-01 model indicate the signature shape stays the same and mostly scales in amplitude with distance going from 8 to 14 semi-spans, and the measurements match these analyses. There seems to be less detail rounding but the nose bluntness spike is also almost gone. These results suggested that extra consideration should be given to improving far measurement accuracy in the LM4 test.

4.2 Ames 11-0249 Boeing Test

4.2.1 Background and Overview

Test 11-249 was conducted at the NASA Ames Unitary 11 ft Transonic Wind Tunnel June 4 to 8, 2012, with single-shift operations. The test was conducted by the Boeing Company and was attended by NASA Analysts and a Lockheed Martin observer. The test was funded by, and in support of, the Fundamental Aerodynamics Supersonics Project based at NASA Langley. This test was an extension of testing performed in the last few years by NASA, Lockheed and Boeing to measure sonic boom signatures in the wind tunnel environment, with most previous testing being conducted at the Ames Unitary 9x7 ft Supersonic Wind Tunnel, with test conditions in the Mach 1.60 to 1.80 range. The 11 ft

Transonic Tunnel was selected to explore the feasibility of measuring sonic boom signatures at Mach 1.20 and 1.40. Existing aircraft and reference models and existing pressure measurement equipment was used. In addition to sonic boom measurements, measurements of transonic drag rise were also obtained.

Test attendees were the following:

- Boeing: Eric Adamson, Alicia Bidwell, Stephen Shaw, Todd Magee, and Pete Wilcox
- Lockheed Martin: Bob Langberg
- NASA Langley: Eric Walker and Alaa Elmiligui
- NASA Ames: Don Durston, Susan Cliff, and Scott Thomas

The test was largely successful with the desired sonic boom signatures being measured. However, the desired test conditions of Mach 1.20 and 1.40 were not attainable. At the tunnel's top speed of Mach 1.40, excessive model lateral dynamic motion was observed with transient loads approaching the internal balance's side force gage limits. As a result measurements desired at 1.40 Mach were taken at 1.30 Mach. At the Mach 1.20 condition, a half-dozen ambient shocks originating on the floor upstream in the test section propagated aft, reflected off the ceiling and adversely affected the flow quality at the location of the models. Testing was conducted initially at Mach 1.20 and later at Mach 1.15, a speed where this flow quality issues did not directly affect the model.

4.2.2 Test Description

The test took place over the course of one calendar week and operated during the day shift, nominally 6:30 to 3:30, but with overtime available at the end of the shift which was used to make up for tunnel downtime periods.

Pretest preparations had taken place in the model buildup and prep area and continued with installation in the 11 ft test section prior to the week of testing. Installation activities were complete by Tuesday afternoon of the test week and testing was completed a few days later, by mid-shift on Friday.

Test conditions were primarily Mach 1.15 to 1.40 at a total pressure, $PT = 2300$ psf, with one brief investigation at $PT = 1450$ psf. In addition, transonic drag rise was investigated between 0.80 to 1.10 Mach.

Three models were used during testing. The two aircraft models are shown in Figure 208:

- “AS2”, an axisymmetric body-of-revolution (“Axi” or “BOR”) model which was a SEEB body with a 0.35 psf flat-top pressure distribution, used as a reference model.
- “BM1” or “Boom 1” was the Boeing aircraft “N+2 Quiet Experimental Validation Concept” model at 0.65 percent scale. It was supported by a swept upper blade support and featured flow through nacelles on the upper surface of the wing. It was the primary model for sonic boom measurement.
- “PM1” or the Performance Model of the Boeing aircraft concept is a 1.79 percent scale sting-supported model which is approximately three times larger than the Boom 1 model and has corresponding greater detail in the loft reproduction. The model aft end is distorted due to the sting mounting, and the model is too long to obtain a clean sonic boom signature with the instrumentation used in this test.

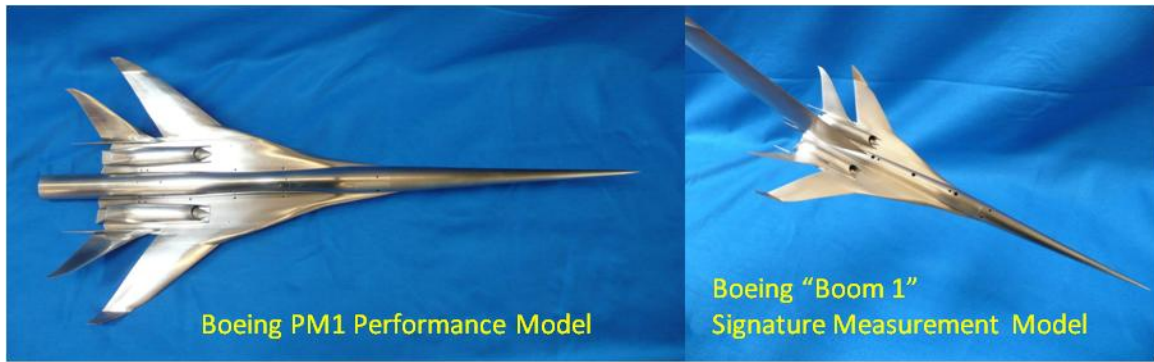


Figure 208.—Aircraft Performance (44 in.) and Boom (16 in.) Models

TABLE 33.—BOEING MODEL REFERENCE DIMENSIONS AND SIZE

	Boom Model	Performance Model
Model Scale, SCALE	0.006496713	0.01786596
Wing Reference Area (ft ²), SREF	0.1064	0.8048
Span (in.), B	6.7111	18.4555
Model Length (in.), LREF	15.7480	43.3071

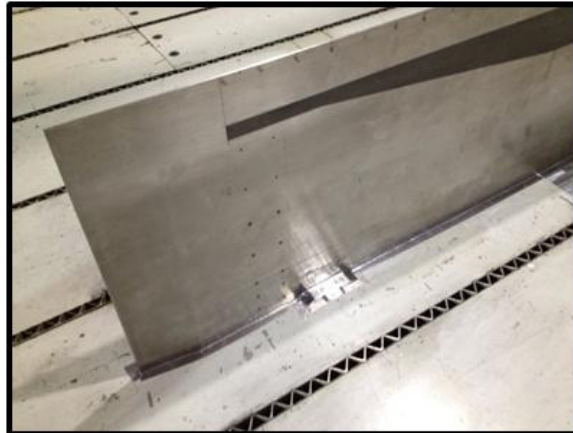


Figure 209.—The 14 in. RF1.0 Rail Attached to Floor of 11 ft Transonic Tunnel (Note Non-Conformal Structural Attachment ~8 in. Aft of LE)

Instrumentation was primarily the 14 in. RF 1.0 pressure rail which is a thin blade, featuring 420 pressure measurement locations along a 66 in. portion of its length. The rail is floor-mounted in the 11 ft tunnel, with pressure ports 14 in. from the tunnel floor. This rail was designed and fabricated for use in the 9x7 transonic tunnel and as a result, the installation in the 11 ft tunnel was a bit different with a nonflush attachment foot and a cantilevered forward edge which normally would have been constrained in the 9x7 installation. Loads were monitored on the cantilevered leading edge portion of the rail and were not a problem in testing. The leading edge of the 14 in. rail as installed on the floor of the test section is shown in Figure 209.

Loads were monitored with the 1.0 in. diameter Task Mk14C six-component balance, located in the balance housing aft of each of the three models. The same balance was used throughout the entire test.

A model fouling circuit was used and model base pressures were measured and corrected.

The model support sting stack was essentially the same as used previously in the 9x7 testing activities and consisted of the Large Model Roll Mechanism, SR-47 Primary Adapter, SR-158 Adapter, Linear Actuator, and the SR-205 Sting.

The test was conducted to measure both X-axis sweeps and Z-axis sweeps.

Humidity was desired to be 300 ± 25 ppm, and within ± 3 ppm of the reference run. In practice, these requirements were changed at the start of testing, and as the test progressed, humidity varied open-loop with the OCPE (Open Circuit Plenum Evacuation) system. Humidity values were substantially drier than the initial plan and will be discussed in greater detail later.

Schlieren images were obtained via live video feed and were viewable in the control room as testing was conducted.

The test section of the 11 ft Transonic Tunnel is presented in Figure 210.

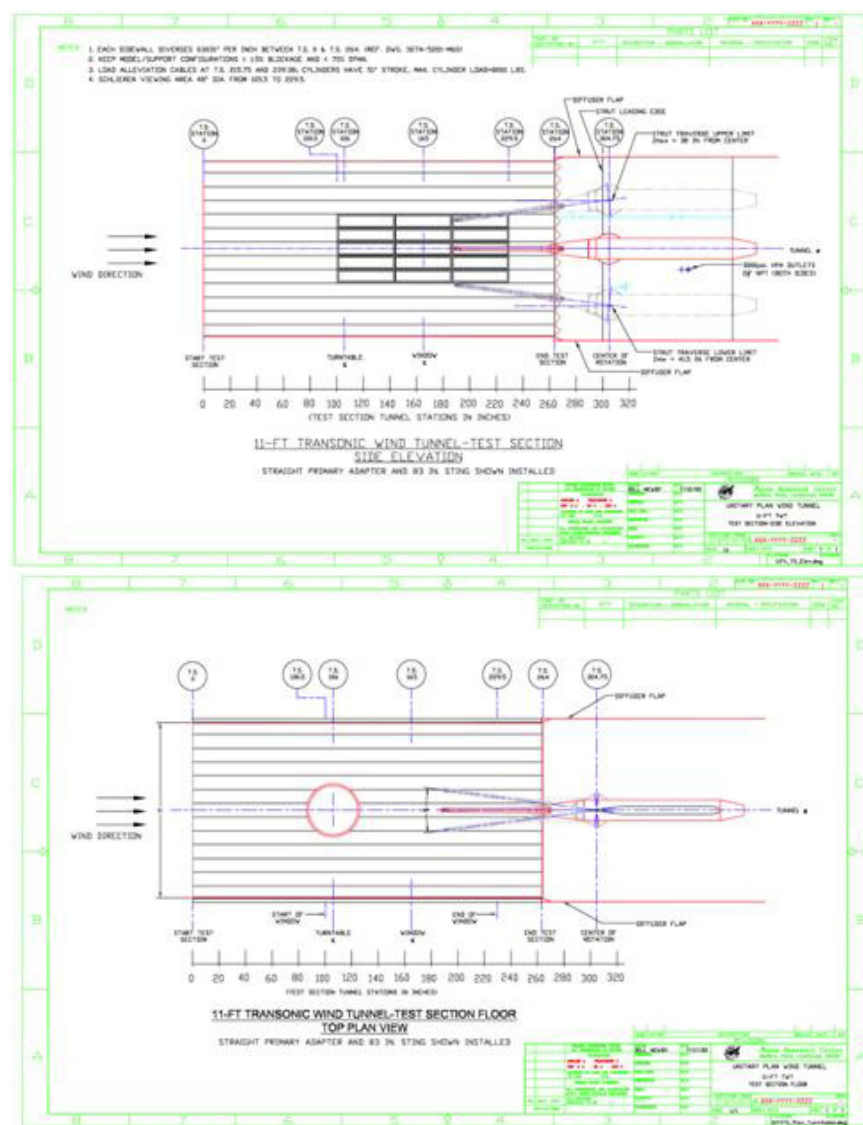


Figure 210.—Drawings of 11 ft Transonic Tunnel Test Section

4.2.3 Test Conduct

4.2.3.1 Pretest Installation Activities

Prior to Monday June 4, 2012, tunnel installation activities were conducted with the usual installation procedures followed. All model support hardware was installed and checked out. The hardware stack was installed in a similar configuration to past test efforts, with the linear actuator, SR-205 sting adaptor and other parts. Check loads were conducted on the balance and were verified to be adequate, and motion and limits verified.

Rail pressure and PSI modules were checked and all leaking ports were fixed. The rail was installed with strain gages to monitor loads during the test. The pressure modules were located under the floor, where the rail was installed. The PSI modules were placed on top of the OCPE (Open Circuit Plenum Evacuation) system's vent exit pipe. The PSI modules were monitored during testing via video feed and were subject to a dynamic environment in the tunnel plenum. In past testing at the 9x7 tunnel, the PSI modules were located outside the tunnel at ambient conditions and were not subject to the tunnel temperature, pressure, and vibration environment. The installation at the 11 ft transonic tunnel appeared to work adequately during the test, despite these conditions.

One note, the pressure line length was left quite long, the same as the previous Parametric 9x7 test in April 2012 (97-250), and the LM3 test from October 2011 (97-231). These pressure line lengths should be subject to lag similar to that observed at the 9x7 tunnel. Later testing in October 2012 at the 9x7 for LM4 (97-254) used shorter line lengths, which reduced pressure lag.

Midway through the 11-0249 test, signatures obtained on the AS2 model were reviewed with Eric Walker's MATLAB plots to compare discrete 2-sec time slices (0 to 2, 2 to 4, 4 to 6, 6 to 8, and 8 to 10 sec) to evaluate the necessary settle time in the pneumatic tubes. Trends were neither orderly nor monotonic, as had been previously observed in the 9x7 data. The 6 sec settle time before 10 sec of data acquisition time was used in the 11 ft testing similar to the April 2012 Parametric Test (97-250).

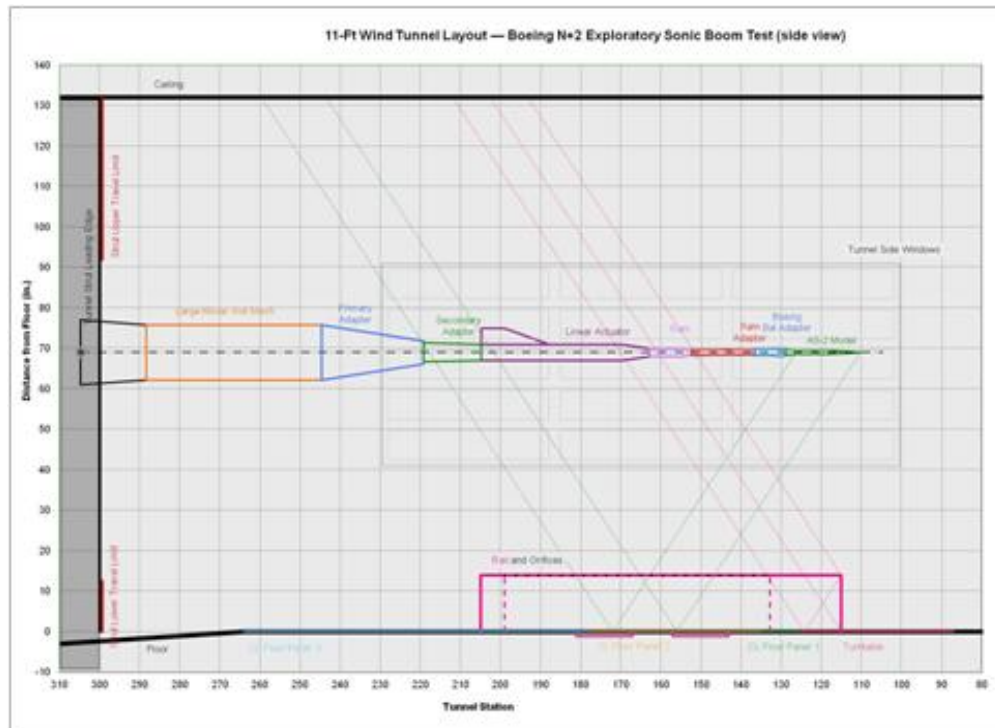


Figure 211.—The 11 ft Wind Tunnel Layout—Boeing N+2 Exploratory Sonic Boom Test (side view).

4.2.3.1.1 Monday, June 4, 2012

Installation activities continued during test week, with the AS2 model installed. Model XYZ measurements were taken and motion and safety checks completed. Although initial runs were expected Monday afternoon, these were not completed until Tuesday afternoon. Occupancy charges began on Monday, June 4, 2012.

4.2.3.1.2 Tuesday, June 5, 2012

By mid-day on Tuesday, motion checks were completed with AS2 from the control room, and the tunnel crew finished prerun inspections, safety briefings and other pretest activities. However multiple tunnel issues prevented running until about 2 pm that day, close to the end of shift.

One issue was a pressure transducer / data acquisition problem related to cavity pressure measurements. Another issue was a problem commanding the IGV (inlet guide vanes) in the main drive rotor / stator required for startup. After solving these issues, an initial shakedown run was accomplished with some initial humidity purge cycles. One reference run and an x-survey were accomplished with the AS2 model at Mach 1.20 / 2300 psf / Hrel = 60 in. Initial plots looked reasonable. As is the case with all axisymmetric models, tunnel angularity measurements upright/inverted are not obtained.

It was observed that as the tunnel approached Mach 1.40, the higher of the two desired test Mach numbers, the AS2 model experienced strong lateral motion, which hit the dynamic balance limits for the side-force gages in BLAMS (balance loads monitoring system). This continued to be a problem for all models at high speeds during this test.

The AS2 model is shown in Schlieren images in Figure 212. Note the model shock structure is traversed near the nose by a half-dozen tunnel ambient oblique shocks which will be discussed later.

4.2.3.1.3 Wednesday, June 6, 2012

Wednesday morning, testing proceeded as planned with the AS2 model and was completed with 190 runs acquired by that afternoon. Due to the large lateral model motion, and problems with the model exceeding BLAMS limits, Mach number was reduced from the desired Mach 1.40, down to 1.30 which still had lateral motion and vibration, but at a more tolerable level. Various X and Z sweeps were acquired at Mach 1.20 and 1.30 with the AS2 model, and Schlieren images were obtained.

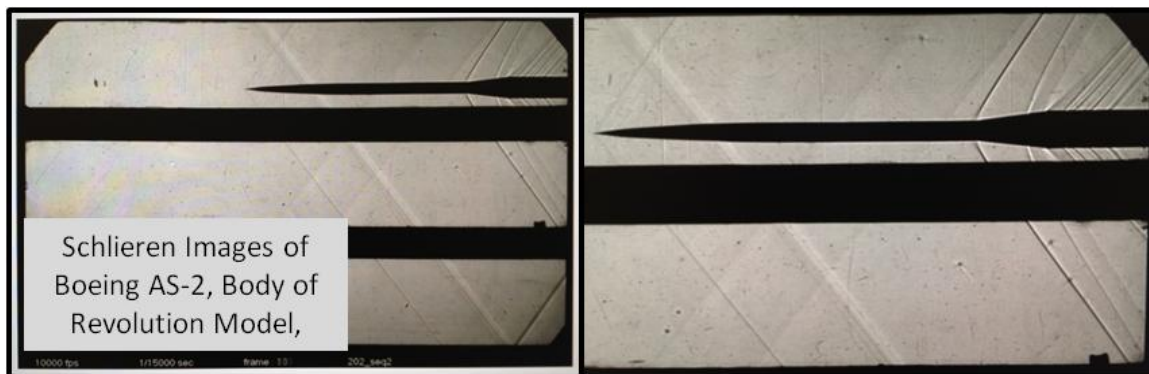


Figure 212.—Schlieren Images from 11 ft Transonic Tunnel

At the Mach 1.20 condition, there was a strong reflected shock from the start of the test section upstream, where the baffled test section slots begin. Based on Schlieren images and the tunnel geometry, it appeared that these ambient shocks originated on the floor, propagated downstream, and reflected off the ceiling, which placed them in a position to run directly across the model, however not necessarily along the tunnel centerline. There appeared to be somewhere between 6 to 8 weak shocks that varied and oscillated slightly in the tunnel flow, and visually appeared to be a loose braid of disturbances. It is believed that these originate at various YBL locations across the tunnel, so the impact on the model signature is unknown. Some similar disturbances were observed originating on the ceiling, but were not as large. If similar shocks originate on the side walls, they would not be visible in the Schlieren images. At the Mach 1.30 speed, the shock angle sweeps back enough that these ambient shocks pass behind the model, and should not adversely affect the data measurements at the higher speed. Because of the problem at 1.20 Mach, data collection was done at Mach 1.15 later in the test instead.

After the AS2 model runs were completed, the model was de-installed, and the blade-mounted Boeing Aircraft, "Boom 1", model installation began. Although the model was ready to run late on Wednesday's day shift, a facility problem prevented running that day. The problem was a tripped motor electrical breaker which failed to close properly. After fixing this issue, one shakedown run was obtained with the Boom 1 model on Wednesday, primarily to observe model dynamics and see if they were similar to the Axisymmetric AS2 model. The Boom 1 model was run up to 1.40 Mach, and displayed similar severe lateral dynamic motion, even when tunnel total pressure was reduced (from $PT = 2300$, down to 1450 psf). All previous AS2 runs had been performed at $PT = 2300$ psf and that total pressure was planned for all models during the 11-0249 test. Because the lower total pressure did not provide any relief, it was not pursued. The Boom 1 model was also run as Mach 1.20 and 1.30 and demonstrated that these conditions could be obtained during the data runs on Thursday.

It should be noted that the Boeing Boom 1 model does not use any trip dots or other boundary layer energizing devices. The Boom 1 model is shown in Figure 213.

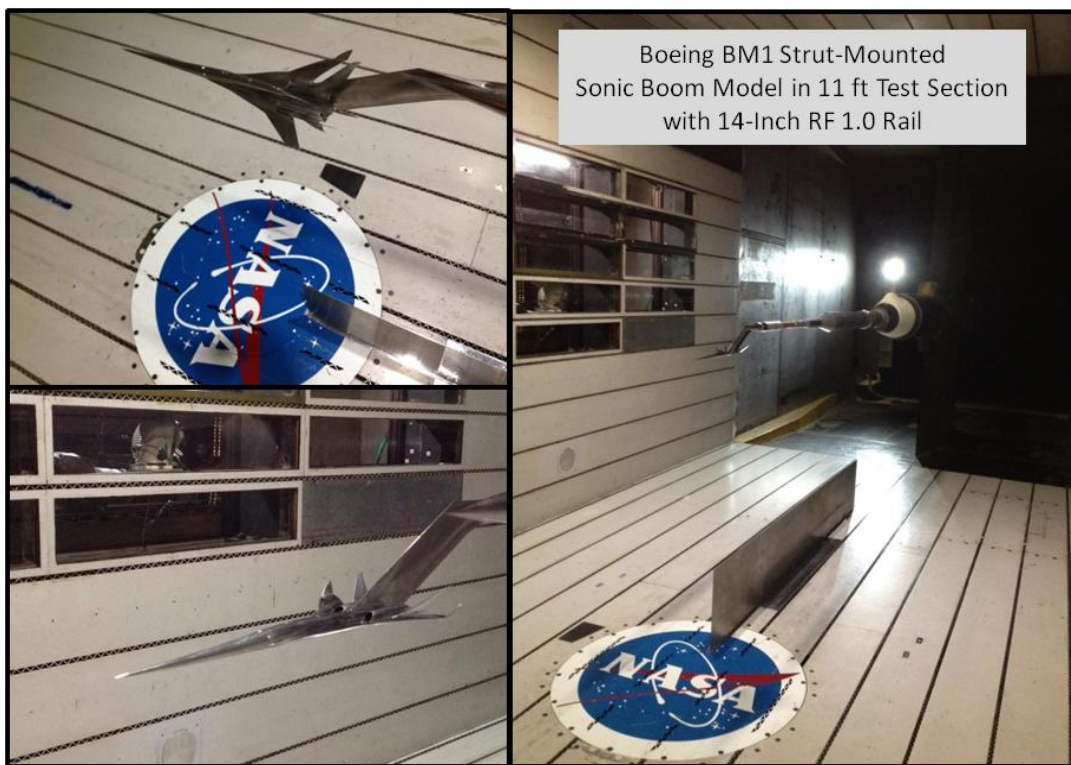


Figure 213.—Boeing Boom1 Model and RF1.0 Rail in 11 ft Transonic Tunnel

As a mitigation strategy for the dynamic motion, stabilizing fins were attached to the balance housing Wednesday night to attempt to provide some aerodynamic damping behind the aircraft model and blade support. As had been expected, testing Thursday morning showed no improvements with the addition of the fins.

By Wednesday afternoon, the test was approximately one day behind schedule, primarily due to tunnel downtime due to facility issues. Some of the cost impact was offset by downtime charges, but the test had fallen behind pace. By running some overtime after the normal end of shift, some of this productivity was made up, but progress was still a bit slower than desired. Additional funds were requested from Peter Coen at the Supersonic Program Office by Don Durston as the current funding level would have been exhausted by Thursday afternoon. The additional funds allowed testing to be completed on all three models by midday on Friday.

4.2.3.1.4 Thursday, June 7, 2012

On Thursday, testing was conducted with the Boeing Boom 1 model from about 08:30 to 11:30. Flow angle checks were conducted at various Mach numbers with the Boeing Boom1 model. To accomplish each model pitch angle change, the model must be translated from a measurement location at $H_{rel} = 38$ in. to the home location at $H_{rel} = 60$ in. and then the pitch angle is changed and the model was translated back down to 38 in. The desired angles ranged from $\text{Alpha} = -1.0^\circ$ to $+5.0^\circ$ in 0.50° increments. As a result of the awkward process, these surveys took a long time to complete. A similar problem exists at the 9x7 tunnel and is an unfortunate consequence of the hybrid model control consisting of the primary tunnel model control and the grafted on model roll mechanism and the x-ram linear translation actuator. These latter two items are not integrated into the standard tunnel model positioning and control software and are operated separately and independently.

During Thursday's testing, both X and Z translation sweeps were conducted at 0° roll, as well as sweeps at 20° , 30° , and 40° roll, all at Mach 1.25. Running at the higher Mach 1.40 speed was not possible due to poor model/sting dynamics, similar to that observed with the AS2 model earlier in the test, even with the "stabilizing" fins on the balance adapter. It was believed that the lateral vibrations were an excitation of the entire sting support system, so the small balance fins did not mitigate the motion much. With the Boom 1 model, runs at Mach 1.25 were avoided because of the ambient tunnel shocks potentially interfering with the model signature. It was thought that Mach 1.25 was a good work around to avoid the tunnel flow quality issue.

By midshift on Thursday, efforts were underway to begin changing to the larger-scale, sting-supported, Boeing Performance Model (PM1), with plans to begin testing this model on Friday. Installation of the PM1 model was completed Thursday at the end of the day shift. The existing sting/balance/Xram assembly was used without any changes. This is the same sting assembly stack as was used for the other two models (AS2 and Boom1). Official installation photos of the Boeing PM1 Performance model were taken Thursday afternoon by a NASA photographer. The PM1 model is shown in Figure 214.



Figure 214.—Boeing PM1 Sting-Mounted Large Scale Performance Model

4.2.3.1.5 Friday, June 4, 2012

On the last day of testing, the larger Boeing PM1 performance model was run. The model is sting-supported, as opposed to the blade support of the smaller Boom 1 model. The PM1 performance model was to be used for transonic drag measurements from Mach 0.80 to 1.20, as well as to measure signatures. It was noted that signatures would be compromised by reflections of the nose signature reflecting from the wall and interfering with the aft-end of the model signatures for this very large model, which is three times the size of the Boom1 signature measurement model (15.75 in. vs. 43.31 in.).

The large PM1 model experienced the same lateral oscillations as were observed with the AS2 axisymmetric model and with the Boom 1 blade-supported model. Although the PM1 model motion was somewhat smaller in angular magnitude, likely due to the increased weight, the larger model's physical size produced higher loads. As a result the PM1 model had similar problems with side force balance limits on the 1.00 in. balance as were observed with the Boom 1 model. Friday's test runs obtained one Z-survey and drag polars to get transonic drag trends. Testing was completed at 12:30.

There was a Boeing-NASA discussion regarding options to replace the Xram or other parts of the stack with tapered spacers, but this was not attempted at the end of the test. The consensus opinion was that this change would not correct the issue. A shorter stack was discussed to change the sting/model natural frequency, but there are limited options for potential locations to mount the 14 in. RF 1.0 rail on the floor of the 11 ft tunnel. This rail location dictates the model location needed, and thus the sting buildup stack cannot be easily shortened. With the sting assembly as installed for the 11-0249 test, there were three models which were all limited to 1.3 Mach.

In addition, testing at 1.2 Mach was hampered by the shocks which originate at the floor at the start of the test section upstream. These shocks reflect off the ceiling and interfere with the model location when the tunnel is run at 1.20 Mach. Testing was conducted at 1.25 and 1.31 as a result of these two limitations. This shock can be seen in Figure 215 crossing the nose of the PM1 model.

4.2.4 Test Observations and Issues

4.2.4.1 Model Dynamics

Model lateral dynamics were a problem at high speeds for each and every model during the 11 ft test. Three models were run, all with distinct and different characteristics, and all three displayed undesirable model lateral (left-to-right) dynamic motion. The lateral motion was worse at higher Mach numbers, and testing was typically limited to 1.31 Mach, rather than the 1.40 Mach desired.

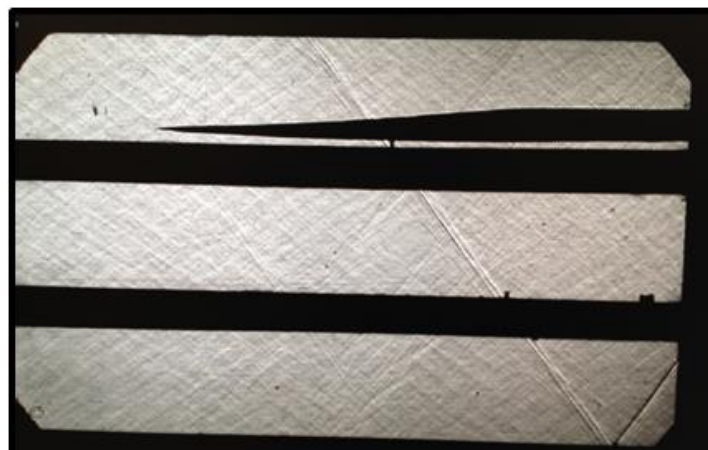


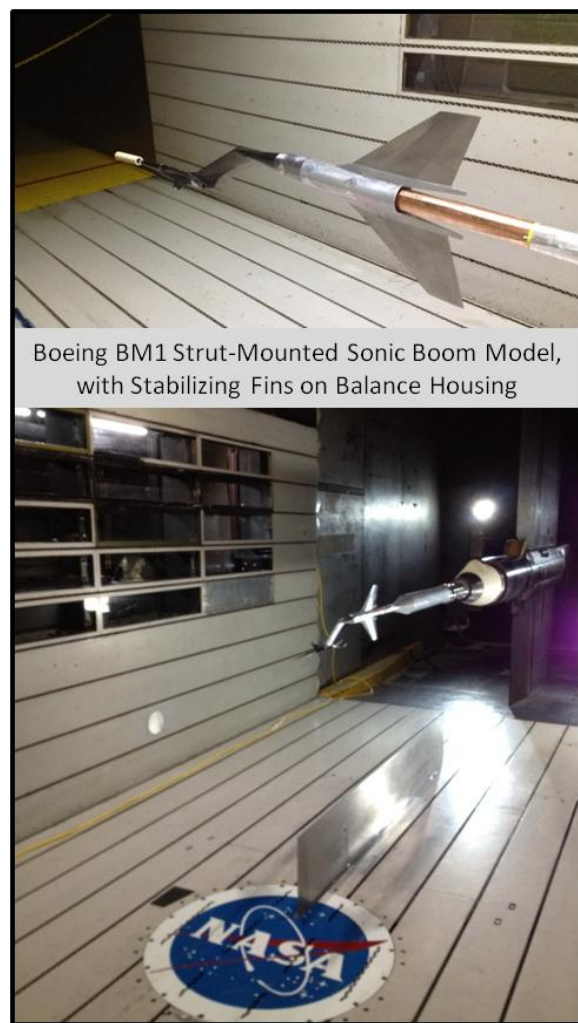
Figure 215.—Schlieren Image of Upstream Shocks Interfering With Boeing PM1 Sting-Mounted Large Performance Model

The AS2 axisymmetric reference model (a nonlifting body) had this tendency, as did the Boom 1 blade-supported aircraft model. The much larger Boeing performance model is approximately three times the size of the Boom 1 model and it sting supported. Because all three models experienced this problem, it is believed to be rooted in the long sting support stack and the relative stiffness and inertia of the components. Some dynamic tap-tests were conducted air-off to observe the natural frequency of the assembly. No free play was observed in the sting assembly when inspected by hand.

Mitigation attempts included the addition of stabilizing fins to the balance housing to provide aerodynamic damping and to improve stability, however these were unable to overcome the sting dynamics. These balance housing fins can be seen in Figure 216.

The addition of lateral damper cables was considered, but it was believed that with the increased blockage due to the 0.50 to 1.00 in. cables, the tunnel maximum speed would be reduced to about 1.30 Mach, which could already be run without excessive model dynamics.

Running at reduced dynamic pressure of $PT = 1450$ psf was attempted but without any substantial reduction in observed sting dynamics.



One work around which helped tunnel productivity was to increase BLAMS (balance loads monitoring system) side-force alarm limits to a higher level before setting off an audible warning and automatically stopping the run and returning the model to a “safe” or “home” position. Model dynamics are mostly observed in the S1 and S2 side force gages, and balance roll loads were well below balance limits. The alarm limits were initially set to 61 percent of balance capacity, and this was increased first to 64 percent and then to 74 percent of balance capacity.

When these hard limits were exceeded, the model was “safed” and was moved to a home position, alpha 0, Hrel 60 in. This doubled the amount of time it took to conduct a sweep survey, due to the fact that after every few points, data acquisition would be stopped, and the model would reset. In one 20 to 30 min time period, 12 safe/resets were observed while attempting to measure 15 to 20 Z-positions, with approximately 50 percent wasted time.

In addition, upon review of the early AS2 signatures, it was apparent that when the model survey was abruptly interrupted by the BLAMS system, the data acquisition was not completed with the full time-averaging desired (6 sec settle time, followed by 10 sec data averaging). The data which was cut short looked suspicious, although the fully-averaged X-surveys looked reasonable. Care must be exercised when using partially-averaged/interrupted data points, and signatures might be improved by removing suspicious stray points.

Increasing BLAMS limits allowed the number of resets to be dramatically reduced to a somewhat tolerable level. At the increased BLAMS settings, the limits are still exceeded on occasion, but at a more acceptable frequency.

Late in the test, there was a discussion regarding options to replace the Xram or other parts of the stack with tapered spacers, but this was not attempted. The hope was that this change might change the sting/model natural frequency or reduce any mechanical freeplay in the existing components. However, the 14 in. pressure rail location dictates the model location needed, and thus the sting buildup stack cannot be easily shortened.

4.2.4.2 Humidity

During the test, we learned that humidity control at the 11 ft tunnel is an “all or nothing” situation. We could not control humidity as was possible in the 9x7 tunnel. The tunnel can have either full injection of very dry air, or none at all. There is no true throttle-ability as was used in the 9x7 by modifying the mass flow of the HPA (high pressure auxiliary air). The initial plans at the start of the 11 ft test proposed running at/about 300 ppm with a 10 ppm tolerance from the reference run. Some discussion followed suggesting 250 ppm. The reality is that the tunnel frequently runs at humidity levels between 100 to 200 ppm, with the actual values trending based on whether the dry air is added or not.

At the start of the test, there was a lively discussion about the desired humidity levels and tolerances to run in the 11 ft tunnel. Originally, Don Durston and Eric Walker reviewed plots and requested that the tunnel should set a target humidity of 300 ppm ± 25 with a tolerance of ± 10 between reference and data runs. It was noted that this tolerance was more than 3x’s what had been used in the recent 9x7 tests. It was hoped that it would be easier to stay within humidity levels with the relaxed tolerance. Alaa Elmiligui recalled that a prior discussion had concluded that a level of 250 ppm or lower was desired. Susan Cliff recommended humidity as low as practical, rather than attempt to control humidity at a level such as 300 ppm. Initial data runs on Tuesday afternoon showed humidity immediately dropping to the mid-200 ppm range, and somewhat stabilizing at this low level.

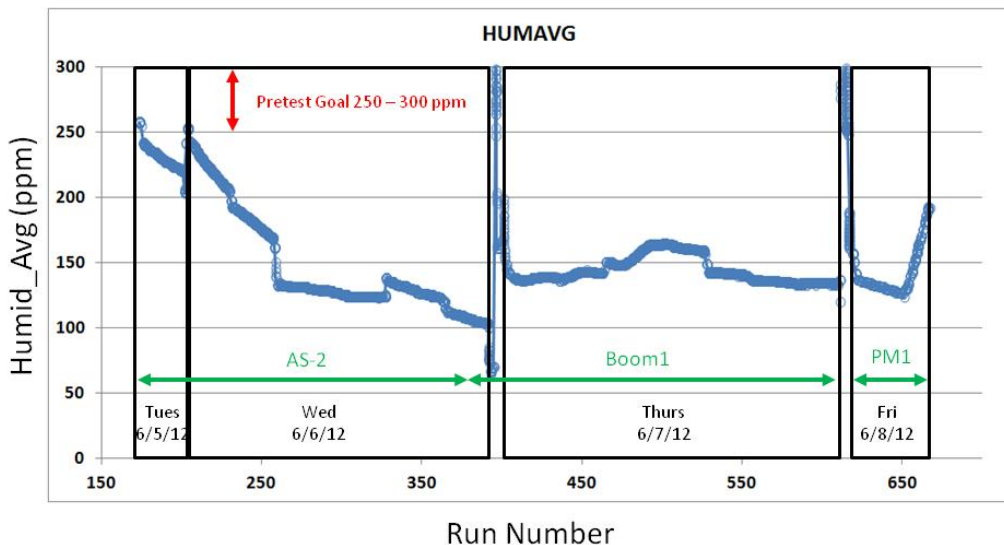


Figure 217.—Humidity per Run Number Throughout Test

On Wednesday, the first full day of running, the humidity control approach was better understood. An initial starting value could be set or established, but there is no way to control this during a run by throttling dry air injection similar to the approach developed in the 9x7 tunnel. At the 11 ft, the only option was to dump a continuous flow of ~30 lb/sec of very dry air into the tunnel. After running in this OCPE (Open Circuit Plenum Evacuation) mode for a few hours, the humidity continued to be reduced, resulting in very low humidity values. For example on Wednesday morning at the start of test runs, (08:30) the initial humidity was set to 250 ppm, and by midday (11:30), the tunnel was down to 100 ppm. There was not any method to actively control this behavior and data was taken as planned, to obtain reference runs, obtain and X or Z sweep, and then another reference run. Often there could be a humidity change of up to 10 to 15 ppm during a sweep. It was believed that the impact on the data would be acceptable because the humidity was at such low overall levels. This tunnel characteristic was similar throughout all testing in the 11 ft on each day that week, from Tuesday through Friday.

The humidity levels throughout the week of testing are presented in Figure 217.

4.2.4.3 Data Reduction Enhancements

The SDS (online data plotting system) had a new capability to plot spatially averaged signatures as data is acquired. Customer attendees were given a tutorial on the software Monday afternoon. This was a good real-time plotting tool and supplemented the analysis conducted by Eric Walker using MATLAB and by Susan Cliff using her methods. The SDS-based plotting was useful for viewing a signature for a quick check, but did not have the complexity, and analysis flexibility that is used with the more-capable MATLAB scripts.

Bob Langberg worked with Eric Walker, NASA Langley to add an additional layer of data reduction to his MATLAB scripts. This extra step removed tunnel residual effects which had not been completely removed by the initial reference run subtraction, but still appeared to be tunnel-fixed artifacts. The cleaner data was then model-aligned and spatially averaged to obtain a cleaner signature.

4.2.4.4 Schlieren Images and Test Section Flow Quality

Testing at 1.2 Mach was hampered by a number of shocks that originated at the floor at the start of the test section. They reflected off the ceiling and were located at the model location when running at 1.20 Mach. These shocks can be seen clearly in Figure 218 and interfere with the model shock signature.

Schlieren images were acquired at 10,000 frames per second and played live at a downsampled rate. The Schlieren images showed the expected shocks off the models and support structure as well as the ambient tunnel conditions similar to that observed in the 9x7 using their RBOS (retro-reflective background-oriented Schlieren) techniques.

The pressure rail leading edge shocks were visible as anticipated, with the shock from the rail/wall junction being the strongest, though a weaker shock from the rail leading edge corner was also visible. Also visible was the shock from the rail leading edge corner, after being reflected off the wall/boundary layer on the tunnel floor. These three shocks showed up and were positioned as had been expected in tunnel layout diagrams.

Curiously, there was a weak and periodic secondary flow phenomenon visible in the Schlieren images. When 200 frames were shown at 10 frames per second, some weak shocks (swept at angles less than the main flow Mach angle) were also visible. They seemed to originate on the floor and ceiling of the tunnel and appeared to translate upstream at an estimated rate of about 0.20 Mach. Speculation was that these may be occurring in the secondary plenum flow, outside the test section due to circulation and air extraction. This phenomenon is curious, and repeatable, but it was not believed to adversely affect the acquisition of the pressure signatures inside the test section itself. Images and video were taken for reference.

Schlieren images were viewed live and the flow phenomenon displayed were interesting. First, when the model was moving side-side, the shocks coming off the model were certainly affected, and this was easily viewed in the Schlieren images. This likely affected measured signatures and was expected to have increased rounding at the peaks. Secondly, the tunnel ambient flow displayed a half-dozen shocks, originating upstream on floor baffle covers. The shocks reflected off ceiling, and returned to cross the tunnel near the model. It was hoped that impact on measured model signatures was minimal, as the tunnel YBL might not be the same as the model which was located at the tunnel centerline. However, the actual impact on the measured pressure data was unknown. Still images and video of the Schlieren images were recorded.

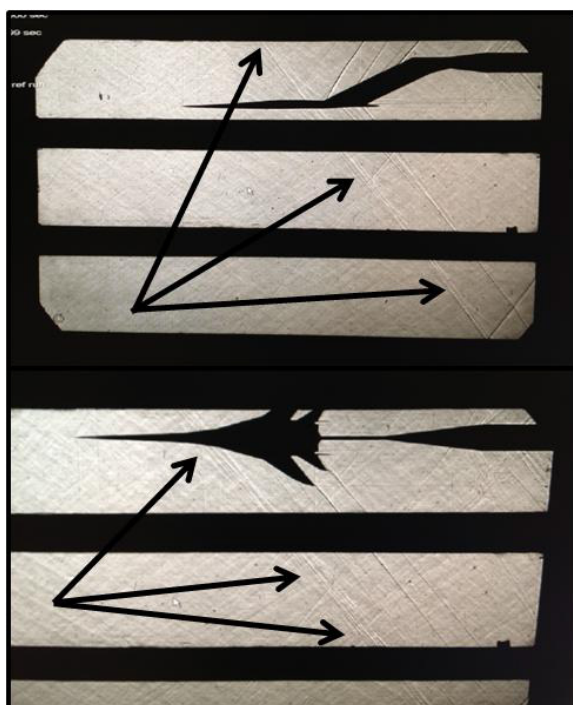


Figure 218.—Schlieren Images Show Ambient Shocks From Upstream Interfering with Boeing BM1 Sonic Boom Model



Figure 219.—The 11 ft Test Section Slot Baffles as Possible Disturbance Sources and Repairs

The suspect slot baffle inserts are shown in Figure 219 during testing, and during an attempt to repair them and make them flush with the test section floor. Only floor-located baffles were adjusted, as they were the suspect source of the oblique shocks which interfered with model measurements at Mach 1.20. By reviewing Schlieren images following the repairs, the problem had not been resolved. It was unknown what the exact source was for the oblique shocks and testing was conducted at higher and lower speeds to locate this flow feature ahead of, or behind the model.

4.2.5 Test Conclusion and Recommendations

The post-test debrief was held Thursday afternoon with all customers and tunnel operations leads present. Overall everyone on both sides of the table was happy with the execution of the exploratory test in the 11 ft transonic tunnel. It was recognized that the tunnel experienced a number of downtime issues, but that the tunnel crew addressed each as it developed and worked through each to resume testing.

A summary of the identified issues and the discussion topics is presented below.

- The 14 in. RF 1.0 pressure rail was said to have “no leaking ports”, whereas in the past, some leaks (typically 5 to 10 ports) could not be fixed and the blame was pointed at the internal hard lines or ferrules, which are a hardware issue that cannot be fixed with the flexible pressure lines or with the PSI module interface. A question was raised if we should confirm that all ports were indeed “good”, or if bad data (leaking ports) had been simply eliminated from the data stream, rather than being flagged with “99’s” as had been standard practice in earlier tests.

- Baffle slot inserts. Repair/adjustment was completed Thursday afternoon. Of the 14 baffle slots, about half (6) were protruding. Two had parts projecting from the wall by up to 1/8th in. Most were on the order of 1/16th of an inch from the flush wall. All may have been casting shocks back towards the model. Schlieren images from Friday's runs showed that, unfortunately, this repair effort did not correct the observed ambient tunnel flow shocks. This should be investigated further and mitigated if possible.
- Lateral sting dynamics problems remained unresolved throughout the test, and were observed with three very different models. Although a higher capacity balance would make it possible to run with the model dynamic motion, without tripping the BLAMS system, the motion would likely have the effect of rounding the measured signatures. It would be best to understand / fix root cause of the structural dynamics and mitigate this effect, rather than just work around it.
- Cavity pressure transducers were wired incorrectly at the start of the test. Downtime was credited, but troubleshooting did not quickly reveal the root cause, instead the data system "1413" card and enclosure were swapped out, thinking this was the glitch. The wiring problem was discovered later. The tunnel should be commended for being forthcoming about the issue and the resolution. This was an example of the great working relationship between the tunnel operators and the NASA analysts and Customer representatives which has developed over the course of testing activities.
- It was noted that with OCPE active, the tunnel dried out a lot, and humidity varied open loop. The air was very dry, but also highly variable and uncontrolled. Humidity during the 11-249 test was normally less than 200 ppm, and was commonly in the range of 130 to 140 ppm. In some of the more extreme cases, humidity was as low as 65 ppm.

The consensus was that this was a very successfully exploratory / shake down test, with issues identified rapidly in this short-duration test, rather than if they had been discovered for the first time in the middle of a more substantial testing effort. Lessons learned from this test should be considered when planning future sonic boom measurement test activities.

Testing was conducted at 1.15 and 1.31 as a result of the flow quality and sting dynamic limitations, rather than the desired 1.20 and 1.40 Mach numbers in the pretest planning.

Boeing stated that despite the challenges and issues encountered in running this exploratory test, that the objectives of this exploratory test were met by "investigating and learning about the particular issues and challenges of how to conduct sonic boom measurement testing in the NASA Ames 11-ft Transonic Wind Tunnel". Data obtained can be used to characterize the spatial and temporal uncertainty in the signatures measured in this tunnel.

It is Lockheed's opinion that the NASA Ames 11-ft Transonic Wind Tunnel can be used to measure sonic boom signatures, but only at specific test conditions, and that care must be exercised in test planning to select desired data runs which can be measured successfully. In particular the following issues were test concerns that should be mitigated if possible before another test:

- The tunnel maximum Mach number of 1.40 may not be achievable due to adverse model / sting dynamics. Efforts should be conducted to understand and possibly mitigate this issue.
- The possible contamination of the measured signatures by easily observed upstream tunnel-ambient shocks are a concern when testing at/near Mach 1.20. Empty-tunnel data runs with the Schlieren system can be used to diagnose and perhaps understand and mitigate this issue. It is possible that the shocks originate in the flow interaction taking place at the initiation of the tunnel wall boundary layer removal baffle slots, and that with these slots open and present this adverse flow behavior may not be easily corrected.

- It is noted that at some lower Mach number, the model shock reflection from the floor will limit testing with the 14 in. RF 1.0 pressure measurement rail.

4.3 Glenn 8x6-12-002 Boeing Test

The NASA Glenn 8x6 tunnel showed promise for covering a greater Mach range (0.3 to 2.0), including continuous coverage of the sonic boom range 1.0 to 2.0, and being able to make sharper sonic boom measurements than the (previous best) 9x7 tunnel. However, drift in the tunnel ambient pressures whenever models were moved, introduced offset errors large enough to spoil measurements. Indications are that keeping the Mach number from drifting when models moved, would result in superior measurements.

The NASA Glenn 8x6 tunnel has several unique features that make it attractive to use for sonic boom measurement. First among them is its tri-sonic ability to run all Mach numbers from 0.3 to 2.0. Supersonic tunnels, like the Ames 9x7, cannot run Mach numbers below 1.55, and the Ames 11 ft transonic tunnel had difficulties taking sonic boom measurements in the Mach 1.0 to 1.4 range, as detailed in the previous Sections 4.2, 5.2.4, Figure 215 and Figure 218. The Glenn 8x6 also has straight, symmetrical flexible walls for its nozzle and a porous transonic test section implemented through angled cylindrical bleed holes of 1 in. diameter (Figure 220). The porosity did not seem to help measurements at Mach 1.6 and there were indications that if the rail had been positioned in the influence of porosity, measurements probably would have been worse. Future testing is likely to try the upstream nonporous test section and perhaps the porous section for Mach's close to 1.0. These facility options provide some advantages; however, there was also previous experience with problems measuring sonic boom in the 8x6.

The DARPA QSP (Quiet Supersonic Platform) program funded the F-5SSSBD (Shaped Sonic Boom Demonstrator) modification and did their sonic boom testing in the 8x6 in 2002. Using the best setup of the time, moving their model past fixed probes (10 in. from the wall), they measured varying, erroneous results. They even made a second entry with somewhat improved results (from changes in probe tunnel location), but the validation accuracy achieved was much worse than our current requirement. Further, Figure 221 shows that the 8x6 has a larger P_{static} variation through its test section (as measured by the RF1.0 rail), which is the cause of flat-top pressure distortions from the tunnel flow-field discussed in the earlier N+2 Phase 1 report (Ref. 10) (section 5.1.1 LM1 and 5.1.3 LM3 descriptions). Consequently, there was concern before the test that this might not be a good facility for the highly precise shaped boom measurements that our advanced designs now require.

During the test, spatially averaged signature calculations were not matching previous measurements, as they had between the LM3 97-0231 and the Parametric 97-0250 tests. After much analysis, a parameter was found with a repeating, proportional relationship to the problem: tunnel Mach number was drifting with model motion (but not proportional to motion) and rail reference pressure changed proportional to the Mach change. Changing the tunnel strut height caused particularly large rail pressures drift of $\pm 0.015 \Delta p/p$. Measurements and references were tried at a fixed strut height using only linear actuator X motion. This reduced rail pressures drift an order-of-magnitude to $\pm 0.0015 \Delta p/p$, as shown in Figure 222 (and expanded in Figure 223). Signature detail from 49 in. distance looked even better than the Ames Test 250 data (scaled from 30 in., blue line), but the level drifts (red arrows) were large enough to cause unacceptable errors, greater than 5 PLdB.



Figure 220.—The 8x6 with Angled Bleed Holes on Walls, Model Hardware on Floor Strut and RF1.0 Rail on Ceiling

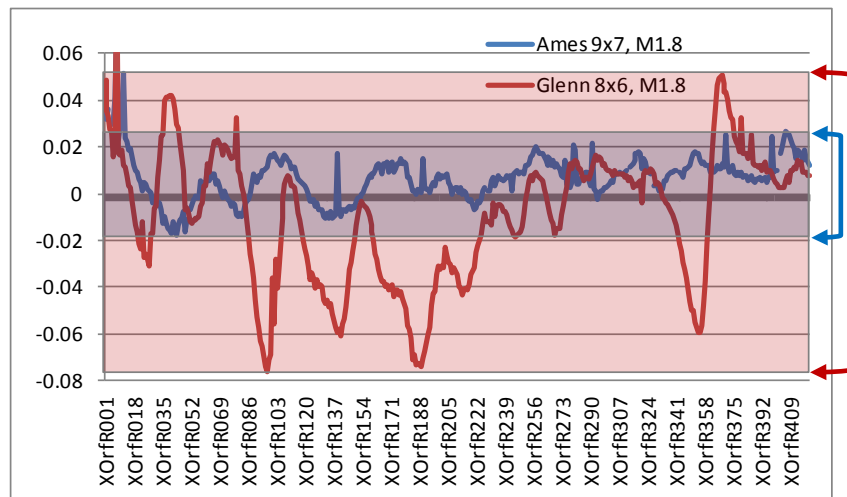


Figure 221.—Glenn 8x6 has Greater P_{static} Variations Than Ames 9x7, Which Distort Slope and Zero of Measurements at Every Rail Orifice

Best 8x6 Signature: G61refG62 ($h = 49''$)

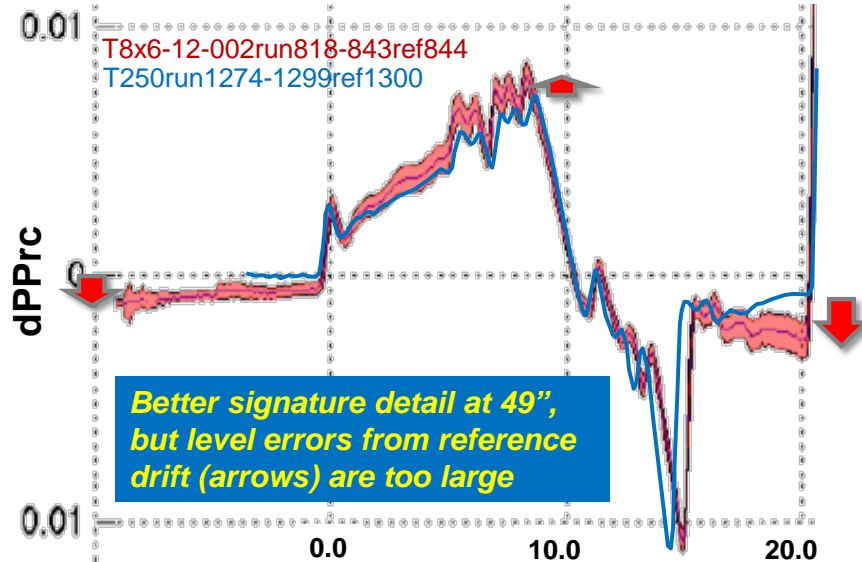


Figure 222.—Better Signature Detail Marred by Varying Level Drift

Looking into more details of this comparison revealed and quantifies some relationships that seem to explain the level drift. From orifices on the measurement rail ahead of the model, the tunnel pressure minus reference is plotted in Figure 223 for these same signature measurement sets. The upper left plot of Figure 223 has 26 lines of pressure through each orifice for the 26 time points that measurements were taken in the 9x7. The upper left plot is the same data from the 8x6 (with fewer orifice repeats toward the right side of the plot). The lower plots show a line with the average value of the above data. Excluding drift, the Glenn 8x6 data has significantly less variation. But averaging the Ames data results in pressure virtually identical to the reference, making the model average measurement minus reference very accurate. Plotting the Mach for the same Glenn 8x6 runs reveals that the reference measurements (X_{ram} at 0 in.) both before and after the model measurement translation (X_{ram} from 16 to 24 in.) are at the same Mach, 0.001 greater than the model measurements, Figure 224 (plotted from dataset column 36 with header “Mach”), and the reference measurements match, unlike measurements when the Mach is 0.001 lower. Figure 225 shows the change in tunnel Mach with change in model position (in this case height change). Unfortunately, pressure changes and tunnel Mach changes are not proportional to model position change and also seems to have a time-dependent lag behavior. However, Figure 226 shows that pressure changes are directly proportional to changes in the measured tunnel Mach—each orifices’ pressure changes in a straight line with changes in tunnel Mach. The proportionality indicates that drifting changes in reference pressure in the Glenn 8x6 would be avoided if the Mach could be held to an average variation less than ± 0.0002 during a measurement and reference set. (More specifically, Mach could vary more than ± 0.0002 as long as the averaged Mach was within ± 0.0002 of the reference measurement Mach; however, less variation should result in sharper spatially averaged measurements.) Ideally, Mach variation should be eliminated even when the strut height is changed, so the best measurement locations and procedures can be used without restrictions.

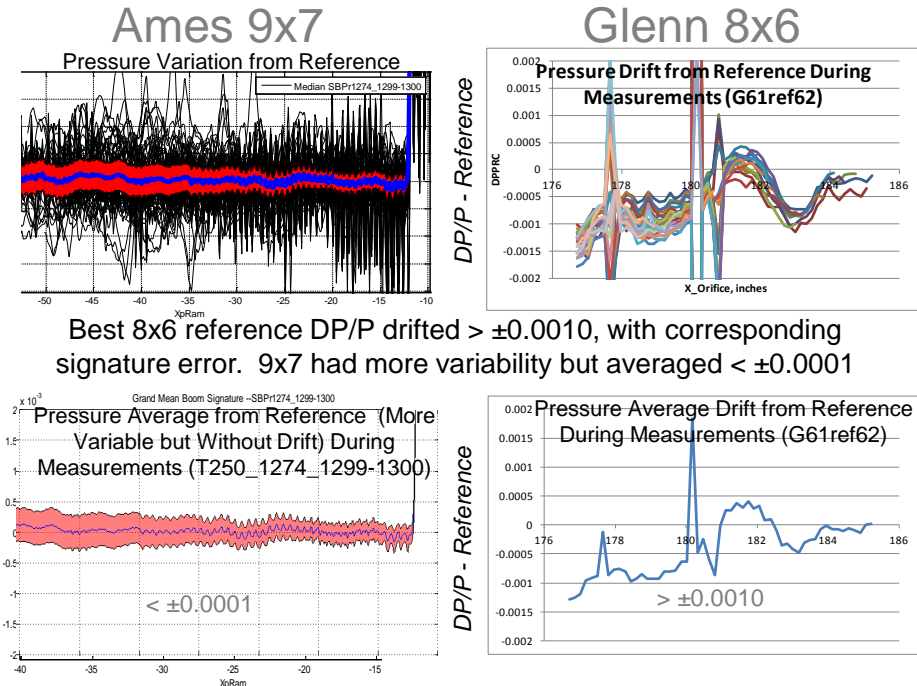


Figure 223.—Glenn 8x6 Ambient/Reference Drift Too Large (even at same strut height)

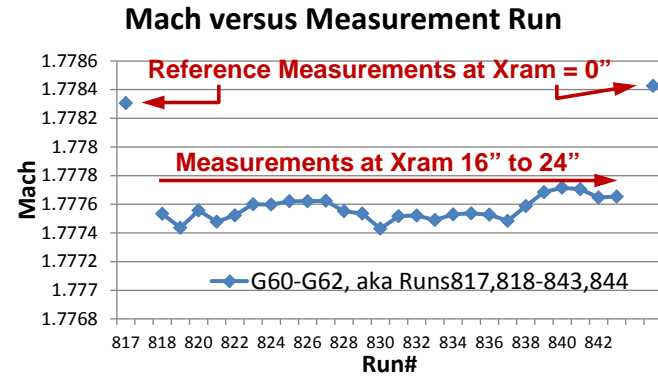


Figure 224.—Change in Reference Measurements Correlates With Change in Tunnel Mach

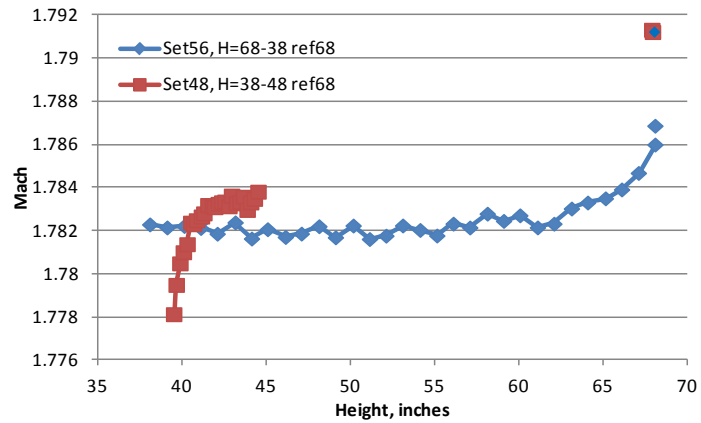


Figure 225.—Mach Change With Model Position Not Proportional (red increasing H, blue decreasing H)

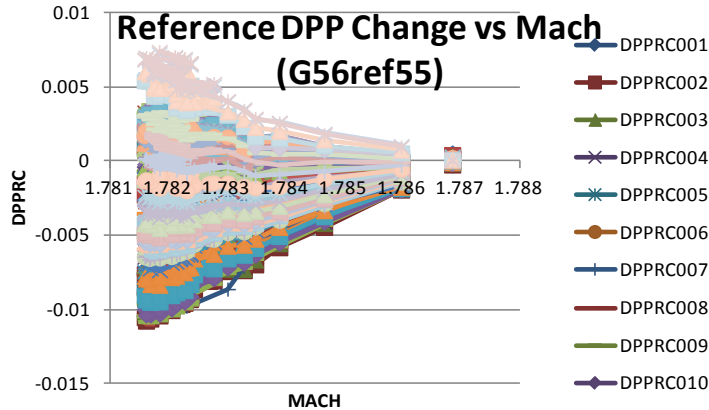


Figure 226.—Orifice Reference Pressures Change in Direct Proportion to Mach Variation

Understanding the extreme sensitivity of shaped sonic boom measurements to tunnel Mach changes (and potentially other parameters like humidity, temperature, etc.) can be derived from understanding the measurement process and supersonic test section flow. The model pressures we are measuring are smaller than the static pressure variations found through all supersonic test sections. We measure model sonic boom from the difference between model propagated pressure (Mach cones) on the rail and reference ambient by moving the model aft and/or up until its propagated pressure (Mach cones) is behind the model pressure when measured. The reference ambient flow-field must be maintained exactly as it was when the model was being measured. One challenge with precisely holding the flow-field condition is that any slight parameter change that changes the Mach will change Mach angle, and thereby, position of the shocks propagating from the nozzle through the test section. All supersonic tunnels have test sections crisscrossed with shocks that form at the tunnel nozzle. The nozzle diverges after its throat to accelerate the flow supersonically, and then, bends the flow back straight with relatively substantial turning angles, often in double digit degrees. Such compression shocks have zero dissipation in the short distance of a wind tunnel. These “shock diamonds” and their static pressure variations (note: little total pressure change since Mach and static pressure titter totter isentropically) tend to be 10 to 20 times larger than subsonic test section variations (unique supersonic consideration for testing of laminar flow, sonic boom, model surface pressure, etc.). During sonic boom measurement, any parameter that slightly changes Mach angle will shift the entire test section flow-field forward or aft. And just an orifice or two displacement of the flow-field at the rail will unacceptably change the reference pressure because of the static pressure oscillations (Figure 221).

4.4 Ames 9x7-0254 LM4 Test

The NASA Supersonics Program’s overall objective was to promote and validate the capabilities needed for supersonic transportation. Shaped sonic boom over land was identified as a “game changing” enabler and was selected for primary development by this N+2 Supersonic Validations contract. Our Phase 1 results validated shaped boom near the quietness expected for over land flight with a very high performance design, showing that shaped boom and high performance are not mutually exclusive. However, that design did not achieve full carpet shaped boom. Its shaped boom shaping broke down for ray roll angles of 30° to 50°, which were louder than 0° to 20°. So for Phase 2, LM had 3 objectives in mind:

1. Validation of a refined, full-carpet shaped boom configuration
2. Accurate shaped boom measurements beyond near-field interference (48 to 80 in.)
3. Improved productivity shaped boom test procedures

These 3 objectives were chosen to demonstrate that total mission shaped boom flight is achievable. The previous LM3 test results validated our CFD predictions in the near-field. To determine how close the measurements matched prediction (expressed in ground sonic boom loudness) compared with the less than 2 PLdB difference requirement, the measured data was substituted for the predicted data where available; then, the mixed measured and predicted data was run through our LMBOOM cylinder/multipole far-field correction method to get a far-field propagated ground signature. We'd like to further boost our methodology validation confidence by matching a second model.

Figure 227 shows an application of the far-field correction to CFD with results extracted at various distances from the vehicle. The far-field corrected solutions are all nearly identical, except a slight difference for the shortest extraction distance of 2.8 semi-spans—which still has a corrected aft signature between the 11 semi-span and ∞ results. At close distances, the multipoles can have difficulty fitting the strong shock discontinuities; so flow-field accuracy suffers, the correction accuracy degrades and the error is multiplied by a larger correction magnitude. But Figure 227 shows the 2.8 semi-span corrected extraction is closer to far-field than the uncorrected extraction from 11 semi-spans. The far-field correction method uses an 11-term Fourier-fit versus roll angle for each X-station's half-circle of CFD data. The method "misfit" error quickly diminishes at greater distances with weaker pressures to fit and a smaller correction magnitude. While a repeatable far-field result is obtained from different extraction distances and the far-field result appears to be a reasonable far distance asymptote, it has never been test validated. And the method's far-field correction almost always results in stronger pressures and greater loudness than uncorrected results. So accurate measurements at distances beyond near-field interference were desired to validate the pessimism of our far-field correction method.

To validate full-mission shaped boom, there are more roll angles and conditions to measure, so productivity improvements make all validations more affordable. Many improvements were successfully identified and implemented in the LM4 test, reducing measurement set time to 5 to 10 min and increasing the number signature sets measured to 5 times greater than LM3 (in slightly less time).

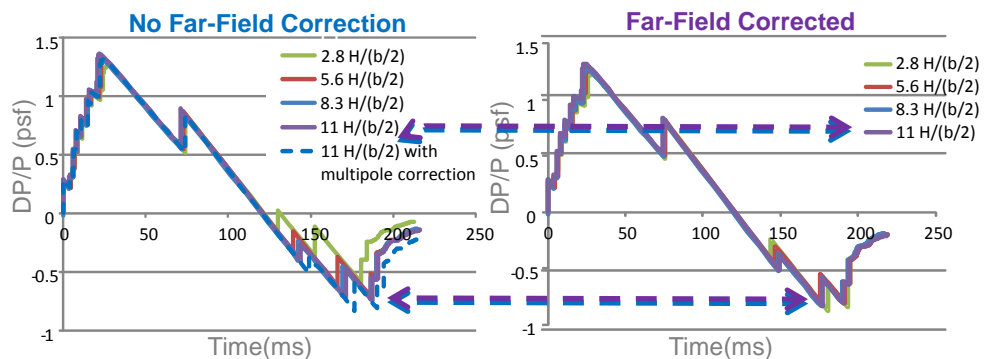


Figure 227.—The Far-Field Correction Method Provides Consistent Results Matching the Uncorrected Data's ∞ Distance Asymptote

4.5 Test Planning (Productivity Tolerances, Test Models, Processing)

Test planning focused on achieving the three objectives, briefly put: 1044-02 validation, accurate far measurements and improved productivity. Near validation measurements were planned similarly to Test 250 to repeat its success with the 1021-01 model. Most new planning focused on ways to improve far measurements and on diagnostics to understand why measurements degrade as measurement distance increases. The smaller 1044-02 model allowed Z sweeps to measure heights from 70 to 42 in. (rail at aft window) and 42 to 20 in. (rail at forward window) for a continuous investigation of measurement height variation. X sweeps were run at heights of 31.8, 42, 54, 61, and 70 in. And to improve far measurement accuracy, the old SEEB-ALR and new 70° Flat-Plate calibration models were run at 54 and 70 in. X sweeps and 70 to 42 in. Z sweeps (both Mach 1.6 and 1.7 with repeats). As illustrated in Figure 228, the 70° Flat-Plate Delta model produces little disturbance below it. Shock reflections from the Flat-Plate are expected to get stronger as the model is translated forward and the shock reflects off an increasing span. The relationship with local span may improve calibration matching to models with wings and tails.

Further improvements to far measurement accuracy were expected from three new data processing refinements that were implemented on this test's measurements termed: automatic reference measurement trimming, elimination of highest/lowest measurements and reverse aging in spatial averaging. Simply put, automatic reference trimming omits any orifices on the rail that still are impacted by model pressures when the model is in its back and up position for reference measurements. Figure 229 shows that during a reference measurement the model pressures may still impact the aft portion of the rail, so rail orifices corrupted by the model during a reference measurement are omitted from spatial averaging. Figure 230 shows the improvement from omitting/trimming the aft rail orifices corrupted by the model.

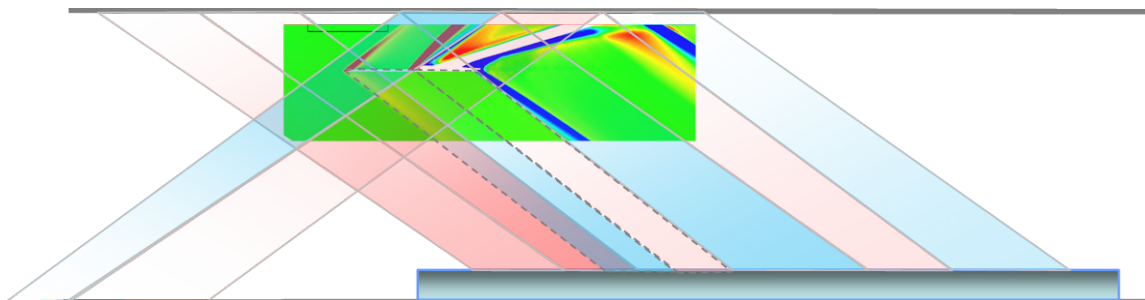


Figure 228.—As the 70° Flat-Plate Model is Advanced Through the Flow-Field, Rail Measurements Quantify How Reflected Shock Strength Varies With Model Span

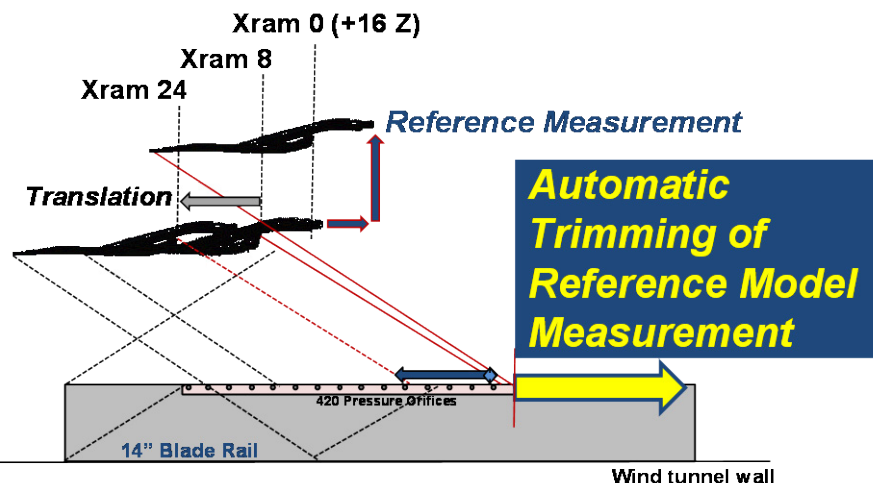


Figure 229.—The Model is Moved Back and Up for a Reference Measurement But May Still be Measured on the Rail—Orifices Not Ahead of the Model are Omitted from Spatial Averaging

Elimination of the outlying highest/lowest measurement extremes before averaging tends to omit the same orifices where the tunnel flow-field distortions are largest. Eliminating the worst 10 to 15 percent of extremes, Figure 231, has been as effective as taking 10 to 15 percent more measurements, so a significant efficiency boost.

Even over the relatively short measurement distances in the wind tunnel, signatures age—meaning that the higher pressures propagate faster while lower pressures propagate slower. When pressures are distorted in amplitude by the flow-field, it affects their aging and leads to a correspondingly distorted position, grey lines in the left plot of Figure 232. Reversing the aging realigns the pressures with the locations where they were produced, grey lines in the right plot. The realigned pressures are averaged and re-aged to produce the final spatially averaged signature. This implementation of reverse aging in spatial averaging is still being refined and may produce even better improvements in future versions. Reverse aging is also particularly important to include when interpolating on CL or alpha, and this routine is being expanded to include CL interpolation. These measurement, calibration and processing improvements were intended to address the objective of improving far measurement accuracy.

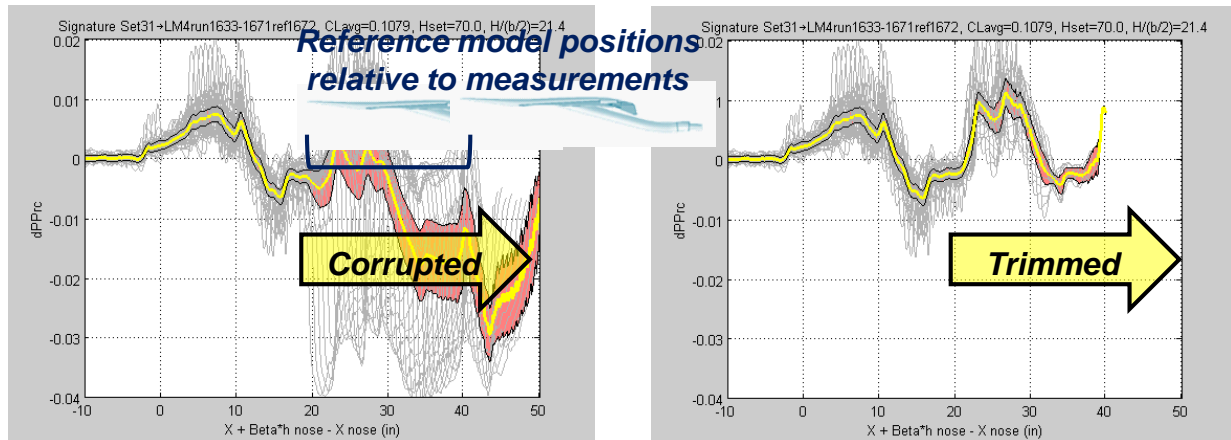


Figure 230.—Automatic Reference Measurement Trimming Removes Only the Data With Model Intrusion and Keeps the Good Data for Resolving the Trailing Signature

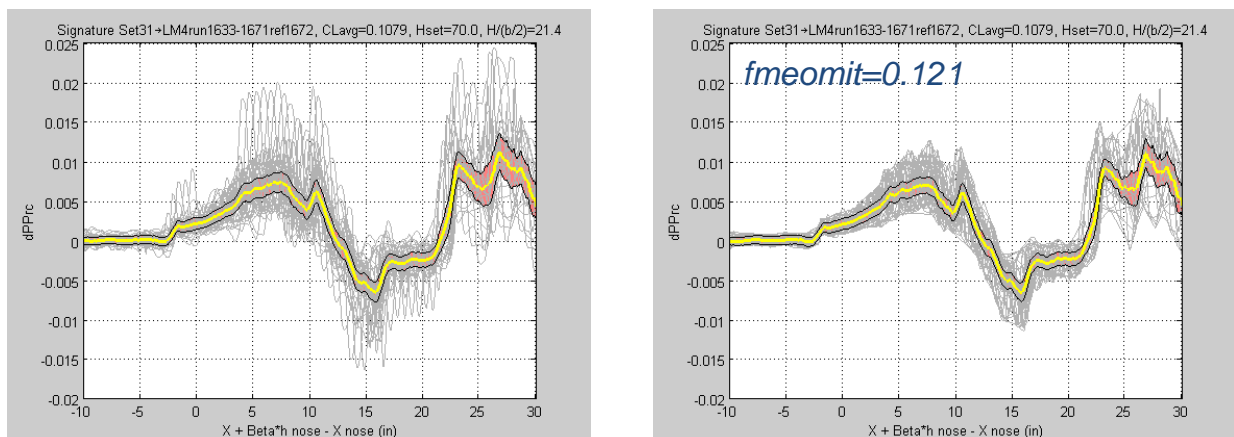


Figure 231.—Omitting a Fraction of the Highest/Lowest Measurements Extremes, Smooths and Sharpens the Spatially Averaged Signature

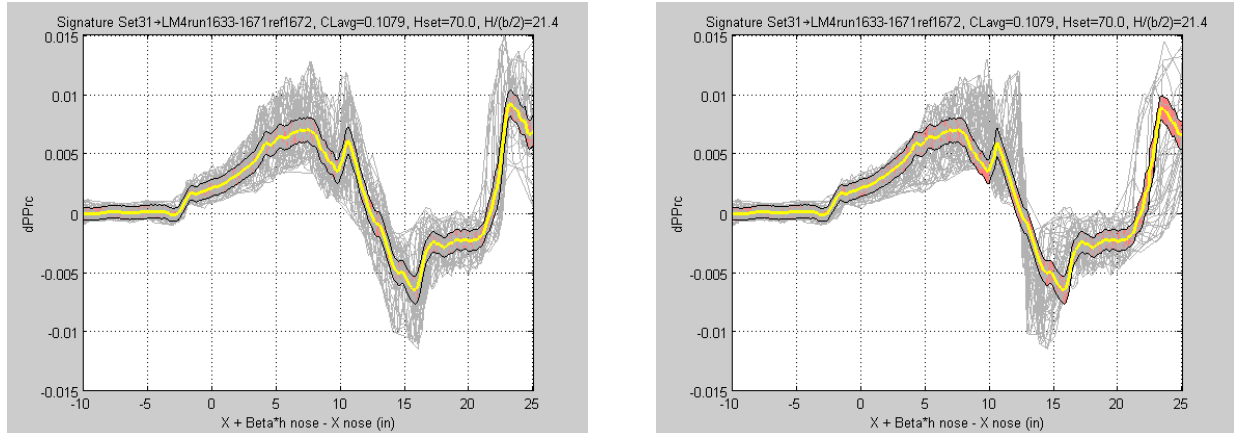


Figure 232.—Reverse Aging, Averaging, then Re-Aging Achieves a Slight Sharpening of the Spatially Averaged Signature

The last objective of improved productivity was addressed through rigorous reconsideration of measurement procedures and tolerances. A thorough investigation was made of tunnel data time stamps to determine where nonproductive time was being consumed. As mentioned previously, much time was lost when humidity or other test conditions could not be maintained within tolerance. Study of Test 250's sensitivities to condition variations, using statistical data analyses by NASA and the high accuracy of spatial averaging, allowed substantial increases in tolerances to be implemented that resulted in no time being lost off-condition. Further, the tolerance and process by which the tunnel crew set a model's CL, alpha, roll angle, etc. could be very time consuming, or not, depending on a string of many factors. Lengthy communications with the tunnel crew to compare their facility capabilities and limitations with our measurement needs, eventually revealed why certain condition specifications were time-consuming. Ways were found in all cases to make changes, which still satisfied our data needs, but were far less time-consuming for the tunnel crew to execute and made more run time productive. While the process analyses consumed a lot of planning time, it was clear that we were going to achieve substantial productivity improvements and a lot of the communications occurred during the 231, 250, and 249 tests. LM4 97-0254 post-test analyses documented the dramatic improvements in productivity achieved since LM3:

	LM3	LM4
Model Changes	5	10
Measurement Runs	671	5377 (8 times more)
Signature Sets	25	137
Shifts Consumed (8-hr)	16	15

In summary, 8 times more measurement runs were taken. Because more measurements were taken per set to try to improve far measurement accuracy, only 5½ times more signature set spatial averages were compiled from those 8 times greater measurement runs. And twice as many model configurations were tested, including a rail location shift from the aft to the forward window. Measurement of a signature set that took 50 min on LM3 was down to 10 min on LM4.

One productivity improvement was not considered early enough to obtain the required funding, but would have eliminated 3 tunnel stops for model changes and eliminated the 4 hr required to move the rail from the aft window to the forward window. The RF1.0 rail was originally designed to span both windows continuously; but to reduce the initial cost of trying the concept, only half of the measurement portion was built with removable leading and trailing edge pieces that would allow the other half to be built and inserted later. In the meantime, near and far measurements are accommodated by moving the half rail from one window to the other. Since spatial averaging is the standard measurement technique, its accuracy is improved by longer lengths of measurements taken in tunnel positions with better flow. As shown in

Figure 233, doubling the rail eliminates a large band of obstructed measurement locations where model measurement translation would cross over the aft/forward rail positions. There is also a 19 in. zone where Xsweeps cannot be run between heights of 35 to 54 in., unless a stack extender (for example the MSA) is used to locate the model farther forward with the forward rail. With a 36 in. extension, the 1044-02 model could be measured at a height of 68 in. on the forward rail but this setup's minimum height would then be 44 in. With the rail doubled, longer translations in better flow can be used for more accurate averaged measurements and all heights can be measured without shutting down the tunnel and moving the rail.

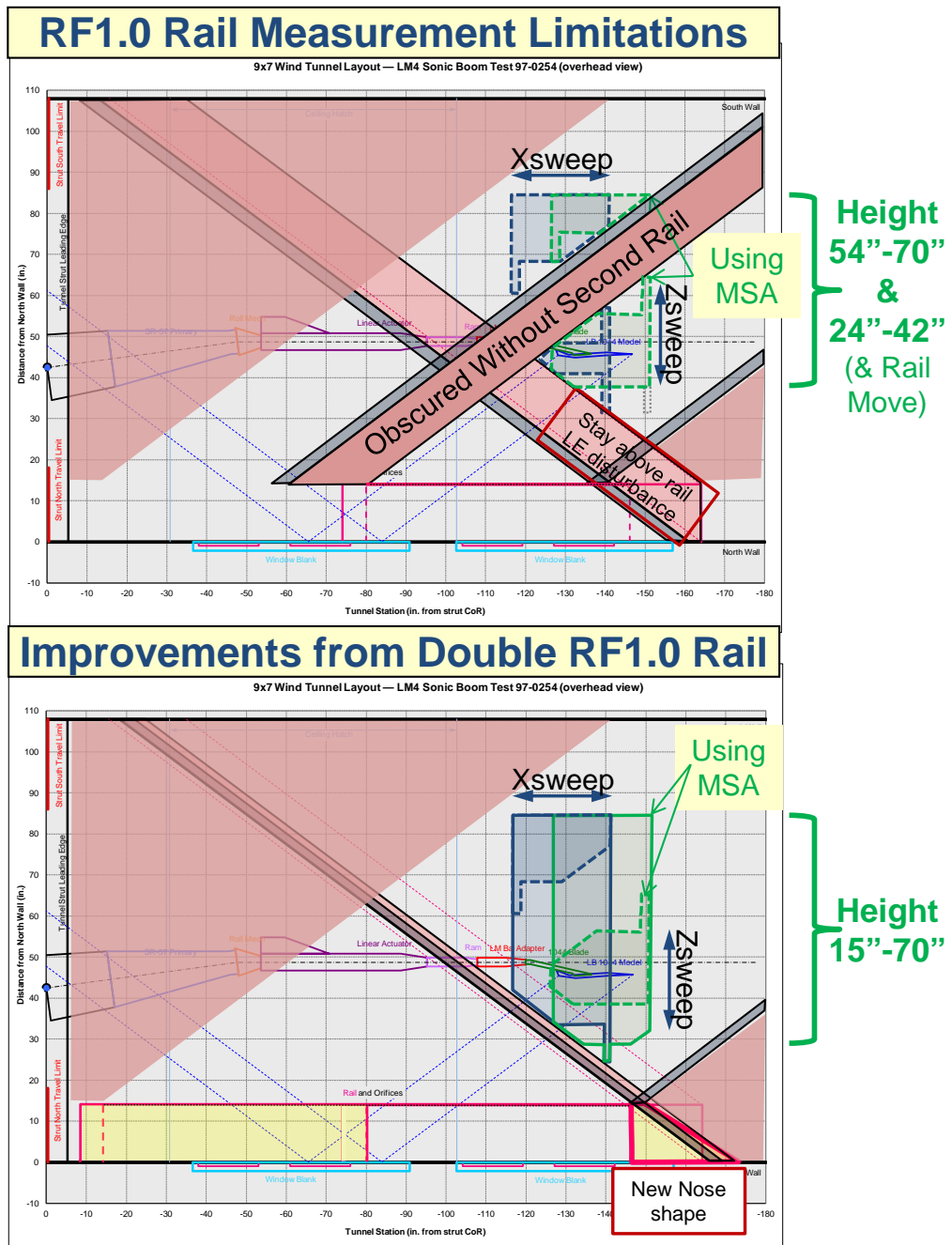


Figure 233.—Doubled Rail Increases Position Options and Translation Length—Improving Measurement Accuracy, Plus No Stopping to Move Rail between Near and Far Measurements

4.6 Model Design

The 0.0065-scale LM4 wind tunnel model offered more location flexibility with wind tunnel support hardware and allowed testing at lower Mach compared to the larger, 0.008-scale LM3 model. The 19-in. long model featured removable flow-through nacelles that allowed exploration of alternate configurations, e.g., centerline nacelle-only and outboard nacelles-only, Figure 234. The highly-swept, LM3-based blade support attaches with no model geometric distortion, and its flow field distortion is minimized by being primarily on the model upper surface and swept greater than the Mach cone angle, illustrated by CFD analysis in Figure 235. The blade thickness was sized to a minimum at the vehicle, which necessitated a slightly increasing thickness going away from the model to counter the increasing moment arm from the running loads. Figure 235 provides a vivid illustration of the model support blade's effect of the flow-field above the vehicle and very small effect below the vehicle. Unlike the LM3 model, no provision was made for a second, alternative model sting support.

Figure 236 compares predicted boom signatures of the supported model with that of a free-floating model in the tunnel. The data show that the blade mount has a minimal impact on the signature out to 40° off-track, with a gradually increasing influence beyond that point due to the compression and expansion generated by the blade spilling over the wing.

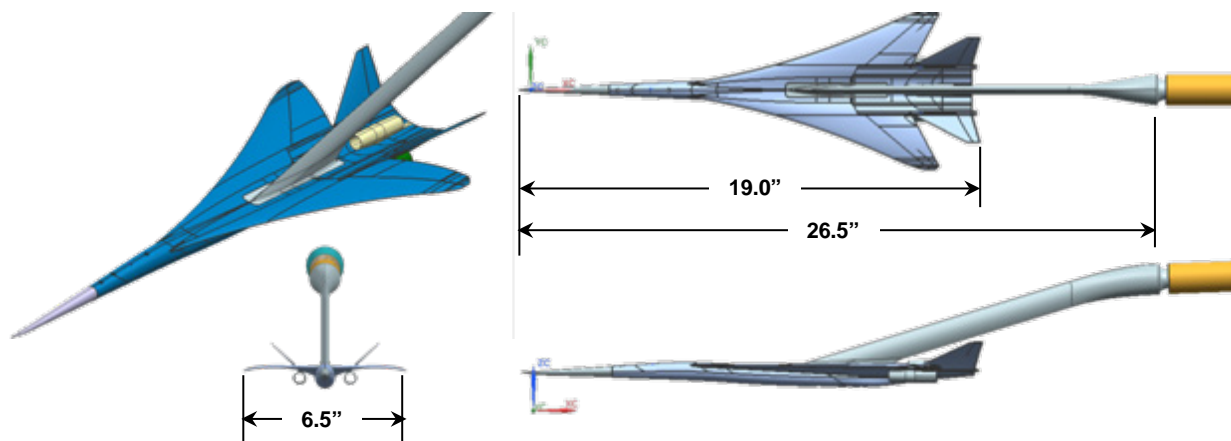


Figure 234.—LM4 Wind Tunnel Model of 1044-2 Configuration

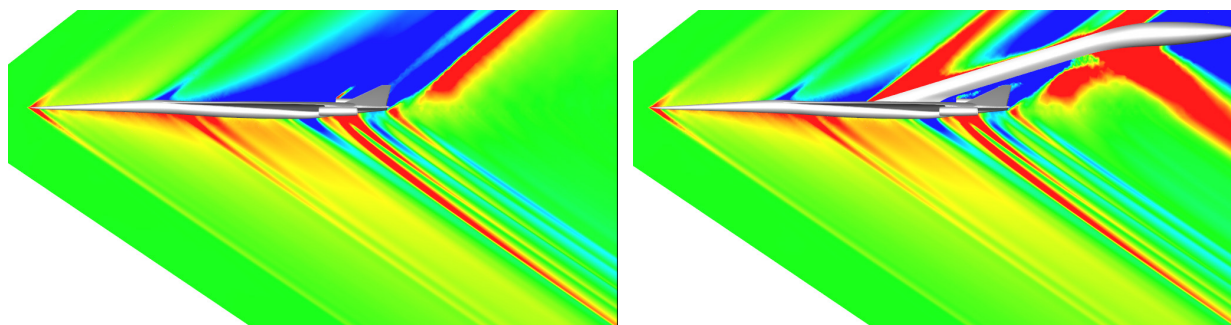


Figure 235.—Symmetry Plane Pressure Contours: No Blade (left) and With Blade (right)

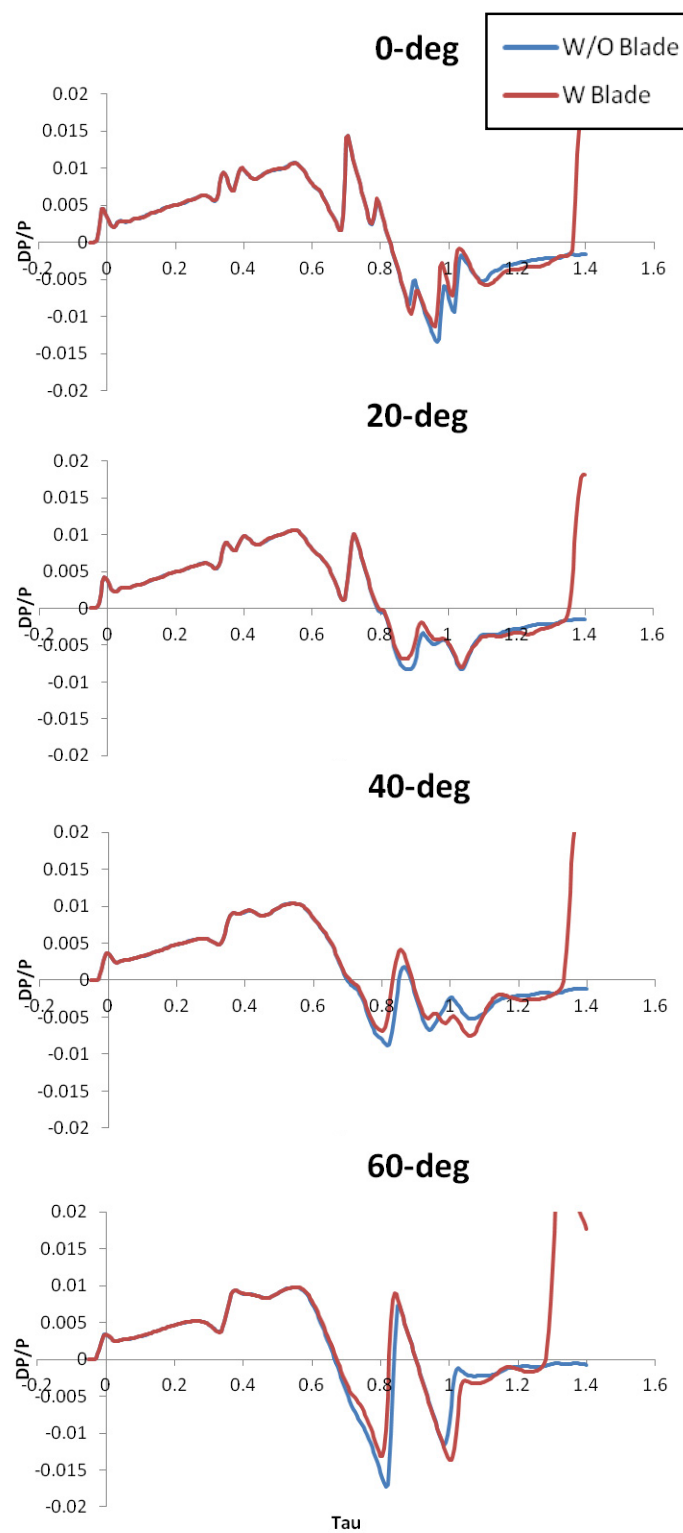


Figure 236.—Blade Effects on Model Signature

Viscous simulations at wind tunnel Reynolds numbers show centerline inlet ingesting the blade wake, strengthening the shocks inside the duct, Figure 237. However, pressure recovery map indicated the flow will not choke, Figure 238. Note that the analysis was done using sharp nacelle LE and TE.

The 0.010-in. edge thickness and 0.030-in corner fillets were incorporated to facilitate model fabrication. Wing, tail and aft-deck edge thickening were accomplished via a simple upper surface offset without changes to the lower surface contour. As of the flow-through nacelles, the thickening involved both OML and IML modifications. To prevent the thickened LE and boundary layer buildup from chocking the flow, the IML was given a small outward expansion after first being offset toward the center. For the centerline nacelle, which has minimal boom signature contribution due to empennage/fuselage shielding, the aft 1/3 of the OML was re-lofted to match the increased exit area with thickness increment. The outboard nacelles, which have significant influence on the signature, required a different approach. Instead of outward expansion of OML that adds compression and intensifies the reflected shock, the OML was held fixed while the exit plane was moved forward until the distance between the IML and OML matches the desired edge thickness. Figure 239 shows the surface pressure distribution of the sharp and thickened models. A stronger yet more diffused lip shock is evident with the thickened model. In the case of the centerline nacelle, the compression from the flare-out weakened the expansion fan at the nacelle closeout. As of the outboard nacelles, pylon shock attenuation was reduced due to weaker expansion coming off the truncated nacelle, resulting in stronger reflected shock. Figure 240 shows the manufacturing-driven modifications have limited effect to the predicted boom signature and can be easily removed with increments.

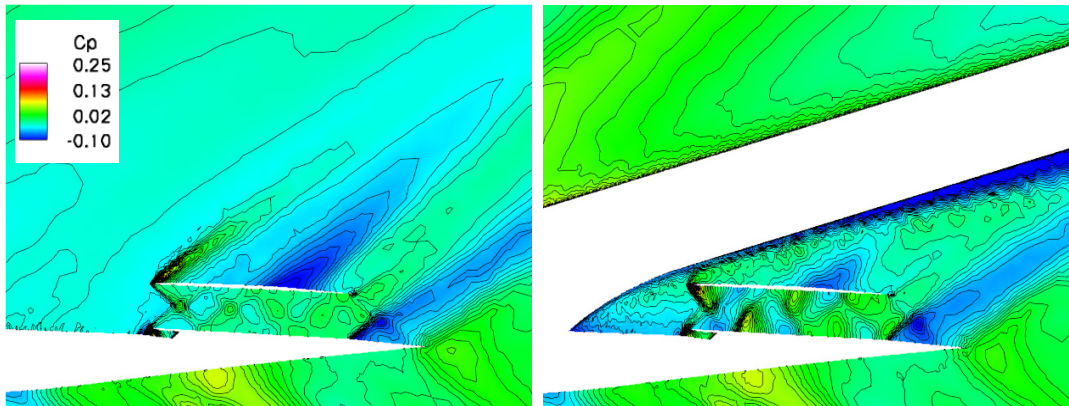


Figure 237.—Blade Effects on Centerline Flow-Through Nacelle

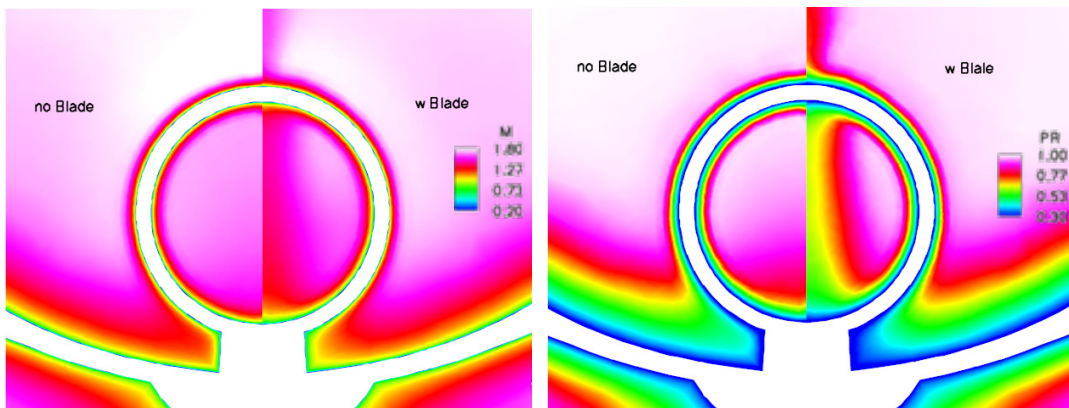


Figure 238.—Centerline Flow-Through Nacelle Mach (left) and Pressure Recovery Map (right)

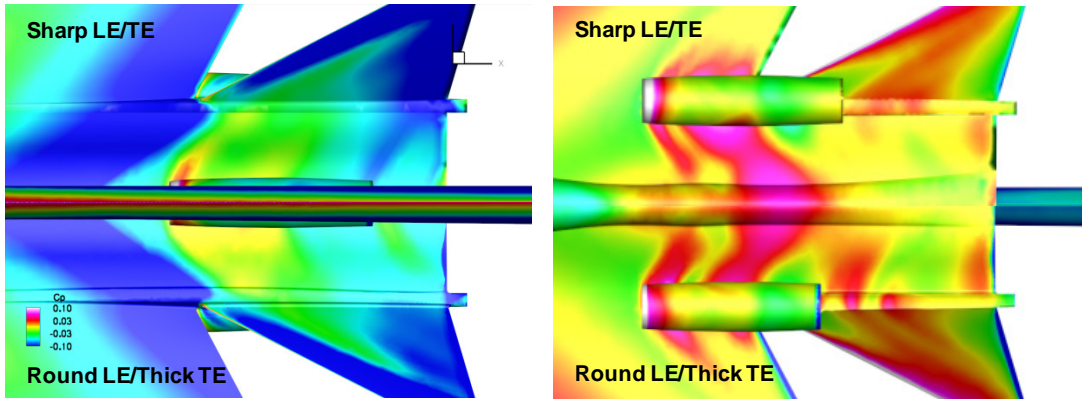


Figure 239.—Surface Pressure Contour Comparison

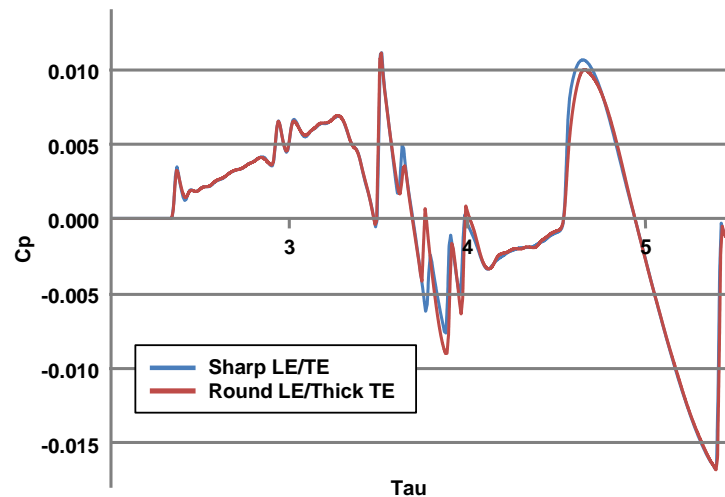


Figure 240.—Edge Thickness Effect on Model Signature [M=1.7, AoA=2.1, H=5.4(b/2)]

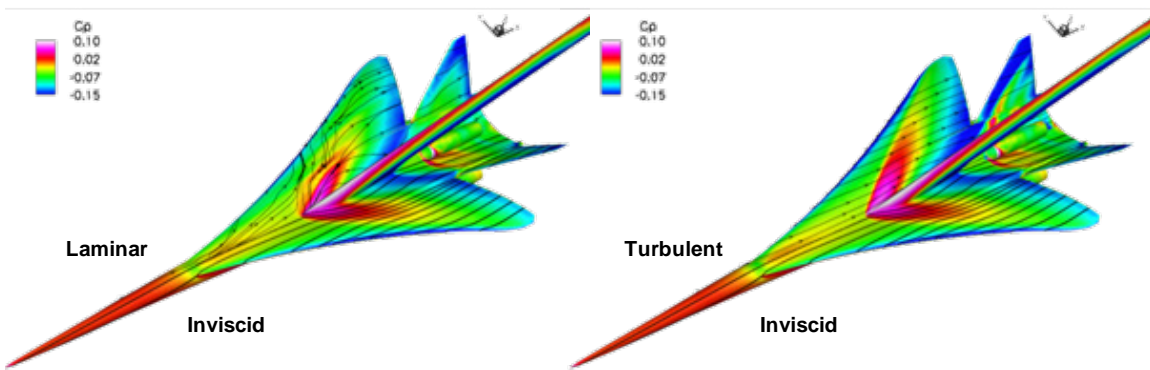


Figure 241.—LM4 Model CFD Boundary Layer Comparisons

Due to the relatively low Reynolds number of the test, significant viscous effects were expected. As such, wind tunnel model-scale boom predictions were made using both laminar and turbulent boundary layers. Surface pressure gradient and streamline traces for the laminar and turbulent runs are shown in Figure 241. For the laminar case, the nacelle cowl and blade support causes shock-induced separation while the flow remains attached for the turbulent condition. Figure 242 compares the predicted boom

signatures of different types of boundary layer. LM3 test experience show that it is desirable to have trip discs on the upper wing surface and blade to energize the boundary layer to inhibit flow separation.

Model fabrication subcontractor was Tri Models, Inc, who also built the tight-tolerance axibody and LM3 models. The model and blade were machined out of 15-5PH and PH13-8 high strength stainless steel, respectively. Both were designed to meet all tunnel stress requirements and have safety factors well above the 4.0 desired by the facility.

The 1044-02 model scale size of 0.0065 was a reduction from the 0.008 of the 1021-01 model, Figure 243. The almost 4 in. reduction in model size to 18.68 in. helped better position the model in the tunnel for spatially averaged measurements. The prior 1021-01 model's signature, allowing 1 in. ahead and 3 in. behind for its recompression, was over 26 in. making it longer than our linear actuator travel. We were able to get more measurements, over greater distance, with better positioning in the tunnel with the new, smaller model that appears to have resulted in better accuracy.

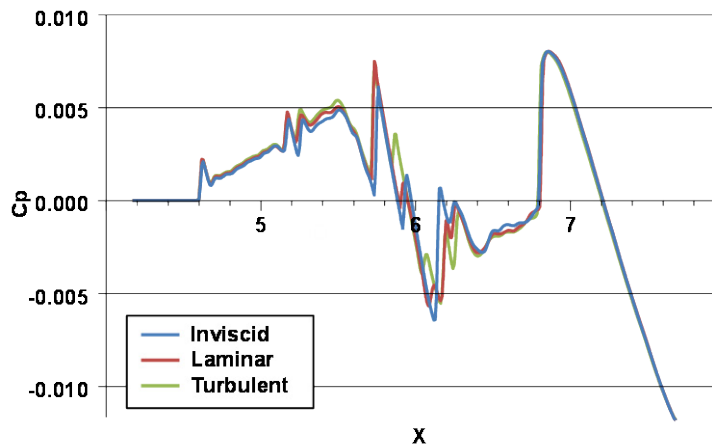


Figure 242.—Predicted Boundary Layer Effects on LM4 Signature



Figure 243.—The 19 Percent Smaller 1044-2 Model Improved Spatial Averaging Positioning



Figure 244.—The 70° Flat-Plate Model Fabricated to Improve Measurement and Calibration of Reflected Shock Distortions

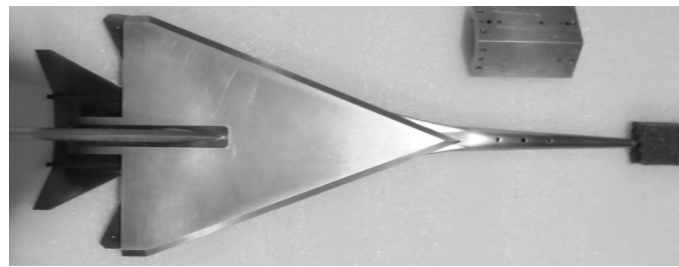


Figure 245.—Flat-Plate Approximates 1044-2 Wing Planform

Five models were tested during LM4. In addition to the 1044-02, the LM3 1021-01 model was retested first to verify that results were matching previous measurements, indicating that the measurement hardware was functioning properly. For far measurements only (with the measurement rail on the aft window) the SEEB-ALR and a new 70° delta planform flat-plate calibration models (Figure 244) were tested next. They provided flow-field characteristics and calibration information useful for improving the processing of the other models' signatures. The delta's varying span with length was planned to characterize how a model's local span affects its reflection of shocks striking its lower surface. The model was inexpensive and produced little pressure change underneath it (Figure 244) so reflections are easier to measure. It also reuses the 1044-02 model's blade support and approximates the 1044-02 planform for improved calibration matching (Figure 245). The final model is a legacy NASA 69° Delta Wing-Body symmetrical model first built and tested in 1972 and reported in NASA TN D-7160, 1973 (Ref. 11). It was built with several other models at the time to investigate wing planform effects on sonic boom.

4.7 Test Description

The LM4 97-0254 test took place October 9 to 19, 2012 at the NASA Ames Research Center's 9x7 ft Unitary Plan supersonic wind tunnel. Two 8 hr shifts were employed each day with the test consuming 15 shifts total. This was exclusively a sonic boom test with sonic boom models and measurements comprising the whole test. A six-component force balance was utilized and flow angularity runs were made to record the CL and alpha of the boom measurements, but no force measurement runs were intended from these small models. Oil surface flow visualization and RBOS flow-field shock photography were performed on most every series at the same time as sonic boom measurements. The test was very successful, achieving continued refinements in measurement accuracy and a large improvement in productivity allowing an early completion with all desired validation data and many more diagnostic measurements than originally conceived.

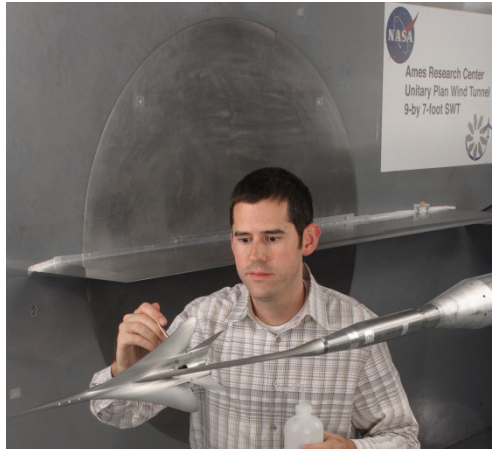


Figure 246.—Hardware and 1044-2 Model Prepared for Testing

The 1021-01 model previously measured in Parametric Test 97-0250 and LM3 Test 97-0231 was measured first to check that all hardware results were matching previous tests. Results repeated previous test measurements with extremely good precision, so only one comparison is shown in the results section. Also, the measurement results of this model are being used for an AIAA sonic boom prediction workshop <http://lbpw.larc.nasa.gov>, so some continued refinement of the measurements will be performed until the workshop takes place in January 2014.

The SEEB-ALR and 70° Flat-Plate Delta were measured next with X sweeps at 54 and 70 in., Z sweeps from 70 to 42, at Machs 1.6 and 1.7, and with repeats of all measurement sets. Results matched previous tests and characterized flow-field distortions for far measurement distances. These models were not used or needed for near measurement distances.

The 1044-02 model was only run at its shaped boom design Mach number of 1.7, as previously described. The 9x7's minimum Mach of 1.55 is only a 4° change in Mach angle, so the boom difference is minimal and the flow quality in the tunnel tends to be worse at lower Machs. Figure 246 shows the model being prepared for testing in the tunnel using the same hardware stack used throughout all tests (also seen in Figure 233).

After finishing testing nine configurations of four LM sonic boom models (two distances and two nacelle-off options), there was time available to re-test the NASA legacy 69° Delta Wing-Body model. This model, like the 1021-01, is also being used for the AIAA Workshop in January 2014. Since it is a smaller model, near (forward rail) measurement distances of 21.2, 24.3, and 31.8 in. corresponded to beyond near-field semi-span, $H/(b/2)$, ratios of 15, 18, and 23.

4.8 Oil and Stereo-RBOS Flow Visualization

Measuring sonic boom has many differences from typical supersonic testing. The first N+2 test, LM1, revealed that the measurement accuracy needed for N+2 shaped boom validations did not exist at the beginning of the program. Prior to N+2, several sonic boom tests yielded completely erroneous results and the cause was not determined at the time. Under N+2, we have discovered sources of measurement error from probe design, from tunnel flow-field distortions and tunnel reference drift. Flow diagnostic information was the key to making such discoveries, so we arranged for oil flow visualization and accommodated one of the first tests with NASA's Stereo RBOS capability. Both provided useful visualizations of different flow aspects.

Oil flow visualization proved very useful for validating model surface flow, was easy and quick to apply and required no run time—running concurrent with sonic boom measurements without interference. NASA provided a powerful LED ultraviolet light source that really improved the contrast of photographs

in the following figures. Oil surface flow visualization was particularly useful for showing that CFD was predicting the correct model flow. Surface oil flow patterns were examined for signs of unpredicted flow separations or other differences with CFD predictions, but care must be taken in interpreting results.

CFD analysis produced different upper wing and blade flow when the boundary layer was switched from turbulent to laminar. Previous testing using sublimation (NASA's HSR program ~1993) to detect boundary layer transition at these flow conditions indicated that several inches of laminar flow can be expected. Prior to testing, trip discs were placed on the wing upper surface, on the blade and ahead of the top-center nacelle. Based on the previous HSR testing, the trip discs (0.0075 in. tall) would not guarantee transition, but hopefully, at least energize the boundary layer enough to prevent separation. (In previous testing, 0.012 to 0.018 in. disc height brought transition to 1 in. behind the trips at a minimum, but the trips were up into supersonic flow at these heights, generating bow shock waves in the surface flow visualization.) N+2 design perturbation studies indicated the trip discs themselves on lower surfaces would affect sonic boom but not on upper surfaces. Further, laminar flow on the lower surface stayed mostly attached and did a better job of replicating the full scale thin boundary layer, so disc were not used there. Figure 247 and Figure 248 show a comparison between CFD analyses, laminar and turbulent, and wind tunnel oil flow. Trip discs helped visualize streamlines, but care must be taken in interpreting results because tunnel start-up artifacts remained in the oil patterns. The dark streaks, starting on the wing inboard of the sweep change and running to the trailing edge just outboard of the lower wind nacelles, form during the very low pressure ($PT=700$ psf, $Re = 1.2M/\text{ft}$) start-up of the tunnel. Testing was originally planned and run at $Re = 2.55M/\text{ft}$, also with attached flow, but the tunnel humidity was easier to reach and hold at $4.5M/\text{ft}$, so extra attachment margin. But the separated flow on start-up proved the uncertainty indicated by CFD. The Figure 248 close-up reveals some cross-flow sweeping streaks around the start of the dark streaks just mentioned. Prominent in both pictures are a rib-like pattern on the inboard wing around the blade support that are formed by the trip discs on the blade and are surprisingly visible from the small discs. Though other trip sizes were available (or none), this trip disc arrangement was kept on this 1021-01 model and repeated on the 1044-02 without variation since the desired flow-fields were achieved.

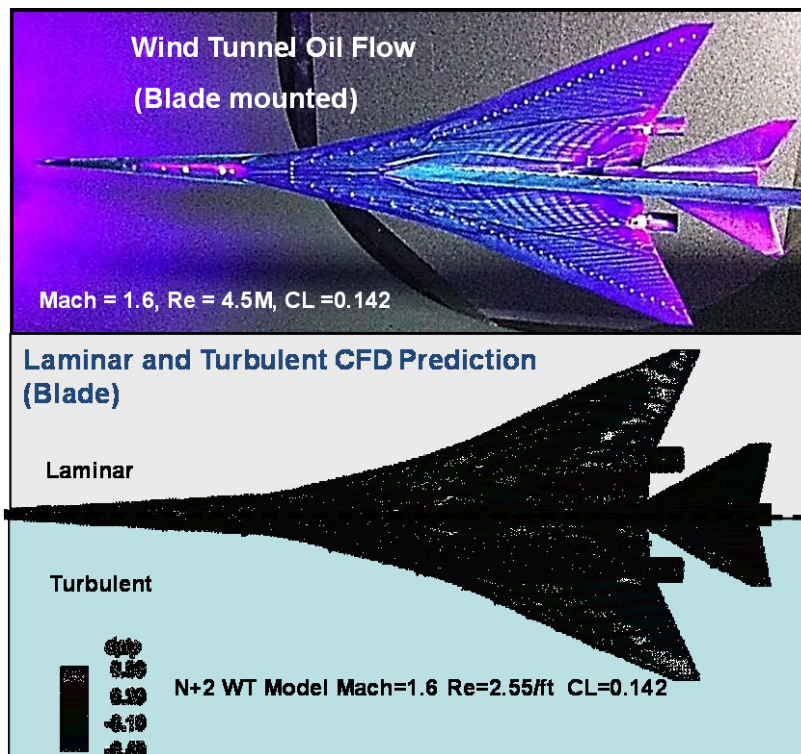


Figure 247.—Test Oil Flow (top) Showed Fully Attached Flow, Like Turbulent CFD (bottom)

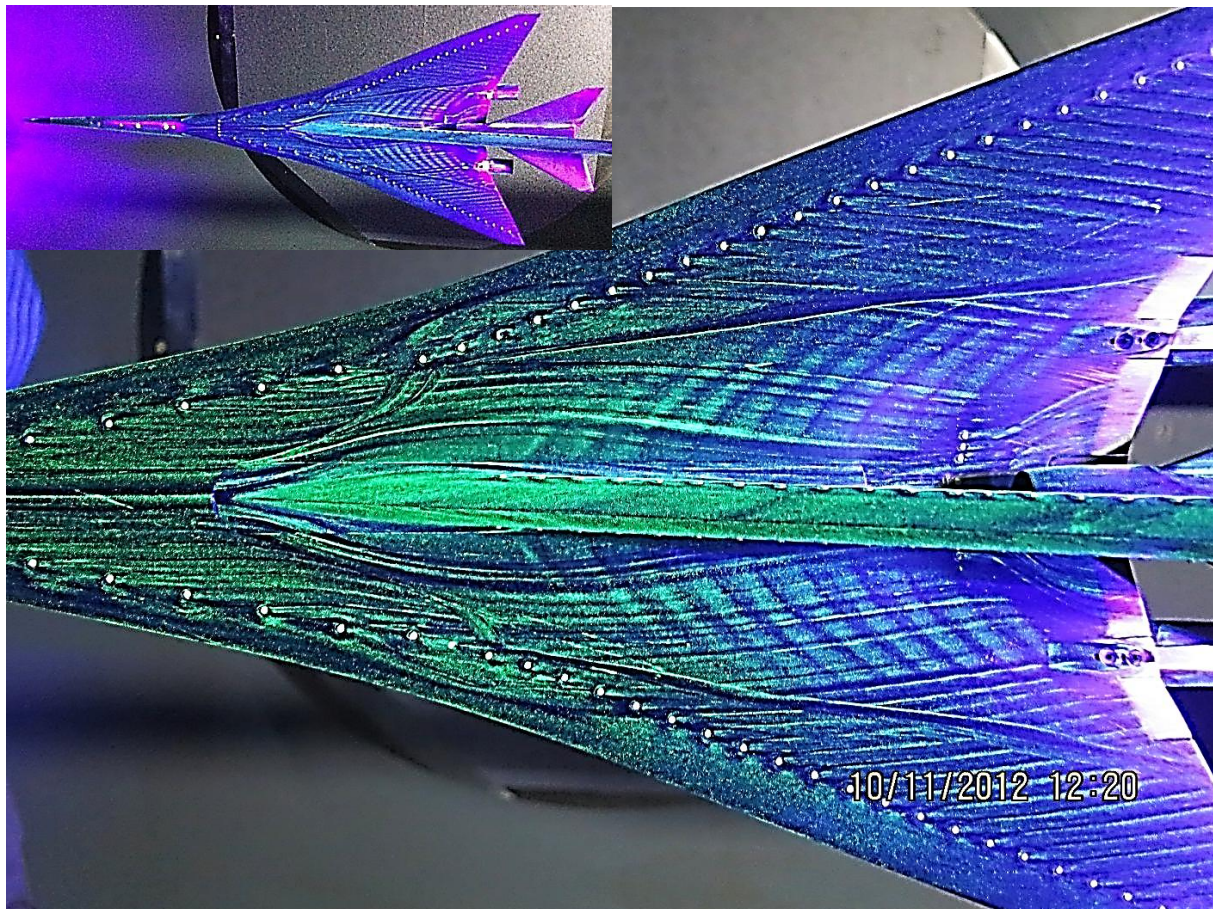


Figure 248.—Close-Up of 1021-01 Oil Streaks Showed Fully Attached Flow, Like Turbulent CFD
(Some persistent separation streaks formed during tunnel start-up at low Re)

After achieving expected measurement results with the 1021-01 model in the aft rail position, the flow calibration models were run for far measurement distances. The tunnel flow-field is different at the two different rail positions and the aft position had not had extensive flow diagnostic measurements taken since (the more limited measurements of) LM1. Oil flow was not deemed worth the tunnel pollution on the high-fineness axisymmetric SEEB-ALR model, but the extreme low-cost 70° Flat-Plate Delta's re-use of the 1044-02 blade support with external, blunt-faced mounting did have some failure modes if the flow did not match CFD predictions. Oil flow of the Flat-Plate (Figure 249 and Figure 250) confirmed that it did isolate upper surface disturbances from the region of calibration measurements underneath the wing. There is also a possibly confusing feature of the oil flow that deserves commentary, the upper surface flow of Figure 249 has dark (oil evacuated) streaks going back streamwise from the blade support bow shock at mid-span that might seem like a separation. We believe there is not a separation (and no separation at the bow shock impingement either, excepting a very small vortex separation and reattachment within the boundary layer) just a point where the boundary layer flow allows the oil to flow streamwise (perhaps a change in the character of the boundary layer vortex that makes the bow shock's dark streak).

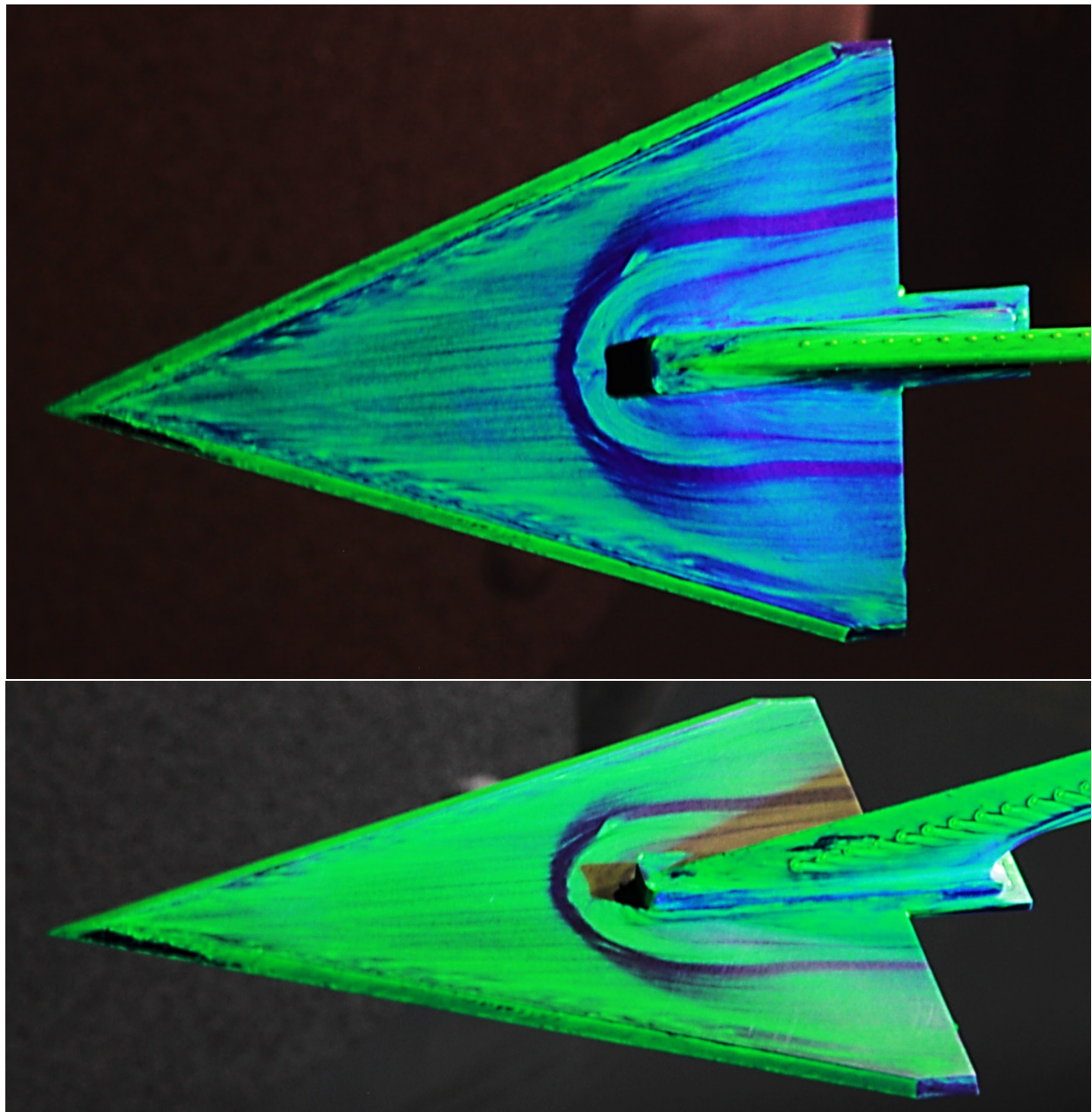


Figure 249.—Dramatic Upper Surface Flow Coloration Showed That Strong Pressure Disturbances are Isolated From Underneath the Wing Until Its Trailing Edge, as Intended

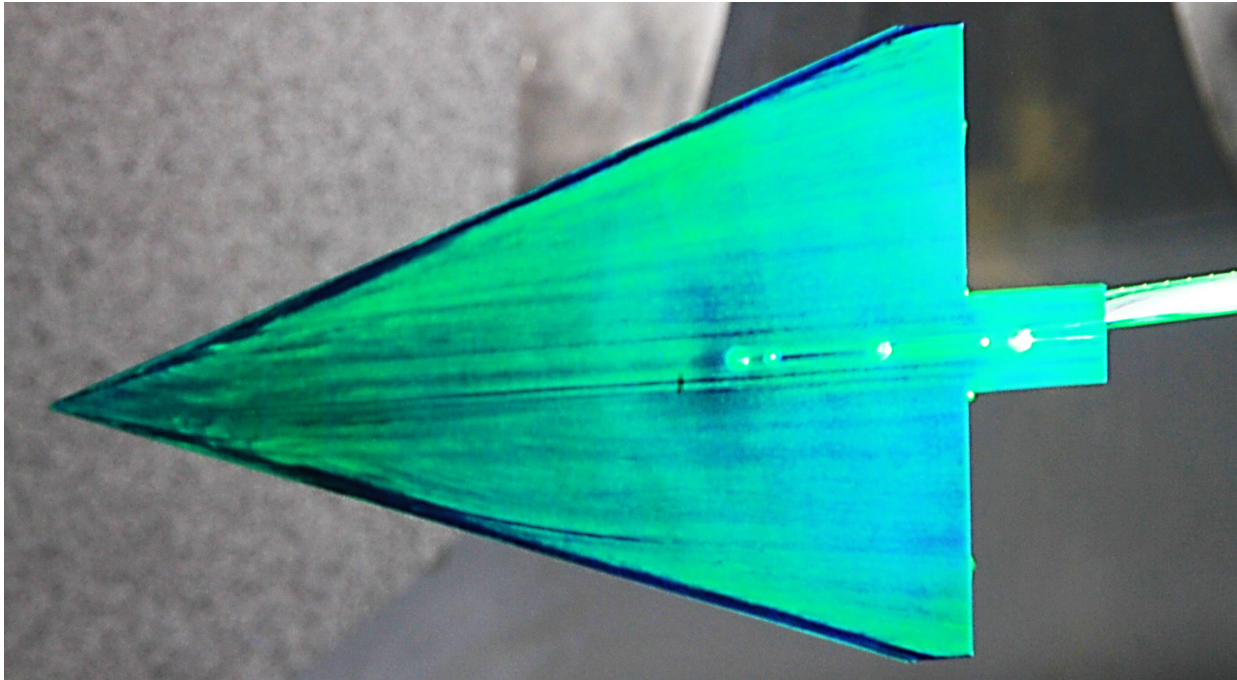


Figure 250.—Lower Surface Produced Little Flow Disturbance, Supporting Its Intended Mission to Quantify Shock Reflection Strength as a Function of Local Span

The 1044-02 blade support was a re-scaled duplicate of the 1021-01 design based on its success and the oil flow images validated its flow, Figure 251. The support blade is expected to and has a separated flow vortex along its trailing edge. With a sweep greater than the Mach cone angle, the trailing edge is inclined to separate; furthermore, when the shock from the center nacelle intersects the blade, separation is almost guaranteed. CFD analysis has shown that enough separated flow ingested into the upper center nacelle can unstart the nacelle's internal flow, creating significant spillage and a consequential flow disturbance. The unswept base of the blade trailing edge keeps flow attached there and keeps the trailing edge vortex from forming until above the nacelle, especially where the nacelle shock intersects.

Figure 252 shows the 1044-02 upper and lower surface oil flows. The streaks indicate fully attached flow everywhere as predicted. The trip discs on the upper surface made high contrast flow streaking. Around the blade support there was some smearing out of the streaking left over from start-up. The lower surface had some oil evacuated dark lines where there were strong nacelle shock impingements, but predictions and streamlines indicated the flow stayed attached straight through these regions. There was also some angled flow indicated on the lower surface visible behind the plaster filled dots that was due to the effect of gravity on the oil before the tunnel flow became strong when the model was rotated 180° from the orientation in which this picture was taken (referring to streaks trailing back and up from the plaster dots in this image orientation). Curiously the oil flow of Figure 252 did not indicate any rib pattern induced by the trip discs on the blade, but the oil flow images in Figure 253 show the rib pattern and show shocks from the wing trip discs themselves. The oil and fluorescent powder were the same, but the proportion could be different, the application thickness could be different, the tunnel time spent at low Re could be different.

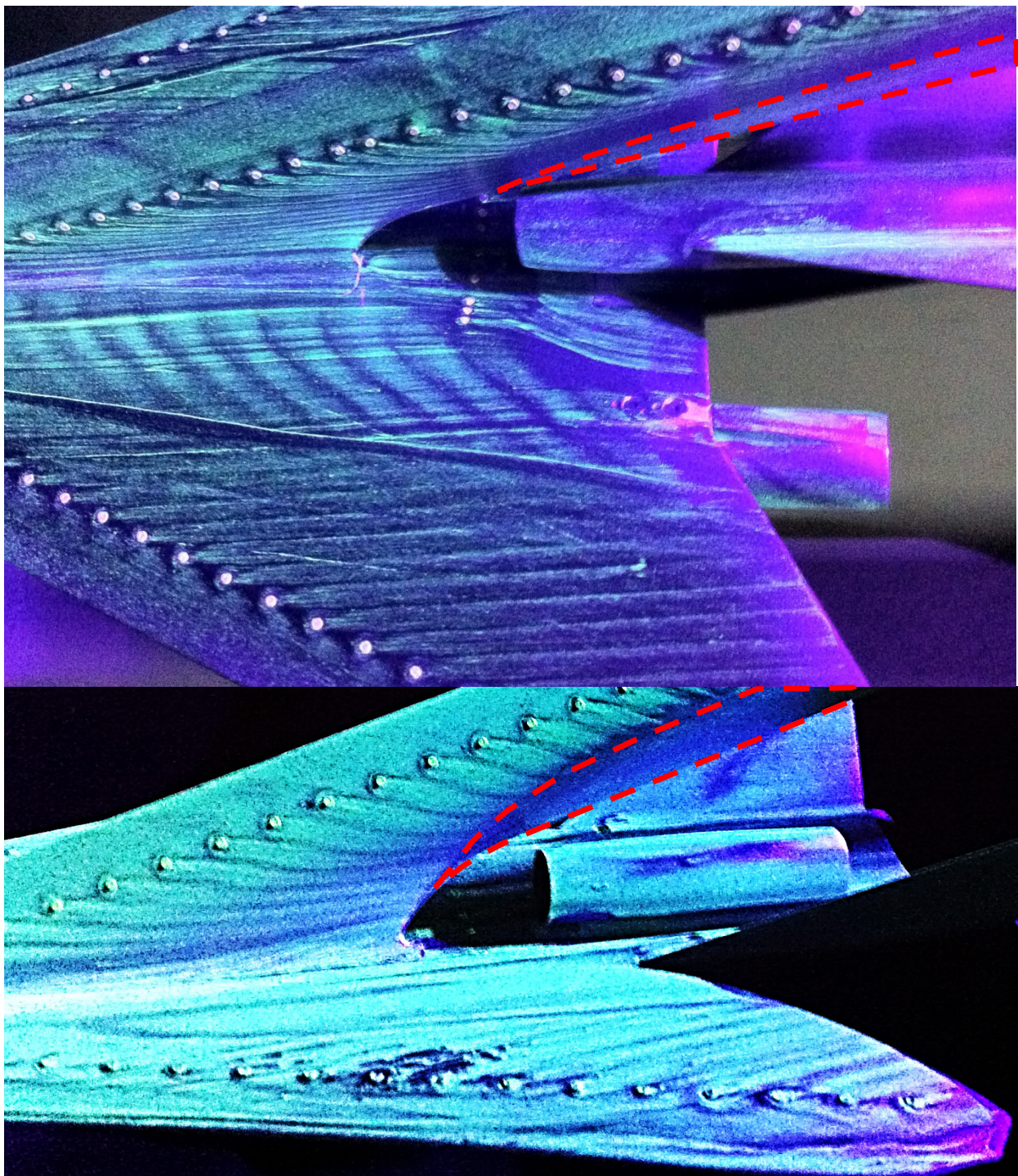


Figure 251.—Blade Support for 1021-01 (top) and 1044-02 (bottom) Showed Attached Flow Until Vortex Separation Region Identified by Dashed Red Line

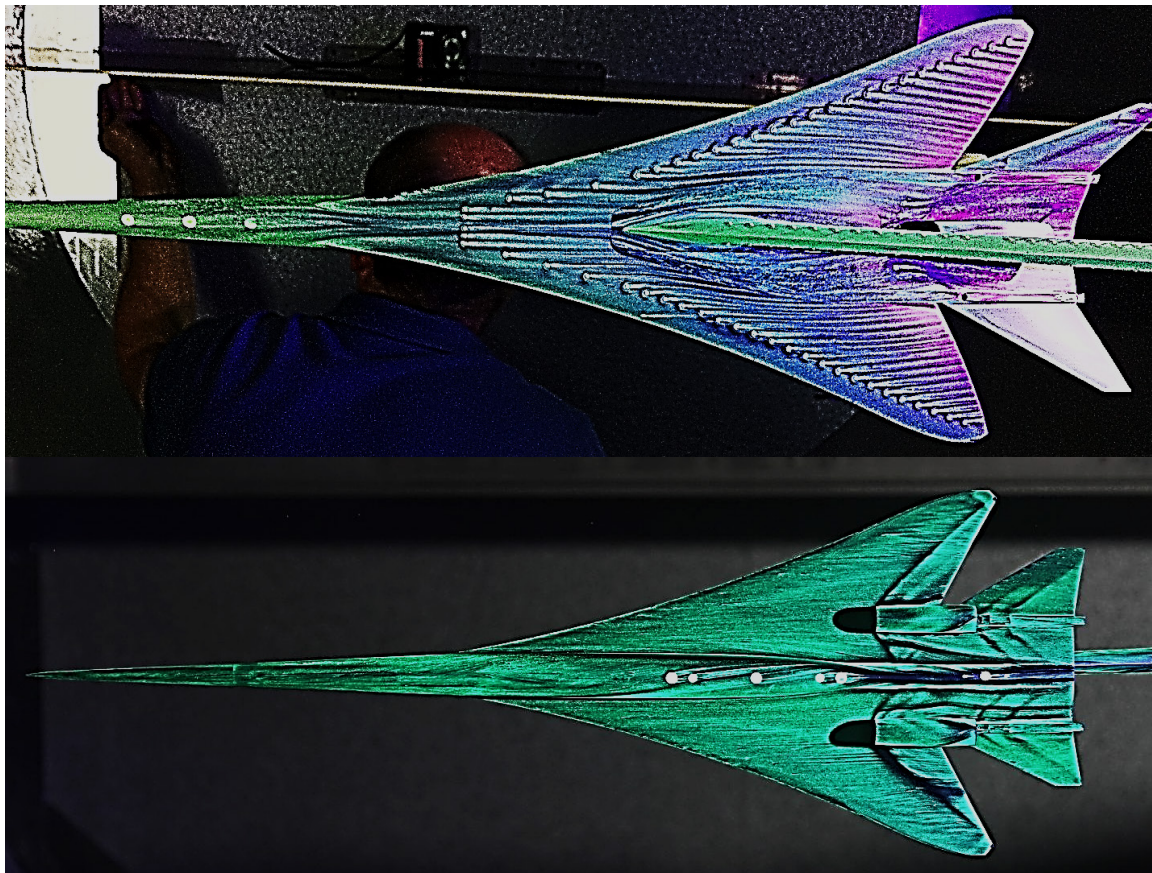


Figure 252.—Upper and Lower Surface Oil Flows on 1044-02 Indicated Fully Attached Flow

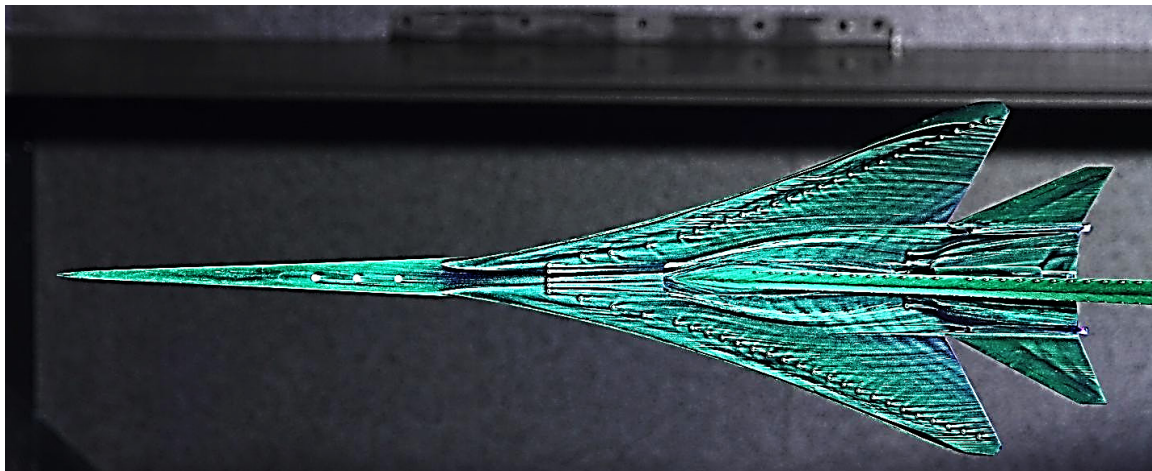


Figure 253.—Upper Surface Oil Flow Strongly Showed Rib Pattern Shocks From Blade Trip Discs and Bow Shock Waves From Wing Trip Discs

The NASA 69° Delta Wing-Body model was run last. It was made top/bottom symmetrical with a 5 percent thick wedge airfoil for the wing, so the maximum thickness at mid-chord has a sudden surface slope change, creating a strong expansion that is highlighted by the oil it evacuates behind the mid-chord ridge as seen in Figure 254. Attached flow is maintained over the model. Care must be taken when interpreting some oil flow features. In Figure 255, some missing and mottled regions of oil flow (below) are left over from the initial oil application (above)—not surface flow features.

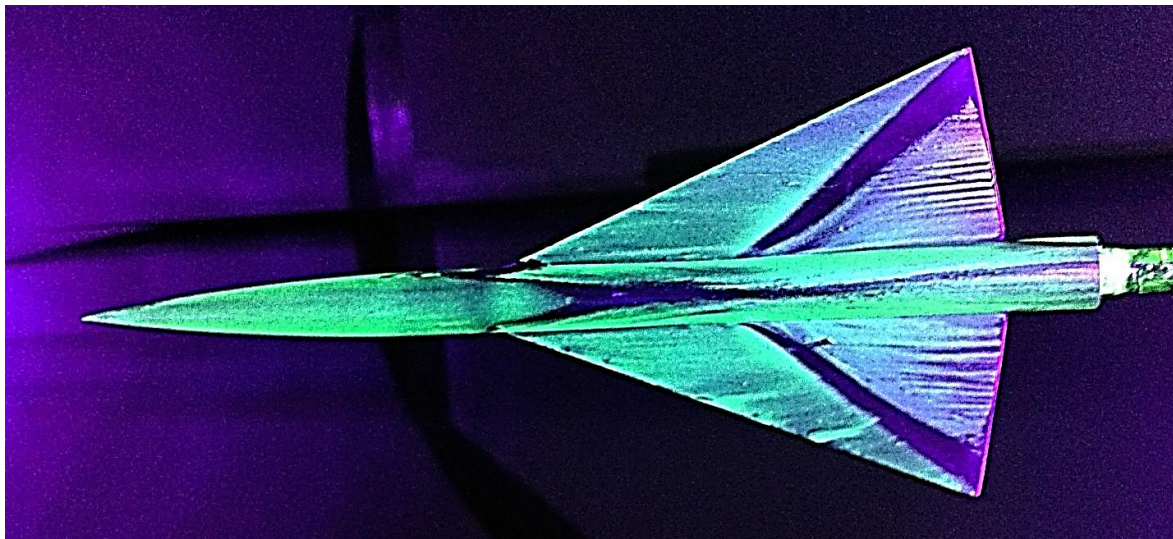


Figure 254.—Legacy 69° Delta Wing-Body Model Oil Streaks Indicating Attached Flow and Dramatic Oil Evacuation Behind Diamond Airfoil Maximum Thickness Ridge

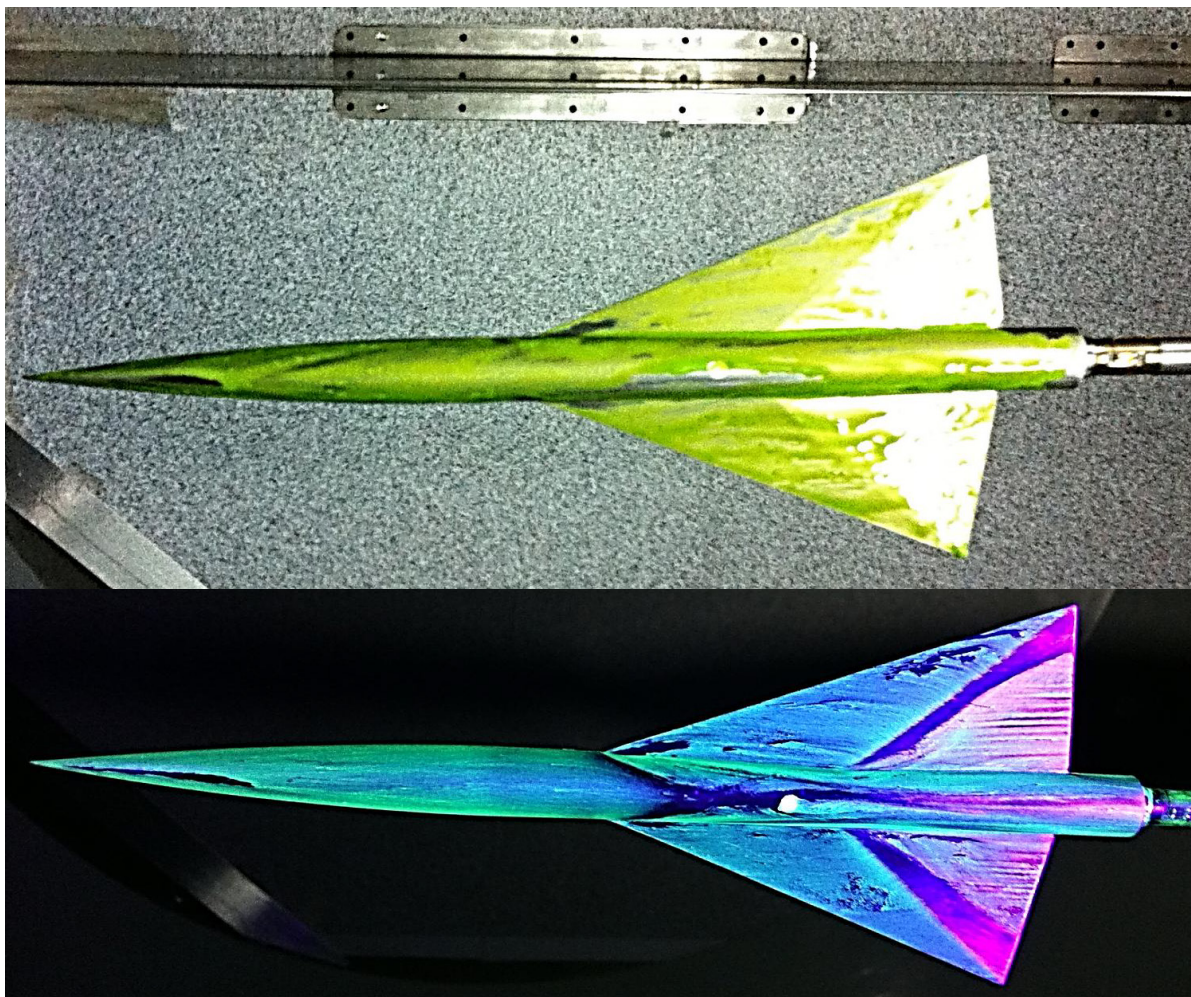


Figure 255.—Mottled Oil at the Root and Outboard Wing and Oil Void Streak at the Nose (bottom) Are Not Flow Phenomena, But Rather, Persistent Features From the Initial Oil Application (top)

The RBOS (Retro-reflective Background Oriented Schlieren) flow visualization technology takes Schlieren-like pictures using pattern recognition technology with some important differences in flow-field sensitivity. A retro-reflective material (strongly reflects light back in the direction from which it came) is speckled with a random pattern of ink blotting (seen in the background of several figures but especially the top image of Figure 255 behind the model) is adhered to the far wall inside the wind tunnel. Pictures taken of the material through the flow-field will have the pattern displaced in position by pressure variations in the test section. However, a pressure change in the middle of the tunnel will displace the wall pattern's position more; while conversely, a pressure change nearer to the wall pattern or camera cause less and less pattern displacement until at the limit of the wall or camera there is no displacement effect at all. (Bending of the light at very short distance from the reflective material results in little pattern displacement at the camera; and near the camera, light rays coming in from the range of angles from the camera's field of view are compressed onto a very small sensor, making small angle changes near the camera also result in little pattern displacement.) Being able to focus on pressure changes in the middle of the tunnel in the vicinity of the model is preferred to Schlieren's that give more equal weighting. Another important consideration when viewing any Schlieren-like images, particularly when comparing the model's disturbances to the background disturbances, is the tunnel's orientation in the photography. Most supersonic tunnels have nozzle contraction/expansion concentrated or completely in one plane more than the other, horizontal or vertical. In this Ames 9x7 tunnel, the side walls are flat and all nozzle contraction/expansion is in the floor and ceiling, making much larger flow disturbance shock diamonds traveling between the floor and ceiling. In this tunnel, models have always been tested rolled 90° so the larger floor/ceiling distortions affect yaw angularity instead of pitch angularity. Sonic boom testing is also done at 90° of roll with the measurement rail mounted on the wall. The larger floor/ceiling shock diamonds are in the measured ambient pressure variation; however, the steadier pitch angularity variations have less interaction with the model and result in improved sonic boom measurements with this tunnel orientation. However, the tunnel's window positions did not allow us to photograph the flow-field, perpendicular to the model-rail, from ceiling to floor. Instead we are RBOS imaging the model disturbances going toward the floor and ceiling (not the wall with the measurement rail) as they propagate in the tunnel's far larger ambient floor/ceiling shock diamonds. Again these floor/ceiling disturbances are in the tunnel's ambient reference pressures, but the orientation makes a big difference when making model to tunnel comparison's or tunnel to tunnel comparisons. Ideally, we would take RBOS images in both wall-to-wall and ceiling-to-floor planes. In this tunnel, the wall-to-wall orientation compares the magnitude of the smaller tunnel disturbances that interact with the model to the magnitude of model disturbances. The ceiling-to-floor orientation compares the magnitude of the larger tunnel disturbances (that change the tunnel yaw angularity running across the model from side-to-side in its measurement orientation) of the tunnel's ambient flow-field to the magnitude of model disturbances.

In these following RBOS images appreciate that we are photographing wall-to-wall along the plane of the strongest ambient flow disturbances created in the contraction/expansion in the ceiling/floor. Most tunnel's measure upright, contract/expand their walls and Schlieren photograph wall-to-wall; so the large magnitude of ambient disturbances is not seen or appreciated. To visualize the actual magnitude of their ambient disturbances compared to the magnitude of model disturbances, they would also need to take Schlieren/RBOS images from ceiling-to-floor. It is these worst-case images that are shown in the following RBOS images.

This first RBOS image, Figure 256, is the larger 1021-01 model in side-view shown with the larger ceiling/floor ambient shock diamonds of the tunnel. The image scale grey-shade is in proportion to the pixel displacement scale shown. The field-of-view clips the back end of the model because of limits to the model positioning (with alpha/height being from the tunnel yaw control in this plane), a limited size and location for the retro-reflective material in the tunnel and limited window position for the camera. Still, the only model shocks of much visibility are the nose shock and some shocks from the underwing nacelles. Some tunnel ambient disturbances are larger than the shaped boom model's nose shock. Model shocks are often only positively identifiable as model shocks because they do not continue upstream. By showing this image sharpened and +40 percent contrast, some subtle model variations to the flow-field

become apparent downstream that did not exist upstream. The following pictures are also enhanced with increased sharpness and contrast.

The 70° Flat-Plate Delta model was made to quantify ambient tunnel disturbance reflection strength off its bottom as a function of local span. As such, it was desired for the model to produce little disturbance itself below its wing. Figure 257, Figure 258, and Figure 259 confirmed the model produces little disturbance below its wing (or even off to the side) until the strong expansion at its trailing edge.

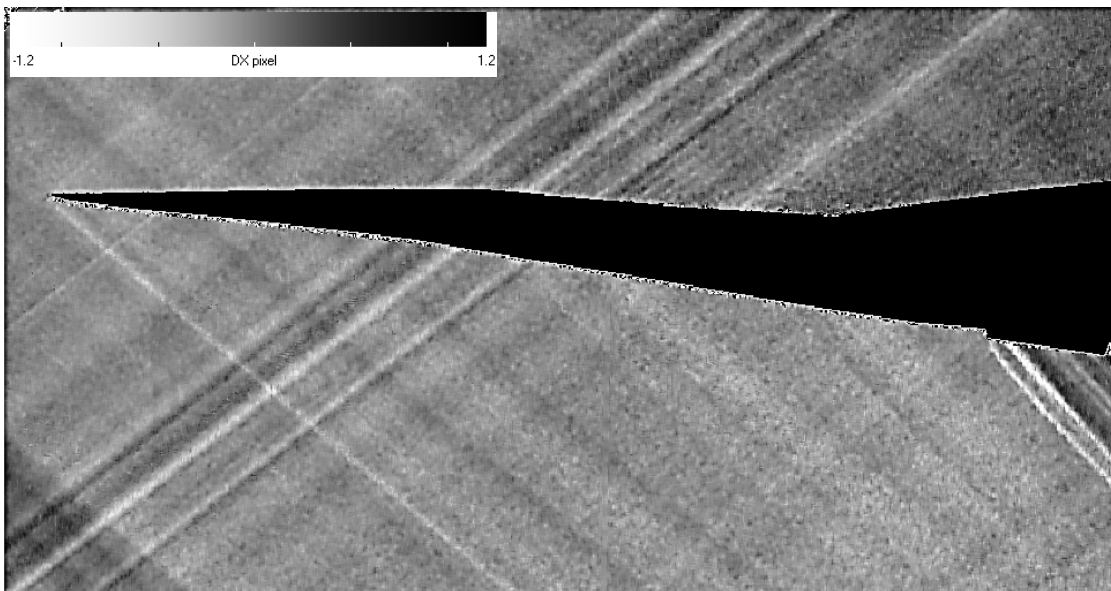


Figure 256.—RBOS of 1021-01 Shaped Boom Model Made Nose and Underwing Nacelle Shocks Apparent, Otherwise, Only Background Flow-Field Variations

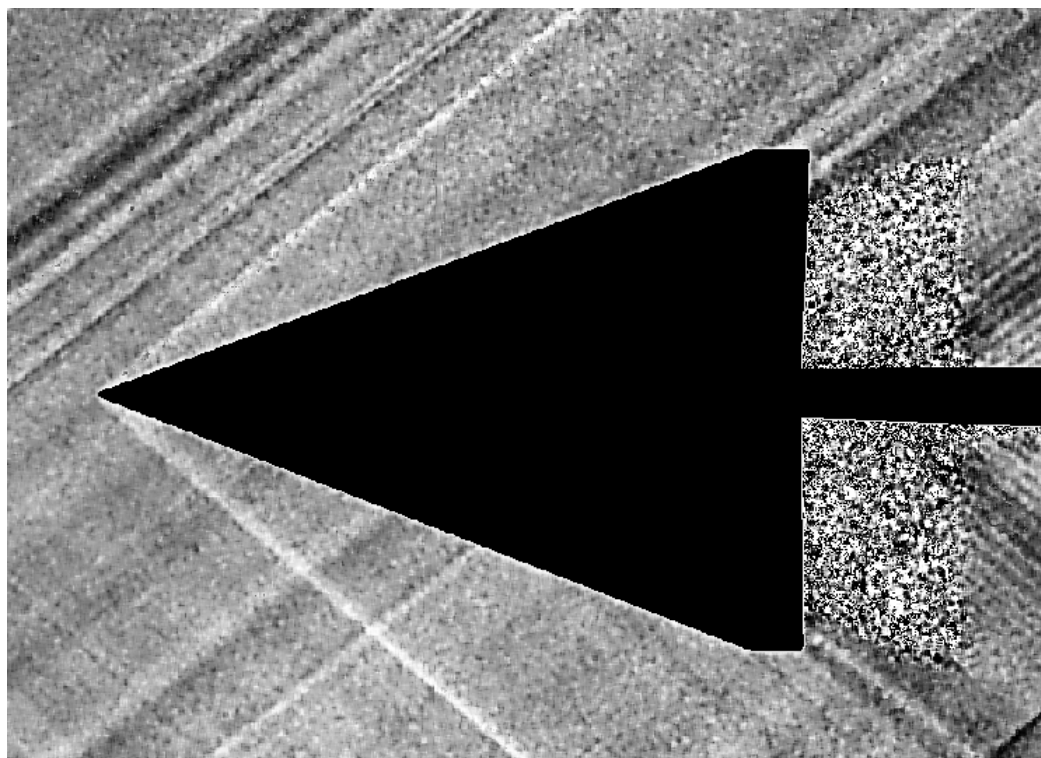


Figure 257.—Flat-Plate Model Created Little Disturbance between Nose Shock and Trailing Edge

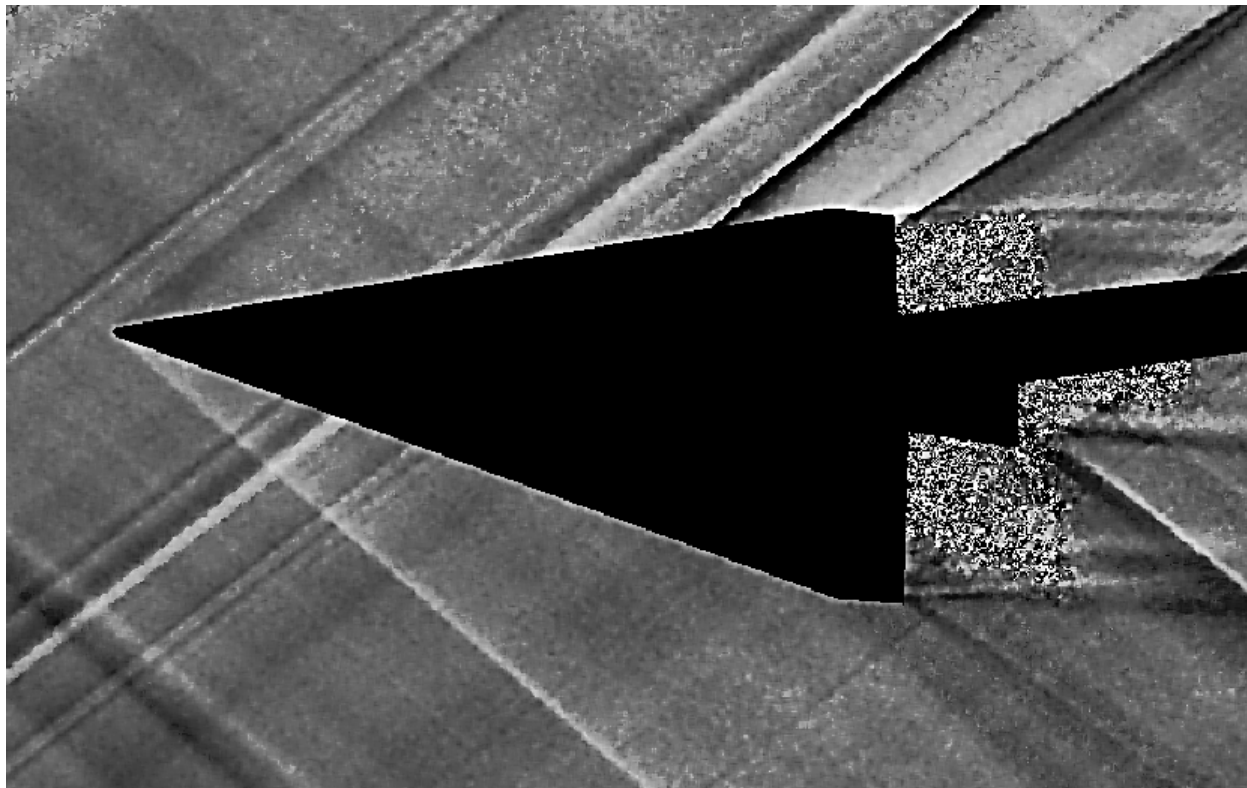


Figure 258.—RBOS Wake Visualization by Shading on DY (see Figure 260)

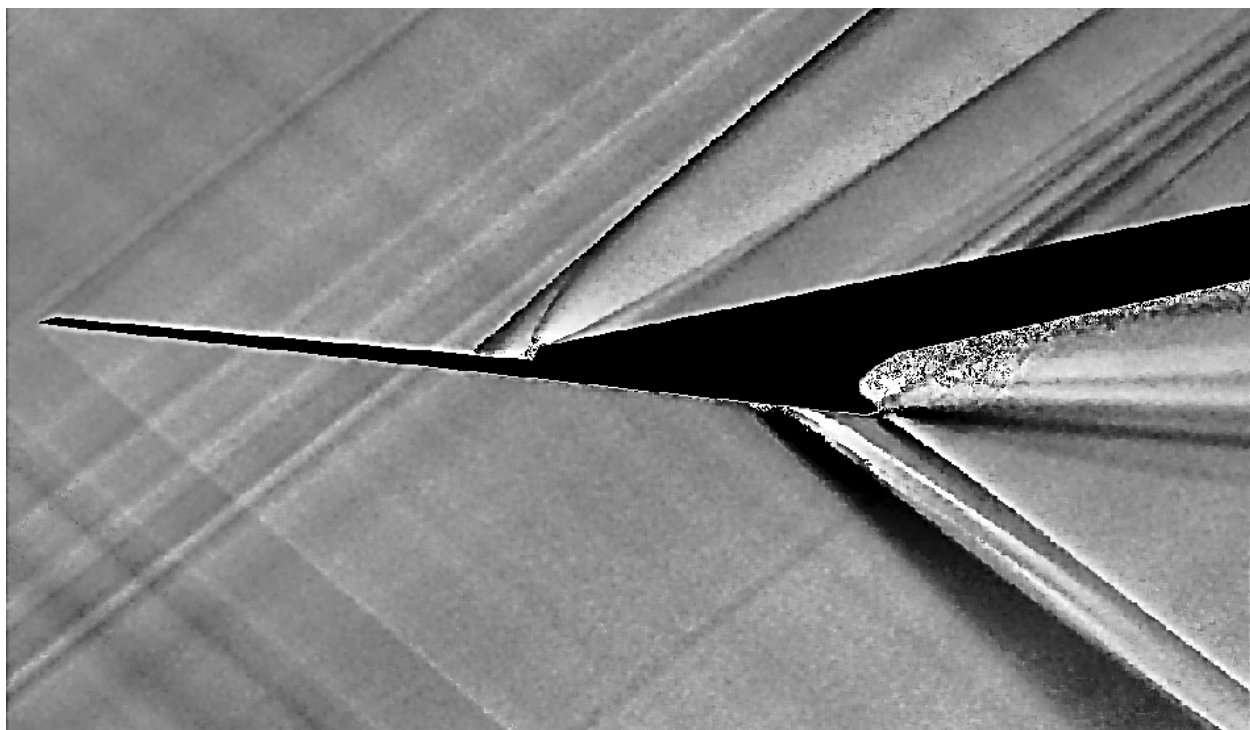


Figure 259.—RBOS Side-View Validated Lack of Disturbance Below Flat-Plate between Nose Shock and Trailing Edge and Successful Isolation of Blade Disturbance

The 1044-02 is shown above twice in Figure 260, the top one was shaded based on pattern displacement distance in X, while the bottom one was shaded based on pattern displacement in Y. Processing the image using only X hides the vehicle wake. Some shades shift between the two images, but results are similar. (We are suggesting an image shaded based on total [$\sqrt{DX^2+DY^2}$] pattern displacement.)

The 1044-02 configuration was designed for very low sonic boom, so in Figure 261 its disturbance was small compared with the ambient tunnel variations (again, RBOS orientation showing tunnel maximum shock strengths, generally 90° off typical tunnel Schlieren orientation). As could be expected from this figure, measuring weak signatures in a supersonic wind tunnel was difficult. This is why spatial averaging measurement processing was necessary to achieve the required measurement accuracy.

Figure 262 showed that the 69° Delta Wing-Body model produced less disturbance because of its smaller (6.9 in. long) size, somewhat offset by its reduced fineness relative to the shaped boom models. Here at angle of attack, a nose and wing disturbance can be seen under the model along with a wing flow-field change above the model. Even over our 20 to 30 in. measurement distances to the rail, the wing disturbance coalesces into a single shock.

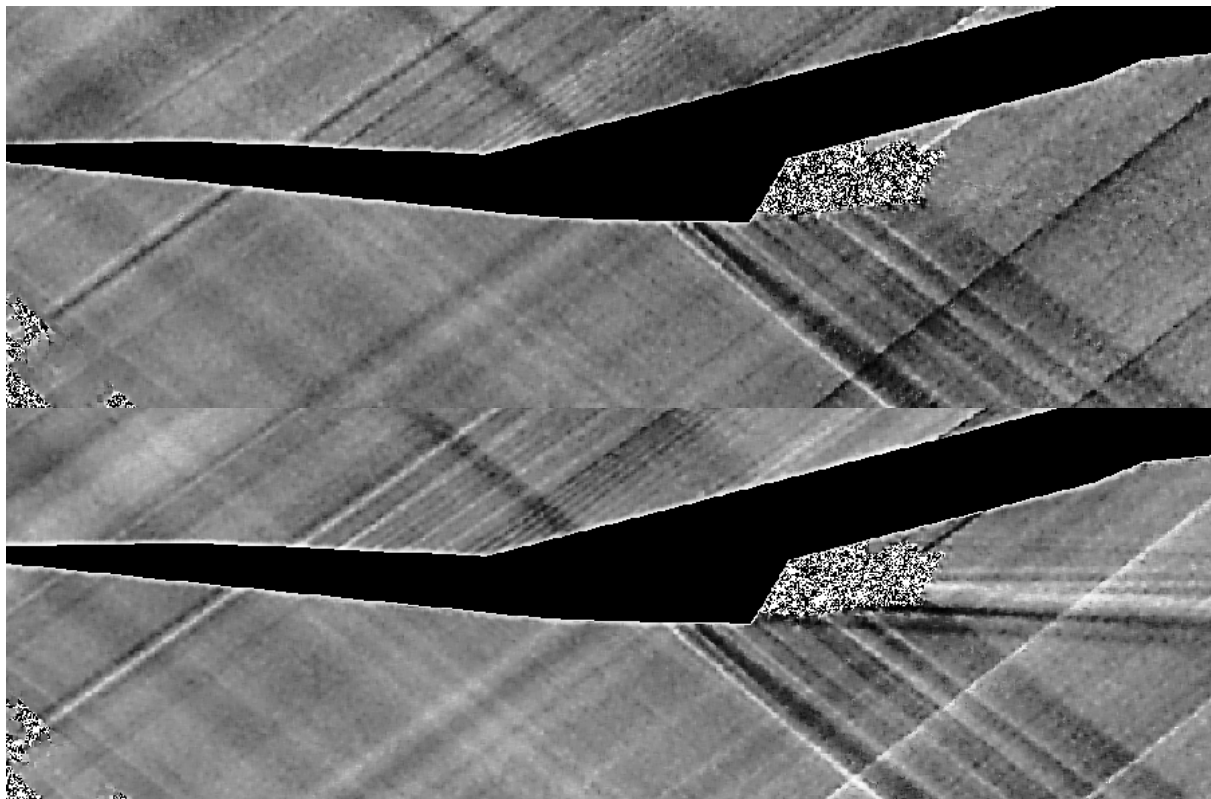


Figure 260.—RBOS of 1044-02 Shaded DX (top) and DY (bottom)

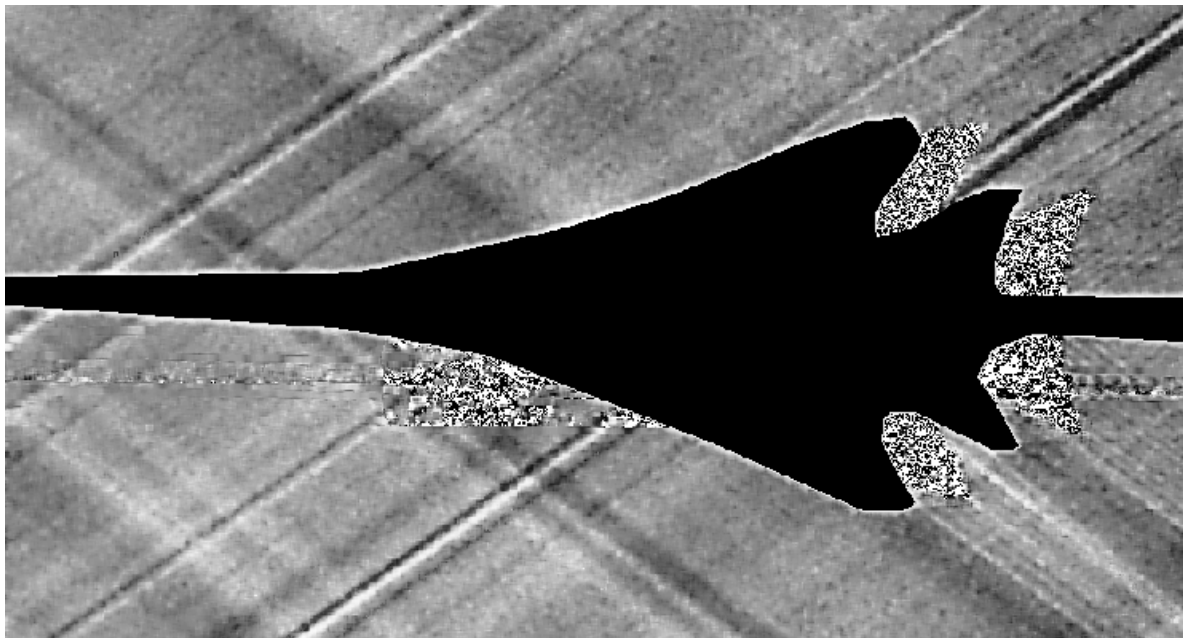


Figure 261.—RBOS of 1044-02 Illustrated that Shaped Boom Disturbances are Lower in Magnitude than Ambient Disturbances and only Subtly Visible Behind the Wing

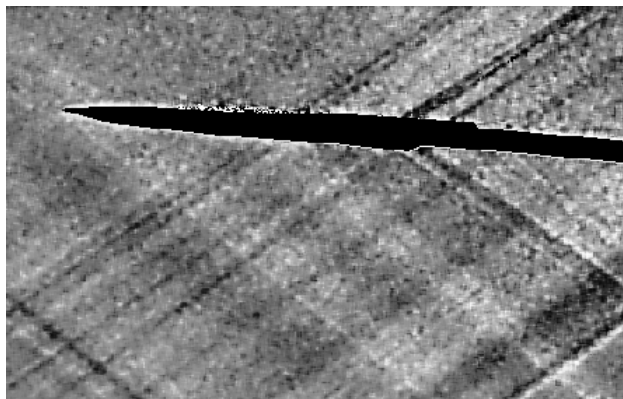


Figure 262.—The 69° Delta Wing-Body Shocks Weakened and Harder to See at Smaller Size

4.9 Test Analysis and Results

There are generally two challenges to CFD for sonic boom: getting the correct vehicle solution and propagating that solution with sufficient resolution to beyond near-field interference (necessary for starting other propagation methodologies). To understand which portion of the solution is responsible for a mismatch, it is desirable to have measurement distances both close, near-field, and far, beyond near-field. Near-field differences are caused by vehicle disturbances that are laterally away from the vehicle centerline—so typically the wing (and anything it contains) is the primary source of near-field differences that go away with enough distance. Though not guaranteed, typically propagating measurements from 15 to 25 semi-spans [$R/(b/2)$] away is sufficient. Much previous technical work has expressed this distance as a ratio of vehicle length [R/L], but since length has nothing to do with the phenomena and semi-span does, we always express measurement or CFD extraction distance as a ratio of semi-span. Part of the January 2014 AIAA Sonic Boom Prediction Workshop's objective is to further investigate and refine the distance needed to be beyond the near-field.

LM4 measured models with the rail mounted on both the aft and forward window blanks to be in position to measure far and near distances, respectively. Measurements started with the 1021-01 model for both rail positions because its measurement results could be compared to other tests to validate that test equipment was working correctly. Figure 263 shows that LM4 results are very closely matching previous LM3 measurements, with the LM4 results being a bit sharper and lower in CL. Excellent 1021-01 test-to-test repeatability provided confidence for proceeding with further testing.

For far measurements, the SEEB-ALR and 70° Flat-Plate Delta models were measured for flow diagnostics at both Mach 1.6 (for 1021-01) and Mach 1.7 (for 1044-02). The gray lines in Figure 264 show individual measurements of the SEEB-ALR flat-top signature. The scatter in flat-top amplitude quantifies variations in local distortion. Some very extreme peaks are seen at X's of -3 to 3 and 7 to 19, but not between 3 and 7. These spikes have a spacing between them that matches the movement spacing between measurements, so the spikes are likely to be repeating from the same 2 spots in the flow-field as the model is moved through them. Dropping data selectively around these strongest flow-field distortions can help reduce rounding in spatial averaging. Methodology is being modified to investigate such improvements.

Rail measurements (Figure 265) of the 70° Flat-Plate Delta model confirmed that the underside of the model produced little disturbance of the flow on its own, making it suitable for its intended purpose of measuring reflections of flow-field disturbances. In fact, the grey lines above from individual measurements were an example of reflections because the model underside did not produce much disturbance on its own, so these variations were mostly reflections. Reflections do not produce the extreme peaking that can come from flow-field distortions.

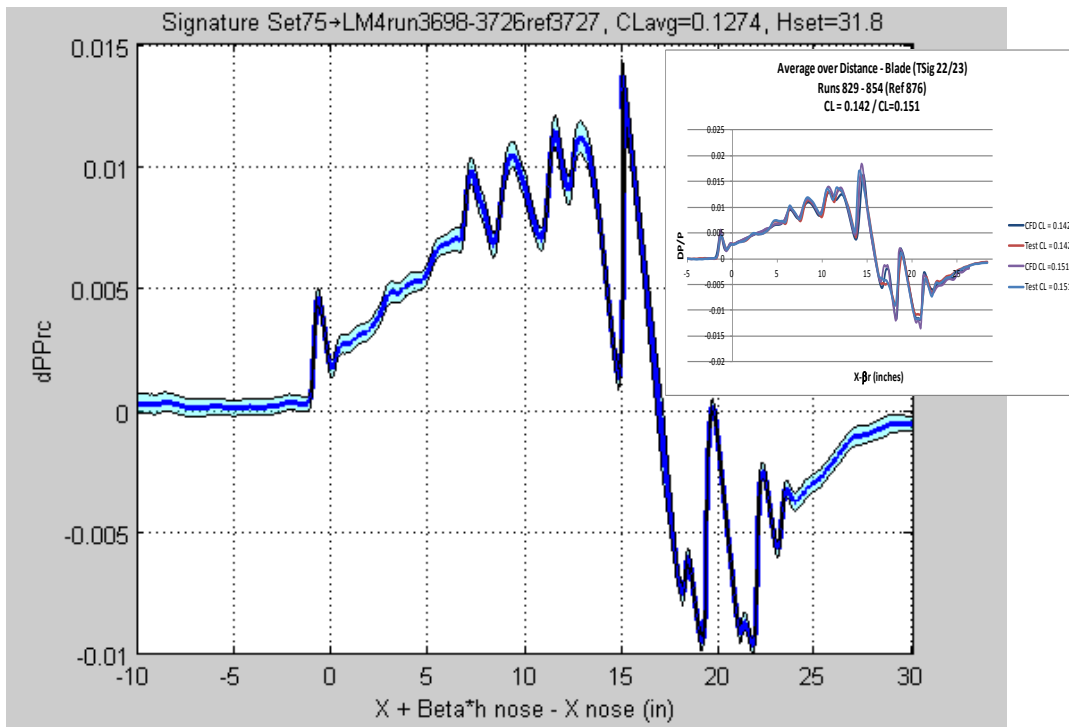


Figure 263.—Excellent Test-to-Test Match (validated before proceeding with LM4)

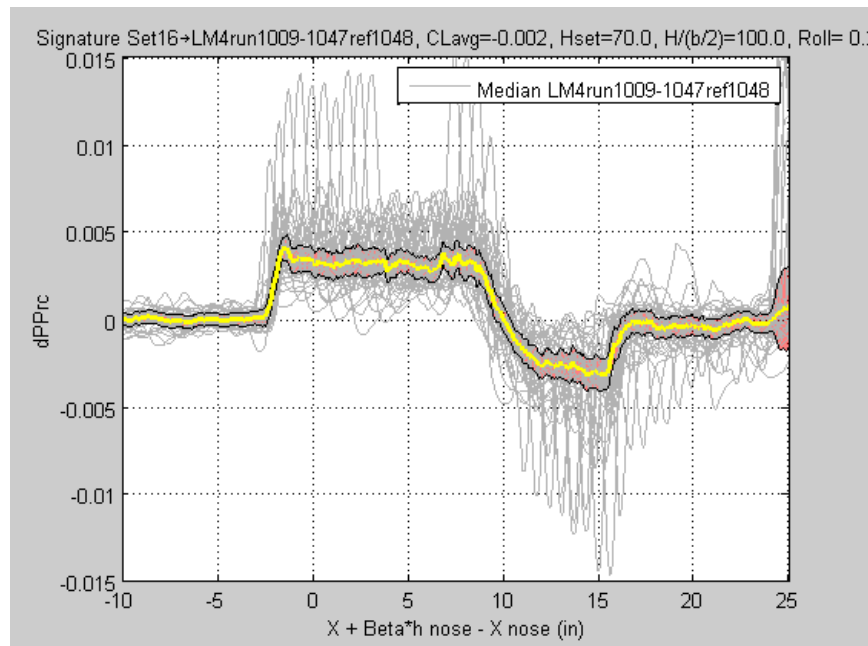


Figure 264.—There Does Appear To Be Better and Worse Locations For Measuring in the Tunnel—Selective Data Processing Might Improve Results

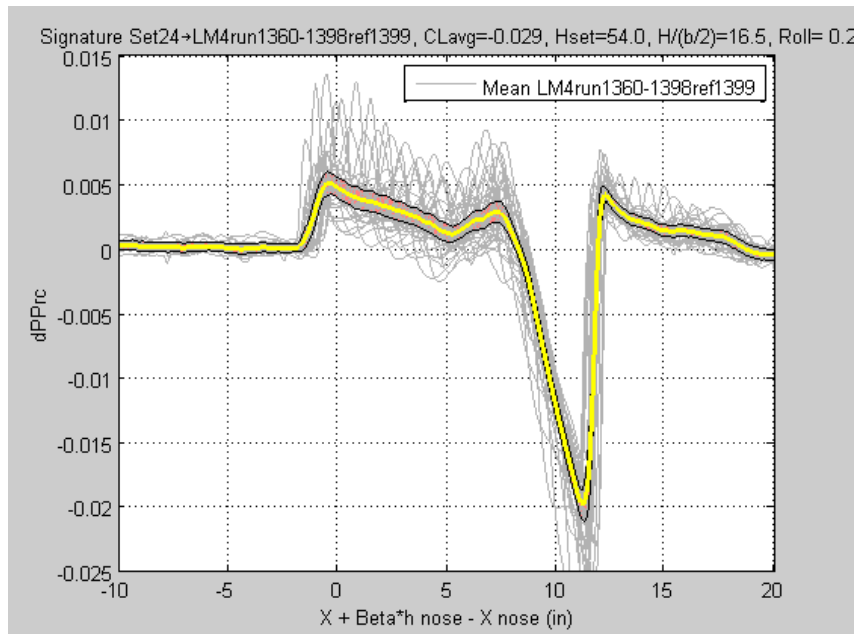


Figure 265.—The 70° Flat-Plate Delta Model Produces Little Disturbance Under Itself So Reflections Could Be Characterized to Improve Flow-Field Calibration

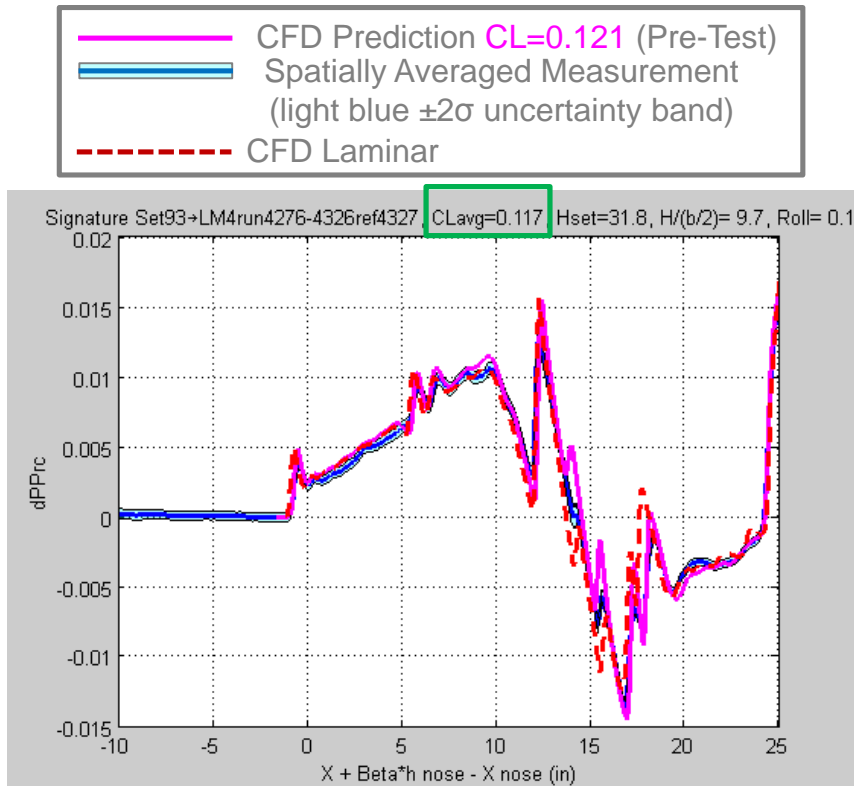


Figure 266.—Measurement Fell Between Turbulent and Laminar Solutions

The 1044-02 model was measured in the tunnel at distances from 6 to 21 semi-spans for near-field and beyond near-field CFD validation. Design of the full-scale 1044-02 configuration included inlets with spillage and nozzles with exhaust. To greatly simplify testing and reduce test cost, flow-through nacelles were used for the model. These simulate typically about 85 percent of the inlet disturbance but produce more nacelle trailing edge expansion than our nozzle exhaust operating at maximum efficiency. The flow-through nacelles do produce a majority of the same flow disturbance according to the small signature difference predicted by CFD. And the model's scale creates a much thicker boundary layer with substantial portions of laminar flow (found in other tests). So the model will always have some signature differences with the full-scale vehicle. We made the model match the vehicle in as many ways as possible, validating as much as possible; and then, use CFD to predict the remaining small differences. For both the 1021-01 and 1044-02 configurations, the difference between models and full-scale were quite small, but still a significant difference to the shaped boom signatures. Further, it was found in general that while full-scale analysis can be done mostly with Euler CFD, matching models requires NS-CFD modeling of the boundary layer. Figure 266 shows a spatially averaged measurement in dark blue for the 1044-02 model at Mach 1.7, near the desired cruise CL of 0.121 and measured 10 semi-spans from the model where good measurement accuracy was evident from the narrow uncertainty band also shown. The magenta prediction used a fully turbulent boundary layer assumption, and mostly matches very well. However, also performing CFD with a fully laminar boundary layer assumption and plotting it in dashed red, created some small signature differences. Significantly, where the turbulent and laminar were different, the measured data tends to fall in between the differences. In reality, the model had mixed flow with substantial portions laminar and turbulent, so the measurement falling in between was exactly what should have been expected. Generally, much of the signature difference between laminar and turbulent is due to the different boundary layer displacement thickness, so differences can be estimated approximately without needing a full analysis. The following figures only plotted turbulent CFD.

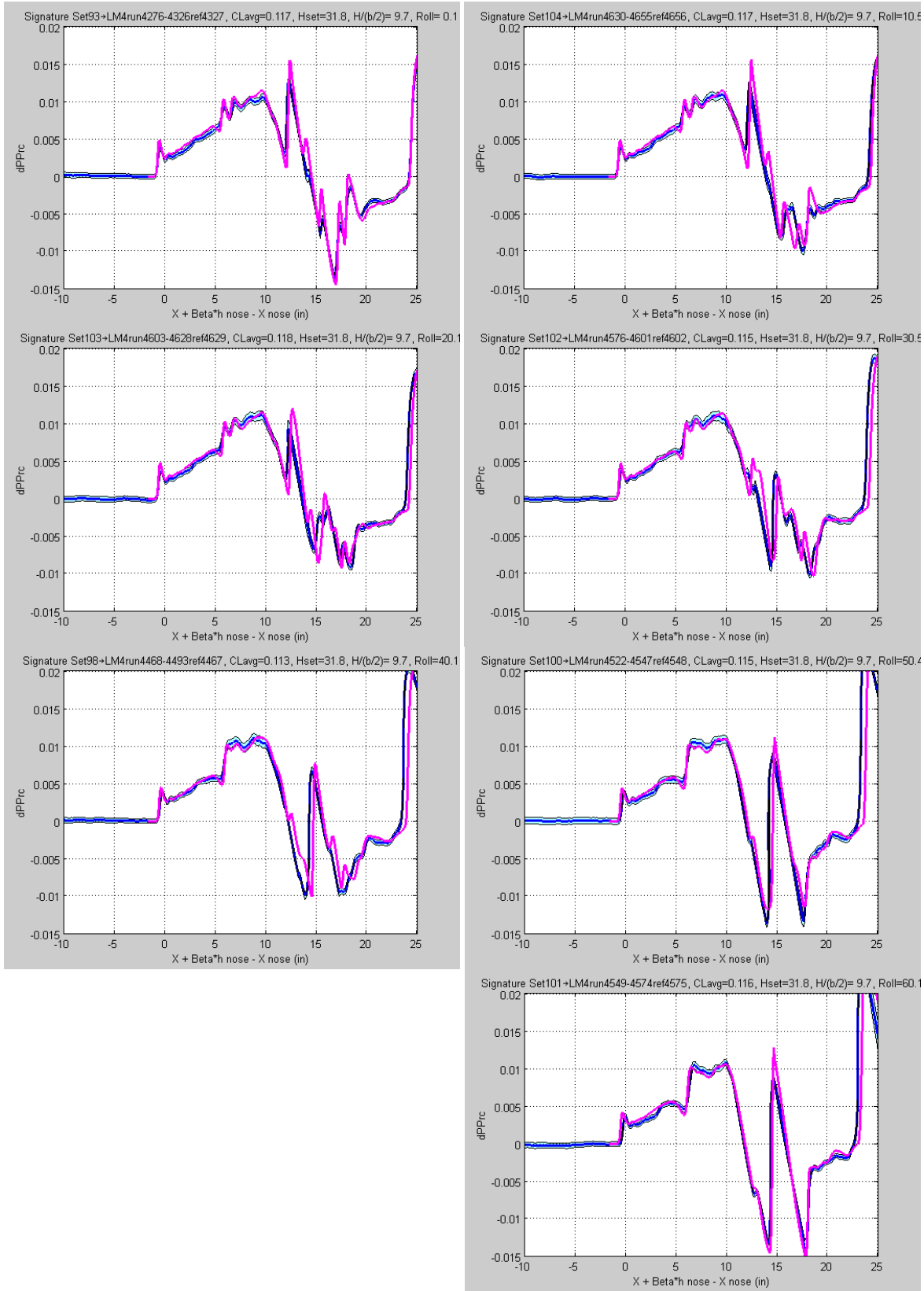


Figure 267.—Predictions Matched Measurements for Roll Angles from 0° to 60°

The undertrack (roll 0°) match is in the upper left corner of Figure 267, along with the other roll angles every 10° to 60° and all achieved excellent matches of sufficient accuracy to match ground sonic boom predictions (applied far-field correction to measurement and prediction based on prediction).

Since nacelle on measurements matched predictions, nacelle off measurements matching is not as significant. The signature tends to be very sensitive to nacelles, especially when mounted under the vehicle, and there are more sources of possible difference between the predicted and wind tunnel nacelle flows. Whenever there is a mismatch between prediction and measurement the nacelles are most often involved; so in such a case, the next match to check is a nacelles off comparison. In the past, the analysis and measurement of the rest of the geometry has matched, allowing focus on the problematic nacelle region thereafter. Our nacelle off CFD analyses matched measurements as shown in Figure 268 at two roll angles.

Measurements were taken at several distances between 7 and 21 semi-spans to understand the worsening of measurement accuracy with distance. The Figure 269 measurements at 13 semi-spans are at the greatest measurement distance possible with the rail in the forward window blank. Figure 270 showed that signature uncertainty increased as measurement distance was increased. More rounding and smearing of signature features also occurred as measurement distance increased. These degradations were expected based on previously measured increased effect of flow-field distortions at increased measurement distance and previously observed measurement accuracy loss with distance. But in addition, Figure 270 indicated that part of the degradation in the 9x7 at greater distance comes from reduced measurement accuracy with the rail on the aft window blank.

Figure 271 showed the match between predictions and measurements for roll angles of 0°, 20°, 40°, 60° at 21 semi-spans distance. The uncertainties are large and there is a substantial mismatch in the peak of the signature at 20° in roll. Matching the CFD CL condition better would help some, but other improvements are needed too. Flow calibration model measurements should be looked into further along with further signature processing improvements.

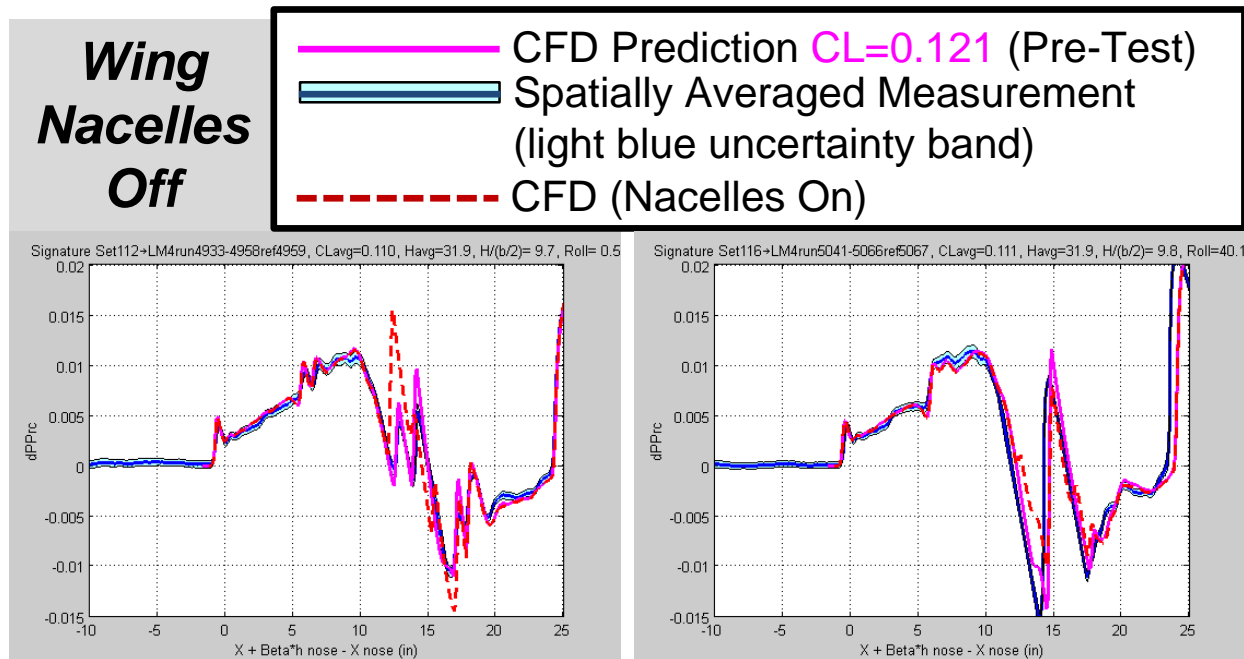


Figure 268.—Large Predicted Nacelle Effect is Matched by Measurements at 0° and 40° Roll

13 Semi-Span Distance

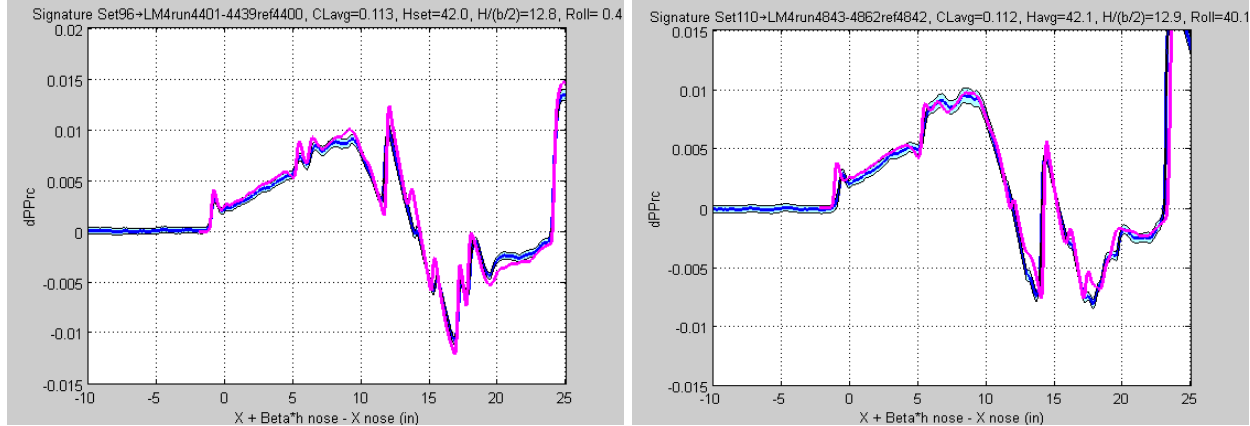


Figure 269.—Still Matching Well at 13 Semi-Span (b/2) Distance at 0° and 40° Roll

Increasing Uncertainty from 13 to 21 Semi-Spans (same 21 H/(b/2) CFD prediction shown for comparison)

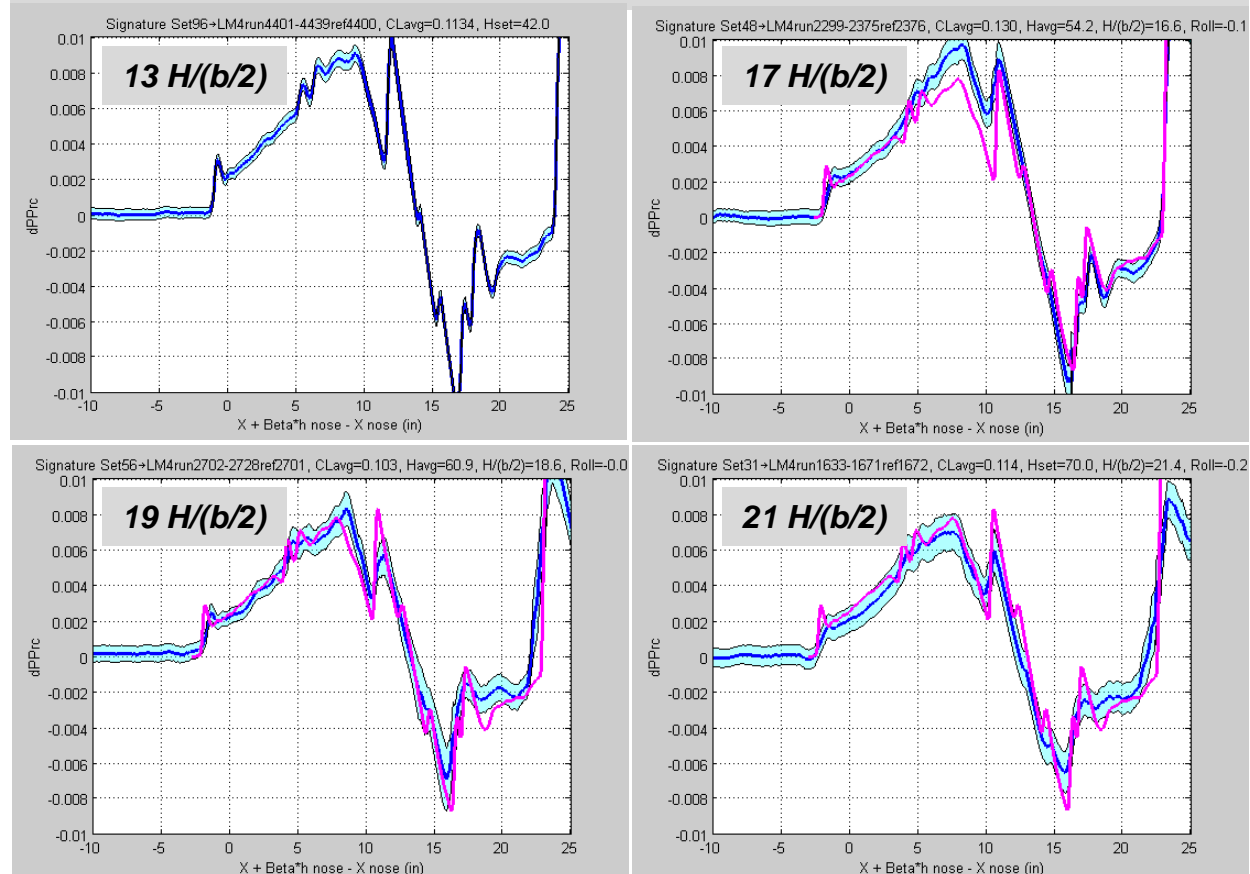


Figure 270.—Signature Uncertainty and Detail Degraded With Increased Measurement Distance but Aft Rail (17 to 21 semi-spans distance) Position Responsible for Part of Degradation

21 Semi-Span Distance (Beyond Near-Field)

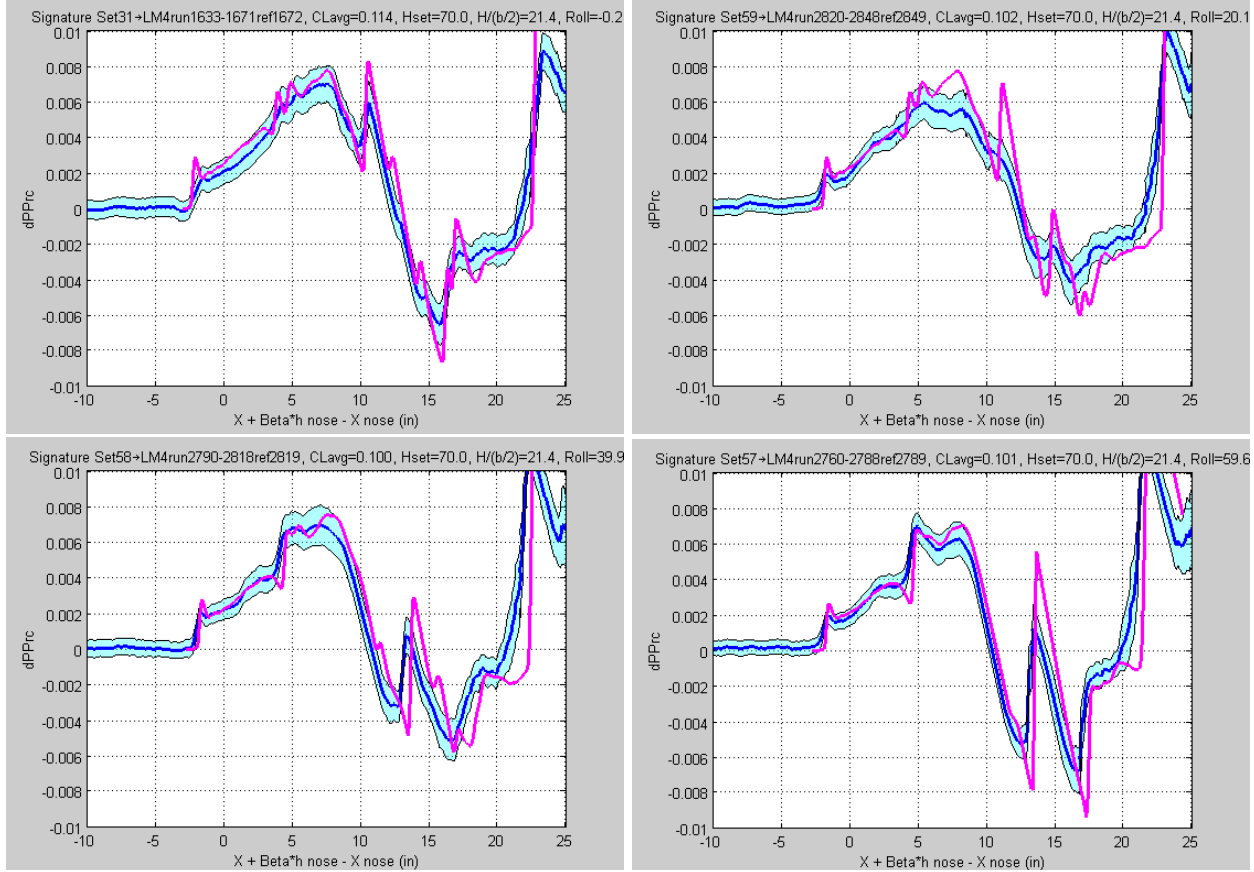


Figure 271.—Measurements and Match Showed More Uncertainty Than Required, Further Measurement Processing Improvements Needed

With some extra time available aided by the large productivity improvements achieved, measurements and flow visualizations were taken of the NASA 69° Delta Wing-Body model. Its signature magnitude and length were reduced relative to the others because of the smaller model size, only 6.9 in. long and 1.36 in. semi-span. But since it is not a shaped boom model, its signature has relatively large shock strengths. The model's signature coalesces into 3 shocks, predominantly from the nose, wing compression (usually coalesced from the first 2/3 - 3/4 of the wing) and wing trailing edge. These three coalesced shocks will average the tunnel distortions located across the ~1/3 of the vehicle length that coalesced into that shock, so tunnel distortions affect a 3 shock signature much less than a shaped boom signature. As seen in Figure 272, individual measurements had far less scatter to begin with even before they were averaged. In the original 1973 paper on this model (and other models investigating the effect of wing planform variations) it was tested using a single orifice probe 8 in. off the wall and measurements were made at three CLs. Figure 273 showed the effect of a CL or alpha change on the model's signature. It mostly increases the magnitude and impulse of the wing compression shock with little change to the signature elsewhere.

Figure 274 shows the signatures that resulted from measuring the model at 0°, 30°, 60°, and 90° of roll. The nose shock did not change at different roll angles because the nose is axisymmetric; but interestingly, the wing compression shock also changed very little at the different roll angles. The wing's leading edge sweep is near the Mach cone angle, so its volume growth is not very different at different roll angles. In contrast, the close to unswept wing trailing edge results in a substantially changing aft

shock that splits into two. As the measurements rolled from 0° to 90°, the wing trailing edge first terminates at nearly the same X station, but as roll angle increases the wing halves on either side of the body shift in position relative to each other in the signature, breaking into two shocks that get farther and farther apart. These kinds of differences are important to notice when trying to design a full-carpet shaped boom vehicle.

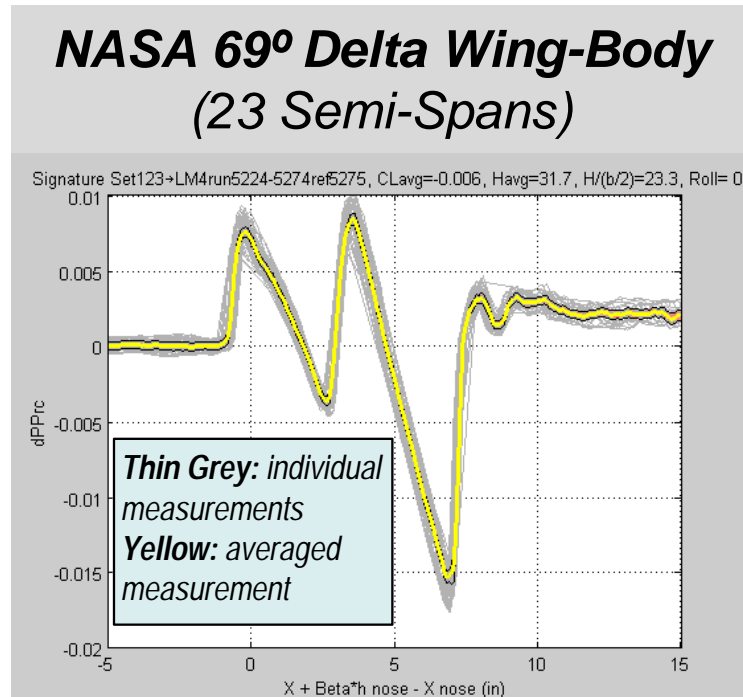


Figure 272.—Despite a Small Model a "Nonshaped" Boom Design of 3 Coalesced Shocks is Far Less Scattered by Tunnel Distortions

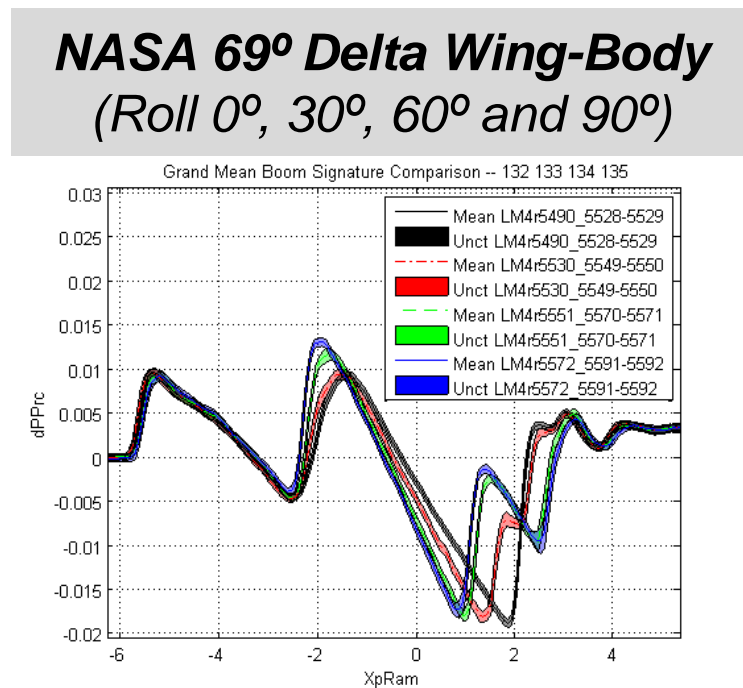


Figure 273.—Effect of Alpha Coalesced Into Only a Shock Magnitude Change and Small Recompression Detail Difference

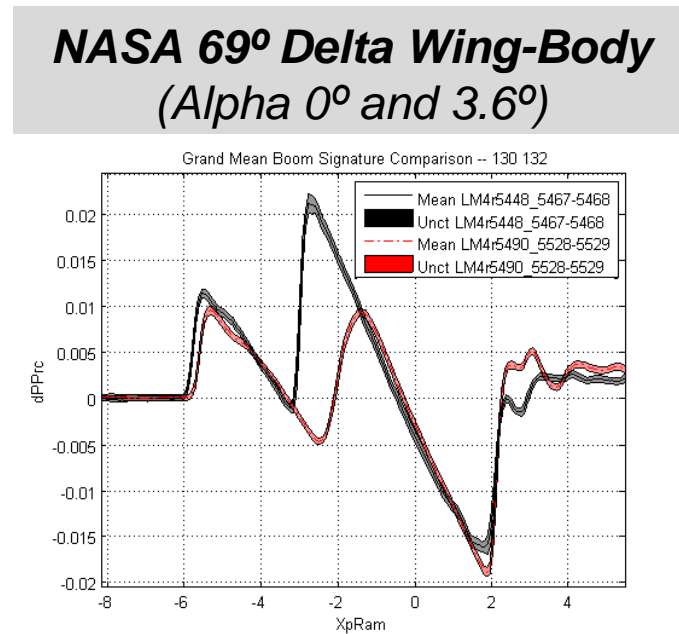


Figure 274.—In Roll, Wing Trailing Edge Shocks Different While Leading Edge Shocks Similar—Because Leading Edge Swept Near Mach Cone

5.0 Summary and Conclusions

5.1 N+2 Configuration Refinement

LM validated that it's refined N+2 Phase 2 1044-X configuration was an environmentally compliant and high efficiency conceptual design. We concluded that such a design could be developed into a viable product; and as such, this 1044-X configuration continues to play a key role in future research as an example of an N+2 product and its characteristics. Those characteristics meet N+2's environmental goals with shaped sonic boom, competitively low airport noise and low cruise emissions.

5.1.1 Quiet Shaped Boom

A key boom shaping improvement, full carpet <85 PLdB, was achieved in Phase 2. Off-track and under-track shaping requirements were simultaneously met. These predicted levels are based on our validated LMBOOM-sBOOM Burger's propagation methodology, which matched NASA and the rest of industry within 1 PLdB (Ref. 12). Plus, there are a number of other factors that impact the typical loudness that would be heard from N+2 operations. Simulating actual operations within an airline city-pair database, a lot of flying is done for shorter trips and by the end of every trip—flight is at reduced fuel weight, which reduces loudness. So the average loudness of the vehicle is biased toward the end-of-cruise (EOC) weight and would be 79 PLdB for this configuration, based on Burger's rounding methodology.

In addition to rounding, in actual flights turbulence and winds scatter sonic boom propagation and cause the actual loudness at any point on the ground to vary several PLdB. Helpfully, turbulence tends to decrease loudness much more often, with median shifts of -3 to -6 PLdB having been measured (from N-waves) in light to heavy turbulence, respectively (Ref. 13). In a comparison between Burger's and 30 weak N-wave dive booms, the flight measurement trend was found to be 5 PLdB quieter than the Burger's prediction. So our best indication from this small dive boom sample is that the N+2 1044-X would average 74 PLdB in practice. Because this increment is so significant, more measurement—prediction comparisons with Burger's should be made to quantify this increment as accurately as possible. (To determine the best flight test correction to Burger's methodology, and incorporate its effect into vehicle design.)

TABLE 34.—N+2 ENVIRONMENTAL AND PERFORMANCE GOALS, AND
VALIDATED PHASE 2 RESULT (TABLE 1 REPEAT)

[Measurements of low N-wave dive booms suggest that Burger's alone may result in loudness as much as 5 PLdB too high.]

	NASA N+2 Supersonic Transport (2018-2020) Goals	LM N+2 Phase 2 Predicted and Validated Status
Environmental Goals		
Sonic Boom	85 PLdB up to 20° off-track (NASA specified goal)	<85 PLdB over full carpet 79* PLdB average (sBOOM)
Airport Noise (cumulative below stage 3)	10 to 20 EPNdB	21.55 (GE - predicted)
Cruise Emissions	<10 EINOx	5 EINOx
Performance Goals		
Cruise Speed	Mach 1.6 to 1.8 shaped boom flight	Mach 1.7 (1.8 over water)
Range	4,000 nmi	5,500 nmi
Payload (passengers)	35 to 70 passengers	82 pax
Fuel Efficiency (passenger-nmi per lb of fuel)	3.0	3.13 (using GE engines)

5.1.2 Quiet, Clean, Efficient Propulsion

In addition to shaping boom, the N+2 Supersonic Validations program also performed large scale acoustic nozzle testing of both Rolls-Royce and GE designs in Phase 1 (Ref. 14). In Phase 2 the GE design was redesigned to overcome some shortcomings found in the first test and the new design was tested. Details of acoustic nozzle redesign and testing are covered in Appendix B. Acoustic nozzle results are particularly important to this vehicle because it is a primary propulsion sizing condition. Typical transport engines are sized for takeoff field length and cruise thrust. A new supersonic transport's engines are sized for take-off noise and cruise thrust, and take-off noise is very dominant when trying to be as quiet as modern subsonic aircraft. Achieving competitive airport noise with a minimal sacrifice in efficiency has meant finding improvement contributions throughout the vehicle system, including operational procedure changes, rule modifications and other changes that don't put all the burden of meeting noise on technology improvements. This whole system solution has required close collaboration with engine suppliers as well as multidisciplinary internal expertise. And our improvements meeting the airport noise challenge are probably the most significant advances toward viability for supersonic transportation. In the late 1990s a supersonic propulsion system was predicted at Stage III – 7 dB, required a take-off thrust-to-weight ratio (T/W) of 0.32 and the propulsion system T/W was 3.2. Our N+2 system is predicted at Stage III – 22 dB, required a take-off T/W of 0.31 and the propulsion system T/W was 4.0—so in summary, the N+2 solution is 15 dB lower in noise and 22 percent lower in weight than that projected late 1990s solution. Our projected N+2 airport noise reduction is consistent with the latest subsonic vehicle levels.

And similar efficiency improvements were achieved by the propulsion system. Again, a combined system solution to propulsion and noise made these remarkable advances possible. A high-recovery, bleed-less inlet allowed the large airflow of a higher BPR (4+) engine to operate efficiently supersonically (contrary to strong past belief). The higher BPR achieves better cruise SFC and is particularly helpful at providing more airport thrust with reduced noise (as quantified above). Overall, this propulsion solution with its many cycle technologies and variability, detailed in Appendix C, combine to achieve a 29 percent SFC improvement over Concorde.

Contrary to most of the N+2 effort, the cruise emissions goal was met by the engine suppliers independently. Combustor technology was being developed in other programs. Under N+2 we were only to show that we could make a successful system solution that integrated that technology. That meant mostly that the engine supplier reduced the combustor temperatures to be compatible with the expected limits of the low NOx designs matching our technology availability date. Accommodating the temperature limits and slightly longer low NOx combustor only incurred a 1.5 percent increase in fuel flow because some of the temperature reduction impact was offset by needing less cooling air, thereby less consequential losses.

5.1.3 Efficient, High Performance Vehicle

For the terminology of this NASA supersonic research, N+1 indicates the first product enabled by these new environmentally compatible and high efficiency technologies. Prospective manufacturers have proposed products from medium cabin business jet size up to small regional jet size for private and public travel. N+2 intends to describe a product that will follow N+1. Typically the next product is made larger for greater efficiency and range and serves growth in existing markets. “One more engine” may determine how much bigger the product can be. There is likely to be more emphasis on public, scheduled service where cost sensitivity is greater, so low recurring cost and high utilization will have increased emphasis. On the N+2 Supersonic Validations program, we found that high efficiency could also be achieved along with the environmental goals. LM’s investment in sonic boom shaping methodology was always developed to achieve quiet shaped boom with minimal impact on efficiency. LM also teamed with Stanford University on N+2 to adapt some new optimization techniques to the design task. The N+2

design also exceeded its 3.0 passenger-nmi/lb fuel goal, which was a 70 percent improvement over Concorde's 1.8. This 1044-X design was made to comprehensively and with good fidelity meet the requirements of an N+2 vehicle. As such, a relatively small amount of effort has gone into its refinement for optimizing its performance. Further efficiency improvements should be readily obtained with additional refinement efforts.

5.2 N+2 Structural and Aeroelastic Analysis

A structural model of the N+2 1044-3 configuration has been developed and sized to preliminary design load cases, consisting of maneuver loads, landing and ground handling loads. Nonstructural mass, representing various system weights, passengers, cargo, fuel, etc., has been included in the model in order that the FEM have representative mass distribution for a credible flutter analysis. After initial sizing of an all-composite FEM to the design load cases, we learned that the tail was deforming significantly under load. Thus we provided a configuration recommendation to thicken the tail and aft deck by about 26 percent. The FEM was also updated to include metallic properties at major load introduction points, such as at gear attachment, wing root spar, tail-to-boom attachment and select areas of the aft deck and boom. The analysis and sizing of this hybrid metallic/composite FEM is presented in this report.

Even after increasing the tail and aft deck thickness we found that the tail was still deforming excessively under a 2.5 g, pull up design load case. Hence, we applied a displacement constraint on the tail to be no more than 10 percent of the tail span and re-sized the model. This FEM was designated FEM017-REV71. This constraint added 1731 lb to the airframe weight or roughly 2 percent of vehicle structural weight. In turn, a flutter analysis of this model showed that the flutter speed increased considerably with a minimum flutter dynamic pressure of 1600 psf (the minimum required flutter margin is roughly 900 psf). Consequently, we performed a flutter survey on the FEM sized without the tail displacement constraint, designated as FEM017-REV70. The flutter speeds for this FEM were lower but still met the required flutter margin. The primary flutter mechanism involved aft deck bending, tail bending and tail torsion.

Given the uncertainty associated with the propulsion system weight, we conducted a sensitivity study of flutter speed to increased engine mass. For a 40 percent increase in engine mass, the flutter dynamic pressure dropped by 12 percent, yet still met the minimum required flutter margin.

The initial open-loop flutter analysis of the N+2 1044-3 configuration has not revealed any show-stopping aeroelastic issues, especially in consideration that with a 2 percent increase in airframe weight we were able to increase minimum flutter dynamic pressure by 24 percent (FEM017-REV70 vs. FEM017-REV71). However, we acknowledge the weaknesses of the linear aerodynamic theory used in this analysis for the transonic regime.

5.3 N+2 Shaped Sonic Boom Testing and Analysis

The N+2 program's comprehensive wind tunnel validation of shaped sonic booms resolved long-standing problems, increased productivity and accuracy by more than an order-of-magnitude and validated efficient shaped boom designs 30 PLdB quieter than Concorde. For the comprehensive shaped boom measurement program planned for N+2, new measurement hardware and diagnostic reference models were built. In many past shaped boom wind tunnel tests, sometimes results were reasonable and sometimes results were unreasonable (Ref. 15). With the new hardware and tenacious analysis of data patterns, it was discovered that small, innate flow variations (found in all supersonic tunnels) are enough to distort weak, shaped signatures. With understanding of the fundamental cause of the measurement problem, a measurement procedure and data processing, termed "spatial averaging," was developed that only slightly increased measurement times while virtually eliminating distortions. By the final LM4 test,

the new RF1.0 rail measured complete signatures with an order-of-magnitude better accuracy in as little as 5 min, instead of the 50+ min required prior to N+2.

Most shaped boom testing was done at the NASA Ames 9x7 ft Supersonic Tunnel. A parametric test was run to optimize test condition variation tolerance, measurement oversample timing, total pressure control schemes and other measurement conditions. What turned out to be most important was that conditions that could affect the test section flow field, like humidity, needed not to change during a measurement set (all spatially averaged measurements and the reference measurement). Measurement procedures for spatial averaging: timing, distance and number of positions were optimized. Measurements and productivity were excellent in the 9x7 in the near-field, but the measurements lost detail and became rounded at distances beyond the near field, $R > 12$ to 15 ($b/2$) semi-spans (or approximately $R > 3$ to $4 L$ to use the old comparison), where validation was also desired. Additionally, the 9x7 tunnel cannot test below Mach 1.55. So tests were run in the Ames 11 ft tunnel and the Glenn 8x6 ft tunnel. The Ames tunnel had some flow disruptions at particular Mach conditions that required changing testing from Mach 1.2 and 1.4 to Mach 1.15 and 1.3. While the 11 ft could be used with such limitations, improvements would be desirable. The Glenn tunnel has the unique capability of testing continuously from Mach 1.0 to 2.0 and has symmetrical flexible walls for its nozzle. During testing though, pressure measurements were drifting with model movement but not proportionally or consistently. In analyses after testing, it was found that the drift was directly proportional to very slight Mach changes, so it is believed that if the Mach changes are eliminated the pressure drift will also be eliminated. Without the drift, 8x6 measurements taken at $R = 12$ ($b/2$) semi-spans look to have better detail and less rounding than 9x7 measurements at that distance, which seems to be due to the 8x6 having about 1/3 the reference pressure variation with time as the 9x7.

6.0 Recommendations

6.1 N+2 Configuration Refinement

- Following the success of this N+2 Supersonic Validations program, a Shaped/Low Boom Flight Demonstration (LBFD) program is being pursued. To support traceability of an LBFD program or system assessments of other continuing supersonic research, a very small effort is recommended to keep this N+2 design up to date with on-going technology refinements.
- Direct on-going indoor shaped boom annoyance research to specifically support and provide guidance for signature shaping to reduce indoor annoyance.
- By the end of March 2015, complete a best assessment of the loudness difference expected between measurements and predictions based on Burger's propagation methodology (to have 6 months until September 2015 to update LBFD design and traceability results to accommodate the increment).
- Continue cooperative airframe-engine system studies to further reduce system weight and noise without increasing propulsion noise stringency by optimizing the many unique aspects of this propulsion system: sideline noise sized, inlet choked/absorbed approach/take-off noise, supersonic exclusive engine rating integrated into noise abatement procedures, integration for sonic boom, packaging for external drag, cruise critical thrust and temperature and emissions, dual-Mach cruise inlet and afterburner noise/climb integration.
- Determine whether validated low noise nozzle and complex cycle performance can buy their way onto a next-gen supersonic vehicle when a turbofan with simple nozzle is adequate.
- Along with propulsion system studies, restart/continue a modest level of highly-leveraged research on weight reduction, laminar drag reduction and design optimization methodology to facilitate increasing vehicle efficiency and avoid enactment of “gas guzzler” restrictions.

6.2 N+2 Structural and Aeroelastic Analysis

As a result, we recommend that additional flutter analysis be performed in the transonic regime with a more suitable aerodynamic method (e.g., Euler, Transonic Small Disturbance, Navier-Stokes). Also, considering that the primary flutter mechanism involves aft-deck bending and because the vehicle is statically unstable in some configurations, we recommend that aeroservoelastic (ASE) analysis be performed with a pitch controller in the loop. It would be of interest to understand how a pitch controller, if the body flap is used for this purpose, interacts with the critical flutter mode since it involves aft deck bending.

All composite—thicken tail and aft deck 26 percent, switched to metallic properties at major load introduction points gear/wing/tail boom/pylon. Displacement constraint not needed. A 40 percent propulsion weight increase accommodated. Recommend: additional flutter analysis transonic with nonlinear, check ASE and flutter with a pitch controller in the loop

Unconventional aft deck stiffening alternative

- As an alternative, remove the aft deck 26 percent thickening (or leave if desired for fuel volume) remove metallic aft deck structure; instead, greatly stiffen the aft deck pitch by increasing the pylon height as described in Section 3.6.4 and Figure 197. The aft fuselage could also be more arbitrarily reshaped for greater height, and thereby pitch stiffness, without changing its cross-sectional area.
- Identify structural mass concentrations and investigate whether stresses can be reduced with design changes (like the above) and redesign the FEM for weight savings. See if reducing or eliminating metallic attachments can reduce weight and cost.
- Redesign the MLG to be mounted to the bottom of the wing and to the fuselage. Eliminate the MLG cut-out in the wing structure.
- Re-run flutter analyses with updated, lighter FEM; and optimize pylon height (pitch) and shape (width) of height blend into aft deck for V-tail support (mostly torsion stiffness).

6.3 N+2 Shaped Sonic Boom Testing and Analysis

- Devise and test Glenn 8x6 ft Mach control improvements, needing only movement of model support strut (no model or RF1.0 Rail needed until control appears to work) for initial testing.
- Build the 2nd half of the RF1.0 Rail and test it in the final 8x6 check (next).
- Implement 8x6 Mach control improvements with RF1.0 Rail x2 and LM4 model measurements at 31.8, 42.0, 50, 60 and 70 in. (or largest possible) at Mach1.7; and if time, measure flow at 1.2, 1.3, 1.4, 1.5 and 1.6 (in this order of priority).

Appendix A.—Acronym List

AIAA	American Institute of Aeronautics and Astronautics
AAPL	Aero-acoustic Propulsion Laboratory
ALR	Aft-Lift Relaxation
ANSI	American National Standards Institute
AoA	Angle of Attack
ARMD	Aeronautics Research Mission Directorate
BFL	Balanced Field Length
BPR	Bypass Ratio
CAD	Computer Aided Design
CATIA	Computer-Aided Three-Dimensional Interactive Application
CFD	Computational Fluid Dynamics
CG	Center of Gravity
DOE	Design of Experiments
EINOx	Emission Index for NOx
EIS	Entry Into Service
EOC	End of Cruise
EPNL	Effective Perceived Noise Level
ESF	Engine Scale Factor
FAA	Federal Aviation Administration
FAR	Fuel/Air Ratio
FOD	Foreign Object Damage
GE	General Electric
GRC	Global Research Center
GE GR	General Electric Global Research
GT	Georgia Tech
GTOW	Gross Take Off Weight
IML	Inner Mold Line
IRAD	Independent Research and Development
LA	Linear Actuator
KEAS	Knots Equivalent Air Speed (constant Q, dynamic pressure)
KTAS	Knots True Air Speed
L/D	Lift to Drag Ratio
LM	Lockheed Martin
MAC	Mean Aerodynamic Chord (often C_ref)
MDAO	Multi-disciplinary Analysis and Optimization
MSA	Model Support Apparatus
MTOW	Max Takeoff Weight
NASA	National Aeronautics Space Administration
NATR	Nozzle Aeroacoustics Test Rig
NLF	Natural Laminar Flow

NRA	NASA Research Announcement
OD	Outer Diameter
OS	Optimum Signature
OEI	One Engine Inoperative
OEW	Operational Empty Weight
OML	Outer Mold Line
OPR	Overall pressure ratio
POD	Point of Departure
PAX	Passenger
PL	Perceived Loudness
PLdB	Perceived Loudness Decibels
PLR	Programmed Lapse Rate
PR	Pressure Ratio
QR	Quarterly Review
QSST	Quiet Small Supersonic Transport
RCD	Rapid Conceptual Design
RH	Relative Humidity
RMS	Root Mean Square
ROC	Rate Of Climb
RRLW	Rolls-Royce Liberty Works
SF	Scale Factor
SFC	Specific Fuel Consumption
SLS	Sea Level Static
SOA	State Of the Art
SOC	Start of Cruise
SST	Supersonic Transport
TC	Technology Configuration
TE	Trailing Edge
TOC	Top of Climb
TOFL	Takeoff Field Length
TOGW	Takeoff Gross Weight
TRL	Technology Readiness Level
WBS	Work Breakdown Structure
ZFW	Zero Fuel Weight

Appendix B.—N+2 NRA—System Level Experimental Validations for Supersonic Transport Aircraft

Jixian Yao, Mugam Murugappan, Umesh Paliath, Lawrence Cheung, Ivan Malcevic, Kishore Ramakrishnan, Nikolai Pastouchenko, and Trevor Wood

GE Global Research
Niskayuna, New York 12309

Steve Martens, Phil Viars, Trevor Tersmette, Jason Lee, Ron Simmons, and David Plybon
GE Aviation
Cincinnati, Ohio 45215

Executive Summary

This final report covers the entire Phase II Effort. GE Global Research and GE Aviation supported Lockheed Martin in this Phase II, NASA sponsored ‘N+2 NRA – System Level Experimental Validations for Supersonic Transport Aircraft’ program.

Based on Lockheed Martin’s updated requirements and targets, GE modified an adaptive cycle engine propulsion system expected to meet or exceed the environmental goals set by NASA, from the recent Phase I program. This propulsion system takes advantage of cooled cooling air to extend the overall pressure ratio of the engine and increase thermal efficiency. A low noise, high performance exhaust system takes advantage of the innovative adaptive feature, to provide a third air stream to feed the inverted velocity profile and fluid shield on the exhaust for lower noise capability. Heat addition is also incorporated in the exhaust to provide augmented transonic thrust.

A limited trade study was performed for various fan pressure ratios. Jet noise assessment played a role in choosing optimal fan pressure ratio.

The flow-path of the IVP/Shield nozzles tested in Phase I was updated to mitigate the overexpansion at low power conditions that led to unsteady flow separation. A new exhaust nozzle configuration was required to fully mitigate this issue. The new exhaust configuration allows the primary exhaust to operate in a purely convergent mode as well as a convergent-divergent mode. This change resulted in higher internal nozzle performance across a wider range of the operational map. Large eddy simulations of the Phase I cutback configuration show very good comparisons to measured acoustic data and Phase II results show a much improved flow field.

Fan noise assessment was performed using a multi-stage fan configuration. Lockheed Martin supplied an inlet boundary condition. The inflow boundary condition is part of Lockheed Martin’s inlet CFD results, at flight Mach of 0.3 of isolated engine configuration. Fan was set at take-off condition.

In the Phase II continuation, a range of continued and new tasks are pursued and accomplished.

The NPSS cycle model was extended to capture transient effects and modified for use as an open loop transient-dynamic model.

A scale model corresponding to the improved sideline and cutback configurations was designed and fabricated. Scale model testing at GRC shows much improved acoustic performance, with an elimination of the unsteady separation seen in Phase I, although some broadband shock noise like component is seen, likely coming off the core cowl expansion surface.

The scale model exhaust nozzle acoustic test was performed at GRC. No evidence of the unsteady separation was seen in the measured Phase 2 acoustic farfield acoustic data. The three stream nozzle resulted in lower noise levels than the reference fully mixed equivalent nozzle. The effect of the shield was measured in the farfield acoustics as a reduction in the higher frequency ranges. A single chevron design was tested on the shield nozzle and on the portion of the primary nozzle not covered by the shield.

No combination with the chevrons resulted in overall (EPNL) noise reduction, although significant low frequency benefit was measured with the chevrons. The azimuthal variation around the three stream nozzle was measured and showed the lowest noise was achieved with the shield aligned with the microphones.

A range of levels of fidelity of CFD from steady RANS, SAS, to DES and to LES was performed on the Phase I exhaust configuration to find the proper fidelity level of simulations for the nozzle flow features to reduce cost of LES simulations. LES simulations were also applied to Phase II nozzle design, and the results were compared to the test, as well as to results of other lower fidelity simulations.

In the Phase II continuation, Lockheed Martin also provided a modified design of the inlet. Analysis was performed of the Lockheed Martin supersonic inlet coupled with the multi-stage fan mentioned above. The flow features of the installed configuration were explored. The acoustic analysis of the installed configuration was also accomplished and compared to the de-coupled analysis. The CFD process for large-scale simulations was developed and verified.

Due to insufficient wake mixing captured by RANS prediction, an effort was made to establish a correction factor using LES simulations and data of GE internal investigations. Both the fan IGV wakes and the inlet strut wakes were analyzed and the correction factors established.

A detailed CAA investigation was carried out for noise transmission through the inlet duct. The far-field projection is then analyzed using the FWH methodology. These analyses provide input to various models for system noise evaluations.

1 INTRODUCTION

GE Global Research and Aviation supported Lockheed Martin's contract from NASA on the N+2 System Level Experimental Validations for Supersonic Transport Aircraft. GE's support included propulsion system support through the modification of the advanced adaptive cycle propulsion system to meet the vehicle requirements and environmental goals. The overall goals are shown in Figure 1. They cover sonic boom, airport noise, fuel efficiency, and emissions. The sonic boom, cruise speed, payload, and range were essentially used by Lockheed Martin to set the propulsion requirements that GE used to design the propulsion system. The airport noise, cruise emissions, and fuel efficiency were targets that GE assessed based on the propulsion system developed.

	N+1 Supersonic Business Class Aircraft (2015)	N+2 Small Supersonic Airliner (2020)	N+3 Efficient Multi-Mach Aircraft (Beyond 2030)
Environmental Goals			
Sonic Boom	65-70 PLdB	65-70 PLdB	65-70 PLdB low boom flight 75-80 PLdB unrestricted flight
Airport Noise (cum below stage 3)	10 EPNdB	10-20 EPNdB	20-30 EPNdB
Cruise Emissions (Cruise NO _x g/kg of fuel)	Equivalent to current Subsonic	< 10	< 5 & particulate and water vapor mitigation
Performance Goals			
Cruise Speed	Mach 1.6-1.8	Mach 1.6 -1.8	Mach 1.3 - 2.0 low boom flight Mach 1.3- 2.0 unrestricted flight
Range (n.mi.)	4000	4000	4000 - 5500
Payload (passengers)	6-20	35-70	100 - 200
Fuel Efficiency (passenger-miles per lb of fuel)	1.0	3.0	3.5 – 4.5

Figure 1 NASA Supersonic Goals.

The baseline propulsion system was an adaptive cycle engine with VAATE Phase III technology assumptions with an approximate 2018 TRL 6 technology availability date. The adaptive engine architecture includes adaptive cycle features such as:

- Adaptive Cycle Features
- Cooled Cooling Air (CCA) with modulated turbine cooling
- Axisymmetric Plug (Axi-Plug) Exhaust with Inverted Velocity Profile, a Fluid Shield, and Chevrons
- Heat Addition

Together these technologies provide a propulsion system anticipated to meet the vehicle requirements and environmental goals.

GE also updated the flow path of axisymmetric plug nozzle with an inverted velocity profile and a fluid shield around 180-deg of the exhaust that was tested in Phase I. This includes the jet noise reduction technologies that are synergistic with the adaptive cycle propulsion system. RANS CFD was run for a number of cycle conditions to ensure good aerodynamic performance over the cycle. The internal nozzle

performance was calculated at each condition. Large Eddy Simulation was completed for the Phase I cutback configuration and limited runs were made with the Phase II nozzle at a cutback cycle condition.

The supersonic inlet was also combined with an existing multi-stage fan configuration that was previously tested to look at the acoustic impact of the wakes from the center-body struts and distortion from the open auxiliary inlet doors.

2 PROPULSION SYSTEM

2.1 PROPULSION SYSTEM OVERVIEW

The technology assumptions for this N+2 propulsion system were adjusted from a TRL 6 date of 2025 for the N+3 model to a TRL 6 date of 2018. The N+2 engine is a lower technology version of the NASA N+3 adaptive cycle engine concept delivered in 2009. The major impact of the lower technology level was designing to lower core temperatures, resulting in an increase in weight. Also, for the N+2 program Lockheed Martin switched to a tri jet configuration and the engine was resized to the higher thrust requirements resulting in an increase in FPR and a larger engine size. In the end, the propulsion system is still designed to meet the N+2 airport noise and emissions goals.

2.1.1 TECHNICAL DESCRIPTION

2.1.1.1 ADAPTIVE CYCLE ENGINE PROPULSION SYSTEM

The advanced Adaptive Cycle Engine (ACE) uses VAATE Phase II level technologies with a TRL 6 date of 2018. The engine architecture includes adaptive cycle features.

2.1.1.2 COOLED COOLING AIR (CCA) ADVANCED THERMAL MANAGEMENT SYSTEM (TMS)

The CCA system, enables the engine to be designed at a higher overall pressure ratio (OPR) for improved thermal efficiency, by keeping the critical blade cooling air down to low levels. The CCA system reduces cooling flow requirements and enhances the high-pressure turbine (HPT) blade life. The system operates by removing a small portion of hot compressor discharge (CDP) air and ducting it out to a Surface Cooler heat exchanger in a bypass duct.

2.1.1.3 ADVANCED Low NOX COMBUSTOR

As part of this program, an advanced low NOx combustor concept was assumed, leveraging work from the NASA Supersonic Low NOx Combustor contract studies. Meeting the N+2 cruise emission goal of EINOx = 10 g/kg fuel will be a challenging goal for the supersonic N+2 program.

To achieve the N+2 NOx goal, an advanced technology development targeting an N+2 timeframe is necessary to reduce combustor residence time, cooling flow, pilot, and fuel/air mixing times.

2.1.2 EXHAUST SYSTEM

The exhaust system design is very important for supersonic vehicles since the nozzle performance is critical to the efficiency of the propulsion system as well as enabling jet noise technologies. The basic exhaust concept is a variable A8 and A9 axi-plug exhaust with a number of technologies added to improve performance and acoustics.

2.1.2.1 VARIABLE GEOMETRY FEATURES

The exhaust has variable A8 and A9 (throat and exit area, respectively) capability through the use of a translating plug and cowl. The translating cowl also provides for a thrust reversing system.

2.1.3 NPSS TRANSIENT CYCLE MODEL

2.1.3.1 INTRODUCTION

Under this task, the NPSS Cycle Model of an Adaptive Engine delivered under the GE Subcontract to LMCO for the NASA NRA N+2 System Validation Study was modified for use as an open loop transient-dynamic model.

2.1.3.2 MODEL DEVELOPMENT

Transient models are used for assessment of engine operation in the development of the engine and aircraft controls and to assess system operational limits. A transient model is critical for engine and aircraft development but is often delayed until late in the program due to the complexity of modeling issues and the lack of component detail required for an accurate simulation. Having a transient model, even with approximate information about the engine, allows important control and engine response issues to be addressed early in the program when configuration and component technology changes are easier and cheaper.

The initial transient modeling is focused on low frequency requirements that meet most engine development needs. The simulation time steps are generally consistent with the sensor sampling rate and the dynamic response of geometry and fuel control hardware. A 10 to 20 ms time step is typically adequate. This time step allows the simulation to capture the movement of bleed valves, variable stators, fuel control action, and acceleration of rotors, heat transfer between the metal and gas path and the impact of flight condition changes on engine fuel burn and thrust response. The simulation ignores fast pressure or temperature perturbations, shock movements and acoustic level responses. These issues can generally be modeled on an average basis for most engine design and control development activities, ignoring the higher frequency content.

The first step in creation of the transient-dynamic model was to implement this low frequency capability. An engine control is created using this low frequency model and a control system model is eventually incorporated into the transient engine simulation. For this effort, open loop inputs of controlled values such as variable geometry and fuel flow vs. time are used to exercise the model.

Transient engine simulation result in different combinations of rotor speeds, component operating lines and flow conditions in the engines than those encountered in steady state operation. A key part of any transient model development is validation of the component models over the extended range of operation that will be encountered transiently. In this study, no component changes were required because the original Steady State simulation utilized components models that considered future transient use and the open loop studies. For example, the model included off-schedule stator effects for all components.

New transient specific information was created based on the system studies and similar engines. Inertias were obtained from the mechanical system studies and engine cross-section and weight. For heat transfer effects, typical values from similar engines were used heat transfer coefficients with surface area and

metal mass values from system studies. Basic validation studies were performed to validate the simulation behaved as expected based on past engine experience.

Dynamic engine simulation refers to high frequency response addressed on an average basis and considered negligible for the normal transient system issues. However, these high frequency events can be important in studying engine stability, stall, blow-out response, engine-aircraft interaction, engine-control feedback or engine failure modes. High frequency perturbations in inlet temperature or pressure and fuel flow or geometry pulses are typical events where a dynamic model can be useful. To address these events the model must be run at a time step consistent with the time scale of the perturbation and the time scale of the transfer of that perturbation across the component models in the engine. For detailed component design studies, this the time scale may be the transition across an individual blade row. For most engine simulations, the time scale is based on the component models where the dynamic effects are considered. In the inlet or nozzle this can be somewhat larger than the time step required for a multi-stage compressor or turbine and much larger than a single stage compressor. Typically the time step must be shorter than the time required for an inlet boundary condition change to traverse the component. This can be based on the overall volume of the component and the time required for changes in mass flow at the entrance to affect the exit mass flow or on the length of the component and the time required for a pressure or temperature perturbation at the component entrance to affect the component model exit value. The key modeling differences in for the components that include high frequency volume dynamics are:

Conventional Transient Component Model

- Flow In = Flow Out (No Mass Retained in Component)
- P,T In = P,T Out = P,T in Component

Dynamic Component Model

- Flow In – Flow Out = Change in Mass in Component Volume (Zero Steady State)
- P,T In vs. Out vs Component Can Vary (Equal Steady State)

In a conventional component model, continuity is satisfied by the simplifying assumptions of the model. The dynamic component model addresses the conditions where these simplifying assumptions are not true and the resulting impact on the component and engine response. For a short period of time, the increase in flow or pressure at the entrance to a component will not impact the exit pressure. An increase in entrance flow will increase the mass in the component volume and may also result in an increase in the component volume P and T. However, without the simplifying assumption of the conventional transient model, the exit flow is calculated based on the downstream boundary conditions and the new component values.

For a small change in flow going into a relative large component volume, this delay in the response can be long. For ground based power generation engines with a large inter-cooler, this difference can be large enough that it must be considered for low frequency operation and control design. For these very large volumes a simplified first order lag in the response across the component is often used to increase the accuracy of low frequency models. For high frequency events the emptying and filling of the component volume and the change P, T in the component and the boundary conditions must be modeled explicitly. For a dynamic model, the entire simulation must be run at the time step required to address the response of the most limiting component while other components can continue to run with conventional assumptions. The initial time step is selected based on the more limiting of the characteristic time to empty the component volume at the operating flow rate and the time for a pressure change to traverse the component. However, numerical stability often requires the time step to be smaller than this value depending on the number of volumes and other response characteristics of the simulation.

The test cases to show the impact of volume dynamics that follow are for a single volume element but the model delivered to NASA includes examples for multiple volumes.

2.1.3.3 MODEL DEMONSTRATION

Figure 2 shows a planar pressure pulse applied to both model the conventional transient and dynamic model. The impact on the engine response is show in Figure 3. Note that the change in core speed is small enough that it would not be noticed or considered important for most studies.

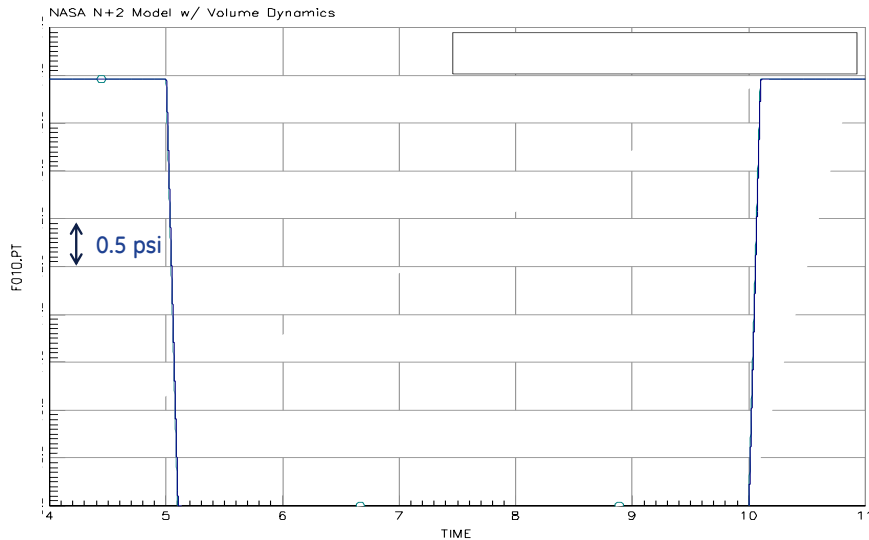


Figure 2 Pressure Perturbation – Conventional Transient vs Volume Dynamics

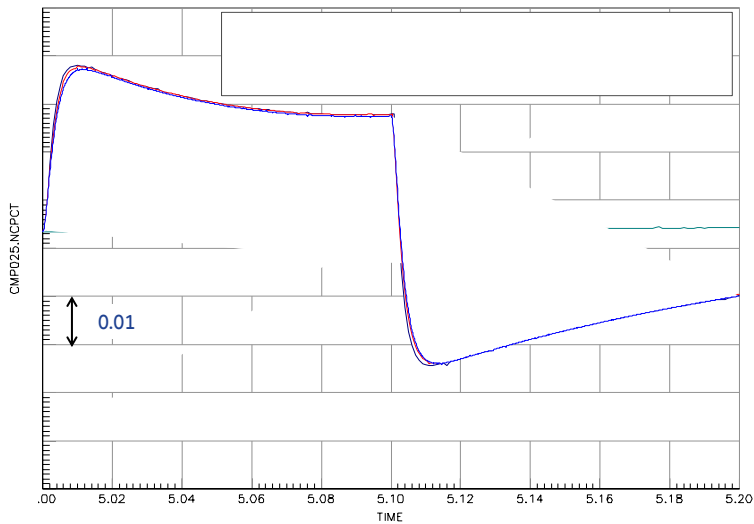


Figure 3 Impact of Time Step on Model Response

Figure 3 also shows the impact of different time steps on the dynamic model response. Only inlet pressure is perturbed but the volume temperature responds briefly to the change in pressure. Figure 4 shows the

very small change in temperature during the start and end of the pressure pulse as the volume equilibrates. Figure 5 shows the core speed response for the conventional transient model and the model with Volume dynamics. Both those the slight slow drop in core speed during the low pressure period and recovery to the original speed as the original pressure resumes. With volume dynamics the impact of the change in temperature at the start and end of the pressure step can be seen in the speed response. Even though this is obviously negligible for most engine studies, it can be important for stability analysis in combination with the high frequency pressure information. Figure 6 shows an inlet temperature pulse and the corresponding change in the volume pressure at the start and end of the pulse. Since the temperature change occurs for the conventional and volume dynamic model, the core speed response is the virtually the same.

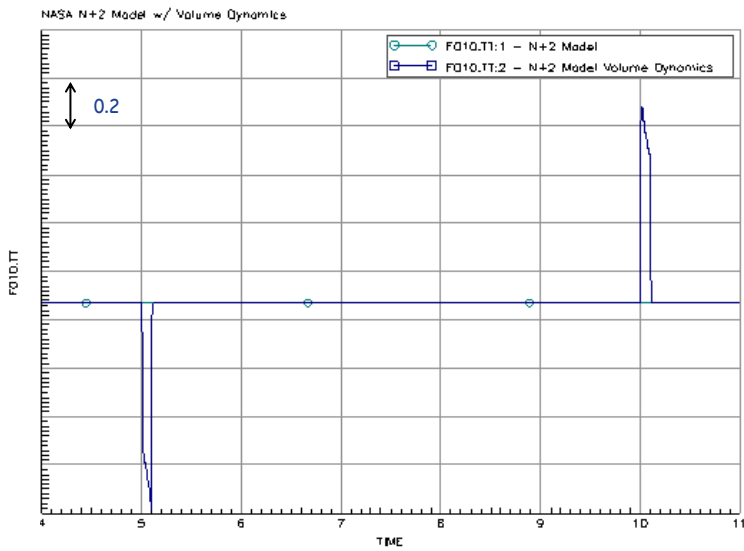


Figure 4 Volume Temperature Response to Pressure Step Change

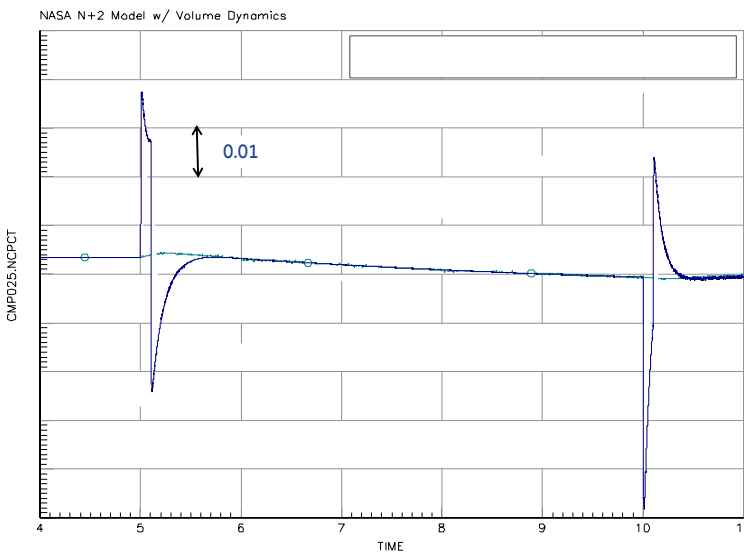


Figure 5 Core Speed Response to Pressure Step Change

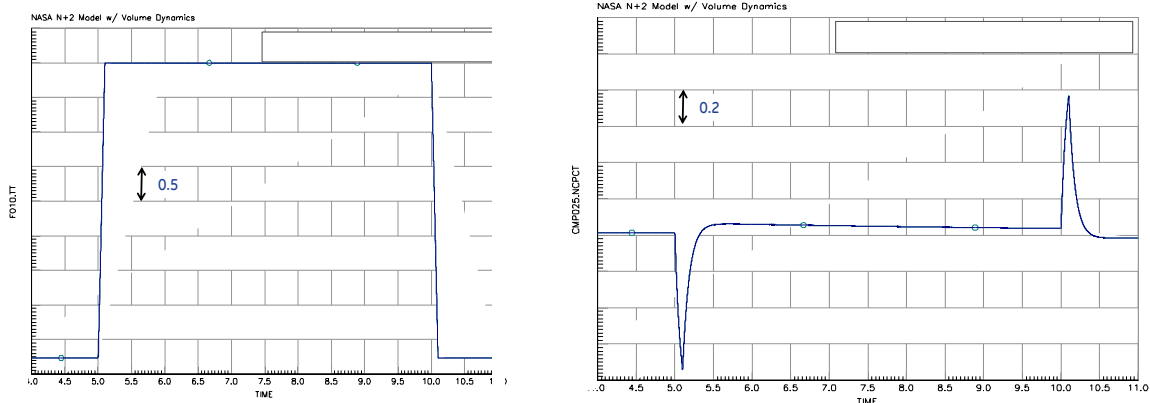


Figure 6 Dynamic Model Response to Temperature Step Change

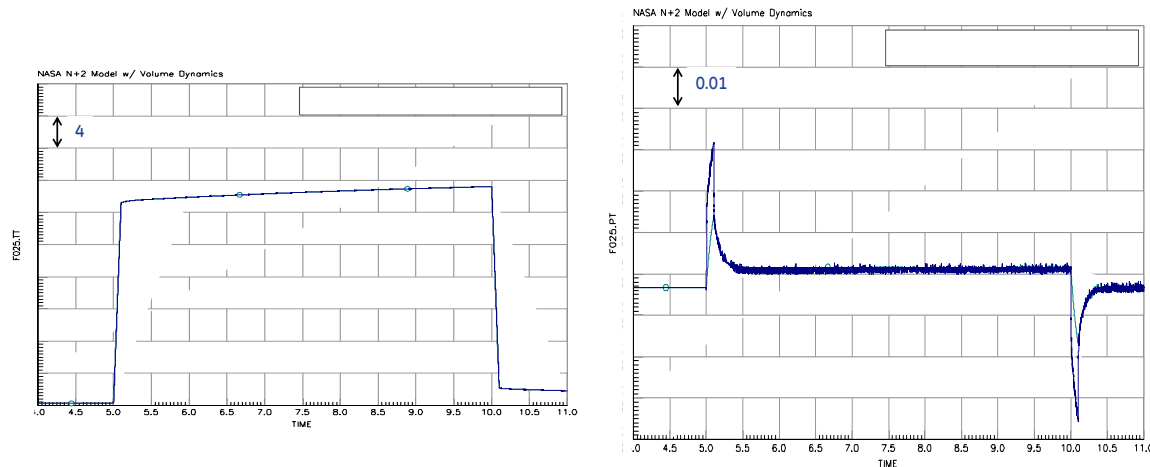


Figure 7 HPC Inlet Response to Temperature Step Change

Figure 7 shows the change in pressure at the HPC inlet in response to the temperature pulse. The primary pressure impact is due to the change in corrected rotor speed due to the temperature pulse but the volume dynamic model has a small delta at the start and end of the pulse. The HPC inlet temperature response is virtually the same.

Figure 8 shows the model response to a slow inlet pressure sine wave input. The response is similar to the step change but now there a more noticeable response to the pressure changes in the conventional transient model. The differences due to volume dynamics are significant but remain small compared to the base levels.

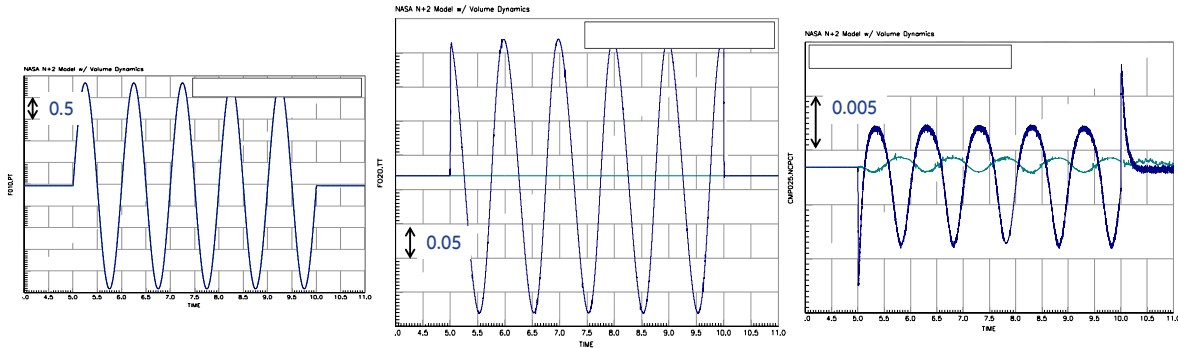


Figure 8 Response to Sinusoidal Planar Wave an Engine Inlet

The frequency of the pressure input causes a significant difference in the response of the engine. A range of frequencies were tested on the model. The results for low frequency showed little impact of the volume calculation as expected. Figure 9 shows that, as the frequency increases, the volume model captured the expected attenuation.

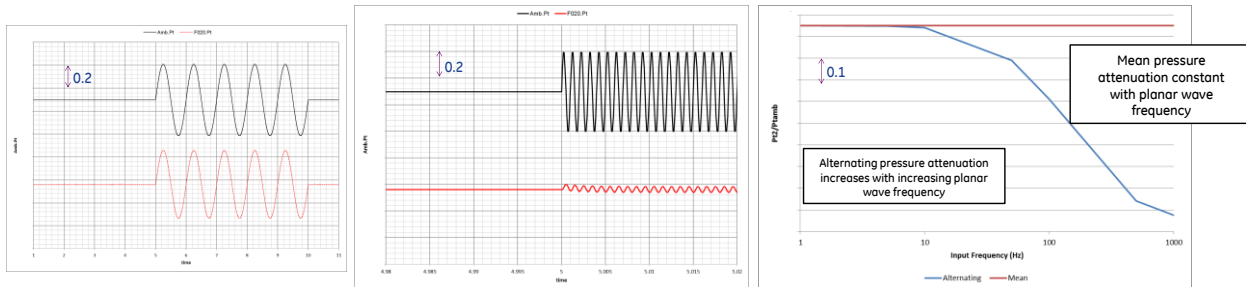


Figure 9 Frequency Impact Sinusoidal Planar Wave Attenuation

2.1.3.4 SUMMARY

As a result of this task, NASA has a transient and dynamic capable NPSS model for the N+2 engine implemented using typical GE practice and a set of test cases and sample studies to use as an example for future efforts.

2.1.4 PHASE 2 SYSTEM NOISE ASSESSMENT

Jet noise estimates were made for the cutback and sideline noise certification points for three fan pressure ratios. Figure 10 shows the estimated margin to Stage 3 for the total jet noise for the cutback configuration for a cutback certification point from a take-off trajectory provided by Lockheed Martin. The same take-off trajectory was assumed for all three fan pressure ratio engine cycles. This is not completely accurate since if the different fan pressure ratio engines were installed and the aircraft sized and reflowed different trajectories would result. The required thrust for this trajectory is shown on the figure and for this relatively low power condition the margins for each fan pressure ratio is fairly close and essentially the same for this level of estimate. Although at higher power settings, clearly the lowest fan pressure ratio engine results in the highest noise margin.

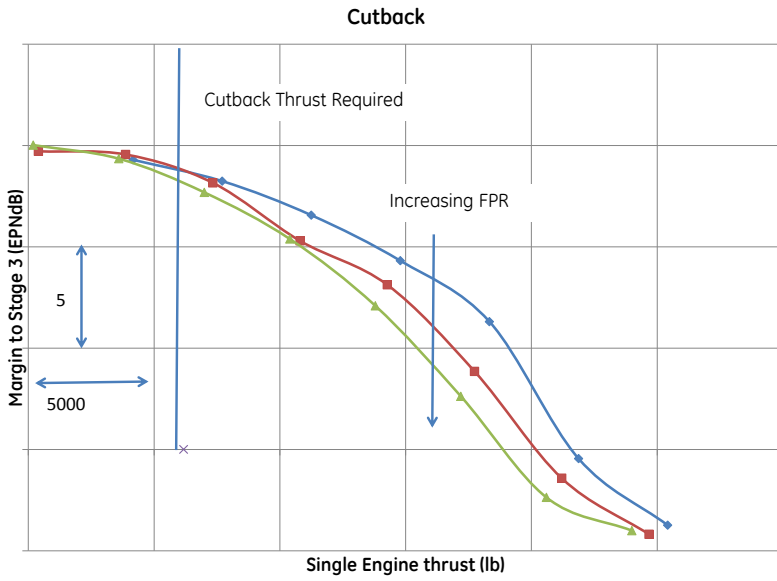


Figure 10 Margin to Stage 3 for Cutback for Jet Noise Only.

Figure 11 shows the jet noise margin to Stage 3 for the sideline trajectory. Again this sideline condition is constant for all three fan pressure ratio power hooks. At this higher power condition the lower fan pressure ratio clearly has the highest margin to Stage 3.

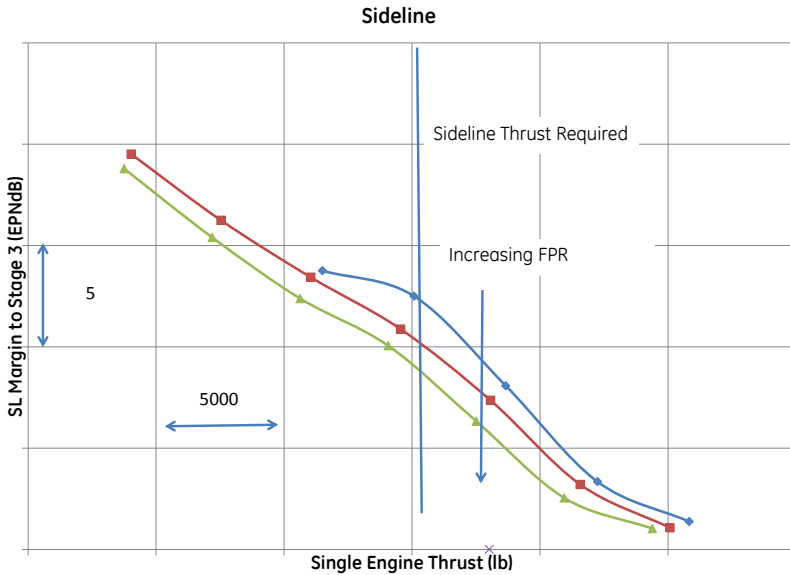


Figure 11 Margin to Stage 3 for Sideline for Jet Noise Only.

Taking into account the additional margin which would be realized when including the landing point and the reduction due to the other engine and airframe noise components it is anticipated that this engine design should meet the N+2 noise goal for cumulative margin to Stage 3.

2.1.5 PHASE 2 CONTINUATION SYSTEM NOISE ASSESSMENT

A system noise assessment including the fan inlet radiated and jet noise components only was made and indicates the current status is expected to meet the NASA N+2 community noise goals. Airframe noise and other engine noise components are not included in this assessment. No margins have been applied as this is a conceptual study only and no guarantees or commitments are implied. This assessment indicates that the fan noise component is important, especially at the cutback condition. A strong suggestion to take a more in depth and detailed look at the fan and inlet is made.

The results of the further refined fan and inlet computational aeroacoustics analysis to be discussed later in this report, including LES strut wake calculations and tone propagation through the inlet struts and the effect of the auxiliary door were applied to the fan inlet estimate in this section and the impact was less than 1 dB at each point.

3 AEROACOUSTIC NOZZLE

3.1 POD MODAL ANALYSIS OF JET PLUME FROM THE PHASE I NASA – IVP TESTS

A Proper Orthogonal Decomposition was performed on the 2D streamwise and 3D cross sectional PIV data at two operating conditions.

3.1.1 POD BACKGROUND

Proper orthogonal decomposition (POD) is a modal reduction technique for extracting or separating large scale structures from background turbulence¹. The mathematical theory for POD is based on the spectral theory of self-adjoint operators, which are widely used in turbulent theories²⁻⁴. This technique provides an optimal basis for the modal decomposition of an ensemble of functions, which in essence allows the extraction of the dominant features (i.e., coherent structures) embedded in an infinite-dimensional process with only a finite number of modes. Mathematically, Lumley indicated that the coherent structure as that structure which has the largest mean square projection on the velocity field. This essentially leads to solving an integral Eigen value problem with the cross correlation tensor as its kernel. The solution to this problem leads to extracting the dominant modes (or flow structures) in the flow field. For the present study POD is used to study the evolution of jet plume.

3.1.2 PIV SET UP

The origin of the coordinate system was the jet centerline at the common nozzle plane. The plane of the laser sheet was vertical, centered on the jet axis for the stream-wise PIV. The first FOV extended from the fluid shield nozzle downstream. The model was mounted such that the fluid shield was on the bottom of the rig to allow laser sheet to illuminate this flow. Due to the model being designed to align with the overhead microphone array, the light sheet crossed in a plane oriented 25° to the symmetry plane of the nozzle. The laser sheet was offset from centerline roughly 5mm to minimize reflection to the cameras. The PIV system was traversed axially 5 times in increments of 14", creating a 1" overlap between acquisitions, providing a total scanned field of 98". The Cross-stream PIV had a nominal field of view of 14" by 17" (360mm x 430mm) per acquisition point. Data was acquired at four axial stations: x = 7.25", 10.875", 14.5", 21.75", but for the current report, POD analysis is only presented at the nearest nozzle location. PIV image pairs were acquired to disk at a rate of 2Hz. Time delays between the matching image pairs was adjusted to make the highest expected velocity produce an 8-pixel displacement on the cameras. 400 image pairs were recorded for each plane of data, requiring 3.5 minutes to acquire a single

plane of data. Subsequent to the acquisition, images were processed using multi-pass correlations with local distortion and, in the case of the cross-stream data, phased-only filtering to minimize the effect of the nozzle image in the background. The final pass of correlation was done on a 32x32 pixel region with 50% overlap.

3.1.3 RESULTS

Figure 12 shows the mean U velocities in the stream-wise plane near the nozzle exit for both the conditions in region 1 (closest to the nozzle/First FOV). The color scale is set the same for both these cases. The shield is at the bottom. All three streams could be observed on the lower half. The outer-most stream is the shield stream which spans the lower half (180 degrees) of the nozzle. The center body blocks the laser light sheet from entering the fan and core streams on the top half, hence only the flow field past the center body is resolved. The separation region at the exit of the fan stream could be observed in both these contours. Comparison of both these cases indicates that the separation region extends further for the sideline case as compared to the cutback condition. Also observable are the shock cells in the sideline condition.

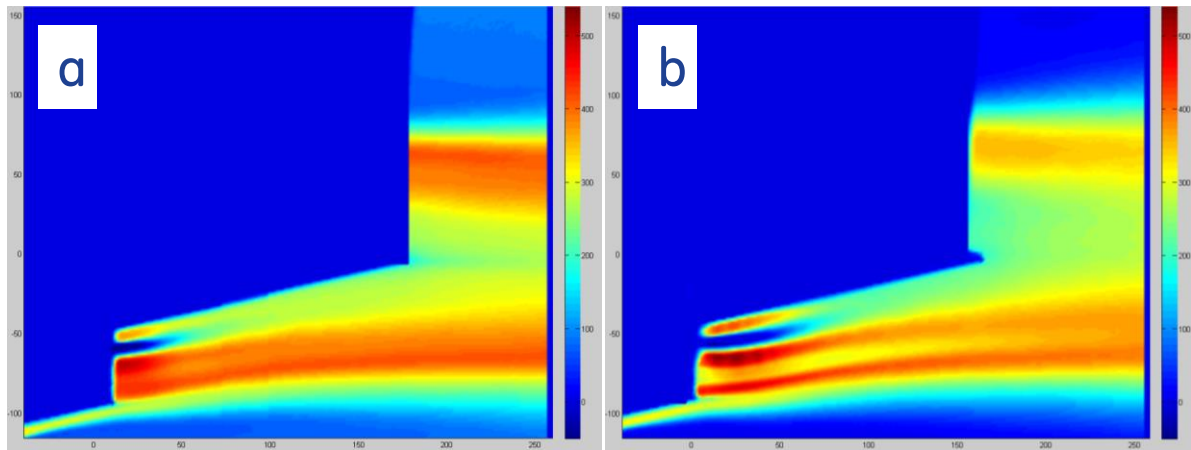


Figure 12 Mean Streamwise, U, Velocity Contours, (a) Cutback, (b) Sideline.

Figure 13 and Figure 14 show the 1st U and V POD modes for the cutback and sideline conditions. The POD modes are normalized. The contours are displayed so that positive is red and blue is negative velocity. The highest POD energy is contained in the structures on the top half of the nozzle. This is expected, since the top half of the nozzle diffuses faster and hence generates larger structures in the POD. Large scale activity is also observed in the region spanned by the separation. The relative energy contained in these structures is much weaker in the sideline case as compared to the cutback case. Due to the higher momentum and larger lateral jet spread of the fan stream for the cutback case the V POD modes show large scale activity that extend further downstream.

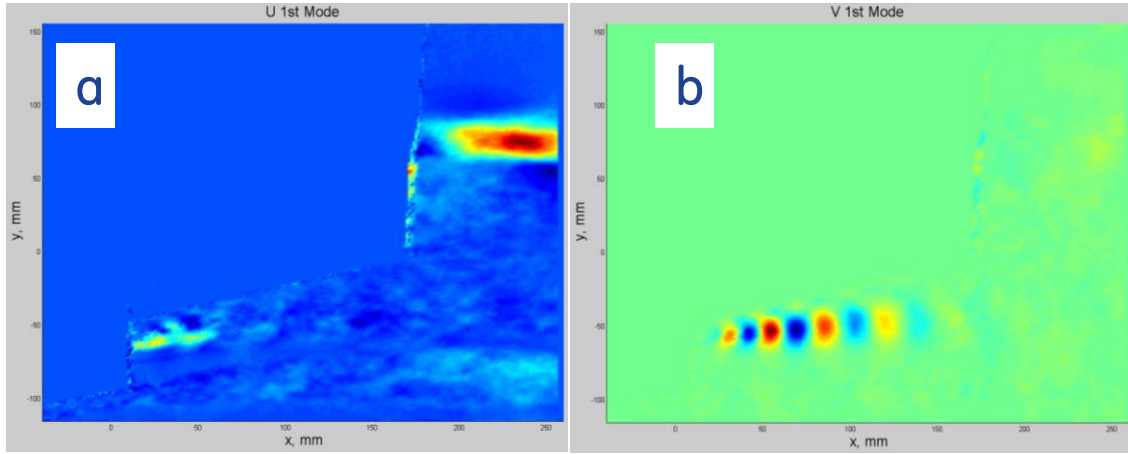


Figure 13 1st (a) U and (b) V POD Mode for the Cutback Condition.

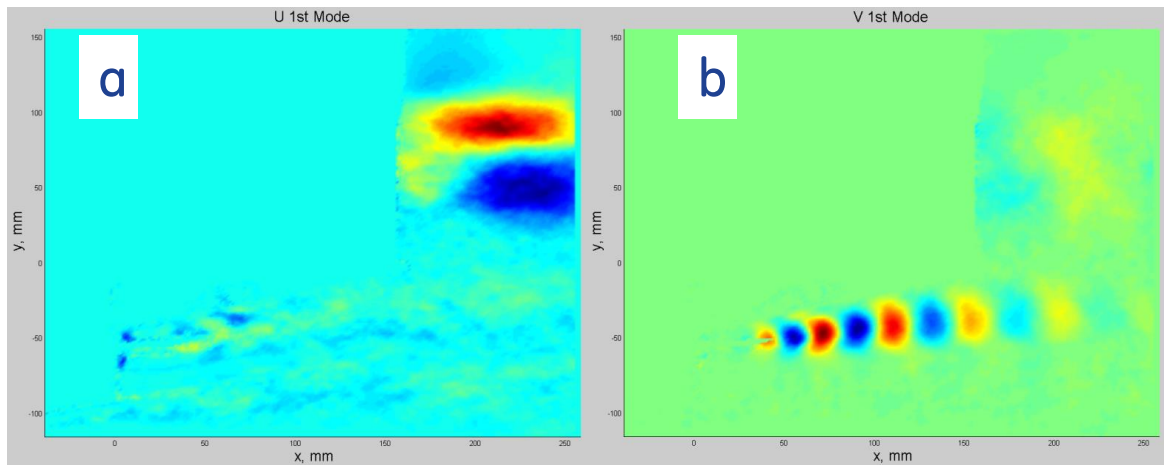


Figure 14 1st (a) U and (b) V POD Mode for the Sideline Condition.

In order to better understand the modal dynamics near the separation region. POD analysis was performed in a small region just spanning the separation. Figure 15 and Figure 17 shows the mean stream-wise velocity contour, 2D TKE and cumulative energy distribution of the cutback and side line condition respectively. Figure 16 and Figure 18 shows the first 3 U and V POD modes in the zoomed region for both cases. The modal energy distribution is found to asymptote in both these cases indicating that the modal content is statistically resolved in this region. A number of features could be observed from these charts. First, the only observable modal activity is on the inside shear layer enclosing the separation region in both the cases. Since the separation region is shorter for the cutback condition, the fan and core streams mix quicker which lead to more distinct modal structures in U POD modes in the cutback condition as compared to the sideline case (compare 3 distinct structures in U POD from Figure 16 c and e as compared to 2 structures in Figure 18 a, c, e). Evidence of increasing structure size with downstream distance is observed in the cutback condition. For the sideline condition, the lower momentum core as compared to the higher momentum fan was found to diffuse quickly and mix with the separated hot fan stream. This led to more coherent modal structures on the top half as compared to lower half. The hot fan stream with higher NPR was found to maintain its momentum for longer distances which suppressed the

jet spread and mixing leading to weaker modal structures (compare the top structures of Figure 18 to the bottom ones).

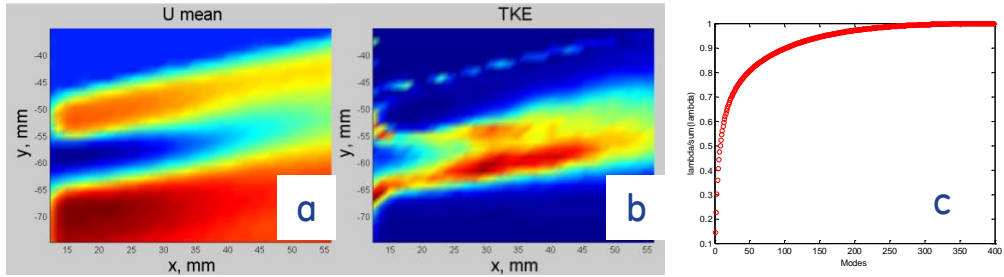


Figure 15 Setpoint 12244 (a) U mean Contours, (b) TKE Contours (c) Cumulative Energy Distribution.

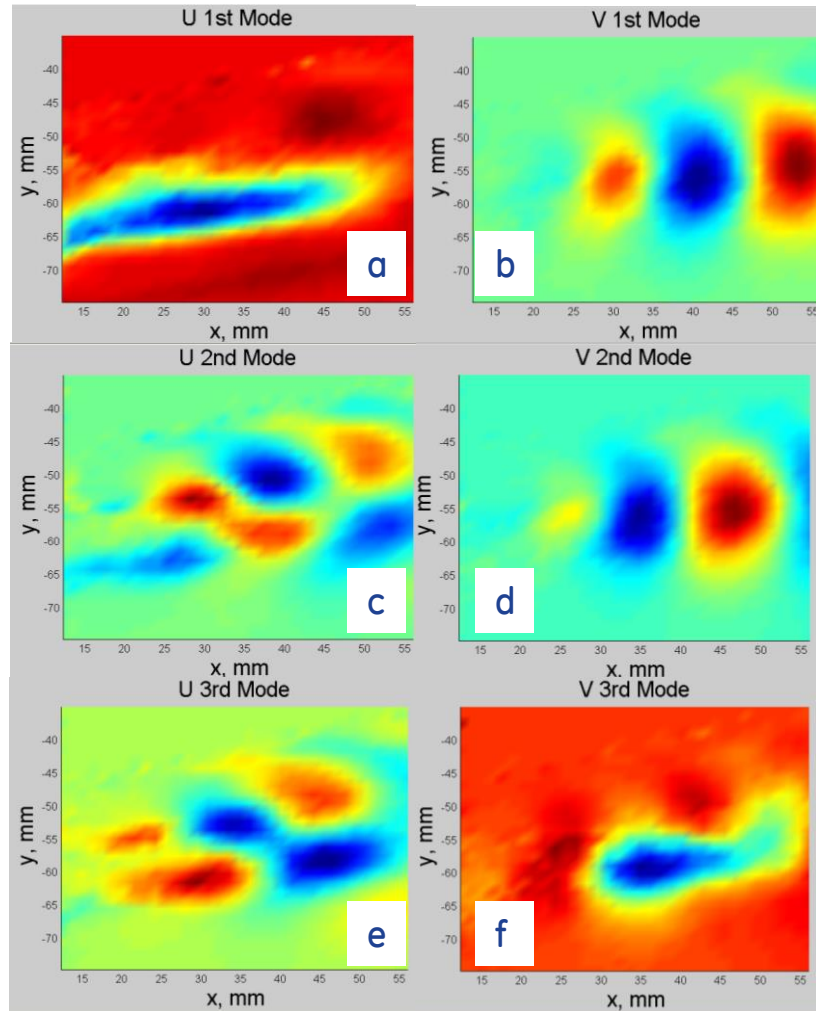


Figure 16 a, c and e: first 3 U POD Modes; b, d and f: first 3 V POD Modes.

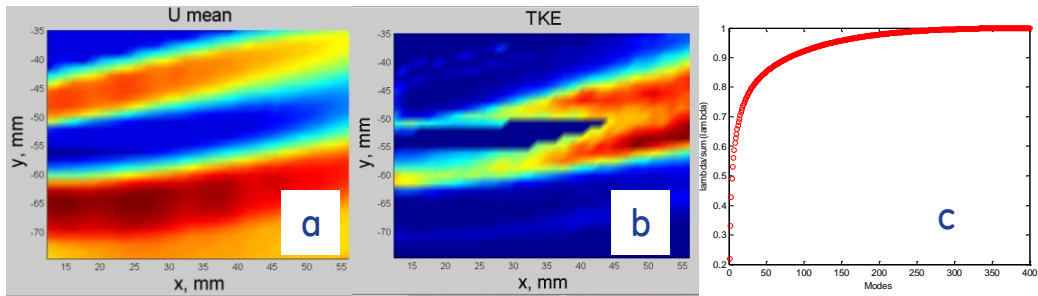


Figure 17 Setpoint 10070 (a) U mean Contours, (b) TKE Contours (c) Cumulative Energy Distribution.

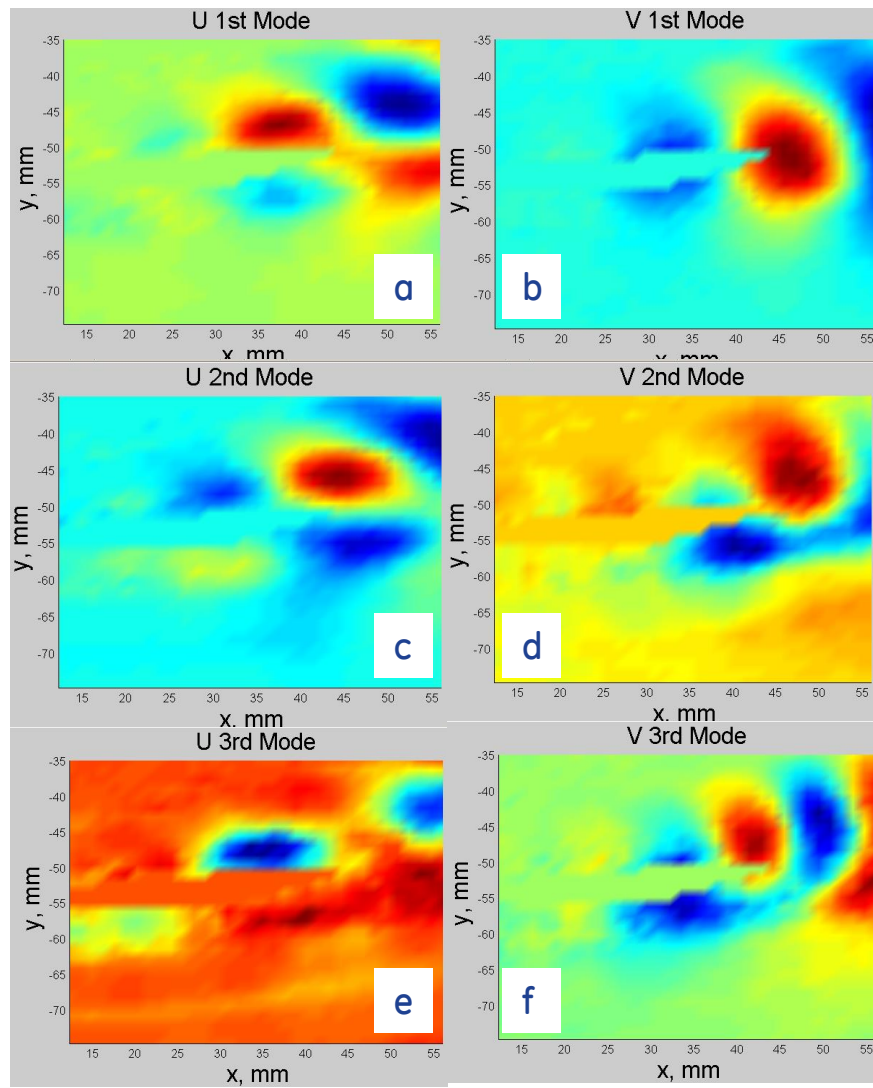


Figure 18 a, c and e: first 3 U POD Modes; b, d and f: first 3 V POD Modes.

The downstream evolution of the nozzle was also studied for the cutback condition. Figure 19 shows the mean U, V and TKE contours for region 2 (downstream of region 1). Clearly the distinction of the different streams is not observed, since the streams are starting to mix. The wake from the center body is

still noticeable in the U contours along the jet centerline. The V mean Contours appear noisy due to small magnitude and small number of instantaneous fields used to reconstruct them. The TKE shows higher magnitude on the unshielded side as compared to the shielded side in this location. This occurs due to the faster diffusion of the jet in the unshielded side. Figure 20 shows the first 3 U and V POD modes. Interestingly, modal activity is only observed on the top half (unshielded side). The bottom half that contains the shielded side shows very weak modal activity for both the U and V components. This is congruent with the higher TKE in the top half shown in Figure 19. This is expected since, the orthogonal basis (i.e. modes) provides the optimal resolution of the TKE (i.e. captures those dominant features that are associated with high TKE). Furthermore, the top half POD magnitudes are much higher than the bottom half hence, on the same color scale bottom half appears to be overwhelmed. In order to support this, POD analysis was performed on only the bottom half. Figure 21 shows the first 3 U and V POD Modes on the bottom half of the measurement region. Clearly the distinct structures were observed that are similar to the top half modal content from whole FOV (Field of View) POD. This confirms the fact that the modal structures are formed at the high shear or velocity gradient region, but the visualization of these features might not be obvious depending on the choice of the region chosen for POD analysis. Figure 22 shows the mean U, mean V and TKE in the fourth region downstream from the nozzle exit. The effect of the shield has started to decay and hence the top and bottom appear symmetric in the mean and turbulence contours. POD analysis was also performed in this region. Figure 23 shows the 3rd U and V POD modes. As expected, modal structures appear to be nearly symmetric of the same size.

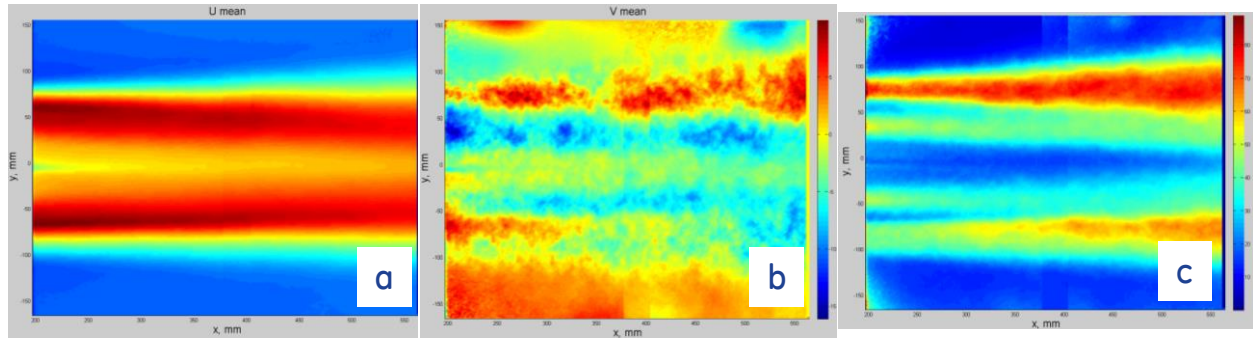


Figure 19 Region 2 (a) U mean Contours, (b) V mean Contours, (c) TKE Contours.

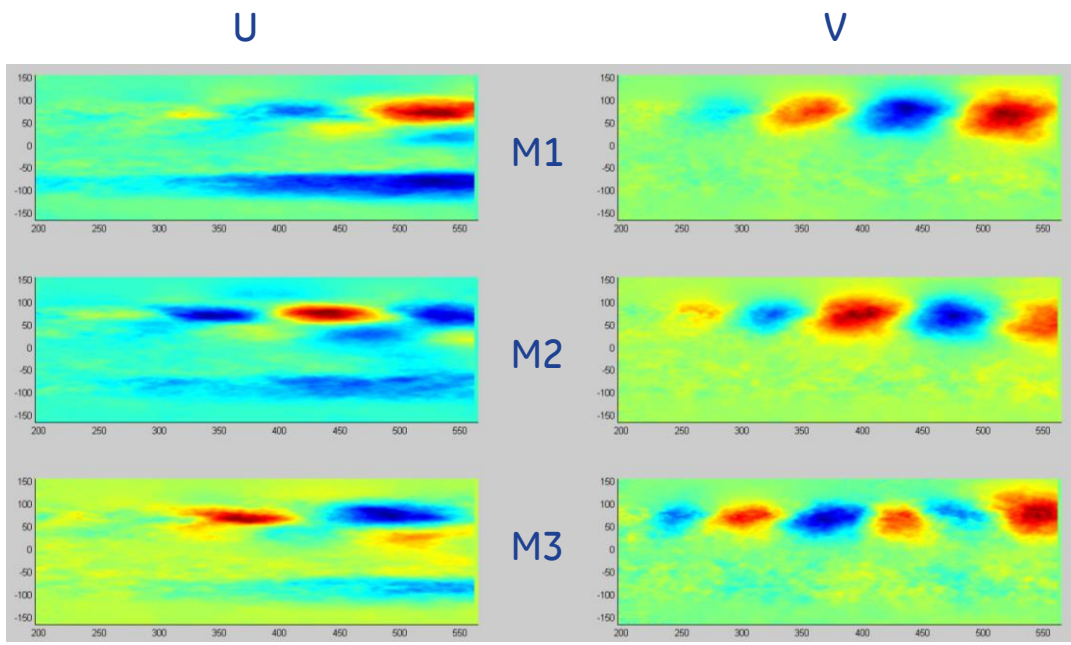


Figure 20 First 3 U and V POD Modes for Full Region 2, M1= Mode 1, M2=Mode 2, M3=Mode 3.

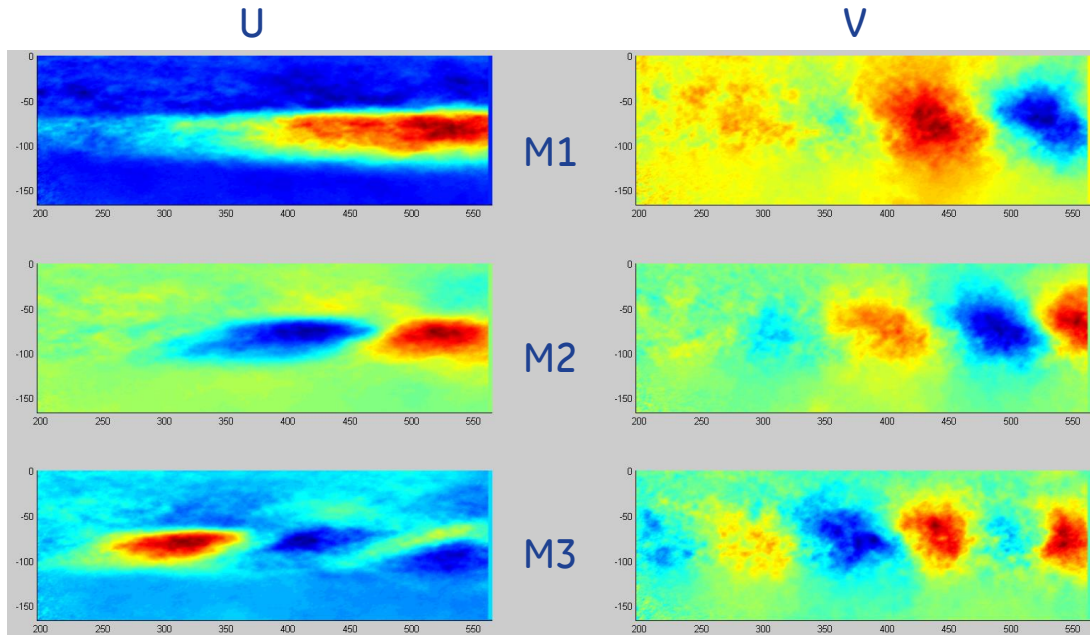


Figure 21 First 3 U and V POD Modes for Bottom Half of Region 2, M1= Mode 1, M2=Mode 2, M3=Mode 3.

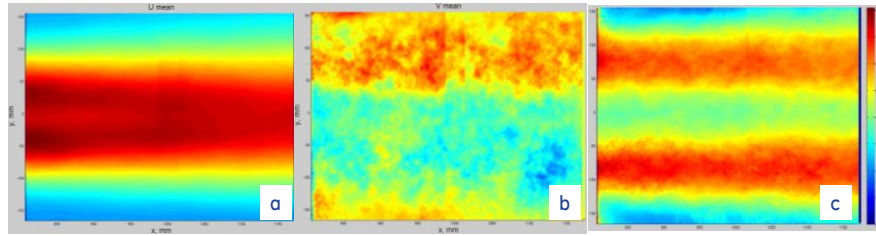


Figure 22 Region 4 (a) U mean Contours, (b) V mean Contours, (c) TKE Contours.

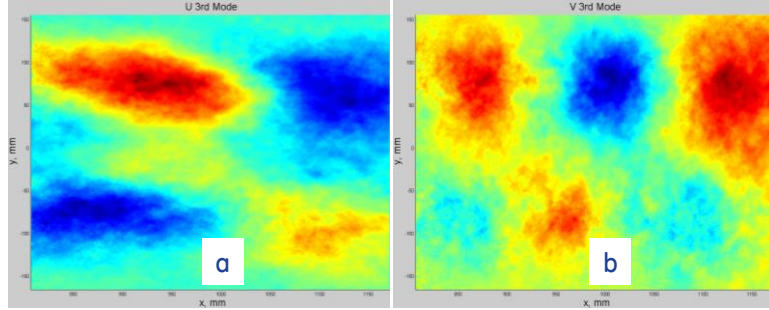


Figure 23 Third U and V POD Modes for Region 4 for cutback condition.

Figure 24 shows the mean W, mean V and TKE at the first cross sectional plane ($X=184$ mm) for set-point 12244. The shield is again at the bottom, but the whole field of view was rotated counter clockwise. Clearly the dominant W mean velocity component appears converged as compared to the lower magnitude mean V velocity component. Higher TKE was found to be on the unshielded side at this nozzle location. The first 4 W mean velocity POD modes are shown in Figure 25. A couple of features could be observed in these contours. First, the higher TKE region on the unshielded side is found to have organized modal activity as compared to the shielded side. Second, the first two W mean velocity component POD modes appear to have a shorter spatial wavelength as compared to POD modes 3 and 4 on the unshielded side. Third, the modal content appears noisy in all the modes and is expected to improve with a higher number of snap shots.

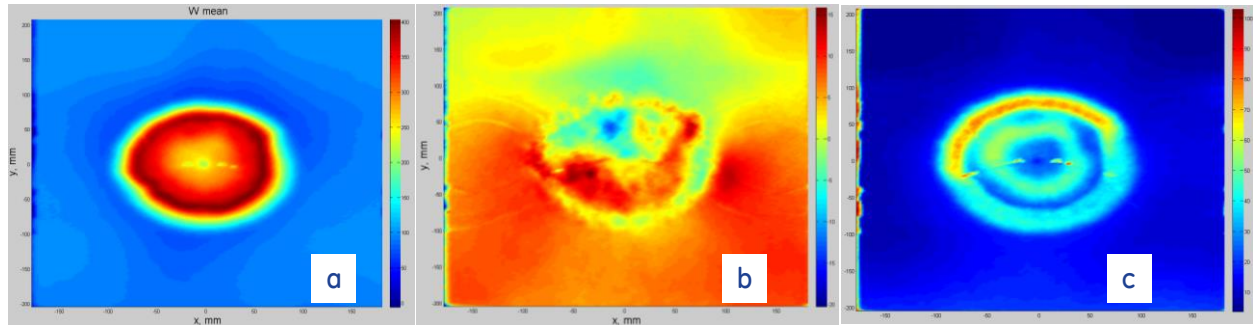


Figure 24 Mean W (a) and V (b) Contours and TKE contours (c) for Region 4.

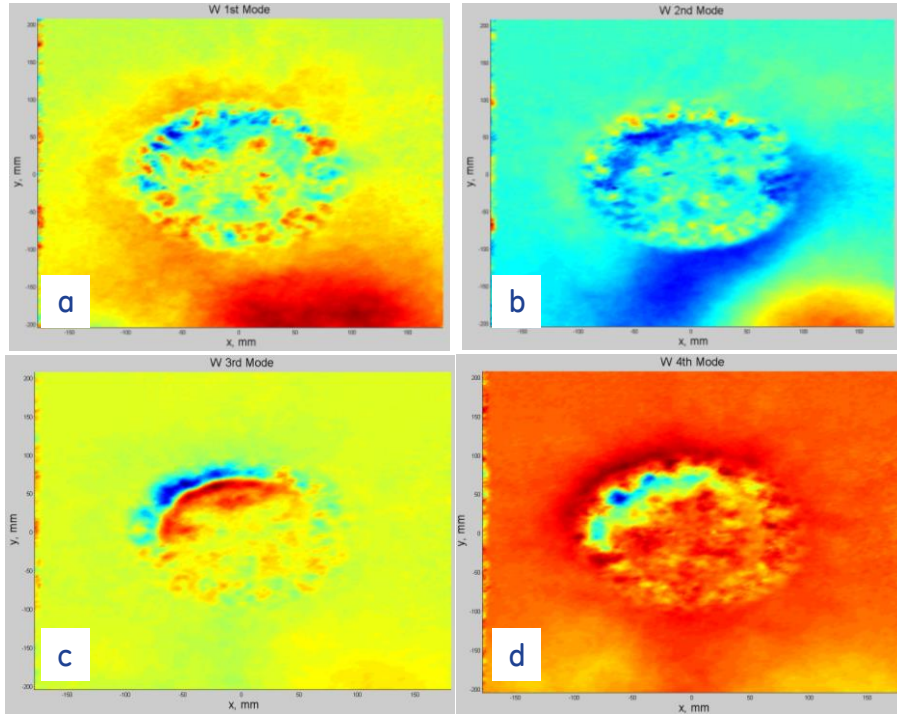


Figure 25 First 4 W POD Models for Axial Cross Section at $Z=184$ mm.

3.1.4 SUMMARY

A POD analysis was conducted on the IVP/shield nozzle at two operating conditions. One corresponded to sideline geometry and other was cutback geometry and operating condition. A separation region was found on the divergent side of the hot nozzle section in both the cases. The separation region was found to extend farther for the sideline condition as compared to the cutback condition. Modal activity was found at the shear and high velocity gradient regions. Near the nozzle exit, both the stream-wise and cross section POD show stronger modal activity on the unshielded region as compared to the shielded region. Higher TKE is expected to be observed farther downstream in the shielded zone as the streams mix, but the effect of shield will eventually decay asymptotizing to symmetric jet profile. This was observed in region 4 (downstream of the nozzle exit) where the Mean, TKE and POD modes appear to be gaining symmetry across the jet axis.

High Modal activity was also observed in region encompassing the separation zone. More number of distinct modal structures is observed in the cutback condition as compared to the side line in the inner shear layer encompassing the separation zone. This occurred due to the shorter separation zone and higher mixing in the region encompassing the separation in the cutback back condition. Though the POD modes and low velocity mean components and TKE appear noisy in several regions due to smaller number of snap shots, we expect that the observed trends will still hold.

3.2 EXHAUST NOZZLE CONFIGURATION

The Phase I nozzle design focused on test hardware to prove the benefits of the inverted velocity profile and fluid shield concepts. A notional geometry was developed and interchangeable primary nozzle inserts were used to set different operating conditions.

CFD analysis of the sideline and cutback configurations showed a strong normal shock in the nozzle due to the large area ratio and relatively low pressure ratio. This behavior was suspected to be the source of a relatively high frequency noise source seen in the test results (Figure 26). The primary goal of Phase II was to refine the nozzle design and mitigate this noise source.

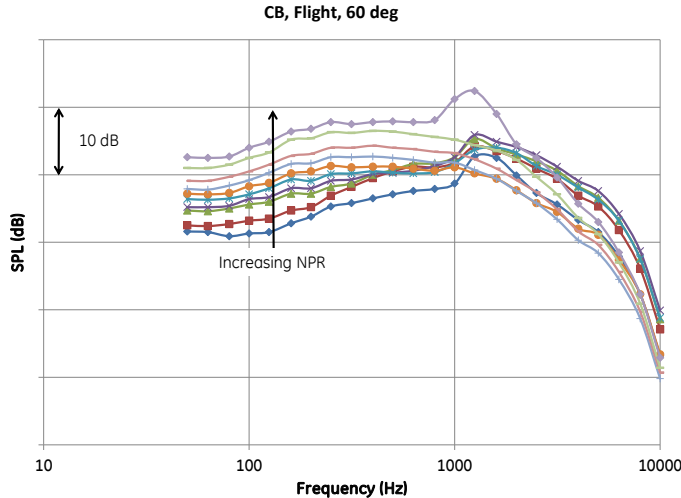


Figure 26 SPL Data Showing Noise Source from Flow Separation near 1 kHz.

3.2.1 PHASE II EXHAUST DESIGN

During the Phase II effort, efforts were made to add fidelity and realism into the nozzle aerodynamics. Geometry changes were limited to only those that could be made with translating actuation of a realistic full scale actuated nozzle. The engine cycle was updated to represent that of a three-engine aircraft. The primary exit area (A9) was allowed to vary independently of A8, as was the IVP exit area. The fluid shield geometry was left fixed. Table 1 shows the A8 and A9 features for each stream.

Table 1 Nozzle Area Features.

Stream	A8	A9
Primary	Variable	Variable
Plug (IVP)	Fixed	Variable
Fluid Shield	Fixed	Fixed

A notional chevron design was applied to the nozzle to supplement the acoustic benefits of the inverted velocity profile and the fluid shield. The focus of the chevron design effort was to increase turbulence and mixing in the near-field in order to increase entrainment and decrease turbulence downstream. Chevrons were only placed on the primary nozzle exhaust not surrounded by the fluid shield and on the outer surface of the fluid shield stream.

Figure 27 and Figure 28 show, quantitatively, the impact of chevrons on these parameters. TKE is increased within two diameters of the nozzle exit but is reduced thereafter which is intended to reduce low-frequency noise. The increased mixing results in a significant but short-lived increase in mass flow entrainment.

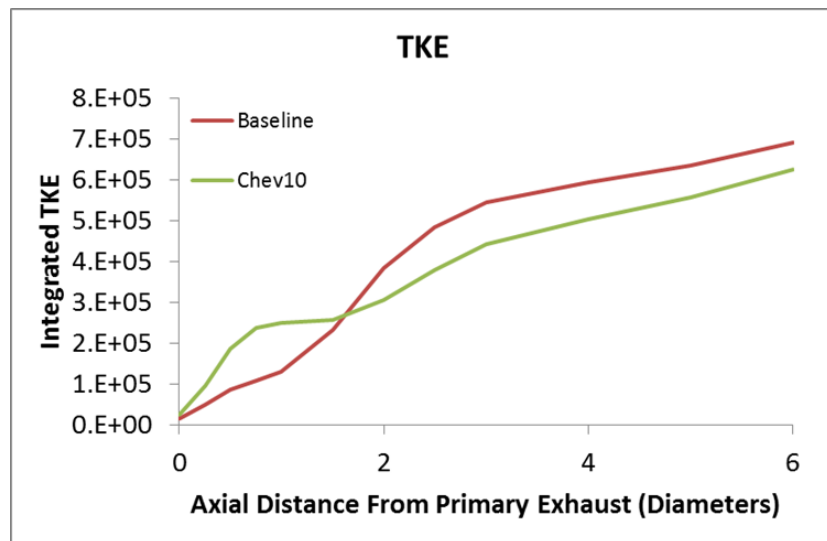


Figure 27 Axial Distribution of Average Turbulent Kinetic Energy.

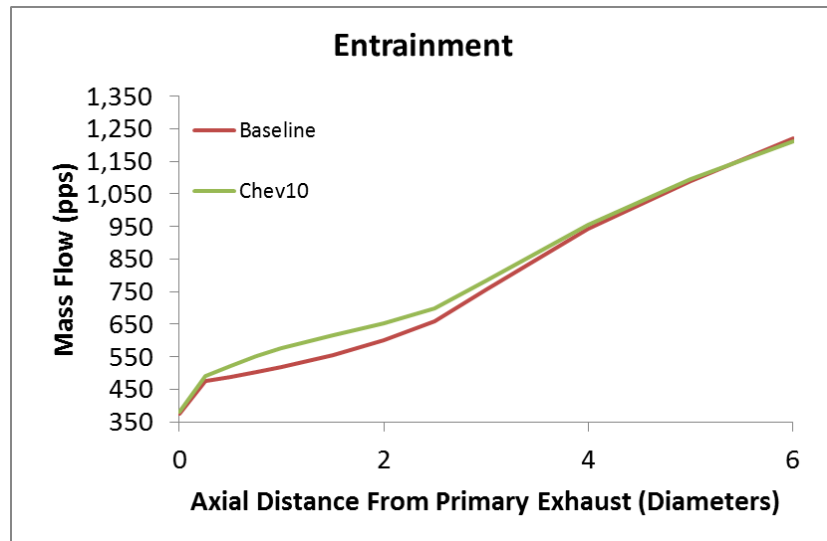


Figure 28 Axial Distribution of Ambient Flow Entrainment.

Steady-state CFD analysis shows good thrust performance over the entire range of conditions and seems to point to better acoustic performance as well.

3.3 RANS AND DES SIMULATIONS

3.3.1 PHASE I SIMULATION APPROACH

The primary objective of this subtask was to conduct a simulation fidelity study of the Phase I nozzle geometry. Through an analysis of various simulation approaches and meshes of various grid resolutions, the necessary CFD requirements can be determined for capturing the features of interest in the nozzle flow. In this case, the primary benchmark for comparison is the experimental visualizations which showed flow separation from the inner nozzle lip and its associated flow unsteadiness. A secondary aim is to capture the far-field tones generated by the flow unsteadiness.

All of the CFD cases examined in this subtask were completed using ANSYS/CFX, version 13.0. This software package contains all of the necessary CFD models and capabilities necessary for the study: structured and unstructured grid capability, steady and unsteady RANS, Scale-Adaptive Simulation (SAS) turbulence model, as well as Detached Eddy Simulation (DES) models. These features allowed for convenient comparisons of results between model outputs, and using ANSYS/CFX also took advantage of prior CFD best practices developed from GE Global Research and GE Aviation.

The meshes for the CFD cases discussed below were generated using Pointwise Gridgen version 15.17. The structured meshes were created for a 180-degree sector surrounding one-half of the nozzle geometry, and symmetry boundary conditions were used on the dividing plane. The outlet plane was placed 30.9 fan diameters downstream, and the far-field boundary was placed 11 fan diameters from the centerline at the exit.

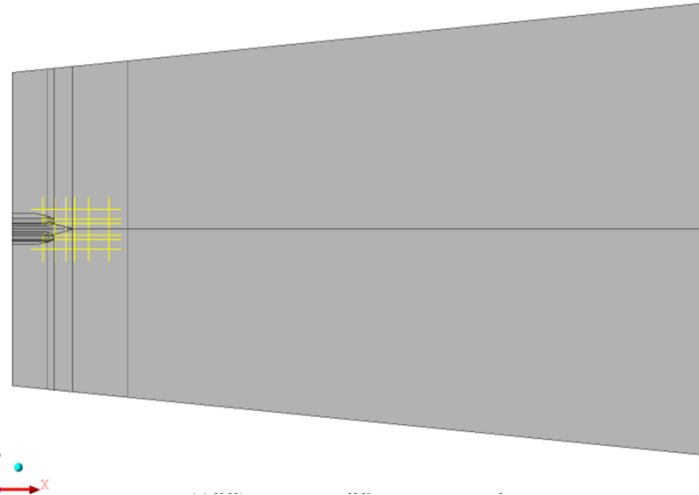


Figure 29 Computational domain for the Phase I nozzle geometry.

To study the effect of grid quality on the resulting solution, varying mesh resolutions were applied to two regions of the domain (Figure 30). The nozzle region consisted of all internal passages of the nozzle before the exit, and the plume region located just downstream of the center-body. Three basic versions of the mesh were created. The baseline mesh resolved both the nozzle and the plume region of the domain with a total of 24.8 million mesh elements. The coarse mesh used only half of the elements in the nozzle region and 2/3 of the elements in the plume region compared to the baseline. In the nozzle refined mesh, more than twice the number of elements was applied to the nozzle region, while sacrificing elements from the plume region to maintain a relatively similar grid count compared to the baseline mesh. In all three

cases, the mesh near the lip line just downstream of nozzle exit was kept constant, in order to resolve the shear layers from the shield, inner and outer streams.

Mesh Name	Nozzle Region	Plume Region	Comments
Coarse	0.6 M	8.5 M	Total: 19.8 M
Baseline	1.2 M	13 M	Total: 24.8 M
Nozzle Refined	2.7 M	8.5 M	Total: 24.3 M

These three meshes were then used in ANSYS/CFX to study the effects from various simulation approaches. Details from the steady RANS, unsteady SAS, and DES calculations are found in sections 3.3.1.1 - 3.3.1.3 below, but the ultimate findings indicated that DES calculations using the baseline and nozzle refined grids were necessary to resolve the separation from the inner nozzle lips.

Although LES and higher fidelity approaches using more conservative, resolved meshes could also be applied to capture the correct separation phenomena, the objective of this study is to determine the minimum necessary fidelity required in the current situation. With mesh counts of approximately 25 million on a 180-degree sector grid, several RANS and DES calculations can be run within a reasonable time frame. Various CFD approaches and nozzles designs can then be tested to select the optimum combination.

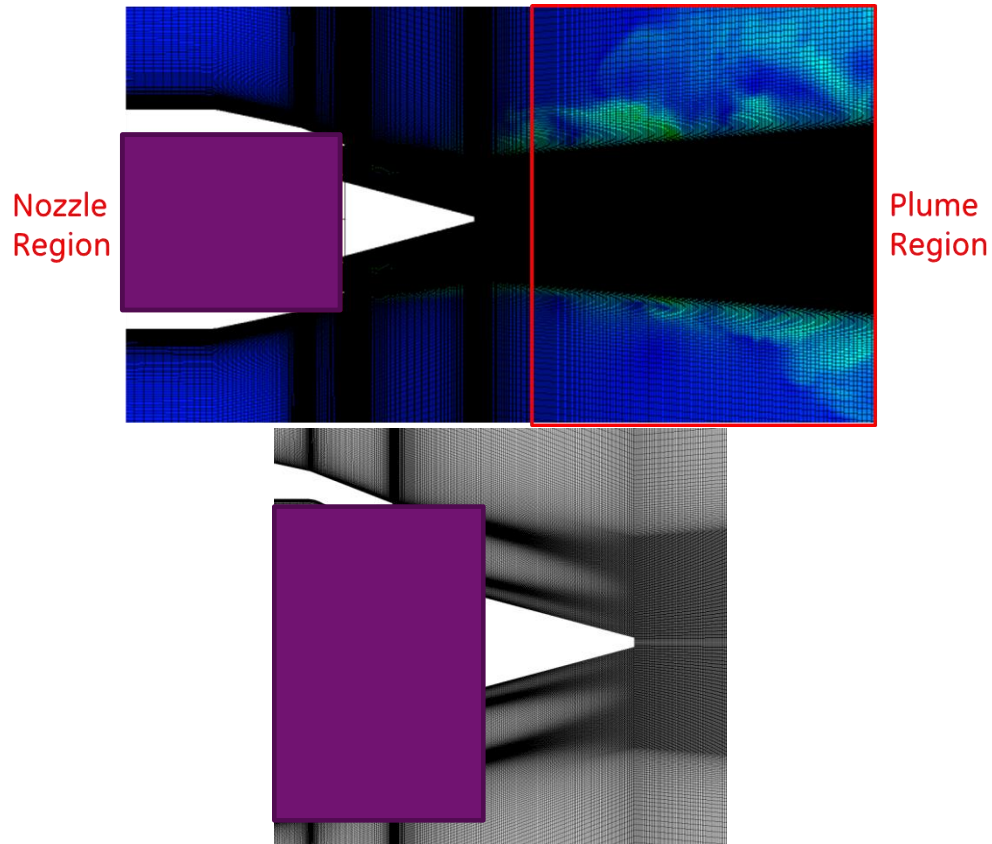


Figure 30 Schematic of the near nozzle mesh, and closeup of the nozzle region for the baseline Phase I nozzle geometry. The grid density in the nozzle region and plume region were modified for the coarse and nozzle refined meshes.

All of the RANS, unsteady SAS, and DES simulations were conducted using the wall function method, based on the work of Launder and Spalding (listed as “automatic near wall treatment” in ANSYS/CFX). Near the shock region on the outer nozzle, the near wall spacing used y^+ values approximately $\sim 20-25$ in the nozzle refined grid, and y^+ values approximately ~ 40 in the baseline grid. Upstream of the nozzle exit, towards the contraction region of the nozzle, the near wall spacing y^+ values were approximately ~ 150 in the nozzle refined grid, and $y^+ \sim 300$ in the baseline grid. This places the first grid point inside the log-law region, existing from about $10 < y^+ < \sim 1,000$.

The axial grid spacing was the determining factor in resolving the shock region, and hence, the point of separation from the nozzle lip. Although finer near wall meshes could be used with lower y^+ values, the study indicated that increased near wall resolution alone would likely be unable to capture the separation behavior.

3.3.1.1 STEADY RANS

Steady RANS calculations were first performed to determine the overall structure of the flow. Using the baseline grid with approximately 25M elements, the CFX calculation was set up using the operating conditions given above and the Shear Stress Transport (SST) turbulence model with default parameters. Outlet boundary conditions were applied to the exit surface, and Entrainment boundary conditions were applied at the radial far-field boundaries. At the ambient inlet surface, a small free-stream velocity of 10 m/s was included to enhance the robustness of the calculation.

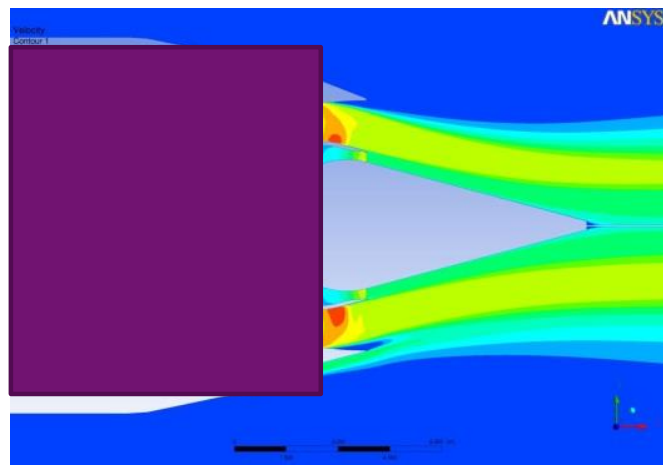


Figure 31 Velocity contours of the steady RANS solution using the baseline grid.

The CFX solution was run for almost 30,000 iterations until the RMS mass and momentum residuals were below 10^{-4} . The results shown in Figure 31, illustrate the velocity contours near the nozzle exit. Contrary to the experimental visualizations, this solution shows the flow separation near the outer nozzle lip on both the shield side and the non-shield side. In addition, the steady RANS solution does not capture any of the unsteady fluctuations associated with the separated flow region. Thus, using steady RANS is unlikely to resolve the primary features of the flow and accurately match the experimental measurements.

3.3.1.2 UNSTEADY RANS WITH SAS MODEL

The next level of simulation involved using unsteady RANS with the Scale Adaptive Simulation (SAS) model to resolve unsteady flow features in the simulation. The SAS model, developed by Menter *et al*, improves upon the unsteady RANS formulation by introducing a von Karman length scale into the

turbulence equation. This length scale is dynamically adjusted to resolve turbulent structures in the unsteady flow-field, providing “LES-like” behavior in specific regions of the domain.

The default SAS formulation in CFX, also used in this steady, couples the two-equation SST model with a dynamic model for the von Karmen length scale L_{vK} . This appears as an additional source term in the transport equation for ω , the turbulence eddy frequency. The length scale L_{vK} depends on the turbulent kinetic energy κ and the scalar invariant S of the strain rate tensor via the relation

$$L_{vK} = \kappa S / U'',$$

where U'' is the magnitude of the velocity Laplacian. More details on the formulation can be found in the CFX-Solver theory guide and the papers by Menter *et al*, and Egorov & Menter.

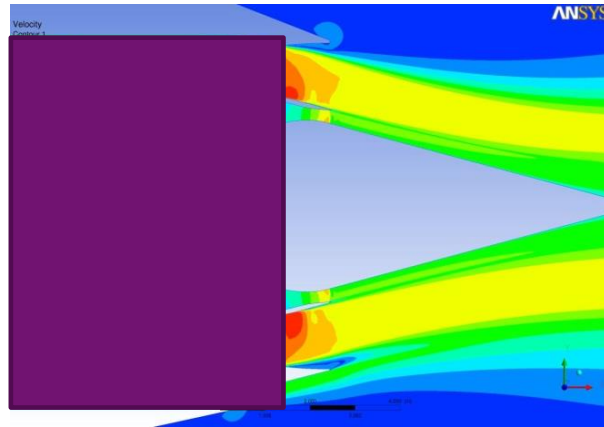


Figure 32 Velocity contours from the unsteady RANS calculation with SAS model (coarse grid)

This formulation was applied on both the coarse and baseline meshes of the Phase I nozzle geometry. The initial flow field was provided from the steady RANS calculation of section 3.3.1.1, and allowed to run until all transients had disappeared from the computational domain. The simulations were run on 64 cores of the local GRC Linux cluster.

The SAS simulations using the coarse mesh returned solutions similar to the steady RANS results of section 3.3.1.1. Flow separation from the outer nozzle lips was visible, but the flow remained attached to the inner nozzle lips (see Figure 32). Better results were obtained using the SAS model on the baseline mesh. As shown in Figure 33, the baseline mesh captured the proper flow separation from the inner nozzle lip and flow attachment at the outer nozzle lip. However, the separated flow region near the nozzle exit only exhibited low-frequency undulations in the jet near field, and none of the high frequency unsteadiness seen in the experimental measurements. Thus, it was concluded that an even higher fidelity approach was necessary to capture the jet dynamics of the Phase I nozzle.

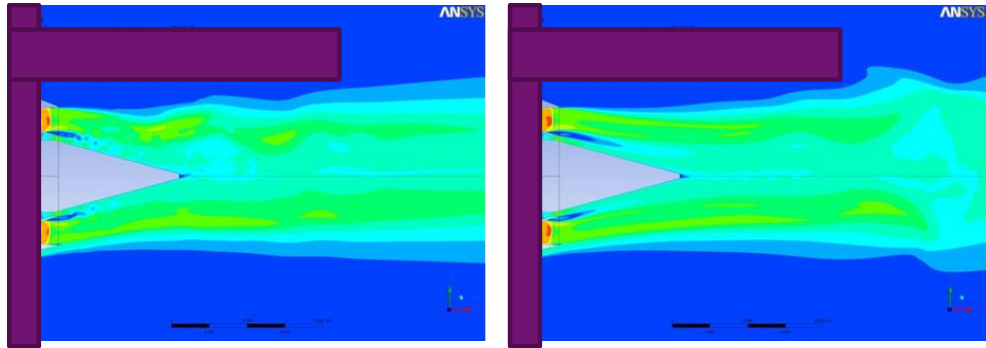


Figure 33 Successive instantaneous velocity fields from the unsteady RANS with SAS model on the baseline mesh.

3.3.1.3 DETACHED EDDY SIMULATIONS

To provide more realistic simulations of the near field turbulent structures in the Phase I nozzle geometry, Detached Eddy Simulations (DES) were explored using ANSYS/CFX. In this approach, both RANS and Large Eddy Simulation (LES) methods are combined in a single formulation. The typical DES model uses the RANS turbulence model inside attached and mildly separated boundary layers, and LES in massively separated regions, where the large scale turbulent structures are the same size as the characteristic geometry.

Combining the two approaches is possible by having the CFD algorithm switch between the SST RANS model to an LES model in regions where the turbulent length scale L_t is larger than the local grid spacing Δ . In the two equation SST RANS model, this alters the dissipation term in the k -equation in the following manner:

$$\epsilon = \beta^* k \omega F_{DES}, \text{ where } F_{DES} = \max\left(\frac{L_t}{C_{DES}\Delta}, 1\right)$$

The default C_{DES} in ANSYS/CFX is given as $C_{DES} = 0.61$. The effect of altering this parameter is discussed later in this section.

For all DES simulations conducted in this study, the Delayed Detached Eddy Simulation (DDES) model was used. The DDES model avoids the problem of grid induced separation, where the boundary layer can separate at arbitrary locations depending on the grid spacing. DDES further modifies the switching function F_{DES} to explicitly force RANS behavior inside the wall boundary and LES behavior away from the wall.

The DES approach was applied to the Phase I nozzle geometry, this time on the coarse, baseline, and nozzle refined meshes. For the baseline mesh, separation was seen to occur at the correct location near the inner nozzle lips, and the proper flow attachment at the outer nozzle lips. Instantaneous snapshots of the velocity flow field also showed that fine-scale turbulent fluctuations were better resolved in the DES compared to the SAS simulations of section 3.3.1.2 (see Figure 34). When compared to the flow field visualizations captured by experiments (Figure 35), the mean velocity profiles showed good agreement. Note that the experimental visualization was captured at operating point SP12244, which includes a free-stream co-flow of Mach 0.30, which is not accounted for in the DES result.

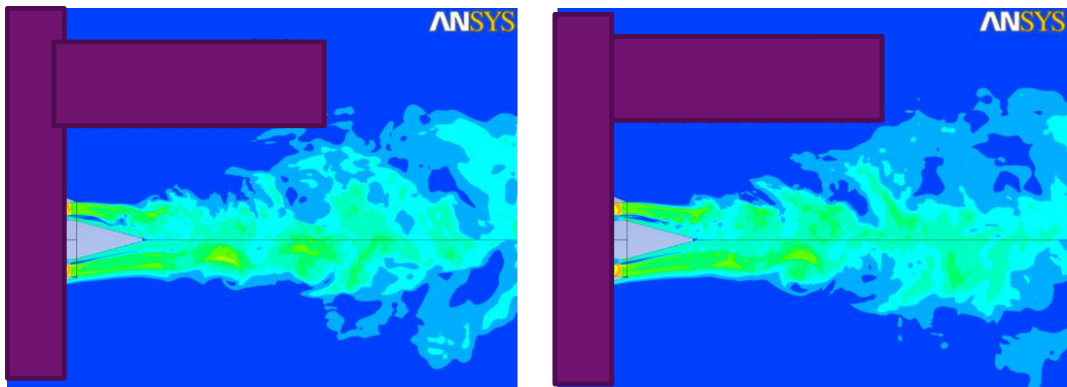


Figure 34 Successive instantaneous snapshots from the DES velocity flow field using the baseline mesh.

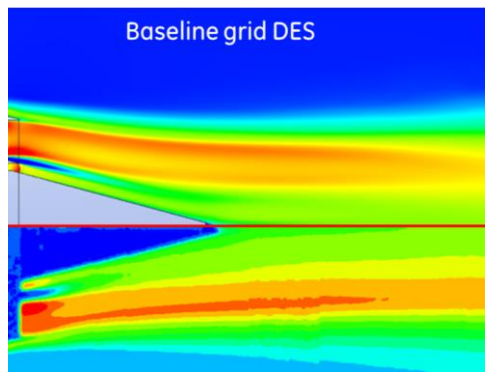


Figure 35 Comparison of the stream-wise U velocity between the DES calculation (upper half) and the experimental visualization (lower half).

The effect of the grid resolution was also examined by comparing the results from the coarse, baseline, and nozzle refined mesh. The grid density in the interior nozzle regions doubles from the coarse to baseline mesh, and more than doubles again for the nozzle refined mesh. This difference is apparent in the overall flow features seen in Figure 36. In both the baseline and the nozzle refined grid, the separated flow region occurs at the inner nozzle lip radial location, while the coarse grid shows the flow separation at the outer nozzle lip.

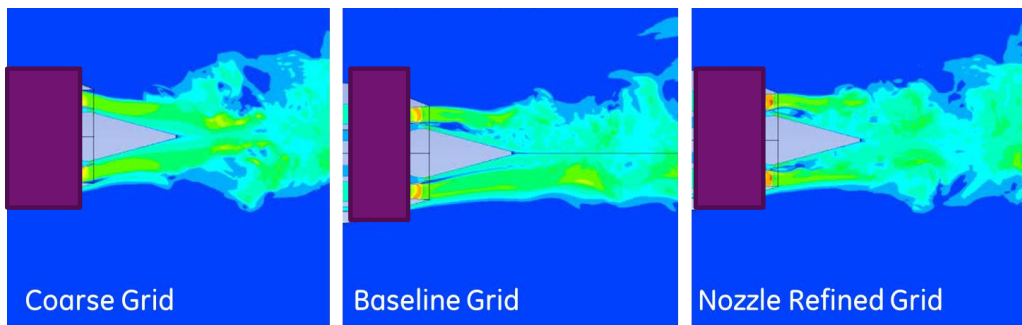


Figure 36 Comparison of the instantaneous velocity flow fields from the DES calculation using the coarse, baseline, and nozzle refined grids.

The unsteady fluctuations in the jet near field were also examined quantitatively. A set of probes was inserted downstream of the nozzle in the nozzle refined DES calculation, and the time history of the pressure and velocity variables was recorded for each one of the probes. An example of the probe locations is shown in Figure 37. Probe 4 is located outside of the jet exhaust plume, probe 4A is located at the shield stream shear layer, and probe 4B is located closest to the centerline near the inner nozzle lip shear layer. A Fourier Transform of the pressure signal at location 4B showed unsteady flow fluctuations causing a peak near 3 kHz. However, the absence of any such peak at the probe 4A and probe 4 locations suggested that these unsteady flow fluctuations are mostly hydrodynamic in nature, and do not propagate to the far-field as acoustic noise. Similar results were seen for the probes located on the no-shield side of the jet.

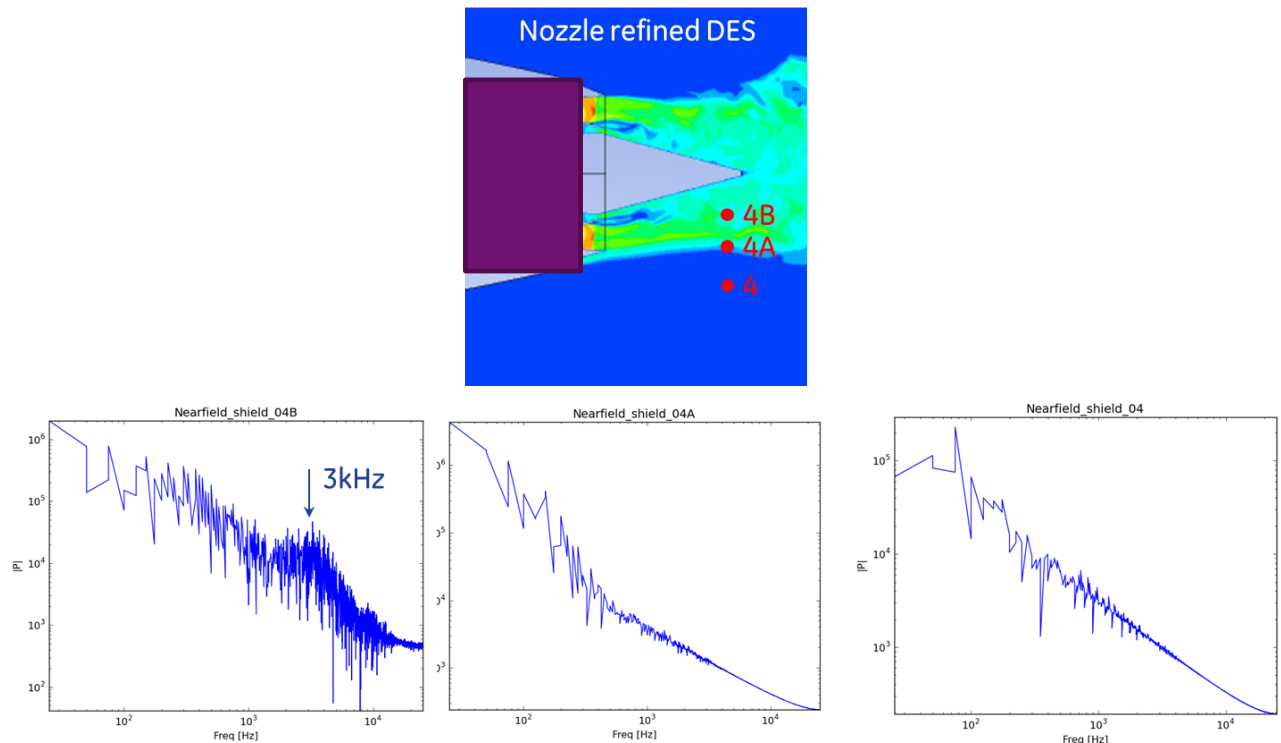


Figure 37 Top: Location of the measurement probes in the nozzle refined DES computation. Bottom: Pressure spectra from the probes located at position 4B (left), 4A (center), and 4 (right).

Taking the DES calculation on the baseline geometry, we were also able to explore the effect of the CDES parameter on the overall solution. By lowering the parameter from the default value CDES=0.61, it was hoped that more “LES-like” behavior could be seen in the solution, and velocity/pressure fluctuations in the near field would be transferred to the acoustic far-field. In addition to the default value of 0.61, two other values were explored on the same grid: CDES=0.51 and CDES=0.31.

Comparing the overall velocity contours in Figure 38, little difference in the flow structures could be seen at the various CDES values. The flow separation points remained largely unchanged, and the near field flow structures were also similar between the DES calculations. However, the differences among the simulations were visible upon examining the DES blending function in Figure 39. This function, which is equal to 1.0 in the RANS region and 0.0 in the LES region, showed some small variations depending on

the value of CDES. As the value of CDES was lowered from 0.61 to 0.31, the blending function displayed greater regions of LES behavior inside the nozzle passages, particularly near the nozzle contractions before the exit. However, aft of the nozzle exit, little difference was seen in the region of LES applicability.

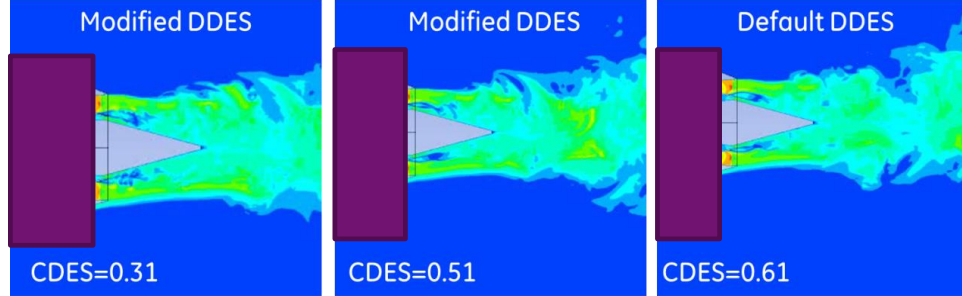


Figure 38 Comparison of the velocity fields from the DES simulation using a CDES parameter of 0.31, 0.51, and 0.61 (default).

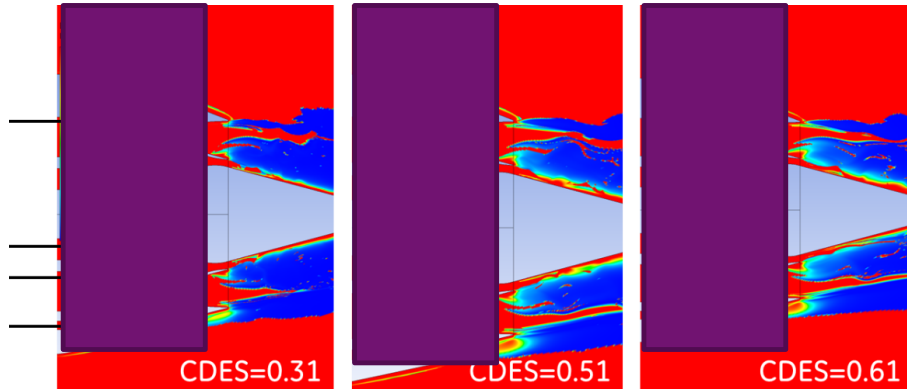


Figure 39 Comparison of the DES blending function from the computations using CDES=0.31, 0.51, and 0.61. Red contours indicate RANS regions while blue contours indicate LES regions. The black arrows on the left indicate regions where the LES region was more dominant in the CDES=0.31 calculation.

3.3.2 PHASE I SIMULATION SUMMARY

From the various RANS and DES calculations performed as a part of this subtask, the best practices for nozzle CFD could be determined. Listed in order of increasing simulation fidelity, the following CFD approaches were applied to the Phase I N+2 nozzle:

1. Steady RANS using SST
2. Unsteady RANS with SAS model
3. Unsteady DDES

The quality of the meshes required for the simulations was also examined by testing a baseline, coarse, and nozzle refined version of the computational grid. For the steady RANS simulations on the baseline grid, it was found that the flow separation points from the nozzle lips were incorrectly predicted. Using unsteady RANS with the SAS turbulence model, the baseline grid was able to correctly capture the flow

separation, however, the unsteady flow features of the nozzle exit did not compare favorably with experimental measurements. Finally, using the DES approach on the baseline and nozzle refined grid captured both the flow separation locations and near field flow unsteadiness in the jet.

Figure 40 provides a summary of the results from the Phase I simulations.

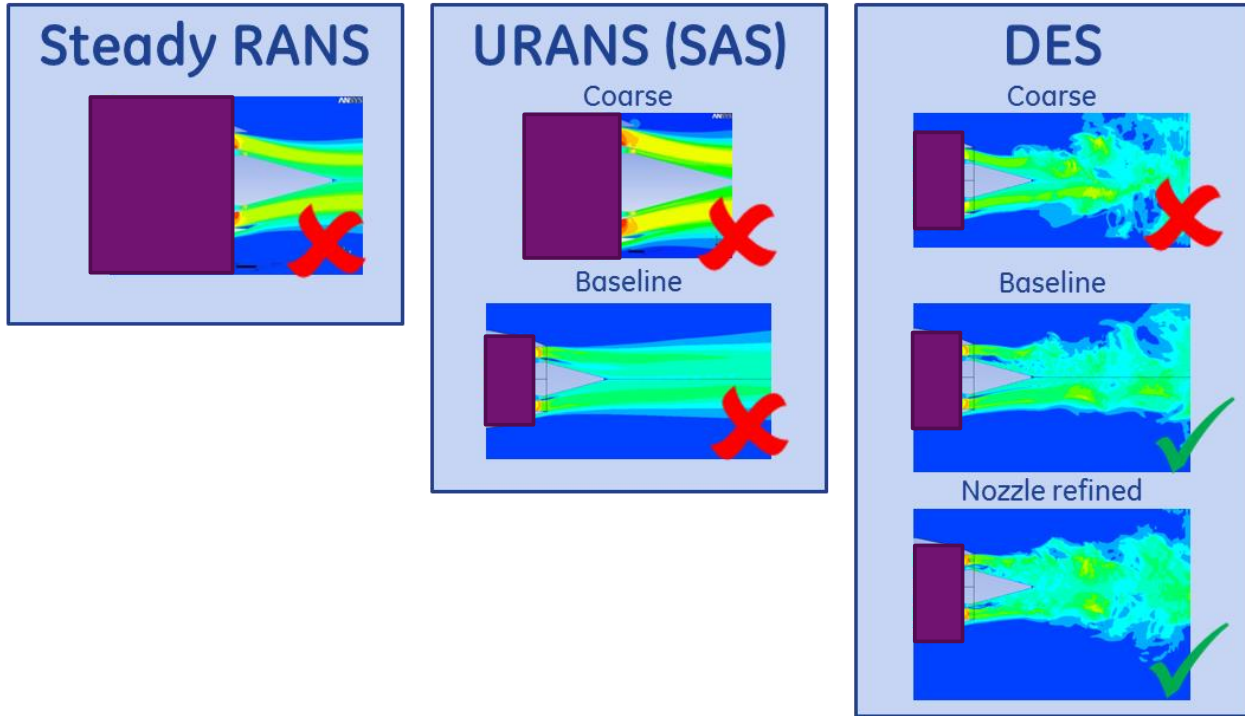


Figure 40 Summary of the steady RANS, SAS, and DES computations done for the Phase I nozzle geometry.

3.3.3 PHASE II CONFIGURATION SIMULATION APPROACH

Using the information obtained from the Phase I CFD simulations, the Phase II nozzle geometry could be simulated in a similar fashion. The objective for this subtask is to confirm that the changes in nozzle geometry removed the separated flow region from the inner nozzle lip exit.

Two DES simulations were conducted for the Phase II study. The first simulation used a baseline mesh, constructed in a similar manner to the Phase I geometry, and the default CDES value in CFX. The second simulation refines the inner nozzle region and also uses a smaller value of CDES, in order to encourage a larger LES-like zone. The ultimate grid counts for the baseline and refined meshes were 29.5 million and 41.2 million elements, respectively.

Mesh Name	Total Size	CDES
Baseline	29.5 M	0.61
Refined	41.2 M	0.31

Results for both meshes are plotted in Figure 41. From the velocity contours in the DES solutions, we can see that flow separation has been eliminated from the inner nozzle lips in both simulations. The overall agreement in the velocity and Mach number fields between the baseline and the refined grid also indicates good grid convergence in the final DES solution.

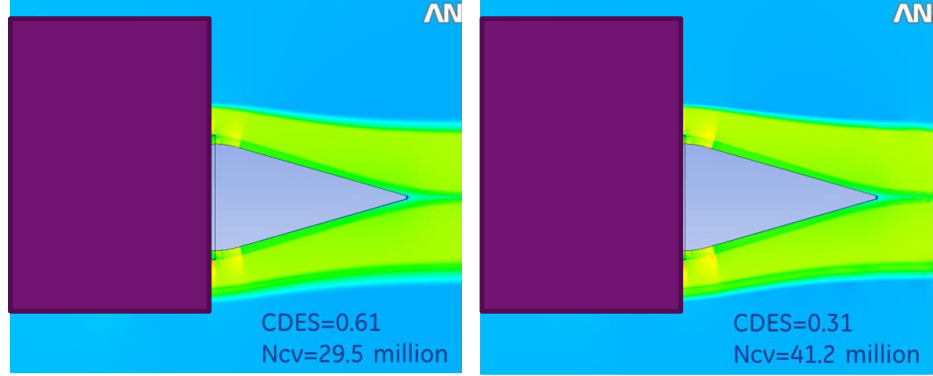


Figure 41 Comparison of the velocity field for the DES computations of the Phase II geometry using the baseline grid (left) and refined grid (right).

It should be noted that these lower values of the CDES parameter were tested with the primary goal of measuring the sensitivity of the solution to the blending function used in the DES model. A number of previous studies by Shur et al (1999) and Travin et al (2006) have examined the general sensitivity of DES to different RANS-LES blending functions as well. In this particular case, the CDES parameter and mesh spacing were appropriate adjustment quantities to quickly assess the sensitivity. The results of the above test, along with the results of section 3.3.1.3, indicate that the DES simulations were insensitive to changes in the RANS-LES blending function, and the default CDES value can be used.

Simulations of the corresponding Phase II nozzle geometry using LES showed unsteadiness in the outer shear layer due to an interaction of a shock with the separated boundary layer from the outer nozzle lip. To see if the DES solution could capture this unsteady phenomenon, a transient pressure fluctuation was applied at the primary stream inlet:

$$P - P_\infty = 0.2 P_\infty \exp\left(-\frac{(t - t_0)^2}{t_w^2}\right)$$

For this case the characteristic width of the Gaussian pulse was $t_w = 0.01$ seconds, and the reference pressure was $P_\infty = 63,125$ Pa. Applying this boundary condition produced a transient shear layer instability in the outer stream, as shown in Figure 42. However, the growth of this instability was not self-sustaining, and eventually decayed at large times. When compared to the LES behavior, we then concluded that a forced impulse at the inlet was not sufficient in the DES to create an acoustic feedback loop which would sustain an oscillatory motion at the outer nozzle lip.

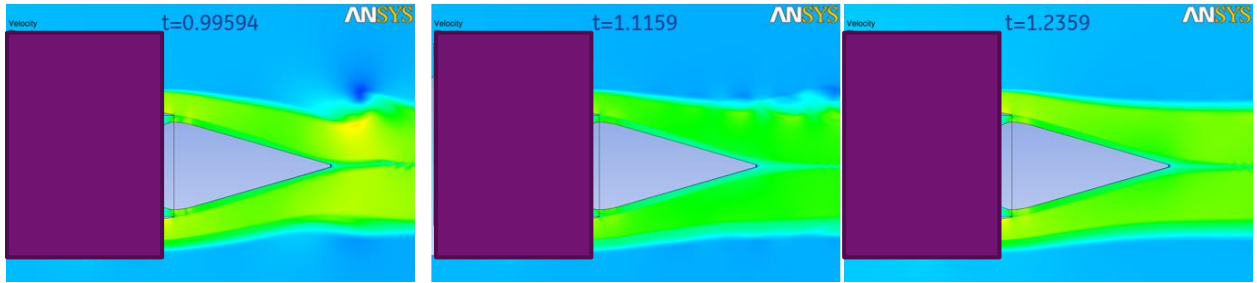


Figure 42 Successive instantaneous snapshots of the DES computation of the Phase II geometry after a Gaussian impulse was applied to the inlet of the primary stream.

3.4 LES SIMULATIONS

3.4.1 PHASE I CONFIGURATION SIMULATION APPROACH

3.4.1.1 FLOW PREDICTION

A LES prediction capability has been developed at GE Global Research Center based on the code (FDL3DI) developed by Gaitonde & Visbal⁵. The code solves the Navier-Stokes equations. It uses a sixth-order accurate compact finite difference scheme for spatial discretization, and has the option to use the second-order Beam-Warming or the fourth-order Runge-Kutta time stepping methods for temporal integration. The higher-order accurate algorithm is desirable because this minimizes the dispersion and dissipation errors for accurate long time integration. Filters of different orders of accuracy (from second- to tenth-order) and the Smagorinsky subgrid scale model are implemented in the solver. This allows the solver to run in either full LES or implicit LES modes. For the current study, all simulations are performed with the use of implicit LES technique. In addition, the code uses a multi-block overset gridding structure to handle complex geometries. This allows a straightforward modeling for realistic engine geometries. For parallel computation, MPI is employed to handle communication between cores/processors.

3.4.1.2 FFWCS WILLIAMS HAWKINGS APPROACH

Having solved for the near field fluctuations in the jet plume using LES, the far-field noise prediction are made using a permeable surface Ffowcs Williams and Hawkings (FWH) solver. This projects the near-field fluctuating quantities on the FWH integration surface to a far field observer location. This alleviates the need to numerically solve for the flow quantities all the way to the far field, resulting in significant resource savings. The FWH control surface is defined as a conical surface just outside the jet plume, such that no significant large-scale noise generating sources go across the surface as seen in Figure 43. The far field solution is computed based on surface integrals of the flow quantities evaluated on the control surface. This approach is superior to traditional acoustic analogy approach, which requires volume integrals. The frequency domain formulation of the FWH solver is used in the present work. The approach used in the current work is the same as that followed by Strelets et.al.⁶

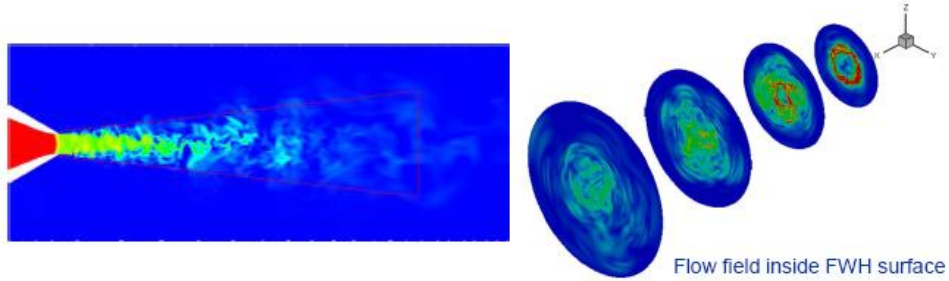


Figure 43 Schematic of FWH surface definition for single flow nozzle configuration.

Details about the validation of the current LES approach and its ability to capture the acoustics effects of nozzle geometry are presented in Paliath et.al⁷. The FWH solver had been validated for configurations with no forward flight effect. This approach was extended recently to include flight effects so as to enable far-field acoustic predictions for some of the configurations in the current work. But detailed validation of this extension is pending.

3.4.2 SIMULATION RESULTS

Simulations were performed for the reference nozzle and the GE IVP/shield nozzle. Simulations were conducted both with and without forward flight. Figure 44 shows a typical mesh used in the computation. The grid topology and count for the simulations was developed based on best practices developed earlier. A conical FWH surface is chosen, where the time accurate unsteady flow field was sampled. The surfaces were not closed on either the upstream or downstream ends. The grid spacing at the FWH surface is specified so as to resolve acoustic waves up to a Strouhal number of 5. The LES simulation was started with zero initial flow-field. Flow was allowed to reach a fully developed state before sampling the unsteady flow field. Farfield acoustic predictions are made, using the FWH formulation, at observer locations matching the experiment, using the data sampled on the FWH surface. Multiple FWH surfaces were evaluated to ensure acoustic prediction convergence.

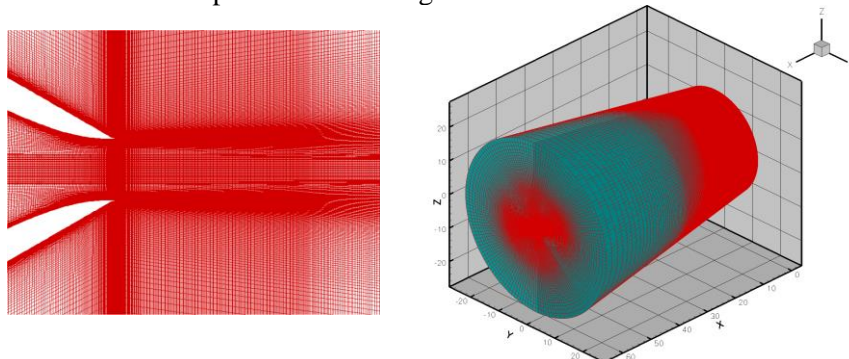


Figure 44 LES grid topology for reference nozzle.

3.4.2.1 REFERENCE NOZZLE

The overset grid topology used is shown in the Figure 44. The grid was designed for a Strouhal number resolution of 5. The grid count for the current configuration was approximately 28 million points. The simulation was run on 2000 cores on GE's internal cluster. Acoustic time sample of approximately 250 time units was used to calculate the spectra. One time unit is the time for a fluid particle to travel 1 nozzle

diameter at the jet exit speed. LES simulations were performed with and without flight effects. Figure 45 show a comparison of the time accurate instantaneous flow fields. Far field acoustic predictions are made at 4 observer locations and comparison with data are shown in Figure 46 and Figure 47. It is seen that the LES methodology is able to predict the spectral shape in both downstream and sideline directions. The large-scale low frequency noise peaks at the downstream directions are over predicted by approximately 2-3 dB, while the small-scale high-frequency noise in the upstream direction is under predicted by about 3-4 dB. It is also seen that the LES based approach is able to capture the reduced broadband spectra due to forward flight. But over prediction of very low frequency part of the spectra is observed though.

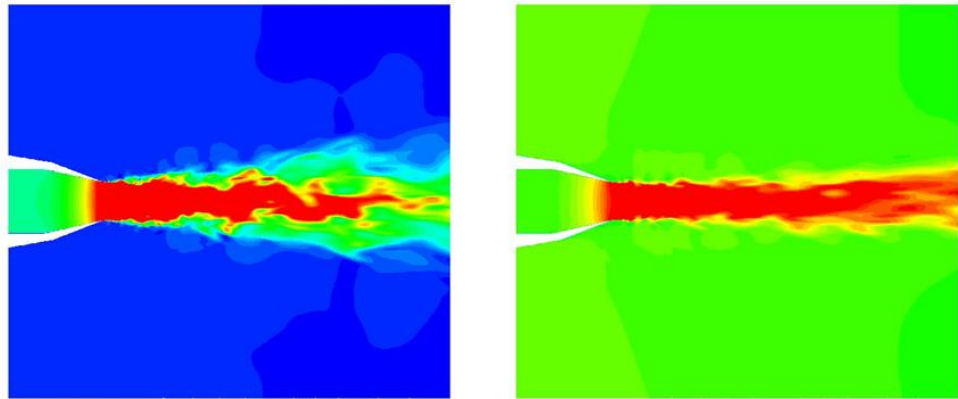


Figure 45 Axial velocity contours for reference nozzle a) $M_f = 0.0$ b) $M_f = 0.34$.

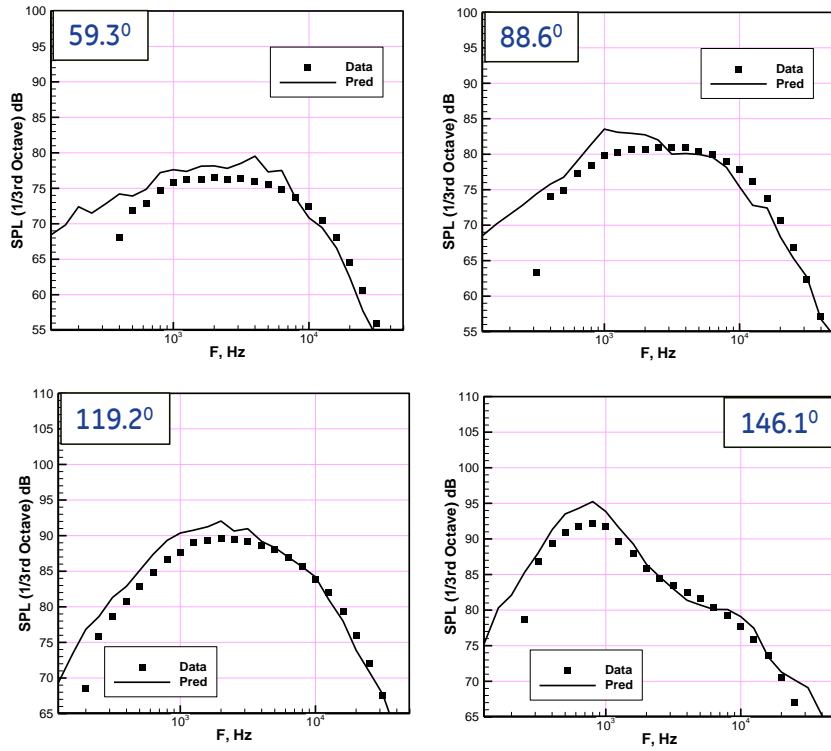


Figure 46 Far field acoustic predictions at 4 different downstream angles for the reference nozzle with $M_f = 0.0$.

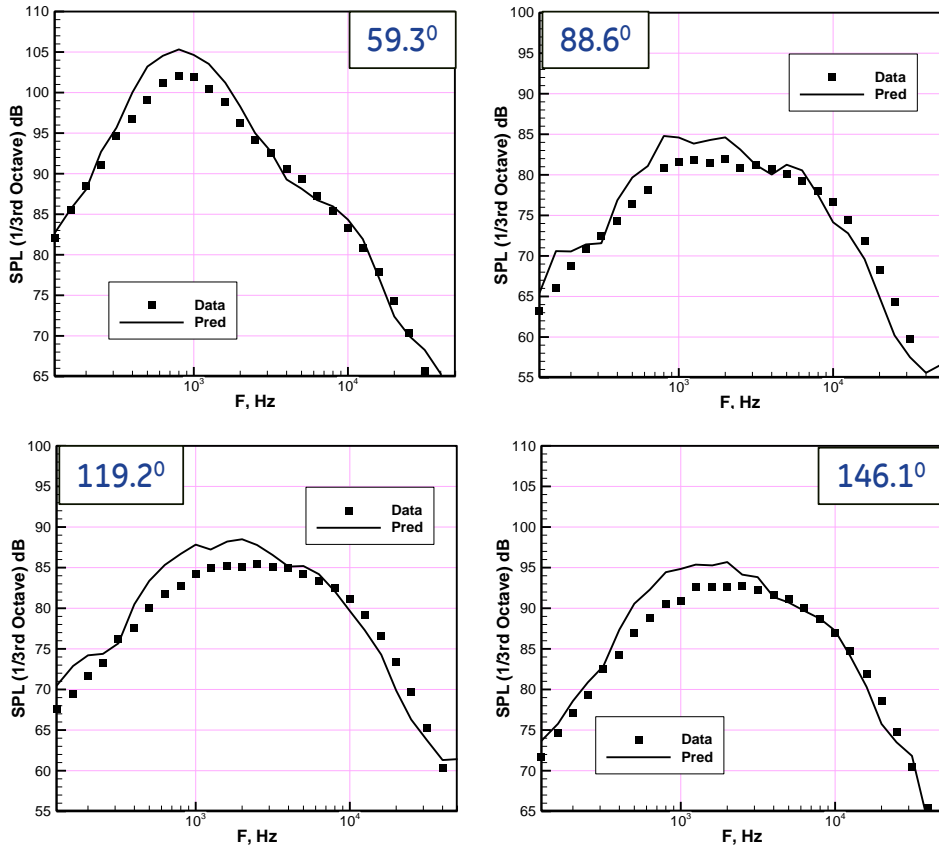


Figure 47 Far field acoustic predictions at 4 different downstream angles for the reference nozzle with $M_f = 0.3$.

3.4.2.2 IVP/SHIELD NOZZLE

The overset grid topology was once again leveraged to define the computational domain and better represent the nozzle with the IVP and fluid shield. The grid was once again designed to achieve similar spectral accuracy as for the reference nozzle configuration. The grid count for the three stream nozzle was considerably larger at 85M pts. Numerical simulations were performed for 2 operating conditions, with and without forward flight. The simulations were once again run on approximately 2,000 cores. The total run time, to obtain a fully developed flow field and for flow sampling, was approximately 2.5 weeks. The run time was larger for the case with forward flight as it started with zero initial velocity. Figure 48 shows the axial flow field along an azimuthal plane for the case without forward flight. Signs of flow separation are seen near the nozzle exit, similar to observations in experimental the PIV data. Data was sampled on four different FWH surfaces of varying radial extent to ensure convergence in prediction. The integral FWH approach was then used to predict the far-field spectra at 4 different observer angles. Figure 49 shows the acoustic prediction comparisons with data for the case with no forward flight. Once again it is seen that the LES based approach does a reasonable job of capturing the spectral shapes and peaks across all observer angles. In addition the numerical approach also picks up a tonal signature being radiated in the downstream direction, possibly related to the flow separation near nozzle exit.

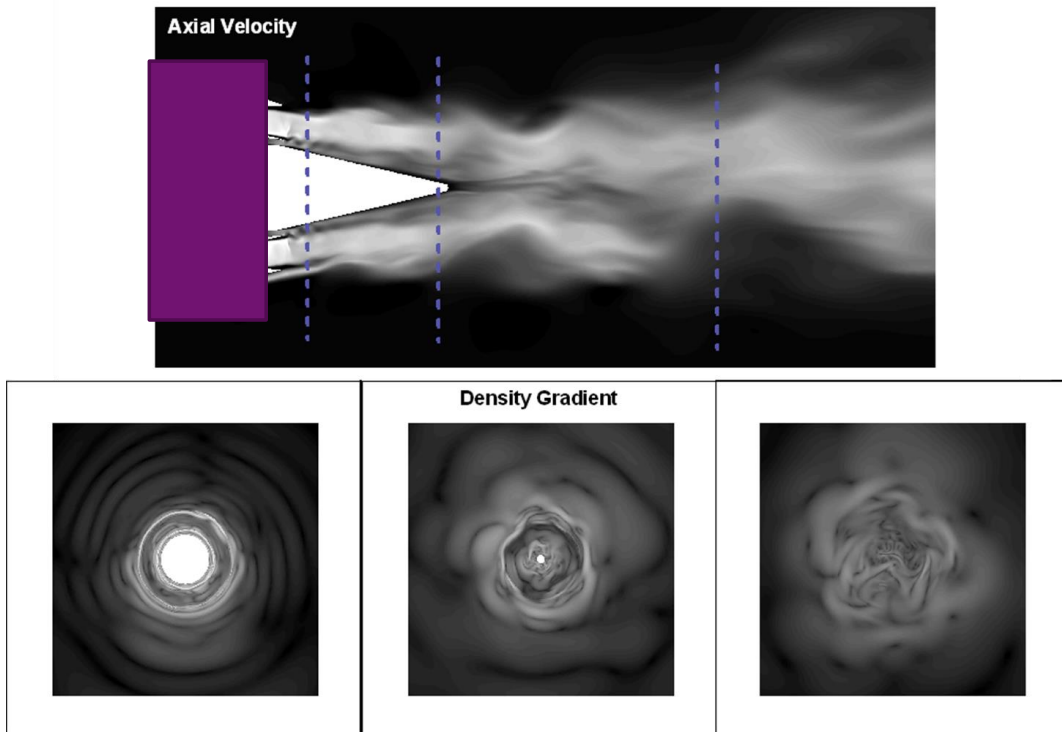


Figure 48 Axial velocity and density gradient contours for cutback nozzle at $M_f=0.0$.

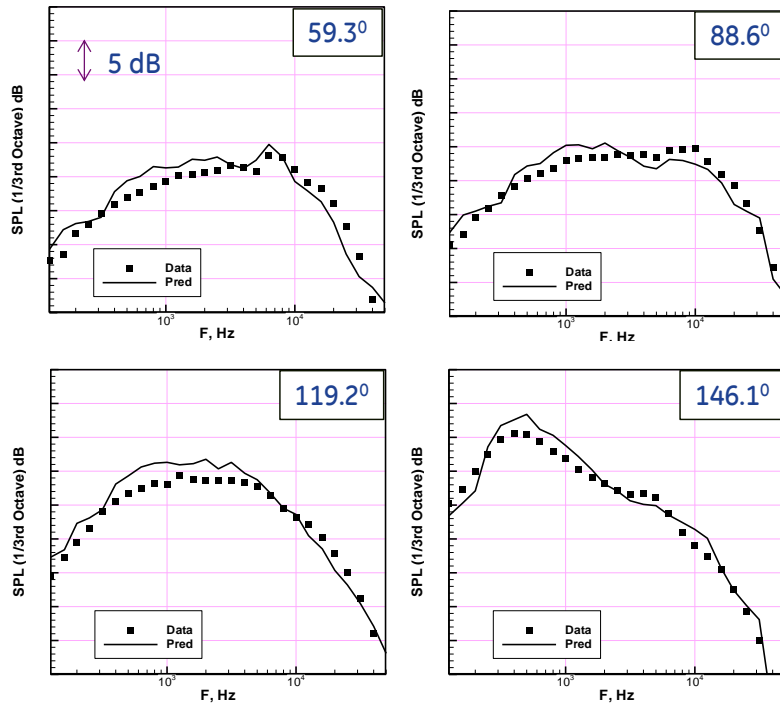


Figure 49 Far field acoustic predictions at 4 different downstream angles for the cutback nozzle at $M_f=0.0$.

Figure 50 shows plots of the reference nozzle noise level minus the IVP/shield nozzle for the four angles shown previously for the measured data as well as the predicted value for cases with and without external flow. The trends for the no external flow case, $M=0$, is predicted extremely well in both amplitude and shape. For the case with external flow the trends are not correct at the low frequency, this is the first time LES has been used with external flow and further investigation is needed to ensure the FWH methodology is being implemented correctly.

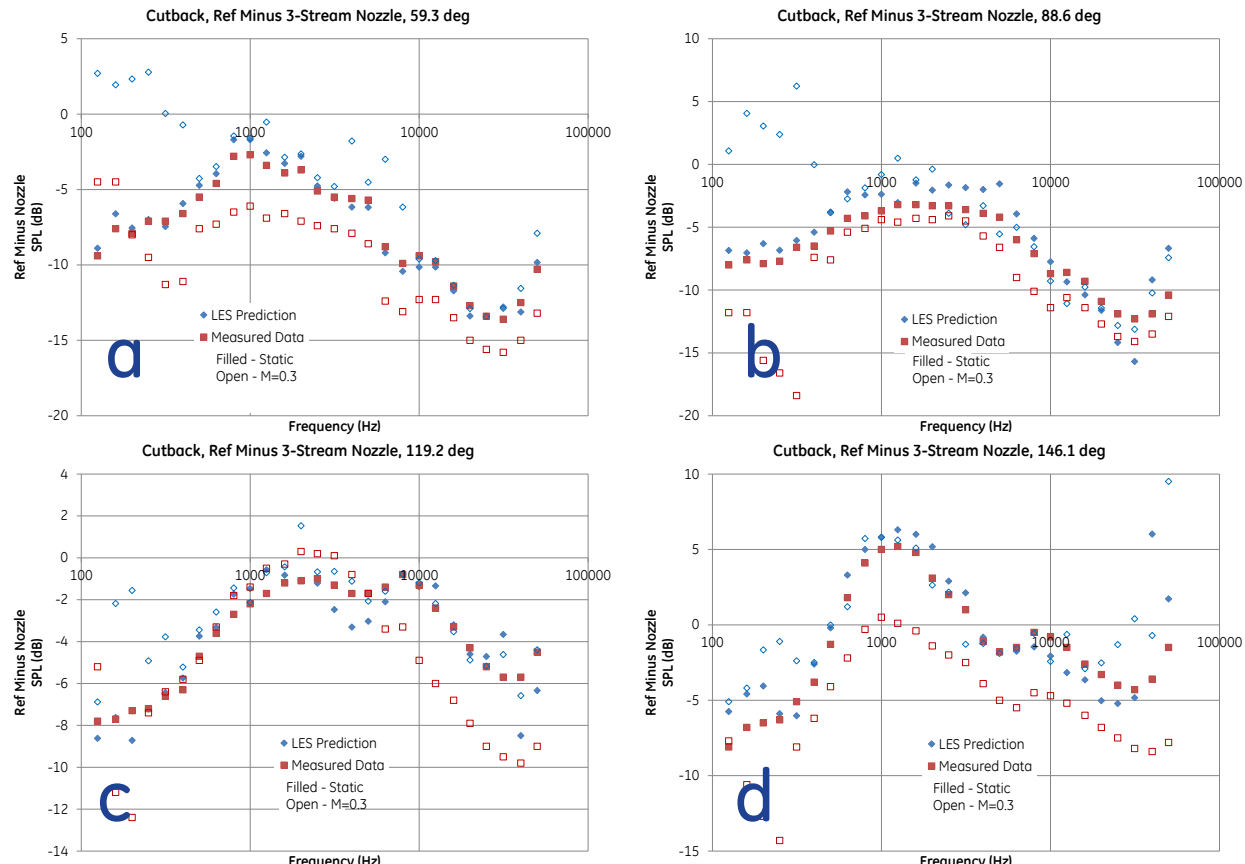


Figure 50 Noise Delta Between Reference Nozzle and IVP/Shield Nozzle, Prediction and Measured Values, (a) 59.3 deg, (b) 88.6 deg, (c) 119.2 deg and (d) 146.1 deg.

3.4.3 PHASE II LES

Aeroacoustic analysis of the Phase II design is in progress using Large Eddy Simulation (LES) with an unstructured flow solver from Cascade Technologies (CTI). A coarse grid of the phase II cutback condition was created in Gridgen using a blocked structure. This grid was then adapted by splitting cells and creating hanging nodes to resolve the critical regions of the flowfield. The final grid count is 78 million points.

The three engine streams (primary, IVP, and shield) were driven with total pressure and total temperature boundary conditions per the engine cycle model. A wall model was used to more accurately predict wall shear and boundary layer growth. A co-flow (simulated flight speed) Mach number 0.3 was applied to the ambient boundaries with temperature of 296K and pressure of 99.4kPa.

The LES solution shows regions of unsteadiness not predicted by the RANS solution, including on the inner and outer surfaces of the primary nozzle, as seen in the instantaneous density gradient shown in Figure 51. Figure 52 shows the instantaneous temperature and velocity in the flowfield near the nozzle. No shocks or regions of gross separation are predicted, which is an improvement over the behavior of the Phase I nozzle. This is expected to result in reduced noise levels for both the LES analysis and the scale model testing. Note this solution is not fully developed throughout the entire computational domain, but in the near nozzle region it is fully developed.

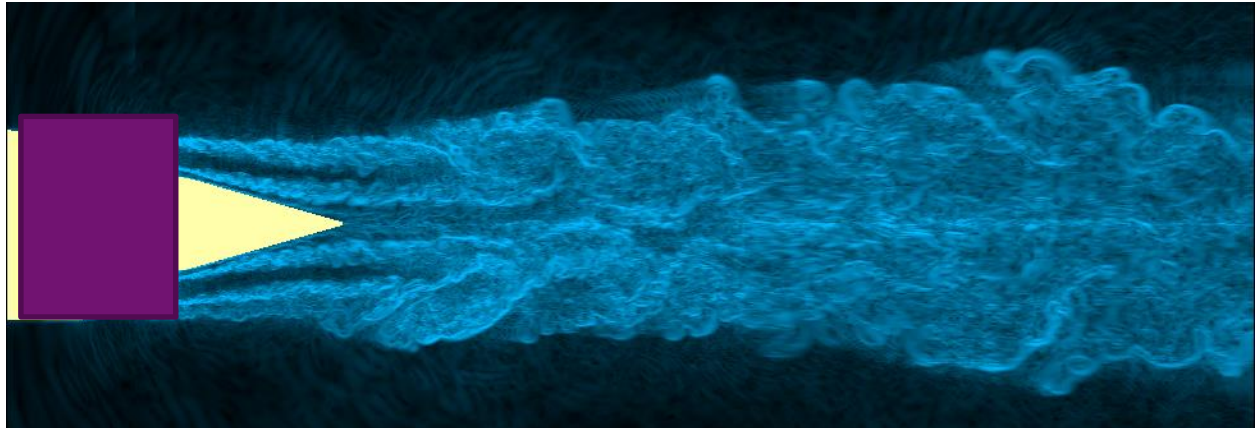


Figure 51 Instantaneous density gradient showing development of mixing structures.

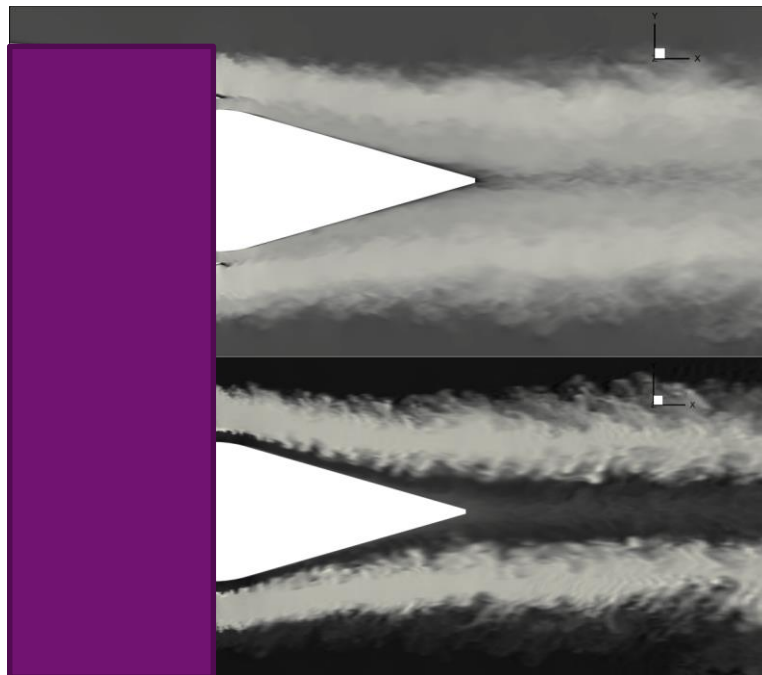


Figure 52 Instantaneous velocity (top) and temperature (bottom).

Figure 53 shows the time averaged mean velocity in the near nozzle flowfield and Figure 54 shows the fluctuating velocity in the same region.

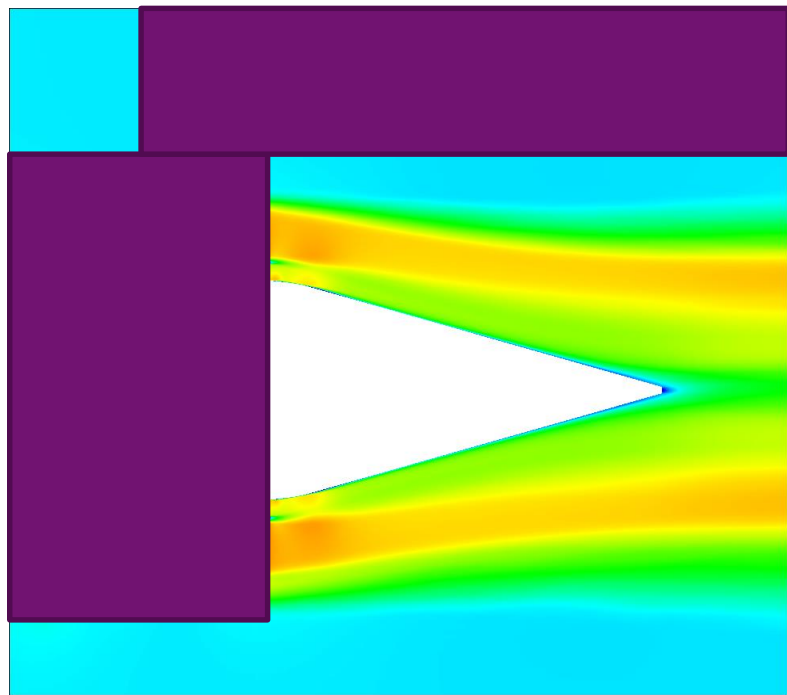


Figure 53 Time-averaged velocity.

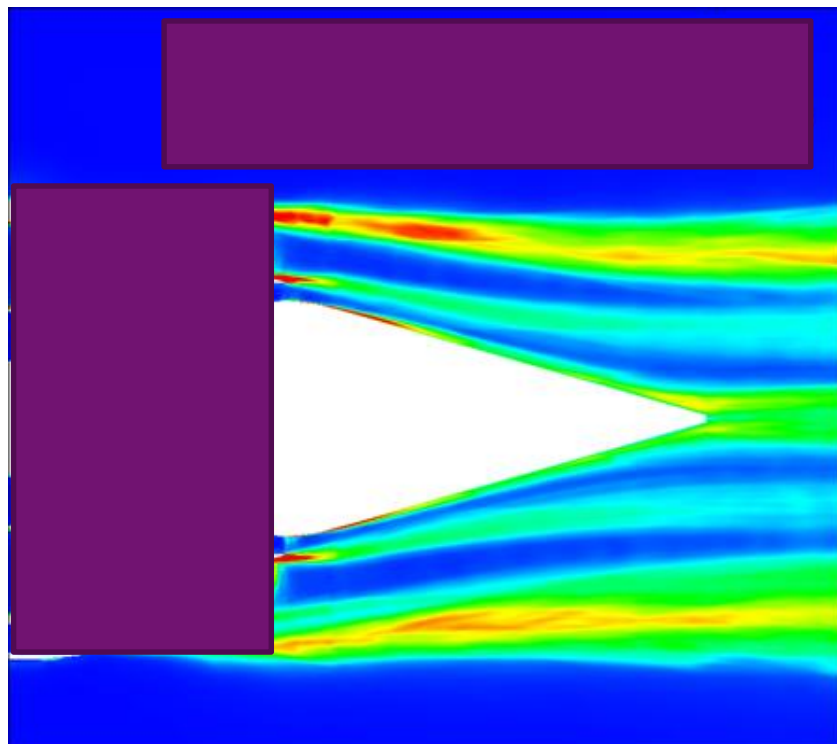


Figure 54 RMS velocity (m/s).

3.5 PHASE II CONTINUATION LES

The LES simulations for the Phase II geometry were run at GE Aviation, where the primary LES code for acoustics is CharLES from Cascade Technologies, Inc. This code solves the compressible Navier-Stokes equations on unstructured grids using a highly-scalable, second-order accurate control volume based finite volume method. Flux is computed at each control volume face by blending a non-dissipative central flux and a dissipative upwind flux. The blending parameter is computed locally based on the grid quality and varies spatially to minimize the introduction of numerical dissipation and dispersion where grid quality is good, and to prevent the introduction of numerical instabilities where grid quality is less than ideal. The explicit Smagorinsky sub-grid scale model is utilized to model the effects of unresolved turbulence on the flow-field, and shocks are captured through a second-order ENO scheme by surgically introducing dissipation where needed. To further improve simulation accuracy, wall modeling is used to account for the effects of boundary layer development on the overall solution. The above combination of low-dissipation schemes allows for high-fidelity LES simulations of complex geometries.

3.5.1 SIMULATION RESULTS

Simulations were performed for the baseline GE Phase II cutback geometry as well as the cutback nozzle with a trimmed primary-stream throat. Both simulations were performed at an ambient Mach number of 0.3 to aid in solution speed. Figure 55 shows a representative mesh for these runs, which was generated in ICEM. Initial grid resolution was set to accurately resolve the nozzle geometry as well as to add sufficient boundary layer grid for use of the CharLES wall modeling, but the volume away from the nozzle walls was left as coarse as possible. The Cascade mesh adaption tool was then used to refine the remaining volume with relatively isotropic hexahedral cells, while introducing hanging nodes that the CharLES solver can handle. This approach allows a high concentration of mesh in regions of interest while limiting the amount of unnecessary mesh resolution outside of the important areas of the flow field. Like the Phase I LES, a conical FWH surface was used to sample the unsteady flow field and the simulation was started with a zero initial flow-field and allowed to fully develop before sampling. Far field acoustic predictions were made with the with observer locations set to mimic the experimental setup. Again, multiple FWH surfaces were investigated to ensure acoustic prediction convergence

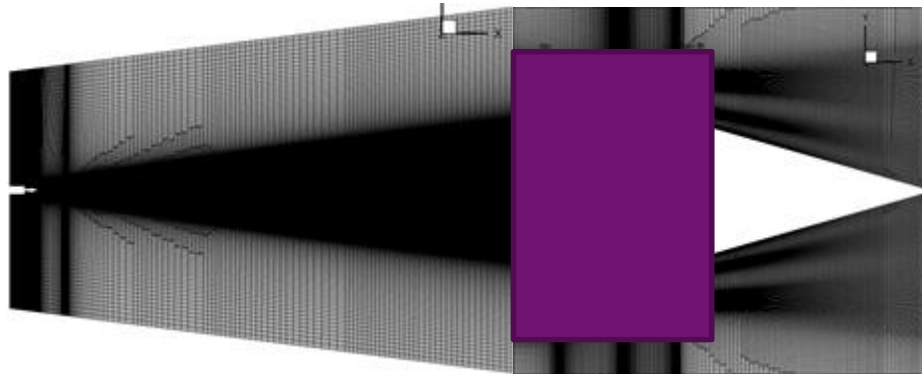


Figure 55 LES Grid Topology for Phase II Continuation LES

3.5.2 BASELINE CUTBACK NOZZLE

The unstructured grid used for the baseline cutback LES simulation is shown in Figure 55. The grid had a total node count of ~76M. The simulation was run on roughly 2000-9000 cores on the AFRL's Spirit supercomputer. Acoustic sampling was performed at a time step of 1.7E-08 seconds for a total of ~1.49M time steps (about 0.0253 seconds).

Figure 56 shows a comparison of the scale model data, to be presented in the next section, with the LES farfield prediction for the cutback geometry and condition, at an angle of 59 deg. The data is shown for the range of cycle conditions tested, referenced with the primary nozzle pressure ratio. In the data some broad humps are seen in the 8 kHz range for some of the mid-range primary nozzle pressure ratios. The LES results also show this broad hump at approximately the same frequency range. This relatively broad noise hump is likely the result of a broad band shock noise from the shocks on the cowl of the IVP nozzle.

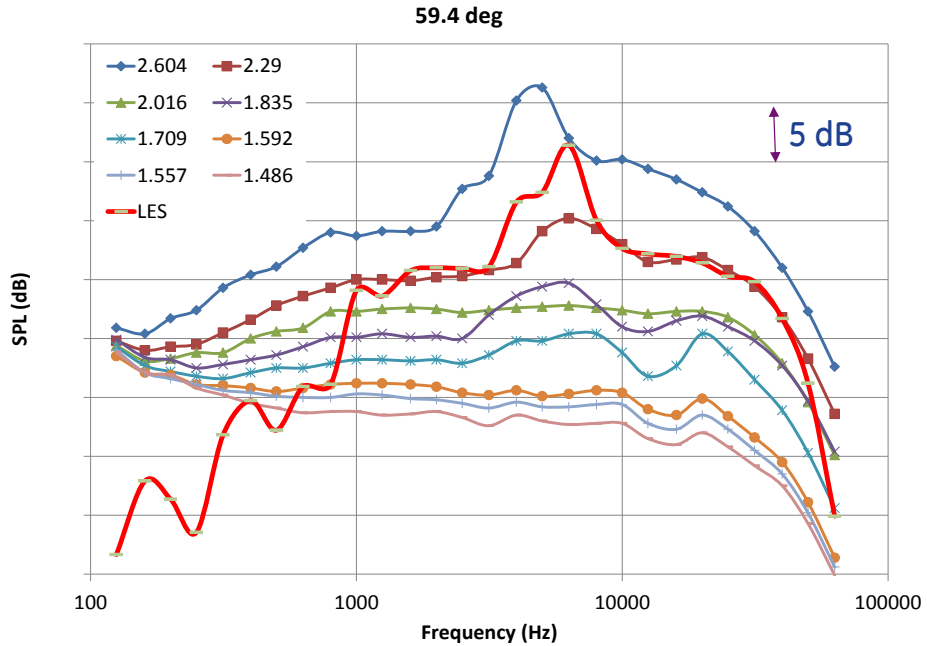


Figure 56 Comparison of LES Acoustic Prediction and Experimental Data at 59.4 deg at Model Scale.

3.6 PHASE 2 CONTINUATION EXHAUST NOZZLE TEST

The exhaust nozzle test was conducted at NASA GRC in the AAPL/NATR facility. Two geometric configurations were available along with a chevron configuration for the primary nozzle exit, where not covered by the shield, as well as for the shield nozzle.

Figure 57 and Figure 58 show photographs of the three-stream nozzle installed at the NASA facility.

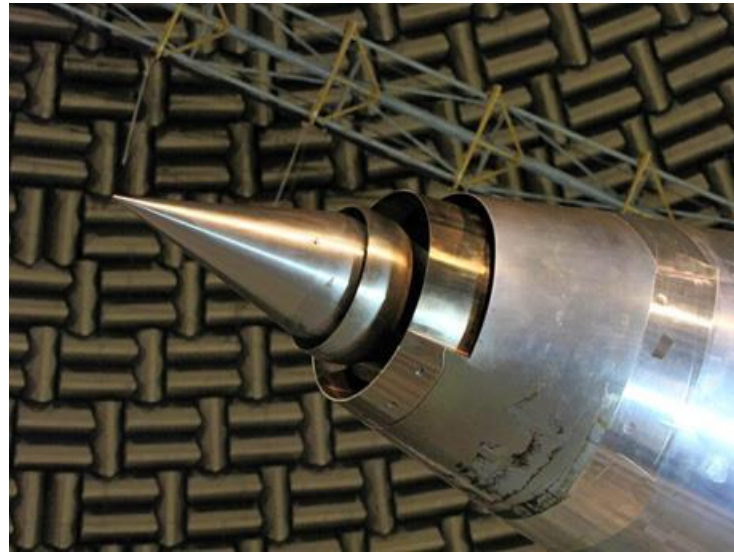


Figure 57 Photo of Three-Stream Nozzles Installed at NASA Facility.

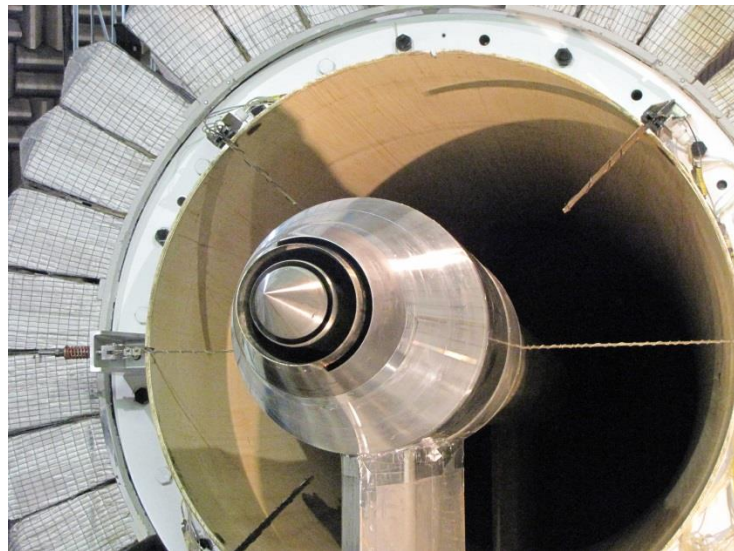


Figure 58 Photo of Three-Stream Nozzle Installed in NASA Facility.

3.6.1 PHASE 1 VS PHASE 2 DATA COMPARISON

Figure 59 shows a comparison of the Phase 1 and Phase 2 cutback configurations and conditions. The model sizes and conditions are not the same between the two phases so the levels should not be compared exactly. The Phase 1 data had an unsteady separation in the flowfield that was generating an extra noise source, seen in the forward angles in the OASPL plot and in the 8 – 12 kHz frequency range in the spectra. Clearly this has been mitigated in the Phase 2 configuration.

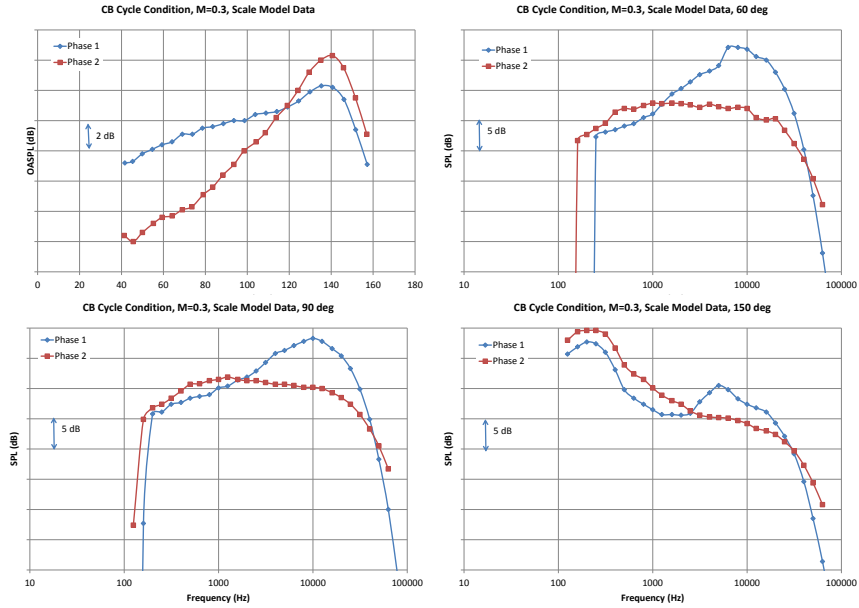


Figure 59 Phase 1 vs Phase 2 Scale Model Test Results for the Cutback Geometry and Condition. Scale Model Data at with Different Nozzle Sizes and Conditions, Shield Aligned with the Microphones.

Figure 60 shows Phase 1 and Phase 2 comparisons of the single engine jet noise EPNL values as a function of mixed velocity, for the cutback configuration. In the Phase 1 figure the unsteady separation issue is seen at lower mixed velocities. The data is compared to data taken with a round conic nozzle run at the same mixed velocity and scaled to provide equivalent thrust levels. At high mixed velocities the three-stream nozzle is quieter than the reference configuration. For Phase 2 the three-stream nozzle is quieter at all velocities.

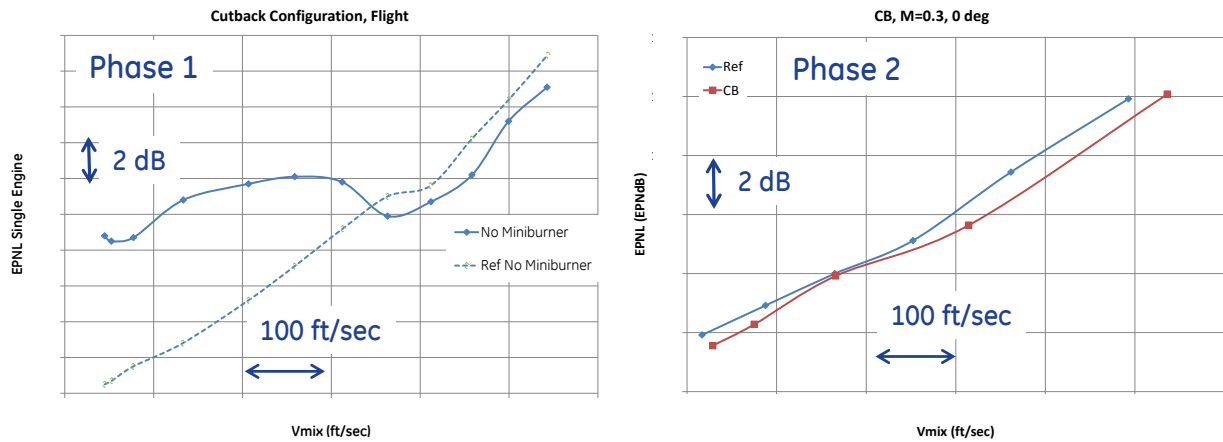


Figure 60 Comparison of Jet Noise EPNL Levels for Phase 1 and Phase 2 Cutback Geometries. Vehicle and Propulsion System Different Between Phase 1 and 2, Shield Aligned with the Microphones.

Figure 61 shows the detailed farfield noise comparisons for the cutback configuration at the cutback cycle conditions compared to the reference nozzle. The PNL plot shows that the three-stream nozzle is quieter than the reference at angles aft of 80 deg. The levels are the same at the forward angles. The spectra

show that the three-stream nozzle is quieter over most frequencies, especially below approximately 5 kHz.

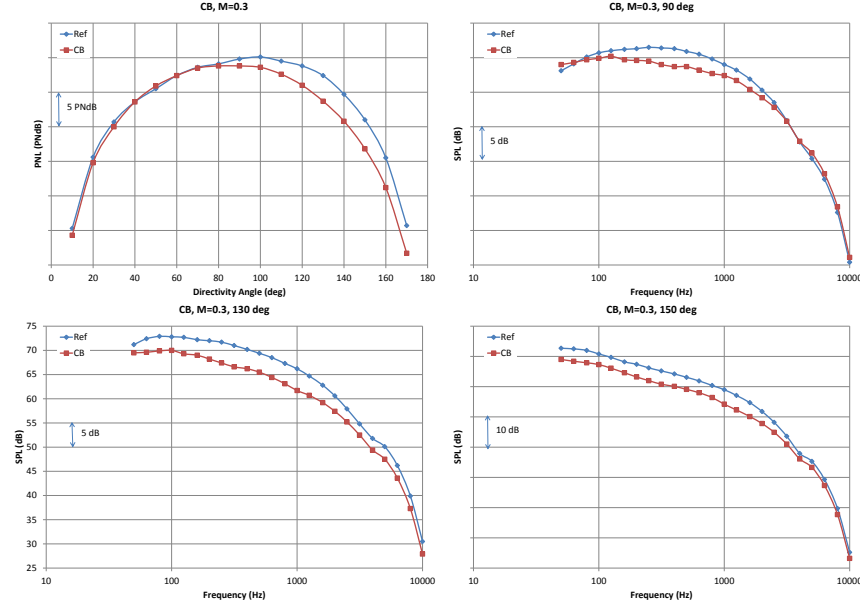


Figure 61 Full Scale Jet Noise Data for Cutback Configuration and Cycle Compared to Reference Nozzle, with Flight Simulation, Shield Aligned with the Microphones.

Figure 62 shows Phase 1 and Phase 2 comparisons of the single engine jet noise EPNL values as a function of mixed velocity, for the sideline configuration. In the Phase 1 figure the unsteady separation issue is seen at lower mixed velocities. At high mixed velocities the three-stream nozzle is quieter than the reference configuration. For Phase 2 the three-stream nozzle is quieter at all velocities.

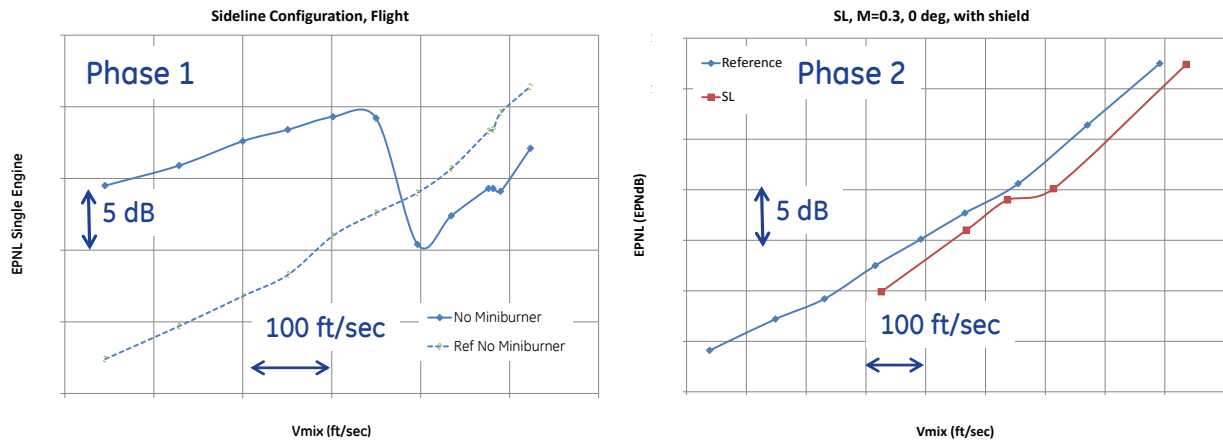


Figure 62 Comparison of Jet Noise EPNL Levels for Phase 1 and Phase 2 Sideline Geometries. Vehicle and Propulsion System Different Between Phase 1 and 2, Shield Aligned with the Microphones.

Figure 63 shows the detailed farfield noise comparisons for the cutback configuration at the sideline cycle conditions compared to the reference nozzle. The PNL plot shows that the three-stream nozzle is quieter than the reference at angles aft of 120 deg. The spectra show that the three-stream nozzle is quieter over

most frequencies, especially below approximately 5 kHz. At forward angles the three-stream nozzle is sometimes louder than the reference nozzle.

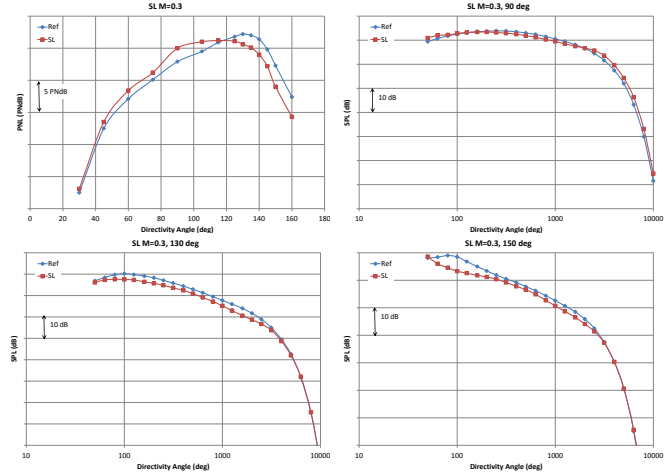


Figure 63 Full Scale Jet Noise Data for Sideline Configuration and Cycle Compared to Reference Nozzle, with Flight Simulation, Shield Aligned with the Microphones.

Figure 64 shows full scale data for the cutback configuration with flight conditions at $M=0.3$ for all of the cycle conditions tested. The PNL plot shows the peak noise directivity is at relatively side angles and only moves forward at the highest nozzle pressure ratios, where the broadband shock noise really picks up. The spectra at 60, 90 and 130 deg show fairly smooth characteristics, although some of the mid-range cycle conditions have some very broad ripples at 8 and 12 kHz. These are thought to be the remnants of the shock like phenomena discussed previously. Although for the current commercial application the operating conditions around noise sensitive operations may only be slightly supersonic, traditional broadband shock noise does not become evident until pressure ratios fairly above supercritical conditions. This is another benefit of the IVP, broadband shock noise really doesn't show up until fairly supersonic conditions are reached.

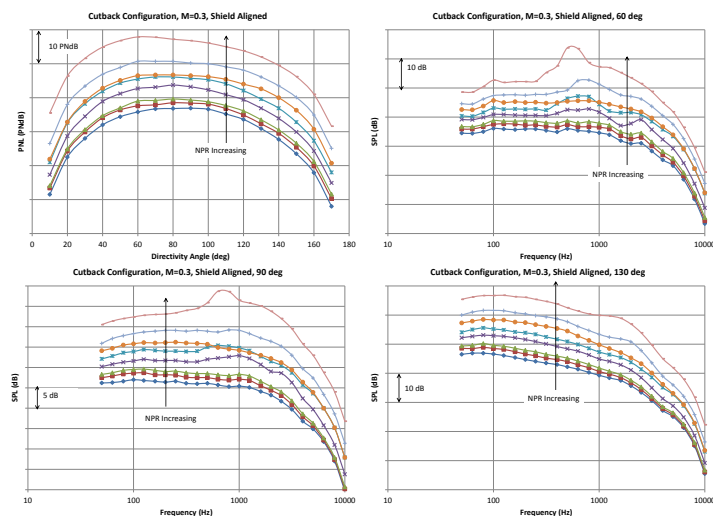


Figure 64 PNL and Spectra at Three Angles for the Cutback Configuration Including Entire Cycle Tested, Simulated Flight Conditions with $M=0.3$, Shield Aligned with Microphones.

Figure 65 shows full scale data for the sideline configuration with flight conditions at $M=0.3$ for all of the cycle conditions tested. The trends are similar for the cutback configuration.

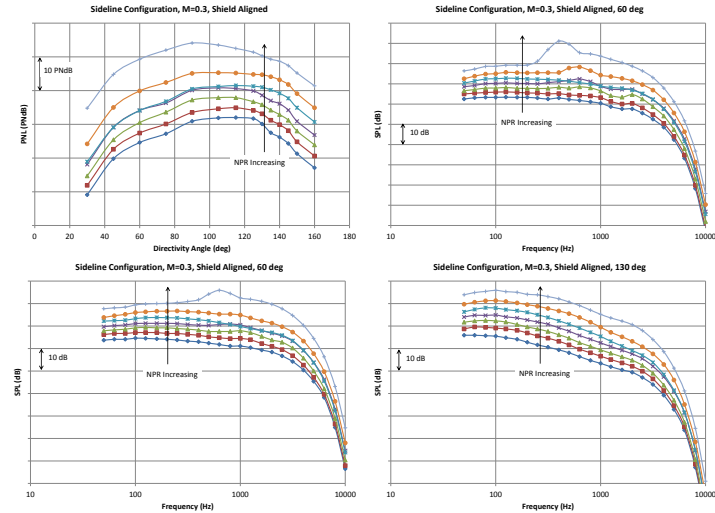


Figure 65 PNL and Spectra at Three Angles for the Cutback Configuration Including Entire Cycle Tested, Simulated Flight Conditions with $M=0.3$, Shield Aligned with Microphones.

Figure 66 shows full scale data for the cutback configuration with static conditions for all of the cycle conditions tested. The PNL plot shows the peak noise directivity is at aft angles and only moves forward at the highest nozzle pressure ratios, where the broadband shock noise really picks up. The spectra at 60, 90 and 130 deg show nice smooth characteristics. Although for the current commercial application the operating conditions around noise sensitive operations may only be slightly supersonic, broadband shock noise does not become evident until pressure ratios fairly above supercritical conditions. This is another benefit of the IVP, broadband shock noise really doesn't show up until fairly supersonic conditions are reached.

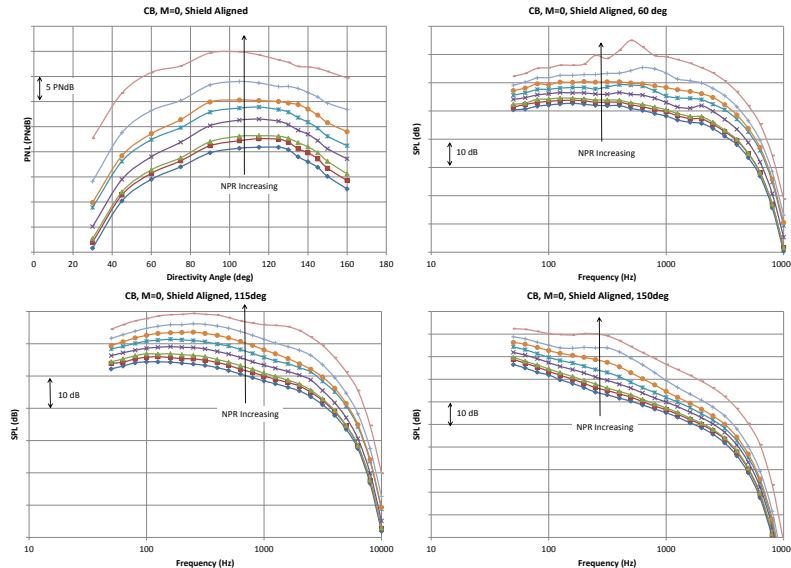


Figure 66 PNL and Spectra at Three Angles for the Cutback Configuration Including Entire Cycle Tested, Static Conditions, Shield Aligned with Microphones.

Figure 67 shows full scale data for the sideline configuration with static conditions for all of the cycle conditions tested. The trends are similar for the cutback configuration.

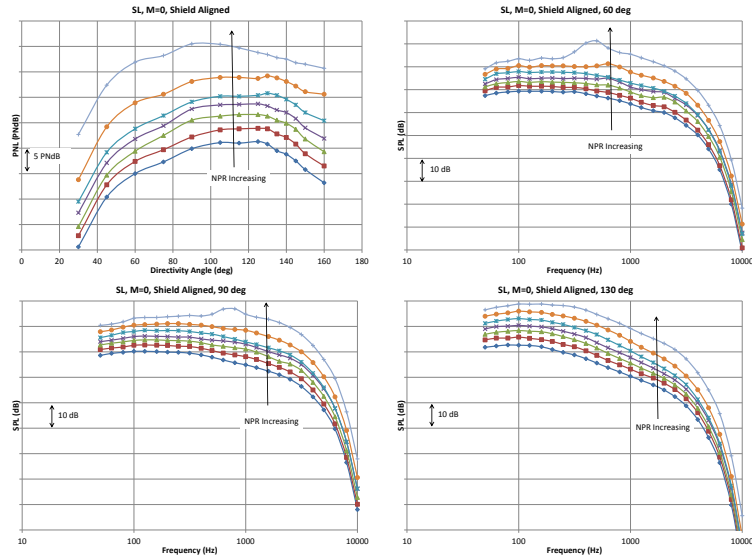


Figure 67 PNL and Spectra at Three Angles for the Sideline Configuration Including Entire Cycle Tested, Static Conditions, Shield Aligned with Microphones.

Figure 68 shows the effect of the shield with the sideline configuration on the EPNL. At this high level metric the effect on the EPNL is fairly small. Figure 69 shows the detailed shield effect at the sideline condition. The PNL plot shows the shield has a benefit over all angles. The SPL spectra show the shield results in the lower noise at the mid-range frequencies, where the shield is expected to reflect noise.

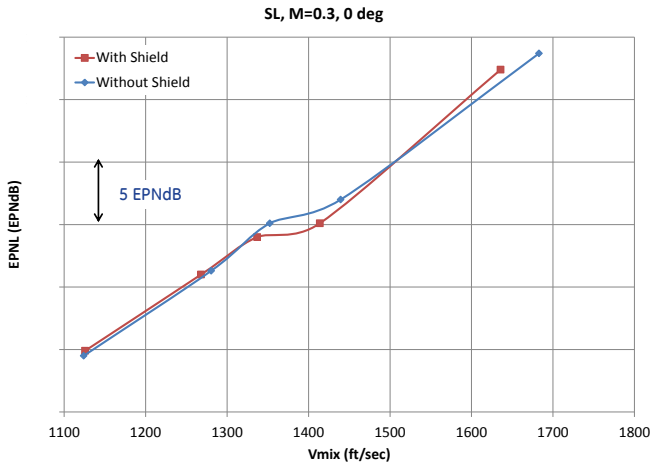


Figure 68 EPNL vs Vmix Showing Effect of the Fluid Shield for the Sideline Configuration with Flight Simulation, Shield Aligned with the Microphones.

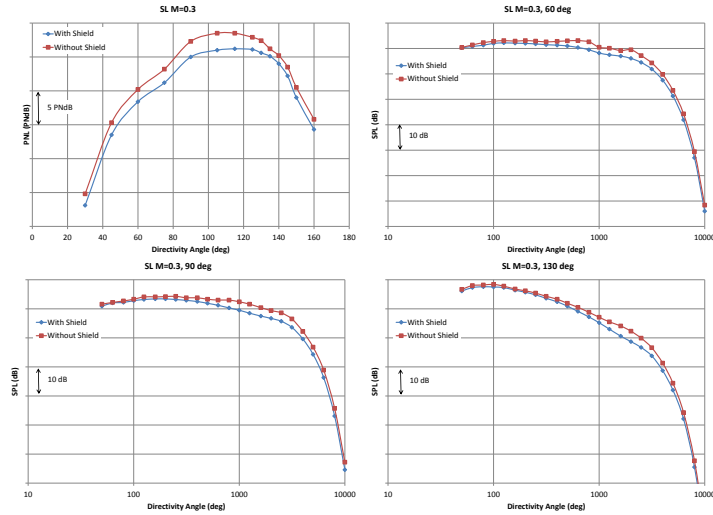


Figure 69 Full Scale Jet Noise Data for Sideline Configuration and Cycle with and without the Fluid Shield, with Flight Simulation, Shield Aligned with the Microphones.

Figure 70 shows the effect of chevrons with the sideline configuration on the EPNL. At this high level metric the effect on the EPNL is fairly small, with no significant benefit seen. Figure 71 shows the detailed chevron effect at the sideline condition. The PNL plot shows the chevrons have a benefit at aft angles. The SPL spectra show the chevrons result in lower noise at the low frequencies, but can increase noise at the higher frequencies. These results show the difficulty with chevrons nozzles that interact with the freestream, great care must be taken with the amount of vorticity generated to balance this low frequency benefit and high frequency penalty.

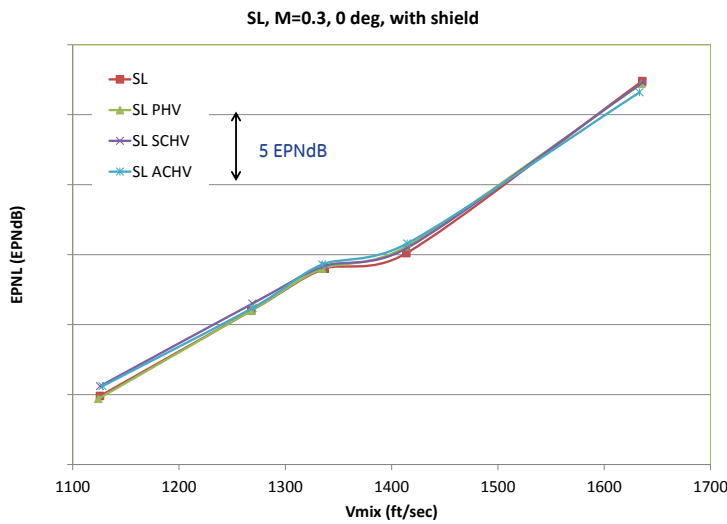


Figure 70 EPNL vs Vmix Showing Effect of the Chevrons for the Sideline Configuration with Flight Simulation, Shield Aligned with the Microphones.

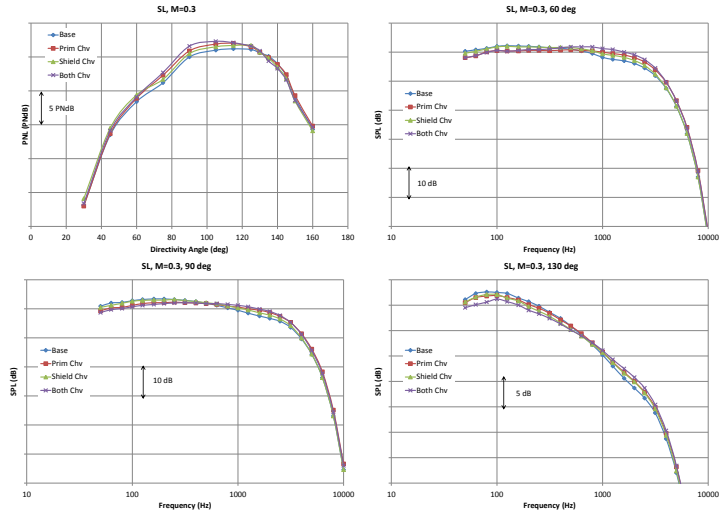


Figure 71 Full Scale Jet Noise Data for Sideline Configuration and Cycle with and without Chevrons, with Flight Simulation, Shield Aligned with the Microphones.

Figure 72 shows the effect of the azimuthal angle with the sideline configuration on the EPNL. At this high level metric the effect on the EPNL is fairly small, but the case with the shield aligned with the microphones generally has the lowest EPNL value. Figure 73 shows the detailed azimuthal angle effect at the sideline condition. The PNL plot shows that with shield aligned with the microphones the benefit is seen at the peak noise radiation angles. The SPL spectra show the shield results in the lower noise at the mid and high frequencies, where the shield is expected to reflect noise. The broad ripples discussed previously at 8 and 12 kHz are also suppressed with the shield aligned with the microphones.

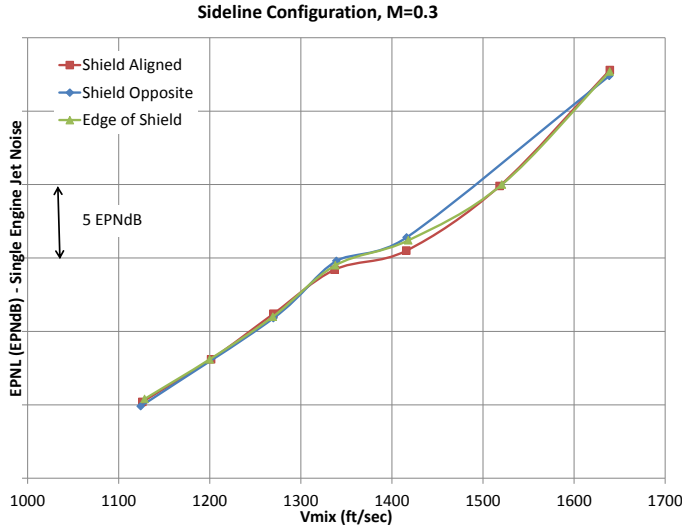


Figure 72 EPNL vs V_{mix} Showing Effect of the Azimuthal Angle for the Sideline Configuration with Flight Simulation, Shield Aligned with the Microphones, Opposite the Microphones and aligned with the edge of the Shield.

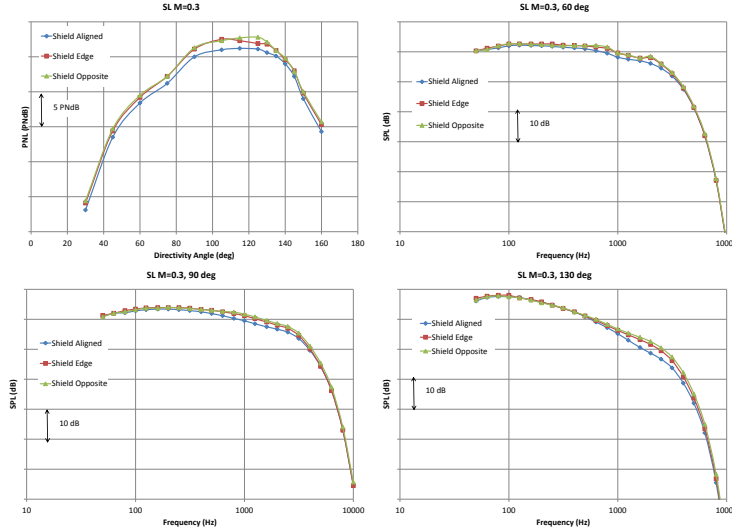


Figure 73 Full Scale Jet Noise Data for Sideline Configuration and Cycle Showing the Effect of the Azimuthal Angle for the Sideline Configuration with Flight Simulation, Shield Aligned with the Microphones, Opposite the Microphones and aligned with the edge of the Shield

4 NUMERICAL SIMULATIONS OF DECOUPLED FAN DOMAIN

A multi-stage fan rig is chosen for the NASA N+2 Phase II program to assess the fan noise. Numerical simulations of this fan rig are then performed using unsteady RANS (URANS) to provide information for fan noise assessment. This report has all the necessary details of the numerical simulations. The details include CFD domain, geometry setup, meshing, operating and boundary conditions, CFD process, convergence check, and post-processing. These details are organized in subsections of this report.

4.1 CFD DOMAIN, MESH, AND BOUNDARY CONDITIONS

The CFD domain includes all the blade rows except for the structural members of the rig at the rear of the two streams. This is a full-annulus model that includes all the blades and vanes contained in the blade rows, with the intention of simulating the distorted flow that enters from the upstream boundary that connects to the supersonic inlet. The LM inlet center-body line is re-scaled slightly to match the fan rig hub profile for a smooth transition. The inlet is also scaled down to match the fan rig scale.

The operating condition for the fan CFD is at a take-off condition. The inflow boundary condition is from CFD of the inlet, generated by Lockheed Martins. Inlet CFD is on unstructured mesh, shown in Figure 74. All five flow variables and two turbulence variables (TKE and Omega) are taken from the inlet solution at above-mentioned AIP. This flow condition is then mapped onto fan domain. Fan CFD is done with GE's in-house turbomachinery code TACOMA, which is a URANS code with structured mesh driven by dual-time stepping algorithm for unsteady calculations. The main numerical scheme in TACOMA is a JST-style 3-stage Runge-Kutta explicit scheme with multigrid and other convergence techniques.

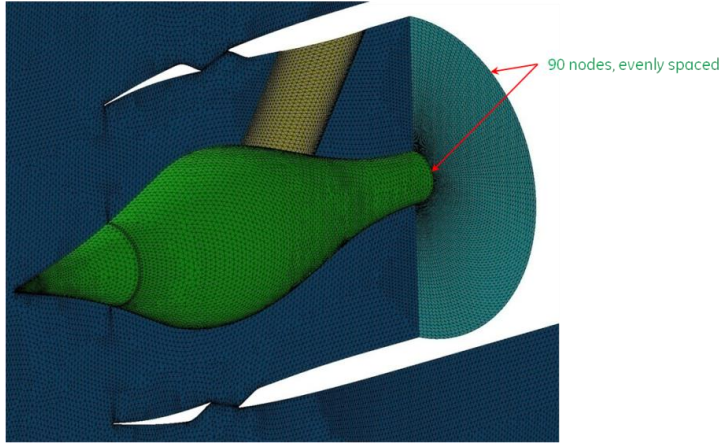


Figure 74 LM inlet grid and AIP location.

The mesh for the fan rig is a structured multi-block topology. Care is taken to provide enough resolution for the expected flow physics, such as wake migration. Proper tip and hub clearances are included, and the relative clocking of stator rows and rotor rows are also checked and placed accordingly. Proper grid spacing in between two adjacent blade rows is also placed in both axial and tangential directions for smooth transition of flow features. Total mesh size is about 600 million cells.

The inflow boundary condition, taken from the Lockheed Martin inlet solution is illustrated in Figure 75. This represents the distorted flow, where the three strut wakes and wakes from the open auxiliary door are shown. Two clean inflow conditions are also derived from this condition. One is a circumferentially averaged condition, labeled as “clean inflow”. The other is a face-averaged clean condition, labeled as “very-clean inflow”. Both clean flow conditions retain the endwall boundary layers.

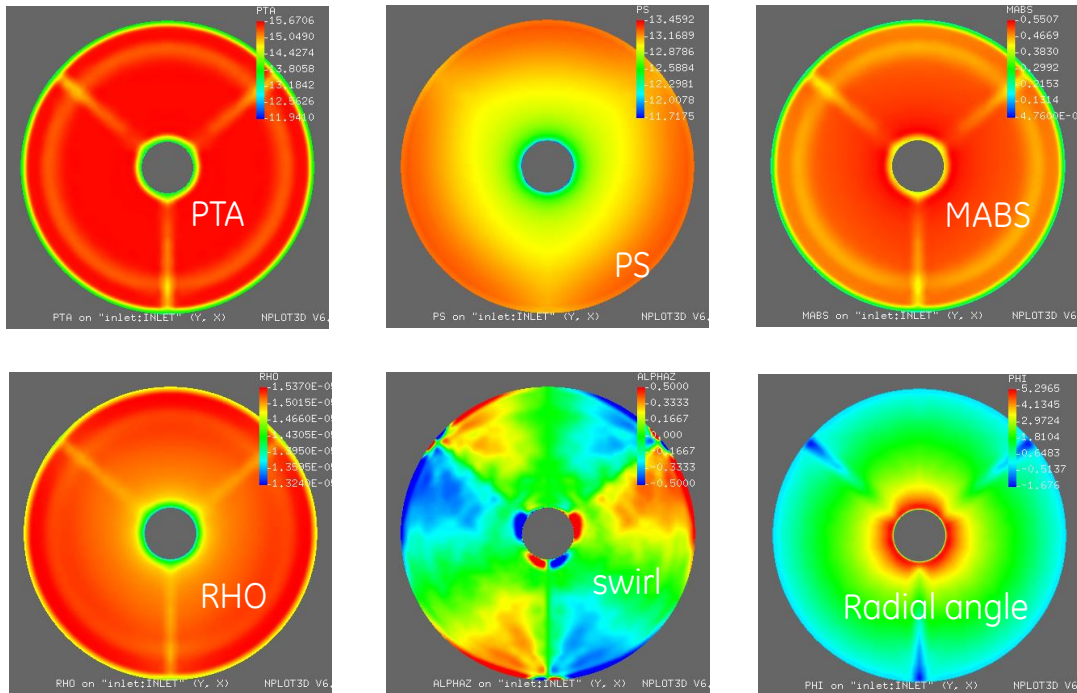


Figure 75 Inflow boundary condition mapped to fan domain.

4.1.1 STEADY-STATE CALCULATION

A steady-state calculation is necessary to establish the basis for unsteady simulations. A mixing-plane approach is adopted in between two adjacent blade rows. This calculation ensures the fan is at the correct operating condition in exit corrected flow.

4.1.2 CONVERGENCE OF UNSTEADY CALCULATIONS

It's important to make sure the unsteady calculations have good convergence. Convergence checks for unsteady calculations should consider multiple aspects rather than a typical error level check. The first rule of thumb is to allow ample time for a fluid particle to pass the entire domain before convergence is checked. Using an averaged velocity and the overall axial length of the domain, the time scale can be calculated, and compared against the physical time step for the unsteady flow calculation to determine how many physical time steps it takes for one particle to pass through. Usually, 4-5 passings is a good measure for the time to establish a converged flow.

Once ample time has passed, a check is performed on the usual error terms of the equations. Beyond the error check, other critical flow properties also need to be checked for proper convergence. The inlet and exit massflows, blade torque, and loss in the domain are examined as well. Figure 76 shows the convergence check of these variables in the blade rows that are near the exit boundary of the CFD domain. These trends show that the flows in all components are properly converged. The solution is extracted after convergence to record blade surface pressure and flow variables at other locations for one revolution.

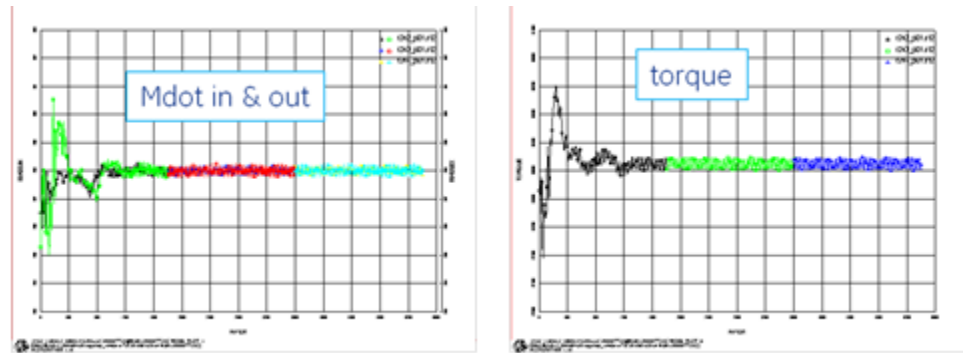


Figure 76 Unsteady flow calculation convergence check.

4.1.3 UNSTEADY RESULTS

The unsteady calculations are carried out on NASA's HPC facility, using 1620 cores, with careful load-balancing. Three major calculations are performed, distorted, clean, and very-clean inflow conditions. These calculations are necessary for the acoustic assessment. Figure 77 illustrates the inflow PTA map corresponding to the three conditions. The results of the three calculations are compared in Figure 78, in which the snapshots of the static pressure distribution upstream of the IGV are compared. With distorted flow, the static pressure map shows the effect from the combined strut (upstream) and fan (downstream).

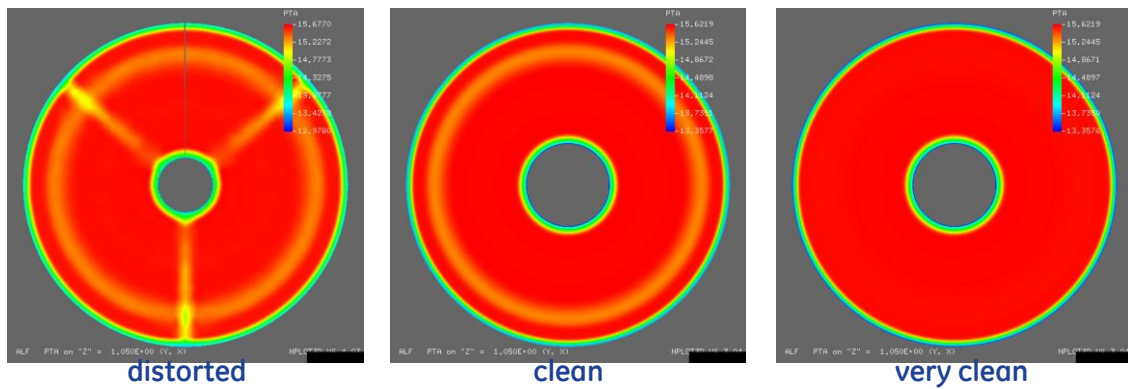


Figure 77 PTA (abs total pressure) of inflow conditions.

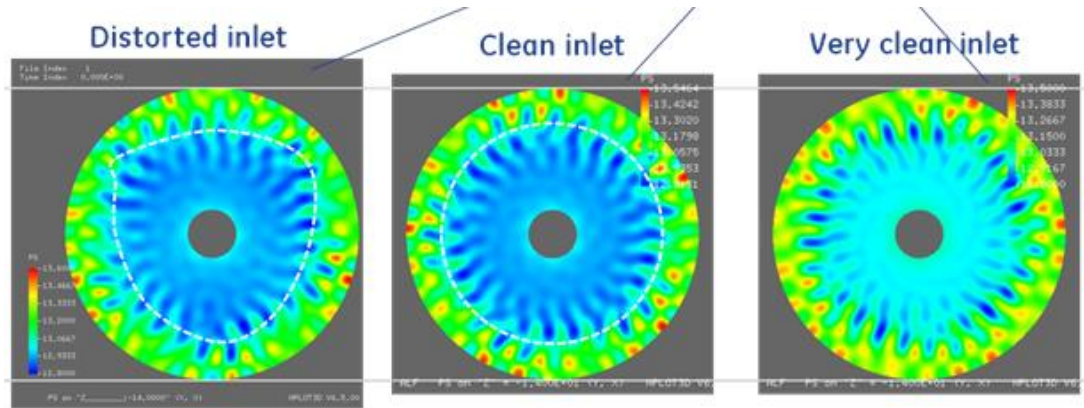


Figure 78 Static pressure maps with clean and distorted inflow conditions.

4.1.4 DETAILED RESULTS WITH DISTORTED INFLOW

The details on the flow field are then investigated, especially for the distorted inflow condition. First the flow in the main stream, upstream of the combined IGV is shown in Figure 79. Rotor 1 shocks interact with the combined IGV and project a complex, non-uniform pattern upstream. The shock impingement and reflection are well captured.

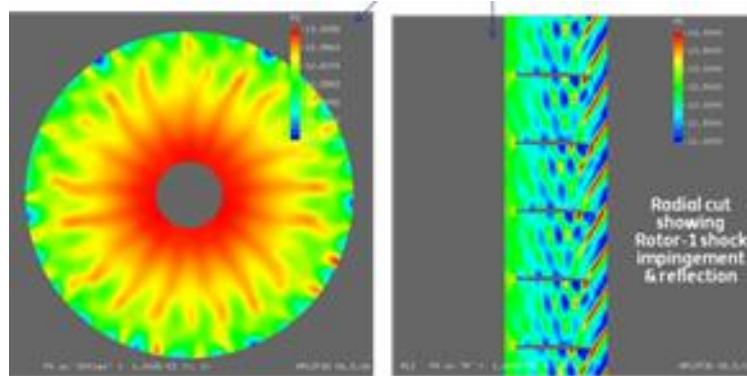


Figure 79 Rotor 1 Shock and IGV Interaction

The combined strut/IGV has a thick wake that travels further downstream, and interacts with Rotor 1, and can be seen in the Rotor 2 domain as well. These flow features are well captured, and are important to resolve for the aero-acoustic assessment which is based on the CFD results. See illustration in Figure 80.

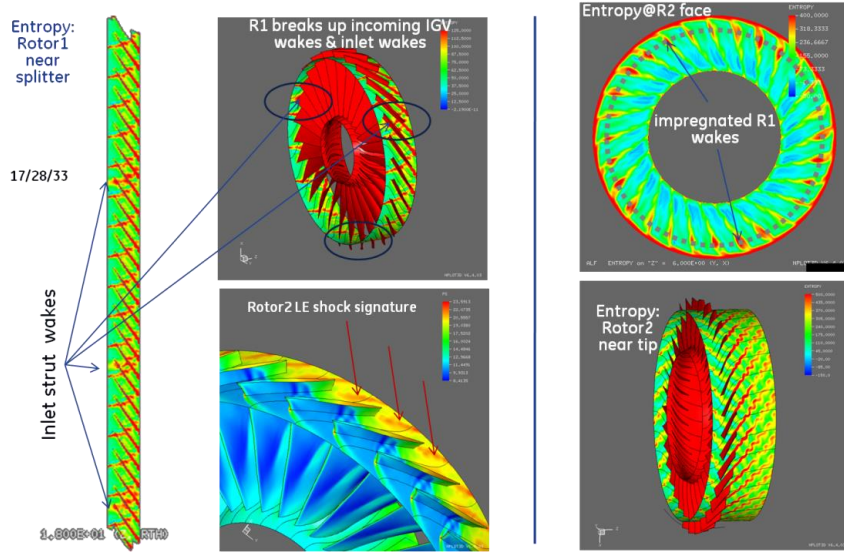


Figure 80 Rotor1/Rotor2 interaction.

4.1.5 POST-PROCESSING AND CONCLUSIONS

Three major unsteady simulations (distorted inflow, clean inflow, and very-clean inflow) have been carried out on the multi-stage fan rig for the acoustic assessment of the flow distortion effects. These calculations capture the flow features in great detail which in turn enables higher confidence in acoustic calculations. These are large-scale calculations that are time-consuming but deliver high-fidelity results.

Unsteady pressure of all the blades in all blade rows are recorded for the extent of one fan revolution. Also recorded are all the flow variables in-between any adjacent blade rows for one revolution. Most importantly, all the flow variables are recorded upstream to the fan rig for one-revolution for the processing of noise projection and comparison under these three different inflow conditions.

5 WAKE SOURCE CORRECTION USING LES SIMULATION OF WAKE DECAY

5.1 MOTIVATION

Blade wake prediction is important to study interaction effects with downstream blade rows. Both aero and acoustic performance of the downstream blade row is impacted due to unsteady wake migration. Typical two equation Reynolds Average Navier Stokes (RANS) models under-predict momentum mixing in the wake, predicting a deeper, narrower wake impinging the downstream blade. This typically results in an overestimation of the tonal noise source generated due to interaction with the aft blade row. Large Eddy Simulation (LES) offers an attractive alternative which predicts better mixing as it directly resolves turbulent structures responsible for flow mixing. GE has internally developed and validated a LES based approach for predicting blade wake evolution. This approach is applied to predict the wake evolution of the strut wake and the IGV wake as they evolve and interact with the downstream blade row. This

improved wake prediction is compared to the RANS based wake prediction to estimate the correction factor that should be applied when estimating the tonal noise source for these two wake interaction problems.

5.2 NUMERICAL APPROACH

The LES solver used is the same solver described in the earlier section (3.4), where it was used for exhaust noise prediction. Details of the solver are given in that section. Significant developments were made in the solver to enable handling the blade wake problem. This included incorporating buffer zone boundary conditions and an ability to specify turbulent boundary condition at the inlet.

Reynolds number for fans in gas turbine engines are typically of the order of a million or more and performing a complete LES or DNS computation of the full fan blade is prohibitively expensive. Therefore a zonal LES approach is adopted, where a portion of the blade trailing edge of a linear blade is simulated, along with the wake convection region. This requires non-trivial boundary condition specification at the edge of the computational domain. This is achieved by using the sponge boundary condition at the spanwise, azimuthal and exit boundaries and driving them to values from a RANS computation of the full blade. In order to provide unsteady disturbances in the blade boundary layer, time accurate turbulence information from a pre-computed flat plate boundary layer is superimposed on the RANS mean flow. This approach is only an idealization since the blade is not a flat plate, but seems to work quite well for wake prediction. A schematic of the computational domain is shown in Figure 81.

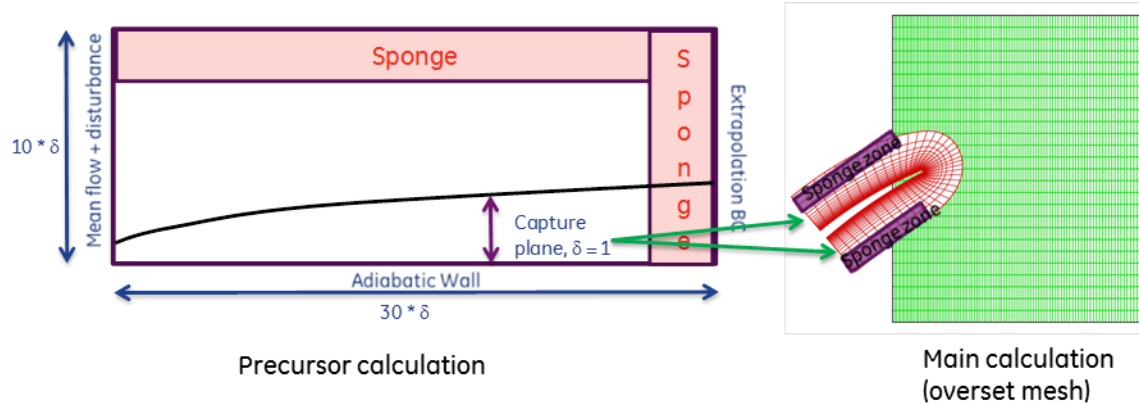


Figure 81 Zonal LES approach, with pre-computed boundary layer turbulence

This approach was validated on a GeNX cascade blade design. Wake profiles predicted at 0.6 chords downstream of the trailing edge is shown in Figure 82. LES predicted wake shape is in excellent agreement with measurement data, while the RANS based wale prediction is deeper and narrow, as expected. This validates the zonal LES approach and provided GE a great cost effective tool for wake prediction which is a huge improvement over traditional RANS based methods.

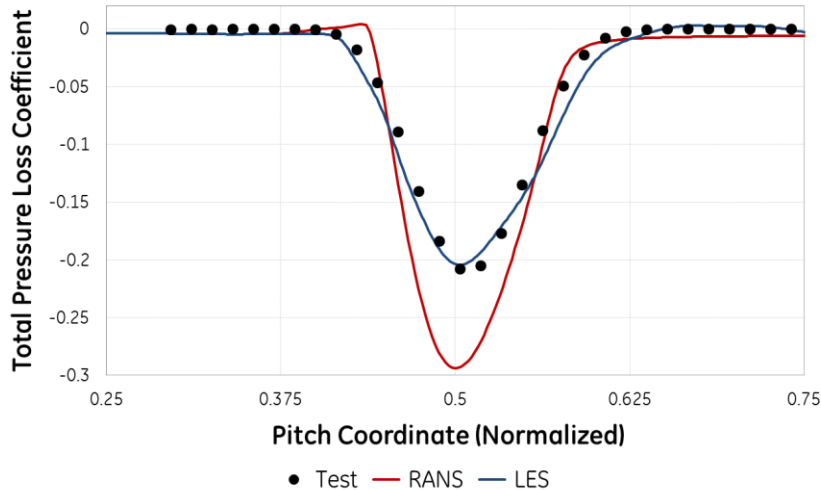


Figure 82 Wake profile at 0.6chods downstream of the trailing edge.

5.2.1 SIMULATION SETUP:

5.2.1.1 IGV WAKE SIMULATION:

As discussed in the earlier section only a fraction of the IGV blade is simulated in the LES calculation to limit the computational cost of the simulation. To determine the spanwise extent of the computational domain two factors were looked at. First the wake strength (acoustic source) at the trailing edge of the IGV was examined. Figure 83 shows the spanwise variation of the wake at four different radial locations. It is observed that the wake strength, i.e., the width and depth of the wake does not vary significantly across most of the outer span region. Next, the rotor loading is examined to evaluate the region of dominant acoustic response. It is found that the flow in the tip region is supersonic, which means the acoustic response will be tip dominated. Based on these factors the spanwise extent of the calculation was chosen to be between the streamlines that pass through from 60% span to 95% span on the IGV. We do not go to 100% span to avoid tip effects.

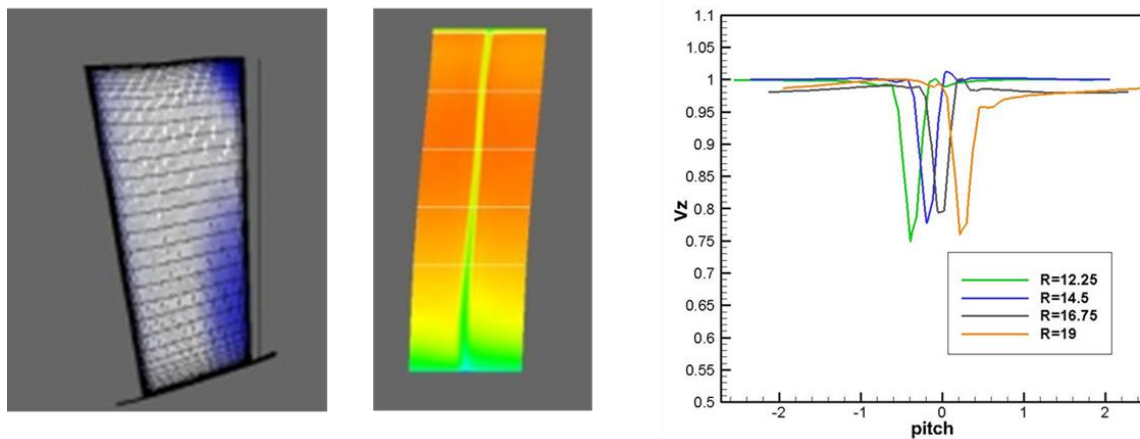


Figure 83 RANS based prediction of wake strength near trailing edge of the IGV

To determine the portion of the IGV blade that should be included in the simulation, the blade loading was examined at the two spanwise boundary locations. The inlet location is then chosen by using the zero pressure gradient criterion as shown in Figure 84. This is done to enable the use of turbulent boundary condition from a separate flat plate calculation as an inlet condition to the current computational domain. A schematic of the two block computational domain is shown in Figure 85. It should be noted that the axial gap between the IGV and rotor one is less than an IGV chord and we are really in the near wake evolution region. The sponge boundary condition is used at the exit and span wise locations and the solution is driven to the predictions based on a full blade RANS calculation. The azimuthal extent is one IGV passage and periodic boundary conditions are imposed at the azimuthal boundaries.

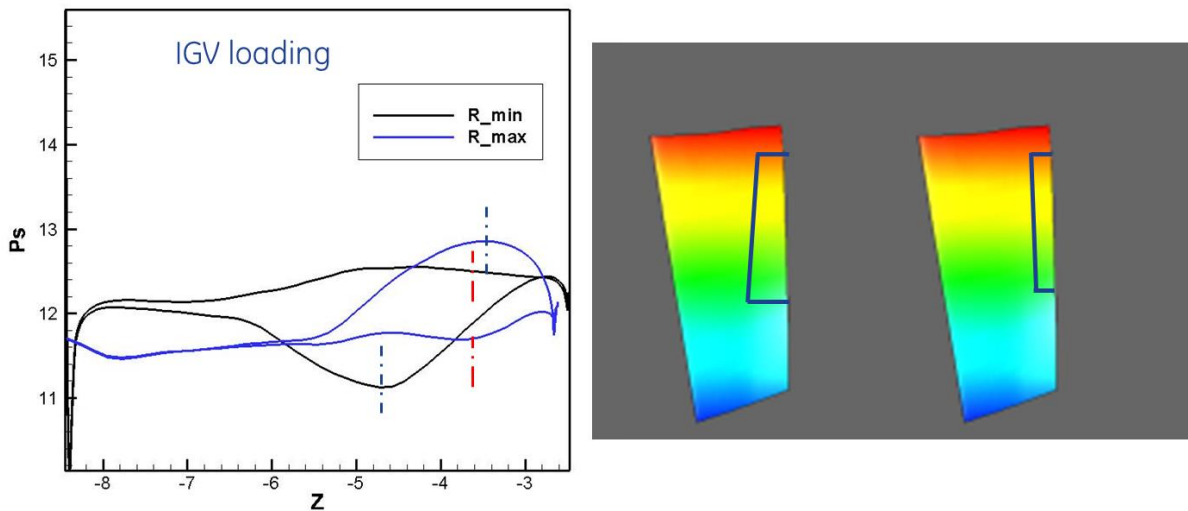


Figure 84 Blade loading at spanwise boundaries of computational domain. Inlet boundary chosen based on pressure gradient being close to zero

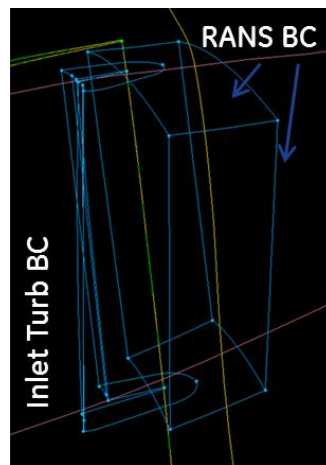


Figure 85 Schematic of two block computational domain for IGV wake simulation

The grid size for the two block computational domain was ~65M points. The computational domain was split into 512 parts and the calculation was run on 512 cores on NASA computer system Pleiades. A separate flat plate boundary layer calculation was initially run internally at GE to get a fully developed solution. The Reynolds number based on the momentum thickness was calculated at the inlet location to block 1 using the RANS solution for either side of the blade. These values were then used to choose two axial locations on the flat plate LES calculations which had the closest match to the Reynolds based momentum thickness. Time accurate data was collected at these two axial locations for three time units. One time unit is defined as the time taken for the flow to go through one IGV chord (at 95% span). This turbulent data was superimposed along with the RANS based mean flow to provide the inlet boundary condition for the C-block (block around the TE of the IGV blade).

The computational domain was first initialized using the RANS solutions and then run to a fully developed state. It took approximately 5 time units of run time to remove all transients. Data was then sampled along a full axial plane located at ~ 85% gap between the IGV and rotor 1. This was done to avoid going into the sponge boundary zone near the exit of the computational domain. Data was sampled for 10 time units.

5.2.1.2 STRUT WAKE SIMULATION:

Once again only a fraction of the strut blade is simulated in the LES calculation to limit the computational cost of the simulation. It was noted that the strut geometry had very little variation in the spanwise direction and was essentially a 2D blade. In addition the wake evolution distance, or the gap between the strut trailing edge and the IGV leading edge was significantly larger than in the previous case. To limit the problem size for such a large evolution region the spanwise extent was limited to be between the streamlines that pass through from 70% span to 98% span on the strut. This was the minimum spanwise extent needed to accommodate the specification of the sponge boundary layers at the spanwise boundaries.

Next, the blade loading on the strut was examined at these radial locations, to once again determine the location for the inlet boundary (portion of strut to be included in computation). A schematic of the two block computational domain is shown in Figure 86. It should be noted that the axial gap/ wake evolution region is significantly larger in this case as opposed to the IGV wake simulation. Once again the sponge boundary condition is used at the exit and span wise locations and the solution is driven to the predictions based on a full blade RANS calculation. Unlike the IGV wake simulation, given the low blade count for the strut, the azimuthal extent of the computational domain is not one strut passage. To maintain the computational cost to manageable levels the azimuthal extent was limited to one IGV passage and sponge boundary/RANS conditions were imposed at the azimuthal boundaries as well.

In spite of these limiting choices on the computational domain the grid size for the strut wake calculation was ~125M grid points. The computational domain was split into 1024 parts and the simulation was carried out on 1024 cores on the NASA computer system Pleiades. An examination of the RANS predicted boundary layer on the strut showed no significant turbulence. Hence in this case, only the RANS based mean flow was used to specify the inlet boundary condition and no additional inlet turbulence boundary condition was used. The simulation was run for 25 time units to obtain a fully developed solution with all initial transients removed. Data was then sampled at an axial location corresponding to ~90% of the gap. Data was sampled for 50 time units.

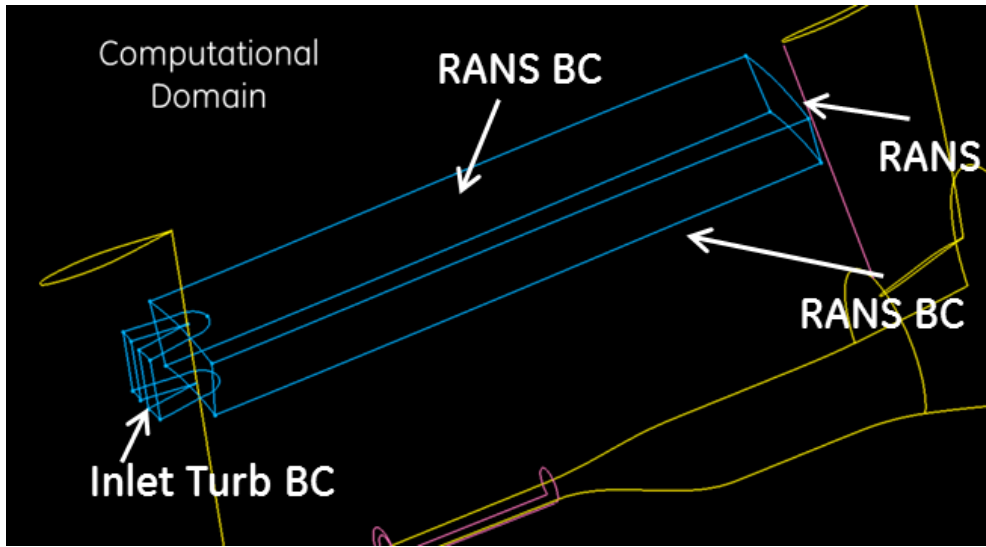


Figure 86 Schematic of two block computational domain for strut wake simulation

5.3 POST-PROCESSING AND RESULTS

The flow variables sampled near the exit plane for the IGV and strut wake calculations was time averaged to obtain the mean flow prediction based on the LES approach. The wake profile at various spanwise locations was compared to the wake profiles predicted by the RANS calculation. Figure 87 shows the comparison of the LES vs. RANS predicted strut wake at 85% span location near the IGV leading edge. It can be seen that the strut wake is not of significant strength, primarily due to the large evolution distance. In addition, the LES approach predicts a marginally higher mixing which translates to a slightly smaller prediction of the wake depth in the far wake region.

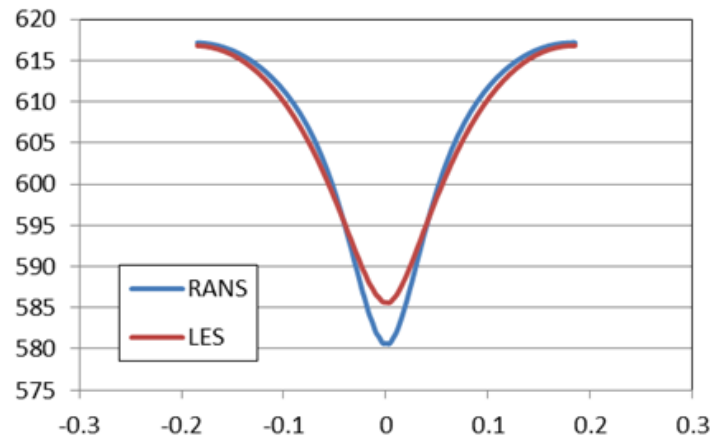


Figure 87 Comparison of RANS vs. LES based prediction for the strut wake at IGV leading edge (85% span location)

To characterize the acoustic source strength for the tone noise generation mechanism based on the wake profile the following steps are followed for both the RANS and LES data sets.

- Multiple constant theta lines are drawn on the 2D axial plane where data was sampled as shown in Figure 88.
- Along each constant line, data was probed at 256 equally spaced points.
- A spatial FFT was done along each line to extract the harmonics at 1st, 2nd & 3rd BPF
- The source strength (V_{2D}) was approximated to be equal to the combination of the azimuthal perturbation (V_{θ}) and axial perturbation (V_z).

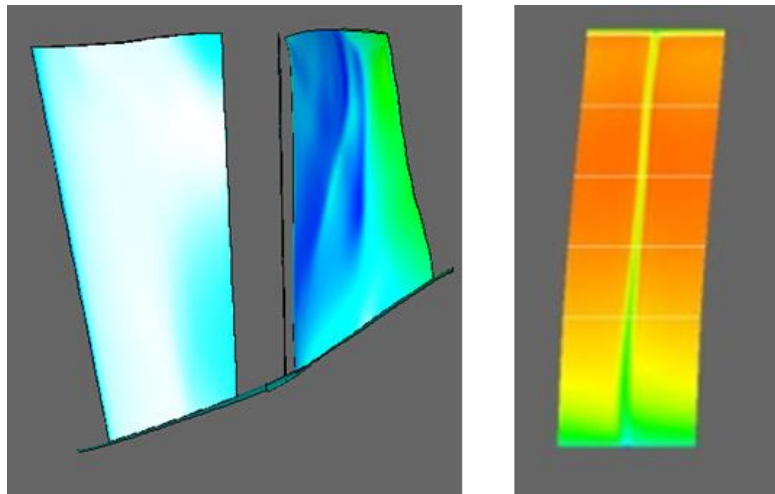


Figure 88 Estimation of wake strength at rotor leading edge using spatial FFT at multiple spanwise locations

This process was repeated on the data sampled from both the IGV wake evolution and strut wake evolution simulation. The spanwise variation of the estimated acoustic source strength for the IGV wake interaction with rotor 1 is shown in Figure 89. The x-axis is chosen to be the $10\log_{10}(V_{2D})$, to provide an estimate in the dB scale. It is seen that, as expected, the LES based prediction of a more mixed out wake results in a reduction in the estimated tonal noise source at the 1st three harmonic frequencies. Comparing the RANS vs. LES predictions, the estimated reduction is observed to be ~ 0.36 dB, 0.58 dB and 1.41 dB for the 1st, 2nd and 3rd BPF tones respectively.

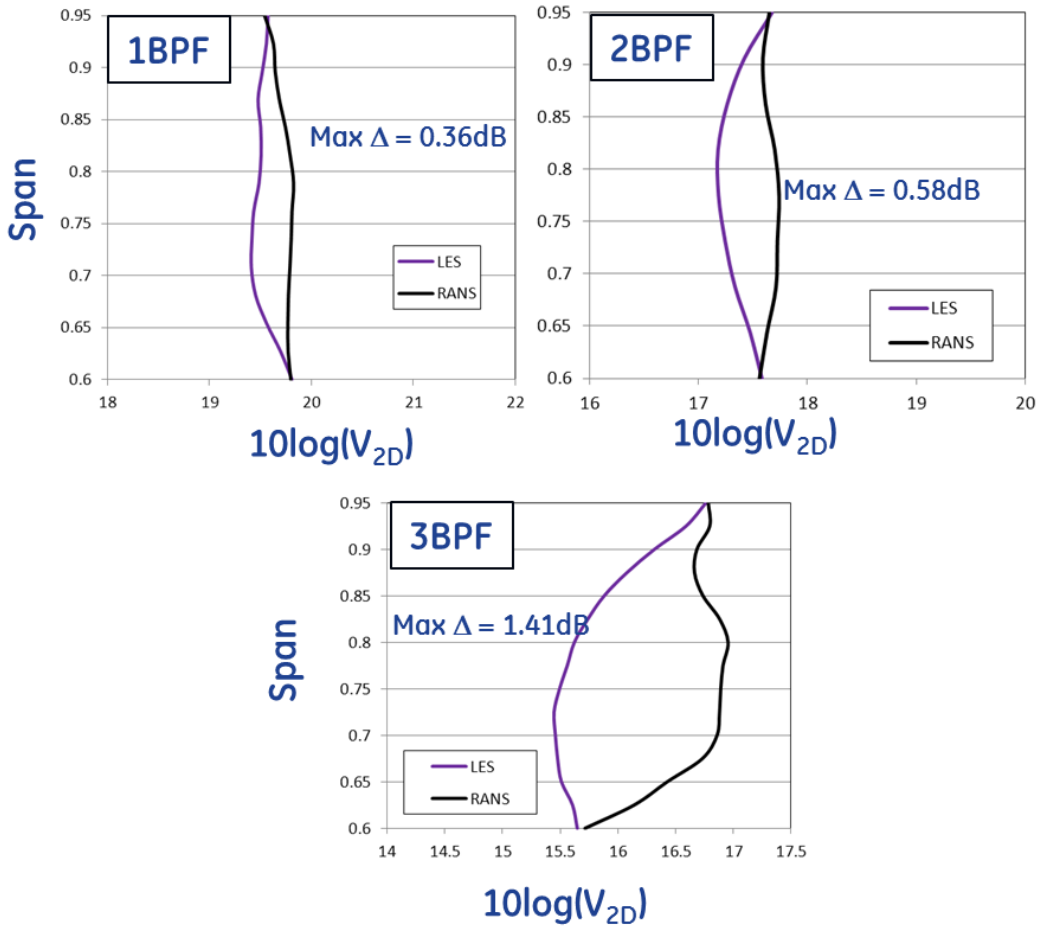


Figure 89 Comparison of 1st, 2nd & 3rd BPF source strength due to IGV wake interaction with rotor one.

Figure 90 shows a similar comparison between the RANS based and LES based prediction of acoustic source strength of the strut wake interacting with the IGV. The first thing to note here is that the absolute values are much smaller than what was observed in the IGV wake case. This is again as expected since the IGV wake strength at rotor one leading edge is much higher than the strut wake strength at the IGV leading edge. This is because of the large gap between the strut and the IGV allowing for a much more mixed out strut wake before it interacts with the IGV. In addition, the LES based wake mixing predicts that the acoustic signature of the strut wake – IGV interaction tones should be $\sim 1.18\text{dB}$, 2.34dB & 6.58dB lower than what is predicted by RANS at the 1st, 2nd and 3rd BPF tones respectively.

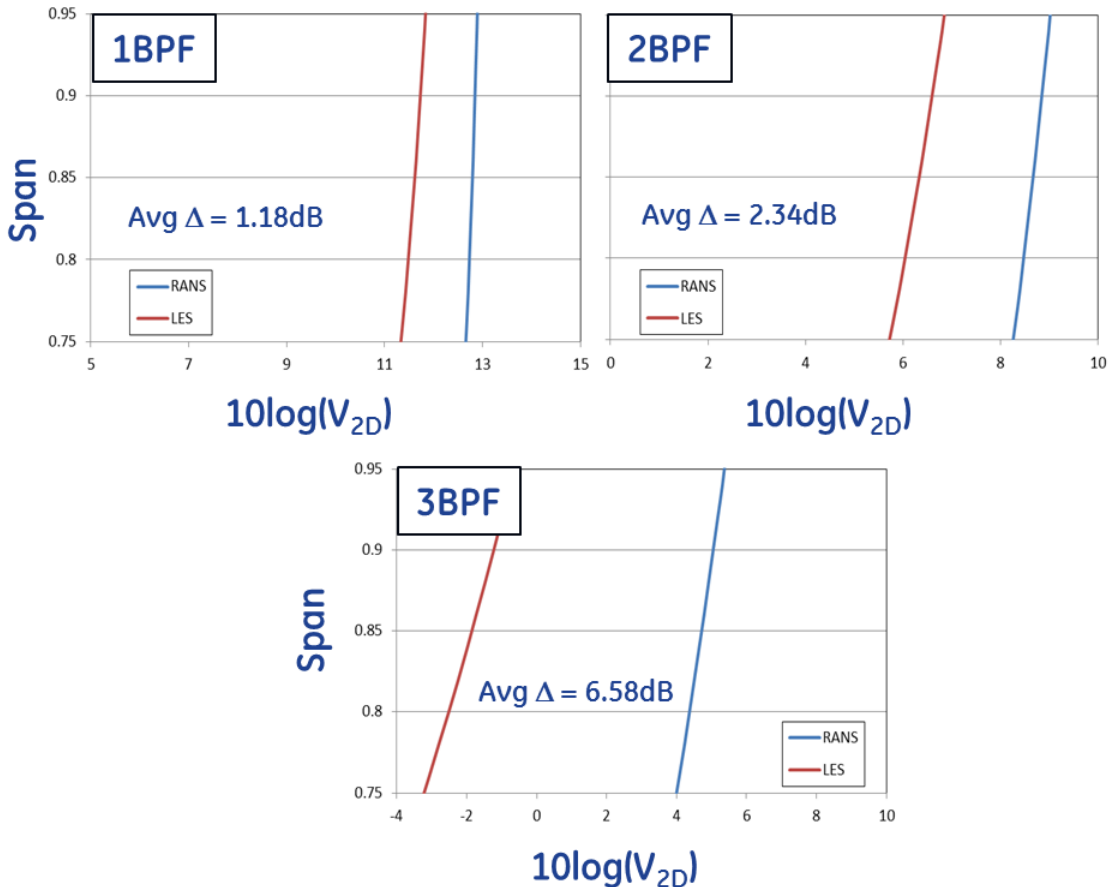


Figure 90 Comparison of 1st, 2nd & 3rd BPF source strength due to strut wake interaction with IGV.

These correction factors will be applied to the Strut wake – IGV interaction tones and the IGV wake - rotor one interaction tones, when computing the system noise.

6 NUMERICAL SIMULATIONS OF COUPLED AIRCRAFT/FAN DOMAIN

6.1 MOTIVATION OF THE INSTALLED CFD

Putting the aircraft and engines in a mutual flowfield is not currently a common practice even though the benefit of doing so is obvious, both to the airframers and to the engine manufacturers. This is primarily due to the barriers of information sharing between commercial companies under increasingly intense competitive pressure, which is a justifiable cause. This is where NASA-led programs can bridge the gap by joining the aircraft and engines in research programs like N+2 for aerodynamic and acoustics evaluations.

One of the purposes of performing the installed CFD within the scope of the N+2 program is to exercise the CFD tools and identify the aspects that CFD excels and the areas that are still in need of improvement. This task in the N+2 Phase II Extension is just the first step in maturing the CFD capability. Large-scale numerical simulations for aircrafts and for engines have significantly different requirements in terms of parallel efficiency and accuracy of prediction. Aircraft CFD software needs to be

efficient in a “strong-scaling” fashion since the CFD code needs to deal with the entire aircraft domain. On the other side, the current industrial CFD software used in engine companies has the benefit of “weak-scaling” due to the nature of turbomachinery which consists of many rows of rotors and stators and for each row, identical or similar blade/vane passages. Internal flows in turbomachinery, however, has the added requirement to capture the inlet and outflow conditions accurately for each row, or the stage-matching can easily go wrong with multi-stage compressors and turbines.

It is a challenge to apply GE’s turbomachinery CFD code to be able to handle very large domains like external flows around aircraft, not due to numerical algorithms but due to data/control structure of GE’s turbomachinery CFD code.

The second purpose of this task is to evaluate the fan face noise level in the installed environment. The operating condition for the installed CFD is determined to be at take-off condition, details of the conditions are presented in the following sections. A logical outcome of the noise level evaluation is to compare the installed noise level to the results that was obtained in Phase II where a fan-alone CFD was performed. The report has a section for this comparison. However, due the design evolution of the nacelle/inlet geometry, the comparison is not directly back-to-back. Also the difference between the standalone fan calculation and the coupled calculation are quite visible for conditions at fan face. This certainly highlights the necessity of coupled simulations. Detailed discussion of the comparison is given in the following sections.

6.2 CFD DOMAIN, GEOMETRY MODEL, MESH AND BOUNDARY CONDITIONS

Geometry model for installed CFD simulation consists of a multi-stage fan rig, and the aircraft model developed by Lockheed Martin. CFD domain is composed of the fan rig domain described in Section 4.2. The location of AIP (Aero-dynamic Interface Plane) is kept at the same location as in Phase II, and inlet portion of the domain described in Section 4.2 is replaced with nacelle / wing / fuselage model. The aircraft model has been scaled and positioned to match the size and orientation of the fan rig portion of the domain. The inlet hub center body has been slightly re-shaped to provide for smooth transition to fan rig domain.

6.2.1 GEOMETRY

Aircraft geometry model developed by LM is shown in Figure 91. Several details considered of no importance for fan/inlet CFD simulation have been modified to allow for simpler CFD model. Since the engine is shielded from the top by the presence of the wing, features above the wing are either simplified or eliminated. The engine at the plane of symmetry has been removed from the model as was the stabilizer at the back side of the wing. In both cases, appropriate smoothing of the fuselage and the top of wing was performed to obtain closed geometry model. The simplified fuselage model is show in Figure 92.

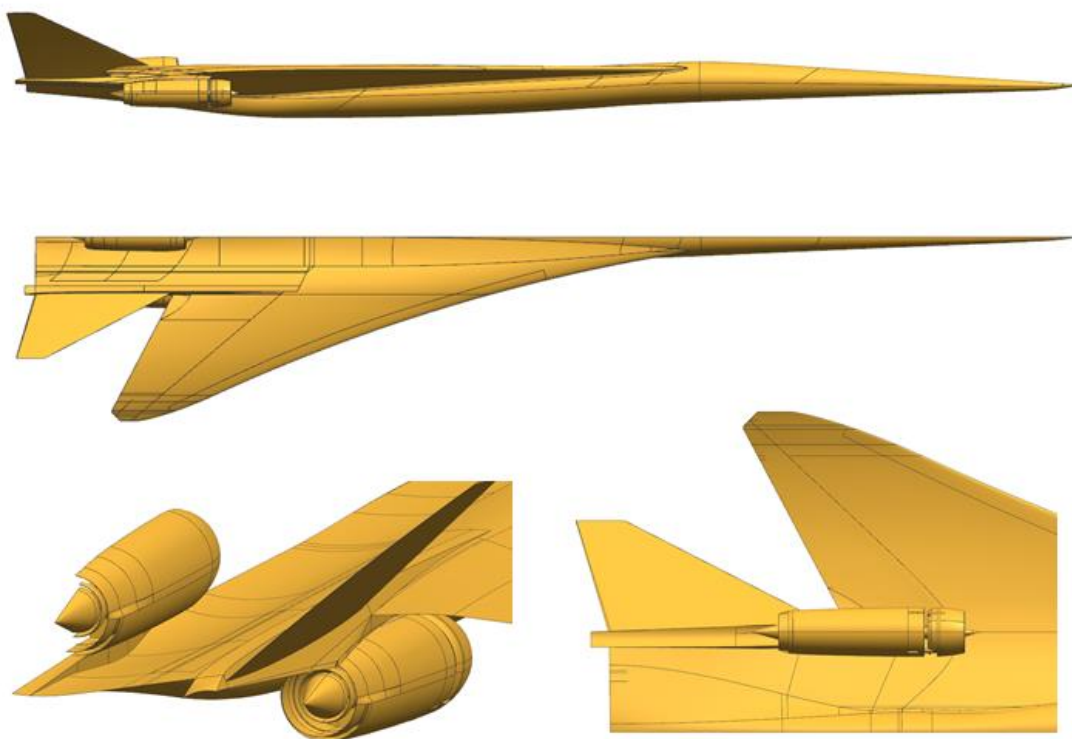


Figure 91 Lockheed Martin aircraft model

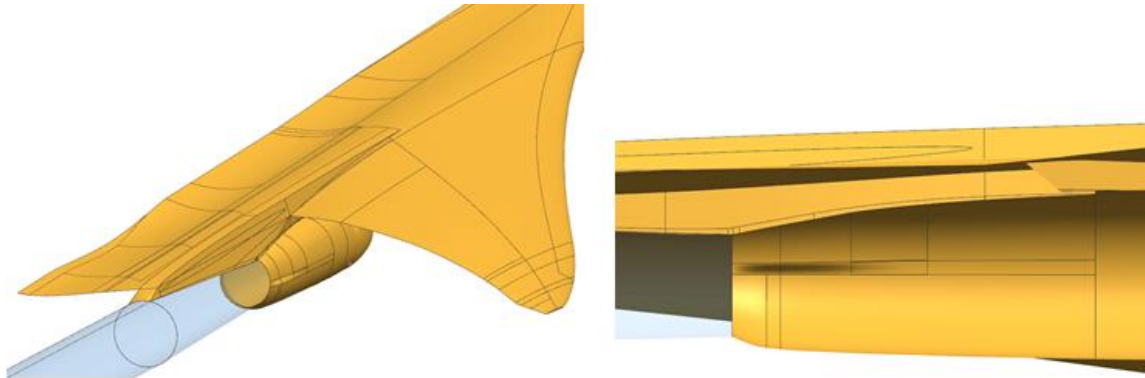


Figure 92 Simplified aircraft model.

6.2.2 CFD DOMAIN

The CFD domain passes through aircraft symmetry plane. Outer boundaries of the domain are set as shown in Figure 93.

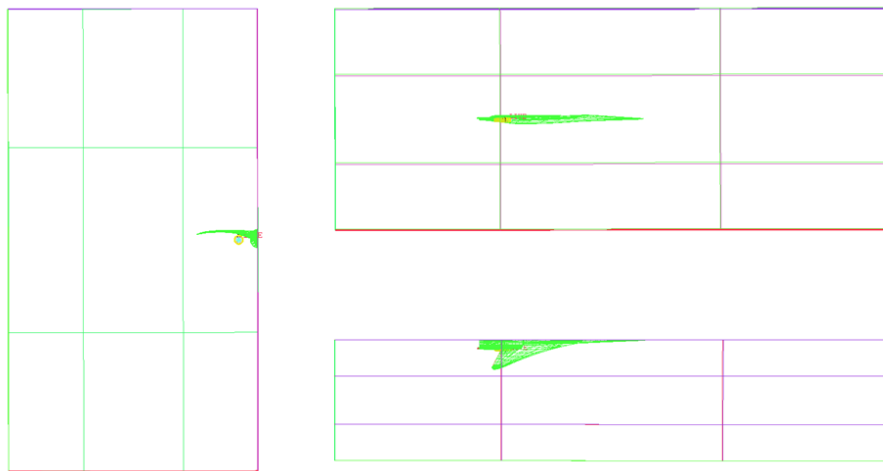


Figure 93 CFD Domain boundaries.

6.2.3 MESH OF THE AIRCRAFT

A manual meshing process was carried out to ensure proper grid resolution in areas of important geometric features. Attention was given to the engine nacelle, pylon, and wing. Farfield boundaries are placed far enough to eliminate potential boundary condition influences on the flow around the nacelle. Total grid points in the aircraft domain are 250 million.

Finite element mesh for the installed CFD consists of the fan rig portion of the domain and inlet-fuselage part of the domain. Mesh for the fan-rig part of the domain has been kept consistent with the Fan/Inlet CFD part of this program, and is described in the section 4.1 of this document. Compared to the mesh described in Section 4.1, the inlet region has been removed and replaced with inlet-fuselage mesh. The inlet fuselage mesh is a multi-block structured mesh suitable for flow the GE flow solver TACOMA. The mesh is generated using ANSYS ICEMCFD meshing software. Care has been taken to properly resolve the AIP interface surface to ensure a smooth transition to the fan-rig part of the domain which is important for unsteady CFD analysis. Relative resolution in all three grid directions does not exceed 1:2. Standard design meshing practices commonly applied to turbomachinery CFD have been applied with respect to strut leading and trailing edge resolution, nacelle lip and wing leading edge areas. To ensure proper flow feature resolution, most of the mesh is concentrated in the inlet / duct / underwing zones which are the focus of the CFD and acoustics analyses.

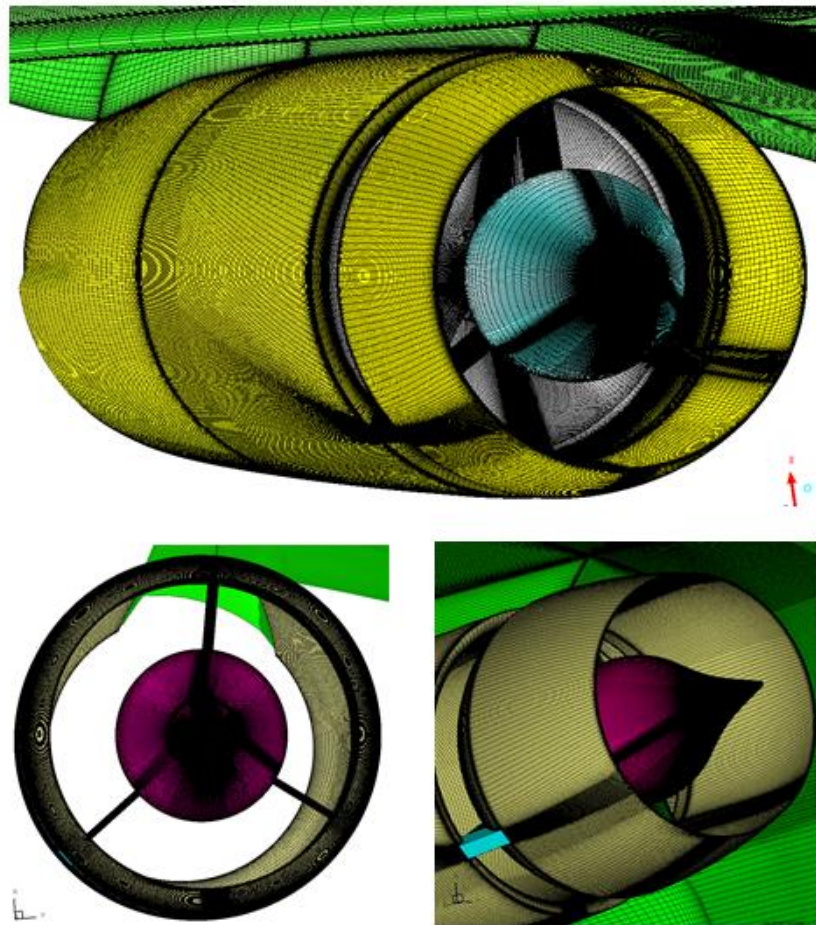


Figure 94 Inlet – fuselage mesh: Engine surface mesh details

Special care has been taken to ensure smooth transition between mesh regions, and to optimize grid quality. Mesh quality has been checked through a standard set of quality checks including determinant, minimum angle, and stretching ratios, and the mesh has been iteratively updated until the quality checks satisfied GE standard design guidelines. Mesh features physically resolved the boundary layers for all surfaces, and care has been taken to control wall cell size distribution off the walls as well as mesh stretching. Total mesh size for the fuselage – inlet domain is approximately 200 million nodes. Details of the inlet-fuselage mesh are shown in Figure 94 (nacelle), Figure 95 (nacelle lip and strut details), Figure 96 (fuselage details) and Figure 97 (details of the interior of the mesh).

- A Nacelle lip detail near strut hinge – side view
- B Nacelle lip and hinge from – outside view
- C Strut leading edge detail
- D Strut trailing edge detail

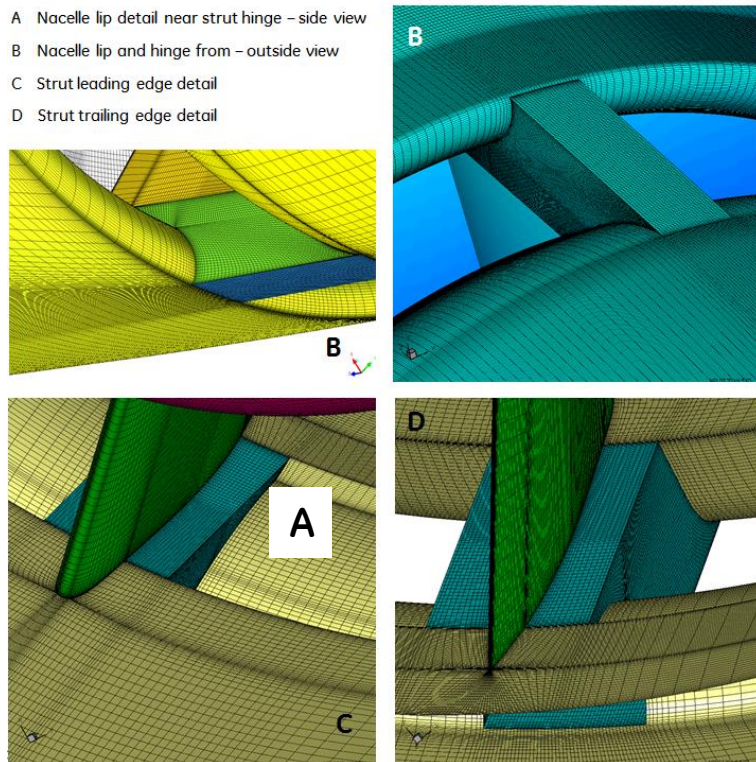


Figure 95 Inlet – fuselage mesh: Nacelle lip and strut details

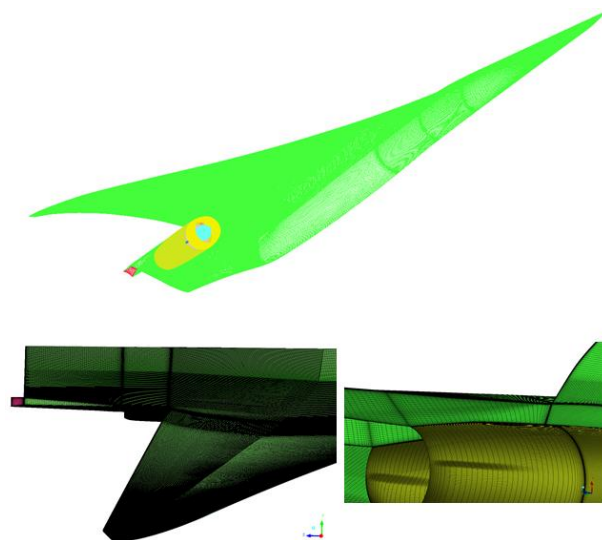


Figure 96 Inlet – fuselage mesh: Aircraft and engine details

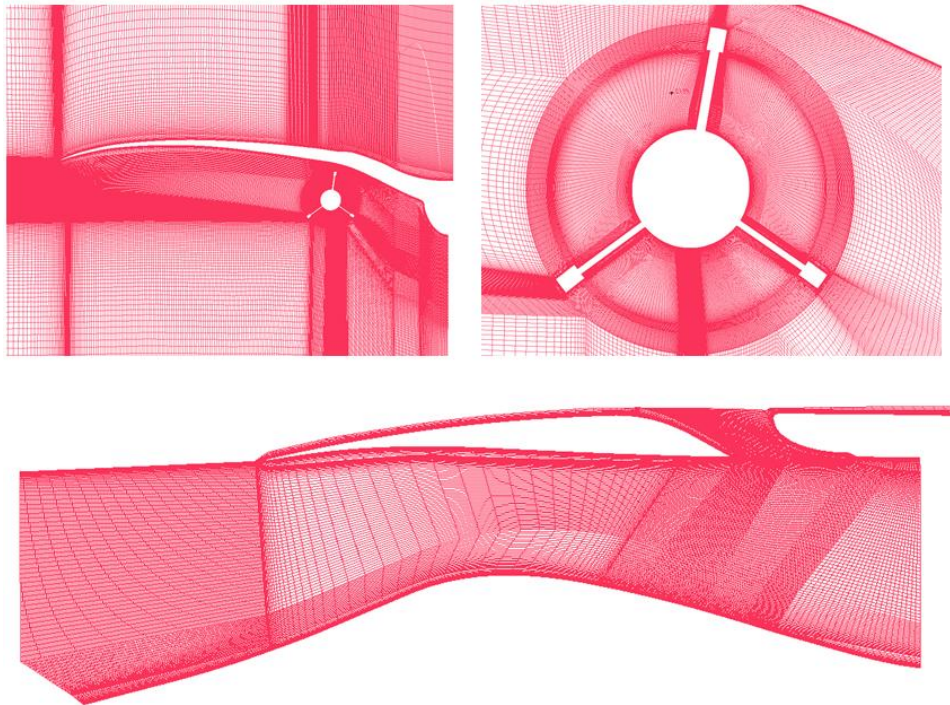


Figure 97 Inlet – fuselage mesh: Details of the interior mesh.

6.2.4 Y+ OF THE AIRCRAFT MESH

Wall boundary layers need to be resolved properly for any potential interaction of viscous effects. Figure 98 shows the statistics of the y^+ 's of all the non-slip walls of the aircraft/nacelle model. Average y^+ ranges from 1.7 to 5, with deviation from 0.7 to 1.4. All y^+ 's are certainly below 30, and a synthesized wall function mode is used in CFD solver to properly resolve the viscous layers.

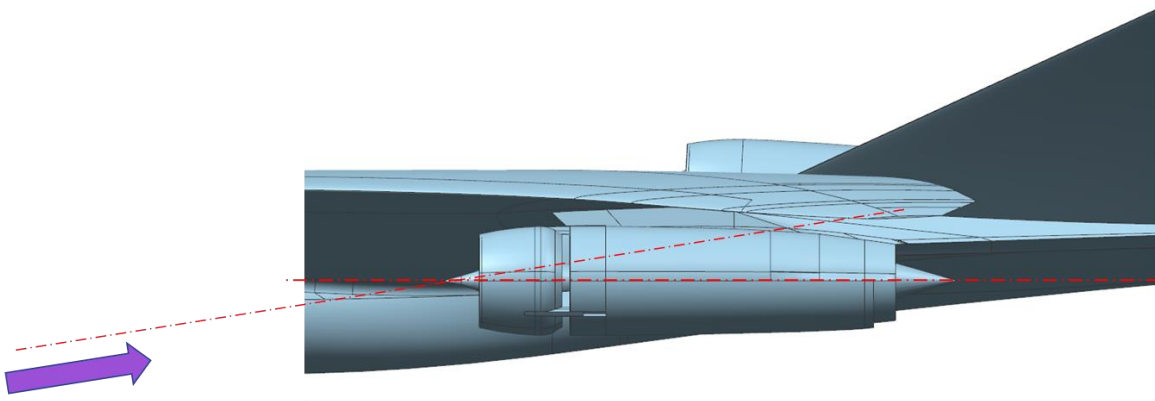
Y+ distribution -							
Surface Type	Tot. #	%<30.	% OK	%>150.	Avg. y+	Std. Dev.	
wall:HUB	163904	100.00	0.00	0.00	4. 949	0. 983	
wall:NAC_FWD	130240	100.00	0.00	0.00	4. 408	1. 795	
wall:NAC_AFT	138368	100.00	0.00	0.00	4. 395	1. 513	
wall:HINGE31	2688	100.00	0.00	0.00	3. 818	0. 992	
wall:HINGE33	3200	100.00	0.00	0.00	3. 783	0. 864	
wall:HINGE34	2816	100.00	0.00	0.00	3. 288	1. 488	
wall:HINGE24	2816	100.00	0.00	0.00	2. 972	1. 036	
wall:HINGE22	3200	100.00	0.00	0.00	3. 860	1. 007	
wall:HINGE21	2688	100.00	0.00	0.00	3. 725	0. 823	
wall:STRUT3	25600	100.00	0.00	0.00	4. 731	1. 137	
wall:STRUT2	25600	100.00	0.00	0.00	4. 664	1. 212	
wall:HINGE32	3200	100.00	0.00	0.00	4. 345	1. 196	
wall:HINGE23	3200	100.00	0.00	0.00	4. 523	1. 200	
wall:HINGE11	3328	100.00	0.00	0.00	3. 388	0. 957	
wall:HINGE12	3200	100.00	0.00	0.00	4. 323	1. 382	
wall:HINGE14	3520	100.00	0.00	0.00	3. 923	1. 402	
wall:STRUT1	26880	100.00	0.00	0.00	4. 590	1. 299	
wall:AIRCRAFT	478208	99.93	0.07	0.00	4. 779	3. 078	
wall:PYLON_FRONT	512	100.00	0.00	0.00	3. 049	0. 855	
wall:PYLON_BACK	512	100.00	0.00	0.00	1. 769	0. 971	
wall:HINGE13	3200	100.00	0.00	0.00	4. 158	1. 029	
wall:WCUT	6144	100.00	0.00	0.00	2. 676	0. 943	
wall:ACCUT	5888	100.00	0.00	0.00	1. 835	0. 680	
All Walls	*****	99.97	0.03	0.00	4. 635	2. 352	

Figure 98 y+ distribution of all surfaces in the aircraft domain: All within 30. Spalding wall function is used (combined sublayer and log-law).

6.2.5 BOUNDARY CONDITIONS OF THE INSTALLED CFD

A take-off condition is designated for the installed CFD simulations. Aircraft angle of attack is 8.1 degrees, flight Mach number is 0.38, as communicated from LM's design team. The condition is equivalent to airspeed of 246.8 KEAS (251.4 KATS). Similar to the numerical simulations that LM had been performing for the nacelle/inlet (in 2012, with flight Mach number of 0.3), a blowing wind tunnel condition is used for the far-field pressure boundary condition, in which the static pressure is set as one atmosphere.

The engine axis is parallel to the reference aircraft axis. The engine has zero degree of toe angle and zero-degree of tilt angle as the current installation model has indicated. These are the conditions that were considered in determining the far-field boundary condition for the aircraft CFD, as illustrated in Figure 99.



Air flow direction, 8.1 deg relative to horizontal (current aircraft axis)

Figure 99 Farfield flow condition for the aircraft model

6.3 STEADY-STATE SOLUTION OF FLOW AROUND THE AIRCRAFT

GE's turbomachinery flow solver, TACOMA, needs to be tested with the aircraft domain before commencing the coupled calculation with the engine. The aircraft domain, as described in earlier sections of the report, consists of the aircraft and the exterior surfaces of the engine nacelle and the forward portion of the interior surfaces. The interface between the aircraft domain and the engine domain is set downstream of the supporting struts inside the nacelle.

The shakedown was performed on a coarse mesh, which is 1/8 of the size of the full mesh by taking every other grid point out from the full mesh. This technique ensures the integrity and topology of the full mesh, and saves time for the trials.

The steady-state run with full mesh was then performed. The proper flow rate at the aircraft/engine interface was specified for the steady-state run. The purpose of the steady-state run is to (a) establish flow of the external domain, which needs to be done before taking on the fully coupled unsteady calculation and, in doing so, saves significant amount of run time compared to starting the fully coupled unsteady run from a uniform solution of the external domain; and (b) establish proper flow condition at the interface to the engine.

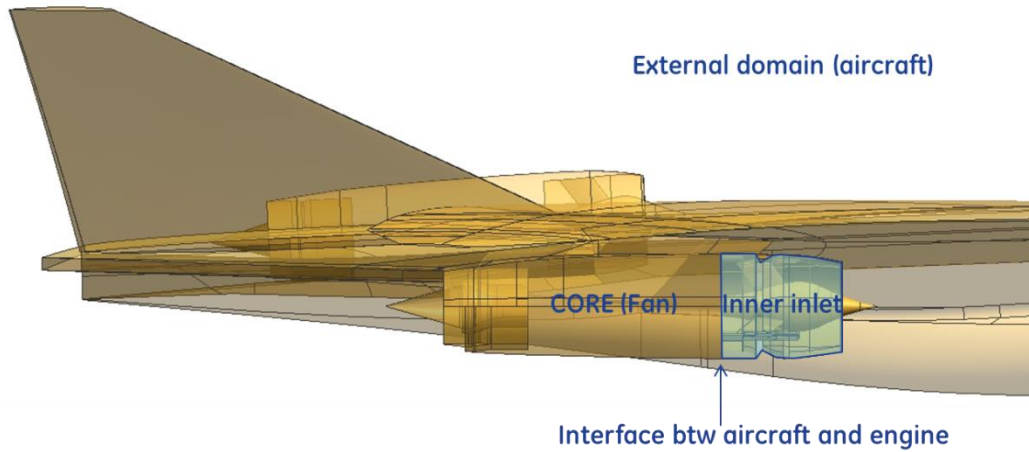


Figure 100 Illustration of interface between aircraft domain and engine domain

The most significant flow feature in this high AoA condition is the significant favorable shielding effect of the wing to the engine nacelle due to the location of engine installation. The engine is completely shielded from the large AoA effect. Under the wing, the flow goes into the engine nacelle in a parallel fashion alleviating severe FWD nacelle lip separation if otherwise exposed to the high AoA condition. Figure 101 shows the streamlines approaching the engine nacelle. The set-back installation of the engine benefits from the under-wing re-direction of the approaching flow with 8.1-deg AoA.

A closer look at the flow near the FWD cowl of the nacelle reveals a very small separation zone of a limited extent of the inlet circumference (near the keel location). The crown portion of the nacelle has no separation due to closer proximity to the underside of the wing, see Figure 102. Also shown in this figure are Mach number, static pressure, and flow vectors. There is a mild static pressure distortion in the circumferential direction at the nacelle lip. This pressure distortion is attenuated as the flow goes through the nacelle. The flow around the aux door is also different at crown than at keel of the nacelle due to the crown portion's close interaction with the wing.

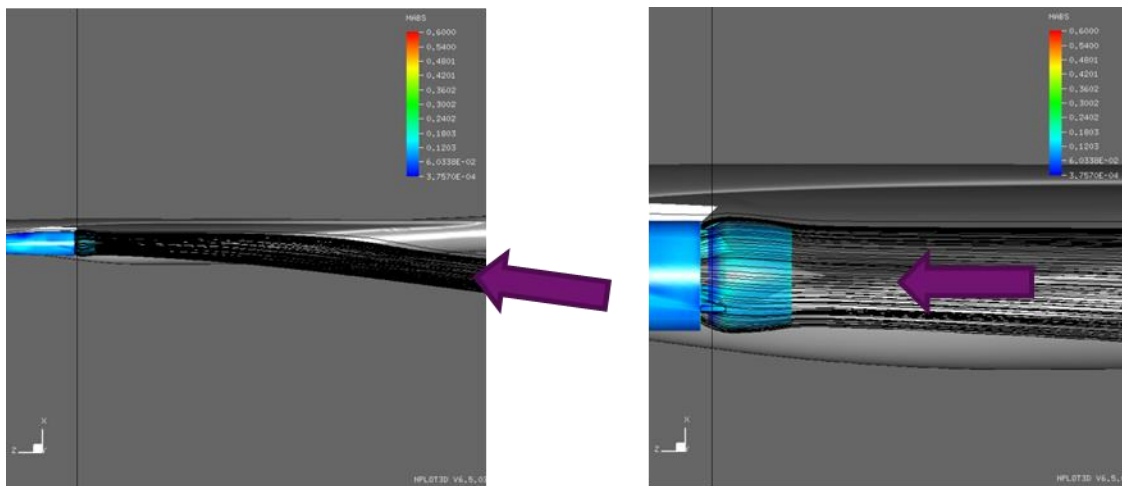


Figure 101 Wing has very favorable shielding effect on the engine nacelle. Static pressure and streamlines are shown.

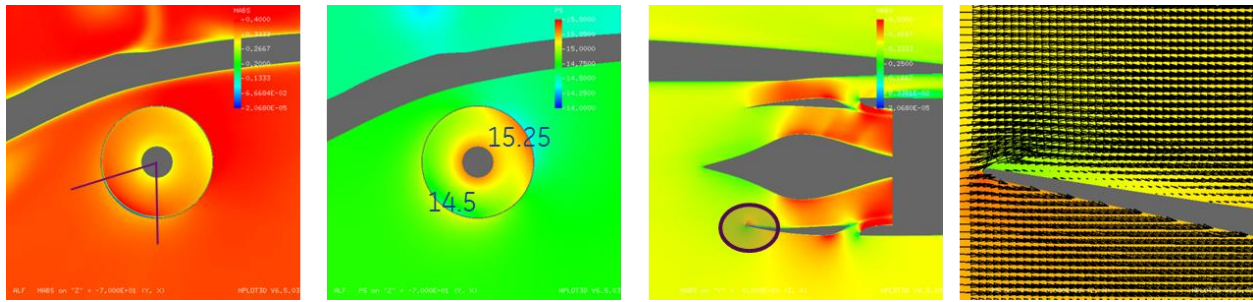


Figure 102 Close examination of flow around the nacelle lip. Plot from left to right are: Mach#, static pressure, Mach#, velocity vectors

As flow progresses inside the nacelle, the mild circumferential pressure distortion at the FWD cowl lip is attenuated. See plots in Figure 103. The flow is not completely uniform in the circumferential direction, but there is no concern of significant distortion in the circumferential direction. The wakes from the aux door convect downstream into the fan domain, so do the strut wakes as well. In all three plots of this figure, one can see the flow features above the wing. That is a predominant wing vortex, details of which are shown later.

Static pressure and absolute Mach number contours at a location that's in the FWD cowl of the nacelle, upstream of the aux door are shown in Figure 104. The mild static pressure distortion we've seen in Figure 102 at the lip of FWD nacelle cowl is attenuated. The pressure and Mach number field represents the flow around the three struts in the nacelle. There are visible differences of the flow around each of the strut, shown both on the pressure and Mach number contours. Higher Mach number is seen around the strut that's closest to the wing. This is mainly due to the higher pressure level near the underside of the wing.

We also observed a swirl distortion on the order of -5 to 5 degrees at the lip of the FWD nacelle, shown in Figure 105. This swirl is driven by the static pressure field described earlier. This swirl distortion is attenuated as the flow progresses further downstream toward the aux door location. Again, since the pressure distortion vanishes, so does the swirl distortion.

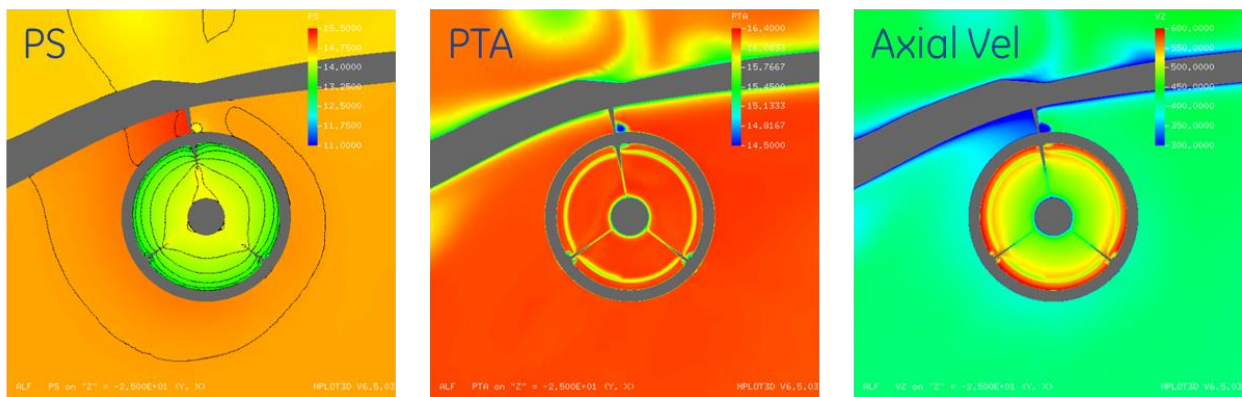


Figure 103 Cross-section of flow in the AFT cowl of the nacelle

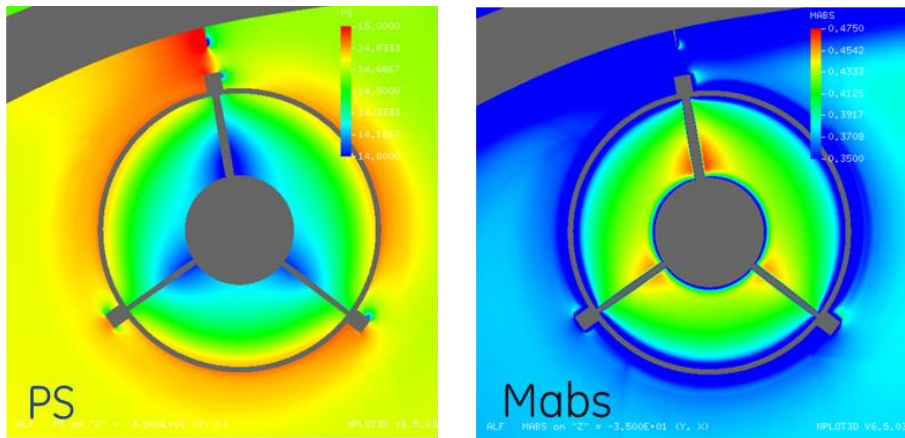


Figure 104 Flow details at upstream of the aux door

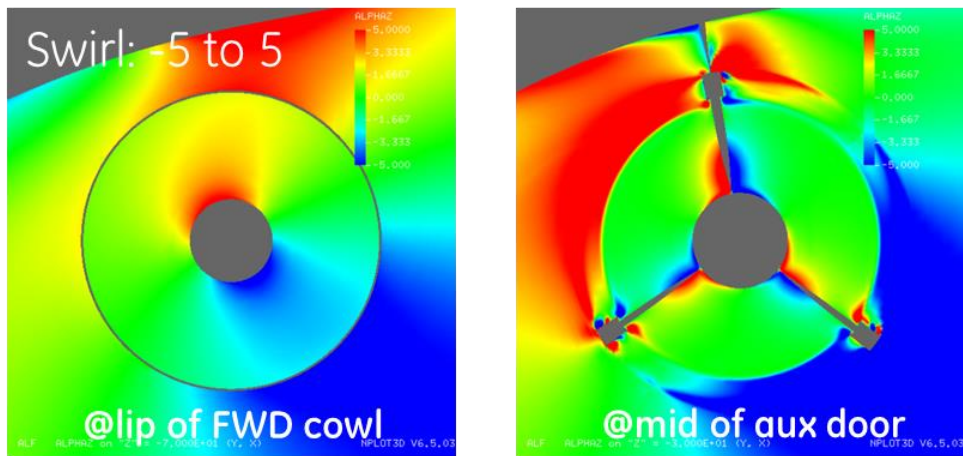


Figure 105 Swirl details at FWD cowl lip, and at middle of the aux door

The open aux door certainly is creating interesting flow features as the flow is entering the engine nacelle through these doors and merging with the main flow that comes from entrance of the nacelle. Under the wing, at the location where the engine is installed, due to the presence of the fuselage, there is a significant cross flow under the wing, as illustrated in Figure 106 on the left. This cross flow moves around the engine nacelle, and enters the nacelle through the open aux doors. As the cross flow enters, it creates a one-per-rev swirl distortion. Remember that the swirl distortion in the FWD cowl has attenuated before flow reaching the aux door. The swirl distortion ranges from -8 to 8 degrees at the location close to the trailing edge of the struts in the inlet. Figure 106 has both contour plots of tangential velocity and swirl from the perspective of the engine. The radial penetration of this swirl distortion, however, is limited the shear-layer that is created by the aux door. This is a favorable effect since the main flow path of the engine is shielded from the distorted flow.

Flow around the “hinge” to which the struts are attached on is also examined. A pair of vortices is observed at each hinge location. These vortices roll up due to the local geometry and two streams of flow merging, one stream is from the FWD cowl of nacelle, and the other is the flow that comes in from the open aux door. Figure 107 shows the PTA (absolute total pressure) signature of the shear layer, the vortices, and strut wakes that are going to enter the turbomachinery.

Finally, an external flow feature that cannot be missed is the large delta-wing vortex that's on the upper surface of the wing on the wing leading edge. This vortex is far from where the engine is installed, and does not have visible interactions to cause flow distortion to the engine. Figure 108 gives the view from both the upper surface and lower surface of the wing, illustrating the wing vortex location and trajectory, and the relative separation of the vortex and flow entering the engine.

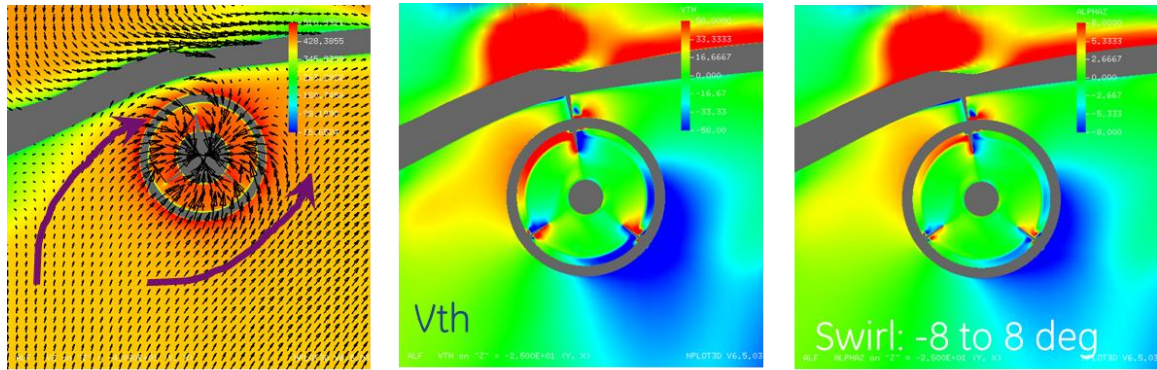


Figure 106 Explanation of elevated swirl distortion level in the AFT cowl

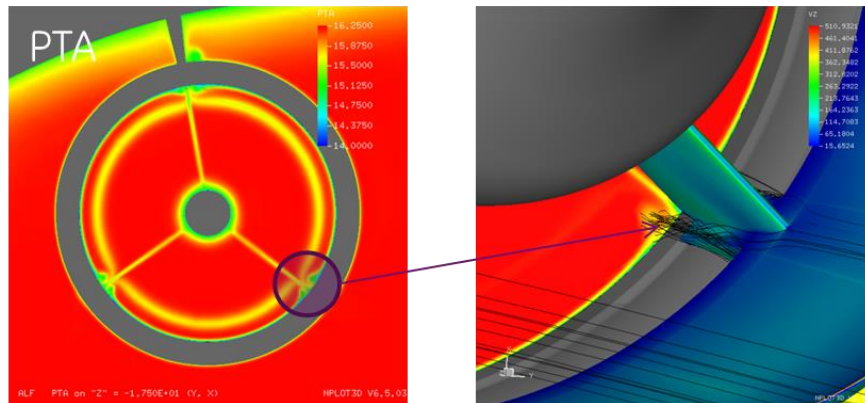


Figure 107 Roll-up of a pair of vortices associated with the strut and aux door

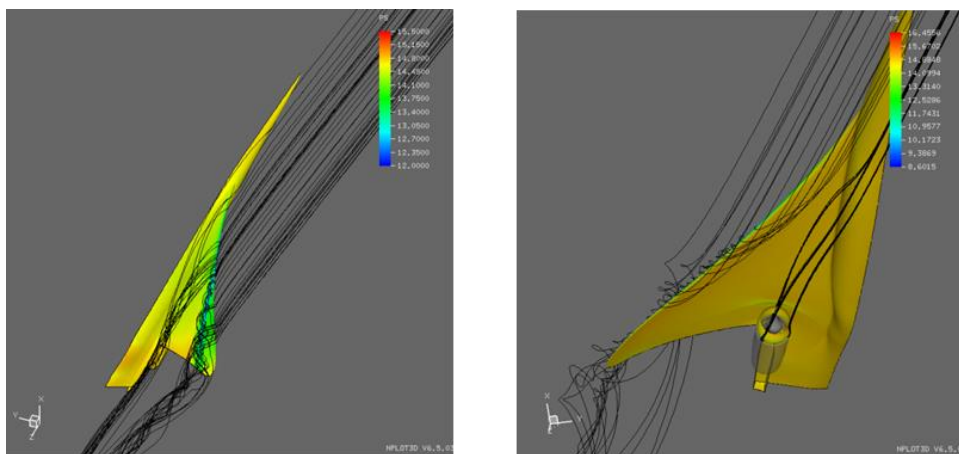


Figure 108 Streamlines illustrating the above-wing vortex

A summary of flow features is as follows:

- The wing has significant favorable shielding effect to nacelle;
- Nacelle only has a minor lip (FWD cowl) separation in a limited sector angle
- Pressure and swirl distortion in FWD cowl of nacelle attenuate before flow entering AFT cowl
- A swirl distortion is seen at fan face, -8 to 8 degrees, due to cross flow under the wing that enters the nacelle via the open aux door
- Fan will see reduced swirl distortion due to IGV and rotation effect;
- Pressure distortion does not seem to be significant
- Wing vortex does not interact with flow entering engine

6.4 SOLUTION OF COUPLED AIRCRAFT/FAN SIMULATIONS

A proper physical time step is chosen to resolve the unsteadiness of blade-row interaction of the turbomachinery. Two hundred (200) time steps per blade passing are used for this purpose. The choice of time step is appropriate for resolving major BPF tone for acoustic purposes. This time step is sufficiently small to be effective for any unsteady flow features in the aircraft domain if there is any.

6.4.1 CONVERGENCE CHECK

A total of 17 fan revolutions have been performed to obtain good convergence. TACOMA uses dual-time stepping for unsteady flow calculations. The inner iteration is converged to a 3-order magnitude drop of the error. Overall convergence is checked using measures of massflow rate of each blade row, the torque of rotors, and the loss in the blade region as well.

As an additional assurance of convergence, many probes are placed in the domain, both internally and externally. Examination of the probe readings indicated that the flow is properly converged. Probes are placed around the nacelle, the aux doors, above and under the wing (tracking for wing vortex unsteadiness), and inside the nacelle at fan face.

6.4.2 CHECK FOR UNSTEADY FLOW FEATURES IN AIRCRAFT DOMAIN

Probes places in the external (aircraft) domain do not have readings that suggest flow unsteadiness. The far-field boundary condition is steady at 8.1-deg angle-of-attack. The grid resolution and time step are effective to capture any unsteady feature, but there is none observed. The unsteadiness mainly comes from the fan/inlet interaction. This interaction has become insignificant at the entrance of the nacelle, where the pressure oscillation is only 0.04 psi, peak-to-peak.

6.4.3 UNSTEADY FLOW AT FAN FACE

The unsteadiness at fan face (location of upstream of IGV's) is more significant. The main fan rotors receive relatively clean flow, with only three strut wakes. And thanks to the wing shielding effect, the fan is not adversely affected by the 8.1-deg aircraft angle-of-attack at take-off. Compared to the steady-state flow in Figure 103, the aux door shear layer now shows the influence of the IGV, which is downstream of the cut-plane, as shown.

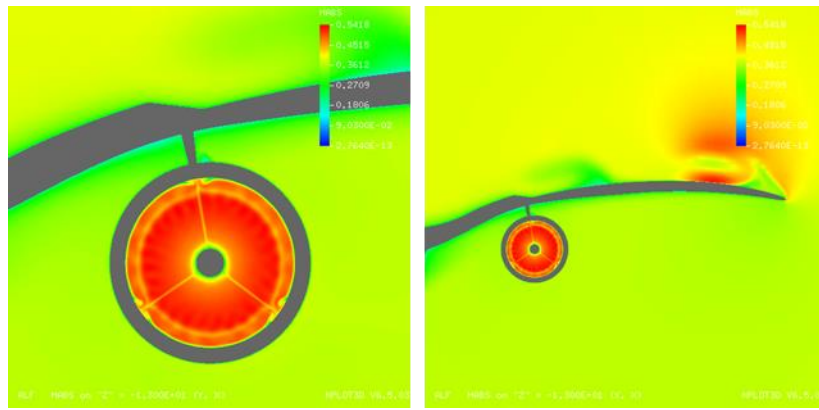


Figure 109 Mach number contours at fan face: range 0-0.54 (blue to red)

The flow properties at the inlet/fan interface plane, which is upstream of the fan IGV, are depicted in Figure 110, including total pressure (absolute), static pressure, swirl, and entropy. The aux door shear layer, the hinge vortices, and the inlet strut wakes are clearly visible. The higher swirl distortion is limited by the shear layer, stay near the casing. The static pressure distribution is a result of fan rotor1 shock waves interacting with the IGV vanes. This interaction is seen in Figure 111, where the fan rotor-1 shock wave is reflected multiple times inside the IGV passage, and propagates upstream of the IGV. Higher levels of pressure variations are seen in the out-board portion of the IGV, this is due to the increased shock strength of the fan tip, intensifying the interaction.

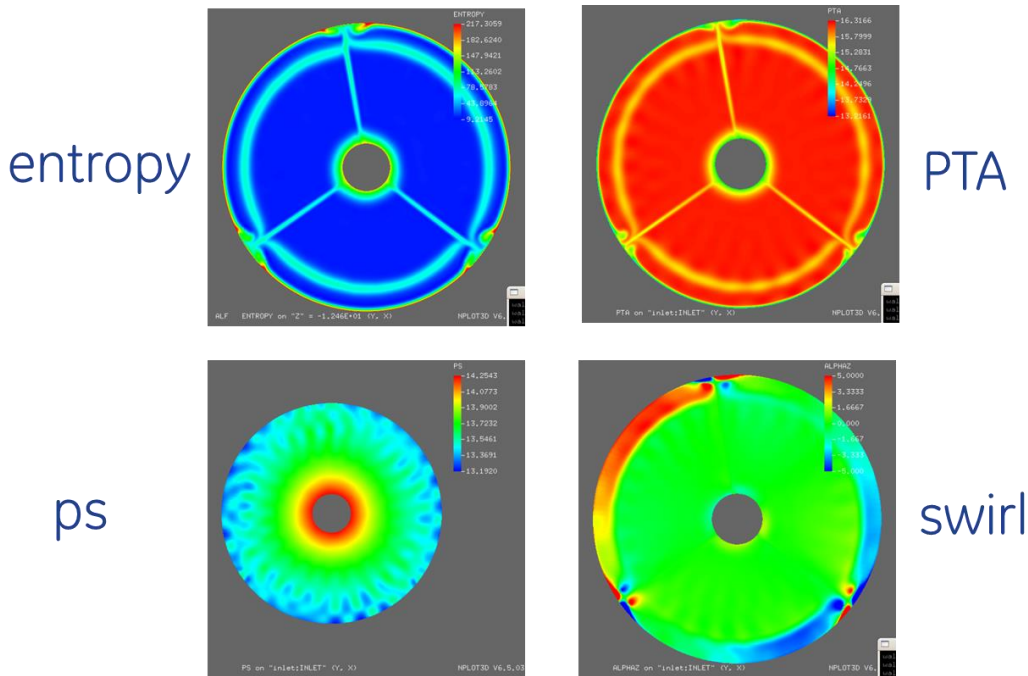


Figure 110 Flow properties at the AIP plane, an interface between the inlet and the fan domain, upstream of the fan IGV's

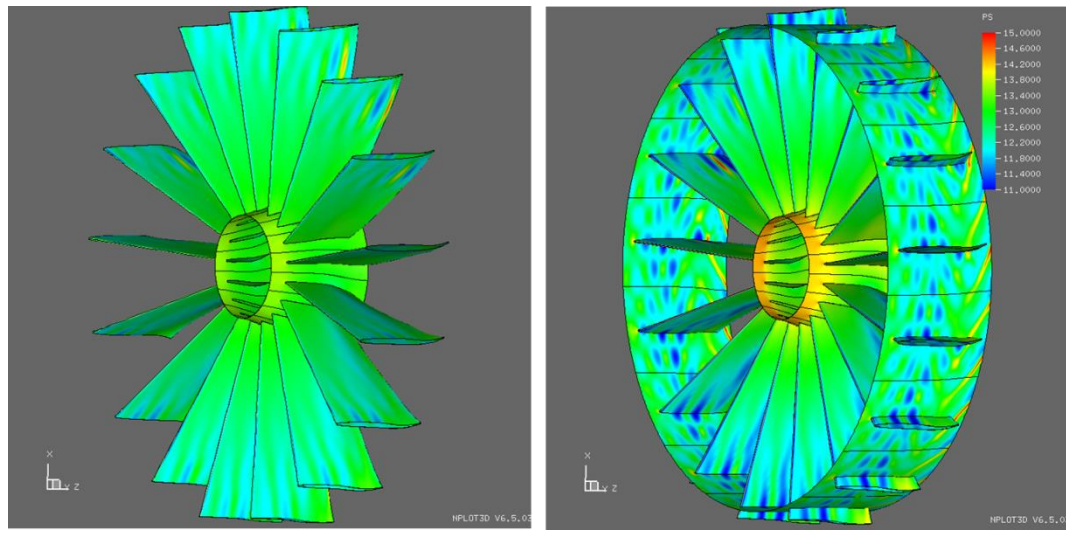


Figure 111 Static pressure on IGV surfaces, showing the fan rotor-1 shock reflecting and propagating upstream

Figure 112 shows more details of the flow in the main flow path, this is taken at a location downstream of the interface place (AIP), as shown in Figure 110. The location is at the inlet to the IGV of the main stream. Total pressure, static pressure, axial velocity and swirl angles are shown. The improved 2013 inlet design has made this possible. When the splitter is bathed in the aux door shear layer, the fan would only see a thickened casing boundary layer. This benefits the fan performance and the noise generation.

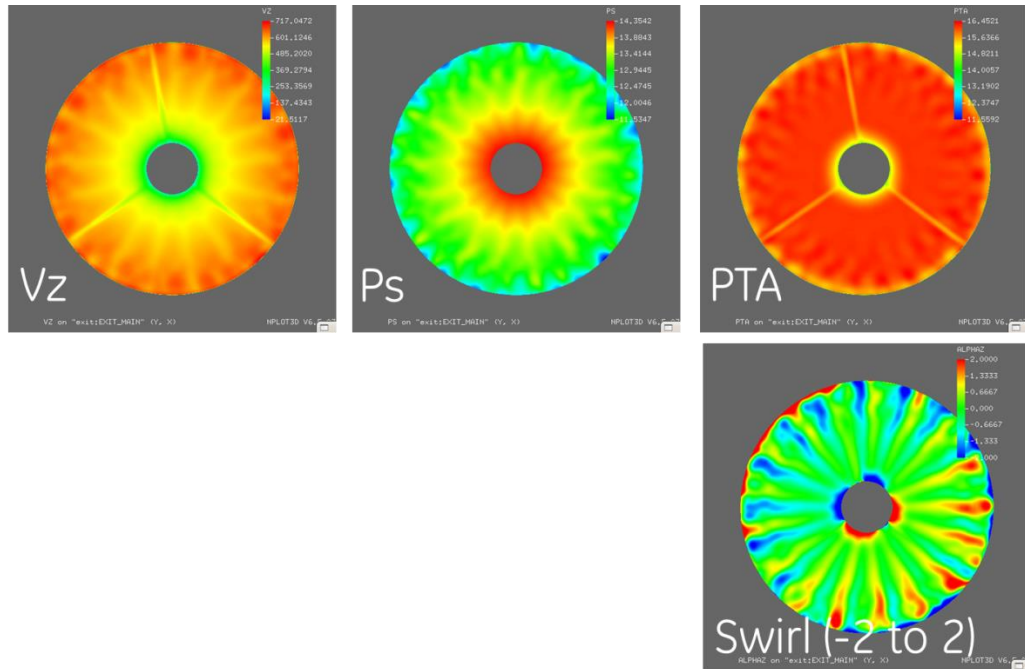


Figure 112 Flow properties of main stream, at inlet to combined IGV.

The circumferential swirl distortion is attenuated by the IGV's in the fan stream. This is one of the major benefits of IGV's. The swirl distortion coming to the main stream is not a large one, only ranging from -2 to 2 degrees. See Figure 113 for a snapshot of the swirl profiles at a near casing radius. The distortion is clearly visible. Downstream of the IGV the per-rev type circumferential distortion is eliminated.

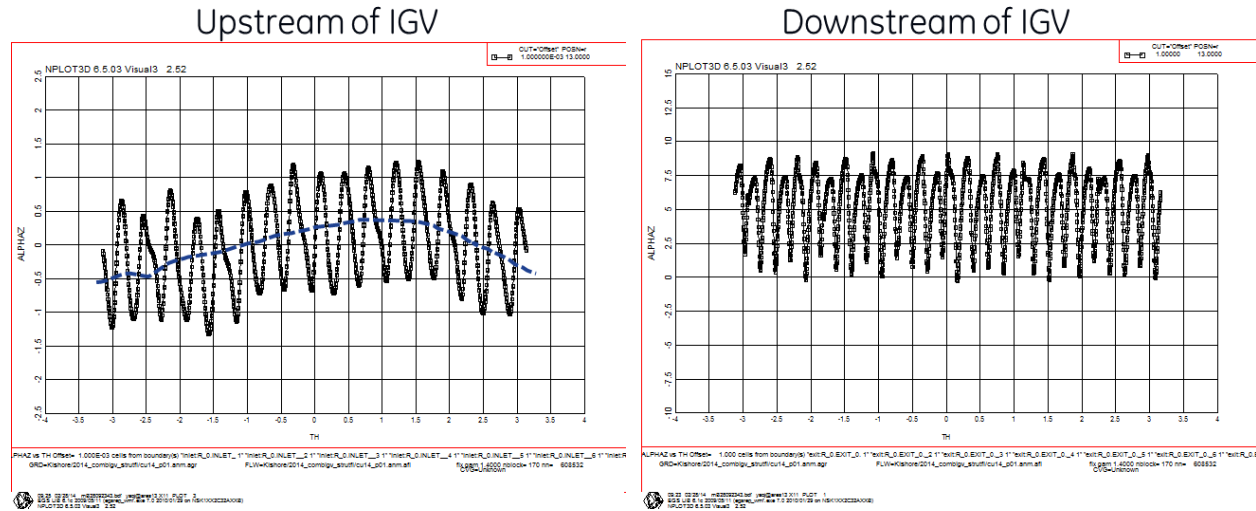


Figure 113 Swirl profile (unsteady snapshot) at inlet and exit of the main stream IGV near casing

6.5 COMPARISON OF INSTALLED CFD RESULTS WITH DECOUPLED CFD RESULTS OF PHASE II

The design improvement of the nacelle/inlet since 2012 is worth noting. Overall, the 2013 design reduces the interactions, improves fan performance, and reduces noise level as well.

The aux door location change has resulted in a more out-board location of the loss core associated with the shear layer. The more out-board location aligns with the splitter of the fan domain very well, so that the splitter is bathed in the shear layer. See Figure 114 for total pressure profile (radial) comparison. This alignment mitigates the risk of a stronger shear layer (stronger due to the shear layer being less mixed out than the 2012 design) being ingested by the fan. The 2012 design has a more FWD aux door location, which results in a mis-alignment of shear layer with splitter, but it has a better mixed state when flow enters the fan. It also has a thicker casing boundary layer. The centerbody profile is also improved, and this improvement has reduced total pressure loss in the hub boundary layer.

At the main stream rotor-1 inlet, the radial profiles of the absolute total pressures are compared in Figure 115, also compared are the Mach number profiles. In the 2012 design, the loss core is ingested by the fan rotor-1, which would generate additional loss. Also, due to the tip section of the fan rotor receiving a more energized flow (higher PTA of 7% immersion), the fan tip would have a strong shock compared to the 2014 results. The main stream fan rotor does not have tip clearance, and this also contributes to higher fan loading. The outcome of this flow difference could explain why the 2014 design, though coupled with the aircraft, actually has a lower fan tone noise level at AIP. Added to this phenomenon, the main stream IGV wakes with the new design are shallower than the wakes from the 2012 design, and this further reduces the IGV wake and fan rotor interaction, hence reducing noise, see Figure 116.

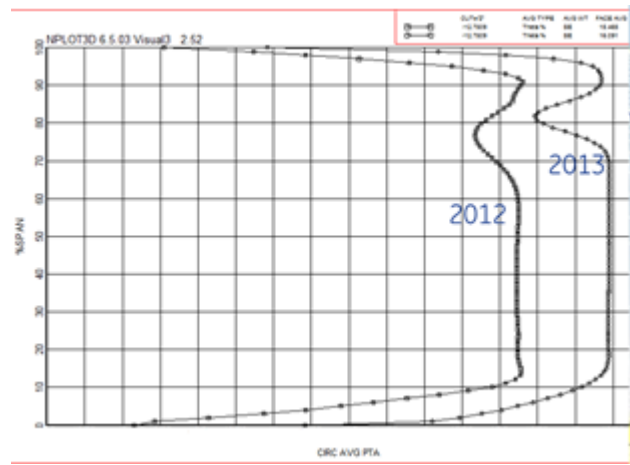


Figure 114 Radial location of the aux door shear layer

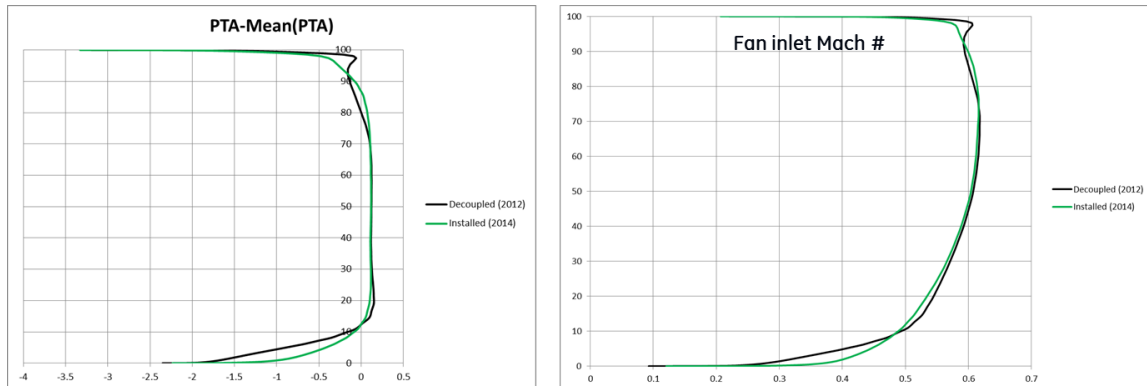


Figure 115 Radial profiles of total pressure and Mach number at main stream rotor-1 inlet

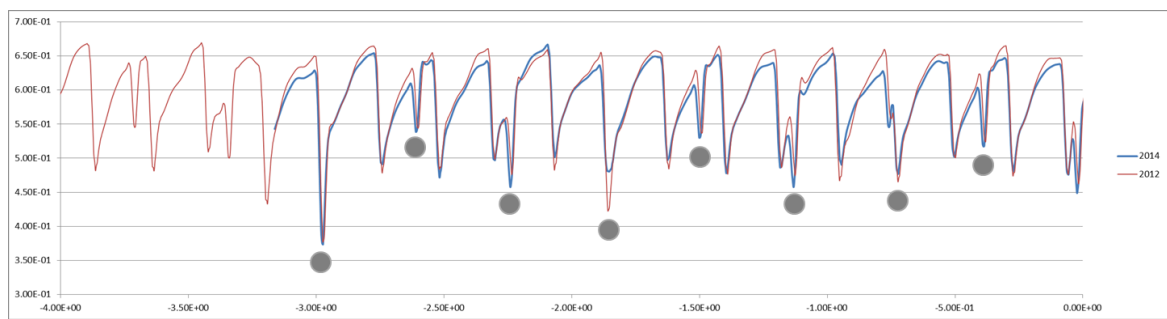


Figure 116 Main stream IGV wake comparison: Mach number profile in circumferential direction near main stream rotor tip ($R=18.6\text{in}$). Blue is new design (2013), Red is old design (2012)

6.6 SUMMARY OF INSTALLED CFD RESULTS

- a) Both macro and microscopic flow features are thoroughly examined in the interest of various level of interactions;
- b) Based on the conditions we chose, there was no unsteady flow observed in the external, aircraft domain;
- c) Aircraft wing provides a significant shielding effect to the engine at high angle-of-attack conditions; the engine only receives mild level of per-rev-type distortion;
- d) The circumferential distortions are effectively attenuated by the IGV's in the fan domain;
- e) Inlet design change has led to better coupling of the aircraft and the engine, reducing the interactions of the inlet and the fan components.

7 ACOUSTICS ANALYSES AND FAN NOISE ESTIMATES

7.1 ACOUSTICS ANALYSES

7.1.1 INTRODUCTION

Computed results from the unsteady fan CFD analysis (Section 4) were used to assess the acoustic impact on the fan noise that can radiate out the inlet and the cowl doors (when open). This assessment provides an initial look at the influence of fan inflow distortion on fan noise. In the sections below, we will briefly overview the analytical methodology used in performing this assessment, and describe the results obtained. First, the effect of the inlet strut wakes on the fan noise is assessed (Section 7.1.3) followed by the impact of installation (Section 7.1.4). The objective of this study is to qualitatively determine whether strut-fan interaction or fan inflow distortion noise potentially dominates over the other components of fan noise (IGV-Fan and rotor-rotor interaction) so as to prioritize subsequent efforts in designing a low-noise fan for this supersonic aircraft configuration.

Note that this assessment does not include broadband noise sources which may be evaluated at a future date. Propagation of fan tones upstream through the inlet and cowl doors is described in Section 7.2. Finally we will provide recommendations for engine noise reduction technologies of greatest potential interest for this program as well as follow-on studies that could be undertaken to reduce the analytical uncertainties in the current assessment prior to testing a technology demonstrator.

7.1.2 METHODOLOGY

The analytical approach follows that employed during Phase I of this program. The full unsteady RANS CFD solution is taken at the Inlet-Fan interface station and harmonics are extracted by temporal Fourier Transforms evaluated at fan blade passing frequencies (R_1 , R_2) as well as R_1 - R_2 interaction tone frequencies. The spatial distribution of acoustic energy is then decomposed into circumferential Fourier modes and projected onto an array of propagating duct modes, as described by the equation below

$$p'(x, t) = \sum_{n_1, n_2, \mu} p_{m\mu} \psi_{m\mu}(r, \omega) e^{i(kz + m\theta - \omega t)}$$

$$\omega = n_1 B_1 \Omega_1 + n_2 B_2 \Omega_2$$

$$m = n_1 B_1 - n_2 B_2$$

This allows us to effectively filter out the hydrodynamic and evanescent energy and integrate only the propagating acoustic power in the duct to provide a relevant assessment of the observable fan noise. This assessment assumes the inlet duct is effectively unchanging in annular geometry and extends far upstream

such that mode cutoff ratios remain unchanged. It also assumes that the flow in the duct is uniform, which is a reasonable approximation at the interface plane. In reality, some evanescent energy will cut-on and the inlet struts will further scatter and reflect a portion of the acoustic energy before the fan noise can radiate to the far-field. However, we expect the first-order effects in comparing different fan configurations is suitably represented by comparing trends of in-duct acoustic power levels in this fashion prior to performing a full analytical propagation to the far-field.

7.1.3 RESULTS – UNINSTALLED FAN NOISE

In Figure 117, an instantaneous view of the pressure at the Inlet—Fan interface station is shown for both the clean and distorted inlet configurations. The influence of the 3 non-equally spaced inlet struts is clearly visible, and the peak pressure fluctuation (spatially) at lines of constant radius is noticeably higher for the distorted case.

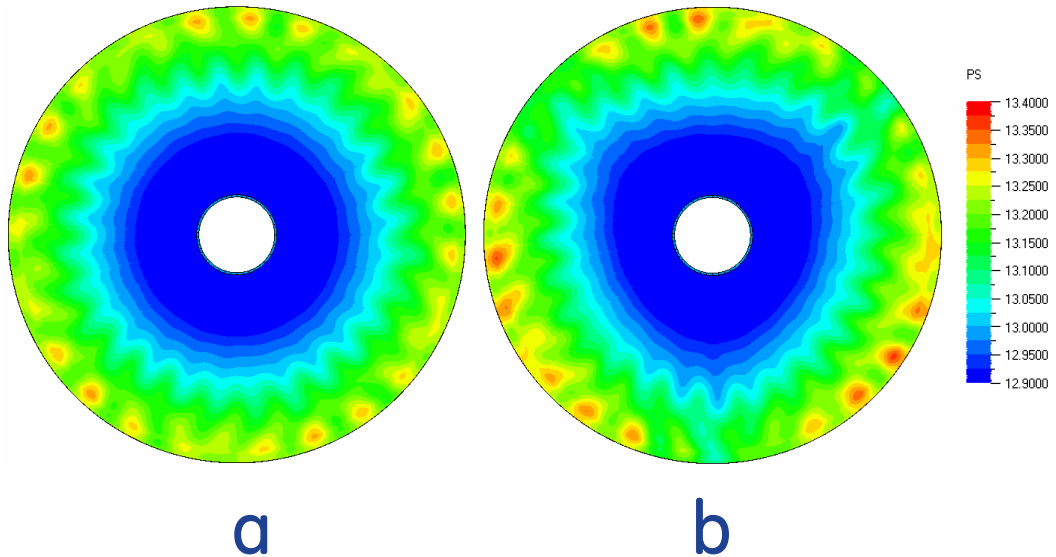


Figure 117: Instantaneous pressure at interface station. (a) Clean inlet; (b) Distorted inlet with struts and open cowl.

Performing the acoustic mode decomposition analyses outlined in Section 7.1.2, the in-duct tone PWL for upstream propagating acoustic waves are calculated for each fan tone frequency of interest. Figure 118 shows the total upstream propagating, cut-on in-duct PWL for all interaction tones corresponding to each blade harmonic index. In Figure 118, the nomenclature is $iFjA$ for the i^{th} R_1 and j^{th} R_2 harmonic, respectively, and this is adopted through the entire section. Also, for all the acoustics results to be presented below, the term “Clean” actually corresponds to the “very-clean” inflow condition described in Section 4.2, the “Circ” configuration has a radial profile distortion due to the circumferentially uniform shear layer created by the opening of the auxiliary door (the “clean” CFD condition described in Section 4.2). The “Distorted” configuration refers to the circumferentially non-uniform conditions prescribed by the strut wakes.

Three observations can be drawn from Figure 118 as follows:

1. First, the upstream radiated tone noise increase due to the shear layer generated by opening the auxiliary door is minimal (at least in a tone OAPWL sense). The effect of the aux door opening is however, significant for acoustic radiation to the far-field as will be shown later. However, at this stage, we are merely referring to the interaction noise caused by the shear layer impinging on the fan. This noise increase is expected to be minimal since the opening of the door creates a circumferentially uniform shear layer (at least in the CFD model) that does not contribute to noise increase. Any noise increase can only be attributed to radial loading profile changes on the fan/IGV brought about by the total pressure distortion of the ingested shear layer.
2. Second, the inclusion of strut wakes increases noise as expected, but only by a small amount (1.1 dB). Thus the dominant sources of fan noise lie in the fan itself (e.g. fan loading, IGV-R1 interaction etc.) rather than installation or distortions upstream.
3. Thirdly, the R_1 blade passing tone and its interactions with R_2 dominate the tone noise spectrum. While the CFD temporal resolution is fine enough to resolve up to 5 times the blade passing frequency of R_1 , spatial resolution is sufficient to only reasonably resolve the 1F0A tone (20 points per wave axially). Higher harmonics are under-resolved. Thus the large excursion of the 1F0A tone in Figure 118 can partly be attributed to numerical dissipation of higher frequency tones.

Because of the dominance of the 1F0A tone, the OAPWL for all fan tones is negligibly impacted by the inclusion of higher frequencies in this CFD/acoustic assessment.

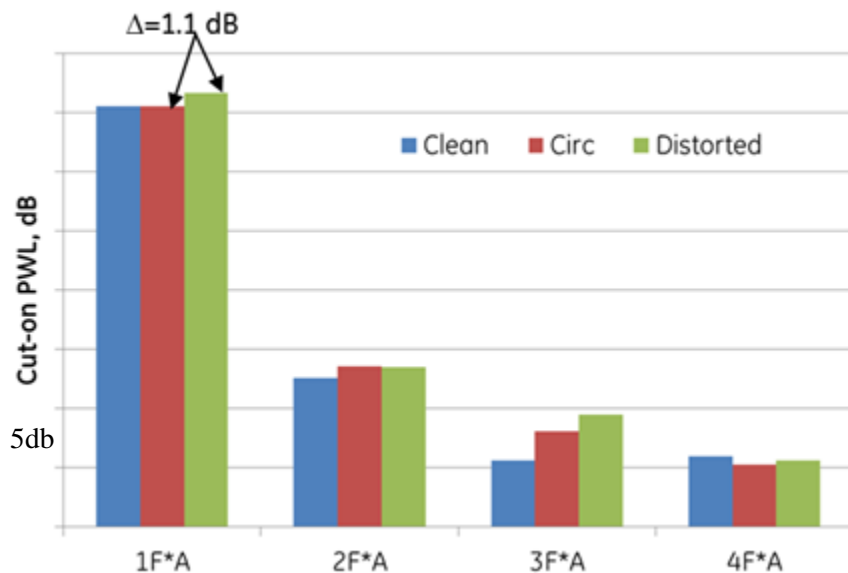


Figure 118: R_1 - R_2 interaction tone in-duct PWL summed over R_2 harmonic index.

The effect of the strut wakes on fan noise can be cross-checked simply by comparing the strengths of the strut and IGV wakes as shown in Figure 119 where the strut wakes just upstream of the IGV are compared to the IGV wakes just upstream of R_1 . The IGV wakes are clearly deeper but the strut wakes are wider. An estimate of the total unsteady vortical energy hitting the fan can be derived as shown below:

$$\Delta(\text{wake energy}) \approx 20\log_{10}[(0.1 \cdot 0.05)/(0.036 \cdot 0.25)] = -5.1 \text{ dB}$$

$$\Delta(\text{blade count}) = 20\log_{10}(17/3) = +15.1 \text{ dB}$$

$$\Delta(\text{source power}) = \Delta(\text{wake energy}) + \Delta(\text{blade count}) = 10 \text{ dB in favor of IGV}$$

Thus, the IGV wakes dominate the vorticity ingested by the fan and any noise increase due to addition of IGV wakes is small as shown in Figure 118.

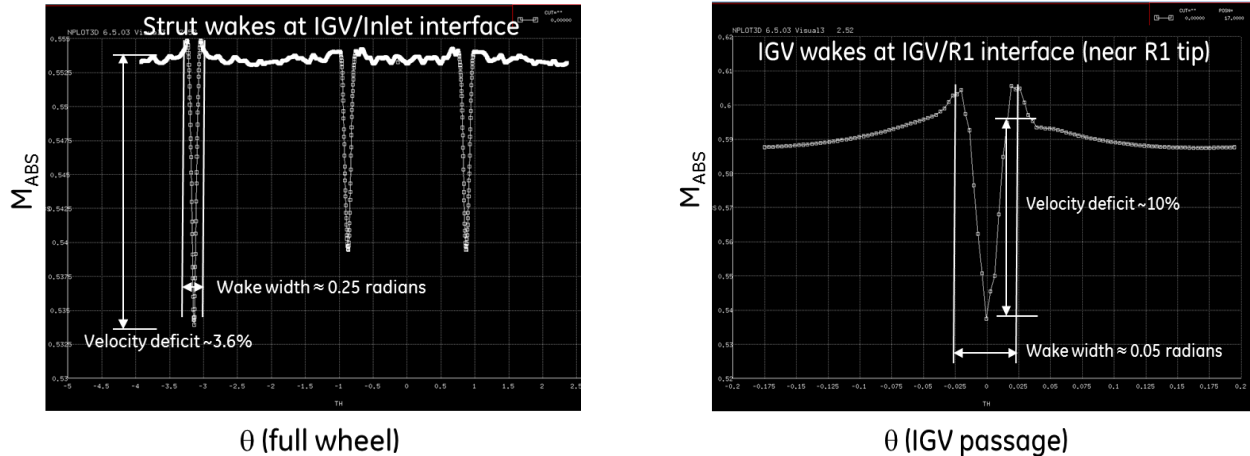


Figure 119: Comparison of strut and IGV wakes near R1.

A breakdown of the interaction tone power levels at the first two R_1 frequencies is shown in Figure 120. The 1F0A tone dominates over all others including other 1F interaction tones. As mentioned previously, part of the reason for this dominance is insufficient numerical resolution of higher frequencies.



Figure 120: R_1 - R_2 interaction tone in-duct PWL.

However, a closer examination of unsteady pressures at the IGV-R₁ interface and just upstream of the IGV shows that the 1F0A tone is significantly louder than the interaction tones even near the turbomachinery, Figure 121. The unsteady pressures in this case are not acoustic, however they are an indication of acoustic levels of the various tones. It is possible that the transonic portion of R₁ acts as a significant source of transmission loss to acoustics propagating forward from R₂.

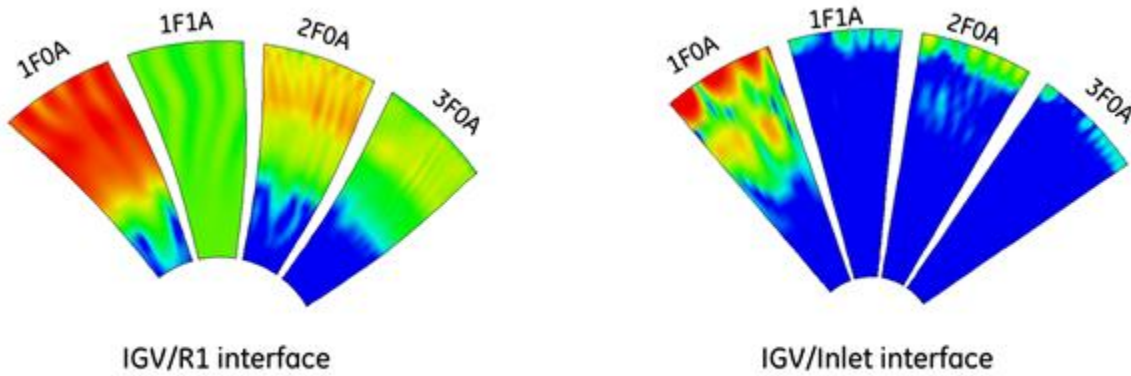


Figure 121: SPL for fan tones near R₁.

Finally, the modal contributions to the 1F0A tone are shown in Figure 122. The dominant tones are m=28 and m=-23 corresponding to the R₁ blade passing tone scattered by the IGVs. For the case without circumferential distortion, all the azimuthal modes shown (in red) correspond to the Tyler-Sofrin theory for scattering of the blade passing tone by the IGVs. For the case with distortion, because of the non-uniform spacing of the struts, additional modes are observed in the decomposition. The increase in noise at the distorted condition is seen across all modes implying a change in the source rather than propagation. However, the increase is small and is consistent with Figure 118.

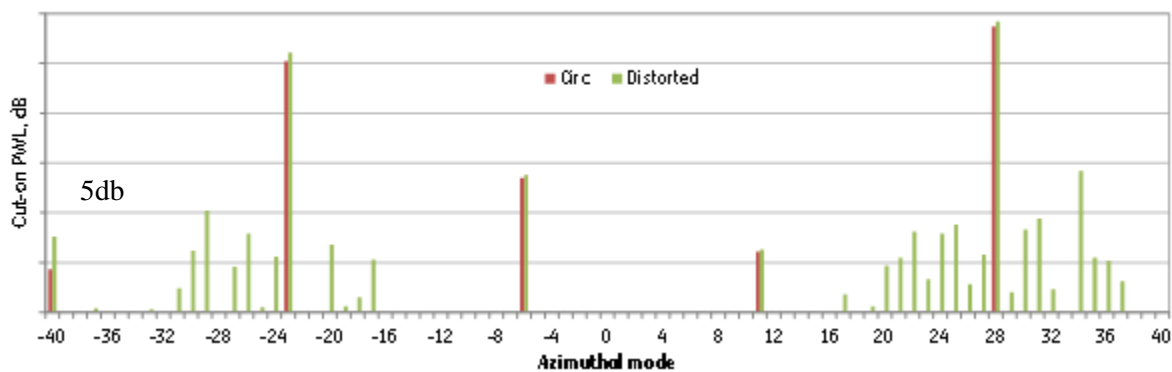


Figure 122: Azimuthal mode content for 1F0A tone.

From Figure 122, only the m=28 and m=-23 modes at the 1F0A frequency need be considered for propagation to the far-field.

7.1.4 RESULTS – INSTALLED FAN NOISE

The acoustic assessment of fan tones at the interface plane is identical for the installed calculations. Due to better matching of the inlet and fan designs, (see Section 0), the installed configuration is expected to be quieter. This is confirmed in Figure 123 and Figure 124 where the reduction in the 1F0A tone at the Inlet-Fan interface plane is 2.2 dB.

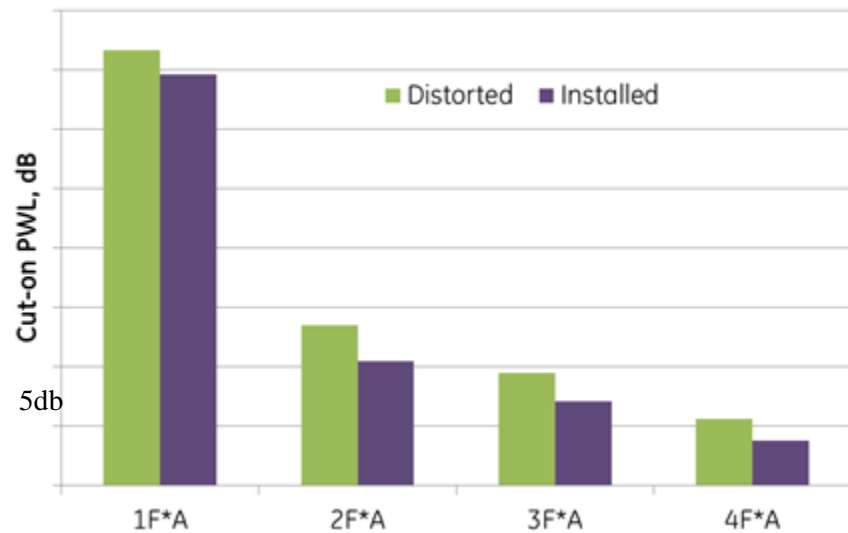


Figure 123: R_1 - R_2 interaction tone in-duct PWL summed over R_2 harmonic index for installed configuration.

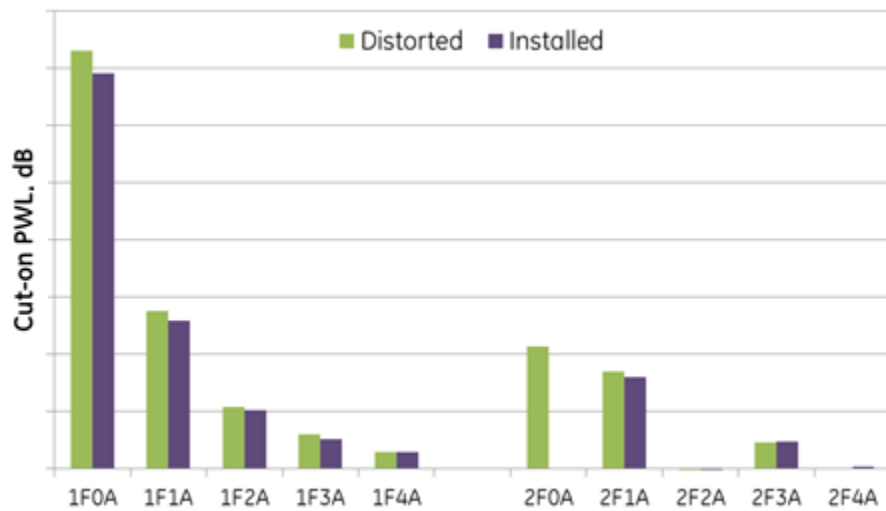


Figure 124: R_1 - R_2 interaction tone in-duct PWL for installed configuration.

7.2 FAN NOISE TRANSMISSION THROUGH INLET

7.2.1 KEY FEATURES OF INLET GEOMETRY FOR ACOUSTIC TRANSMISSION

With the fan face acoustics quantified via unsteady CFD simulations, it is of interest to assess fan noise propagation upstream and scattering by the inlet struts. Two configurations, one with the struts, and one without, but both with the auxiliary door open are assessed to quantify the scattering effect of the struts. The aux door is open in both cases because it is expected that this condition would be noisier.

Figure 125 shows a schematic of how the fan noise transmits upstream. The aux door opening has an area that is slightly more than 50% of the inlet area upstream, hence it is critical to model noise radiation through the door opening. The other feature of the inlet transmission problem is that the struts are non-identical and non-axisymmetric (Figure 126). This ideally requires a full annulus model to accurately capture the scattering into low-order azimuthal modes that could propagate more efficiently through the inlet duct. However, because the grid requirements for propagation are rather severe and the struts are only slightly non-uniform, a single blade passage model assuming identical struts was ultimately used. This would slightly degrade the accuracy, however, the first order effect of strut scattering should be captured.

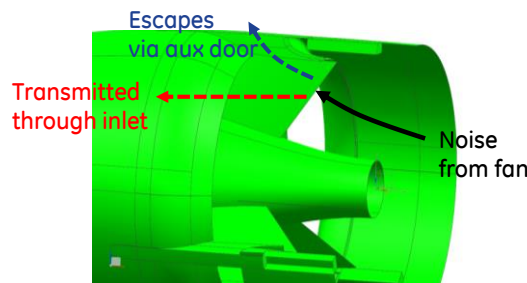


Figure 125: Schematic of fan noise upstream transmission.

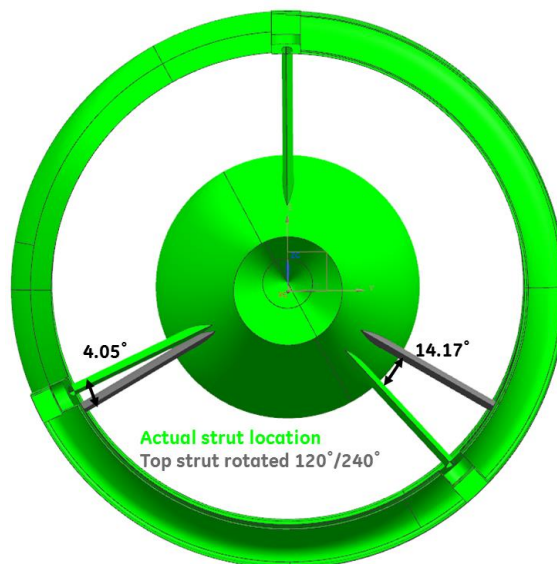


Figure 126: Inlet Struts (aft looking forward).

7.2.2 CAA MODEL AND BOUNDARY CONDITIONS

Because the aux door is open, it is necessary to model the external flow around the nacelle to obtain the correct entrainment into the inlet. The geometry model for noise transmission analysis has been derived from the inlet part of the installed CFD model described in Section 0. The model consists of inlet/nacelle. Geometry updates related to details around strut hinges are as described in Section 6.2.3. The only addition relative to the model used for installed CFD is the presence of a hub surface at the extension of the inlet center body. This feature is used to preclude potential numerical difficulties with the CAA model at the axis of rotation. The radius of the surface has been set at 0.1 inch and the surface is modeled as an inviscid wall. The model used is illustrated in Figure 127.

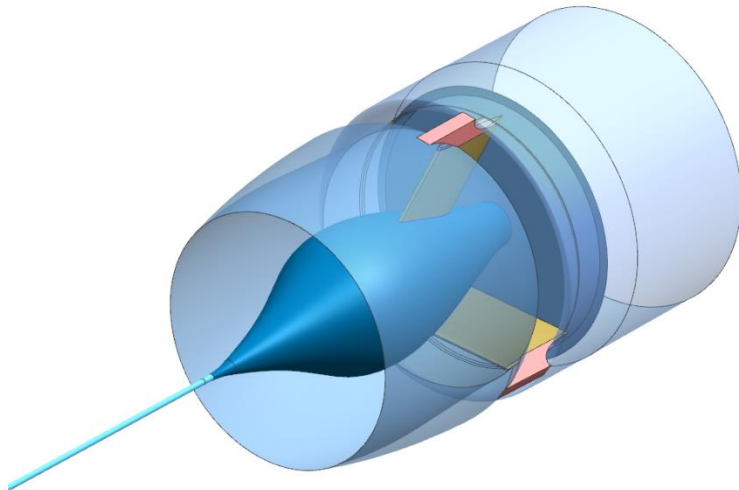


Figure 127: CAD model for noise transmission analysis.

The domain exit in the core region is set at the same aerodynamic interface plane described in Section 6.2. Compared to the installed CFD analysis, the model does not include the pylon, wing and fuselage. The far-field domain boundary has been set per standard GE aero acoustics practice with the inlet placed far upstream. A second exit (in the external flow) is placed at a convenient location just far enough downstream of the auxiliary door. Two different inlet models have been generated for the purpose of this calculation: nacelle only model without struts and corresponding hinges, and model including the struts. The no-strut model has been modeled as a 20^0 periodic sector while the strut model has been modeled as a 120^0 periodic sector. The domain boundaries and CFD domains for both strut and nacelle only model are shown in Figure 128.

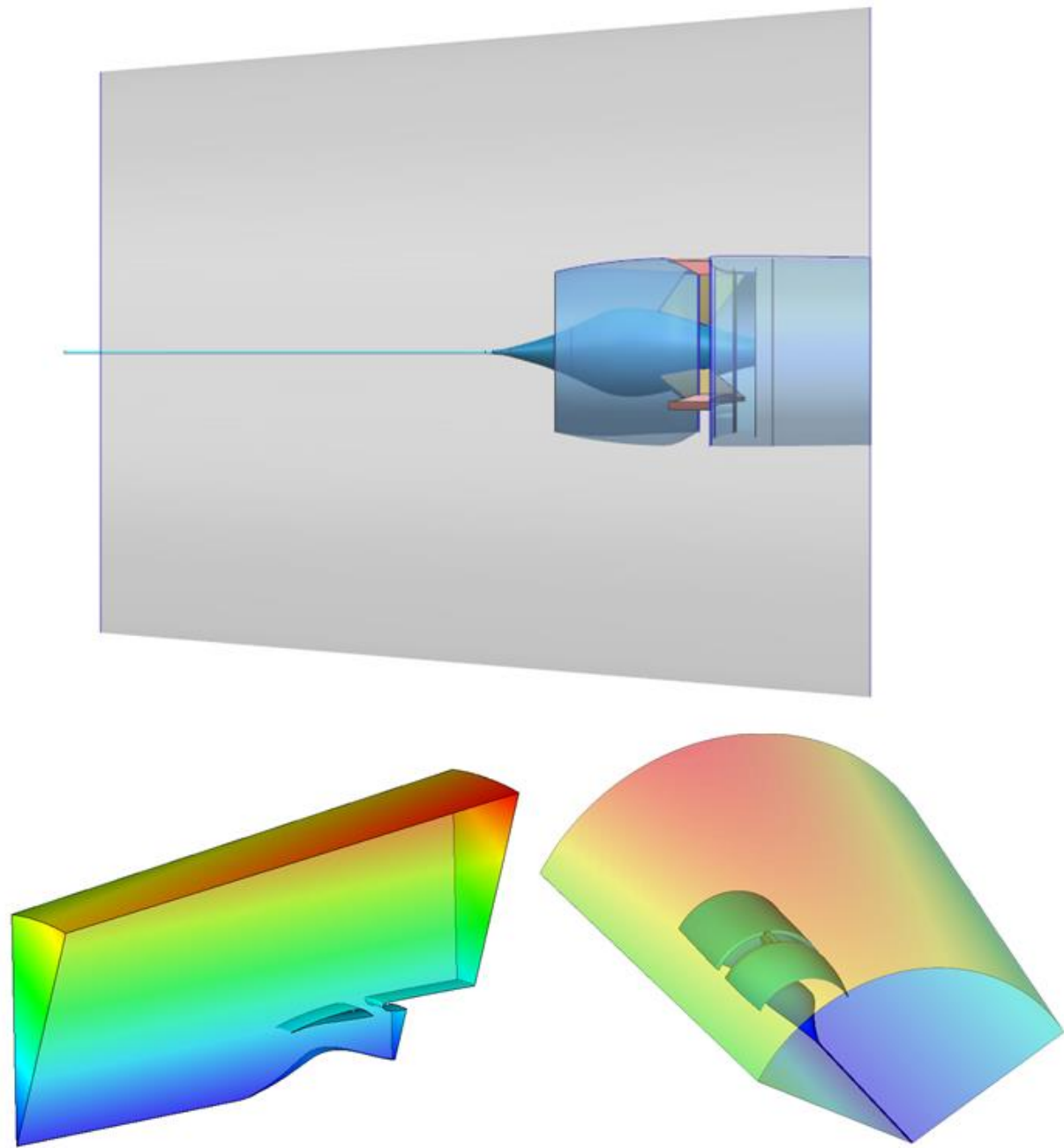


Figure 128: Noise transmission model: domain boundaries for no-strut and strut domains.

A schematic of the boundary conditions used is shown in Figure 129. A far-field boundary condition similar to those used in past GE studies on propellers and open rotors is employed at radial boundary with the static pressure held at ambient. This boundary is sloped radially outward to ensure unambiguous inflow. Far upstream, the inflow is purely axial at the flight Mach number of 0.3 with static flow variables at standard day conditions. The artificial inviscid hub surface upstream of the inlet is not expected to significantly alter the acoustic behavior of the inlet (since acoustic energy is concentrated near the casing) or the steady flow characteristics with axial inflow. On the external flow exit, ambient static pressure is imposed with a steady non-reflecting boundary condition. On the internal exit (at the Inlet-Fan interface

plane, also referred to sometimes as “fan-face” in this report), the radial static pressure profile from the 2012 de-coupled CFD analysis is enforced to entrain the correct mass flow.

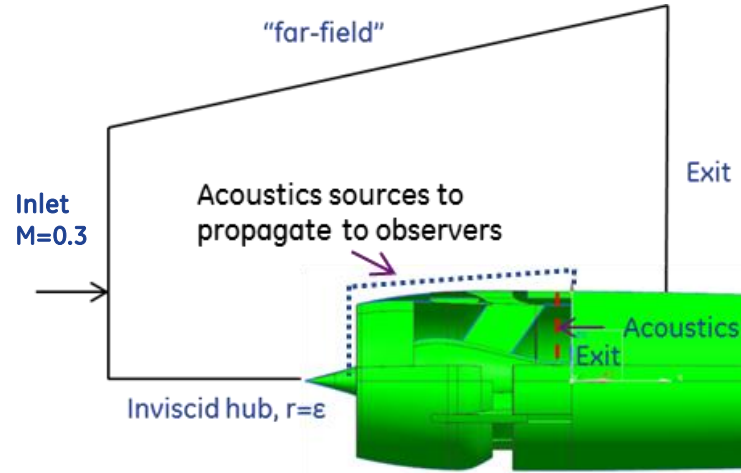


Figure 129: Domain for CAA analysis.

The CAA propagation is performed using a linearized Navier-Stokes solver for turbomachinery acoustics. First a steady flow analysis of the inlet with the aux door open is performed. This forms the base flow about which the linearized acoustic calculation is performed. Then, the perturbation variables extracted from the fan face acoustic processing (Section 7.1.3) are imposed via a 3-D non-reflecting boundary condition that allows upstream propagating acoustic modes to travel into the inlet domain while minimizing numerical reflections. The acoustic solver has been validated previously for ducted as well as unducted fan tone noise predictions [12, 13]. A simplified 1-D non-reflecting boundary condition is used at the exterior inlet whereas a far-field boundary condition is used at the radial boundary. At the exterior exit, the 3-D non-reflecting boundary condition is again used to maintain consistency with the interior exit boundary. While the 1-D boundary conditions can generate numerical reflections when acoustic waves are incident, they are located sufficiently far away from the sources near the nacelle. Furthermore, the grid is coarsened rapidly away from the nacelle as shown in Section 7.2.3, dissipating any acoustic waves propagating towards the boundary and reflecting back towards the sources.

Acoustic propagation to the far-field is handled by sampling the near-field sources on a surface enclosing the nacelle and propagating using the Ffowcs-Williams and Hawkings equation. This process will be described in detail in Section 7.3.1.

7.2.3 MESH DETAILS

Multi-block structured meshes have been generated for both nacelle-only and strut models. The CFD mesh has same block topology as the nacelle region of the installed mesh described in section 6.2.3. Care has been taken for proper boundary layer resolution of all wall surfaces, as well proper nacelle lip and strut leading and trailing edge resolution per GE compressor aero design practice. For the purposes of acoustic sensitivity studies, several acoustic-level refined meshes have been generated by varying mesh resolution in axial, radial (span-wise) and circumferential direction. Mesh resolution details for each level

of refinement for both models are shown in Figure 130. Details of the mesh cross section for no-strut and strut models are shown in Figure 131 and Figure 132 respectively.

Nacelle Only Model (20 degree sector)				
Refinement level	Axial (nacelle-core exit)	Radial	Circumferential	Size (million cells)
Base	1300	128	48	35
Refinement 1	1300	272	48	47
Refinement 2	1800	272	48	62

Nacelle and Strut Only Model (120 degree sector)				
Refinement level	Axial (nacelle-core exit)	Radial	Circumferential	Size (million cells)
Base	800	100	184	64
Refinement 1	1026	192	232	129
Refinement 2	1400	216	272	195

Figure 130: Mesh resolution data for nacelle only and nacelle-strut model.

Accurate propagation of high frequency acoustic waves over long distances is a challenge numerically, particularly for standard turbomachinery solvers like the one used in this analysis. A key factor that affects accuracy is how well the acoustic waves are resolved. The mesh resolution was chosen so as to satisfy a minimum requirement of 20 points per wave in the axial and circumferential directions for a nominal axial wavelength of 1.6", and nominal circumferential mode order of 28 for the 1F0A tone. Even so, perceptible changes in the far-field power were observed with grid refinement. Thus, quantitative comparisons of strut scattering must be performed only at consistent grid resolution.

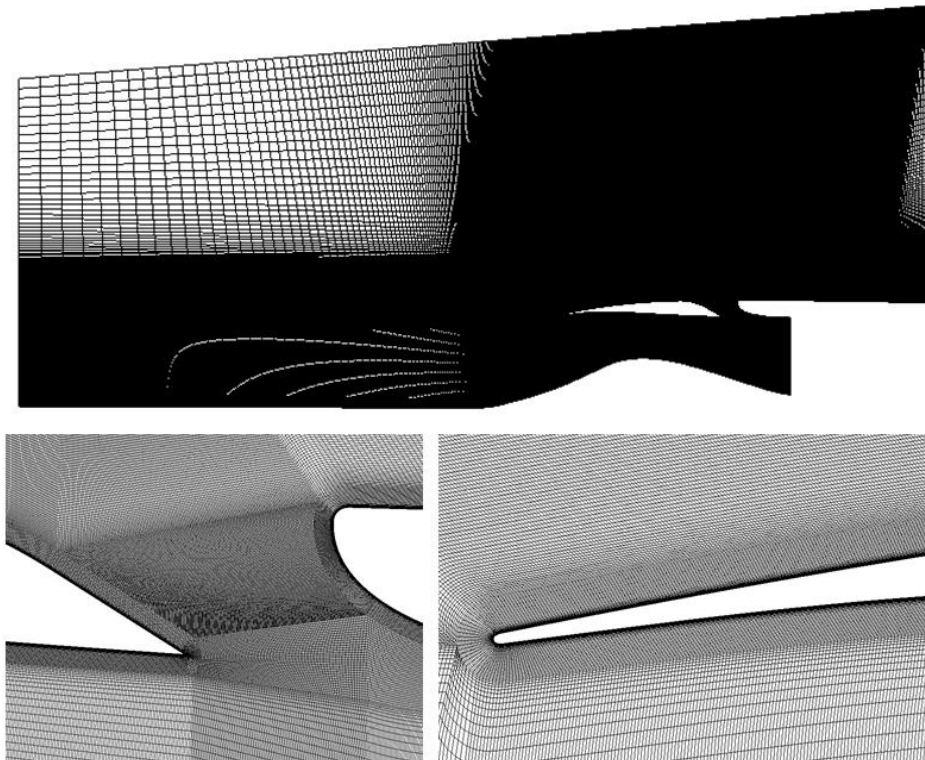


Figure 131: Cross-section of the CFD mesh for nacelle only model.

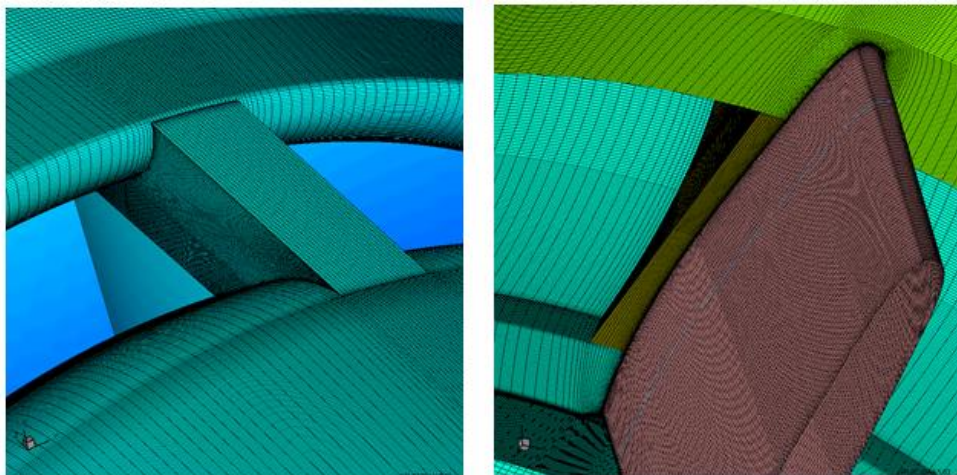


Figure 132: Strut and hinge details of the nacelle – strut noise transmission model.

7.2.4 STEADY FLOW

The steady CFD is performed at the conditions listed in Section 7.2.2. Figure 133 shows a cross-section of the flow Mach numbers for a coarse mesh check-out run. Entrainment of mass flow through the auxiliary door increases the Mach number at the fan face. A lip separation is also observed due to the low incidence sensitivity of the sharp lip designed for supersonic cruise conditions. Fortunately even though the predicted bubble is long, it did not destabilize the linearized acoustic propagation calculations for this

geometry. But note that this lip separation was substantially smaller in the installed analysis, hence it is not expected to be a significant acoustic source or destabilizing effect in reality either.

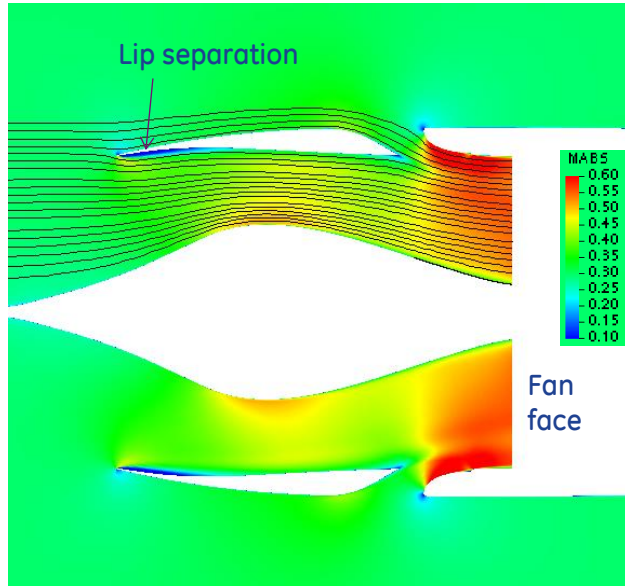


Figure 133: Inlet takeoff Mach number distribution (no-struts).

Figure 134 shows the circumferentially averaged Mach number profiles as a function of span at the Inlet-Fan interface plane. Since the static pressure this plane is the same as the decoupled 2012 CFD analysis, the Mach number profiles should be identical. The differences at the hub and case are likely due to the boundary layer interference losses that are absent in the no-strut simulation shown. Overall, the agreement is acceptable and the steady flow in the inlet and exterior is consistent with the decoupled fan analysis from which acoustic signals are extracted for the propagation calculation.

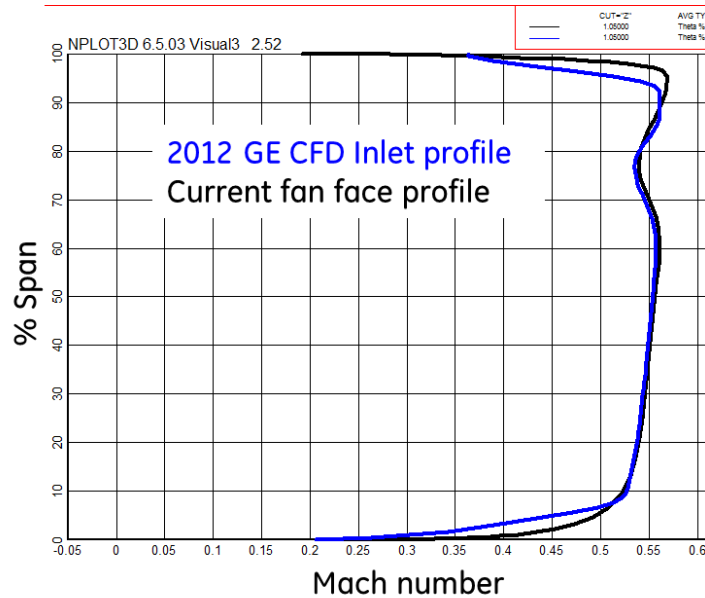


Figure 134: Fan face circumferentially averaged flow profiles.

7.2.5 CAA ANALYSIS

After the steady flow analyses are complete (with and without struts), the fan face perturbation variables corresponding to the dominant acoustic modes for the 1F0A tone (Section 7.1.3) with and without struts are extracted to be input to the CAA calculation. Only the $m=28$ and $m=-23$ azimuthal modes are considered because of their dominance. Note that the perturbations can contain both propagating and evanescent acoustic energy although only the upstream propagating part is reported in Section 7.1.3.

7.2.5.1 TRANSMISSION WITHOUT STRUTS

Figure 135 and Figure 136 show the real part of the unsteady pressure corresponding to the $m=28$ and $m=-23$ acoustic modes at the 1F0A frequency from the CAA analysis. Red and blue contours indicate positive and negative unsteady pressures respectively with the distance between two red or blue contours being the wavelength in the direction of propagation. The need for high grid resolution is apparent in the number of wavelengths an acoustic wave must travel from the fan face before it reaches the inlet lip.

Several interesting features can be observed in the analysis. Both figures show that the most intense acoustic radiation emanates from the auxiliary door at approximately 60° - 70° from the inlet axis, validating the decision to model the auxiliary door. The direction of the dominant beam depends on diffraction around the side AB of the door opening as shown in Figure 137, refraction by the mean flow entrained into the aux door and reflections from the forward end of the door opening. For $m=-23$, the radiation issuing from the auxiliary door bifurcates into two beams whereas the radiation through the inlet is more axial compared to $m=28$. This difference in behavior between $m=28$ and $m=-23$ could be related to the azimuthal and radial mode content of the two modes drawing from acoustic radiation from typical commercial fan inlets [14].

Finally, it is worth noting that the acoustic field is azimuthally uniform due to absence of struts.

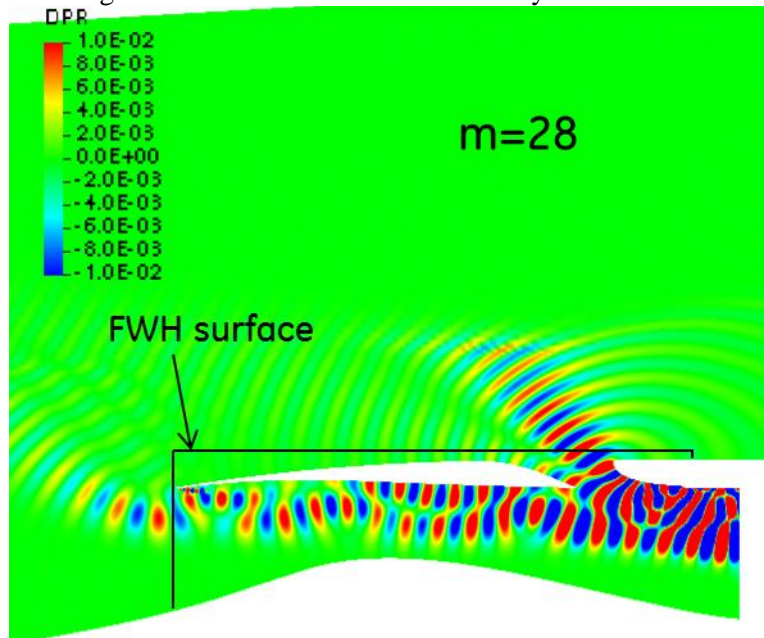


Figure 135: Real part of unsteady pressures for $m=28$ mode (1F0A tone).

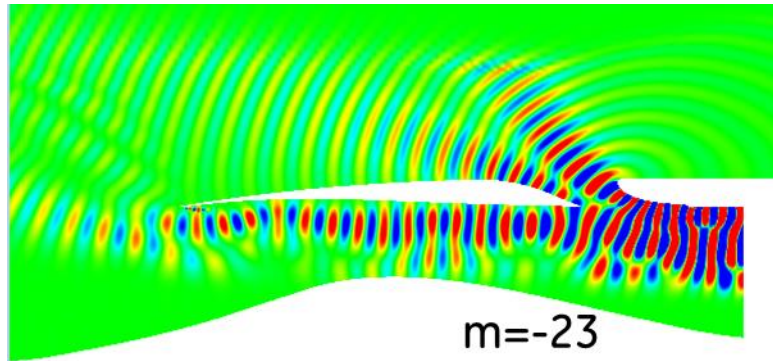


Figure 136: Real part of unsteady pressures $m=-23$ mode for 1F0A tone (same contour levels as Figure 135).

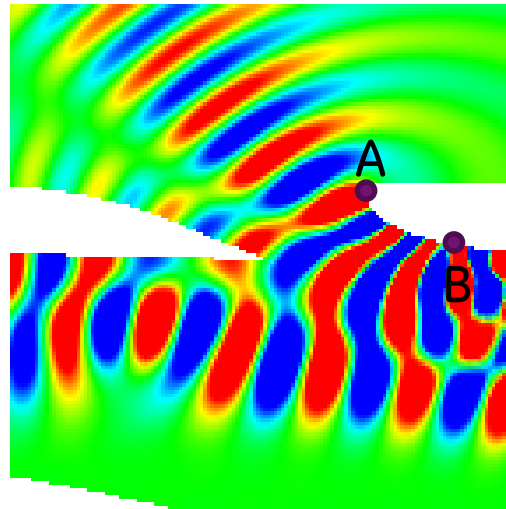


Figure 137: Real part of unsteady pressures for $m=28$ mode (1F0A tone), with detail around auxiliary door opening.

7.2.5.2 TRANSMISSION WITH STRUTS

For the geometry with struts, the dominant modes are again $m=28$ and $m=-23$ for the 1F0A tone (Section 7.1.3). Since there is only a small axial overlap between the struts and the auxiliary door, the presence of the struts is not expected to qualitatively change the physics observed in the previous analysis without struts. However, the amount of energy scattered into the duct can change as can the fraction radiating through the aux door.

Figure 138 shows the unsteady pressure contours at a plane mid-way between two struts for the $m=28$ mode (only). Recall that the struts were made uniform, affording a single passage simulation at a manageable mesh size (195 MM elements, Figure 130). This picture is qualitatively similar to Figure 135 except that there is less structure near the inlet lip (possibly due to superposition of multiple scattered

azimuthal modes). However, there is significant variation in the azimuthal direction due to scattering by the struts as shown in Figure 139. There are acoustically active spots, followed by zones of silence. Since the far-field pattern is non-uniform, noise deltas due to strut scattering will be computed by averaging the far-field power circumferentially.

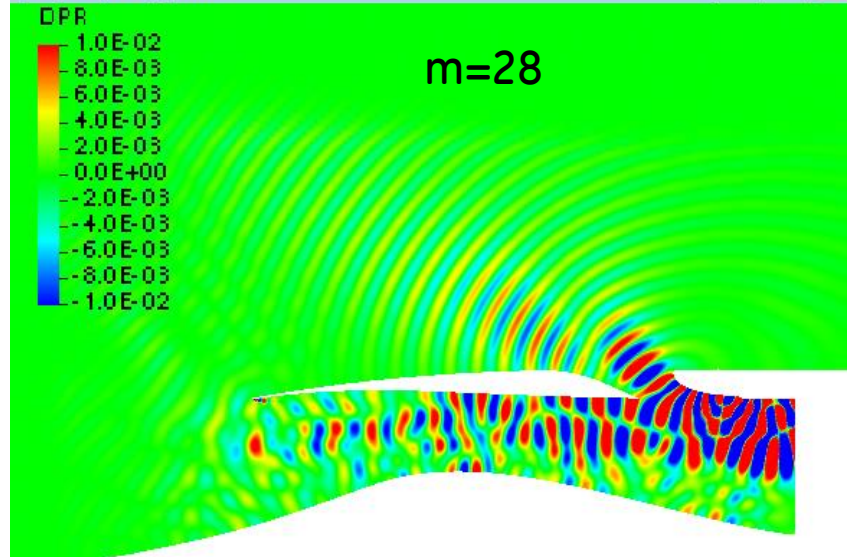


Figure 138: Real part of unsteady pressures for $m=28$ mode (1F0A tone) with struts. Cutting plane location is mid-way between struts.

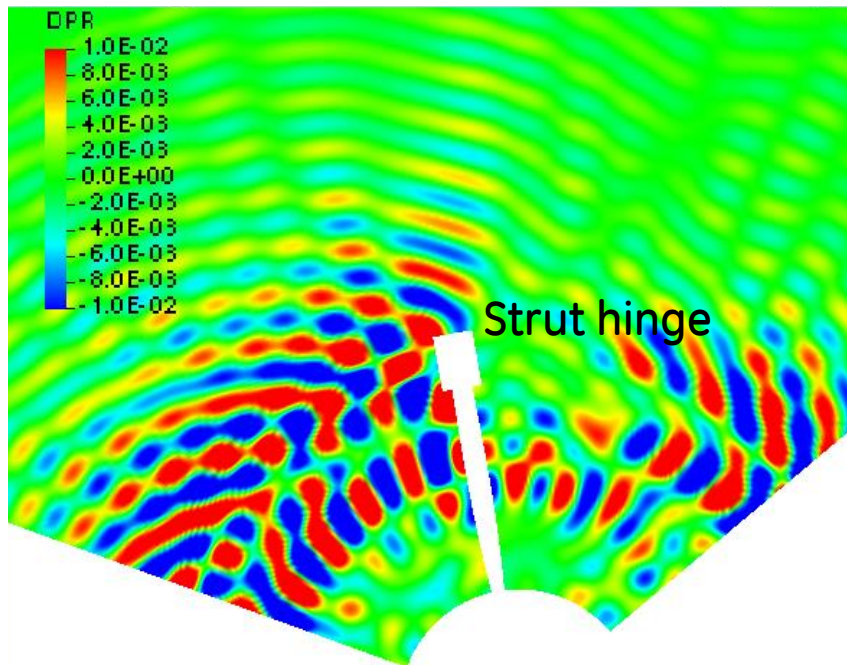


Figure 139: Real part of unsteady pressures for $m=28$ mode (1F0A tone) with struts. Cutting plane location is over aux door, aft looking forward.

7.3 NOISE PROPAGATION TO FAR-FIELD

7.3.1 PROCEDURE

To project the solution to the far-field, a permeable formulation of the Ffowcs-Williams and Hawkings (FWH) equation is used. The amplitude and phase of the unsteady acoustic pressure is extracted on the cylindrical surface surrounding engine inlet shown in Figure 135. The extracted solution is replicated with the appropriate phasing over the full annulus, and decomposed into a Fourier series for different azimuthal modes to take into account the scattering by the struts when applicable. Given the frequency of the mode, the time history of the unsteady pressure, velocities, and density is built on the cylindrical surface. This is then projected to the far-field using the FWH formula by integration over the cylindrical surface for a specified frequency, ω , and a set of observer locations:

$$4\pi|\mathbf{x}|\hat{p}\left(\mathbf{x}, \frac{\omega}{1-M_r}\right) = i\omega \frac{x_i}{c|\mathbf{x}|} \int [p'n_i + \rho\widehat{u_i}(\widehat{u_j} - U_j)n_j] \exp\left\{-\frac{i\omega}{1-M_r}\left(-\frac{\mathbf{x}\cdot\mathbf{y}}{c|\mathbf{x}|}\right)\right\} d\Sigma \\ + i\omega \int [(\rho_0 u_i + \rho'(\widehat{u_i} - U_i))n_i] \exp\left\{-\frac{i\omega}{1-M_r}\left(-\frac{\mathbf{x}\cdot\mathbf{y}}{c|\mathbf{x}|}\right)\right\} d\Sigma,$$

A frequency domain formulation of the FWH equation is used here and is derived in [12]. In the above formula, subscript zero denotes the mean flow, M_r is the projection of the mean flow Mach number in the direction of the observer, and the hat denotes the time Fourier time transform. This formulation has been validated for canonical cases and used extensively for open rotor tone noise prediction within GE [12].

A sensitivity study has been performed on the length of the time sample, time sampling rate, and spatial resolution of the sampled solution on the cylindrical surface and the position of the FWH surfaces. It was found that the solution converges and becomes insensitive to the choice of the parameters for the sampling rate of 10 points per time period of the acoustic wave, and time history of 10 periods. Spatial sampling should be done on a grid fine enough to allow at least seven points per acoustic wave length both axial and azimuthal directions. The effect of FWH surface location is described in Section 7.3.2.1.

7.3.2 FAR-FIELD RESULTS

A sideline array of observers at a 450 meter distance was used to obtain the far-field SPLs. The far-field observers are located starting at 20° from the inlet axis and ending at 160° . Between 30° and 150° , the observer locations are spaced every 5° .

7.3.2.1 FWH SENSITIVITIES

It is found that the far-field PWL is particularly sensitive to grid resolution and FWH sampling locations. Figure 140 shows the far-field PWL for the $m=28$ mode (no struts, base grid) as a function of where the acoustic sources are sampled (Figure 135). In Figure 140, increasing surface number corresponds to increasing volume of sources sampled and each surface is offset by $1''$ ($\sim 60\%$ of the 1FOA tone acoustic wavelength) radially and axially. It is interesting to note that the far-field PWL displays an oscillatory behavior. It is possible that this happens because of phase interference effects due to a large number of wavelengths being sampled especially on the radial surface. Notice also that the amplitude of

the PWL oscillation is decreasing and the far-field PWL appears to be converging to a constant value with sampling location.

In order to obtain a more robust estimate of the far-field PWL that is not subject to such numerical uncertainties, the far-field power levels are averaged successively over increasing number of surfaces (the red line in Figure 140). This value does not oscillate much (less than 0.5 dB) over the entire range of surfaces averaged. While the highest value of this averaged line (most acoustic power) corresponding to averaging over 3 surfaces is used for comparison purposes to the configuration with struts, this highlights the level of uncertainty in the assessment.

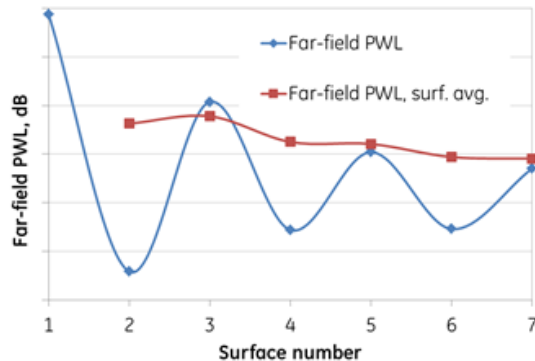


Figure 140: Far-field PWL for $m=28$ mode (1F0A tone) without struts for baseline grid.

Sensitivity to grid is shown in Figure 141. Here, the complex pressures corresponding to $m=-23$ and $m=28$ modes are added in the far-field prior to averaging over 3 FWH surfaces. There is a 1.7 dB noise increase by going to a more refined grid and a further increase of 0.9 dB with additional grid refinement (Figure 130). Obviously, more grid is required to achieve grid convergence, however, matching this resolution on the strut model is already challenging. Since our objective is to quantify the scattering effect of the struts, further mesh refinement was not attempted.

Thus, comparison of the strut scattering effects is accurate only when the underlying mesh resolution is identical. However, as Figure 130 shows, a direct comparison is not possible. The closest match is to compare the finest grid on the struts (Refinement level 2) with an average of the base and the first level refinement on the no-strut geometry as quantified by the resolutions in the axial, circumferential and radial directions within the nacelle.

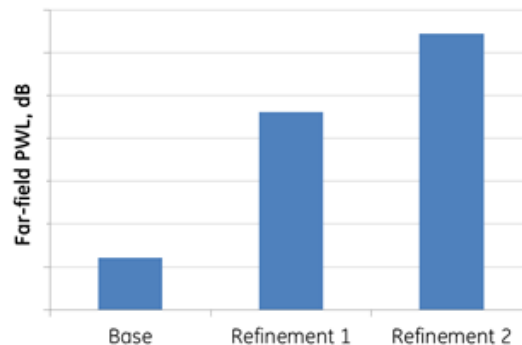


Figure 141: Grid sensitivity of far-field PWL for 1F0A tone for no-strut CAA.

For the case with struts, the far-field SPL is azimuthally varying due to strut scattering. Hence the far-field power is averaged azimuthally for each FWH surface location. Contrary to the oscillatory behavior observed in Figure 140 (no struts), the far-field PWL is monotonically reducing with increasing surface number (Figure 142). In Figure 142, both $m=28$ and $m=-23$ modes are added with appropriate phase. The fact that the curve is monotonically decreasing is an indication that we are losing acoustic power due to grid dissipation with increasing FWH surface distance for the strut mesh. Thus, the far-field results for the struts use the predictions from the FWH surface closest to the geometry. Unlike the no-strut case, averaging to reduce phase interference errors is not needed because an azimuthal average is inherently performed.

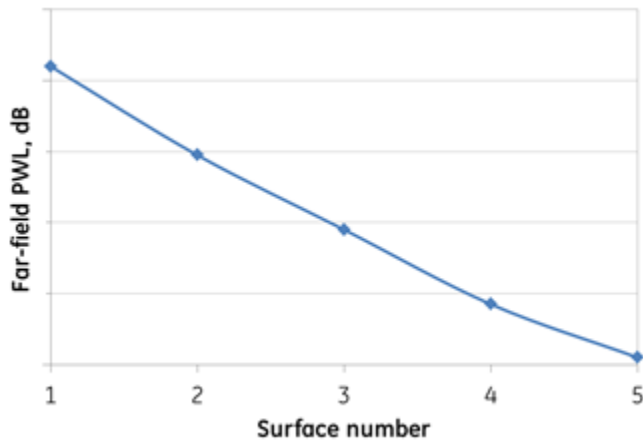


Figure 142: Far-field PWL for 1F0A tone with finest strut mesh.

To summarize, the following process is used to arrive at the far field SPL/PWL:

1. Add $m=23$ and $m=28$ mode far-field complex pressures at each observer location to account for interference effects.
2. For the strut scattering case, average resulting far-field power over the azimuth on the closest FWH sampling surface. In the case without struts, no such averaging is required. Rather, an average is performed over three FWH surfaces to smooth spatial jitters in the far-field directivity due to FWH surface sampling sensitivities in the source field.
3. For the no-strut case, a further average over the baseline and first level refined grids is performed to match the grid resolution of the finest strut mesh.

7.3.2.2 EFFECT OF STRUT SCATTERING

In both the strut and no-strut cases, we report only the highest far-field PWL obtained using the above process (Figure 143). Strut scattering actually lowers far-field acoustic power by 1.3 dB. This is a little counter-intuitive because normally one would expect scattering to conserve power or potentially increase it due to more efficient radiation caused by generation of lower order azimuthal modes. However, the struts do add more shear layers to the flow, and it is possible that there is some dissipation of acoustic energy. In any case, the reduction in power is only slight and is well within the uncertainties of the assessment.

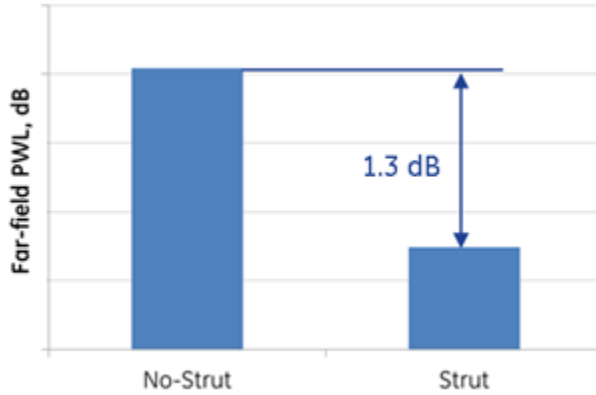


Figure 143: Far-field PWL due to strut scattering (1F0A tone).

Figure 144 shows the far-field directivity for the two geometries. The peak near 60° - 70° is the strong beam radiating through the auxiliary door. Without struts, the radiation drops steeply away from the peak particularly towards the inlet. With struts, the directivity is flatter, and more energy beams through the inlet axis. As a consequence, even though the PWL for the strut case is lower, the flatter directivity could cause the EPNL levels due to strut scattering to be higher.

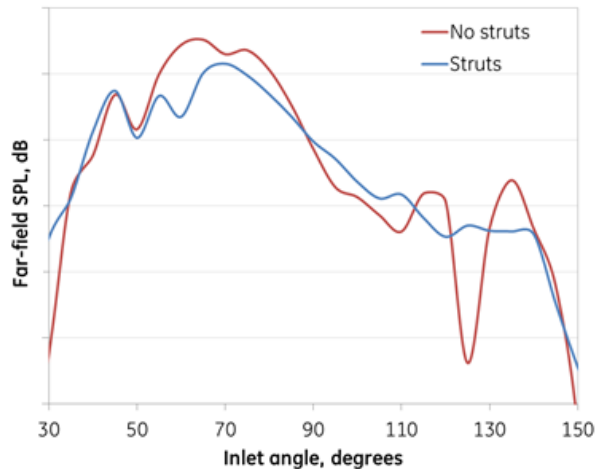


Figure 144: Far-field SPL as a function of inlet angle.

7.3.2.3 ACOUSTIC POWER SPLIT BETWEEN AUX DOOR AND INLET

Since the dominant beam of radiation issues through the aux door, it is of interest to assess the effect of closing the door on the far-field noise. In reality, closing the door would reduce the mass flow to the fan, and the steady flow inside the inlet would change. The resulting effect on noise however, is expected to be beneficial. An accurate assessment of the flow field and acoustic change would entail a new

CFD/CAA calculation. However, the effect of noise radiating out through the inlet only can be qualitatively assessed by repeating the FWH propagation by neglecting the sources on the radial FWH surface and the axially aft surface. Such a calculation shows that the power radiating through the inlet is 46% of the total power, i.e. almost equal power radiates through the aux door as well as the inlet.

We previously mentioned that the area of the aux door opening is approximately 50% of the inlet area. Therefore the intensity of sound escaping through the aux door is twice that emanating from the inlet. In addition, this noise radiates almost normal to the flight direction. Thus, this is the portion of the inlet geometry that likely contributes the most to EPNL. Hence, any efforts on noise reduction in the inlet should first focus on attenuating acoustics upstream of the aux door by say acoustic liners, and then adding treatment further upstream.

7.4 CONCLUSIONS

Results from fully-coupled unsteady RANS-based CFD predictions were post-processed to assess fan tone noise for a counter-rotating fan configuration subject to inflow distorted by the presence of inlet struts and a translatable inlet cowl to entrain exterior flow when opened. The analysis shows that the upstream radiated noise is governed by the fan system sources rather than interaction with the inlet struts. Improving the inlet design and installation under the wing allows for better matching between the inlet and the fan, reducing the noise generated.

The noise generated by the fan in the un-installed scenario was propagated upstream through the inlet and to the far-field using a linearized tone CAA analysis. Results show that a little more than 50% of the acoustic power radiates through the aux door at an angle of approximately 60°-70° from the inlet axis. The inlet struts merely direct more energy through the inlet resulting in a flatter directivity. While the tone PWL is reduced slightly (within the fidelity of the numerical assessment), the EPNL change due to strut scattering is likely smaller than the observed far-field PWL reduction (possibly even a penalty to system noise) on account of the more uniform directivity. Application of acoustic treatment in the inlet duct and axial positioning of the aux door is thus likely to have significant impact on noise transmission.

It is important to note that these predictions were obtained by extending a standard tone noise analysis process for ducted and unducted turbomachinery to a challenging problem of high frequency acoustic propagation over long distances. Thus it is critical to thoroughly validate the results of this analysis to improve confidence in the ability of the predictions to guide low noise fan design both in terms of source reduction and transmission. In addition, the following need to be addressed to obtain a more accurate picture of installed fan noise levels:

- Prediction of broadband noise levels generated by the fan leveraging current GE broadband noise prediction tools for fan-OGV interaction.
- Tone scattering due to installation effects (which would be an extension of the current analysis to include the installed geometry).

Finally, the results of this analysis suggest that low noise fan design efforts for this application should be pursued along the following directions:

- Fan inlet radial profile tailoring to reduce tip shock strengths.
- Designing the IGV to increase rotor noise transmission loss and reduce IGV wake strengths.
- Application of acoustic treatment in the inlet duct and nacelle aft of cowl door opening in conjunction with axial re-positioning of the aux door further forward, and variations in door opening/geometry.

8 SUMMARY

This report covers the activity in Phase II of the N+2 NRA – System Level Experimental Validations for Supersonic Transport Aircraft. Three main activities were included in this portion, an updated conceptual design of a propulsion system to meet the N+2 goals with technologies appropriate with the associated timeframe, a redesign of the flow lines for the inverted velocity profile nozzle with a fluid shield, and an assessment of the noise impact of the Lockheed Martin supersonic inlet with a multi-stage fan module.

The proposed engine concept incorporated advanced technologies such as Cooled Cooling Air (CCA) with modulated turbine cooling flow, variable area bypass injector (VABI), Axi-Plug inverted velocity profile (IVP) exhaust with a fluid shield and chevrons, and heat addition. The maximum T4 of the engine was set to meet the cruise NOx requirement.

Testing of the exhaust nozzle with the inverted velocity profile and a fluid shield around 180 deg of the exhaust in Phase I indicated that the primary nozzle flowpath was too divergent at lower power settings for quiet operation. The flowpath was redesigned to mitigate the unsteady separation seen due to the overexpansion. This resulted in the adoption of the dual mode nozzle, where the nozzle can operate in a purely convergent mode as well as a convergent-divergent mode. Large Eddy Simulations of the Phase I reference and IVP/shield nozzle provided very accurate prediction of the farfield acoustics. LES of the Phase II geometry indicates a much cleaner flowfield at the cutback conditions, although it did pick a tone and an additional primary nozzle flowpath was fabricated and tested.

A scale model corresponding to the improved sideline and cutback configurations was designed and fabricated. Scale model testing at NASA GRC shows much improved acoustic performance, with an elimination of the unsteady separation seen in Phase I, although some broadband shock noise like component is seen, likely coming off the core cowl expansion surface.

The scale model exhaust nozzle acoustic test was performed at NASA GRC. No evidence of the unsteady separation was seen in the measured Phase 2 acoustic farfield acoustic data. The three stream nozzle resulted in lower noise levels than the reference fully mixed equivalent nozzle. The effect of the shield was measured in the farfield acoustics as a reduction in the higher frequency ranges. Single chevron designs were tested on the shield nozzle and one the portion of the primary nozzle not covered by the shield. No combination with the chevrons resulted in overall (EPNL) noise reduction, although significant low frequency benefit was measured with the chevrons. The azimuthal variation around the three stream nozzle was measured and showed the lowest noise was achieved with the shield aligned with the microphones.

A less-expensive alternative to LES was found. This alternative approach, grid-proper DDES can indeed capture the flow separation in the Phase I nozzle. URANS and SAS failed to capture this significant flow development. Sufficient grid resolution is needed for the DDES to be able to predict this flow feature. Key learning of the proper grid resolution was to resolve shock wave with 6 points across shock width, and a wall $y+$ less than 40 in the shock impingement region.

Noise correction factors were established for acoustics assessment using RANS/URANS predictions in which the wakes from inlet struts or IGVs were not mixed properly. The correction was based on LES wake decay which matched available wake decay test results.

Analysis was performed of the Lockheed Martin supersonic inlet coupled with a multi-stage fan configuration. The simulations were carried out in two steps. In step 1 (Phase II), Lockheed Martin supplied an inlet/boundary condition with inlet auxiliary doors open, downstream of the inlet center-body and struts. And the decoupled calculation was performed for the fan component using the pre-determined inflow boundary conditions. In step 2 (Phase II extension), a new inlet design was provided by Lockheed Martin. The fan, nacelle, and the aircraft are coupled in the installed configuration. A take-off condition of Mach 0.38 and 8.1-deg angle-of-attack is simulated in the installed configuration. It is found that, due to the engine location, the wing provides a significantly favorable shielding effect to the engine. The large angle-of-attack (8.1 degrees, take-off condition) did not affect the nacelle and fan significantly. The under-wing cross-flow does, however, introduce a strong swirl distortion, which is ingested by the fan via the open aux door. The swirl distortion mainly stays within the near-casing stream, no the effect to main flow fan blades is minimal. The struts and IGVs in the fan domain attenuate the swirl distortion effectively.

The inlet design evolution in Phase II extension has improved the aerodynamic interaction with the fan. The acoustics analysis is carried out for the installed CFD result. The improvement of main fan tip flow has resulted in reduced overall fan tone noise level.

Results from fully-coupled unsteady RANS-based CFD predictions were post-processed to assess fan tone noise for a counter-rotating fan configuration subject to inflow distorted by the presence of inlet struts and a translatable inlet cowl to entrain exterior flow when opened. The analysis shows that the upstream radiated noise is governed by the fan system sources rather than interaction with the inlet struts. Improving the inlet design and installation under the wing allows for better matching between the inlet and the fan, reducing the noise generated.

The noise generated by the fan in the un-installed scenario was propagated upstream through the inlet and to the far-field using a linearized tone CAA analysis. Results show that a little more than 50% of the acoustic power radiates through the aux door at an angle of approximately 60°-70° from the inlet axis. The inlet struts merely direct more energy through the inlet resulting in a flatter directivity. While the tone PWL is reduced slightly (within the fidelity of the numerical assessment), the EPNL change due to strut scattering is likely smaller than the observed far-field PWL reduction (possibly even a penalty to system noise) on account of the more uniform directivity. Application of acoustic treatment in the inlet duct and axial positioning of the aux door is thus likely to have significant impact on noise transmission.

A cumulative system noise assessment including the fan inlet radiated and jet noise components was made, indicating the NASA community noise goals for N+2 should be achievable with this propulsion system.

9 SUGGESTED FUTURE WORK

Based on the work conducted in this program some suggested follow-on activities are included:

- Flowfield testing of exhaust nozzle including schlieren measurements to look for shocks on the IVP cowl.
- Exhaust Nozzle fine tuning of the core cowl geometry to eliminate the shocks seen.
- More detailed fan and inlet integration studies and noise estimates
 - More detailed analysis with inlet treatment

- Propulsion/Airframe Integration Studies to look at noise reflection and shielding, depending on location
- Wind Tunnel test with the supersonic inlet concept with auxiliary doors to validate the high fidelity assesments
- Fan wind tunnel acoustic test.

10 ACKNOWLEDGEMENTS

This work was funded by the NASA N+2 Supersonic program administered by Peter Coen at the NASA Langley Research Center under prime contract (Lockheed Martin) NNC10CA02C. The authors recognize numerous individuals from both GE Global Research and GE Aviation, and Lockheed Martin for their technical guidance.

11 REFERENCES

1. Lumley, J.L., The structure of inhomogeneous turbulence, *Atmospheric turbulence and wave propagation*, edited by Yaglom, A., and Tatarsky, V., Nauka, Moscow, pp. 167-178, 1967.
2. "Stochastic Estimation and Proper Orthogonal Decomposition: Complementary Techniques for Identifying Structures", Bonnet, J.P., Cole, D.R., Delville, J., Glauser, *Experiments in Fluids*, vol.17, p307-314, 1994.
3. "Low dimensional characteristics of a transonic jet. Part 1. Proper orthogonal decomposition", Tinney, C.E., Glauser, M.N., Ukeiley, L.S., *Journal of Fluid Mechanics*, Vol. 612, pp. 107-141, 2008.
4. Sirovich, L., Turbulence and the dynamics of coherent structures Part 1: Coherent Structures, *Quarterly of Applied Mathematics*, Vol. 45, No. 3, pp. 561-571, 1987.
5. Visbal, M. R. and Gaitonde, D. V., "On the Use of Higher-Order Finite-Difference Schemes on Curvilinear and Deforming Meshes," *Journal of Computational Physics*, Vol. 181, 2002, pp. 155-185.
6. Shur, M. L. et. al, "Analysis of jet-noise-reduction concepts by large-eddy simulation," *International Journal of Aeroacoustics*, Vol. 6, No. 3, 2007, pp. 243-285..
7. Paliath,U., Shen, H., Avancha, R. & Shieh, C " Large Eddy Simulation for jets from chevron and dual flow nozzle," AIAA 2011 -2881
8. J. Yao, P. Cargill, D. G. Holmes, S. Gorrell, "Aspects of Numerical Analysis for Unsteady Flows in Aircraft Engines", Invited paper AIAA-2010-1603, 48th AIAA Aerospace Sciences Meeting Including the New Horizons Forum and Aerospace Exposition, 2010
9. J. Yao, S. Gorrell, A. Wadia, "High-Fidelity Numerical Analysis of Per-Rev-Type Inlet Distortion Transfer in Multistage Fans - Part II: Entire Component Simulation and Investigation", ASME Turbo Expo 2008: Power for Land, Sea and Air, June 2008, Berlin, Germany, GT2008-50813, Also published on J. of Turbomachinery, Vol 132, No 4, Oct. 2010
10. J. Yao, S. Gorrell, A. Wadia, "High-Fidelity Numerical Analysis of Per-Rev-Type Inlet Distortion Transfer in Multistage Fans - Part I: Simulations with Selected Blade Rows", ASME Turbo Expo 2008: Power for Land, Sea and Air, June 2008, Berlin, Germany, GT2008-50812, Also published on J. of Turbomachinery, Vol 132, No 4, Oct 2010
11. J. Yao, S. Gorrell, "A Time-Accurate CFD Analysis of Inlet Distortion Induced Swirl in Multistage Fans", 43rd AIAA/ASME/SAE/ASEE Joint Propulsion Conference & Exhibit, AIAA Paper 2007-5059.

12. Sharma, A., and Chen, H., "Prediction of Tonal Aerodynamic Noise from Open Rotors" *Journal of Sound and Vibration*, Vol. 332, No. 16, pp. 3832–3845, 2013.
13. Sharma, A., Richards, S.K., Wood, T.H., and Shieh, C.M., "Numerical Prediction of Fan Tone Interaction Noise from High Bypass Aircraft Engines," *AIAA Journal*, Vol. 47, No. 12, pp. 2866-2878, 2009.
14. Tam, C.K.W., Parrish, S.A., Envia, E., and Chien, E.W., "Physical Processes Influencing Acoustic Radiation from Jet Engine Inlets", *Journal of Fluid Mechanics*, Vol. 725, pp. 152-194, 2013.
15. Menter, F. R, Kuntz, M., Bender R., "A scale-adaptive simulation model for turbulent flow predictions", AIAA Paper 2003-0767, 2003
16. Egorov, Y., and Menter, F., "Development and Application of SST-SAS Turbulence Model in the DESIDER Project", Second Symposium on Hybrid RANS-LES Methods, Corfu, Greece, 2007

Appendix C.—Development of Design Capabilities Within the NASA/LMCO N+2 Supersonics Effort

Juan J. Alonso, Francisco Palacios, Trent Lukaczyk, and Gerald Carrier*
Stanford University
Stanford, California 94305

Abstract

This report describes the efforts of the Stanford University (SU) Team during the entire Phase II of the Supersonic Validations Study, pursued in collaboration with the Lockheed-Martin Corporation. Contained in this report is a description of our efforts in the development of cutting-edge, high-fidelity techniques for the design of supersonic aircraft that must match a particular equivalent area distribution at pre-specified lift coefficients and while retaining high aerodynamic performance. The report focuses on the description of the complete capability including the flow analysis, grid adaptation technique, the formulation of an adjoint solver for the equivalent area distribution (at different azimuth angles), the optimization strategy (gradient based, and response surface modeling with Gaussian process regression) and the practical shape design process of the supersonic aircraft proposed by LMCO. This shape design effort is challenging due the complexity of the geometric details involved that require a full unstructured direct and adjoint flow solver with grid adaptation capabilities to capture the propulsion system effects and the shock and expansion waves in the near-field. It is important to highlight that the application of the continuous adjoint methodology to the equivalent area objective function is novel, and the technique developed in this project includes filtering methodologies to manage the gradient inaccuracies while enhancing the response surface model. Moreover, even though in our earlier work we had relied on LMCO's capabilities to compute the ground sonic boom metrics, in this report we include the results of our own computations of sonic boom loudness metrics, and we make a number of observations about the computed sonic boom intensities.

*Visiting Research Engineer from Onera/Meudon, France.

Contents

1	Introduction	2
2	High-fidelity flow analysis	3
2.1	Solver description	4
2.2	Adaptive mesh refinement	6
3	Gradient computation and design variables	7
3.1	Gradient evaluation using control theory	8
3.2	Adjoint method applied to engine simulations	10
3.3	Design variable definition, and mesh deformation	13
3.4	Managing gradient inaccuracies	14
4	Optimization framework	16
4.1	Gradient based optimization	16
4.2	Surrogate Based Optimization	17
4.3	Response surface modeling with Gaussian process regression	17
4.4	Methodology for surrogate based optimization	20
4.5	Python package	22
5	Numerical results	22
5.1	Grid adaptation	22
5.2	Shape optimization maintaining equivalent area	23
5.3	Unconstrained surrogate-based optimization	27
5.4	Recovering boom performance after including structurally-motivated changes	27
6	Sonic boom assessment of the different aircraft configuration geometries	29
6.1	Objective	29
6.2	Description of the methods and tools used for ground propagation of sonic booms	32
6.3	Flight conditions used for the sonic boom analysis	34
6.4	Set-up and verification of the sonic boom evaluation process	35
6.5	Summary of the sonic boom evaluation results for the different configurations investigated	41
7	Conclusions	44

1 Introduction

As part of the NASA Supersonics Project N+2 effort (Supersonic Validations) and in collaboration with LMCO, SU had agreed to develop and demonstrate an adjoint-based capability for the inverse shape design of supersonic configurations that must match a number of target equivalent area distributions at different azimuth angles (chosen for their beneficial ground-boom properties). The long-term intent is to incorporate such a capability into a generic multi-disciplinary analysis and optimization (MDAO) framework that, in addition to aerodynamic performance and sonic-boom considerations, accounts for other important aspects of the design in order to reach a balanced, realizable, low-boom aircraft. The main objective of our effort during Phase II of this program has been to improve and test the techniques developed during Phase I of the project. In particular, the starting point was a preliminary version of an adjoint solver that was able to produce sensitivities (gradients) of cost functions derived from the aircraft equivalent area distributions with respect to arbitrary numbers of design variables that parameterize the shape of the aircraft. Owing to the properties of adjoint solvers, the entire vector of sensitivities (the gradient) can be obtained with a single flow solution followed by a single adjoint solution, thus leading to large computational efficiencies. To analyze both the performance and the boom loudness, high-fidelity CFD analyses were performed all the way to a near-field location (typically between 2 and 3 body lengths beneath the aircraft) and then the pressure signature was extracted at a number of azimuthal locations (see Fig. 1). Based on classical linearized supersonic aerodynamics theory[1], these signatures were converted into equivalent area distributions that can then be compared to target distributions known to have good loudness characteristics. In order to carry out design / optimization exercises, the shape of the aircraft is parameterized using arbitrary Free Form Deformation (FFD) control boxes so that we are able to alter the aircraft configuration to minimize drag (while maintaining lift and ensuring that the pitching moment is no worse than that we started with) and ensure that the aircraft equivalent area distributions do not deviate from the target by more than a permitted amount. In contrast,

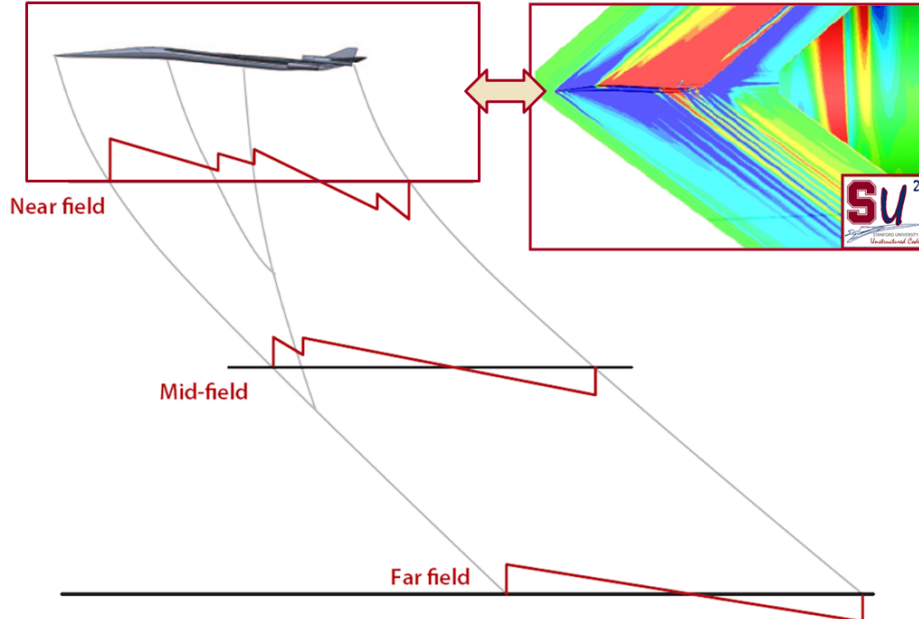


Figure 1: Schematic of CFD-based Supersonic Boom Propagation Simulations

design approaches that are based directly on the minimization of sonic boom loudness measures on the ground can lead to difficult design spaces with multiple local minima and sharp discontinuities as was shown by Chung et al. [2]. Additionally, equivalent area analyses for low boom have a well-established history,

have led to design approaches for supersonic aircraft, and have been used extensively by Lockheed Martin to shape this design and to generate the favorable pressure signature it has today. Starting with a baseline adjoint implementation, the following features have been developed/implemented during the course of Phase II: equivalent area design at multiple azimuthal locations, integration of the engines (and engine inflow and exhaust) in the simulation and design process, grid adaptation during the analysis and optimization processes to capture the engine effects, and substantial improvements in the computational infrastructure (see Fig. 2) and design process (gradient based, and response surface modeling with Gaussian process regression). In addition, we have used a loudness computational capability that is separate from the at LMCO in order to better understand the differences in equivalent area distributions (and their derivatives) that can be tolerated without significant changes in the perceived loudness of the ground boom. In particular, this report focuses

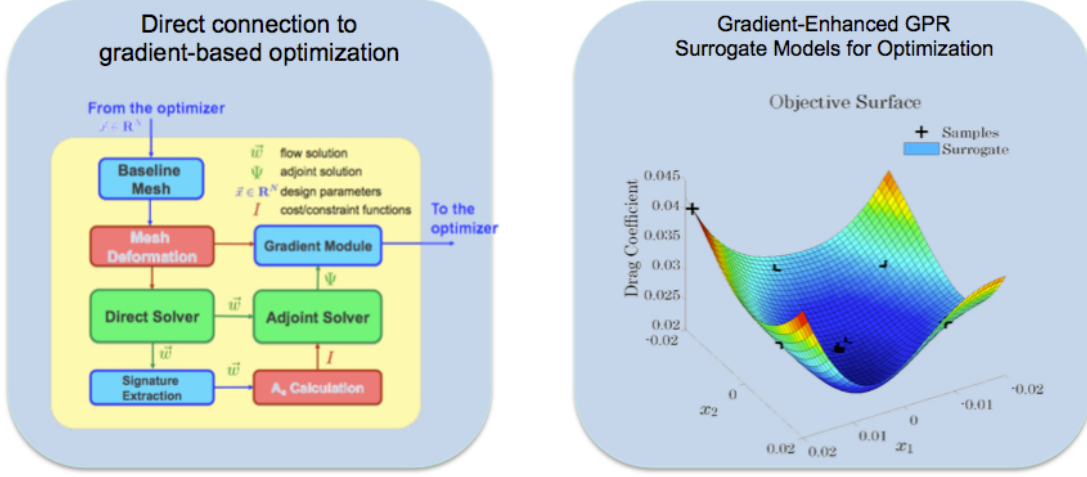


Figure 2: Overall methodology for supersonic low-boom shape optimization (gradient-based method, and response surface modeling with Gaussian process regression)

on:

- The description of direct flow solver (including the grid adaptation methodology),
- The formulation of the adjoint solver for low-boom design (based on cost functions related to the equivalent area distribution at different azimuthal angles),
- The description of the response surface modeling with Gaussian process regression,
- The results of various demonstration optimization runs that we have been pursuing and that leverage all other components, and
- The calculation of loudness metrics of the various computed ground booms.

As in our Phase I report, this document does not focus on the details of the unstructured flow solver that we are using [3], or the optimization algorithms that drive the results presented.

2 High-fidelity flow analysis

The solution of challenging multi-disciplinary problems involves the interaction between separate simulation modules that represent different physical models and procedures. In order to avoid problems with efficiency and integration, it can be beneficial for the modules to share a common set of numerical solution algorithms

and a code architecture. Additionally, adjoint equations might need to be solved for each system, and the entire problem may require an infrastructure for shape design (shape parameterization, grid deformation, and optimization algorithms) to be available. In supersonic low-boom design, the ability to integrate multiple physics, parameterize the resulting system, and design/optimize the outcome is of utmost importance and must be accomplished with minimum effort. In this work we use the open-source solver SU^2 developed in the Aerospace Design Laboratory at Stanford University. SU^2 is a general purpose partial differential equation solver equipped with tools for optimal shape design including flow and adjoint solvers, free-form mesh deformation, goal-oriented adaptive mesh refinement, and a constrained optimization environment. These tools are wrapped in the Python language to efficiently manage the input and output of data and the exchange of information between the different modules in the SU^2 suite. In order to overcome challenges and develop a lasting infrastructure for future efforts, the basic philosophy in the development of the SU^2 framework has been to ensure:

- An open-source model: while the Aerospace Design Laboratory (ADL) at Stanford University has provided the basic formulation with a reasonable set of initial capabilities, we would like to see contributions from the community to further enhance the capabilities of the suite, and we will ensure that all of these developments are available to all users in the future.
- Portability: SU^2 has been developed using ANSI C++ and only relies on widely-available, well-supported, open-source software including OpenMPI, Metis, and Python. As such, SU^2 is able to run on any computing platform for which a C++ compiler is available.
- Reusability and encapsulation: SU^2 is built so that the main concepts (geometry, grids, solution algorithms, numerical implementations, etc.) are abstracted to a very high-level. This abstraction promotes reusability of the code and enables modifications without incorrectly affecting other portions of the modules in the suite.
- Performance: we have attempted to develop numerical solution algorithms that result in high-performance convergence of the solver in SU^2 . Although some level of performance is traded for reusability and encapsulation, the loss in performance is minor.
- Gradient availability: for many applications (optimization, response surface formulations, and uncertainty quantification, among others) it is important to obtain gradients of the responses computed by SU^2 to variations of, potentially, very large numbers of design parameters. For this reason, SU^2 relies on adjoint solver implementations that can be used to compute the necessary gradients. In addition, these adjoint solutions can be used to compute functional-driven mesh adaptation techniques.

Using this philosophy within SU^2 , we are able to develop both Finite Volume Method (FVM) or FEM solvers, their corresponding adjoint systems, and, if needed, multi-physics solvers that can combine both approaches. The use of a clearly-structured set of classes allows for the easy identification of the main pieces of the code that will need to be re-implemented or enhanced for new models without interfering with the main code. A library of numerical schemes and linear solvers reduces the development time required for a new implementation (e.g., agglomeration multigrid, line-implicit relaxation, and goal-oriented grid adaptation are generic capabilities provided by SU^2 that can be reused in many numerical simulations.) Additionally, the solver structure and parallelization methodology are shared by all the members of the suite. It is important to highlight that the ability to easily integrate these solvers ensures that new features or updated models can be included without affecting the main infrastructure and with a reasonably low degree of difficulty.

2.1 Solver description

SU^2 is built to enable vertical integration with optimizers and to reduce the amount of user overhead required for setup. There are five levels of components in the optimization control architecture, and most rely on Python scripts to modify the configuration input, execute lower-level components and post-process any resulting data. To simplify and shorten overhead time during problem setup, all levels start from a common

configuration file, which is modified as needed when passed to lower levels. Listed in order from lowest to highest, these levels are:

- Core tools - These contain all of the SU² binary executables, which are the core tools of the suite. As input, they take a custom format ASCII configuration file. For output, they write data such as integrated forces, moments and other objectives to an iteration history file, field data to files for plotting, or deformed, adapted, or decomposed meshes in the native format, for instance.
- Solution decomposition/recomposition - Many of the core solvers (i.e., SU2_CFD, SU2_MDC, SU2_GPC, SU2_MAC) can operate in parallel on a partitioned mesh. The management of pre- and post-processing tasks such as mesh decomposition and plot-file merging for the output data (and for other tasks) is handled by the 'parallel_computation.py' and 'parallel_deformation.py' Python scripts ('parallel_adaptation.py' is under development).
- Sensitivity analysis - This level manages the pre- and post-processing needed for calculating performance sensitivities with respect to user-specified design variables. Both continuous adjoint and finite differencing approaches have been implemented, and the discrete and hybrid adjoint approaches are under development. For the adjoint approach, both a direct and adjoint solution are computed, and the resulting adjoint surface sensitivities must be projected into the design space during a post-processing step. In the case of finite differencing, multiple-but-independent evaluations of the direct problem are required before the performance sensitivities can be calculated.
- Design evaluation - For easier integration with optimization packages, SU² has a design management class that wraps a black box around the previous components and only takes design vectors for input. This interprets special configuration file options for design variables which allow it to set up mesh deformation. When it receives a design vector from the optimizer, it then executes mesh deformation, direct solution, and sensitivity analyses as needed, and then finally returns performance data. As it operates, it archives restart and plot data in an organized folder structure, which may be useful for secondary analyses or debugging. Evaluations of multiple design requests can be submitted in parallel if the resources are available, for example on a high-performance computing cluster.
- Design optimization - Single-objective design optimization is the highest level of architecture that we have developed at the moment. Two optimization strategies have been adopted for use with SU². The first is gradient-based optimization using SciPy's SLSQP optimizer, which adds complexity by requiring separate function handles for the objective function, constraints and their sensitivities. The second is surrogate based optimization, where an in-house gradient-enhanced Gaussian Process Regression based optimizer is used.

The core tools of the SU² suite are the C++ modules, a brief description of each binary is presented below:

- SU2_CFD (Computational Fluid Dynamics Code) - Solves direct, adjoint (steady or unsteady) problems for the Euler, Navier-Stokes and Reynolds-Averaged Navier-Stokes (RANS), plasma, free-surface, electrostatic, etc., equation sets. SU2_CFD can be run serially or in parallel using MPI. It uses either the FVM or FEM approaches and an edge-based structure. Explicit and implicit time integration methods are available with centered or upwinding spatial integration schemes. The software also has several advanced features to improve robustness and convergence, including residual smoothing, agglomeration multigrid, linelet and low-speed preconditioning, and Krylov space methods for solving linear systems.
- SU2_GPC (Gradient Projection Code) - Computes the partial derivative of a functional with respect to variations in the aerodynamic surface. SU2_GPC uses the surface sensitivities computed using SU2_CFD, the flow solution and the definition of the geometric design variables to evaluate the derivative of a particular functional (e.g. drag, lift, etc.) with respect to a given design parameter.

- SU2_MDC (Mesh Deformation Code) - Computes the geometric deformation of surfaces within the computational mesh and the surrounding volumetric grid. Once the type of deformation is defined, SU2_MDC performs the grid deformation using different strategies. Three-dimensional deformations use a method called Free Form Deformation (FFD), while two-dimensional problems typically use bump functions, such as Hicks-Henne.
- SU2_MAC (Mesh Adaptation Code) - Performs grid adaptation using various techniques (including goal-oriented) based on the analysis of a converged flow, adjoint or linearized solution to strategically refine the mesh about key flow features.
- SU2_DDC (Domain Decomposition Code) - Partitions the specified volumetric grid for use with several of the other core tools when performing simulation or design in parallel. SU2_DDC is built around the METIS [4] software that will identify and assign nodes to each processor for achieving load balancing with minimal communication (edge cuts). Once that information is received, SU2_DDC prepares the communication between nodes on different partitions and generates the appropriate computational grid partitions required by the other core tools for executing in parallel.
- SU2_PBC (Periodic Boundary Code) - Creates ghost cells in the computational domain for performing simulations with periodic boundary conditions and outputs a new mesh containing the proper communication structure between periodic faces. This module must be run prior to SU2_CFD for any simulation that uses such boundary conditions.
- SU2_SMC (Sliding Mesh Code) - Creates ghost cells in the computational domain for performing simulations with sliding surfaces and outputs a new multi-zone mesh containing the proper communication structure between sliding interfaces. As in the case of SU2_PBC, this module must be run prior to SU2_CFD.

2.2 Adaptive mesh refinement

In combination with the apriori-adapted grid, an adaptive mesh refinement procedure has been implemented to capture the effects of the propulsion system on the near-field pressure distributions. Using this method, an existing mesh can be dynamically modified by the code to improve the accuracy of the solution without an excessive increase in computational effort. In particular, we are interested in the impact of the details of the engine flows (inflow and exhaust) on the sonic boom signal. The procedure we have implemented [5] uses anisotropic adaptation of the grid based on an edge binary system that identifies the right division for each element. This methodology is important to maintain the coherence in the division of the common faces between control volumes. Some of the main important characteristics of this adaptation strategy are:

- Robust adaptation. The method should allow multiple adaptation cycles, using classical two-dimensional and three-dimensional finite volume elements (tetrahedra, hexahedra, pyramids and wedges).
- Fully automated and easy to use.
- No “hanging” nodes: the final grid should be conforming.

A method based on a flexible element division has been implemented in addition to tetrahedral and hexahedral division methods which might not give optimum results in some cases. The tetrahedral division procedure is based on the detection of edge division patterns that are prescribed in the code. However, the anisotropic division of tetrahedra can significantly deteriorate the quality of the mesh. This is a serious problem when directional flow-field features are present. The main challenge of hexahedral division methodologies is the so-called refinement propagation problem (the buffer zone between an adapted element and the non-adapted grid is greater than one cell.) This occurs when more than one set of edges in the same hexahedron are marked for adaptation non-uniformly and “hanging” nodes are not allowed. To prevent the refinement propagation, the implementation uses a flexible element division technique [5]. Once an

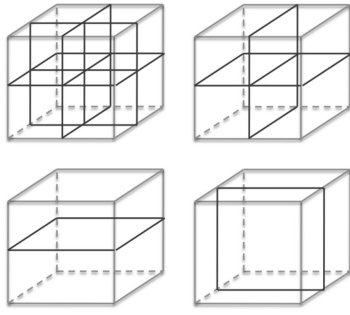


Figure 3: Allowed hexahedral divisions. The last division requires a new vertex in the middle of the hexahedron.

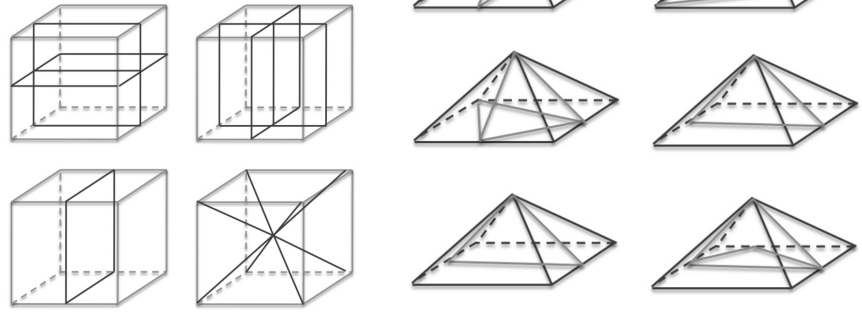


Figure 4: Allowed pyramidal divisions: a total number of 16 combinations are possible.

edge-based structure is in place, the allowed hexahedral division is identified. Fig. 3 shows the seven divisions/combinations implemented in the code. The last division is a special division with a vertex inserted in the middle of a marked hexahedron. The special hexahedral division into pyramids is required to connect the adapted with the non-adapted grid. Furthermore, each pyramid will later be divided into tetrahedrons (see Fig. 4). The error estimate of integral outputs of partial differential equations can be used as goal-oriented grid adaptation indicators [6, 7]. These techniques produce good (and even optimal) numerical grids for the accurate estimation of an output functional. To illustrate the main idea behind this technique, suppose that a nonlinear function $J(U)$ (e.g. heat flux, temperature, or pressure distributions on a body surface) is to be evaluated, where U is the exact solution of a set of nonlinear equations $R(U) = 0$. Given an approximate solution, \bar{U} , we define u as the error of the solution, $u = \bar{U} - U$, and linearize both the nonlinear equation and the functional as follows:

$$R(\bar{U}) = R(U + u) \approx \frac{\partial R}{\partial U} u, \quad (1)$$

and

$$J(\bar{U}) = J(U + u) \approx J(U) + \frac{\partial J}{\partial U} u. \quad (2)$$

This can be re-written as $Au \approx f$, where $A = \partial R / \partial U$, $f = R(\bar{U})$, and $J(U) \approx J(\bar{U}) - g^T u$ where $g^T = \partial J / \partial U$. If u satisfies the primal equation and v satisfies the dual or adjoint equation then $A^T v = g$. Hence,

$$J(U) \approx J(\bar{U}) - v^T f \approx J(\bar{U}) - v^T R(\bar{U}), \quad (3)$$

where $J(\bar{U}) - v^T R(\bar{U})$ is a more accurate estimate for $J(U)$ than $J(\bar{U})$. This computable correction $v^T R(\bar{U})$ is the sensor for our goal-oriented adaptation. This goal-oriented adaptation, and a more classical feature-based (solution gradient) grid adaptation has been used in this project to increase the accuracy of the solution without an excessive increase in computational effort.

3 Gradient computation and design variables

In this project two optimization techniques has been used: Gradient Based Optimization (GBO), and Response Surface Modeling (RSM) with gradient-enhanced Gaussian Process Regression (GPR). Both methods rely on the calculation of sensitivities of the objective and constraints in the design space. In the following subsections we will examine the use of adjoint formulations to perform sensitivity analyses, and the definition of the shape design variables.

3.1 Gradient evaluation using control theory

The adjoint method was originally applied to aerodynamics by Jameson [8], adapting ideas originally formulated by Lions [9] on optimal control of systems governed by partial differential equations (PDEs). The adjoint equations can be conveniently formulated in a framework to calculate the sensitivity of a given objective function \mathcal{J} (f for the RSM problem) to parameters α in a problem governed by the set of equations which can be represented by $\mathcal{G}(U, \alpha) = 0$, where U is the solution. The additional computational cost of solving the adjoint problem is generally of the order of one additional flow solution, and the adjoint variables represent the sensitivities of \mathcal{J} to changes in all of the parameters that define the problem at every point in the domain. There are two main ways to pose the adjoint equations. First, we often speak of a discrete adjoint method, in which the discretized governing equations are used to derive the adjoint equations. Secondly, we often use the continuous adjoint method, in which the adjoint equations are derived from the analytical PDEs. The discrete and continuous approaches are found to have relative advantages and disadvantages over each other. In theory, a discrete method can handle PDEs of arbitrary complexity without significant mathematical development and can treat arbitrary functionals. However, this method requires the evaluation of discrete Jacobians, which we denote as $\frac{\partial}{\partial}$ to distinguish from their continuous alternatives $\frac{\partial}{\partial}$, and there are two main ways to do this. The first is to analytically derive these terms from the discretized forms of the flow residuals and then develop code based on this knowledge, and the second it to use algorithmic Automatic Differentiation, either via source code transformation[10] or operator overloading[11]. The former approach requires significant development, more than that generally required in the continuous method[12], while the latter is computationally expensive, with large memory storage requirements. In comparison, the continuous adjoint requires significant theoretical development but is better connected to the underlying physics, can be solved using a numerical method independent of the flow solution scheme, and, what is more important from the shape design perspective, it provides a closed formula based on a surface integration to evaluate the functional sensitivity. The objective of this section is to describe the way in which we quantify the influence of geometry modifications on either the pressure distribution on the aircraft surface or at an arbitrary location within the domain of interest (namely the near-field, which can be used to derive the equivalent area distribution). Conventional adjoint implementations are typically aimed at reducing a cost function computed from the pressure distribution on the surface that is being modified [13, 14]. In our current work, apart from the traditional functionals defined on the airplane surface (drag, lift, etc.), we will use two objective functions that depend on the near-field pressure distribution: the pressure coefficient distribution on the near-field [15], and the equivalent area distribution calculated from this pressure distribution. The fluid domain Ω is bounded by a disconnected boundary $\delta\Omega$ which is divided into a “far-field” component, Γ_∞ , and a solid wall boundary, S . Ω has been further divided into two subdomains Ω_i and Ω_o separated by the “near-field” boundary Γ_{nf} . Note that Γ_{nf} will remain fixed throughout the optimization process, but the solid surface S will change as needed to meet the optimization criteria. A typical optimization problem seeks the minimization of a certain cost function J with respect to changes in the shape of the boundary S . We will concentrate on functionals defined as integrals over the solid surface S , and integrals over the near-field boundary Γ_{nf} ,

$$J = \int_S \vec{d} \cdot (P \vec{n}_S) ds + \int_{\Gamma_{nf}} g(x, P) ds = \int_S j_S ds + \int_{\Gamma_{nf}} j_{nf} ds, \quad (4)$$

where P is the value of the pressure, \vec{n}_S is a normal vector to the solid surface S pointing outside the domain, $g(x, P)$ is a function that depends on the spatial coordinates and the pressure at the near-field, and \vec{d} is an arbitrary constant vector that we will define later on. The goal is to compute the variation of the above functional caused by arbitrary (and multiple) deformations of S . Upon an infinitesimal deformation δS of the control surface S along the normal direction \vec{n}_S , the cost function varies due to the changes in the solution induced by the deformation:

$$\delta J = \int_S \vec{d} \cdot \delta P \vec{n}_S ds + \int_{\Gamma_{nf}} \frac{\partial g(x, P)}{\partial P} \delta P ds + \int_S (\vec{d} \cdot \vec{\nabla} P) \delta S ds. \quad (5)$$

In the last expression we note that the objective function variation depends on the linearized steady Euler flow equations, $\vec{\nabla} \cdot (\vec{F}) = 0$, where \vec{F} are the convective fluxes. And we resort to the adjoint state $\Psi = (\psi_1, \vec{\varphi}, \psi_5)$

to tackle the variation of the flow variables δP in the objective function:

$$\begin{aligned}\delta J &= \int_S (\vec{d} \cdot \vec{n}_S) \delta P \, ds - \int_S (\vec{n}_S \cdot \vec{\varphi}) \delta P \, ds + \int_{\Gamma_{nf}} \frac{\partial g(x, P)}{\partial P} \delta P \, ds - \int_{\Gamma_{nf}} \Delta \Psi (\vec{n}_{nf} \vec{A}) \delta U \, ds \\ &+ \int_S (\vec{d} \cdot \vec{\nabla} P + (\partial_n \vec{v} \cdot \vec{n}_S) \vartheta + \nabla_S (\vec{v} \vartheta)) \delta S \, ds,\end{aligned}\quad (6)$$

where $\Delta \Psi = \Psi_i - \Psi_o$ is the difference between the values of Ψ above and below the near-field boundary, \vec{A} is the jacobian matrix of the fluxes, and $\vartheta = (\rho \psi_1 + \rho \vec{v} \cdot \vec{\varphi} + \rho H \psi_5)$. Finally, the following adjoint system should be solved

$$\vec{A}^T \cdot \vec{\nabla} \Psi = 0. \quad (7)$$

where the boundary equations will be discussed below. Using a pressure base functional on the surface, the vector \vec{d} is defined as

$$\vec{d} = \begin{cases} \left(\frac{1}{C_\infty} \right) (\cos \alpha \cos \beta, \sin \alpha \cos \beta, \sin \beta), & C_D \quad \text{Drag coefficient,} \\ \left(\frac{1}{C_\infty} \right) (-\sin \alpha, \cos \alpha, 0), & C_L \quad \text{Lift coefficient,} \end{cases} \quad (8)$$

where α is the angle of attack, β is the angle of sideslip, $C_\infty = \frac{1}{2} v_\infty^2 \rho_\infty A_z$, and v_∞ and ρ_∞ denote the infinity values of velocity and density. Using this particular definition of \vec{d} , the boundary condition for the adjoint equations are:

$$\vec{n}_S \cdot \vec{\varphi} = \vec{d} \cdot \vec{n}_S, \quad \text{on } \Gamma_S \quad (9)$$

Apart from surface pressure based functionals, in this work the equivalent area distribution is used in the optimization problems. The equivalent area distribution $A_e(x, \theta)$ at a particular azimuthal angle θ is given by

$$A_e(x, \theta) = \int_0^x C(P - P_\infty)(x - t)^{1/2} \, dt, \quad (10)$$

where $C = 4 \frac{\sqrt{2\beta r}}{\gamma P_\infty M_\infty^2}$, and the line integral is evaluated on a near-field line characterized by an azimuthal angle θ . In order to pose an inverse design problem whereby we attempt to match a target equivalent area distribution, the logical approach is to formulate the problem using a least-squares minimization formulation. Let's minimize the weighted sum of the square of the differences between the computed equivalent area and the target equivalent area at N different points x_i ($i = 0, \dots, N-1$), and different azimuthal angles $k = 0, \dots, M$, with weights ω_{ik} , and target equivalent areas $A_t(x_i, \theta_k)$. The objective function can be written as:

$$J = \sum_{k=0}^M \sum_{i=0}^{N-1} \omega_{ik} [A_e(x_i, \theta_k) - A_t(x_i, \theta_k)]^2, \quad (11)$$

The variation of Eq. 11 is given by:

$$\delta J = \sum_{k=0}^M \sum_{i=0}^{N-1} 2\omega_{ik} [A_e(x_i, \theta_k) - A_t(x_i, \theta_k)] \delta A_e(x_i, \theta_k). \quad (12)$$

On the other hand, the variation of the equivalent area, $A_e(x, \theta)$, with respect to the pressure yields:

$$\delta A_e(x, \theta) = \int_0^x C(x - t)^{1/2} \delta P \, dt. \quad (13)$$

Using this last expression it is possible to separately evaluate the variation of the non-zero equivalent areas at the chosen points as follows:

$$\delta A_e(x_i, \theta) = \sum_{j=0}^{i-1} \int_{x_j}^{x_{j+1}} C(x_i - x)^{1/2} \delta P \, dx, \quad (14)$$

where, for the sake of simplicity, we have substituted the dummy variable of integration t by x . Using the variation of the equivalent area that we have computed in Eq. 12, it is possible to rewrite the variation of the objective function as:

$$\delta J = \sum_{k=0}^M \sum_{i=0}^{N-1} \left[2\omega_{ik} [A_e(x_i, \theta_k) - A_t(x_i, \theta_k)] \sum_{j=0}^{i-1} \int_{x_j}^{x_{j+1}} C(x_i - x)^{1/2} \delta P dx \right], \quad (15)$$

where, to simplify the notation, we will use:

$$\Delta A_e(x_i, \theta_k) = 2C\omega_{ik} [A_e(x_i, \theta_k) - A_t(x_i, \theta_k)]. \quad (16)$$

Rearranging the integrals in Eq. 15, it is possible to write the variation of the objective function as

$$\delta J = \sum_{k=0}^M \sum_{j=0}^{N-2} \int_{x_j}^{x_{j+1}} \sum_{i=j+1}^{N-1} (\Delta A_e(x_i, \theta_k)(x_i - x)^{1/2}) \delta P dx. \quad (17)$$

Using this final expression, the admissible adjoint boundary condition that eliminates the dependence on the fluid flow variation in the inverse equivalent area shape design problem is:

$$\vec{\nabla} \Psi (\vec{n}_{nf} \cdot \vec{A}) = h(x, \theta, P), \quad \text{on } \Gamma_{nf} \quad (18)$$

and the function $h(x, \theta, P)$ is defined at each discrete azimuthal angle θ_k as

$$h(x, \theta_k, P) = \begin{cases} 0 & , \text{ if } -L < x < x_0, \\ \sum_{i=j+1}^{N-1} \Delta A_e(x_i, \theta_k)(x_i - x)^{1/2} & , \text{ if } x_0 \leq x \leq x_{N-1}, \\ 0 & , \text{ if } x_{N-1} < x < L, \end{cases}$$

where x_j is the closest discrete lower value to x .

3.2 Adjoint method applied to engine simulations

The simulation of propulsion systems in SU² is based on the specification of the fan face Mach number at the inflow surface (located somewhere close to the actual location of the fan face), and total nozzle temperature and pressure in the exhaust surface (typically located inside the exit nozzle.) These boundary conditions are imposed in the direct problem using a method based on the local characteristics (see Fig. 5). In the direct problem, characteristic-based boundary conditions are imposed at the outer boundaries where the fluid states are updated depending on the sign of the characteristic speeds, or eigenvalues, given by the well-known diagonalization of the flux Jacobian matrix. Incoming characteristics correspond to the propagation of information into the flow domain, and at these locations, physical boundary conditions, such as mass flow, stagnation conditions, or back pressure, are prescribed. Outgoing characteristics correspond to information propagation out of the domain, and numerical boundary conditions are imposed at these locations that extrapolate the characteristic variable information from within the domain, often using Riemann invariants. However the adjoint implementation is far from trivial [16] and requires a non-standard treatment of adjoint term on the boundaries. Let us return to the integral over the boundaries that was assumed to vanish with the appropriate choice of adjoint boundary conditions. This integral will indeed vanish if the scalar integrand is satisfied at every point on the boundary:

$$\Psi^T (\vec{A} - \bar{I} \vec{u}_b) \cdot \vec{n} \delta U = 0. \quad (19)$$

Therefore, we seek the adjoint state, Ψ , at the boundary that eliminates any contribution from this integral to the variation of the functional through the satisfaction of the preceding expression. A common strategy for the removal of this integral is the imposition of a homogeneous adjoint boundary condition, $\Psi = \mathbf{0}$.

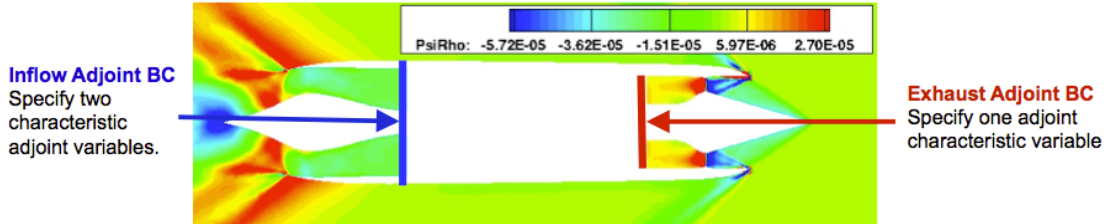


Figure 5: Boundary conditions in the direct simulation of an engine.

Table 1: Number of physical (P) and numerical (N) boundary conditions required for the direct and adjoint problems in three dimensions (the state vector, U , has five components).

	Supersonic Inflow	Subsonic Inflow	Subsonic Outflow	Supersonic Outflow
Direct	5 P, 0 N	4 P, 1 N	1 P, 4 N	0 P, 5 N
Adjoint	0 P, 5 N	1 P, 4 N	4 P, 1 N	5 P, 0 N

While this does force Eqn. 19 to be true, it may be an over-specification and does not take into account the mathematical character of the equations at the boundary. Before further consideration, we will revisit the handling of boundary conditions in the direct problem and the relationship between the direct and adjoint characteristic behavior. The sign of the characteristic velocities has been flipped in the adjoint problem, causing characteristic information to propagate in the reverse direction. This sign reversal occurs due to the integration by parts procedure during the adjoint derivation. The result is that the required type of boundary conditions for the direct and adjoint problem are also reversed, i.e. physical conditions in the direct problem become numerical ones in the adjoint problem and vice-versa, and the reversal implies the existence of a complementary set of well-posed conditions for the adjoint problem. This relationship is summarized for inflow and outflow boundaries in Tab. 1.

Based on this idea, it is possible to propose suitable physical adjoint boundary conditions involving the characteristic speeds based on a manipulation of Eqn. 19 after introducing the diagonalization of the flux Jacobian (see Fig. 6). Recent work by Hayashi et al, advances the notion of characteristic-based boundary conditions for the adjoint equations by connecting the direction of information propagation to the imposition of physical conditions at the boundaries in the direct problem. That is to say, rather than impose conditions using the characteristic variables, one should consider the realizable perturbations in the flow solution, δU , allowed at the boundaries given the particular choice of physical boundary conditions in the direct problem. The latter derivation approach will now be further detailed and extended in a systematic fashion. Consider the boundary, Γ_∞ , to be split into a subsonic inflow and subsonic outflow region for the direct problem. At

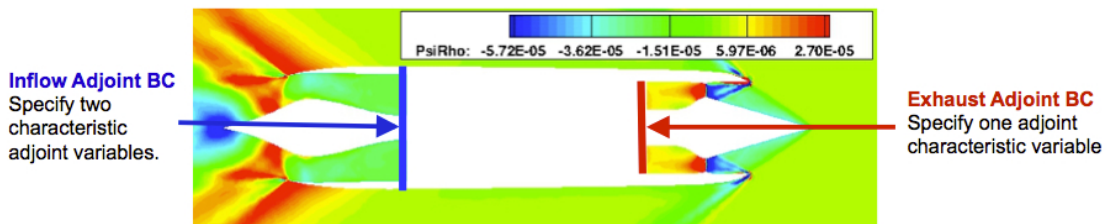


Figure 6: Boundary conditions in the adjoint simulation of an engine.

the inflow, 4 physical conditions can be prescribed, and for clarity in the derivation, we will choose to specify mass flow (ρ and \vec{v}) at this boundary. At the outlet boundary, the typical physical condition of back pressure (p) is imposed. The type of physical conditions chosen for the direct problem has therefore constrained the allowable perturbations at the boundaries. More specifically, we have prescribed $\delta\rho = \delta\vec{v} = 0$ at the inlet and $\delta p = 0$ at the outlet. Therefore, to derive the suitable adjoint boundary conditions for this situation, we must introduce these primitive variable perturbations into Eqn. 19:

$$\Psi^T \left(\vec{A} - \bar{\vec{I}}\vec{u}_b \right) \cdot \vec{n}_\infty M \delta V = 0, \quad (20)$$

where $M = \frac{\partial U}{\partial V}$ is the transformation matrix from conservative to primitive variables and $\delta V = \{\delta\rho, \delta\vec{v}, \delta p\}^\top$ is the vector of primitive variable perturbations. After taking the transpose of Eqn. 20 and evaluating $(\vec{A} - \bar{\vec{I}}\vec{u}_b) \cdot \vec{n}_\infty M$ in three dimensions, the expanded result can be written as

$$\left\{ \begin{array}{c} \delta\rho \\ \delta u \\ \delta v \\ \delta w \\ \delta p \end{array} \right\}^\top \left[\begin{array}{ccccc} v_n & uv_n & vv_n & wv_n & \frac{\vec{v}^2}{2} v_n \\ \rho n_x & \rho u n_x + \rho v_n & \rho v n_x & \rho w n_x & \rho H n_x + \rho u v_n \\ \rho n_y & \rho u n_y & \rho v n_y + \rho v_n & \rho w n_y & \rho H n_y + \rho v v_n \\ \rho n_z & \rho u n_z & \rho v n_z & \rho w n_z + \rho v_n & \rho H n_z + \rho w v_n \\ 0 & n_x & n_y & n_z & \frac{1}{\gamma-1} [\gamma(\vec{v} \cdot \vec{n}) - (\vec{u}_b \cdot \vec{n})] \end{array} \right] \left\{ \begin{array}{c} \psi_\rho \\ \psi_{\rho u} \\ \psi_{\rho v} \\ \psi_{\rho w} \\ \psi_{\rho E} \end{array} \right\} = 0, \quad (21)$$

where $v_n = (\vec{v} - \vec{u}_b) \cdot \vec{n}_\infty$ as a shorthand, $\vec{n}_\infty = \{n_x, n_y, n_z\}^\top$, and $\vec{v}^2 = u^2 + v^2 + w^2$. In this format, physical boundary conditions for Ψ are easily recovered by imposing the constraints on the flow perturbations resulting from the choice of direct boundary conditions and then manipulating the remaining expressions. For example, at the inlet, the imposition of mass flow forces $\delta\rho = \delta\vec{v} = 0$, and therefore, the terms associated with the products in the first four rows of Eqn. 21 are all zero. As δp is the only allowable perturbation in the flow variables remaining, in order to completely remove contributions from the boundary integral the following expression must be satisfied

$$\delta p \left\{ \vec{\phi} \cdot \vec{n}_\infty + \frac{\psi_{\rho E}}{\gamma-1} [\gamma(\vec{v} \cdot \vec{n}) - (\vec{u}_b \cdot \vec{n})] \right\} = 0, \quad (22)$$

and because δp is arbitrary, we recover the admissible physical boundary condition at the mass flow inlet:

$$\psi_{\rho E} = -\frac{\gamma-1}{\gamma(\vec{v} \cdot \vec{n}) - (\vec{u}_b \cdot \vec{n})} \vec{\phi} \cdot \vec{n}_\infty. \quad (23)$$

Using the same derivation approach, physical boundary conditions for the adjoint variables at the outlet can be found. At the outlet, only $\delta p = 0$, and all other flow variable perturbations are allowable. This eliminates any contributions from the final row of the expression in Eqn. 21, and leaves a system of four equations with five unknowns from the first four rows of Eqn. 21 that must be set equal to zero in order to remove any dependence on the remaining perturbations. Choosing $\psi_{\rho E}$ free variable and solving the other four equations in terms of it gives the following four physical boundary conditions:

$$\psi_\rho = \psi_{\rho E} \left[\frac{\gamma e (\vec{v} \cdot \vec{n})}{(\vec{v} - \vec{u}_b) \cdot \vec{n}} + \frac{\vec{v}^2}{2} \right], \quad (24)$$

$$\psi_{\rho u} = -\psi_{\rho E} \left[\frac{\gamma e n_x}{(\vec{v} - \vec{u}_b) \cdot \vec{n}} + u \right], \quad (25)$$

$$\psi_{\rho v} = -\psi_{\rho E} \left[\frac{\gamma e n_y}{(\vec{v} - \vec{u}_b) \cdot \vec{n}} + v \right], \quad (26)$$

$$\psi_{\rho w} = -\psi_{\rho E} \left[\frac{\gamma e n_z}{(\vec{v} - \vec{u}_b) \cdot \vec{n}} + w \right], \quad (27)$$

where $e = E - \frac{\vec{v}^2}{2}$ is the internal energy per unit mass. While they also pursue a characteristic form of the adjoint equations to provide numerical boundary conditions, we will use the values for the free variables ($\vec{\phi}$

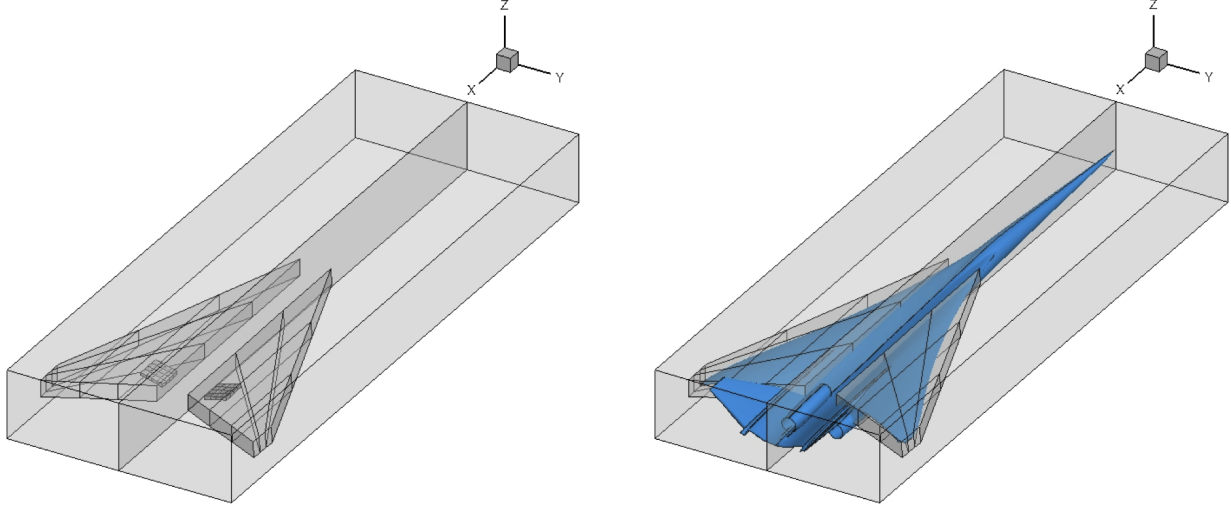


Figure 7: Nested Free-Form Deformation example (volume, main, and secondary boxes are shown).

and $\psi_{\rho E}$) found at the boundaries that satisfy the discretized adjoint Euler equations within the domain. Other sets of subsonic inflow and outflow conditions for the adjoint equations can be derived using the same approach above when choosing different types of physical boundary conditions for the direct problem (such as prescribing stagnations conditions at an inlet). One must simply introduce the perturbation of the chosen quantities and the appropriate transformation matrix from the conservative variables into Eqn. 19 and solve for the admissible conditions in the same manner. Supersonic inlet and outlet boundaries are straightforward in comparison. At a supersonic inlet, all of the flow variables can be prescribed as physical boundary conditions in the direct problem (all characteristics are incoming) which means that none of the adjoint variables will have prescribed values in the adjoint problem. This approach assumes that $\delta U = 0$ due to the direct problem boundary conditions, and therefore, Eqn. 19 is automatically satisfied. In the case of a supersonic outlet, no flow variables can be specified in the direct problem (all characteristics are outgoing), so all of the adjoint variables can be prescribed with $\Psi = \mathbf{0}$ being the choice that exactly satisfies Eqn. 19.

3.3 Design variable definition, and mesh deformation

As we have seen, using the continuous adjoint methodology, SU² can compute the variation of an objective function with respect to infinitesimal surface shape deformations in the direction of the local surface normal at points on the design surface. While it is possible to use each surface node in the computational mesh as a design variable capable of deformation, this approach is not often pursued in practice. A more practical choice is to compute the surface sensitivities at each mesh node on the design surface and then to project this information into a design space made up of a smaller set (possibly a complete basis) of design variables. This procedure for computing the surface sensitivities is used repeatedly in a gradient-based optimization framework in order to march the design surface shape toward an optimum through gradient projection and mesh deformation. In three dimensions, a Free-Form Deformation (FFD) strategy [17, 18] has been adopted. Here an initial box encapsulating the object (wing, fuselage, tails, pylons, nacelles, etc.) to be redesigned is parameterized as a Bézier solid. A set of control points are defined on the surface of the box, the number of which depends on the order of the chosen Bernstein polynomials. The solid box is parameterized by the

following expression

$$X(u, v, w) = \sum_{i=0}^l \sum_{j=0}^m \sum_{k=0}^n P_{i,j,k} B_i^l(u) B_j^m(v) B_k^n(w), \quad (28)$$

where l, m, n are the degrees of the FFD function, $u, v, w \in [0, 1]$ are the parametric coordinates, $P_{i,j,k}$ are the coordinates of the control point (i, j, k) , and $B_i^l(u)$, $B_j^m(v)$ and $B_k^n(w)$ are the Bernstein polynomials. The Cartesian coordinates of the points on the surface of the object are then transformed into parametric coordinates within the Bézier box. Control points of the box become design variables, as they control the shape of the solid, and thus the shape of the surface grid inside. The box enclosing the geometry is then deformed by modifying its control points, with all the points inside the box inheriting a smooth deformation. With FFD, arbitrary changes to the thickness, sweep, twist, etc. are possible for the design of any aerospace system. Once the deformation has been applied, the new Cartesian coordinates of the object of interest can be recovered by simply evaluating the mapping inherent in Eq. 28. To increase the flexibility of the definition of three-dimensional design variables, a nested Free-Form Deformation (FFD) capability has been implemented in Phase II of this project. The key idea of this methodology is the use of a set of nested FFD boxes to explore the design space, with each FFD box corresponding to a different objective (see Fig. 7).

- The volume box (which embeds the entire aircraft surface) is useful for rotating the entire geometry, adjusting the area of the different sections or the total length of the aircraft.
- The main box (which embeds the main wing, fuselage, tail, etc.) is useful for redefining the camber and thickness of the wing, or applying some deformations like twist, sweep, etc.
- The secondary box (in small localized areas) is useful for removing shock waves in those areas (e.g., shocks induced by the nacelles and pylons).

3.4 Managing gradient inaccuracies

Our derivations of the adjoint equations for shape design rely on an assumption of smoothness of the adjoint variables. Discontinuous flow features like shocks violate this assumption and can result in high-frequency oscillations or noise in the surface sensitivities which introduce errors that decorrelate the objective and gradients. These errors can be important in both guiding gradient-based optimization techniques and in the construction of surrogate models that benefit from the calculation of the gradient to reduce the total number of functions evaluations required for a pre-specified accuracy level.

A key assumption in gradient-enhanced Response Surface Modeling is that the correlation of all input information can be modeled by a covariance function. Typically, when performing gradient enhanced RSM with Kriging or GPR, an exact correlation model is used to relate the function and its gradients[19]. As identified by Dwight[20], violations of this model have adverse effects on the quality of the fit.

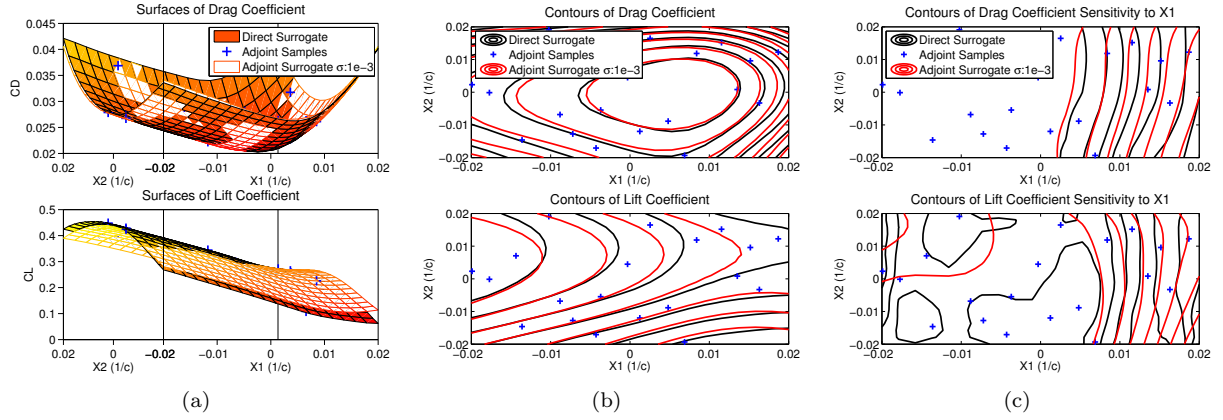
Decorrelation of objectives and gradients can affect gradient-based optimization as well. However, many modern methods approximate Hessians with an under-fitting surrogate model, such as a quadratic polynomial, which expresses a weak assumption of the behavior of the data in small regions. Along with various relaxation techniques, this makes GBO more robust, but not insensitive, to gradient errors.

A key problem that we have identified, explored and addressed during this project is the quality degradation of optimization methods that occurs when using function and gradient data that are decorrelated because they possess varying levels of “physical” exactness [21].

Here we define physical exactness as the ability of the numerical model to describe the real physical flow. We include the governing flow equations, adjoint equations, and even finite differencing in this set of numerical models. Each numerical model has limits of physical exactness, based on, for example, numerical scheme or step size. In this limit, we describe a digit of precision as “physically representative” if an engineer would use it to make a decision between two candidate designs. Experience is largely a determining factor in setting the maximum level of physical representativity. These factors will negatively affect the performance

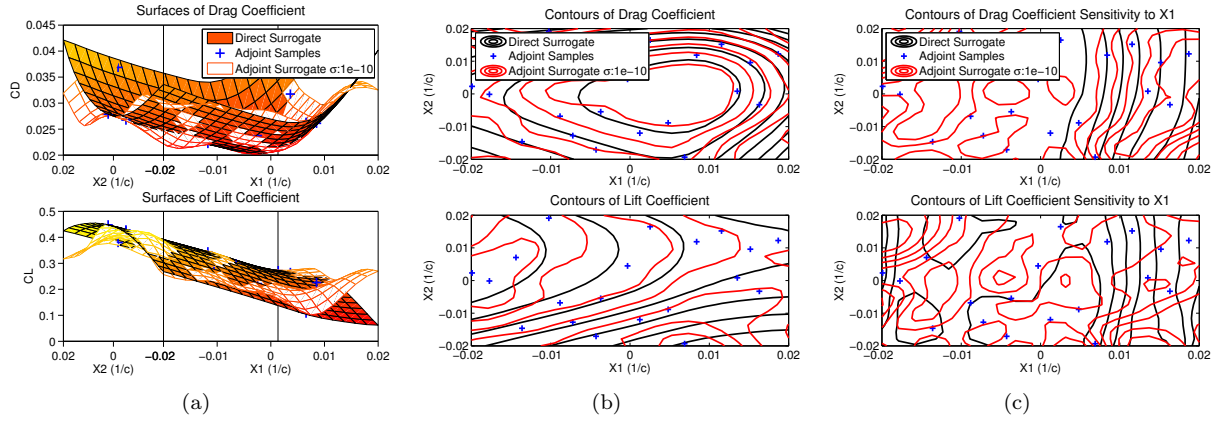
of a response surface and can hamper the convergence of SBO and GBO optimizations without methods to manage gradient inaccuracies.

For example, we apply a gradient-enhanced GPR technique to training data from a NACA0012 test case with two Hicks-Henne bump functions on the top and bottom of the airfoil at mid-chord. In Fig.8 and Fig.9, we generate response surfaces for drag and lift with 20 latin hypercube sampled training data with continuous adjoint-based gradients. We then compare the effect of changing the amount of noise the response surface is allowed to model. For reference we compare the fits to a response surface generated from a 10x10 grid of direct solution data only. The data shows that if a noise of 1e3 (in dimensions of the design variable) is allowed in the response surface, a reasonable quality fit is achieved with 3.3% mean estimation error in the lift objective, and 1.2% mean estimation error in the drag objective. If noise is not allowed, or restricted to be very low, then the accuracy of the response surface degrades significantly. A methodology that we have derived for this work allows a certain level of noise in the gradients to ensure both the accuracy of the resulting fit and the beneficial effects of exploiting the gradient information during the construction of response surface models.



Mean Errors: Lift Objective: 3.3%; Lift Gradient: 10.9%; Drag Objective: 1.2%; Drag Gradient: 3.4%

Figure 8: Example RSM with Adjoint Gradients, Noise Tolerance = 1e-3



Mean Errors: Lift Objective: 5.5%; Lift Gradient: 50.8%; Drag Objective: 4.8%; Drag Gradient: 12.8%

Figure 9: Example RSM with Adjoint Gradients, Noise Tolerance = 1e-10

4 Optimization framework

We have used two optimization approaches in this work. The flow chart in Fig. 10 compares the eXtended Design Structure Matrices (XDSMs) of the two approaches [22]. Central to both approaches is the physical model, in this case the SU² suite, which accepts design variables, performs the various analyses (deformation, direct and adjoint solutions) and returns performance variables and their derivatives. The first approach, Gradient Based Optimization (GBO), directly drives the physical model. The second approach, Surrogate Based Optimization (SBO), uses a response surface model constructed using Gaussian Process Regression (typically enhanced with gradient information) to guide the physical model. The intent of this additional complexity is to reduce function evaluations and wall time required to perform global optimization. The approach has been programmed in Python, which easily interfaces with the SU² suite.

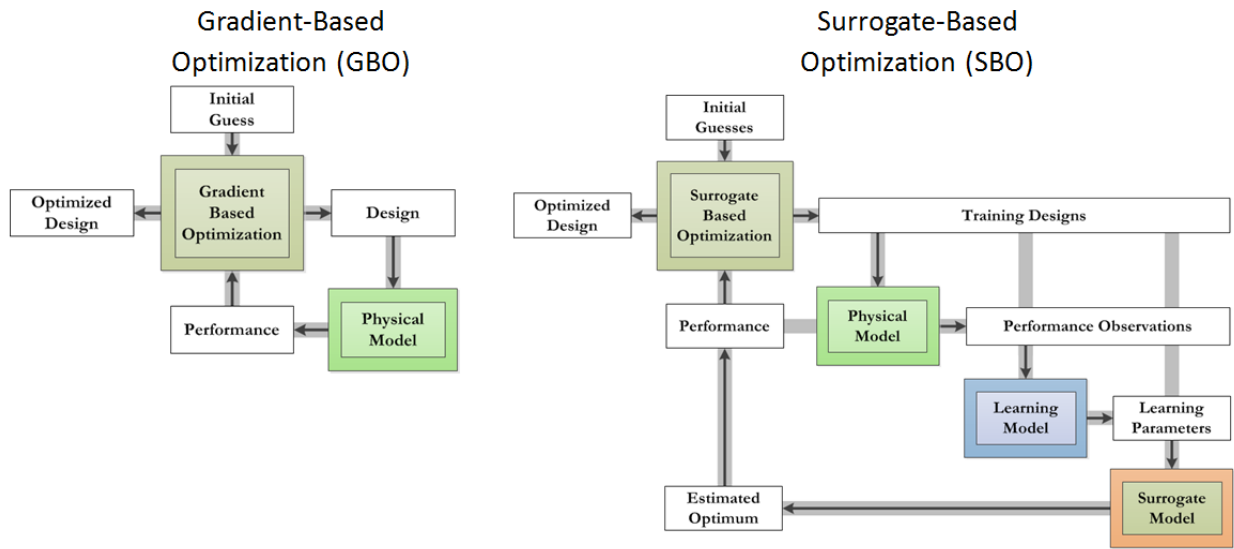


Figure 10: Comparison of Optimization Frameworks.

4.1 Gradient based optimization

Compared to SBO, gradient based optimization can require fewer function evaluations in higher-dimensional design spaces at the cost of performing local optimization. In this study, we use a sequential quadratic programming (SLSQP) optimizer built into the Scientific Python (scipy) toolbox [23, 24], a well-established open-source software for mathematics, science and engineering. The SciPy library provides many user-friendly and efficient numerical routines for the solution of non-linear constrained optimization problems, such as conjugate gradient, Quasi-Newton or sequential least-squares programming algorithms.

At every iteration, the SLSQP code chooses a search direction based on the constrained optimization of a second-order least-squares response surface (the quadratic program). It then performs a line search in this direction to find a point that satisfies first- and second-order optimality conditions. At each major iteration the response surface is updated with the BFGS update rule. Convergence is declared when improvement of the objective, or norms of the gradients and Hessian fall below a tolerance.

The SciPy routines require as inputs the values and gradients of the objective functions as well as the chosen constraints, but not necessarily in a sequential order. Thus the physical model must also keep track of what simulations have been run to avoid unnecessarily repeating an analysis. This is handled by the SU² suite's optimization wrappers.

4.2 Surrogate Based Optimization

To address the high computational cost of the CFD simulations and to enable global design space optimization, we are using Response Surface Modeling (RSM) with gradient-enhanced Gaussian Process Regression (GPR) [25]. Gradient information available from an adjoint solution is used to increase the accuracy of the RSM at lower computational cost. With the solution of one flow and one adjoint simulation, we are able to provide $1 + d$ pieces of information to the response surface model. This is much more efficient than running $1 + d$ flow solutions to yield approximately the same amount of information.

A large body of work has been built around RSM approaches, especially using a stochastic modeling technique known as Kriging[26, 27] and its gradient enhanced relative known as Co-Kriging[2, 19]. GPR is a superset of Kriging, and is formulated by conditioning a probability distribution over random functions. In general both GPR and Kriging result in the same mathematical fitting models[27, 28]. However, GPR is built within the context of machine learning, which allows more flexibility when dealing with complex design spaces[29].

Response surface models can be used in what is known as Surrogate-Based Optimization (SBO) (see Sec.4.4) to search for optimum designs in a global design space. To generate an initial response surface, a set of designs are sampled using Design of Experiment (DOE) techniques such as Latin Hypercube Sampling. Because the locations of these points are not dependent on each other, they can be run in parallel, dramatically reducing wall-clock time if the resources are available. After this initial sample, additional design points are chosen using an Infill Sampling Criterion (ISC). It is common to take advantage of the uncertainty information available from stochastic response surface models like GPR to efficiently add points that attempt to improve the accuracy of the model near regions of optimal design[30].

An equally large body of work has been built around surrogate-based optimization. Forrester provides a thorough summary of different infill sampling criterion[31]. Several studies describe its application to aircraft design problems [32, 33, 34, 35]. In previous work, we explored the use of ISCs to further improve the SBO process using a hybrid infill sampling criteria with expected improvement and estimated optimum[25].

4.3 Response surface modeling with Gaussian process regression

Gaussian Process Regression is a super-set of Kriging. It approaches regression from a Bayesian standpoint by conditioning a probabilistic function to training data[36]. For example, it can be shown that in the case where the probabilistic prior is assumed to be a Gaussian process with a stationary zero mean, the resulting model matches that of Simple Kriging (SK). Because GPR is posed as a conditioning problem and not an expected error minimization problem, it may have more flexibility when handling poorly behaved design spaces, such as discontinuities as found by Chung[2], or in our case noisy response functions. This is one of the key motivations for our exploration of Gaussian Process Regression.

Following the derivation given by Rasmussen[36], Gaussian Process Regression is approached by conditioning a multivariate normal distribution

$$f \sim \mathcal{N}(\mu, [\sigma]), \quad (29)$$

where f is a normally distributed function with mean vector μ and standard deviation matrix $[\sigma]$. In this work, we take a uniformly zero mean vector, and populate the standard deviation matrix with a covariance submatrix k that is a function of training and estimated data:

$$\begin{bmatrix} f_p \\ f_k^* \end{bmatrix} \sim \mathcal{N} \left(0, \begin{bmatrix} k(x_p, x_q) & k(x_p, x_j^*) \\ k(x_k^*, x_q) & k(x_k^*, x_j^*) \end{bmatrix} \right), \quad (30)$$

$$\{ f_i(x_i) \mid i = 1, \dots, n \}, \{ f_t^*(x_t^*) \mid t = 1, \dots, m \}.$$

The notation $(\cdot)^*$ is used to distinguish the estimated data from the training data. Additionally, index notation is used to describe the sub-blocks of the covariance matrix, where $k(x_p, x_q)$ would be equivalent to the matrix k_{pq} . There are n training point vectors x with function values $f(x)$, and m estimated data point vectors x^* with function values $f^*(x^*)$.

Of the data, we do not know the estimated function values f^* . We do know the training data locations x and function values $f(x)$, as well as the desired estimated data locations x^* . Following Rasmussen's derivation [36], we condition the normal distribution with the data we do know

$$f|x^*, x, f \sim \mathcal{N}(f^*, \mathbb{V}[f^*]), \quad (31)$$

which allows us to identify useful relations for estimating a function fit,

$$\begin{aligned} f_k^* &= k(x_k^*, x_q) k(x_p, x_q)^{-1} f_p \\ \mathbb{V}[f_k^*] &= (k(x_k^*, x_j^*) - k(x_k^*, x_q) k(x_p, x_q)^{-1} k(x_p, x_j^*))_k \end{aligned} \quad (32)$$

where $\mathbb{V}[f^*]$ is the covariance of the estimated value f^* . These are the relations needed for coding a GPR program. Rasmussen provides an example algorithm that simplifies these relations by using Cholesky decomposition [36]. The covariance function models the spatial correlation between data points. It is chosen based on the types of functions that are going to be modeled. Highly-smooth or weakly-smooth functions would be examples of different types of functions that would require different choices of covariance functions. A common covariance function is the Gaussian function of the Euclidean distance between points:

$$\begin{aligned} k(x_p, x_q) &= k(p, q) = \theta_1^2 \exp \left(-\frac{1}{2\theta_2^2} \sum_{z=1}^d (p_z - q_z)^2 \right) \\ &\quad \{p_i, q_i, \frac{\partial}{\partial x_i} \mid i = 1, \dots, d\}, \end{aligned} \quad (33)$$

where d is the number of dimensions, and p and q are the position vectors chosen from the design space x . There are two degrees of freedom in the covariance function. These are known as hyper-parameters. In terms of their effect on the function fit, the nominal variance θ_1 is a measure of the amount of variance allowable between points, and the length scale θ_2 is a measure of the range of influence of a point.

Modeling the influence of gradients on the fit involves adding information to the covariance matrix. This requires finding a covariance function to model the correlation between points and derivatives. One approach to do this is shown for Co-Kriging by Chung[37] by deriving the covariance functions from the definitions of variance and derivative. Another approach suggested by Papoulis[38] and used for gradient enhanced GPR by Solak[39] exploits the theorem that the linear operation of an expected value is the expected value of the linear operation. The result from either approach is the same. To include gradient information in the fit, simply take the derivatives of the covariance function:

$$\begin{aligned} k\left(\frac{\partial p}{\partial x_v}, q\right) &= \left. \frac{\partial k(p, q)}{\partial x_v} \right|_q \\ k\left(p, \frac{\partial q}{\partial x_w}\right) &= \left. \frac{\partial k(p, q)}{\partial x_w} \right|_p \\ k\left(\frac{\partial p}{\partial x_v}, \frac{\partial q}{\partial x_w}\right) &= \left. \frac{\partial}{\partial x_w} \left(\left. \frac{\partial k(p, q)}{\partial x_v} \right|_q \right) \right|_p. \end{aligned} \quad (34)$$

This is where the assumption of a correlation model between function value and its gradient is made. It is a natural and powerful assumption. However, because there will be d -times more gradient information than function values, inaccurate gradients can override the behavior of the fit.

The gradient information must be packed into the covariance matrix. This can be done by updating the definition for the covariance function as follows:

$$k(p, q) \rightarrow \begin{bmatrix} k(p, q) & k\left(p, \frac{\partial q}{\partial x_w}\right) \\ k\left(\frac{\partial p}{\partial x_v}, q\right) & k\left(\frac{\partial p}{\partial x_v}, \frac{\partial q}{\partial x_w}\right) \end{bmatrix} \quad f_p \rightarrow \begin{bmatrix} f_p \\ \frac{\partial f_p}{\partial x_d} \end{bmatrix}, \quad (35)$$

where submatrix $k(p, q)$ has dimension $n \times n$, and submatrix $k\left(\frac{\partial p}{\partial x_v}, \frac{\partial q}{\partial x_w}\right)$ has dimension $n d \times n d$.

A useful extension of this formulation is estimating the gradients of the response surface given only objective information. This simply involves omitting the blocks associated with the training data gradients

but keeping those associated with the estimated data gradients. Given a reasonable amount of objective data, this can be used to build an analytic estimate of the gradients in the design space for those data. While the curse of dimensionality unfortunately constrains this method to low-dimensional design spaces, it is still useful for generating an accurate reference when evaluating the errors of the various sensitivity analysis methods.

We are able to model several types of noise within the GPR framework. Allowing noise can relax the assumption of exact correlation between objective and gradient information. The effect on the response surface will have the form:

$$f_N^*(x) = f^*(x) + \epsilon, \quad (36)$$

where ϵ is a noise model. Adding noise to our model requires us to update our covariance matrix structure:

$$[\sigma] = [k] + [k_N], \quad (37)$$

where $[k]$ is the full covariance matrix for functions and gradients, and $[k_N]$ is the noise component of the covariance matrix.

A simple but useful model is an independent identically-distributed Gaussian noise with zero mean and given variance. This will only affect the self-correlated covariance terms along the diagonal of $[k_N]$. The noise covariance matrix will then take the form:

$$[k_N] = \begin{bmatrix} \theta_3^2 I_{n',n'} & 0_{n',m'} \\ 0_{m',n'} & \theta_4^2 I_{m',m'} \end{bmatrix}, \quad (38)$$

where I and 0 are identity and zero matrices with $n' = n(1+d)$ and $m' = m(1+d)$. Note we have allowed two separate noise hyper-parameters for the function values and gradients. Adding this diagonal component to the covariance matrix relaxes the requirement that the fit exactly honors the training data. Depending on the magnitude of the noise hyper-parameter, the fit will be allowed to stray a certain distance away from the data. This will allow us to model noise in the gradients due to inaccuracies from mesh refinement or the particular sensitivity method.

Steps are taken to improve numerics and generality of the method by scaling the data based on the initial LHC sample. The sampled objective function range, and design variable bounds are linearly scaled according to:

$$\begin{aligned} f &= f' \cdot f_{ref} + f_{off} & s.t. \quad [min(f), max(f)] &\rightarrow [0, 1] \\ x_z &= x'_z \cdot x_{z,ref} + x_{z,off} & s.t. \quad [min(x_z), max(x_z)] &\rightarrow [0, 1], z = 1, \dots, d \\ \frac{\partial f}{\partial x_z} &= \frac{\partial f'}{\partial x'_z} \cdot \frac{f_{ref}}{x_{z,ref}}. \end{aligned} \quad (39)$$

Several benefits are realized from scaling the data past improving the condition of the covariance matrix, if we can assume the response surface is smooth with a nominal amount of variation. First, we can approximately say the variation of data is brought to be the same order of magnitude. This allows us to assume isotropy of variation in each dimension and reduce the number of length scale parameters to one. This significantly reduces the computational cost of hyperparameter learning. Second, this allows us to claim that the scaled magnitude of the noise parameters for f and $\frac{\partial f}{\partial x}$ are of the same order of magnitude. This is important since the value of the noise in the gradients is difficult to estimate *a-priori*. Finally, it makes the problem robust to more design problems, where different design parameters of different scales can be mixed without having to learn separate length scales.

To use the covariance function, the hyper-parameters θ_{1-4} must be chosen. Different values will yield different fits, each being a different view of the data. We present the method of tuning the required hyperparameters by maximizing Marginal Likelihood[36].

Marginal Likelihood measures how well a given set of hyperparameters describes the training data. Finding its argument maximum is a common way to select hyperparameters for GPR. It can be defined mathematically with:

$$\log p(f_p | x_p, \theta) = -\frac{1}{2} f_p^\top [\sigma]^{-1} f_p - \frac{1}{2} \log |[\sigma]| - \frac{n}{2} \log 2\pi, \quad (40)$$

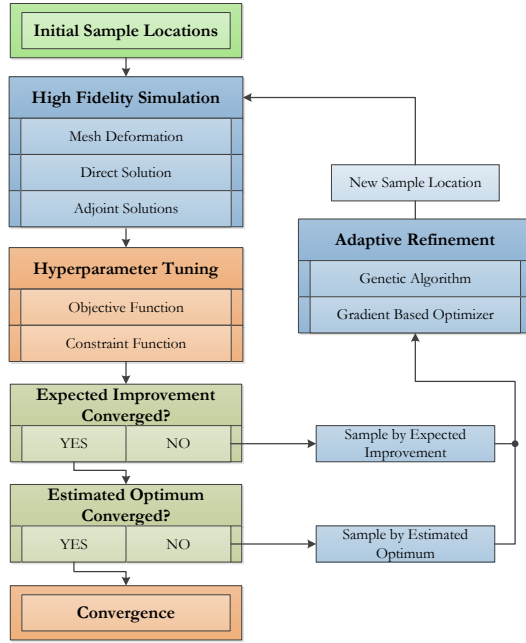


Figure 11: Surrogate Based Optimization Process.

where θ is a vector of hyper-parameters. Maximizing the marginal likelihood is itself an optimization problem. This problem can be solved with a gradient based optimizer, however the space is not guaranteed to be convex. This study used modified Newton's method with multiple starting locations chosen with Latin Hypercube sampling to account for multiple local minima.

In order to avoid honoring the gradient information over the objective function information, we constrain the noise hyperparameters according to

$$\theta_3 < \theta_4. \quad (41)$$

If we had not scaled the gradient data to the same order of magnitude as the objective data, this constraint would not be appropriate. The constraint is especially important in a problem with inaccurate gradient information, as the presence of high-dimensional gradients can overpower the objective data and result in a response surface with high error at the training data locations.

4.4 Methodology for surrogate based optimization

We have developed a surrogate based optimization approach that follows the basic process flow shown in Fig. 11. A summary of this process is first described, and detail on modifications to the traditional process are then given. Our approach to surrogate based optimization involves three sampling stages - first an initial sample, second an efficient global refinement, and last a refinement of the estimated minimum. These stages are designed to efficiently dissect the design space and attempts to yield the best estimate of the optimum only in the last sample. The main motivation of this construction is to build in a sense of convergence that is similar to that of gradient-based optimization.

In the first stage, the design space is sampled with a set of well-spread initial design points chosen with Latin Hypercube (LHC) sampling restricted to the hypercube,

$$x_k^l < x_k < x_k^u, \quad k = 1, \dots, d. \quad (42)$$

The initial $x = 0$ design is included with this sample as the first point. Given enough computational resources, this first phase is nicely parallelizable as each design point can be run independently. The number of samples to take should depend on the expected complexity of the design space. For the problems explored in this study, two samples per dimension has worked well.

Second, the surrogate model is refined using an Infill Sampling Criteria (ISC) based upon Expected Improvement (EI). This sampling criteria is well known for its ability to leverage both estimated function value and uncertainty to balance design space exploration (targeting global accuracy) and exploitation (targeting local optimality)[31, 40]. Expected improvement is commonly expressed as:

$$\begin{aligned} E[I(x)] &= E[\max(f_{\min} - F, 0)] \\ &= (f_{\min} - f^*)\Phi\left(\frac{f_{\min} - f^*}{s^*}\right) + s^*\phi\left(\frac{f_{\min} - f^*}{s^*}\right). \end{aligned} \quad (43)$$

In the above, $\Phi(\cdot)$ and $\phi(\cdot)$ are the standard normal distribution and density functions, $s^* = \mathbb{V}[f^*(x)]$ is the estimated variance of the response surface, and f_{\min} is the minimum of the current training point sample.

If additional information in the form of constraints is available in the problem, it can be added to the infill sampling criterion by searching in locations of high probability of feasibility. Following the method described by Shimoyama[41], this is done by building a second surrogate model and evaluating the expected improvement, conditioned by the probability of feasibility,

$$P[c(x) < 0] = \phi\left(\frac{c^*}{s_c^*}\right), \quad (44)$$

where the constraint is formulated as $c(x) < 0$, and c^* is the estimated constraint value with estimated variance, s_c^* .

In our experience, the expected improvement infill sampling criteria often added training data near the box boundaries and corners of the design space. This is inefficient because at least half of a training point's region of influence is wasted modeling the response surface outside the boundaries. To encourage sampling inside the design space, we apply a penalty function,

$$B(x) = 1 - \exp\left(-\frac{1}{2}\min\left(\frac{x_k - x_k^l}{b_k^2}, \frac{x_k^u - x_k}{b_k^2}, k = 1, \dots, d\right)\right), \quad (45)$$

which is a Gaussian function of the distance from the nearest hypercube boundary. In this study, the length-scale b_k is set to $0.1(x_k^u - x_k^l)$, or 1% of the hypercube dimension k 's length. The above penalty function is greatly simplified in the non-dimensional space constructed in the previous section.

Combining the Expected Improvement, Constraint Penalty, and Boundary Penalty results in the first infill sampling criterion:

$$\begin{aligned} ISC_1(x) &= E[I(x)] \cdot P[c(x) < 0] \cdot B(x) \\ x_{new} &= x \mid \max(ISC_1(x)), \end{aligned} \quad (46)$$

The response surface is refined by sampling $f(x_{new})$ and $c(x_{new})$ in this way until the criterion converges to a small value,

$$R_1(i) = ISC_1(x_i) < T_1, \quad (47)$$

where T_1 is a specified tolerance.

While indeed efficient, our experience with GPR-based SBO has suggested that after expected improvement has converged to some preset value, it becomes difficult to discover the sharp and narrow wells that develop in its surface. For this reason, it can be more efficient to switch to an infill sampling criteria based on pure exploitation.

Thus the final phase of our method's design space sampling is based on refining around the estimated deterministic optimum of the surrogate model:

$$\begin{aligned} ISC_2(x) &= f^*(x), \\ x_{new} &= x \mid \min(ISC_2(x)), \text{ s.t. } c^*(x) < 0. \end{aligned} \quad (48)$$

This procedure continues until the measured improvement of the design sample converges to a small value

$$R_2(i) = \max (f_{best} - f_i, R_2(i-1)) < T_2, \quad (49)$$

or until the sampling stalls after not finding an improvement for a predetermined number of iterations. In the above equation, T_2 is another specified tolerance, and f_{best} is the minimum of the training data that came before f_i . We use similar monitors on the change in location of the best point, and the norm of the gradient of the best point, but often the function value of best point converges the fastest.

Both the second and third sampling stages use a two-part optimization of the surrogate model. First a genetic algorithm is used to find a reasonable estimate of the global minimum. This estimate is fed as the initial guess to a gradient based optimizer, which returns a better estimate of the global minimum. This process requires several thousand function evaluations of the response surface, but is far less expensive than evaluating an additional high-fidelity design point.

4.5 Python package

The above methods have been implemented in a python package called "pyGPR" to allow for greater portability. The package api is built in a similar architecture to the XDSM flow chart in Fig. 10. The basic steps for using the package involve defining "Models" for each objective or constraint. Each Model is defined by a Kernel, and a set of Training data. Code listing 1 below shows an example of defining one such model. In

Listing 1: pyGPR Model Definition

```
Y,DY = Func_Y(X)
Train = pyGPR. Training(XB,X,Y,DY)
Kernel = pyGPR. Kernels. Gaussian(Train)
Model_Y = pyGPR. Modeling(Kernel)
```

this listing, training data locations X are chosen using latin hypercube sampling, Y and DY are the objective and gradients at X, and XB is a matrix defining the upper and lower bounds of the design space.

The function and model are then used to execute the sampling strategy described earlier. The present code implements adaptive refinement using expected improvement and estiamted minimum and has been abstracted such that it can accept multiple constraints constraints. Listing 2 shows an example of starting this process. Monitoring of the optimization process is provided with convergence plots. An example convergence

Listing 2: pyGPR Sampling Execution

```
Sample = pySBO. Sampling( Model_Y , Func_Y , [ Model_C1 , Model_C2 ] , [ Func_C1 , Func_C2 ] )
Sample . Optimize()
```

plot shown in Fig.12 monitors the reduction in expected improvement, as well as the change in best training point objective, gradient, and location. It shows here that the objective function was converged to 1e-6% in 27 function evaluations. This plot is from the optimization example presented in Sec.5.3.

5 Numerical results

5.1 Grid adaptation

The gradient-based adaptation methodology was also tested with highly-complex geometries. For example, the adaptation techniques were used to study the effects of propulsion integration for the Lockheed N+2

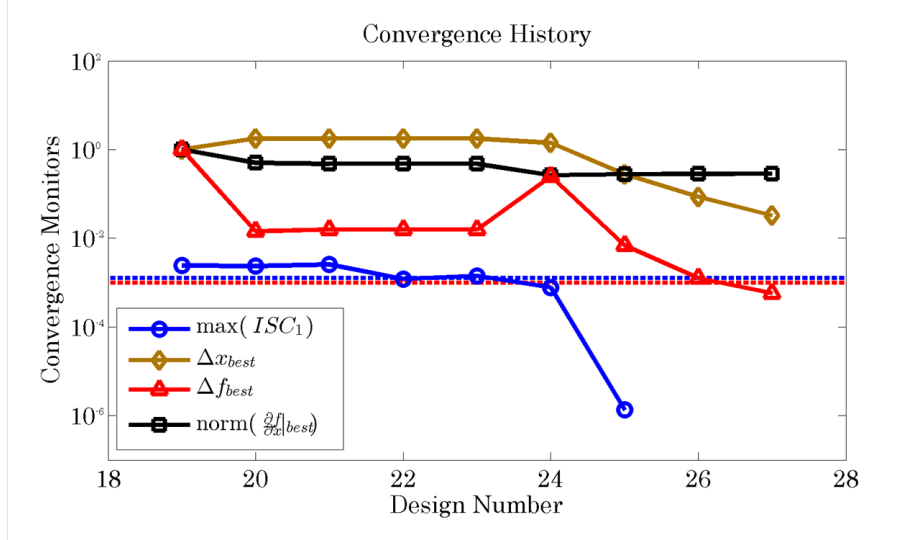


Figure 12: Example Surrogate Based Optimization Convergence Plot

aircraft geometry ($M_\infty = 1.7$, angle of attack 2.1°). Here the final target was to evaluate the pressure signature in the near-field, and two levels of solution adaptation were used to capture minor effects due to the propulsion. In Fig. 13 and Fig. 14 the baseline and two levels of adaptation are shown. The baseline mesh has 1.3 million nodes, while the adapted grids have 1.5 and 1.8 million nodes, respectively. The effect of the adaptation is also reflected in the near-field pressure signature, plotted at different azimuthal angles in Fig. 15, which shows minor differences. The effects of propagating the resulting near-field signatures at varying levels of adaptation are presented in Sec. 6.

5.2 Shape optimization maintaining equivalent area

The objective of this particular problem is to demonstrate the ability of the adjoint formulation to enable design optimization while maintaining a target equivalent area distribution across multiple azimuths [25]. More specifically, a gradient-based, multi-objective optimization of the Lockheed N+2 design was performed ($M_\infty = 1.7$, angle of attack 2.1°). This was done for 9 iterations with azimuths varying from 0° to 60° (pressure disturbances above 60° do not reach the ground) and the coefficient of drag was reduced from 0.00875 to 0.00850, a 3% reduction. The ability to compute sensitivities is a fundamental capability and very useful output of SU². Fig. 18 and Fig. 19 show the sensitivities of C_D and C_L with respect to variations of the geometry in the local normal direction. The magnitude of the surface sensitivity is related to changes in the cost function caused by changes in geometry, and designers can use this sensitivity information to determine appropriate parameterizations of the configuration prior to optimization. Figs. 16 and 17 show a comparison of the near-field pressure distributions, and Fig. 20 and Fig. 21 show a comparison of equivalent areas between the baseline and final design. The plots for equivalent area distribution show at most a 2% change from the target. The overlay of the baseline and final geometry in Fig. 22 shows that the upper wing surface was flattened and the lower fuselage deformed inwards in order to reduce the drag. To compensate for the fuselage effect on the equivalent area, the lower wing surface was deformed downwards as well. A comparison of surface pressures for the design study is given in Fig. 23, and contours of the density and adjoint density fields are shown in Fig. 24 and Fig. 25.

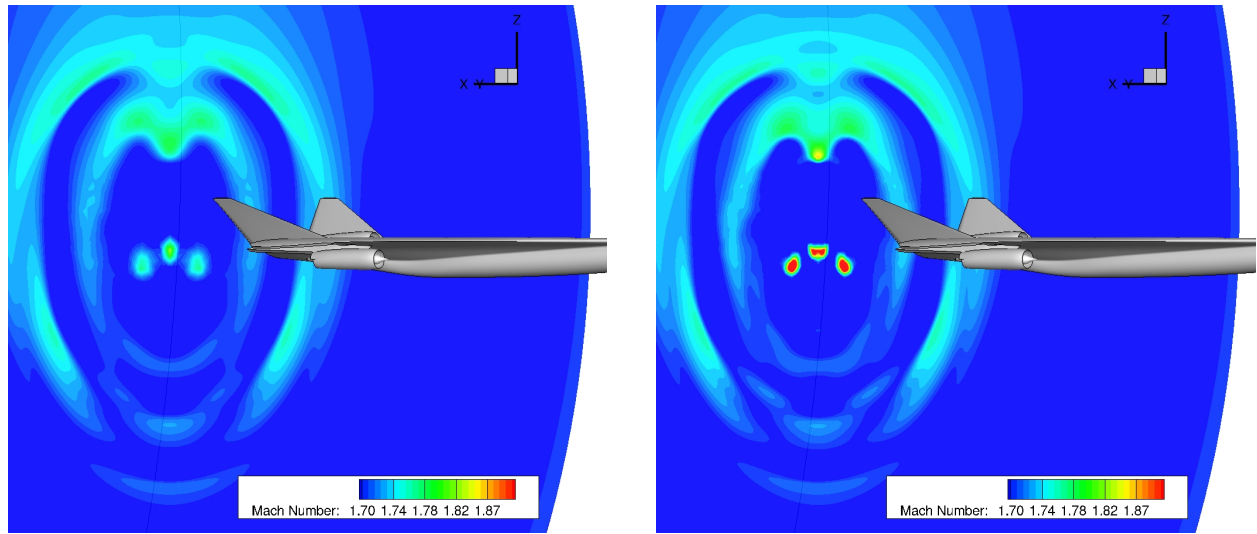


Figure 13: Gradient-based mesh refinement for the Lockheed N+2 aircraft geometry ($M_{\infty} = 1.7$, AoA 2.1° , with engine propulsion effects), showing the change in the Mach number contours.

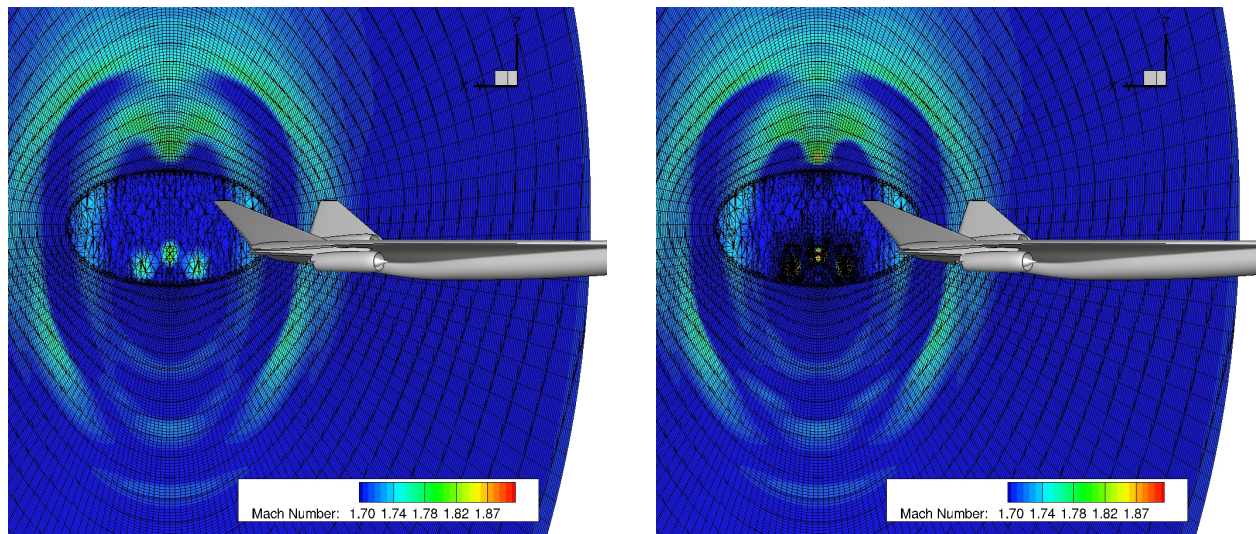


Figure 14: Gradient-based mesh refinement for the Lockheed N+2 aircraft geometry ($M_{\infty} = 1.7$, AoA 2.1° , with engine propulsion effects), showing the change in the grid.

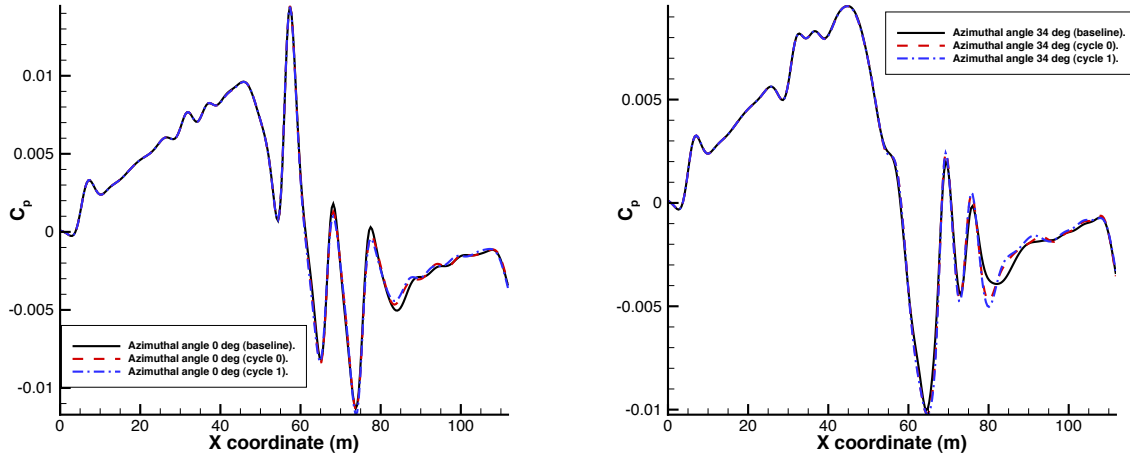


Figure 15: Near-field pressure signatures with different levels of grid adaptation.

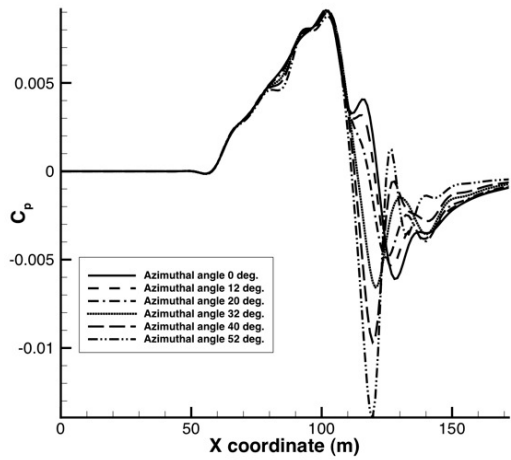


Figure 16: Baseline near-field pressure signatures.

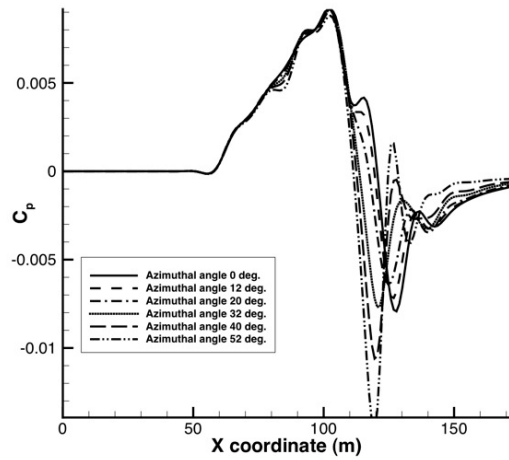


Figure 17: Final near-field pressure signatures.

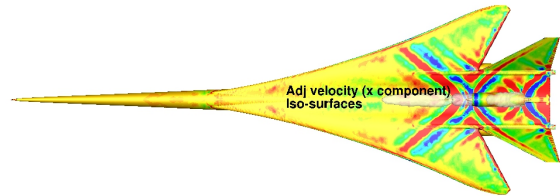
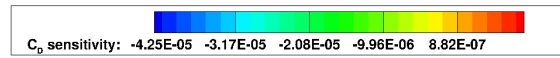


Figure 18: Drag sensitivity ($M_\infty = 1.7$, AoA 2.1°), including propulsion effects.

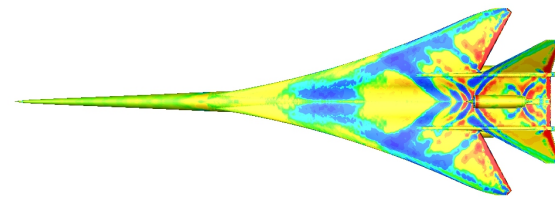
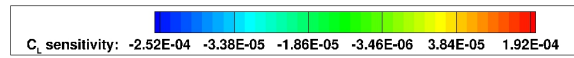


Figure 19: Lift sensitivity ($M_\infty = 1.7$, AoA 2.1°), including propulsion effects.

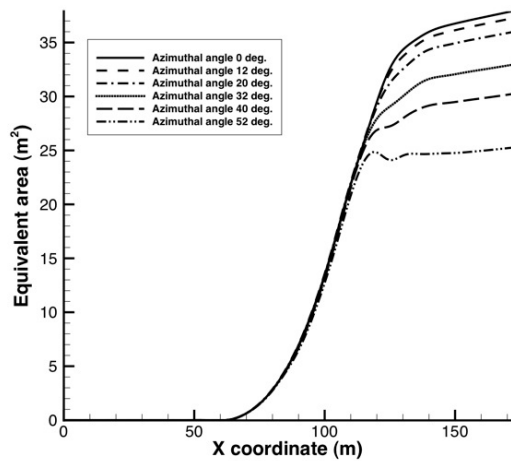


Figure 20: Baseline target equivalent area distributions.

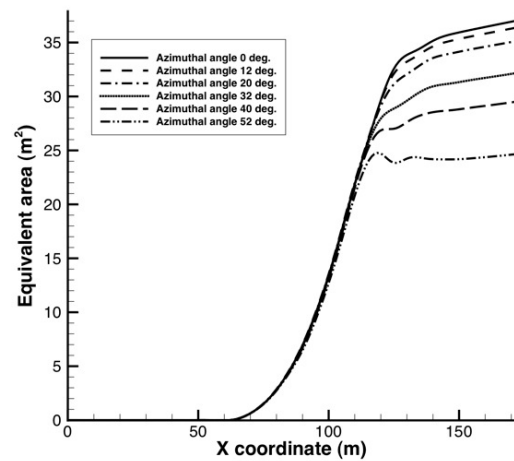


Figure 21: Final target equivalent area distributions.

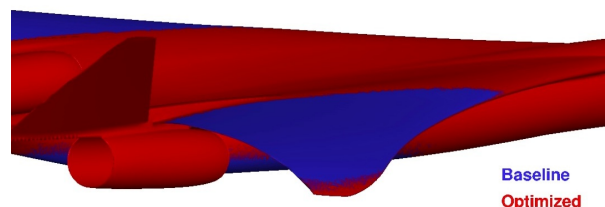


Figure 22: Baseline and final N+2 geometry comparison.

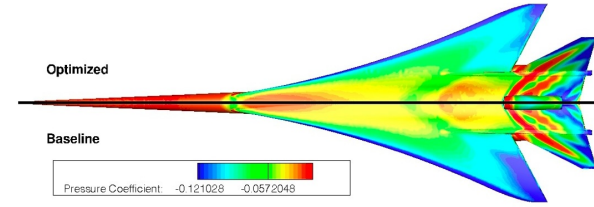


Figure 23: Baseline and final N+2 surface pressures.

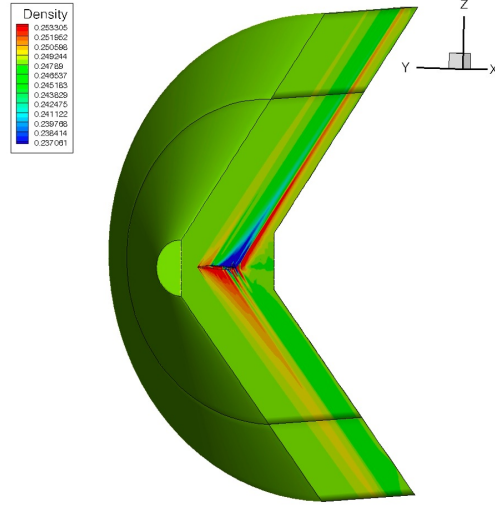


Figure 24: Contour plot of density for the N+2 baseline configuration.

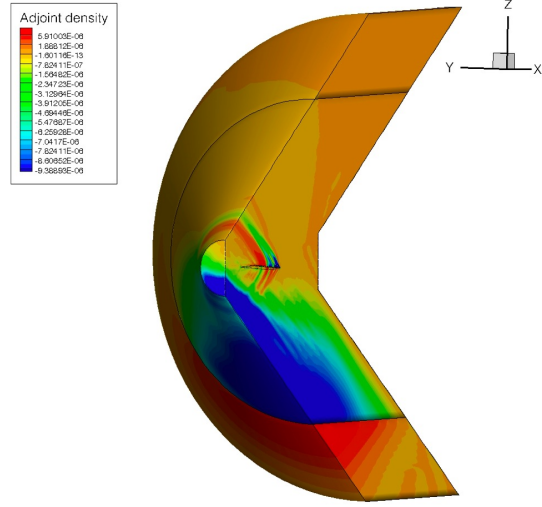


Figure 25: Contour plots of density adjoint variable for the N+2 baseline configuration and equivalent area as objective function.

5.3 Unconstrained surrogate-based optimization

An unconstrained, surrogate-based drag optimization was performed on the N+2 configuration using the 9 Free-Form Deformation control points placed on the upper wing surface (see Fig. 26). A comparison of the convergence history with a gradient-based optimization of the problem is shown in Fig. 27. The surrogate-based optimization procedure was able to discover a 4.6% reduction in drag in 20 fewer iterations than a gradient-based optimization. The first 21 design points are chosen by latin hypercube sampling and are independent. They can be simulated simultaneously given enough computing resources, which further reduces the wall time spent optimizing. The six adaptive refinement iterations after the initial sample show that the response surface allows rapid convergence to the minimum. The use of an expected improvement sampling criteria also allows us to claim with reasonable certainty that this is the global minimum within the box bounds of the problem. A comparison of the geometry change between the baseline and final design in Fig. 28 shows that the drag reduction was accomplished by reducing the thickness of the wing.

5.4 Recovering boom performance after including structurally-motivated changes

In the course of this project, a Lockheed Martin structures team suggested design changes for the aircraft outer mold line to strengthen the wing-body joint and General Electric provided an updated engine nacelle geometry. These changes required the re-optimization of the aircraft in order to attempt to recover the original target equivalent area distribution and drag. To accomplish this, we used the developed design methodology to recover the boom performance after including the structurally-motivated and engine modifications to the baseline aerodynamic shape. This calculation was used as the final demonstration of our efforts in Phase II. If Fig. 29 a comparison of the initial design (1044-1) and the modified design (1044-3b) is shown. Note that LM 10440-3b was modified to take advantage of better wing-body blending and improved load paths through the aft strut. The engine nacelle/nozzle designs were also updated based on work by GE. The result, as described above, was a modification of the ground boom signatures that significantly increased the boom loudness. The purpose of this optimization was to perform an inverse design that attempted to recover the equivalent area distributions (at a number of azimuthal locations) of the original design, denominated LM 1044-1. The optimization problem is defined at $Ma=1.7$, $AoA = 2.1\text{deg}$, $H = 50,000 \text{ ft}$, and the objective

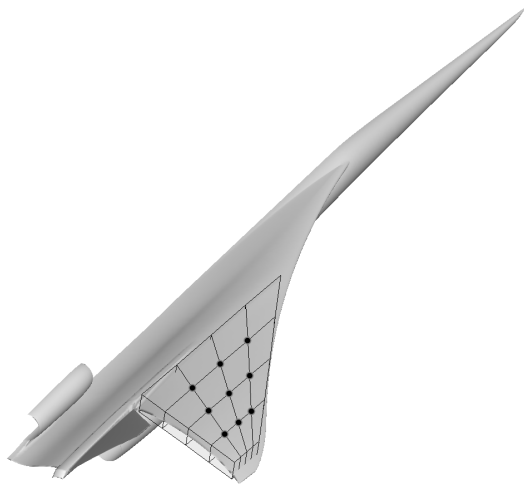


Figure 26: Location of the design variable (control points of the FFD box).

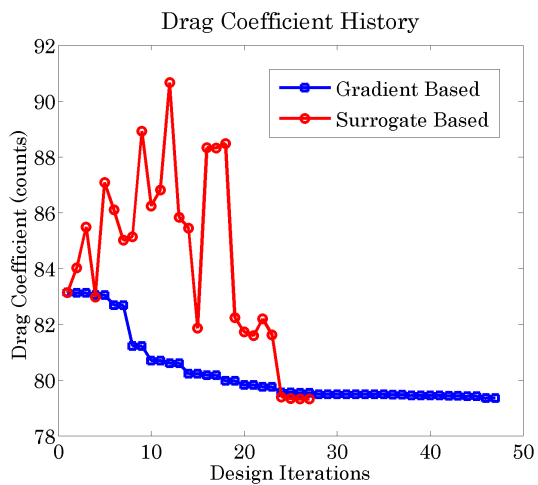


Figure 27: Comparison of unconstrained drag GBO and SBO.

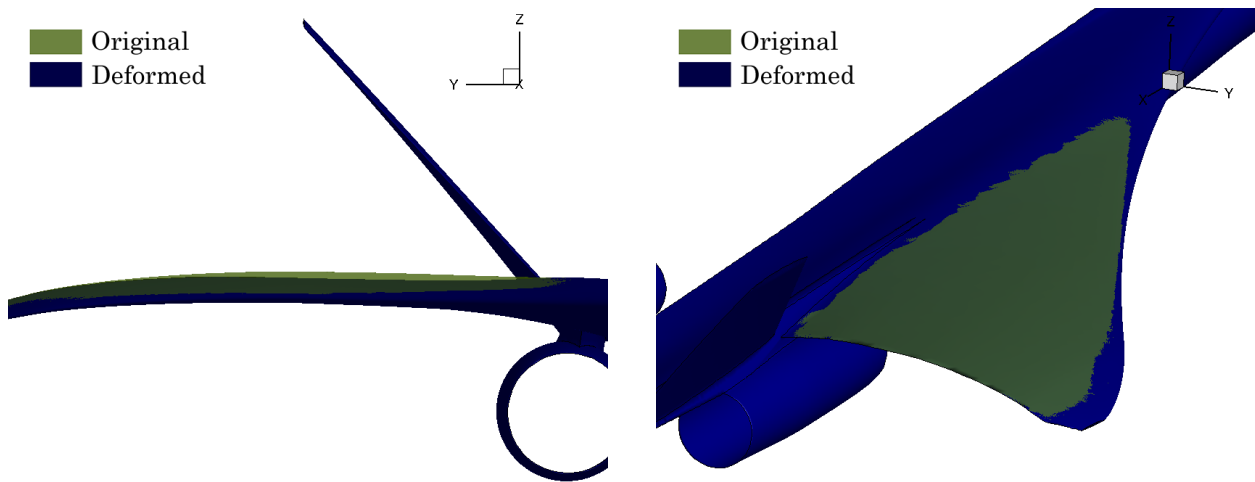


Figure 28: Original and deformed N+2 surfaces, unconstrained drag SBO.

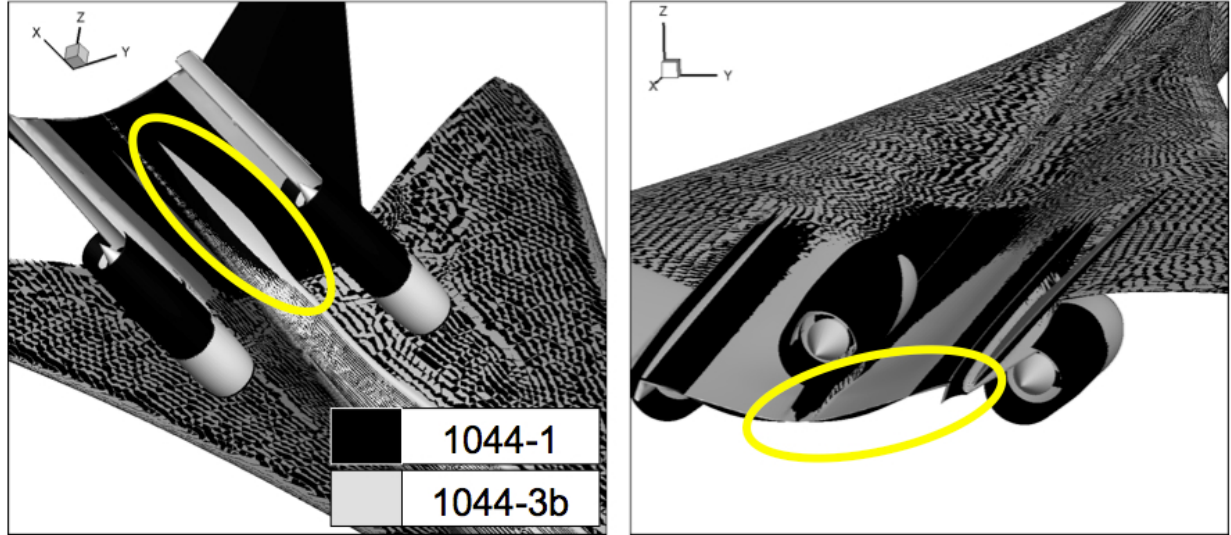


Figure 29: Comparison of 1044-1 and 1044-3 geometries.

is to recover 1044-1 target equivalent area distribution (computed at 2 body lengths), while maintaining the value of the original lift coefficient. A total of 74 Free-Form Deformation (FFD) design variables (see Fig. 30) were used. The optimization history is shown in Fig. 31, and Fig fig:OptimizationHistory. In particular, different sets of design variables have been used: 12DV (tail), 24DV (tail, aft deck), and 74DV (tail, aft deck, main wing, fuselage, un-scaled). When 74 design variables were used it was possible to obtain a 85.5% reduction in the equivalent area objective (a 100% reduction would have implied the exact recovery of the original equivalent area distributions), with an increase in the lift of 1.8% and 1.1% in drag. By considering the calculated value of the lift-curve slope, the increase in drag is almost entirely attributable to the increase in lift of the resulting design. However, the drag may be further minimized by an optimization with A_e and lift constraints that was not attempted here. The resulting geometry is presented in Fig. 33, in the new configuration the main wing dihedral has been increased, the trailing edge de-cambered, the tail angle of attack increased near root, and the fuselage volume has been increased. The formulation developed in this work allows a multiple azimuth formulation maintaining the off-track performance which is fundamental in this kind of problem. In Fig. 34 the equivalent area at different azimuth angles is shown, note that for angles between 0 and 40 degrees the target equivalent area has been recovered. Note that disturbances radiated at azimuths greater than 55 degrees do not contribute to the boom loudness. In Fig. 35 a detailed contour map of the Mach number is presented. As final step of the optimization process the ground signature has been computed and compared with the target configuration. The results of this comparison are presented in Fig. 36, Fig. 37, and Fig. 38, in all the cases the optimized geometry has the shocks in the same location (and with a similar amplitude) than in the target configuration.

6 Sonic boom assessment of the different aircraft configuration geometries

6.1 Objective

The achievement of a low-boom configuration is one of the primary objectives of these design efforts. The adjoint-based sonic boom minimization performed using the SU² CFD code used a set of target equivalent area distributions to achieve a low sonic boom signature in the cruise condition. The target equivalent ar-

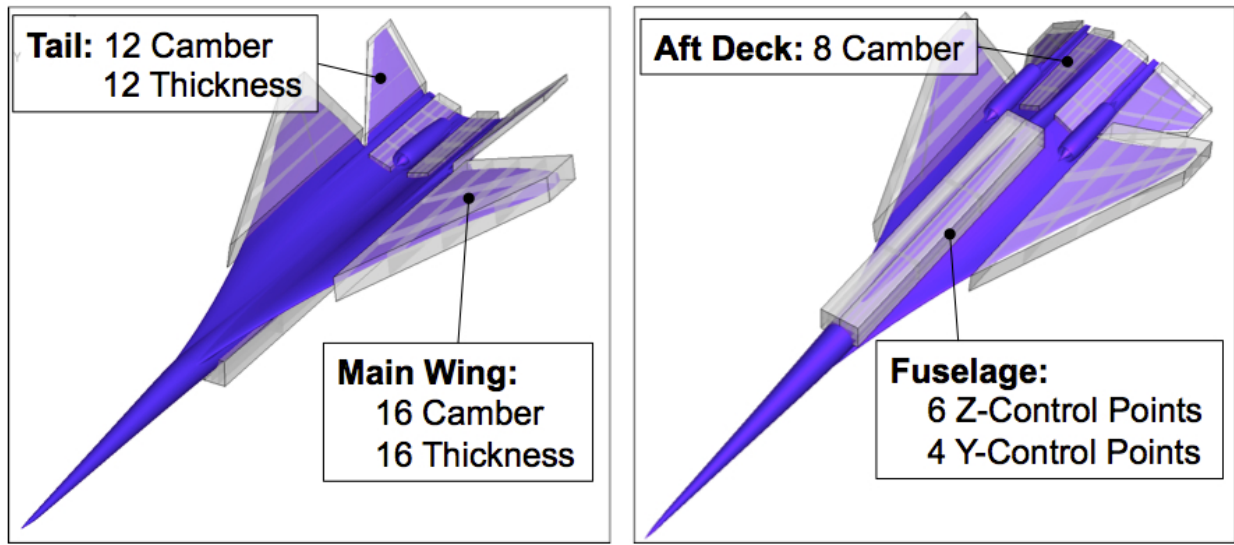


Figure 30: 1044-3b Design Parameterization. A total of 74 free-form deformation control points available.

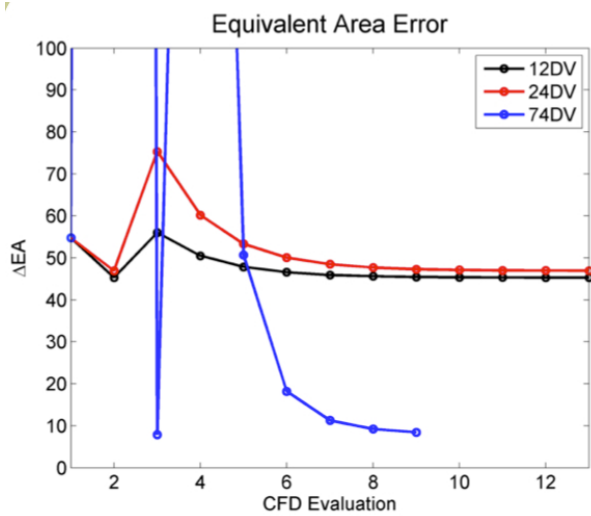


Figure 31: Optimization history (equivalent area error).

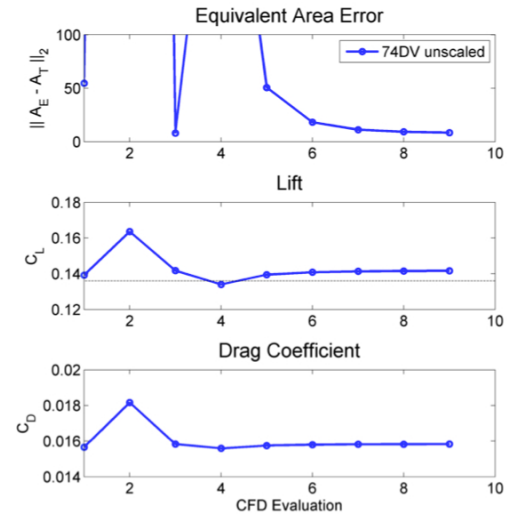


Figure 32: Optimization history (force coefficients).

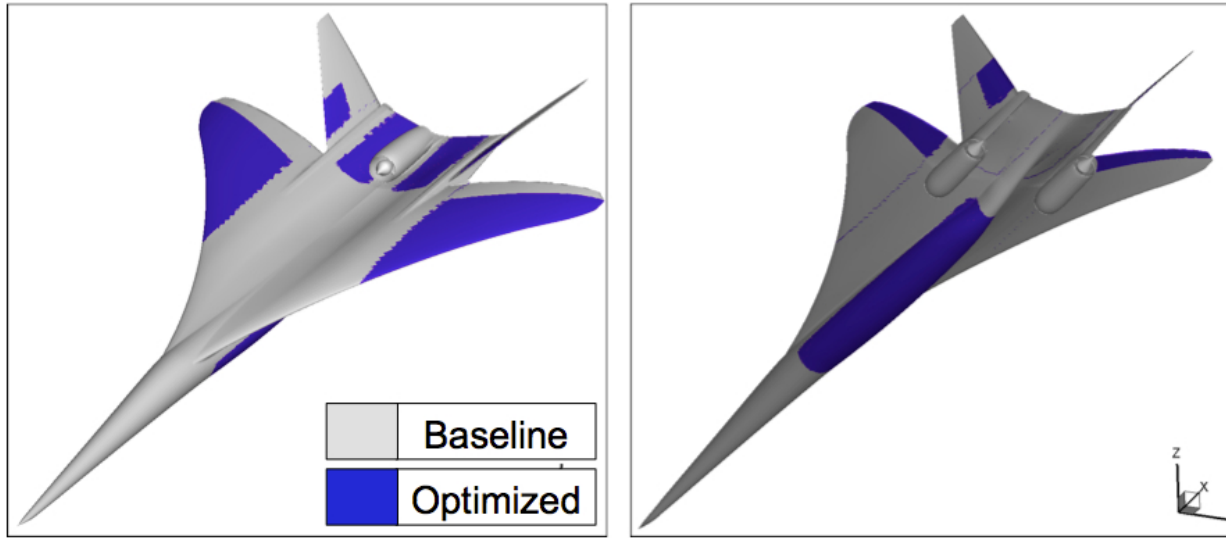


Figure 33: Baseline and optimized shape (74 Design variables)

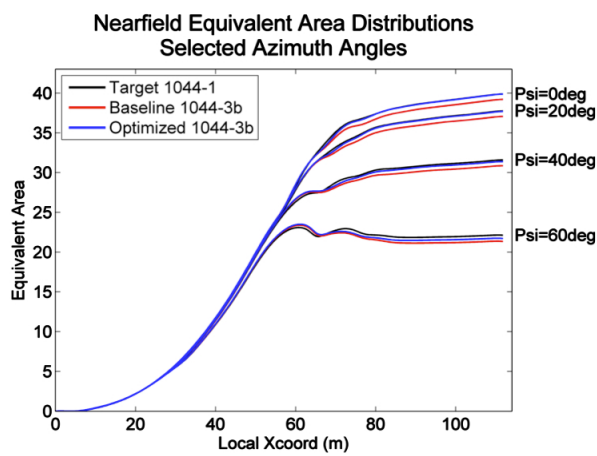


Figure 34: Equivalent area distributions at different azimuth angles.

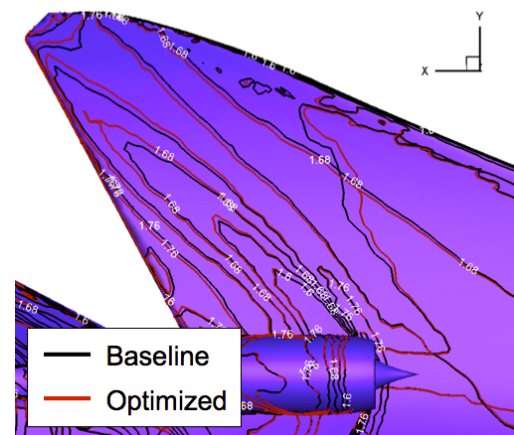


Figure 35: Initial and final surface Contours (wing detail).

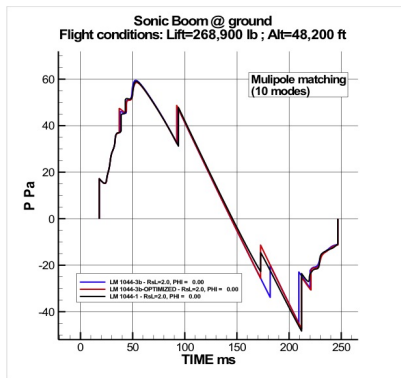


Figure 36: Comparison of ground signatures (azimuth angle 0 deg.).

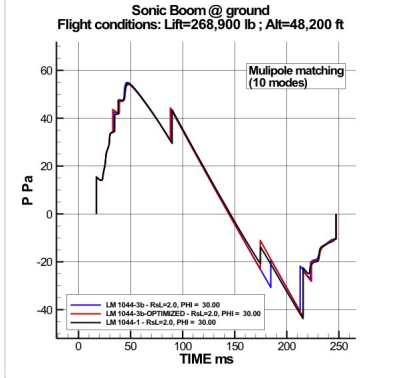


Figure 37: Comparison of ground signatures (azimuth angle 30 deg.).

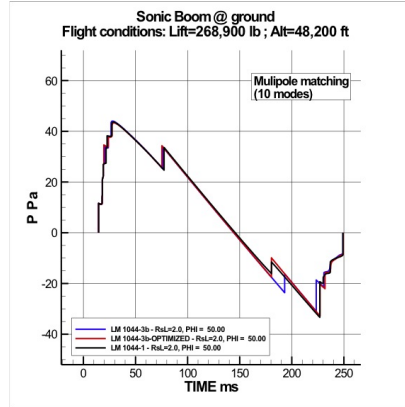


Figure 38: Comparison of ground signatures (azimuth angle 50 deg.).

eas used for this optimization were defined to recover the low-boom characteristics of a previously-designed configuration. Although, this optimization successfully reduced the difference between the actual and the target equivalent area distributions, a perfect match was not obtained. The differences in the equivalent area distributions motivate a careful evaluation of the actual loudness of the ground-propagated sonic boom achieved by the final optimized configuration, and a comparison with the sonic boom of the other configurations that have been investigated at Stanford University over the reporting period (Phase II) with the SU² code.

6.2 Description of the methods and tools used for ground propagation of sonic booms

Simulating the sonic boom is an intricate task involving complex physical phenomena and very different length scales. Accurate modeling of sonic boom first requires an adequate prediction of the acoustic source: the aerodynamic pressure disturbances generated in the close vicinity of the aircraft. In this region, the aerodynamic flow is governed by the non-linear Euler equations and it includes three-dimensional features with scales proportional to the aircraft length. Therefore, CFD methods are perfectly suited and necessary to predict these near-field aerodynamic perturbations that create the sonic-boom. Because the prediction of the sonic boom requires propagating this pressure signal from the near field down to the ground over tens of kilometers, several hundred aircraft lengths, conventional CFD methods are inadequate to perform this long distance propagation. They would require a tremendous number of mesh points and would eventually fail to capture important effects occurring during the propagation (such as molecular relaxation). Therefore, a specifically-tailored acoustic code is necessary to carry out this long-distance propagation of the sonic boom signal through the standard atmosphere, which in these calculations is assumed to be stratified and include the standard temperature and density variations with altitude. A suite of ONERA sonic boom evaluation methods and tools have been used for this portion of the study. This method is based on a three-layer approach, as illustrated in Figure 39. Layer 1 corresponds to the near-field aerodynamic flow prediction with CFD. Layer 3 is the atmospheric propagation of the sonic boom with an acoustic code, while layer 2 ensures a natural matching between the near-field aerodynamic data and the native inputs of the acoustic code.

Layer 1: Near-field aerodynamic calculation by CFD

First, the aerodynamic pressure field in the near field of the aircraft flying in the supersonic cruise condition is calculated by solving the three-dimensional steady Euler equations using the SU² CFD code. To obtain

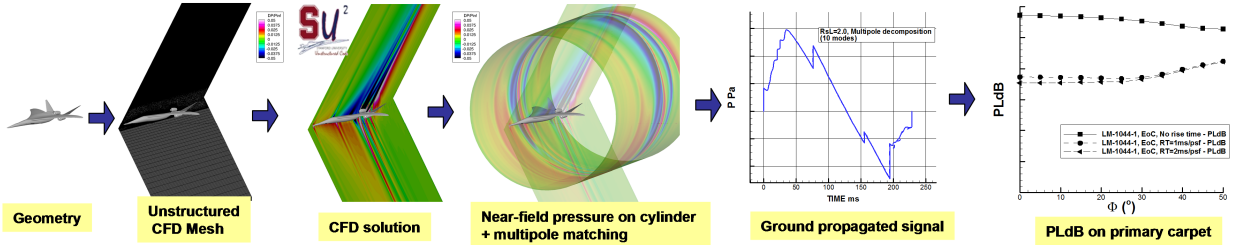


Figure 39: ONERA Sonic Boom evaluation methodology

an accurate evaluation of the near-field aerodynamic pressure perturbations, careful attention must be paid to the quality of the CFD mesh which must have features adapted to the flow physics of these perturbations traveling along flow characteristics. The computational domain of this CFD calculation typically extends between twice and four times the aircraft length below the aircraft.

Layer 2: Multipole matching method

The CFD aerodynamic pressure field is extracted on a cylinder surrounding the aircraft, aligned with the flow direction, whose radius is a user-specified parameter varying between one half to one body length. The pressure perturbations on this cylinder are then post-processed using the multipole decomposition method originally introduced by Plotkin and Page [42, 43] and applied by Salah El Din [44]. This decomposition method proceeds through a development of the near-field pressure signature on the cylinder according to the azimuthal variable Φ . Thereby, it allows to rebuild a Whitham function equivalent, at long distance, to the pressure perturbation generated by the aircraft, while accumulating the diffraction effects associated with the non-axisymmetric near-field flow. The ground signature computed from this equivalent rebuilt Whitham function is observed to converge much faster with the matching distance between the CFD and the acoustic theory (i.e. the radius of the cylinder) than the ground signature from a direct CFD/acoustic match (without the use of the multipole expansion). This justifies the use of this second layer which, in addition to providing a theoretically-correct near-field/far-field match, greatly reduces the CFD grid size needed for the near-field computation, thus saving significant computing time.

Layer 3: Atmospheric non-linear acoustic propagation method

The ground signature is computed by propagating the near-field aerodynamic pressure perturbations matched with the multipole decomposition method (layer 2) with the acoustic propagation code TRAPS. TRAPS [45, 46] is a dedicated sonic boom propagation code based on inviscid non-linear acoustic theory. It uses a ray-tracing approach to account for the refraction phenomena occurring during propagation through a stratified atmosphere with vertical temperature and density gradients, and to evaluate the extent of the *primary carpet*, i.e. the width of the corridor underneath the aircraft trajectory directly affected by the sonic boom. Along each acoustic ray, a signal aging process (first-order correction to linearized supersonic theory) is used to predict the evolution of the shape of the sonic-boom pressure signal. The ground pressure signature is finally obtained by post-processing the previous aged pressure signal to identify and locate the different shocks with the equal-area rule [45] and by applying a multiplication factor of 2.0 to account for a perfect reflection on the ground. Finally, from this ground sonic boom pressure signature (having infinitely steep shocks), corrections for rise time are applied to each shock composing the signature. A hyperbolic-tangent shape is introduced for the actual shocks and the rise time is assumed to be inversely proportional to the pressure jump. From this corrected ground signature, a spectral analysis is performed and classical sonic boom metrics such as ASEL, CSEL and PLdB can be calculated. The process of calculating SEL and PLdB sonic boom metrics follows the procedure described by Shepherd and Sullivan in [47] and is depicted in Figure 40.

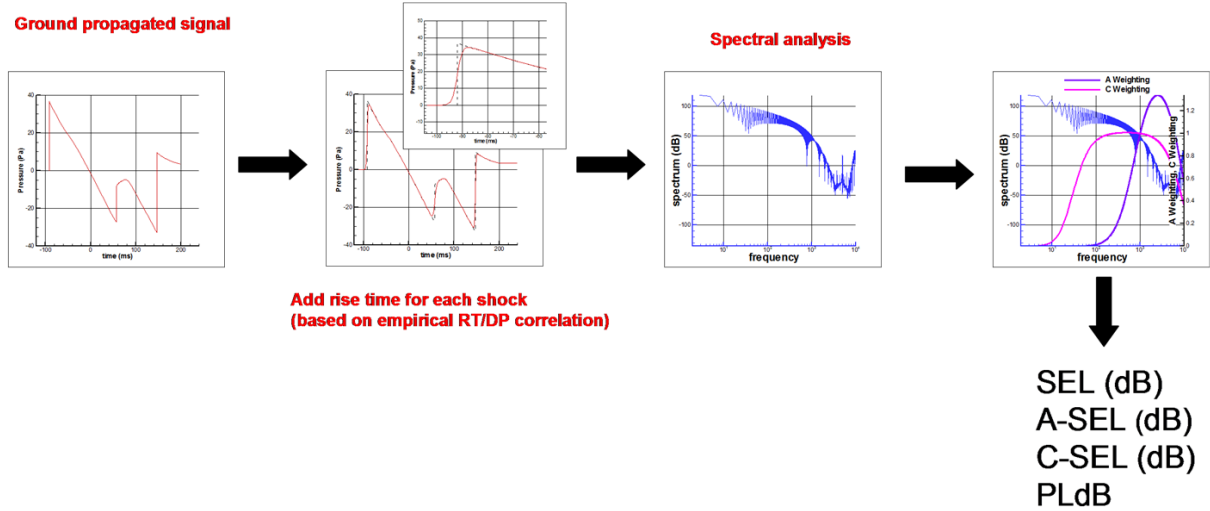


Figure 40: PLdB calculation process from ground propagated (inviscid) pressure signature

6.3 Flight conditions used for the sonic boom analysis

All sonic boom evaluations presented hereafter have been performed using the results of SU^2 CFD calculations (Euler) obtained for a Mach number of 1.7 and an angle of incidence of 2.1 degrees, corresponding to the cruise conditions and a lift coefficient of about 0.136. The CFD meshes used for these calculations were meshes specifically generated for sonic boom analysis in term of density and extent. A view of the mesh and the CFD pressure field in the symmetry plane is given in Figure 41.

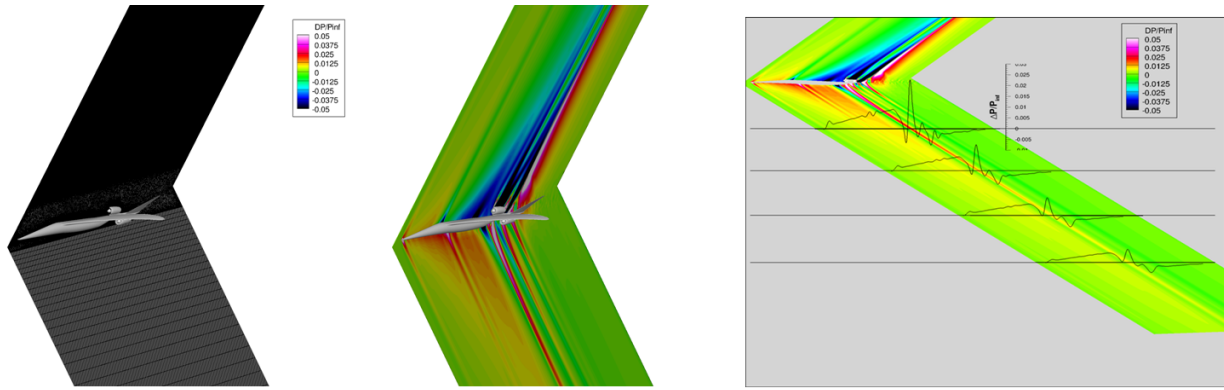


Figure 41: View of the Euler CFD mesh and CFD solution in the symmetry plane. The rightmost figure shows the full extent of the mesh (in the symmetry plane)

The changes in the aerodynamic forces with angle of attack, calculated using two different meshes (for configuration LM 1044-3b) are presented in Figure 42.

Two flight altitudes have been considered for the evaluation of sonic boom: the start-of-cruise (SoC) at 48,200 feet and the end-of-cruise (EoC) at 57,000 feet.

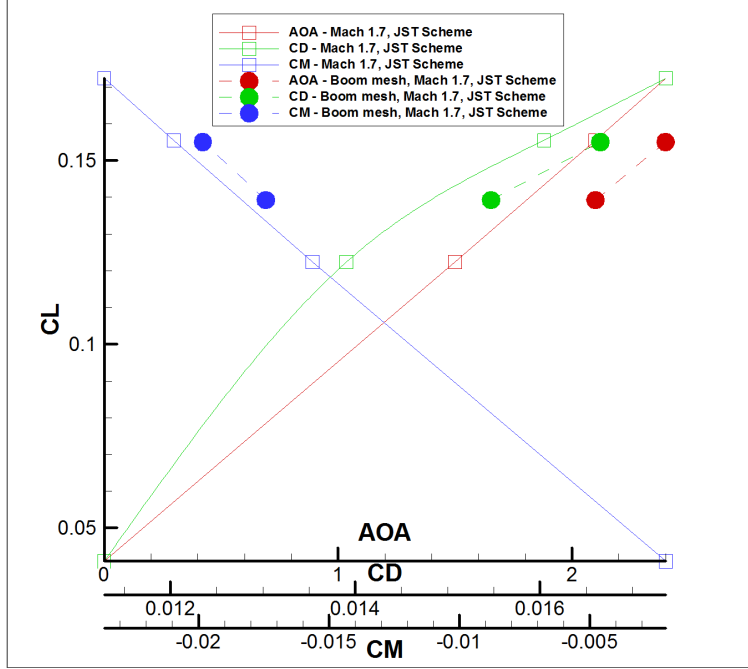


Figure 42: Aerodynamic polars for the LM 1044-3b configuration. The results using two meshes are compared. Only the finest mesh (sonic boom mesh) has been used for the present sonic boom analyses.

6.4 Set-up and verification of the sonic boom evaluation process

Prior to presenting the results obtained for the ground propagated sonic booms of the different designs investigated recently at SU, some verifications and the set-up of the ONERA sonic boom calculation procedure are described in this section. The effects of the major parameters or options offered by the different tools composing the complete sonic boom evaluation process are presented. To illustrate these effects, the CFD solution of the LM 1044-3b configuration is used and we focus more precisely on the effects of:

- The distance at which the near-field pressure is extracted in the SU² CFD solution;
- The multipole decomposition and the number of Fourier modes used to reconstruct the data;
- The rise time of shocks in the ground sonic boom signature on the Decibel metrics.

The first analysis conducted was used to evaluate the quality of the CFD solution in the near-field by extracting the CFD pressure on cylinders of increasing radii, aligned with the free stream and surrounding the aircraft, as illustrated in Figure 43. The evolution of the pressure signal with distance from the aircraft, under the flight track ($\Phi = 0$ deg) and off-track at azimuth ($\Phi = 45$ deg) is shown in Figure 44 and Figure 45. By plotting $\Delta P \times \sqrt{R/L}$, an indication of the diffusion of the forming shocks in the signature can be obtained. Indeed, if the signal were fully axisymmetric, it would remain unchanged. Therefore any decrease in the amplitude of the compression in the signal with R can only be due to numerical dissipation or three-dimensional effects (non-axisymmetry). A non-negligible reduction of the strongest shock (under-track) can be observed. Although it is not directly possible to evaluate the contribution of the non-axisymmetric effects on this reduction, an indication is given by looking at the evolution of the signal at other azimuthal angles. In this case, it appears clearly that the overpressure associated with this shock wave (wing leading edge shock) is also reduced at azimuthal angles 15deg and 30deg. This tends to indicate that numerical dissipation is the main reason for the decrease of this shock. This situation illustrates the typical compromise to be made

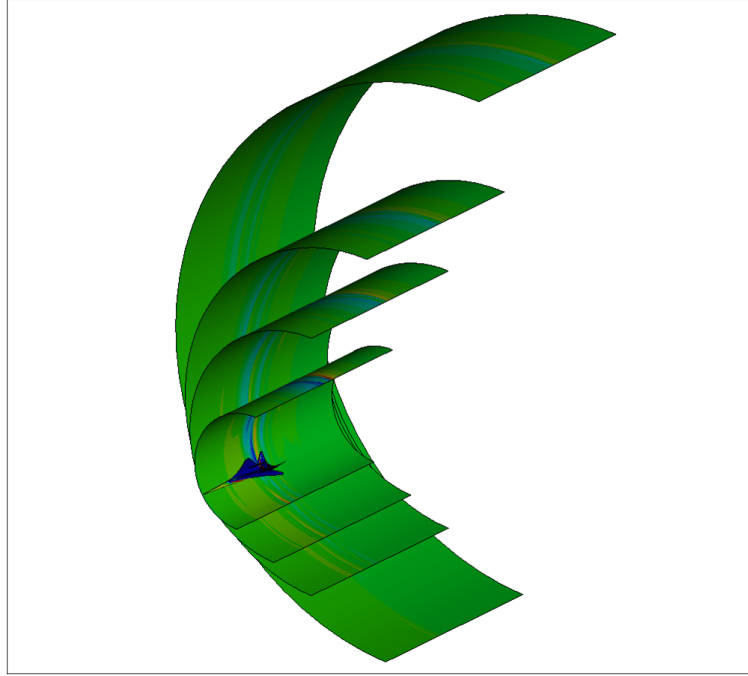


Figure 43: Cylinders on which the aerodynamic near-field pressure is extracted from the SU² CFD solution. The radius (R) of these cylinders varies from 0.5 to 2.5 times the aircraft length (L)

when choosing the distance at which the pressure is extracted from the CFD solution: if extracted too far, the CFD solution is affected by the spurious numerical dissipation of shocks; if extracted too close, the near-field solution is still far from being locally axisymmetric (three-dimensional effects are still important), which is the assumption made by the acoustic propagation code.

The multipole matching method offers an interesting solution to help solve this dilemma in choosing the right distance for extracting pressure in the CFD solution. Indeed, by accounting for the three-dimensional effects occurring between the cylinder where the pressure is extracted in the CFD solution and the far-field (by using the asymptotic behavior of each azimuthal mode), this method allows to actually extract the CFD data very close to the body, typically $R/L = 1.0$, where the CFD solution does not yet suffer from significant spurious attenuation of shocks. The advantage of using this multipole matching method is directly illustrated in Figure 44 which shows the propagated ground sonic boom calculated with data extracted from the CFD at different distances R/L , with and without use of the method, respectively. The faster convergence of the ground signature with distance of extraction of the near-field pressure is observed when the multipole method is used to generate the inputs for the acoustic code TRAPS. When using the multipole decomposition method, the number of (azimuthal) Fourier modes used to reconstruct the signal must be chosen by the user. A perfect reconstruction would require the use of an infinite number of modes, which is practically impossible. Usually, the number of modes that can be used is limited by the appearance of numerical oscillations during the treatment of high-order modes. In the present case, using 20 modes was not possible because of the numerical oscillations produced by the method. However, as illustrated in Figure 45 and Figure 46, the convergence of the reconstructed near-field signal with increasing numbers of modes is fast and the use of 10 modes proved to be sufficient. Therefore, this parameter has been frozen to 10 during the remainder of the study.

Figure 49 summarizes, for the start-of-cruise conditions, the effect of the distance of extraction R/L on the under-track ground-propagated sonic boom signatures obtained with the multipole matching method (for the LM 1044-3b configuration). Figure 50 gives the off-track evolution of the ground-propagated sonic

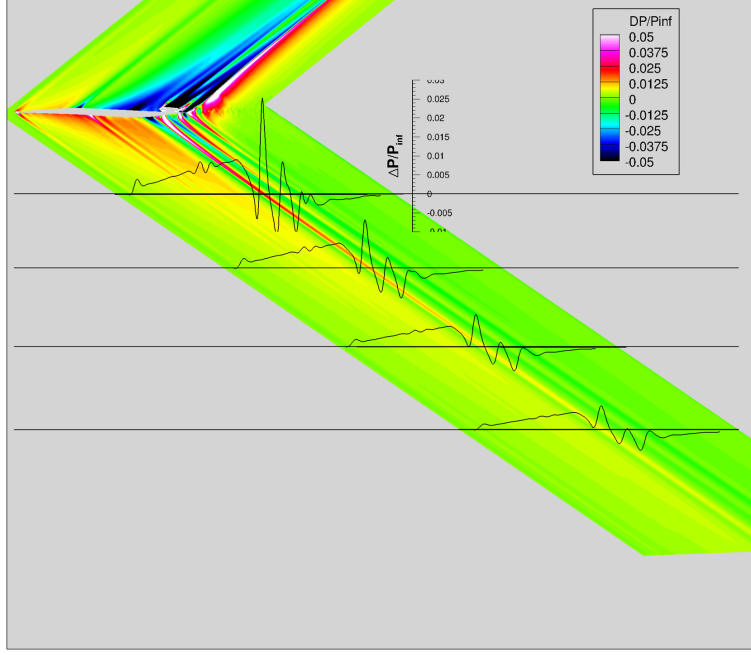


Figure 44: Visualization of the evolution of the near-field pressure signal under-track as distance from the body increases from $0.5L$ to $2.0L$. Configuration LM 1044-3b

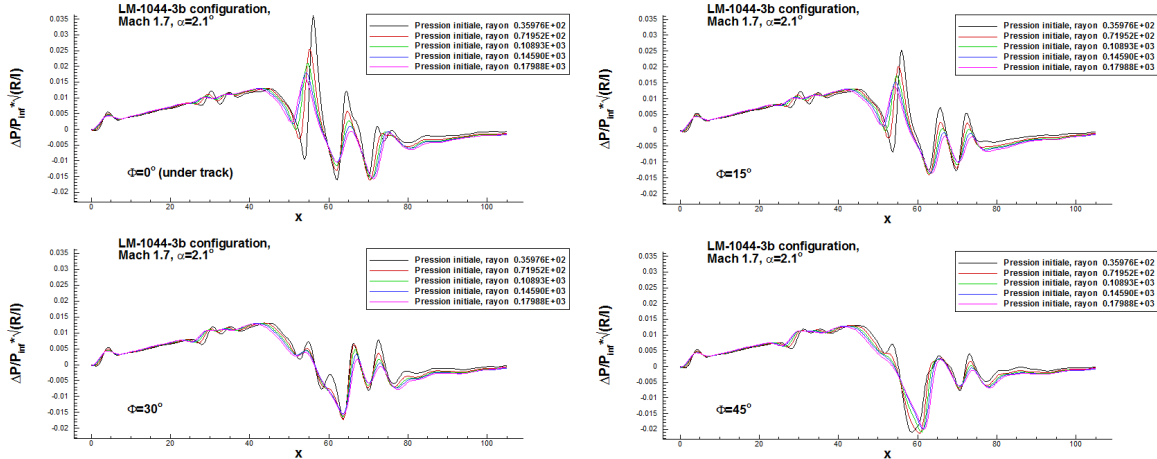


Figure 45: Evolution of the near-field pressure with distance from the aircraft (radius of the cylinder on which pressure is extracted from the CFD solution). Under-track (left) and off-track at azimuth 45deg. Direct extraction results (top) and results of multipole matching extrapolation (bottom) are presented.

boom signatures for the same configuration, using the exact same evaluation procedure. The evolution of the overpressure with azimuthal angle exhibits a typical decrease. However this overpressure decrease is also accompanied by a decrease of the mean rise time of the initial shock that can also be detected in these results (which will have an adverse impact on the PLdB and other decibels metrics). Note that the results in Figure

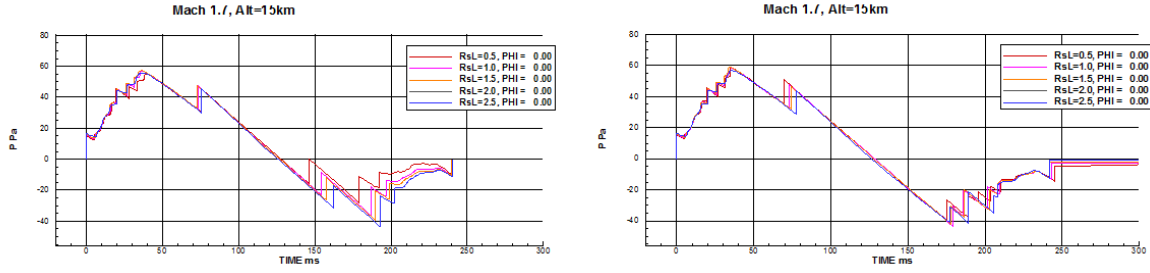


Figure 46: Influence of the distance at which the pressure is extracted in the CFD solution on the under-track ground sonic boom signatures. Left: direct matching from the CFD results to the acoustic code; Right: use of multipole matching method (with 10 Fourier modes).

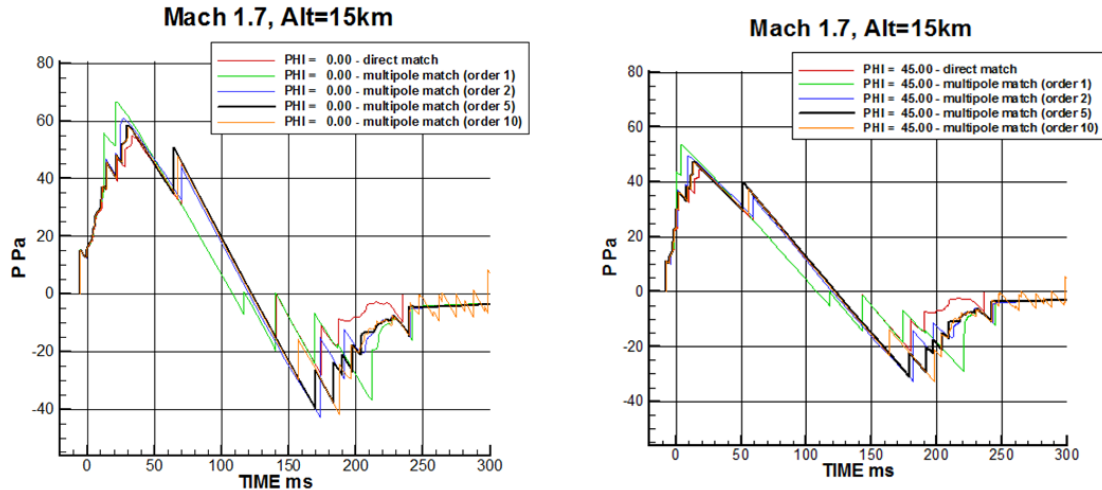


Figure 47: Influence of the number of modes used in the multipole matching method applied on near-field pressure data extracted at $R/L = 0.5$. Under-track results (left) and at azimuth 45deg (right).

50 correspond to the direct output of the TRAPS propagation code and the dissipative effects occurring during the propagation through the atmosphere are not captured in these results. This rise time effect actually comes from the careful low-boom design of the aircraft nose to produce a progressive compression instead of a strong initial shock.

The pressure signatures obtained with the TRAPS propagation code shown in Figure 50 have been post-processed in term of decibels metrics. The results are presented in Figure 51 and Figure 52 which show the evolution with azimuth angle (over the complete primary carpet) of ASEL, CSEL and PLdB. Figure 51 shows the influence of the addition of a physical rise-time to the TRAPS invicid results. The impact is negligible for the CSEL metric which is mostly sensitive to low-frequencies, but is important on the ASEL and PLdB metrics which are reduced by almost 10 dB while accounting for a rise time modeled by a simple empirical tanh-shaping of each shock in the TRAPS signatures. The coefficient actually used in this empirical model (number of ms per psf of the shock overpressure) does have an impact on the decibel evaluations, but it is not as important as whether a correction is made or not (going from 1 ms per psf to 2 ms per psf reduces the PLdB by about 1 dB, under-track). The value of 1 ms per psf has been retained for the rest of the study. Finally, since the use of the multipole method has been shown to significantly reduce the impact of the choice

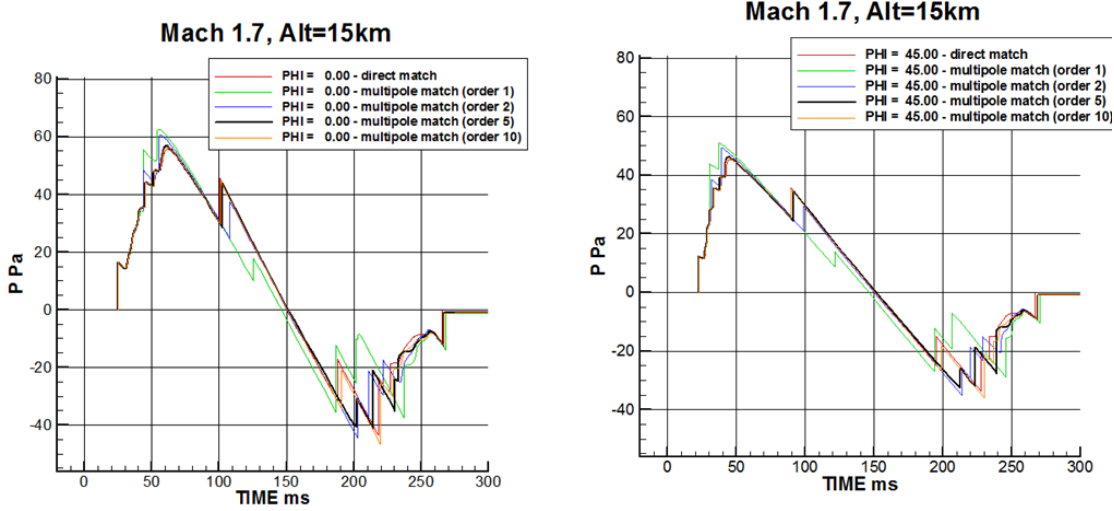


Figure 48: Influence of the number of modes used in the multipole matching method applied on near-field pressure data extracted at $R/L = 2.0$. Under-track results (left) and at azimuth 45deg (right).

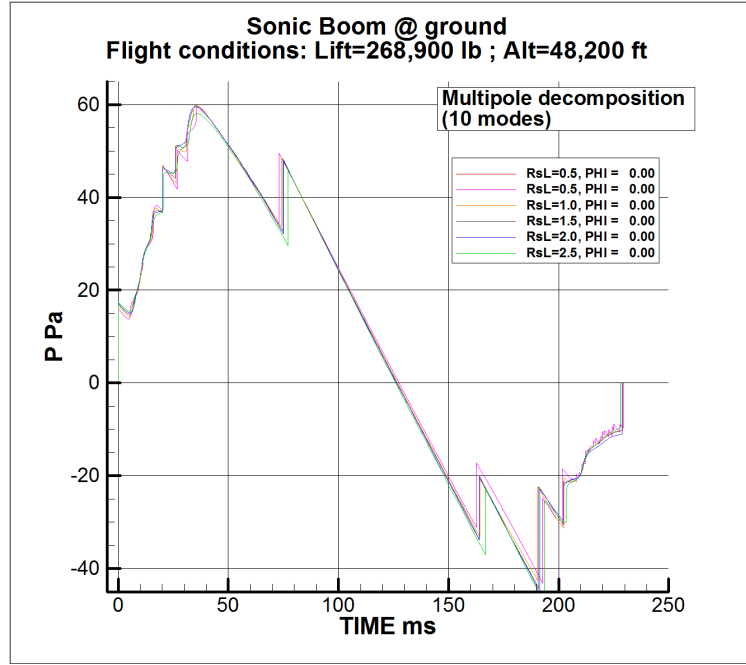


Figure 49: Influence of the distance of extraction of pressure data in the CFD solution on the under-track ground sonic boom signature with the use of the multipole matching method (10 Fourier modes)

of the distance of extraction of the near-field pressure in the CFD solution, the remaining sensitivity of the ground signature to this parameter R/L has an impact on Decibels metrics, as it is shown in Figure 52. This proves the high sensitivity of these metrics evaluation to different parameters of the sonic boom evaluation process.

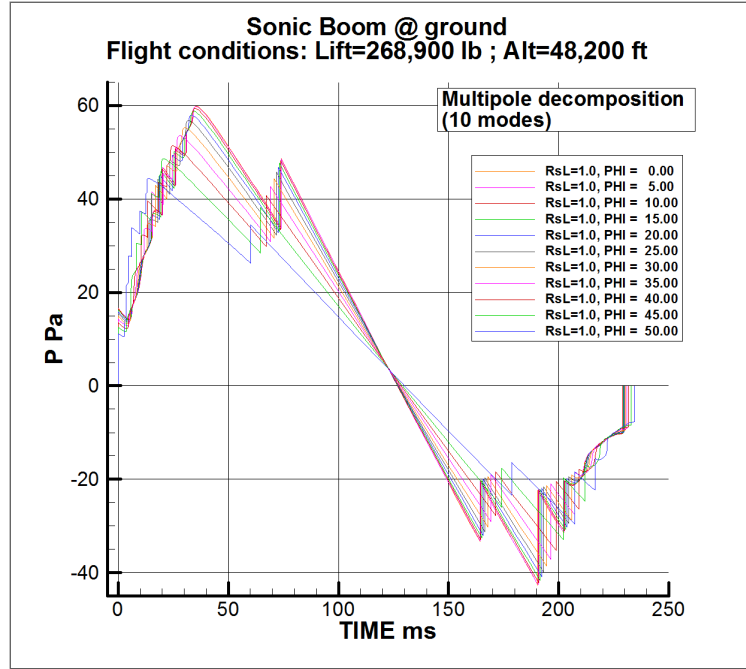


Figure 50: Ground-propagated sonic boom signatures under-track and at different azimuthal angles (off-track). Results obtained from pressure data extracted at $R/L = 2.0$ and using the multipole matching method (with 10 Fourier modes)

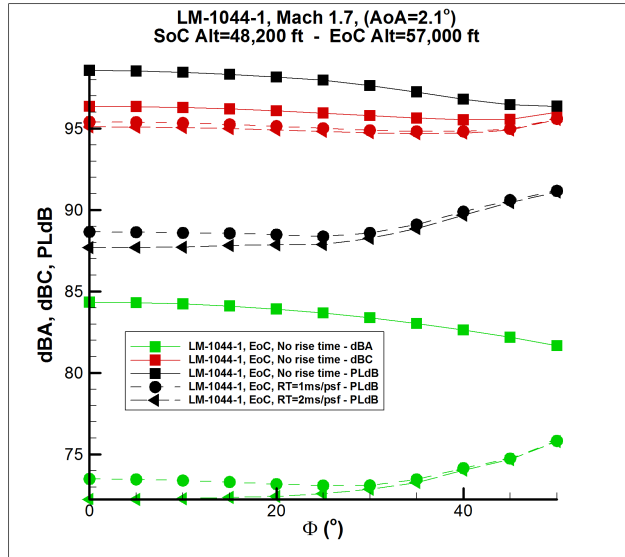


Figure 51: Effect of the assumption made for the empirical rise time correction of the ground pressure signal on the ASEL, CSEL and PLdB metric over the full primary carpet (under- and off-track).

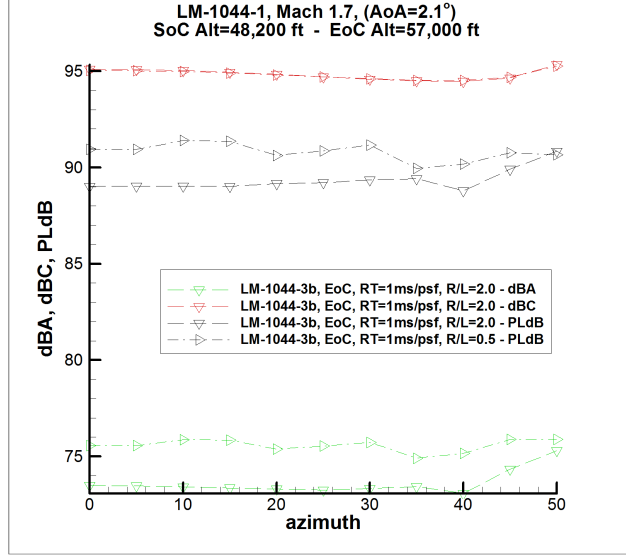


Figure 52: Effect of the extraction distance of the near-field CFD pressure on the ASE, CSEL and PLdB metric over the full primary carpet (under- and off-track).

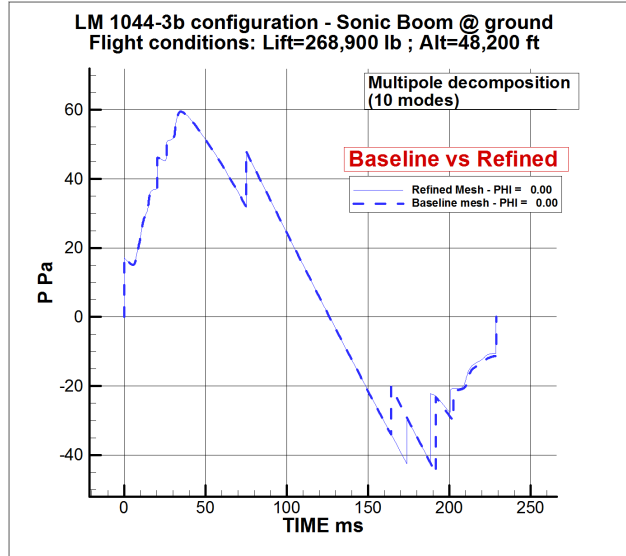


Figure 53: Effect of mesh adaptation (in the region of the engines) on the ground-propagated sonic boom of configuration LM 1044-3b (multipole matching method).

6.5 Summary of the sonic boom evaluation results for the different configurations investigated

Presentation of the different aircraft configurations studied

The geometry differences between the three configurations investigated are shown in Fig. 54 and correspond to:

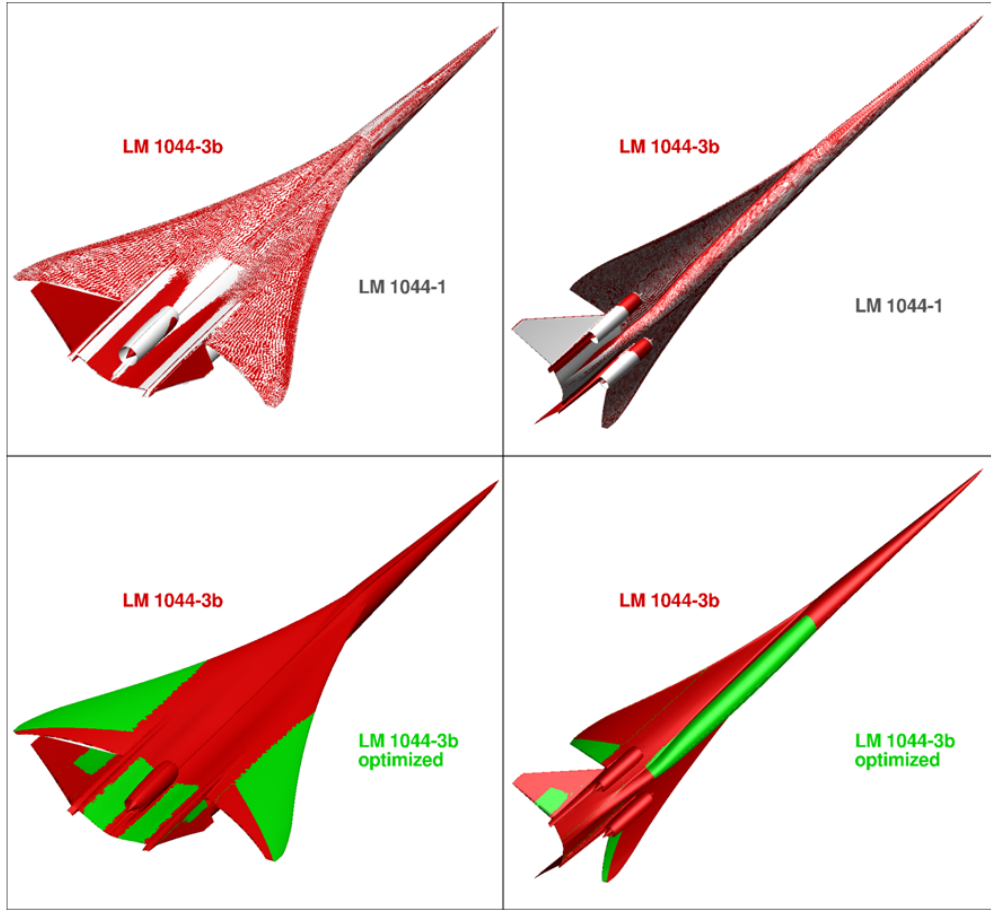


Figure 54: Comparison of the geometries of the 3 aircraft configurations studied: LM 1044-1, LM 1044-3b (before optimization) and LM 1044-3b-opt (optimized to recover the equivalent area of LM 1044-1).

- LM 1044-1;
- LM 1044-3b;
- LM 1044-3b after sonic boom optimization (equivalent area target),

Effect of the cruise angle

The effect of cruise altitude on the ground sonic boom signatures propagated with the TRAPS code are illustrated in Figure 55 for the LM 1044-1 configuration.

Analysis of the configuration effect on the near-field and ground propagated sonic boom

The comparison of the evolution of near-field pressure signatures extracted from the SU² CFD solution for the three configurations investigated are shown in Figure 57 (under-track) and Figure 58 (off-track).

The configuration effects on the ground propagated sonic boom signatures are presented in Figure 59. These results confirm the efficiency of the optimization started from the initial LM 1044-3b to recover the ground sonic boom of LM 1044-1. The effects on the ASEL, CSEL and PLdB metrics are illustrated in Figure 60. The analysis of these configuration effects has to be made in light of the relatively high sensitivity

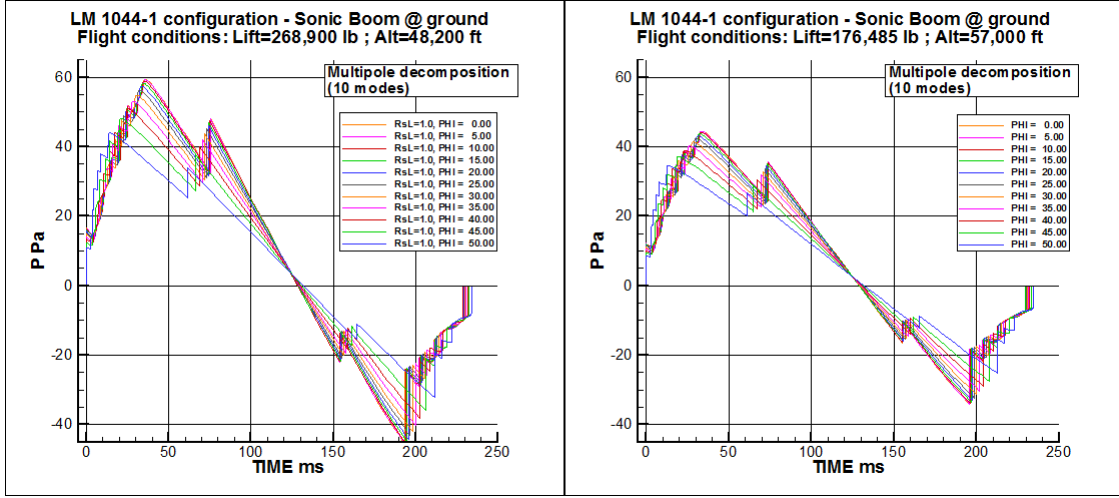


Figure 55: Ground sonic boom signature for configuration LM 1044-1 under-track and off-track for start-of-cruise (left) and end-of-cruise (right) altitudes.

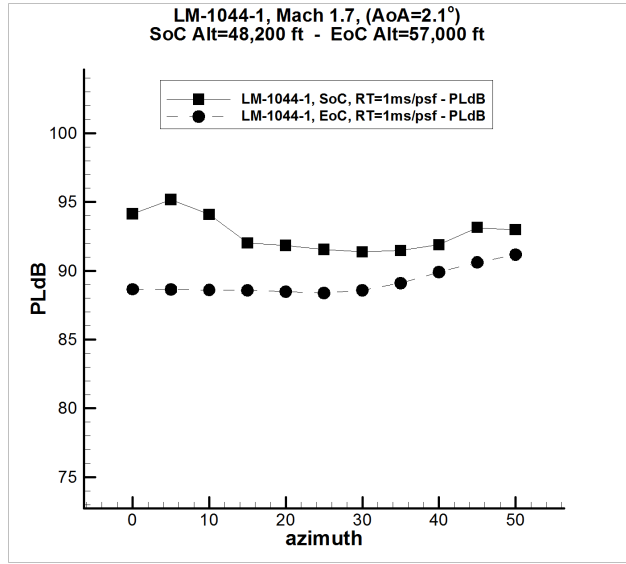


Figure 56: Under-track and off-track PLdB evolutions with azimuthal angle for configuration LM 1044-1 for start-of-cruise and end-of-cruise altitudes.

of these metrics to various parameters in the simulation process. Indeed, differences of the order of 1 dB are observed from one configuration to the other, which is really close to the reasonably achievable accuracy of these evaluations. The analysis of CSEL clearly shows the convergence of -3b OPTIM results towards the -1 configuration results. However, the ASEL and PLdB results analysis are not as straightforward, since the behavior evolves with the azimuth angle. It should also be noted that the present results show an advantage of the -1 configuration over the -3b configuration in term of the ASEL and CSEL metrics, but a slight drawback in terms of PLdB.

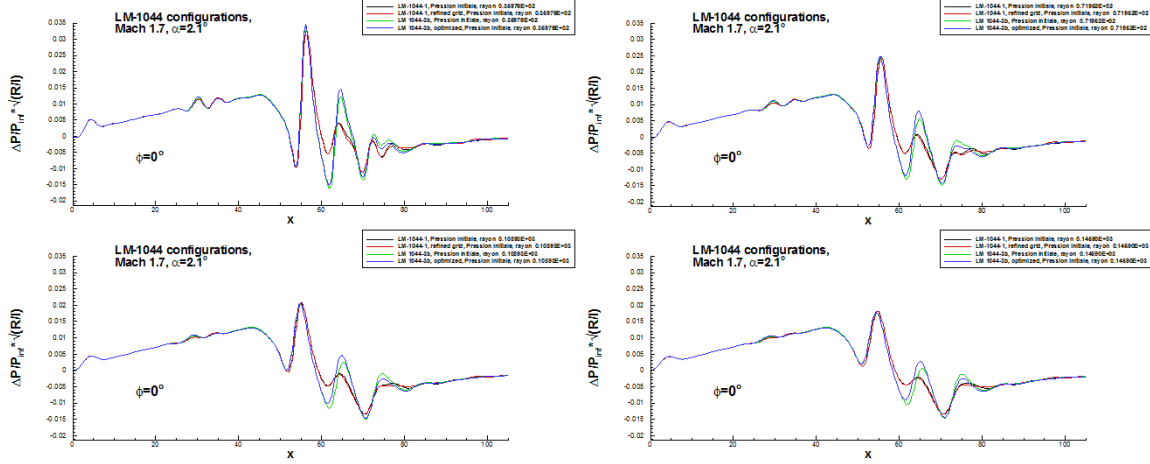


Figure 57: Comparison of the under-track near-field pressure for the three aircraft geometries investigated at different distances from the aircraft.

7 Conclusions

In this work we have improved the methodology for the simulation and optimal shape design of supersonic aircraft using objective functions derived from the equivalent area distribution (and within the framework of an adjoint methodology). We have also implemented a new methodology for the development of gradient-enhanced Gaussian Process Regression surrogate models for MDO including noise tolerance. A grid adaptation methodology has been implemented, and the engine effects have been introduced in the direct and adjoint problem with the implementation of new engine (and adjoint-engine) boundary conditions for powered simulations / optimizations. Careful calculations of the effect of these configuration optimizations on the actual loudness metrics for the ground sonic boom have been performed and presented, and shows that the recovery of equivalent area distributions has the desired effect on the reduction of the calculated loudness metrics, although further work to define more effective equivalent area error measures should be pursued. Finally the entire methodology has been tested in different equivalent-area based design problems.

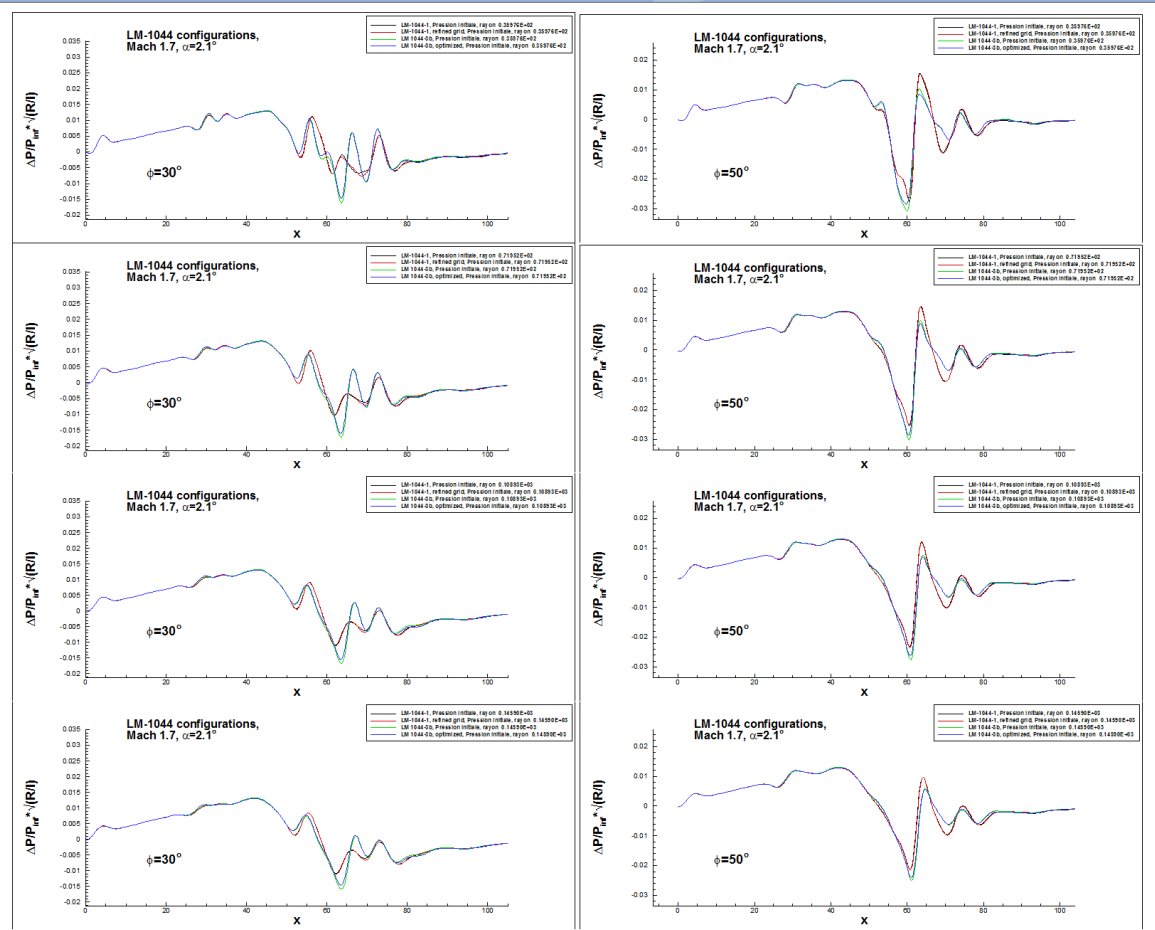


Figure 58: Comparison of the near-field pressure at azimuth 30deg (left) and 50deg (right) for the three aircraft geometries investigated at different distances from the aircraft.

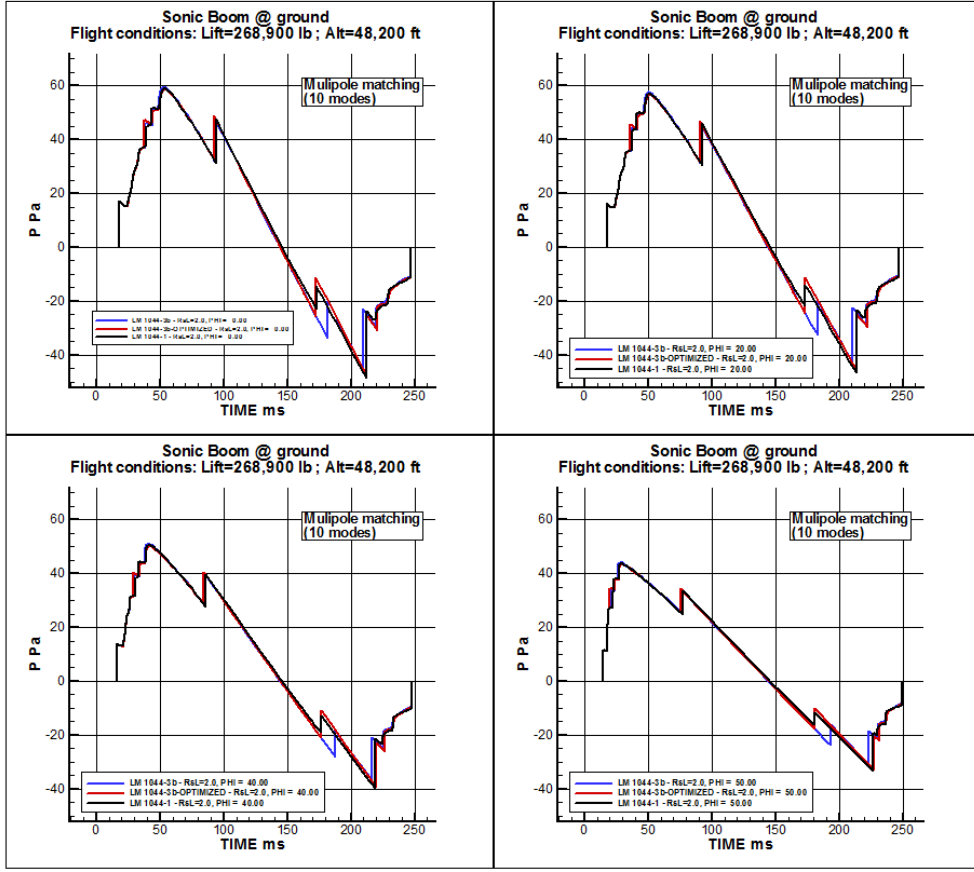


Figure 59: Ground-propagated sonic boom for the three investigated configurations under-track and for three off-track azimuth angles.

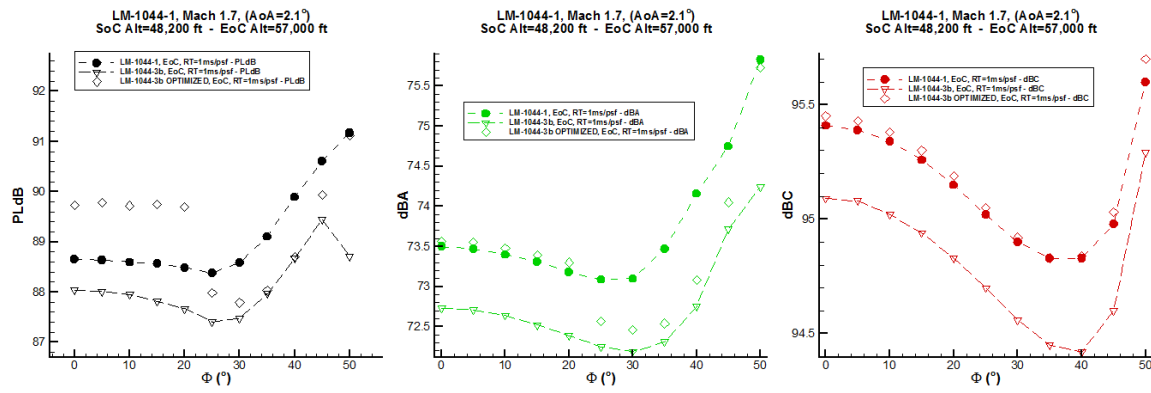


Figure 60: Comparison of PLdB, A- and C-SEL metrics over the primary carpet for the three aircraft configurations

Bibliography

- [1] Seebass, R., "Sonic Boom Theory," *Journal of Aircraft*, Vol. 6, 1969, pp. 177–184.
- [2] Chung, H. and Alonso, J., "Design of a Low-Boom Supersonic Business Jet Using Cokriging Approximation Models," *9th AIAA/ISSMO Symposium on Multidisciplinary Analysis and Optimization*, AIAA Paper 2002-5598, Atlanta, GA, September 2002.
- [3] Palacios, F., Colombo, M., C. Aranake, A., Campos, A., Copeland, S. R., Economou, T. D., Lonkar, A. K., Lukaczyk, T. W., Taylor, T. W. R., and Alonso, J. J., "Stanford University Unstructured (SU2): An open-source integrated computational environment for multi-physics simulation and design," *51st AIAA Aerospace Sciences Meeting including the New Horizons Forum and Aerospace Exposition*, AIAA Paper 2013-0287, Grapevine, Texas, January 2013.
- [4] Karypis, G. and Kumar, V., "MeTis: Unstructured Graph Partitioning and Sparse Matrix Ordering System, Version 4.0," <http://www.cs.umn.edu/~metis>, 2009.
- [5] Biswas, R. and Strawn, R., "Tetrahedral and hexahedral mesh adaptation for CFD problems," *Applied Numerical Mathematics*, Vol. 26, 1998, pp. 135–151.
- [6] Giles, M. B. and Pierce, N. A., "Adjoint error correction for integral outputs," *Error Estimation and Adaptive Discretization Methods in Computational Fluid Dynamics*, 2002.
- [7] Palacios, F., Duraisamy, K., Alonso, J. J., and Zuazua, E., "Robust Grid Adaptation for Efficient Uncertainty Quantification," *AIAA Journal*, Vol. 50, No. 7, 2012, pp. 1538–1546.
- [8] Jameson, A., "Aerodynamic Design via Control Theory," *Journal of Scientific Computing*, Vol. 3, No. 3, 1998, pp. 233–260.
- [9] Lions, J. L., *Optimal Control of Systems Governed by Partial Differential Equations*, Springer Verlag, New York, 1971.
- [10] Hascoët, L. and Pascual, V., "TAPENADE 2.1 user's guide," Technical Report 0300, INRIA, <http://www.inria.fr/rrrt/rt-0300.html>, 2004.
- [11] Griewank, A., Juedes, D., and Utke, J., "Algorithm 755: ADOL-C: A Package for the Automatic Differentiation of Algorithms Written in C/C++," *ACM Transactions on Mathematical Software*, Vol. 22, No. 2, 1996, pp. 131–167.
- [12] *A Comparison of the Continuous and Discrete Adjoint Approach to Automatic Aerodynamic Optimization*, No. AIAA-2000-0667, Reno, NV., January 2000.
- [13] Jameson, A., "Aerodynamic Design via Control Theory," *Journal of Scientific Computing*, Vol. 3, No. 3, Sept. 1988, pp. 233–260.
- [14] Bueno-Orovio, A., Castro, C., Palacios, F., and Zuazua, E., "Continuous Adjoint Approach for the Spalart-Allmaras Model in Aerodynamic Optimization," *49th AIAA Aerospace Sciences Meeting and Exhibit*, No. AIAA-2011-1299, Orlando, Florida, Jan. 2011.

- [15] Nadarajah, S., Jameson, A., and Alonso, J. J., "An Adjoint Method for the Calculation of Remote Sensitivities in Supersonic Flow," *40th AIAA Aerospace Sciences Meeting and Exhibit*, No. AIAA-2002-0261, Reno, Nevada, Jan. 2002.
- [16] Economou, T. D., Palacios, F., and Alonso, J. J., "Unsteady Aerodynamic Design on Unstructured Meshes with Sliding Interfaces," *51st AIAA Aerospace Sciences Meeting including the New Horizons Forum and Aerospace Exposition*, AIAA Paper 2013-0632, Grapevine, Texas, January 2013.
- [17] Sederberg, T. W. and Parry, S. R., "Free-Form Deformation of Solid Geometric Models," *Proceedings of SIGGRAPH 89 (Computer Graphics)*, Vol. 20, No. 4, 1986, pp. 151–159.
- [18] Samareh, J. A., "Aerodynamic shape optimization based on Free-Form deformation," *AIAA Paper*, Vol. 2004-4630, 2004.
- [19] Yamazaki, W. and Mavriplis, D., "Derivative-Enhanced Variable Fidelity Surrogate Modeling for Aerodynamic Functions," *49th AIAA Aerospace Sciences Meeting including the New Horizons Forum and Aerospace Exposition*, AIAA Paper 2011-1172, Orlando, FL, Jan 2011.
- [20] Dwight, R. P. and Han, Z., "Efficient Uncertainty Quantification using Gradient Enhanced Kriging," *50th AIAA/ASME/ASCE/AHS/ASC Structures, Structural Dynamics, and Materials Conference*, AIAA Paper 2009-2276, Palm Springs, CA, May 2009.
- [21] Lukaczyk, T., Palacios, F., and Alonso, J. J., "Managing Gradient Inaccuracies while Enhancing Response Surface Models," *51st AIAA Aerospace Sciences Meeting and Exhibit*, AIAA Paper 2013-1042, Texas, January 2013.
- [22] Lambe, A. B. and Martins, J. R. R. A., "Extensions to the Design Structure Matrix for the Description of Multidisciplinary Design, Analysis, and Optimization Processes," *Structural and Multidisciplinary Optimization*, Vol. 46, 2012, pp. 273–284.
- [23] Jones, E., Oliphant, T., Peterson, P., et al., "SciPy: Open source scientific tools for Python," 2001–.
- [24] Kraft, D., "A software package for sequential quadratic programming," *Forschungsbericht- Deutsche Forschungs- und Versuchsanstalt fur Luft- und Raumfahrt*, 1988.
- [25] Lukaczyk, T., Palacios, F., and Alonso, J. J., "Response Surface Methodologies for Low-Boom Supersonic Aircraft Design using Equivalent Area Distributions," *12th AIAA Aviation Technology, Integration, and Operations (ATIO) Conference and 14th AIAA/ISSM Multidisciplinary Analysis and Optimization Conference*, AIAA Paper 2012-5705, Indianapolis, IN, September 2012.
- [26] Myers, R. H., Montgomery, D. C., and Anderson-Cook, C. M., *Response surface methodology: process and product optimization using designed experiments*, John Wiley & Sons, Hoboken, NJ, 2009.
- [27] Sacks, J., Welch, W., Mitchell, T., and Wynn, H., "Design and Analysis of Computer Experiments," *Statistical Science*, Vol. 4, The Institute of Mathematical Statistics, 1989, pp. 409–423.
- [28] Parzen, E., "A new approach to the synthesis of optimal smoothing and prediction systems," *Mathematical Optimization Techniques*, edited by R. Bellman, University of California Press, Berkley, CA, 1963, pp. 74–108.
- [29] Paciorek, C. and Schervish, M., "Nonstationary Covariance Functions for Gaussian Process Regression," *Advances in Neural Information Processing Systems 16*, edited by S. Thrun, L. K. Saul, and B. Schoelkopf, MIT Press, Cambridge, MA, 2004, pp. 273–280.
- [30] Jones, D., "A Taxonomy of Global Optimization Methods Based on Response Surfaces," *Journal of global optimization*, Vol. 21, No. 4, 2001, pp. 345–383.

- [31] Forrester, A. I. J. and Keaney, A. J., "Recent advances in surrogate-based optimization," *Progress in Aerospace Science*, Vol. 45, January 2009, pp. 50–79.
- [32] Han, Z.-H., Zimmerman, R., and Goertz, S., "A New Cokriging Method for Variable-Fidelity Surrogate Modeling of Aerodynamic Data," *48th AIAA Aerospace Sciences Meeting Including the New Horizons Forum and Aerospace Exposition*, AIAA Paper 2010-1225, Orlando, FL, Jan 2010.
- [33] Choi, S., Alonso, J. J., Kroo, I., and Wintzer, M., "Multifidelity Design Optimization of Low-Boom Supersonic Jets," *Journal of Aircraft*, Vol. 45, 2008, pp. 106–118.
- [34] Wintzer, M. and Sturdza, P., "Conceptual Design of Conventional and Oblique Wing Configurations for Small Supersonic Aircraft," *44th AIAA Aerospace Sciences Meeting and Exhibit*, AIAA Paper 2006-0930, Reno, NV, January 2006.
- [35] Ordaz, I. and Rallabhandi, S. K., "Boom Minimization Framework for Supersonic Aircraft Using CFD Analysis," *48th AIAA Aerospace Sciences Meeting Including the New Horizons Forum and Aerospace Exposition*, AIAA Paper 2010-1506, Orlando, FL, January 2010.
- [36] Rasmussen, C. and Williams, C., *Gaussian Processes for Machine Learning*, MIT Press, Cambridge, MA, 2006, pp. 13–30.
- [37] Chung, H., *Multidisciplinary Design Optimization of Supersonic Business Jets Using Approximation Model-Based Genetic Algorithms*, Ph.D. thesis, Stanford University, March 2004.
- [38] Papoulis, A., *Probability, Random Variables, and Stochastic Processes*, McGraw-Hill, New York, 1991, p. 310.
- [39] Solak, E., Murray-Smith, R., Leithead, W. E., Leith, D. J., and Rasmussen, C. E., "Derivative Observations in Gaussian Process Models of Dynamic Systems," *Advances in Neural Information Processing Systems 15*, edited by S. Becker, S. Thrun, and K. Obermayer, MIT Press, Cambridge, MA, 2003, pp. 1033–1040.
- [40] Jones, D. R., Schonlau, M., and Welch, W. J., "Efficient Global Optimization of Expensive Black-Box Functions," *Journal of Global Optimization*, Vol. 13, 1998, pp. 455–492.
- [41] Shimoyama, K., Sato, K., Jeong, S., and Obayashi, S., "Comparison of the Criteria for Updating Kriging Response Surface Models in Multi-Objective Optimization," *WCCI 2012 IEEE World Congress on Computational Intelligence*, Brisbane, Australia, Jun 2012.
- [42] Plotkin, K. and Maglieri, D., "Sonic Boom Research: History and Future," *33rd AIAA Fluid Dynamics Conference and Exhibit*, AIAA Paper 2003-3575, Orlando, FL, June 2003.
- [43] Plotkin, K. and Page, J., "Extrapolation of sonic boom signatures from CFD solution," *40th Aerospace Sciences Meeting and Exhibit*, AIAA Paper 2002-0922, Reno, NV, January 2002.
- [44] Salah El Din, I., Le Pape, M.-C., Minelli, A., Grenon, R., and Carrier, G., "Impact of multipole matching resolution on supersonic aircraft sonic boom assessment," *Eucass 2011 Conference*, St. Petersburg, July 2011.
- [45] Taylor, A., "The TRAPS sonic boom program," Technical memorandum erl-arl-87, NOAA, July 1980.
- [46] Hayes., W., Haefeli, R., and Kulsrud, H., "Sonic boom propagation in a stratified atmosphere, with computer program," Cr-1299, NASA, April 1969.
- [47] Shepherd, K. P. and Sullivan, B. M., "A Loudness Calculation Procedure Applied to Shaped Sonic Booms," Tp-3134, NASA, 1991.

References

1. Morgenstern, John; Buonanno, Michael; Chai, Sonny and Marconi, Frank; “Overview of Sonic Boom Reduction Efforts on the Lockheed Martin N+2 Supersonic Validations Program.” AIAA Summer Conference, AIAA-2014-2138.
2. Morgenstern, J; Norstrud, N.; Sokhey, J.; Martens, S. and Alonso, J.; “Advanced Concept Studies for Supersonic Commercial Transports Entering Service in the 2018 to 2020 Period” – Phase I Final Report. NASA/CR—2013-217820, PMF-01766, February 2013.
3. National Research Council; “U.S. Supersonic Commercial Aircraft: Assessing NASA’s High Speed Research Program.” National Academies Press, July 25, 1997; p. 94, section title: Aero/Propulsive/Servo/Elastic Phenomenon.
4. Silva et al., “The NASA High Speed ASE Project: Computational Analyses of a Low-Boom Supersonic Configuration,” AIAA SciTech Conference, Kissimmee, FL, January 5-9, 2014, AIAA-2015-0684.
5. Perry, B., Silva, W. A., Florance, J. R., Wieseman, C. D., Pototzky, A. S., Sanetrik, M. D., Scott, R. C., Keller, D. F., Cole, S. R., and Coulson, D. A., “Plans and Status of Wind-Tunnel Testing Employing an Aerovielastic Semispan Model,” 48th AIAA/ASME/ASCE/AHS/ASC Structures, Structural Dynamics, and Materials Conference, Honolulu, HI, April 23-26 2007, AIAA-2007-1770.
6. De La Garza, A.P., McCulley, C.M., Johnson, J.C., Hunten, K.A., Action, J.E., Skillen, M.D., and Zink, P.S., “Recent Advances in Rapid Airframe Modeling at Lockheed Martin Aeronautics Company,” NATO Research and Technology Agency, Presented at NATO RTO Meeting AVT-173 – Virtual Prototyping of Affordable Military Vehicles Using Advanced MDO, Sophia, Bulgaria, May 16-19, 2011.
7. QSST Report
8. Love, M., De La Garza, A., Charlton, E., Egle, D., “Computational Aeroelasticity in High Performance Aircraft Loads.” ICA481.1, ICAS 2000 Congress.
9. De La Garza, A., Skillen, M., Zink, P., Voorhees, S., Snyder, R., Reed, C., “High-Fidelity Flutter Analysis of a Re-Usable Launch Demonstrator with Wing-Tip Vertical Tails,” 51st AIAA/ASME/ASCE/AHS/ASC Structures, Structural Dynamics, and Materials Conference, Orlando, FL, April 12-15, 2010, AIAA-2010-2953.
10. Norstrud, Nicole; Buonanno, Michael; Morgenstern, John; Chai, Sunny; Langberg, Robert; et al.; “N+2 Supersonic Validations – Phase 1 Final Report.” 2011.
11. Hunton, Lynn W.; Hicks, Raymond M. and Mendoza, Joel P., “Some Effects of Wing Planform on Sonic Boom,” Moffett Field, CA, NASA TN D-7160, 1973.
12. Loubeau, Alexandra; “Sonic Boom Propagation and PL Calculation Check Results Comparison Memo.” June 3, 2013, pp 7.
13. Plotkin, K.J., “The effect of Turbulent Distortion on the Loudness of Sonic Booms,” NASA High-speed Research Sonic Boom Workshop, NASA CP3172, May 1992.
14. Norstrud, Nicole; Buonanno, Michael; Morgenstern, John; Chai, Sunny; Langberg, Robert; et al.; “N+2 Supersonic Validations – Phase 1 Final Report.” 2011.
15. Graham, David; Dahlin, John; Page, Juliet; Plotkin, Kenneth and Coen, Peter; “Wind Tunnel Validation of Shaped Sonic Boom Demonstration Aircraft Design.” AIAA Aerospace Sciences Meeting, January 2005, AIAA-2005-0007.

